

NUREG/CP-0097  
Vol. 2  
R1, R5, RF

Proceedings of the U.S. Nuclear Regulatory Commission

---

---

# Sixteenth Water Reactor Safety Information Meeting

## Volume 2

- Industry Safety Research
- Non-Destructive Evaluation
- Materials Engineering
  - Pressure Vessel Research
  - Radiation Effects
  - Degraded Piping

Held at  
National Institute of Standards and Technology  
Gaithersburg, Maryland  
October 24-27, 1988

---

---

Date Published: March 1989

Compiled by: Allen J. Weiss

**Office of Nuclear Regulatory Research  
U.S. Nuclear Regulatory Commission  
Washington, DC 20555**

Proceedings prepared by  
Brookhaven National Laboratory





## ABSTRACT

This five-volume report contains 141 papers out of the 175 that were presented at the Sixteenth Water Reactor Safety Information Meeting held at the National Institute of Standards and Technology, Gaithersburg, Maryland, during the week of October 24-27, 1988. The papers are printed in the order of their presentation in each session and describe progress and results of programs in nuclear safety research conducted in this country and abroad. Foreign participation in the meeting included twenty different papers presented by researchers from Germany, Italy, Japan, Sweden, Switzerland, Taiwan and the United Kingdom. The titles of the papers and the names of the authors have been updated and may differ from those that appeared in the final program of the meeting.



PROCEEDINGS OF THE  
16th WATER REACTOR SAFETY INFORMATION MEETING

October 24-27, 1988

Published in Five Volumes

**GENERAL INDEX**

VOLUME 1

- Plenary Session
- Decontamination and Decommissioning
- License Renewal
- Human Factors
- Generic Issues
- Risk Analysis/PRA Applications
- Innovative Concepts for Increased Safety of Advanced Power Reactors

VOLUME 2

- Industry Safety Research
- Non-Destructive Evaluation
- Materials Engineering
  - Pressure Vessel Research
  - Radiation Effects
  - Degraded Piping

VOLUME 3

- Nuclear Plant Aging
- Structural and Seismic Engineering
- Mechanical Research
- Environmental Effects in Primary Systems

VOLUME 4

- Code Uncertainty for ECCS Rule
- International Code Assessment Program
- Thermal Hydraulics
- 2D/3D Data Applications

VOLUME 5

- NUREG-1150
- Accident Management
- Recent Advances in Severe Accident Research
- TMI-2
- BWR Mark I Shell Failure



REGISTERED ATTENDEES (NON-NRC)  
16th WATER REACTOR SAFETY INFORMATION MEETING

J. A. ADAM  
STONE & WEBSTER  
245 SUMMER ST  
BOSTON MA 02107  
USA

S. L. ADDITON  
TENERA  
2011 EYE STREET N.W., SUITE 300  
WASHINGTON DC 20006  
USA

M. J. ADES  
SAVANNAH RIVER LABORATORY  
BLDG. 733-43A  
AIKEN SC 29808  
USA

D. W. AKERS  
EG&G IDAHO INC.  
P.O. BOX 1625  
IDAHO FALLS ID 83415  
USA

H. AKIMOTO  
JAPAN ATOMIC RESEARCH INST.  
TOKAI-MURA, NAKA-GUN  
IBARAKI-KEN 319-11  
JAPAN

N. S. AKSAN  
PAUL SCHERRER INSTITUTE  
WUERENLINGEN CH5303  
SWITZERLAND

R. P. ALLEN  
PACIFIC NORTHWEST LABORATORY  
P.O. BOX 999  
RICHLAND WA 99352  
USA

R. A. ALLEN  
SAVANNAH RIVER LABORATORY  
AIKEN SC 29808  
USA

K. ALMENAS  
UNIVERSITY OF MARYLAND  
COLLEGE PARK MD 20742  
USA

A. ALONSO  
MADRID POLYTECHNIC UNIVERSITY  
JOSE GUTIERREZ ABASCAL, 2  
MADRID 28006  
SPAIN

H. ALSMEYER  
KERNFORSCHUNGSZENTRUM, IRB/PRS  
POSTFACH 3640  
7500 KARLSRUHE 1  
FRG

J. G. ANDERSEN  
GENERAL ELECTRIC CO.  
175 CURTNER AVE  
SAN JOSE CA 95125  
USA

J. M. ANDERSON  
BECHTEL POWER CORP.  
15740 SHADY GROVE ROAD  
GAITHERSBURG MD 20874  
USA

K. B. ANDERSSON  
SWEDISH NUCLEAR POWER INSPECTORATE  
BOX 27016  
STOCKHOLM SW S-10252  
SWEDEN

C. E. APPERSON  
SAVANNAH RIVER LABORATORY  
1635 ALPINE DR.  
AIKEN SC 29801  
USA

K. J. ARAJ  
BDM  
7915 JONES BRIDGE DRIVE  
MCLEAN VA 22102  
USA

W. C. ARCIERI  
ENSA  
15825 SHADY GROVE ROAD  
ROCKVILLE MD 20850  
USA

W. W. ASCROFT-HUTTON  
HINI  
BAYNARDS HOUSE/WESTBOURNE GROVE  
LONDON ENGLAND W2 4TF  
UK

B. ATEFI  
SCIENCE APPLICATIONS INT'L CORP.  
1710 GOODRIDGE DR.  
MCLEAN VA 22102  
USA

N. I. AVDOSHKIN  
USSR EMBASSY  
1125 16TH ST NW  
WASHINGTON DC 20036

S. M. BAJOREK  
WESTINGHOUSE POWER SYSTEMS DIVISION  
P.O. BOX 355  
PITTSBURGH PA 15230-2728  
USA

K. K. BANDYOPADHYAY  
BROOKHAVEN NATIONAL LABORATORY  
BLDG 129  
UPTON NY 11973  
USA

R. A. BARI  
BROOKHAVEN NATIONAL LABORATORY  
BLDG. 197C  
UPTON NY 11973  
USA

G. P. BAROIS  
FRAMATOME  
TOUR FIAT - CEDEX 16  
PARIS LA DEFENSE FR 92084  
FRANCE

J. H. BARON  
MADRID POLYTECHNICAL UNIVERSITY  
JOSE GUTIERREZ ABASCAL, 2  
MADRID 28006  
SPAIN

B. R. BASS  
OAK RIDGE NATIONAL LABORATORY  
PO BOX 2003  
OAK RIDGE TN 37831  
USA

J. A. BAST  
GENERAL ELECTRIC CO.  
P.O. BOX 1072, BLDG. F3-8  
SCHENECTADY NY 12301  
USA

P. D. BAYLESS  
EG&G IDAHO INC.  
P.O. BOX 1625  
IDAHO FALLS ID 83415  
USA

P. BEDNARIK  
SCIENCE & TECHNOLOGY  
3900 LINNEAN AVE., NW  
WASHINGTON DC 20008  
CZECHOSLOVAKIA

K. D. BERGERON  
SANDIA NATIONAL LABS.  
P.O. BOX 5800  
ALBUQUERQUE NM 87185  
USA

R. F. BEYER  
WESTINGHOUSE  
206 NAVAJO RD.  
PITTSBURGH PA 15241  
USA

V. M. BHARGAVA  
VIRGINIA POWER  
5000 DOMINION BLVD.  
GLEN ALLEN VA 23060  
USA

W. BINNER  
AUSTRIAN RESEARCH CENTER  
SEIBERSDORF A-2444  
AUSTRIA

D. P. BIRMINGHAM  
BABCOCK & WILCOX CO.  
1562 BEESON STREET  
ALLIANCE OH 44601  
USA

D. BIZZAK  
CARNEGIE-MELLON UNIVERSITY  
386 HUNTINGDON AVENUE  
N. HUNTINGDON PA 15642  
USA

R. J. BOHL  
LOS ALAMOS NATIONAL LABORATORY  
P.O. BOX 1663, MS K560  
LOS ALAMOS NM 87545  
USA

T. C. BORDINE  
CONSUMERS POWER COMPANY  
1945 WEST PARNALL RD.  
JACKSON MI 49201  
USA

R. B. BORSUM  
BABCOCK & WILCOX CO.  
1700 ROCKVILLE PIKE, #525  
ROCKVILLE MD 20852  
USA

B. E. BOYACK  
LOS ALAMOS NATIONAL LAB  
PO BOX 1663  
LOS ALAMOS NM 87545  
USA

D. R. BRADLEY  
SANDIA NATIONAL LABS.  
P.O. BOX 5800  
ALBUQUERQUE NM 87185  
USA

R. J. BRANDON  
GE NUCLEAR CORP  
6728 LOOKOUT BEND  
SAN JOSE CA 95120  
USA

P. A. BRATBY  
NATIONAL NUCLEAR CORP.  
BOOTH'S HALL, CHELFORD ROAD  
KNUTSFORD  
UK

R. J. BREEDING  
SANDIA NATIONAL LABS., DIV. 6410  
P.O. BOX 5800  
ALBUQUERQUE NM 87185  
USA

S. J. BRETT  
CEGB, GENERATION DEV. & CONSTRUCTION  
GEN. DEV. & CONST. DIV., BARNWOOD  
GLOUCESTER GL47RS  
UK

I. BRITTAIN  
UKAEA/AEE WINFRITH  
DOERCHESTER  
DORSET DT28DH  
UK

J. M. BROUGHTON  
EG&G IDAHO INC.  
P.O. BOX 1625  
IDAHO FALLS ID 83415  
USA

S. BRYANT  
CENTRAL ELECTRICITY GENERATING BD.  
BOOTH'S HALL, CHELFORD RD  
KNUTSFORD, CHESHIRE WA1680Q  
UK

C. E. BUCHHOLZ  
GENERAL ELECTRIC CO.  
175 CURTNER AVE  
SAN JOSE CA 95125  
USA

B. BUESCHER  
EG&G IDAHO INC.  
P.O. BOX 1625  
IDAHO FALLS ID 83415  
USA

L. C. BUFFARDI  
GEORGE MASON UNIVERSITY  
4400 UNIVERSITY DRIVE  
FAIRFAX VA 22030  
USA

J. D. BYRON  
ELECTRIC POWER RESEARCH INSTITUTE  
3412 HILVIEW AVE.  
PALO ALTO CA 94303  
USA

J. I. CALVO  
CONSEJO SEGURIDAD NUCLEAR  
SOR ANGELA DE LA CRUZ 3  
MADRID 28020  
SPAIN

A. L. CAMP  
SANDIA NATIONAL LABS. DIV. 6412  
P.O. BOX 5800  
ALBUQUERQUE NM 87185  
USA

D. D. CARLSON  
SANDIA NATIONAL LABS., DIV. 6513  
P.O. BOX 5800  
ALBUQUERQUE NM 87185  
USA

R. CARO  
CONSEJO DE SEGURIDAD NUCLEAR  
C/SOR ANGELA DE LA CRUZ, 3  
MADRID 28020  
SPAIN

D. E. CARROLL  
SANDIA NATIONAL LABS.  
P.O. BOX 5800  
ALBUQUERQUE NM 87185  
USA

R. CARUSO  
NUCLEAR ENERGY AGENCY  
38 BLYD. SUCHET  
PARIS 75016  
FRANCE

D. A. CASADA  
OAK RIDGE NATIONAL LABORATORY  
PO BOX 2009, BLDG. 9104-1  
OAK RIDGE TN 37831  
USA

J. H. CHA  
KOREA ADVANCED ENERGY RESEARCH INST.  
PO BOX 7, DAEDUK-DANJI  
TAEJON CHUNG-NAM  
KOREA

S. CHAKRABORTY  
PAUL SCHERRER INSTITUTE  
WUERENLINGEN CH5303  
SWITZERLAND

R. CHAMBERS EG&G IDAHO INC. P.O. BOX 1625 IDAHO FALLS ID 83415 USA	D. CROUCH BROOKHAVEN NATIONAL LABORATORY BLDG. 130 UPTON NY 11973 USA	M. DIMARZO UNIVERSITY OF MARYLAND MECHANICAL ENGINEERING DEPT. COLLEGE PARK MD 20016 USA	F. A. ELIA STONE AND WEBSTER PO BOX 2325 BOSTON MA 02014 USA
Y. I. CHANG ARGONNE NATIONAL LABORATORY 9700 S. CASS AVE. ARGONNE IL 60439 USA	W. H. CULLEN MATERIALS ENGINEERING ASSOCIATES 9700-B M. L. KING HIGHWAY LANHAM MD 20706 USA	M. R. DINSEL BECHTEL POWER CORP. 15740 SHADY GROVE ROAD GAITHERSBURG MD 20874 USA	G. T. EMBLEY GENERAL ELECTRIC BOX 1092 SCHENECTADY NY 12301 USA
D. CHAPIN MPR ASSOCIATES, INC. 1050 CONNECTICUT AVENUE, N.W. WASHINGTON DC 20036 USA	G. E. CUMMINGS LAWRENCE LIVERMORE NATIONAL LAB P.O. BOX 808, L-198 LIVERMORE CA 94526 USA	S. R. DOCTOR PACIFIC NORTHWEST LABORATORY P.O. BOX 999 RICHLAND WA 99352 USA	T. C. ENG DEPARTMENT OF ENERGY EH-35, MAIL STOP F-137 WASHINGTON DC 20545 USA
S. C. CHENG TAIWAN POWER COMPANY TAIPEI  ROC	H. D. CURET ADVANCED NUCLEAR FUELS 2101 HORN ROAD RICHLAND WA 99352 USA	C. V. DODD OAK RIDGE NATIONAL LABORATORY PO BOX 2008 OAK RIDGE TN 37831 USA	R. G. ESPEFALT SWEDISH STATE POWER BD. VATTENFALL VALLINGBY S-16287 SWEDEN
L. Y. CHENG BROOKHAVEN NATIONAL LABORATORY BLDG 703 UPTON NY 11973 USA	B. D. CURRY PHILADELPHIA ELECTRIC CO. PO BOX A SARATOGA BR. POTTSTOWN PA 19464 USA	T. F. DORIAN DOUB, MUNTZING & GLASGOW, CHARTERED 808 17TH STREET, N. W., SUITE 400 WASHINGTON DC 20006 USA	C. R. FARRAR LOS ALAMOS NATIONAL LAB. MS J576 LOS ALAMOS NM 87545 USA
R. D. CHEVERTON OAK RIDGE NATIONAL LABORATORY PO BOX 2009 OAK RIDGE TN 37831 USA	R. A. CUSHMAN NIAGRA MOHAWK POWER CORP. 301 PLAINHELD ROAD SYRACUSE NY 13212 USA	J. DRCEC NPP KRSKO PO VRBINA 12 KRSKO 68270 YUGOSLAVIA	H. E. FILACCHIONE SCIENTECH 11821 PARKLAWN DR. ROCKVILLE MD 20878 USA
W. G. CHOE TU ELECTRIC 400 N. OLIVE STREET DALLAS TX 75201 USA	D. A. DAHLGREN SANDIA NATIONAL LABS., ORG. 6442 P.O. BOX 5800 ALBUQUERQUE NM 87123 USA	S. S. DUA GENERAL ELECTRIC M/C 769, 175 CURTNER AVE. SAN JOSE CA 95125 USA	S. R. FISCHER MIDDLE SOUTH UTILITIES 188 E. CAPITOL STREET, SUITE 600 JACKSON MS 39201 USA
O. K. CHOPRA ARGONNE NATIONAL LABORATORY 9700 S. CASS AVE., BLDG 335 ARGONNE IL 60439 USA	J. DALLMAN EG&G IDAHO INC. P.O. BOX 1625 IDAHO FALLS ID 83415 USA	S. W. DUCE EG&G IDAHO INC P.O. BOX 1625 IDAHO FALLS ID 83415 USA	R. G. FITZPATRICK BROOKHAVEN NATIONAL LABORATORY BLDG 130 UPTON NY 11973 USA
B. CHUNG KOREA ADVANCED ENERGY RESEARCH INST. NSC, DAE DUK DAN-JI, BOX 7 CHOONG-NAM KOREA	R. DAMERON ANATECH 10975 TORREYANA RD., SUITE 301 SAN DIEGO CA 92121 USA	J. J. DUCO CEA FRENCH ATOMIC ENERGY COMMISSION DAS/SASC, GEN/FAR, BP NO. 6 FONTENAY-AUX-ROSES 92265 FRANCE	C. W. FORSBERG OAK RIDGE NATIONAL LABORATORY P.O. BOX 2008, BLDG 4500N OAK RIDGE TN 37831 USA
D. T. CHUNG SCIENTECH 11821 PARKLAWN DR. ROCKVILLE MD 20878 USA	J. DARLSTON CENTRAL ELECTRICITY GENERATING BD. BERKLEY NUCLEAR LABS GLOUCESTER GL139PB UK	R. B. DUFFEY EG&G IDAHO INC. P.O. BOX 1625 IDAHO FALLS ID 83415 USA	E. FOX OAK RIDGE NATIONAL LABORATORY P.O. BOX 2009 OAK RIDGE TN 37831-8063 USA
H. CHUNG ARGONNE NATIONAL LABORATORY 9700 S. CASS AVE. ARGONNE IL 60439 USA	W. L. DAUGHERTY SAVANNAH RIVER LABORATORY PO BOX A AIKEN SC 29808 USA	K. K. DWIVEDI VIRGINIA POWER 5000 DOMINION BLVD. GLEN ALLEN VA 23060 USA	G. FREI SIEMENS HAMMERBACHERSTR. 12 ERLANGEN 852 FRG
J. P. CHURCH SAVANNAH RIVER LABORATORY BLDG. 773-41A AIKEN SC 29808 USA	N. W. DAVIES UKAEA, RISLEY LABORATORY WARRINGTON CHESHIRE WA3 6AT. UK	J. L. EDSON EG&G IDAHO INC. P.O. BOX 1625 IDAHO FALLS ID 83415 USA	B. C. FRYER ADVANCED NUCLEAR FUELS 1930 CYPRESS RICHLAND WA 99352 USA
D. B. CLAUSS SANDIA NATIONAL LABS. DIV. 6442 P.O. BOX 5800 ALBUQUERQUE NM 87122 USA	M. A. DAYE BECHTEL POWER CORP. 15740 SHADY GROVE RD. GAITHERSBURG MD 20877 USA	G. R. EIDAM BECHTEL/SPUN P.O. BOX 72 MIDDLETOWN PA 17057 USA	H. FUJIMOTO COMPUTER SOFTWARE DEVELOPMENT CO. 4-1, SHIBAKOJEN 2-CHOME, MINATO-KU TOKYO 105 JAPAN
M. COLAGROSSI ENEA/DISP VIA VITALIANO BRANCATI, 48 ROME 00144 ITALY	J. A. DE MASTRY FLORIDA POWER AND LIGHT CO. BOX 14000 JUNO BEACH FL 33408 USA	D. M. EISSENBERG OAK RIDGE NATIONAL LABORATORY PO BOX 2009, BLDG. 9104-1 OAK RIDGE TN 37831 USA	P. J. FULFORD NUS CORPORATION 910 CLOPPER ROAD GAITHERSBURG MD 20878 USA
M. W. CONEY CENTRAL ELECTRICITY GENERATING BD. C.E.R.L., KELVIN AVENUE LEATHERHEAD SURREY KT227SE UK	L. O. DeIGEORGE COMMONWEALTH EDISON P.O. BOX 767 CHICAGO IL 60690 USA	Z. J. ELAWAR ARIZONA NUCLEAR POWER PROJECT, 7202 P.O. BOX 52034 PHOENIX AZ 85072 USA	R. R. FULLWOOD BROOKHAVEN NATIONAL LABORATORY BLDG 130 UPTON NY 11973 USA
W. R. CORWIN OAK RIDGE NATIONAL LABORATORY PO BOX 2009 OAK RIDGE TN 37831 USA	L. V. DeWITT SAVANNAH RIVER LABORATORY 1313 WILLIAMS DR. AIKEN SC 29801 USA	G. ELETTI ENEA/DISP VIA VITALIANO BRANCATI, 48 ROME 00144 ITALY	F. M. GANTENBEIN CEA FRENCH ATOMIC ENERGY COMMISSION GEN-SACLAY DEMT/SMIS/EMSI GIF-SUR-YVETTE 91191 FRANCE

F. GELBARD  
SANDIA NATIONAL LABS.  
P.O. BOX 5800  
ALBUQUERQUE NM 87185  
USA

D. I. GERTMAN  
EG&G IDAHO INC.  
P.O. BOX 1625  
IDAHO FALLS ID 83415  
USA

T. GINSBERG  
BROOKHAVEN NATIONAL LABORATORY  
BLDG 820  
UPTON NY 11973  
USA

T. GINZBURG  
APPLIED BIOMATHEMATICS INC.  
100 NORTH COUNTRY ROAD  
SETAUKET NY 11733  
USA

B. GITNICK  
ENSA, INC.  
15825 SHADY GROVE RD., STE. 120  
ROCKVILLE MD 20850  
USA

H. G. GLAESER  
GESELLSCHAFT FUR REAKTORSICHERHEIT  
FORSCHUNGSGELANDE  
D-8046 GARCHING  
FRG

J. GLEASON  
WYLE LABORATORY  
7800 GOVERNORS DRIVE WEST  
HUNTSVILLE AL 35807  
USA

D. W. GOLDEN  
EG&G IDAHO INC.  
P.O. BOX 1625  
IDAHO FALLS ID 83415  
USA

M. GOMOLINSKI  
CEA FRENCH ATOMIC ENERGY COMMISSION  
CEN/FAR, BP NO 6  
FONTENAT-AUX-ROSES 92265  
FRANCE

C. GONZALEZ  
MADRID POLYTECHNICAL UNIVERSITY  
JOSE GUTIERREZ ABASCAL, 2  
MADRID 28006  
SPAIN

E. D. GORHAM-BERGERON  
SANDIA NATIONAL LABS.  
P.O. BOX 5800  
ALBUQUERQUE NM 87185  
USA

T. C. GORRELL  
SAVANNAH RIVER LABORATORY  
RX TECH, DU PONT (SRP)  
AIKEN SC 29808  
USA

G. A. GREENE  
BROOKHAVEN NATIONAL LABORATORY  
BLDG. 820M  
UPTON, NY 11973  
USA

P. GRIFFITH  
MIT  
ROOM 7-044  
CAMBRIDGE MA 02139  
USA

F. GRIMM  
SIEMENS  
HAMMERBACHERSTR. 12  
ERLANGEN 852  
FRG

C. GRIMSHAW  
BROOKHAVEN NATIONAL LABORATORY  
BLDG. 130  
UPTON NY 11973  
USA

W. W. GUNTHER  
BROOKHAVEN NATIONAL LABORATORY  
BLDG 130  
UPTON NY 11973  
USA

S. HABER  
BROOKHAVEN NATIONAL LABORATORY  
BLDG. 130  
UPTON NY 11973  
USA

D. R. HAFFNER  
WESTINGHOUSE HANFORD CO.  
P.O. BOX 1970 A3-30  
RICHLAND WA 99352  
USA

F. M. HAGGAG  
OAK RIDGE NATIONAL LABORATORY  
P.O. BOX 2008, BLDG 4500-5  
OAK RIDGE TN 37831-6151  
USA

A. N. HALL  
HM NUCLEAR INSTALLATIONS INSPECTORATE  
ST PETER'S HOUSE, BALLIOL RD  
BOOTLE, MERSEYSIDED L203LZ  
UK

R. J. HAMMERSLEY  
FAUSKE & ASSOCIATES  
16W070 WEST 83RD STREET  
BURR RIDGE IL 60521  
USA

A. M. HASHIMOTO  
JAPAN INST. OF NUCLEAR SAFETY  
3-17-1 TOYANOMON  
MINATOKU, TOKYO 105  
JAPAN

Y. A. HASSAN  
DEPT OF NUCL ENERGY, TEXAS A & M  
COLLEGE STATION TX 77843  
USA

J. R. HAWTHORNE  
MATERIALS ENGINEERING ASSOCIATES  
9700-B M. L. KING HIGHWAY  
LANHAM MD 20706  
USA

H. D. HAYNES  
OAK RIDGE NATIONAL LABORATORY  
PO BOX 2009, BLDG. 9201-3  
OAK RIDGE TN 37831  
USA

J. HAZELTINE  
WYLE LABORATORY  
7800 GOVERNORS DRIVE WEST  
HUNTSVILLE AL 35807  
USA

R. E. HENRY  
FAI  
16W070 WEST 83RD STREET  
BURR RIDGE IL 60521  
USA

G. F. HEWITT  
UKAEA/HARWELL LABORATORY  
THERMAL HYDRAULICS DIV., BLDG 392  
OXON OX11 0RA  
UK

J. HIBBARD  
MPR ASSOCIATES, INC.  
1050 CONNECTICUT AVENUE, N.W.  
WASHINGTON DC 20036  
USA

D. E. HIDINGER  
GENERAL ELECTRIC  
14 CORONET CT.  
SCHENECTADY NY 12309  
USA

J. C. HIGGINS  
BROOKHAVEN NATIONAL LABORATORY  
BLDG 130  
UPTON NY 11973  
USA

C. J. HIGGINS  
APPLIED RESEARCH ASSOCIATES, INC.  
4300 SAN MATEO NE, STE B 380  
ALBUQUERQUE NM 87111  
USA

P. R. HILL  
PENNSYLVANIA POWER & LIGHT CO.  
2 N. NINTH STREET  
ALLEN TOWN PA 18101  
USA

J. E. HINTON  
DU PONT DE NEMOURS  
SRP 707-C, RM. 329  
AIKEN SC 29808  
USA

T. J. HIRONS  
LOS ALAMOS NATIONAL LABORATORY  
P.O. BOX 1663, MS E561  
LOS ALAMOS NM 87545  
USA

M. HIROSE  
NUCLEAR POWER ENG'G TEST CTR  
FUJITA KM'KO BLDG., TORANOMON, MINATO-  
TOKYO 105  
JAPAN

S. A. HODGE  
OAK RIDGE NATIONAL LABORATORY  
PO BOX 2009, BLDG. 9104-1  
OAK RIDGE TN 37831  
USA

P. G. HOFMANN  
KERNFORSCHUNGSZENTRUM, IMF  
POSTFACH 3640  
7500 KARLSRUHE  
FRG

C. H. HOFMAYER  
BROOKHAVEN NATIONAL LABORATORY  
BLDG 129  
UPTON NY 11973  
USA

G. S. HOLMAN  
LAWRENCE LIVERMORE NATIONAL LAB  
P.O. BOX 808, L-197  
LIVERMORE CA 94550  
USA

K. R. HOOPINGARNER  
PACIFIC NORTHWEST LABORATORY  
P.O. BOX 999  
RICHLAND WA 99352  
USA

R. G. HOPPE  
WESTINGHOUSE ELECTRIC CORP.  
P.O. BOX 79  
W HIFFLIN PA 15122  
USA

K. G. HORNBERGER  
OAK RIDGE NATIONAL LABORATORY  
P.O. BOX 2009  
OAK RIDGE TN 37831-8056  
USA

P. J. HOSEMANN  
PAUL SCHERRER INSTITUTE  
WUERENLINGEN CHS303  
SWITZERLAND

B. J. HSEIH  
ARGONNE NATIONAL LABORATORY  
9700 SO CASS AVE.  
ARGONNE IL 60439  
USA

A. H. HSIA  
USA  
240 MONROE STREET  
ROCKVILLE MD 20854  
USA

H-N HSIAU  
TAIWAN POWER COMPANY  
TAIPEI TAIWAN  
ROC

K. HU  
BROOKHAVEN NATIONAL LABORATORY  
BLDG. 475B  
UPTON NY 11973  
USA

D. S. HUMPHRIES  
SCIENTECH  
11821 PARKLAWN DR.  
ROCKVILLE MD 20852  
USA

M. L. HYDER  
SAVANNAH RIVER LABORATORY  
AIKEN SC 29808  
USA

C. R. HYMAN  
OAK RIDGE NATIONAL LABORATORY  
PO BOX 2009, BLDG. 9104-1  
OAK RIDGE TN 37831  
USA

T. IGUCHI  
JAPAN ATOMIC RESEARCH INST.  
TOKAI-MURA, NAKA-GUN  
IBARAKI-KEN 319-11  
JAPAN

R. L. IMAN  
SANDIA NATIONAL LABS. DIV 6415  
P.O. BOX 5800  
ALBUQUERQUE NM 87185  
USA

J. R. IRELAND  
LOS ALAMOS NATIONAL LAB  
PO BOX 1663, MSK 551  
LOS ALAMOS NM 87544  
USA

M. ISHII  
PURDUE UNIVERSITY  
WEST LAFAYETTE ID  
USA

S. K. ISKANDER  
OAK RIDGE NATIONAL LABORATORY  
P.O. BOX 2008  
OAK RIDGE TN 37831-6151  
USA

R. IVANY  
COMBUSTION ENGINEERING, INC.  
1000 PROSPECT HILL RD.  
WINDSOR CT 06095  
USA

J. M. IZQUIERDO  
CONSEJO SEGURIDAD NUCLEAR  
SOR ANGELA DE LA CRUZ 3  
MADRID 28020  
SPAIN

M. J. JACOBUS  
SANDIA NATIONAL LABS., DIV. 6447  
P.O. BOX 5800  
ALBUQUERQUE NM 87185  
USA

J. F. JANSKY  
B7B-LEONBERG  
RIKKESTRASSE 5  
LEONBERG D-7250  
FRG

D. B. JARRELL  
PACIFIC NORTHWEST LABORATORY  
P.O. BOX 999  
RICHLAND WA 99352  
USA

G. W. JOHNSEN  
EG&G IDAHO INC.  
P.O. BOX 1625  
IDAHO FALLS ID 83415  
USA

A. B. JOHNSON  
PACIFIC NORTHWEST LABORATORY  
P.O. BOX 999  
RICHLAND WA 99352  
USA

E. R. JOHNSON  
WESTINGHOUSE ELECTRIC CORP  
P.O. BOX 2728  
PITTSBURGH PA 15230-2728  
USA

H. V. JULIAN  
VOLIAN ENTERPRISES, INC.  
PO BOX 410  
MURRYSVILLE PA 15668  
USA

J. E. KALINOWSKI  
SAVANNAH RIVER LABORATORY  
AIKEN SC 29808  
USA

P. S. KALRA  
ELECTRIC POWER RESEARCH INSTITUTE  
3412 HILLVIEW AVE.  
PALO ALTO CA 94303  
USA

F. B. KAM  
OAK RIDGE NATIONAL LABORATORY  
PO BOX 2008  
OAK RIDGE TN 37831  
USA

H. KAMATA  
JAPAN ATOMIC RESEARCH INST.  
TOKAI-MURA, NAKA-GUN  
IBARAKI-KEN 319-11  
JAPAN

D. D. KANA  
SOUTHWEST RESEARCH INSTITUTE  
6220 CULEBRA ROAD  
SAN ANTONIO TX 78284  
USA

L. D. KANNBERG  
PACIFIC NORTHWEST LABORATORY  
P.O. BOX 999  
RICHLAND WA 99352  
USA

S. KARIMIAN  
BROOKHAVEN NATIONAL LABORATORY  
BLDG. 130  
UPTON NY 11973  
USA

W. Y. KATO  
BROOKHAVEN NATIONAL LABORATORY  
BLDG 197C  
UPTON NY 11973  
USA

K. R. KATMA  
EG&G IDAHO INC.  
P.O. BOX 1625  
IDAHO FALLS ID 83415  
USA

G. KATZENMEIER  
KERNFORSCHUNGSZENTRUM, PHDR  
POSTFACH 3640  
7500 KARLSRUHE 1  
FRG

W. R. KEANEY  
GENERAL ASSOCIATES CORP.  
1314 OAKVIEW DR.  
WORTHINGTON OH 43085  
USA

J. E. KELLY  
SANDIA NATIONAL LABS. DIV. 6418  
P.O. BOX 5800  
ALBUQUERQUE NM 87185  
USA

C. R. KEMPF  
BROOKHAVEN NATIONAL LABORATORY  
BLDG. 197-C  
UPTON NY 11973  
USA

W. L. KIRK  
LOS ALAMOS NATIONAL LABORATORY  
P.O. BOX 1663, H-DO, MS E561  
LOS ALAMOS NM 87545  
USA

E. KNOGLINGER  
PAUL SCHERRER INSTITUTE  
WUERENLINGEN CH5303  
SWITZERLAND

A. KOHSAKA  
JAPAN ATOMIC RESEARCH INST.  
TOKAI-MURA, NAKA-GUN  
IBARAKI-KEN 319-11  
JAPAN

M. J. KOMSI  
IMATRAN VOIMA OY  
P.O. BOX 112  
VANTAA 01601  
FINLAND

C. A. KOT  
ARGONNE NATIONAL LABORATORY  
9700 S. CASS AVE., BLDG 335  
ARGONNE IL 60439  
USA

G. S. KRAMER  
BATTELLE COLUMBUS  
505 KING AVE.  
COLUMBUS OH 43201  
USA

T. S. KRESS  
OAK RIDGE NATIONAL LABORATORY  
P.O. BOX 2009  
OAK RIDGE TN 37831-8063  
USA

C. A. KROPP  
ENEA/DISP  
VIA ANGUILLARESE K 1+300  
ROME 00060  
ITALY

G. A. KRUEGER  
PHILADELPHIA ELECTRIC  
2301 MARKET ST., N2-1  
PHILADELPHIA PA 19101  
USA

R. C. KRYTER  
OAK RIDGE NATIONAL LABORATORY  
P.O. BOX 2008  
OAK RIDGE TN 37831-6010  
USA

R. KUBOTA  
HITACHI  
SAIWAICHO 3-1-1  
IBARAKI-KEN 317  
JAPAN

C. A. KUKIELKA  
PENNSYLVANIA POWER & LIGHT CO.  
2 N. NINTH STREET  
ALLENTOWN PA 18101  
USA

D. S. KUPPERMAN  
ARGONNE NATIONAL LABORATORY  
9700 S. CASS AVE.  
ARGONNE IL 60439  
USA

K. F. KUSSMAUL  
UNIVERSITY OF STUTTGART  
PFAFFENWALDRING 32  
STUTTGART 80 7000  
FRG

P. S. LACY  
URA  
51 MONROE STREET  
ROCKVILLE MD 20854  
USA

T. K. LARSON  
EG&G IDAHO INC.  
P.O. BOX 1625  
IDAHO FALLS ID 83415  
USA

D. LEAVER  
TANERA  
1340 SARATOGA-SUNNYSIDE ROAD, SUITE 2  
SAN JOSE CA 95129  
USA

R. E. LECKENBY  
UKAEA, RISLEY LABORATORY  
WARRINGTON  
CHESHIRE WA36AT  
UK

M. LEE  
BROOKHAVEN NATIONAL LABORATORY  
BLDG. 130  
UPTON NY 11973  
USA

N. E. LEE  
COMBUSTION ENGINEERING  
1000 PROSPECT HILL RD  
WINDSOR CT 06095  
USA

J. R. LEHNER  
BROOKHAVEN NATIONAL LABORATORY  
BLDG. 130  
UPTON NY 11973  
USA

K. M. LEIGH  
UKAEA/SRD  
WIGSHAW LANE, CULCHETH  
WARRINGTON WA34NE  
UK

S. J. LEVINSON  
BABCOCK & WILCOX CO.  
3315 OLD FOREST RD  
LYNCHBURG VA 24506  
USA

P. M. LEWIS  
PACIFIC NORTHWEST LABORATORY  
P.O. BOX 999  
RICHLAND WA 99352  
USA

K. LIESCH  
GESELLSCHAFT FUR REAKTORSICHERHEIT  
FORSCHUNGSGELANDE  
D-8046 GARCHING  
FRG

J. N. LILLINGTON  
UKAEA/AEE WINFRITH  
DOERCHESTER  
DORSET DT28DH  
UK

C. L. LIN  
ELECTRIC POWER RESEARCH INSTITUTE  
3412 HILLVIEW AVE.  
PALO ALTO CA 94303  
USA

L. LINDSTROM  
SWEDISH NUCLEAR POWER INSPECTORATE  
BOX 27016  
STOCKHOLM SW S-10252  
SWEDEN

Y. Y. LIU  
ARGONNE NATIONAL LABORATORY  
9700 S. CASS AVE.  
ARGONNE IL 60439  
USA

R. LOFARO  
BROOKHAVEN NATIONAL LABORATORY  
BLDG 130  
UPTON NY 11973  
USA

J. P. LONGWORTH  
CENTRAL ELECTRICITY GENERATING BD.  
COURTNEY HSE., WARWICK LA  
LONDON  
UK

F. J. LOSS  
MATERIALS ENGINEERING ASSOCIATES  
9700-B, M. L. KING HIGHWAY  
LANHAM MD 20706  
USA

A. L. LOWE, JR.  
BABCOCK & WILCOX CO.  
PO BOX 10935  
LYNCHBURG VA 24506  
USA

T. S. LUBNOW  
MPR ASSOCIATES  
1050 CONNECTICUT AVE., NW  
WASHINGTON DC 20036  
USA

W. J. LUCKAS, JR.  
BROOKHAVEN NATIONAL LABORATORY  
BLDG. 130  
UPTON NY 11973  
USA

H. L. MAGLEBY  
EG&G IDAHO INC.  
P.O. BOX 1625  
IDAHO FALLS ID 83415  
USA

A. P. MALINAUSKAS  
OAK RIDGE NATIONAL LABORATORY  
P.O. BOX 2008  
OAK RIDGE TN 37831-6135  
USA

R. M. MANDL  
SIEMENS  
HAMMERBACHERSTR. 12  
ERLANGEN 852  
FRG

C. F. MARKUS  
WESTINGHOUSE ELECTRIC CORP.  
P.O. BOX 79  
W. MIFFLIN PA 15122-0079  
USA

C. W. MARSCHALL  
BATTELLE COLUMBUS  
505 KING AVE.  
COLUMBUS OH 43201  
USA

P. MARSILI  
ENEA/DISP  
VIA VITALIANO BRANCATI, 48  
ROME 00144  
ITALY

B. MAVKO  
J. STEFAN INSTITUTE  
JAMOVA 39  
LJUBLJANA 61000  
YUGOSLAVIA

D. E. MCCABE  
MATERIALS ENGINEERING ASSOCIATES  
9700-B, M. L. KING HIGHWAY  
LANHAM MD 20706  
USA

L. D. McCANN  
WESTINGHOUSE ELECTRIC CORP.  
P.O. BOX 79  
W. MIFFLIN PA 15122-0079  
USA

R. K. McCARDELL  
EG&G IDAHO INC.  
P.O. BOX 1625  
IDAHO FALLS ID 83415  
USA

D. J. McCLOSKEY  
SANDIA NATIONAL LABS.  
P.O. BOX 5800  
ALBUQUERQUE NM 87122  
USA

K. P. McKAY  
WESTINGHOUSE ELECTRIC CORP.  
P.O. BOX 79  
W. MIFFLIN PA 15122  
USA

N. R.H. McMillan  
UKAEA/SRD  
WIGSHAW LANE, CULCHETH  
WARRINGTON WA34NE  
UK

C. MEDICH  
SIET  
VIA NINO BIXIO 27  
PIACENZA ITALY 29100  
ITALY

H. B. MEIERAN H B MEIERAN ASSOCIATES 458 SOUTH DALLAS AVENUE PITTSBURGH PA 15208 USA	S. A. NAFF SIEMENS AG-UB.KWU.UBS POSTFACH 3220 ERLANGEN 8520 FRG	C. F. OBENCHAIN EG&G IDAHO INC. P.O. BOX 1625 IDAHO FALLS ID 83415 USA	M. Z. PODOWSKI RENSELEAR POLYTECHNIC INSTITUTE TROY NY 12180-3590 USA
M. MERILO ELECTRIC POWER RESEARCH INSTITUTE 3412 HILLVIEW AVE. PALO ALTO CA 94303 USA	C. NAKAMURA JAPAN ATOMIC RESEARCH INST. TOKAI-MURA, NAKA-GUN IBARAKI-KEN 319-11 JAPAN	T. OHNO NUCLEAR POWER ENG'G TEST CTR BLDG. 4-3-13, TORANOMON, MINATO-KU TOKYO 105 JAPAN	A. Y. PORRACCHIA CEA FRENCH ATOMIC ENERGY COMMISSION CEN CADARACHE-DERS/SEMAR BP NO. 1 SAINT PAUL LEZ DURANCE 13108 FRANCE
J. G. MERKLE OAK RIDGE NATIONAL LABORATORY P.O. BOX 2009 OAK RIDGE TN 37831-8049 USA	R. K. NANSTAD OAK RIDGE NATIONAL LABORATORY PO BOX 2008, MS 6151 OAK RIDGE TN 37831 USA	M. OHUCHI JAPAN SYSTEMS CORP. NOMURA BLDG., 4-8 YOMIBANCHO, CHIYODA- TOKYO 102 JAPAN	D. A. POWERS SANDIA NATIONAL LABS. P.O. BOX 5800 ALBUQUERQUE NM 87185 USA
J. F. MEYER SCIENITECH 11821 PARKLAWN DRIVE ROCKVILLE MD 20852 USA	A. NATLIZIO ATOMIC ENERGY OF CANADA SHERIDAN PARK RSCH. COMM. MISSISSAUGA ONTARIO L5K1B2 CANADA	T. OKUBO JAPAN ATOMIC RESEARCH INST. TOKAI-MURA, NAKA-GUN IBARAKI-KEN 319-11 JAPAN	N. PRASAD WESTINGHOUSE POWER SYSTEMS DIVISION P.O. BOX 2728 PITTSBURGH PA 15230-2728 USA
A. MEYER-HEINE CEA FRENCH ATOMIC ENERGY COMMISSION CEN CADARACHE-DERS/SEMAR BP NO. 1 SAINT PAUL LEZ DURANCE 13108 FRANCE	D. J. NAUS OAK RIDGE NATIONAL LABORATORY P.O. BOX 2009, BLDG 9204-1 OAK RIDGE TN 37831-8056 USA	R. C. OLSON BALTIMORE GAS & ELECTRIC CO. CCNPP-NGF PO BOX 1535 LUSBY MD 20657 USA	T. PRATT BROOKHAVEN NATIONAL LABORATORY BLDG. 130 UPTON NY 11973 USA
S. M. MIHAIU YANKEE ATOMIC ELÉCT. CO. 508 MAIN ST. BOLTON MA 01740 USA	E. NEGRENTI ENEA/DISP V. ANGUILLARESE, 301 ROME 00060 ITALY	A. OMOTO TOKYO ELECTRIC POWER 1901 L ST., NW, STE. 720 WASHINGTON DC 20036 USA	D. A. PRELEWICZ ENSA, INC. 15825 SHADY GROVE RD. (SUITE 170) ROCKVILLE MD 20850 USA
J. S. MILLER GULF STATES UTILITIES P.O. BOX 220 ST. FRANCISVILLE LA 70775 USA	D. B. NEWLAND NATIONAL NUCLEAR CORP. BOOTHS HALL, CHELFORD ROAD KNUTSFORD ENGLAND UK	N. R. ORTIZ SANDIA NATIONAL LABS., DIV. 6410 P.O. BOX 5800 ALBUQUERQUE NM 87185 USA	J. G. PRUETT OAK RIDGE NATIONAL LABORATORY P.O. BOX 2008 OAK RIDGE TN 37831-6135 USA
A. MINATO ENERGY RESEARCH LAB., HITACHI LTD. 1168 MORIYAMA-CHO HITACHI-SHI IBARAKI-KEN 316 JAPAN	L. Y. NEYMOTIN BROOKHAVEN NATIONAL LABORATORY BLDG 475B UPTON NY 11973 USA	J. PAN UNIVERSITY OF MICHIGAN 2250 G. G. BROWN BLDG., MECH. ENG. ANN ARBOR MI 48108 USA	J. PUGA UNITED ELECTRICIA, S. A. (UNESA) FRANCISCO GERVAS, 3 MADRID 28020 SPAIN
S. M. MODRO FZS-AUSTRIA C/O EG&G P.O. BOX 1625 IDAHO FALLS ID 83415 USA	Y. NOGUCHI CHUBU ELECTRIC POWER CO. INC 900 17TH ST. N.W., SUITE 714 WASHINGTON DC 20006 USA	R. K. PAPESCH BECHTEL-KWU ALLIANCE 15740 SHADY GROVE RD. GAITHERSBURG MD 20877 USA	C. E. PUGH OAK RIDGE NATIONAL LABORATORY P.O. BOX 2009 OAK RIDGE TN 37831 USA
T. MOMMA JAERI C/O GENERAL ELECTRIC SAPS RT. 168 S. BEAVER PA 15077 USA	P. NORTH EG&G IDAHO INC. P.O. BOX 1625 IDAHO FALLS ID 83415 USA	C. PARK BROOKHAVEN NATIONAL LABORATORY BLDG. 130 UPTON NY 11973 USA	W. J. QUAPP WESTINGHOUSE HANFORD CO. PO BOX 1970 RICHLAND WA 99352 USA
F. J. MOODY GE NUCLEAR ENERGY 175 CURTNER AVE. MAIL CODE-769 SAN JOSE CA 95125 USA	H. NOURBAKHSH BROOKHAVEN NATIONAL LABORATORY BLDG. 130 UPTON NY 11973 USA	W. R. PEARCE CONSULTANT 6846 GLENBROOK ROAD BETHESDA MD 20814 USA	P. J. QUATTRO MBZ, INC. 1175 HERNDON PKWY., STE. 150 HERNDON VA 22070 USA
R. J. MOORE SAVANNAH RIVER LABORATORY BLDG. 707C AIKEN SC 29808 USA	S. P. NOWLEN SANDIA NATIONAL LABS. PO BOX 5800, DIV. 6447 ALBUQUERQUE NM 87185 USA	G. A. PERTMER UNIVERSITY OF MARYLAND DEPT. OF CHEMISTRY & NUCLEAR ENGR. COLLEGE PARK MD 20742 USA	Z. H. QURESHI SAVANNAH RIVER LABORATORY 786-SA AIKEN SC 29808 USA
F. I. MOPSIK NAT'L INST. OF STDS. & TECH. GAITHERSBURG MD 20899 USA	E. I. NOWSTRUP CONSULTANT 17605 PARK MILL DR ROCKVILLE MD 20855 USA	G. PETRANGELI ENEA/DISP VIA VITALIANO BRANCATI, 48 ROME 00144 ITALY	H. J. REILLY IDAHO NATIONAL ENGINEERING LAB PO BOX 1625 IDAHO FALLS ID 83402 USA
M.J. MOREAU GENERAL ELECTRIC P.O. BOX 1072 SCHENECTADY NY 12301 USA	A. NUHM TECHNICATOME CEN CADARACHE CADARACHE 13115 FRANCE	J. L. PIERREY CEA FRENCH ATOMIC ENERGY COMMISSION CEN/FAR, BP NO. 6 FONTENAT-AUX-ROSES 92265 FRANCE	L. RIB LNR ASSOCIATES 8605 GRIMSBY CT. POTOMAC MD 20854 USA
Y. MUBAYI BROOKHAVEN NATIONAL LABORATORY BLDG. 130 UPTON NY 11973 USA	J. O'HARA BROOKHAVEN NATIONAL LABORATORY BLDG. 130 UPTON NY 11973 USA	A. PINI ENEA/DISP VIA VITALIANO BRANCATI, 48 ROME 00144 ITALY	B. RIEGEL GESELLSCHAFT FUR REAKTORSICHERHEIT FORSCHUNGSGELANDE D-8046 GARCHING FRG
Y. MURAO JAPAN ATOMIC RESEARCH INST. TOKAI-MURA, NAKA-GUN IBARAKI-KEN 319-11 JAPAN	K. R. O'KULA SAVANNAH RIVER LABORATORY BLDG. 773-41A AIKEN SC 29808 USA	M. G. PLYS FAUSKE & ASSOCIATES 16W070 WEST 83RD STREET BURR RIDGE IL 60521 USA	D. E. ROBERTSON PACIFIC NORTHWEST LABORATORY P.O. BOX 999 RICHLAND WA 99352 USA

S. B. RODRIGUEZ  
EG&G IDAHO INC.  
1646 GRANDVIEW #1  
IDAHO FALLS ID 83402  
USA

U. S. ROHATGI  
BROOKHAVEN NATIONAL LABORATORY  
BLDG 475B  
UPTON NY 11973  
USA

B. ROSENSTROCH -  
EBASCO SERVICES INC.  
2 WORLD TRADE CENTER 89E  
NEW YORK NY 10048  
USA

S. T. ROSINSKI  
SANDIA NATIONAL LABS, DIV. 6513  
P.O. BOX 5800  
ALBUQUERQUE NM 87185  
USA

J. C. ROUSSEAU  
CEA FRENCH ATOMIC ENERGY COMMISSION  
CEN/GRENOBLE  
GRENOBLE 38000  
FRANCE

D. RUBIO  
ELECTRIC POWER RESEARCH INSTITUTE  
3412 HILLYVIEW AVE.  
PALO ALTO CA 94303  
USA

K. A. RUSSELL  
EG&G IDAHO INC.  
1520 SAWTELLE  
IDAHO FALLS ID 83415  
USA

J. RUTHERFORD  
CENTRAL ELECTRICITY GENERATING BD.  
BOOTH'S HALL, CHELFORD ROAD  
KNUTSFORD CHESHIRE WA16 806  
UK

B. F. SAFFELL  
BATTELLE COLUMBUS DIVISION  
505 KING AVENUE  
COLUMBUS OH 43201  
USA

R. T. SAIRANEN  
TECHNICAL RSCH CTR OF FINLAND  
POB 169  
HELSINKI SF-00181  
FINLAND

K. SAKANA  
JAPAN INST. OF NUCLEAR SAFETY  
FUJITA KANKOU TORANOMON MINATO  
TOKYO 105  
JAPAN

K. SAKANO  
JAPAN INSTITUTE OF NUCLEAR SAFETY  
FUJITA KANKON TOR. BLDG. 3-17-1  
TOKYO 105  
JAPAN

A. SALA  
HIDROELECTRICO ESPANOLA  
HERMOSILLA 3  
MADRID 28001  
SPAIN

J. SALUJA  
VIKING SYSTEMS INTERNATIONAL  
2070 WM PITT WAY  
PITTSBURGH PA 15238  
USA

L. SCHOR  
YANKEE ATOMIC ELECT. CO.  
508 MAIN ST.  
BOLTON MA 01740  
USA

D. G. SCHRAMMEL  
UFK  
WEBERSTR. 5  
KARLSRUHE  
FRG

S. SETH  
MITRE CORP.  
7525 COLSHIRE DR.  
MCLEAN VA 22102  
USA

W. J. SHACK  
ARGONNE NATIONAL LABORATORY  
BLDG 212  
ARGONNE IL 60439  
USA

V. N. SHAH  
EG&G IDAHO INC.  
P.O. BOX 1625  
IDAHO FALLS ID 83415  
USA

R. H. SHANNON  
CONSULTING ENGINEER  
P.O. BOX 2264  
ROCKVILLE MD 20852  
USA

R. S. SHARMA  
AMERICAN ELECTRIC POWER  
ONE RIVERSIDE PLAZA  
COLUMBUS OH 43017  
USA

D. A. SHARP  
SAVANNAH RIVER LABORATORY  
AIKEN SC 29801  
USA

D. L. SHAW  
BALTIMORE GAS & ELECTRIC COMPANY  
CALVERT CLIFFS NPP, P.O. BOX 1535  
LUSBY MD 20657  
USA

L. SHEN  
ATOMIC ENERGY COUNCIL, ROC  
NO 67, LANE 144, KEELUNG RD. SEC. 4  
TAIPEI TAIWAN 107  
ROC

G. L. SHERWOOD  
U.S. DEPT. OF ENERGY  
GERMANTOWN MD 21701  
USA

P. SHEWMON  
ACRS  
2477 LYTHAM ROAD  
COLUMBUS OH 43220  
USA

K. SHIBATA  
JAPAN ATOMIC RESEARCH INST.  
TOKAI-MURA, NAKA-GUN  
IBARAKI-KEN 319-11  
JAPAN

K. SHIMIZU  
HITACHI, LTD.  
1-1 SAIWAI-MACHI  
HITACHI  
JAPAN

A. SHIMIZU  
OHYASHI CORP.  
777 RIVERVIEW DR., APT. 9  
ROCHESTER PA 15074  
USA

J. J. SHIN  
EBASCO SERVICES, INC.  
2 WORLD TRADE CENTER  
NEW YORK NY 10048  
USA

M. S. SHINKO  
EMERGENCY RESPONSE TEAM  
PO BOX 129  
WASHINGTON GROVE MD 20880  
USA

B. S. SHIRALKAR  
GENERAL ELECTRIC CO.  
175 CURTNER AVE (M/C 186)  
SAN JOSE CA 95125  
USA

D. A. SIEBE  
LOS ALAMOS NATIONAL LABORATORY  
P.O. BOX 1663, MS K555  
LOS ALAMOS NM 87545  
USA

E. G. SILVER  
OAK RIDGE NATIONAL LABORATORY  
P.O. BOX 2009, BLDG 9201-3  
OAK RIDGE TN 37831-8065  
USA

F. A. SIMONEN  
PACIFIC NORTHWEST LABORATORY  
P.O. BOX 999  
RICHLAND WA 99352  
USA

F. B. SIMPSON  
EG&G IDAHO INC.  
P.O. BOX 1625  
IDAHO FALLS ID 83415  
USA

L. SLEGERS  
SIEMENS KWU  
BERLINER STR 295-303  
OFFENBACH 6000  
FRG

G. L. SMITH  
WESTINGHOUSE HANFORD CO.  
P.O. BOX 1970 X0-44  
RICHLAND WA 99352  
USA

A. W. SNYDER  
SANDIA NATIONAL LABS., ORG. 6500  
P.O. BOX 5800  
ALBUQUERQUE NM 87185  
USA

P. SOO  
BROOKHAVEN NATIONAL LABORATORY  
BLDG 830  
UPTON NY 11973  
USA

H. SPECTER  
NEW YORK POWER AUTHORITY  
123 MAIN STREET  
NEW YORK NY 10601  
USA

J. E. SPEELMAN  
ECN  
3 WESTERDUINWEG, P.O. BOX 1  
PETTEN NEW HOLLAND 1755 ZG  
THE NETHERLANDS

K. E. ST. JOHN  
YANKEE ATOMIC ELECTRIC CO.  
1671 WORCESTER RD  
FRAMINGHAM MA 01701  
USA

H. STADTKE  
JOINT RESEARCH CENTRE-ISPRA ESTABLISH  
ISPRA 21020  
ITALY

D. D. STEPNEWSKI  
WESTINGHOUSE HANFORD CO.  
P.O. BOX 1970 NI-31  
RICHLAND WA 99352  
USA

E. J. STUBRE  
TRACTABEL  
31 RUE DE LA SCIENCE  
BRUSSELS 1040  
BELGIUM

R. K. SUNDARAM  
YANKEE ATOMIC ELECT. CO.  
508 MAIN ST.  
BOLTON MA 01740  
USA

J. D. SUTTON  
YANKEE ATOMIC ELECTRIC CO.  
580 MAIN ST.  
BOLTON MA 01740  
USA

T. SUZUKI  
TOSHIBA  
SHINSUGITA 15060-KU  
YOKOHAMA  
JAPAN

I. SZABO  
C.E.A.  
C.E.N CADARACHE  
ST. PAUL LES DURAN 43  
FRANCE

A. TAKAGI  
TOSHIBA  
4921 NORWALK DR., APT Y202  
SAN JOSE CA 95125  
USA

K. TASAKA  
JAPAN ATOMIC RESEARCH INST.  
TOKAI-MURA, NAKA-GUN  
IBARAKI-KEN 319-11  
JAPAN

J. H. TAYLOR  
BROOKHAVEN NATIONAL LABORATORY  
BLDG 130  
UPTON NY 11973  
USA

B. J. TOLLEY  
COMM. OF THE EUROPEAN COMMUNITIES (CJ)  
200 RUE DE LA LOI  
BRUSSELS 1049  
BELGIUM

J. S. TONG  
ATOMIC ENERGY CONTROL BOARD  
PICKERING NGS OPERATIONS  
PICKERING ONTARIO L1V2R5  
CANADA

L. S. TONG  
TAI  
9733 LOOKOUT PLACE  
GAITHERSBURG MD 20879  
USA

F. M. TOUBOUL  
CEA FRENCH ATOMIC ENERGY COMMISSION  
CEN-SACLAY DEMT/SMTS/RDM5  
GIF-SUR-YVETTE 91191  
FRANCE

H. E. TRAMMELL  
OAK RIDGE NATIONAL LABORATORY  
104 OGLETHORPE PL.  
OAK RIDGE TN 37830  
USA

J. D. TROTTER  
GROVE ENGINEERING  
15215 SHADY GROVE RD.  
ROCKVILLE MD 20878  
USA

C-K TSAI  
WESTINGHOUSE POWER SYSTEMS DIVISION  
P.O. BOX 355  
PITTSBURGH PA 15230-2728  
USA

T. TSUJINO  
JAPAN ATOMIC RESEARCH INST.  
TOKAI-MURA, NAKA-GUN  
IBARAKI-KEN 319-11  
JAPAN

B. D. TURLAND  
UKAEA CULHAM  
CULHAM LABORATORY  
ABINGDON  
UK

G. TYROR, DIRECTOR  
UKAEA/SRD  
WIGSHAW LANE, KNUTSFORD  
WARRINGTON WA34NE  
UK

R. E. UHRIG  
OAK RIDGE NATIONAL LABORATORY  
113 CONNORS DRIVE  
OAK RIDGE TN 37830  
USA

R. A. VALENTIN  
ARGONNE NATIONAL LAB - BLDG. 208  
9700 S. CASS AVE  
ARGONNE IL 60439  
USA

G. L.C.M. VAYSSIER  
MINISTRY OF SOCIAL AFFAIRS  
P.O. BOX 69  
VOORBURG 2270MA  
THE NETHERLANDS

O. VESCOVI  
SIET  
VIA NINO BIXIO 27  
PIACENZA 29100  
ITALY

G. L. VINE  
ELECTRIC POWER RESEARCH INSTITUTE  
3412 HILLVIEW AVE.  
PALO ALTO CA 94303  
USA

D. S. WALLS  
OAK RIDGE NATIONAL LABORATORY  
P.O. BOX 2009, MS-8057  
OAK RIDGE TN 37831-8065  
USA

S. F. WANG  
INST. OF NUCLEAR ENERGY RSCH.  
PO BOX 3-3, LUNG TAN  
TAIPEI TAIWAN 32500  
ROC

O. J. WANG  
WESTINGHOUSE HANFORD CO.  
P.O. BOX 1970 X0-44  
RICHLAND WA 99352  
USA

R. WANNER  
PAUL SCHERRER INSTITUTE  
WUERENLINGEN CH5303  
SWITZERLAND

E. A. WARMAN  
STONE & WEBSTER  
245 SUMMER ST.  
BOSTON MA 02107  
USA

K. E. WASHINGTON  
SANDIA NATIONAL LABS.  
P.O. BOX 5800  
ALBUQUERQUE NM 87185  
USA

W. L. WEAVER  
EG&G IDAHO INC.  
P.O. BOX 1625  
IDAHO FALLS ID 83415  
USA

E. O. WEINER  
WESTINGHOUSE HANFORD CO.  
P.O. BOX 1970, L2-57  
RICHLAND WA 99352  
USA

P. A. WEISS  
SIEMENS AG / UB KWU  
HAMMERBACHERSTR. 12+14  
ERLANGEN 8520  
FRG

H. J. WELLAND  
EG&G IDAHO INC.  
442 JOAN AVENUE  
IDAHO FALLS IDAHO 83401  
USA

E. T. WESSEL  
CONSULTANT  
312 WOLVERINE STREET  
HAINES CITY FL 33844  
USA

H. WESTPHAL  
GESELLSCHAFT FUR REAKTORSICHERHEIT  
SCHWERTNERGASSE 1  
D-5000 COLOGNE 1  
FRG

A. M. WHITE  
SAVANNAH RIVER LABORATORY  
BLDG. 773-11A  
AIKEN SC 29808  
USA

J. D. WHITE  
OAK RIDGE NATIONAL LABORATORY  
P.O. BOX 2008  
OAK RIDGE TN 37831-6009  
USA

G. M. WILKOWSKI  
BATTELLE COLUMBUS  
505 KING AVE.  
COLUMBUS OH 43201  
USA

W. K. WINEGARDNER  
PACIFIC NORTHWEST LABORATORY  
P.O. BOX 999  
RICHLAND WA 99352  
USA

F. J. WINKLER  
SIEMENS  
RINGSTRASSE 19  
SPARDORF  
FRG

L. WOLF  
KERNFORSCHUNGSZENTRUM, PHDR  
POSTFACH 3640  
7500 KARLSRUHE 1  
FRG

A. J. WOLFORD  
EG&G IDAHO INC.  
P.O. BOX 1625  
IDAHO FALLS ID 83415  
USA

D. N. WOODY  
SAVANNAH RIVER LABORATORY  
AIKEN SC 29808  
USA

R. O. WOOTON  
BATTELLE COLUMBUS  
505 KING AVE.  
COLUMBUS OH 43201  
USA

J. WREATHALL  
SAIC  
2929 KENNY RD.  
COLUMBUS OH 43221  
USA

D. W. WRIGHT  
ANCHOR/DARLING VALVE  
701 FIRST ST.  
WILLIAMSPORT PA 17701  
USA

W. WULFF  
BROOKHAVEN NATIONAL LABORATORY  
BLDG 475B  
UPTON NY 11973  
USA

H. XU  
BROOKHAVEN NATIONAL LABORATORY  
BLDG. 130  
UPTON NY. 11973  
USA

Y. YAMAMOTO  
TAKENAKA CO.  
21-1 8CHOME CHUO-KU  
TOKYO  
JAPAN

H. YASOSHIMA  
JAPAN ATOMIC RESEARCH INST.  
TOKAI-MURA, NAKA-GUN  
IBARAKI-KEN 319-11  
JAPAN

M. YOKOTA  
JAPAN ATOMIC RESEARCH INST.  
TOKAI-MURA, NAKA-GUN  
IBARAKI-KEN 319-11  
JAPAN

Y. YOSHIMOTO  
HITACHI, LTD.  
SAIWAI-CHO 3-H  
HITACHI-SHI 316  
JAPAN

R. W. YOUNGBLOOD  
BROOKHAVEN NATIONAL LABORATORY  
BLDG 130  
UPTON NY 11973  
USA

R. ZIPPER  
GESELLSCHAFT FUR REAKTORSICHERHEIT  
SCHWERTNERGASSE 1  
D-5000 COLOGNE 1  
FRG

P. C. ZMOLA  
C&P ENGINEERING  
5409 NEWINGTON RD.  
BETHESDA MD 20816  
USA

R. ZOGRAN  
MPR ASSOCIATES, INC.  
1050 CONNECTICUT AVENUE, N.W.  
WASHINGTON DC 20036  
USA



PROCEEDINGS OF THE  
SIXTEENTH WATER REACTOR SAFETY INFORMATION MEETING

October 24-27, 1988

TABLE OF CONTENTS - VOLUME 2

	<u>Page</u>
ABSTRACT. . . . .	iii
GENERAL INDEX . . . . .	v
REGISTERED ATTENDEES. . . . .	vii

INDUSTRY SAFETY RESEARCH

Chairman: W. B. Loewenstein (EPRI)

Meeting Evolving Reactor Safety Requirements. . . . .	1
A. Rubio and R. C. Vogel (EPRI)	
Scrubbing of Aerosols by Water Pools. . . . .	57
M. Merilo (EPRI), J. A. Gieseke (BCD), and A. T. Wassel (SAIC)	
Validation of FREY for the Safety Analysis of LWR Fuel Using Transient Fuel Rod Experiments. . . . .	71
R. O. Montgomery and Y. R. Rashid (ANATECH), J. A. George and K. L. Peddicord (Texas A&M), and C. L. Lin (EPRI)	
EPRI Operator Reliability Experiments Program . . . . .	95
V. Joksimovich et al. (Accident Prevention Group), and D. H. Worledge (EPRI)	
STARRS: A Methodology to Evaluate Consequences of Steam Generator Tube Ruptures . . . . .	107
S. P. Kalra (EPRI)	
Risk Management for the BWR Plant . . . . .	125
R. A. Cushman (Niagara Mohawk), P. R. Hill (PP&L), H. Specter (NYPA), and I. B. Wall (EPRI)	

NON-DESTRUCTIVE EVALUATION

Chairman: J. Muscara (NRC)

Evaluation and Improvement in Nondestructive Examination (NDE) Reliability for Inservice Inspection of Light Water Reactors. . . . .	145
S. R. Doctor et al. (PNL)	
Final Developments, Validation and Technology Transfer for AE and SAFT-UT. . . . .	171
S. R. Doctor et al. (PNL)	

NON-DESTRUCTIVE EVALUATION  
(Cont'd)

	<u>Page</u>
Final Evaluation of Advanced and Current Leak Detection Systems . . . . .	181
D. Kupperman et al. (ANL)	
Eddy-Current Inspection for Steam Generator Tubing Program Annual Progress Report for Period Ending December 31, 1988. . . . .	193
C. V. Dodd, W. E. Deeds and J. R. Pate (ORNL)	
Review of the Status of Nondestructive Measurement Techniques to Quantify Material Property Degradation Due to Aging and Planning for Further Evaluation . . . . .	201
S. R. Doctor et al. (PNL)	

MATERIALS ENGINEERING/PRESSURE VESSEL RESEARCH  
Chairman: M. Mayfield (NRC)

Progress in Research and Standards Activities in the Materials Engineering Branch for 1988 . . . . .	207
C. Z. Serpan, Jr. (NRC)	
Impact of Radiation Embrittlement on Integrity of Pressure Vessel Support for Two PWR Plants . . . . .	211
R. D. Cheverton et al. (ORNL)	
Fracture Resistance Characterization for LWR Materials. . . . .	237
E. M. Hackett (DTRC) and J. A. Joyce (USNA)	
Advances in Crack-Arrest Technology for Reactor Pressure Vessels. . . . .	263
B. R. Bass and C. E. Pugh (ORNL)	
HSST Wide-Plate Test Results and Analysis . . . . .	291
D. J. Naus, B. R. Bass and J. Keeney-Walker (ORNL), and R. J. Fields, R. deWit and S. R. Low III (NIST)	

MATERIALS ENGINEERING/RADIATION EFFECTS  
Chairman: A. Taboada (NRC)

Summary of the Heavy-Section Steel Technology Program Irradiation Series. . . . .	319
R. K. Nanstad (ORNL)	
Results of Irradiated Cladding Tests and Clad Plate Experiments . . . . .	355
F. M. Haggag and S. K. Iskander (ONRL)	

MATERIALS ENGINEERING/DEGRADED PIPING  
Chairman: M. Mayfield (NRC)

General Developments from NRC's Degraded Piping Program . . . . .	371
G. M. Wilkowski et al. (BCD)	

## MEETING EVOLVING REACTOR SAFETY REQUIREMENTS

A. Rubio and R. C. Vogel  
Electric Power Research Institute

### ABSTRACT

This paper gives an overview of the work being conducted by the Electric Power Research Institute (EPRI) in the reactor safety field.

Topics covered include nuclear seismic research, nuclear reload management, systems reliability analysis, severe accident management, safety margins and testing (i.e., water hammer), source term investigations and control and diagnostics.

The general philosophy behind the work is to be of help to the utilities which support EPRI in such a way that safety is enhanced, firstly, in protecting the public and, secondly, in protecting the very large investment represented by a nuclear power plant.

### 1.0 INTRODUCTION

This paper reviews the work of the Safety and Technology Department of the Electric Power Research Institute (EPRI). The space is too limited to cover all the work. Here, we will cover some of the work in the areas of nuclear seismic studies, reload management, accident management, systems reliability analyses, severe accident studies, safety margins, control and diagnostics.

It is the general approach in our work to be of help to the utilities which support EPRI in such a way that safety is enhanced, firstly, in protecting the public, and secondly, in protecting the very large investment represented by a nuclear power plant.

NRC issued a Severe Accident Policy Statement (50 FR-32138) on August 8, 1985, whose objectives were: (1) to reduce the probability of a severe accident; and (2) should a severe accident occur, to mitigate its consequences to the public. The policy statement provides for a generic letter requiring individual plant evaluations (IPEs). During the past year, we have all been waiting for the issuance of the generic letter which will give guidance to the utilities for the individual plant evaluations. At the time this paper is being written the generic letter has not been issued. Therefore, at this point, it is too early to comment in any detail on the generic letter.

Another important activity this year has been the NRC's efforts in reworking NUREG-1150. EPRI has participated in this effort. We are impressed with the effort which NRC has put into this difficult task and await final publication of this document.

## 2.0 NUCLEAR SEISMIC STUDIES

The goals of the seismic research conducted at the Electric Power Research Institute (EPRI) are to reduce costs and provide the technological bases for safe operation of nuclear power plants with respect to seismic phenomena. With no new plants on order, the current principal focus of EPRI's seismic research is to support the needs of operating plants. In the long term, however, the program addresses the major strategic need to stabilize the regulatory process and reduce costs of licensing delays and plant reevaluations.

### 2.1 Probabilistic Seismic Hazard

The purpose of EPRI's probabilistic seismic hazard research is to provide a documented basis for informed decision making about ground motions appropriate for seismic design at a given site. Seismic hazard is represented by probabilities that given levels of ground shaking will be exceeded at a site in a given time (usually annually). Uncertainty on the hazard at any site may be large; therefore, procedures are required to quantify uncertainty that reflects uncertain input parameters and computational models.

Recently, a probabilistic seismic hazard methodology has been completed specifically to characterize seismic hazard at low probabilities ( $<10^{-3}$  per year) at locations in the central and eastern United States, using multiple input interpretations (1).

The probabilistic computational structure permits expression of alternative, scientifically supported interpretations of earthquake causes and observed seismicity (figure 1). The interpretation procedure provides a step-by-step, structured approach leading to seismic source representations that are fully trackable and amenable to scientific peer review.

The methodology incorporates rigorous statistical analyses of an earthquake catalog to maximize its use in estimating the sizes and rates of occurrence of future earthquakes in any given seismic source. Flexibility has been retained for the user to express alternative interpretations. The main features of the assessment are:

- a. An evaluation of the internal consistency of earthquake size assessments and the establishment of a uniform measure of earthquake size, with error estimate;
- b. Discrimination of independent main shocks from dependent events (foreshocks and aftershocks);
- c. Analysis of the historic earthquake database for completeness in time, space and magnitude;
- d. Methods to estimate seismicity parameters to account for error in magnitude estimates and to permit spatially nonhomogeneous reoccurrence rates within a source; and,

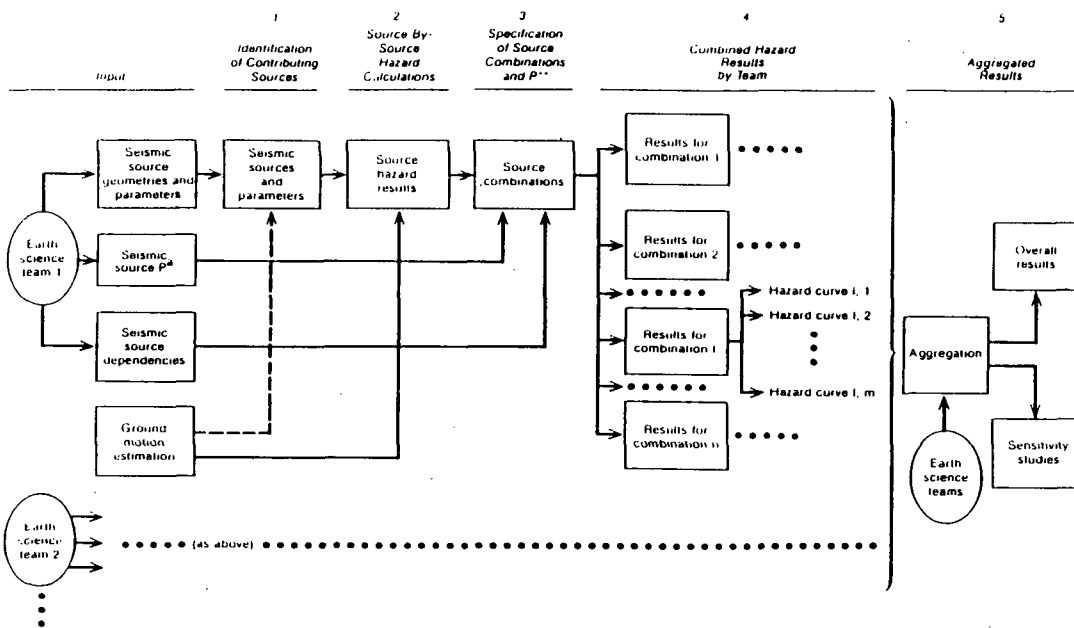


Figure 1. Steps Required for Seismic Hazard Analysis at a Site.

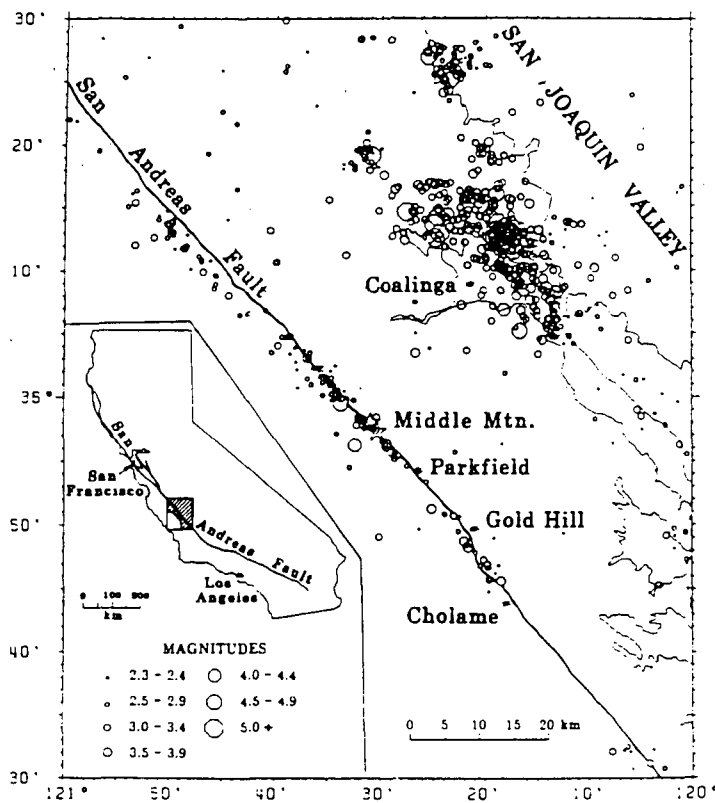


Figure 2. Map of Earthquake Epicenters (1975 to June 1985) Relative to the Trace of the San Andreas Fault.

- e. Flexibility to allow prior (in a Bayesian sense) estimates of seismicity parameters to be specified by the user.

The methodology is believed to be completely general. It can be applied to any site by any team of researchers knowledgeable in earth sciences and probability analysis.

## 2.2 Seismic Design Ground Motion

The main objective of the research on seismic design ground motion is to reduce conservatism in seismic design standards for the development of reliable operating basis earthquake/safe shutdown earthquake (OBE/SSE) guidelines for nuclear power plants.

The resolution of these issues requires the development of procedures to reliably determine ground-motion time histories and associated response spectra. This requires a fundamental understanding of all elements contributing to ground motion at a site: earthquake source properties, propagation of seismic energy and site response. Present and planned research may be divided into three areas: (1) field and laboratory experiments to collect data; (2) data analysis and model synthesis; and (3) integration of results into topical reports or technical positions as bases for modifying regulatory practice.

Currently, EPRI's largest effort toward collecting free-field ground-motion and soil-response data is at Parkfield, California, the site of a predicted magnitude 5.5-6.0 earthquake in 1988  $\pm$ 5 years (figure 2). EPRI is participating in installing and maintaining two arrays installed at Parkfield: (1) a dense 3-dimensional seismic engineering array (figure 3); and (2) a vertical soil liquefaction array (figure 4). The seismic engineering array is located 6 km east of the San Andreas Fault and is designed to study dynamics of earthquake rupture and spatial coherence of near-field seismic wave propagation. The soil liquefaction array is located on soft sediments less than 1 km from the fault and is designed to study the effects of strong ground shaking on saturated, cohesionless soils.

Data analysis and model synthesis can be broken down into investigations of earthquake source processes, the propagation path and site response. In terms of sources, EPRI is looking very hard at scaling relationships, with a special emphasis on characterizing similarities and differences between intra- and interplate earthquakes. Reliable seismic hazard prediction in the eastern United States depends on an understanding of intraplate earthquakes; however, because intraplate events are relatively rare, it is important to understand when it is appropriate to apply data from the more common interplate events to hazard estimation for potential eastern United States sources.

The investigations of path properties have been focused on developing models of attenuation in the eastern United States. Regional investigations have looked at attenuation of Lg waves (crustal Love wave) at distances greater than 100 km from earthquake sources and at models for ground motion attenu-

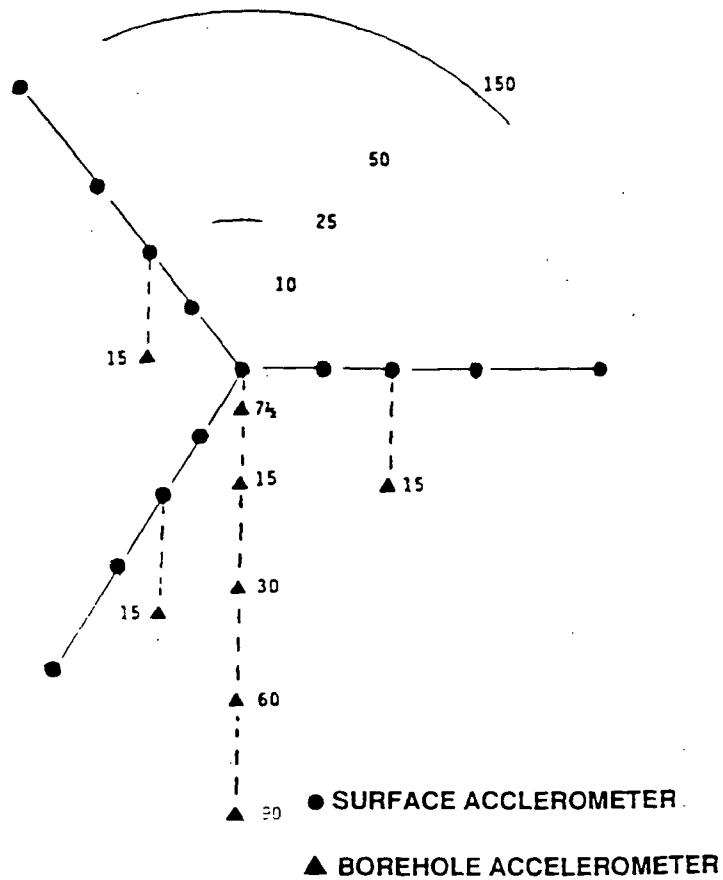


Figure 3. Parkfield 3-Dimensional Seismic Engineering Array. Numbers in meters.

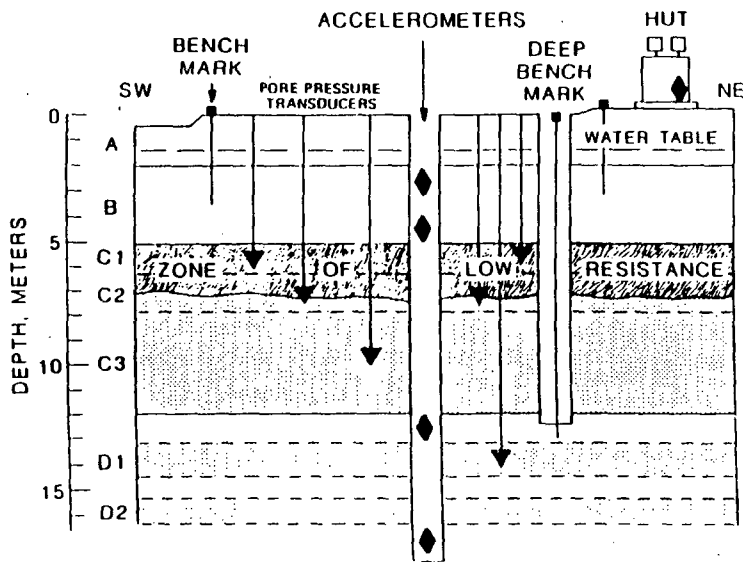


Figure 4. Cross Section of Parkfield Site Liquefaction Array.

ation of body-wave phases at closer ranges. Effort has also been aimed at resolving controversies over sources of high-frequency attenuation and appropriate models for ground motion estimation.

Site response is the least understood contributor to ground motion and the least developed aspect of the analysis program. EPRI is now initiating projects to investigate nonlinear soil response (from arrays at Parkfield and Lotung), the effects of shallow crustal structure, and the spatial coherence of ground motion of dimensions of a typical nuclear plant embedment.

In terms of integration of results of ground motion studies, EPRI held a symposium in April 1987 on the subject of "Earthquake Ground Motion Estimation in Eastern North America." Investigators from a variety of disciplines and organizations were invited to make presentations, the results of which are published in an EPRI technical report (2).

### 2.3 Piping Design Improvement

Overly conservative and inefficient piping seismic design has often led to overstiffened systems with excessive numbers of snubbers. The EPRI research strategy is aimed at achieving the following two objectives: (1) reducing snubbers by relaxation of design criteria, and (2) replacing snubbers by using alternative support design.

EPRI and NRC have cosponsored a piping and fitting dynamic reliability program (PDFDRP) aimed at developing a set of defensible and improved criteria for more realistic piping designs with fewer snubbers (3, 4). To provide the necessary experimental database that would support design rule changes, the project conducted an extensive test program on components, systems, and material specimens. The component test program consisted of 41 tests on elbows, tees, reducers, nozzles and welded attachments. Each component was pressurized and dynamically tested to leakage failure under extreme high seismic, hydrodynamic or water hammer loads. A typical seismic test setup for an elbow element is shown in figure 5. The piping system test program consisted of four system tests: two seismic/hydrodynamic tests, and two water hammer load tests. The test results from both component and system tests have demonstrated that nuclear piping has excessive dynamic capacity and the major failure mode is fatigue ratcheting rather than collapse.

Some typical results from component tests are summarized in table 1. It can be seen that the dynamic load level could reach as high as 15 to 25 times of the level D load before through-wall cracks developed from fatigue ratcheting. Also, the results have shown that the recorded dynamic moments always exceed the static limit moments. Based on the test evidence, two code cases on removal of OBE from the equation in the ASME code have been approved by ASME. Additional code rule changes will be proposed to allow higher code stress limits and to permit the use of simpler analysis methods.

Research on alternative support design includes the development of simplified piping support systems using limit-stops (5) and the application of an energy-absorbing support device (6). EPRI has participated in the NRC program to

Table 1

PIPING AND FITTING DYNAMIC RELIABILITY PROGRAM - COMPONENT TEST SUMMARY  
(6 in. Components - Seismic Input)

No.	Type	Mat	Sch	Press	Load Dir	DYN MON LIM MON	Input X Level D	No TH	Fail Mode	Residual Strain
1	Elbow (Retest)	CS	80	1500	I-P	1.21	15	5	NF	No data
			80	2600	I_P	1.21	15	0.5	FR	No data
2	Elbow (Retest)	CS	80	1500	O-P	1.04	15	5	NF	No data
			80	2600	O-P	1.04	15	4.5	FR	No data
3	Elbow	SS	10	400	I-P	2.36	21	3.5	FR	7.0%
4	Elbow	CS	40	1000	I-P	1.83	18	2.5	FR	No data
5	Elbow	CS	40	1700	I-P	2.06	21	3.5	FR	27%
6	Elbow	SS	40	1700	I-P	2.00	19	3.5	FR	32%
7	Elbow	SS	40	1000	I-P	1.80	23	4.5	FR	18%
8	Elbow	SS	40	0	I-P	1.80	24	5	NF	3%
9	Tee Fix-2	SS	40	1700	O-P	2.50	21	1.5	FR	8%
10	Tee Fix-2	SS	40	1000	O-P	2.40	21	2.5	FR	6.5%
11	Tee Fix-2	SS	10	400	O-P	1.00	16	0.5	FR	5%
12	Tee Fix-2	SS	40	1700	I-P	2.30	27	2.5	FR	11%
13	Short Elb.	CS	40	1000	I-P	2.30	22	2.5	FR	6%
14	Tee Fix-2	CS	40	1700	O-P	2.46	18	1.5	FR	10%
15	Reducer	SS	40	1700	N/A	1.18	13	5	FR	18%
23	Strut	CS	40	1000	I-P	2.0	N/A	5	NF	1.5%
25	Elb-Mid	SS	10	800	MIX	6.0	27	7	NF	4%
35	Elb High	CS	40	1700	I-P	1.65	18	5	FR	No data
37	Elb 1.4 Hz	SS	10	0	I-P	1.03(4)	10	2	RB	4.0%
38	Tee Fix-1	CS	40	1700	O-P	1.92	20	3.6	FR	20%
39	Tee Fix-1	SS	40	0	O-P	1.84	21	4	NF	10%
40	Reducer	SS	40	0	N/A	1.2	22	2	RB	9%

I-P = In-Plane

O-P = Out-of-Plane

NO TH = No. of high-level input test runs to cause failure.

FR = Fatigue ratcheting failure.

NF = No failure.

Residual strain = measured by 2-inch scratch marks.

Input x Level D = calculated stress using linear response spectrum analysis, 2% damping,  $\pm 15\%$  broadening and actual sled input. Use the calculated stress,  $(B_2M/Z)$ , divided by Level D allowable,  $35_m$  to determine multiple of Level D allowable.

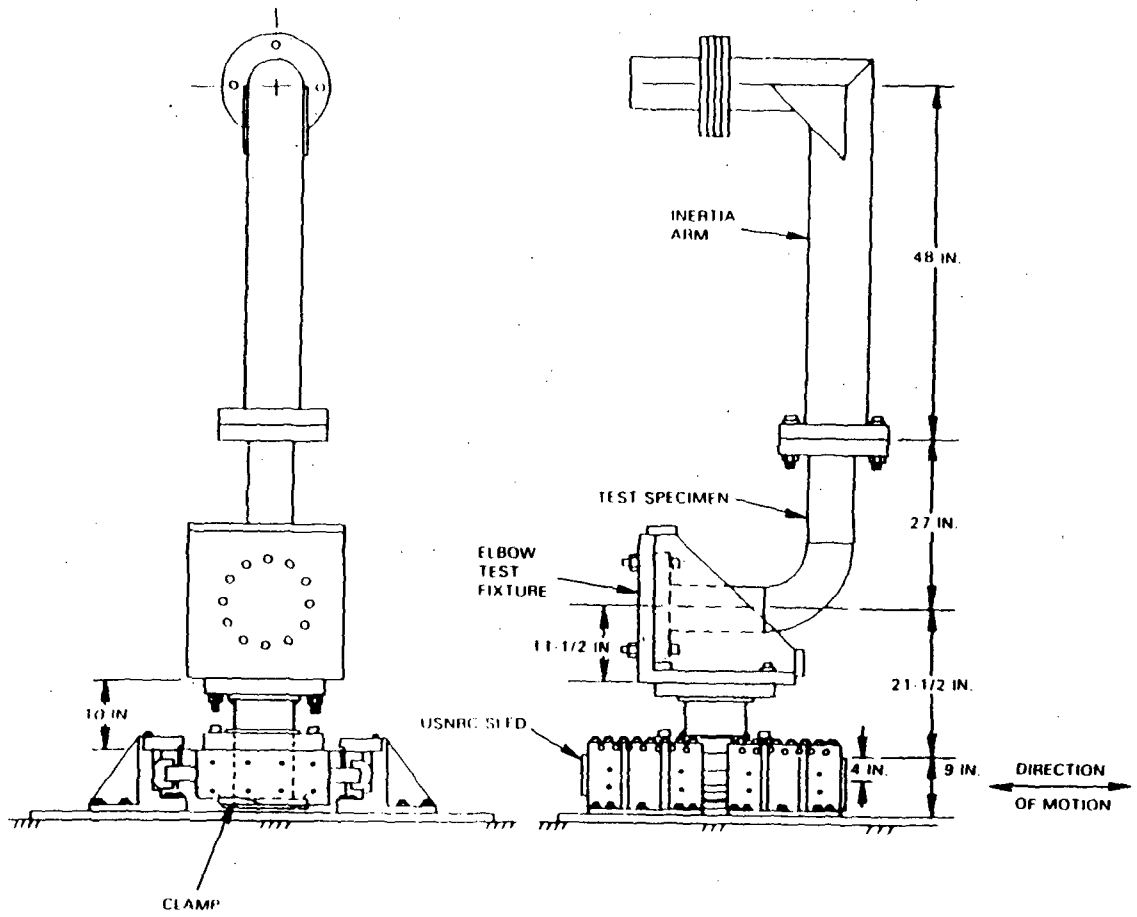


Figure 5. In-Plane Elbow Test Setup.

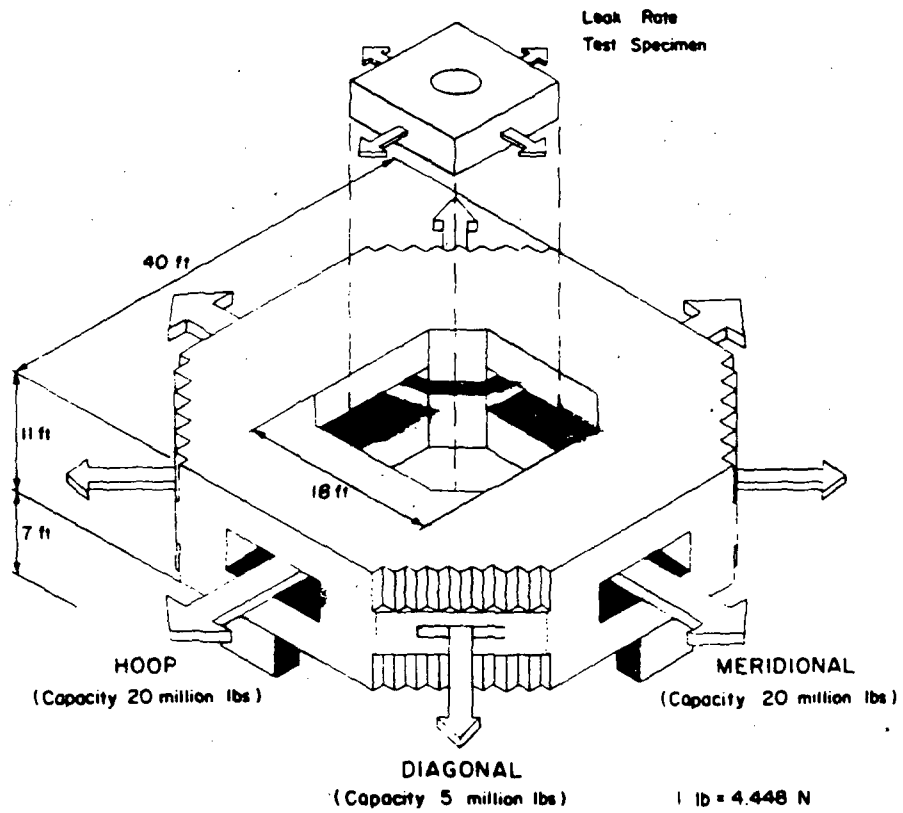


Figure 6. Multiaxial Test Frame Load Capacity.

test these alternative passive designs on actual piping systems at the HDR plant in West Germany (7). Such passive piping support systems could help reduce or eliminate widely used snubbers and thus, help achieve substantial cost savings in power plant construction and, operation. Further software development and hardware design of the limit stop support is underway for product commercialization.

The piping system damping reevaluation is aimed in critically evaluating the available damping data to form a technical basis for recommending piping system damping values for formal ASME code (Appendix N) adoption. The study was motivated by some concerns surrounding the ASME Code Case N-411.

Based on engineering insights and judgment, using regression judiciously and factoring the practicality of application into consideration, the following damping recommendations have been submitted to ASME (8):

### 2.3.1 For LWR Piping.

$$\beta = \beta_0 + 0.24 D + 1.66 \text{ (RL)} \quad \text{(A)}$$

where

D = pipe diameter (in.)

$\beta_0$  = 1.43\* first mode without on-line equipment  
 = 0.53\* higher modes without on-line equipment  
 = -0.47\*\* first mode with on-line equipment  
 = -1.37\*\* higher modes with on-line equipment

RL = response level--extreme fiber stress normalized against yield stress

\*Applicable also to small bore piping with on-line equipment.

\*\*Applicable only when no special equipment supports are provided and to only those modes that have a dominant equipment response.

Maximum diameter dependent damping are determined by the intersection of Eq. (B) below with the above equation for a similar LMR configuration.

### 2.3.2 For LMR Piping.

$$\beta = \beta_0 - 0.31 D + 4.0 \text{ (SR)} \quad \text{(B)}$$

where

D = pipe diameter (in.)

SR = ratio of snubber supports to total supports in terms of pipe support density (PSD)

$\beta_0$  = 8.09 first mode

= 5.89 higher modes

One key point to be observed here is that damping increases as response level increases. Another key point is that the damping for first mode is larger than the one for higher modes. Although the definition of first mode and higher modes is a much more rigorous one than frequency in terms of assessing the physical response of the piping system, the results presented here do not conflict with Code Case N-411.

Other ongoing and planned research activities in support of overall piping improvement include development of simplified inelastic analysis method (9, 10), analysis of NRC/EPRI/NUPEC (Nuclear Power Engineering Test Center) high-amplitude piping tests at Tadotsu, dynamic testing of eroded and corroded piping, and development of improved support design criteria. EPRI has also sponsored studies on relaxing snubber testing specifications to reduce snubber maintenance costs.

#### 2.4 Concrete Containment Integrity

The goal of EPRI's research is to provide industry with a test-verified analytic tool for evaluation of concrete containment integrity under various postulated severe accident scenarios. The approach of the EPRI research program is to conduct tests and analysis in parallel. To avoid uncertainties associated with using small-scale models to study detailed structural response of prototypical structures, the test program focuses on testing of large- and full-scale segments, starting with simple uniaxial and biaxial tension tests on square structural elements to define material behavior and then following up with more systematic testing of prototypical containment segments with penetrations and structural discontinuities to produce a database on leakage through local liner tearing. A 50-million pound multiaxial reaction rig, as shown in figure 6, was fabricated at Construction Technology Laboratory (CTL) for testing. As shown in figure 7, a leakage monitoring fixture was also installed to obtain information on leakage through liner and concrete crack. Seven specimens of various configurations were tested. The results have been reported (11, 12) and have demonstrated that:

- The liner will develop cracks in the discontinuity region such as around penetrations where high strain concentration is induced;
- The liner crack will not develop in regions where no high strain concentration is expected;
- A preexisting liner crack or a crack initiated at the strain concentration region will arrest (instead of propagating in an unstable manner) due to concrete-liner interaction; and,

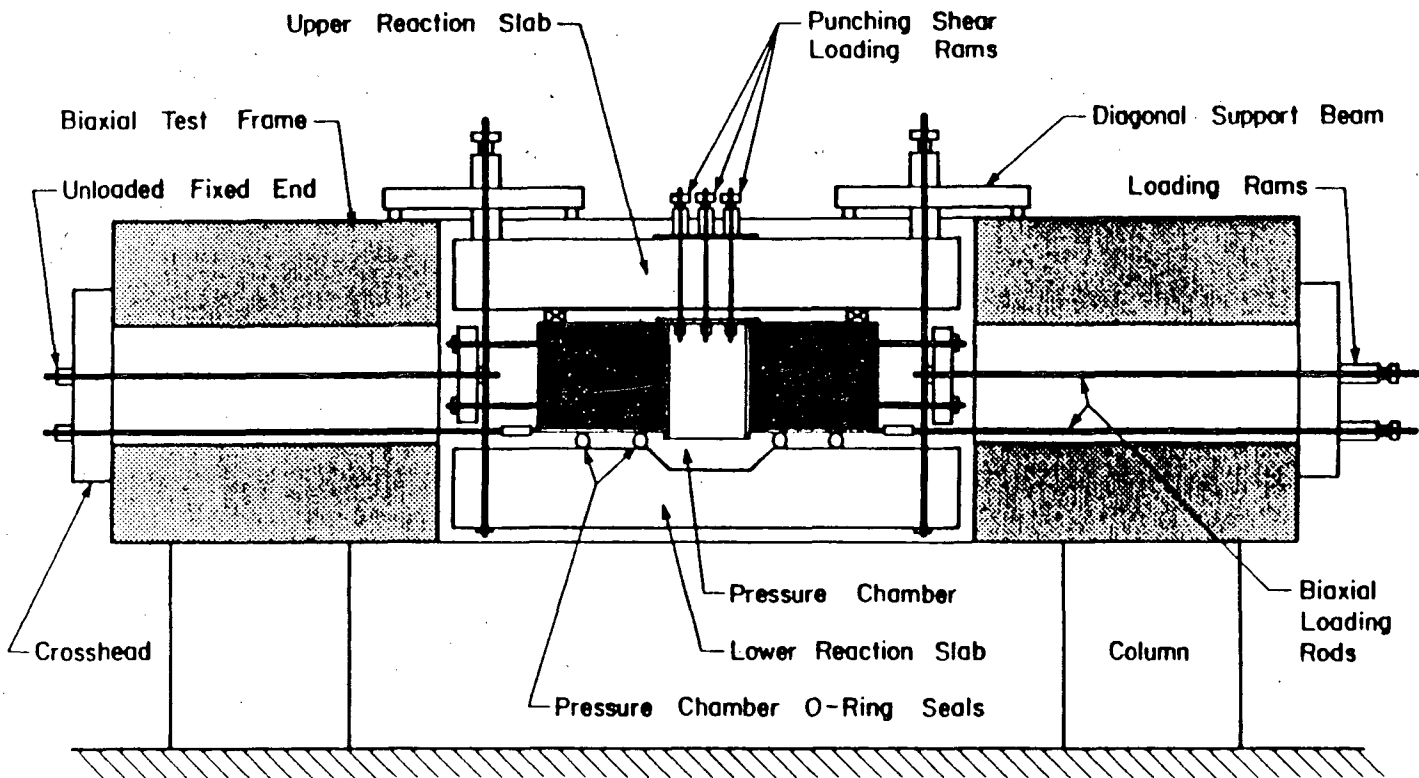


Figure 7. Cross-Section of Air Leak Rate Test Fixture and Multiaxial Test Frame.

- Liner anchorage plays a critical role in liner crack initiation and arrest.

These experimental findings have also been observed in the NRC/Sandia 1/6-scale reinforced concrete containment model testing where about 10 cracks developed in the liner in the strain concentration regions. One, therefore, can conclude that the ultimate "failure" mode of a concrete containment under internal overpressurization will most likely be "leak" instead of catastrophic "break."

The analytical development has resulted in capabilities in ABAQUS-EPGEN (13) for nonlinear concrete containment integrity evaluation. These capabilities have been qualified by correlating analysis with test (14-16).

The qualified capabilities were applied to performing pretest analysis of the NRC/Sandia 1/6-scale reinforced concrete containment overpressurization test. The ABAQUS results correctly predicted the failure mode (liner tear at strain concentration regions rather than catastrophic unstable sudden failure) and failure pressure level (~145 psi, the level the liner tear occurred) observed in the test (17).

With the release of the test data, posttest correlations were performed. The 8-inch constrained penetration gage measurements are plotted with an analysis liner strain profile at the 145-psi pressure reading in figure 8. In general, very good agreement is observed between the test and analysis.

The best profile of gages that is available on the model is a closely spaced line of gages near equipment hatch A. The comparison between analysis and experiment given in figure 9 shows the same strain concentration trend.

The EPRI concrete containment integrity program has yielded significant results for concrete containment evaluation under beyond design basis severe core loading conditions.

### 3.0 NUCLEAR RELOAD MANAGEMENT

#### 3.1 Evaluation of Differences Between Current Lattice Physics Codes

Utility reactor analysis staffs utilize a variety of cross-section generator codes and libraries with nodal codes to perform core analysis. Inter-comparisons of some of these codes have yielded, in some circumstances, differences in results that were larger than expected. The accuracy of these methods can potentially impact reload core analysis and plant operations support.

The computer codes used in reactor analysis are usually developed for specific applications and benchmarked for a range of relevant parameters. This approach has been used for the cross-section generator codes involved in this study. Fuel enrichment and burnable poison loadings are being extended outside the range of earlier designs, upon which much of the benchmarking has been based.

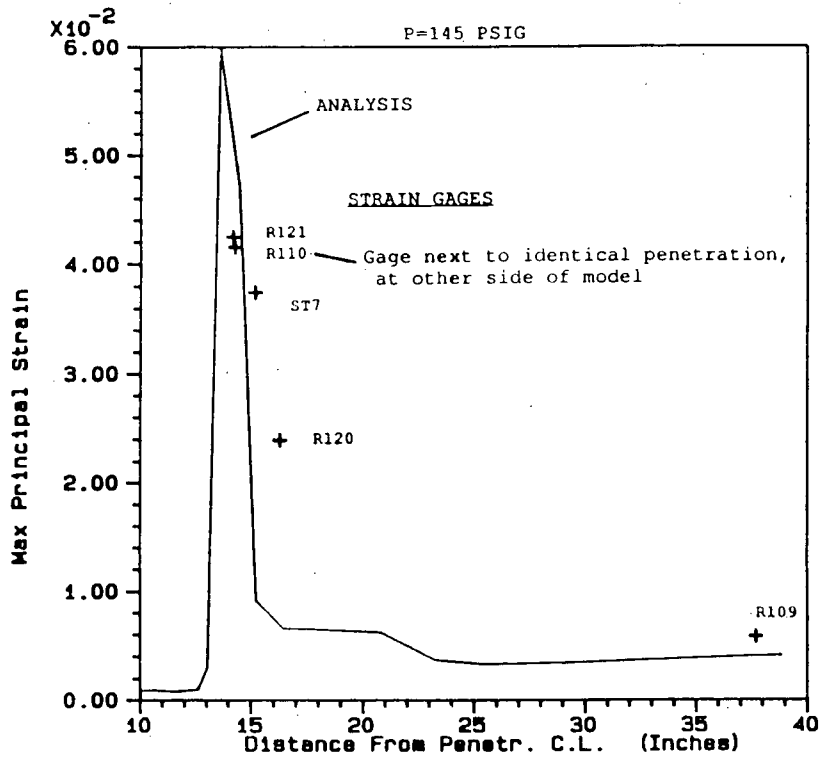


Figure 8. Strain Measurements at End of Test Versus Pretest 3D Local Effects Analysis - 8" Diameter Penetrations.

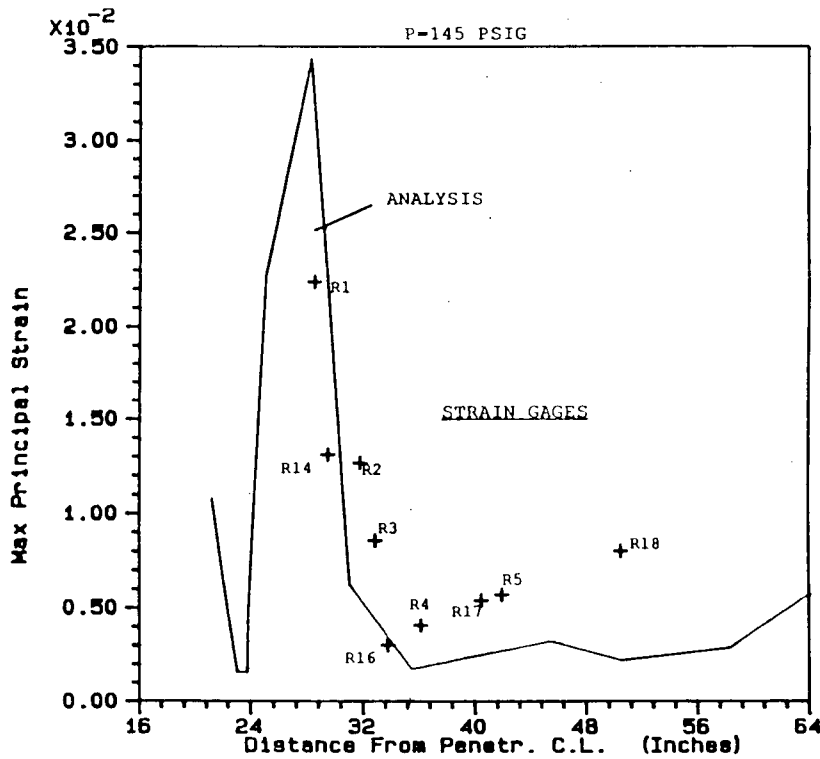


Figure 9. Strain Measurement at End of Test Versus Pretest 3D Local Effects Analysis - Equipment Hatch A.

As applications were being made to the wider range of parameters, larger differences in the results given by the various codes were observed. It was not known whether the differences were systematic, the result of different cross-section libraries, the code methodology, or how the codes had been applied by the user. EPRI was encouraged by various utilities to help sort out the source of the differences.

The evaluation of cross-section generator codes, includes the identification of differences in results from the EPRI-CELL, CELL2, CPM1, CPM2, CASMO2, CASMO3, and LATTICE codes. The differences in code results caused by the use of the ENDF/V library in CELL2 and the CPM library in CASMO2 were also evaluated.

This investigation of cross-section generators is based on six different utility companies running BWR and PWR pin cell and multipin cell calculations with controlled input specification options. Fuel enrichment, burnable poison, Gd or burnable poison rods (BPRs), control rod and soluble poison effects were evaluated over a range of moderator temperatures, moderator void, fuel burnup, power level, and xenon conditions.

Significantly, different results were obtained from the codes/libraries for  $K_{\infty}$  vs. enrichment, cold (68°F)  $K_{\infty}$ ,  $K_{\infty}$  vs. fuel burnup and reactivity worths for Doppler, burnable poison vs. burnup, and control rods. Examples of some of those differences are shown in figure 10. Results obtained for reactivity worths for soluble boron, xenon, void, and temperature history effect were in good agreement.

### 3.2 Analytical Methods for Transient Fuel Behavior

Established procedures for licensing fuel reloads require that each licensee demonstrate that the new fuel reload or proposed operating procedure will not violate previously established limits. In some cases, such as reactor plant changes that affect the fuel limits, the transient fuel analysis of the design basis accidents (DBAs), for which acceptable fuel limits have been specified, becomes a necessary part of the total reload licensing analyses. The FREY code has been developed to address this need.

In addition to fuel licensing analysis, the need of fuel integrity evaluation under plant operation conditions has also been the incentive of FREY development. FREY employs two-dimensional finite formulation with fully coupled thermal-mechanical modeling which is especially suitable for fuel diagnostic analyses as in the case of pellet-clad interaction (PCI). FREY's application in plant operation support is in the ramp rate evaluation, fuel procurement evaluation, and post transient fuel integrity evaluation areas.

An extensive FREY V&V effort covering both steady-state and transient validations is now ongoing. Code predictions are compared with plant irradiation test data, the Halden reactor test data, the power ramp test data, and the severe transient test data obtained in the Power Burst Facility (PBF) and the Transient Reactor Test Facility (TREAT). The scope of this V&V effort is

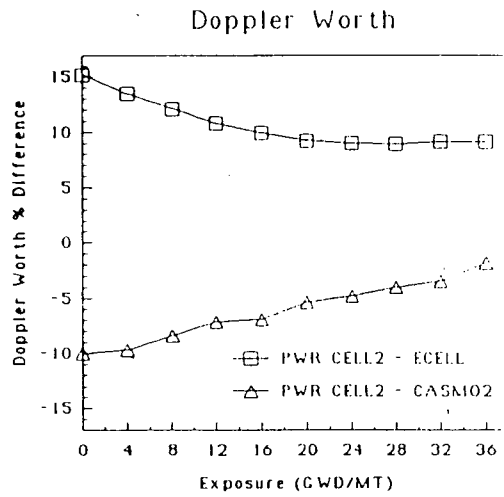
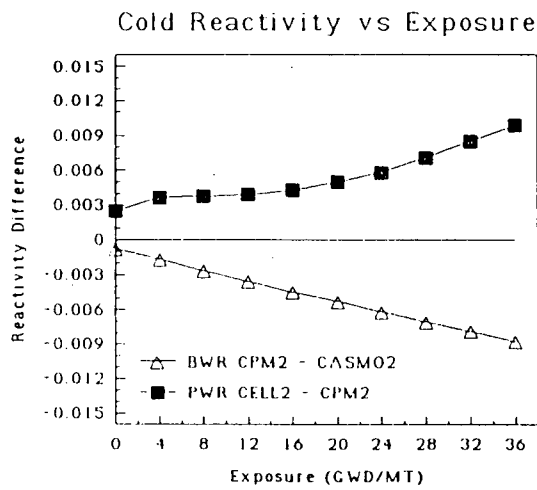
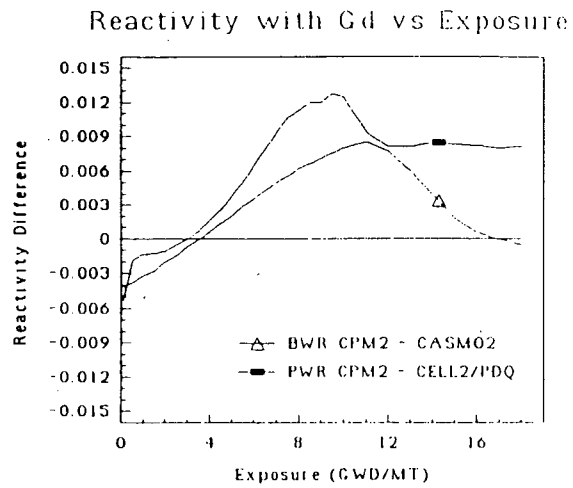
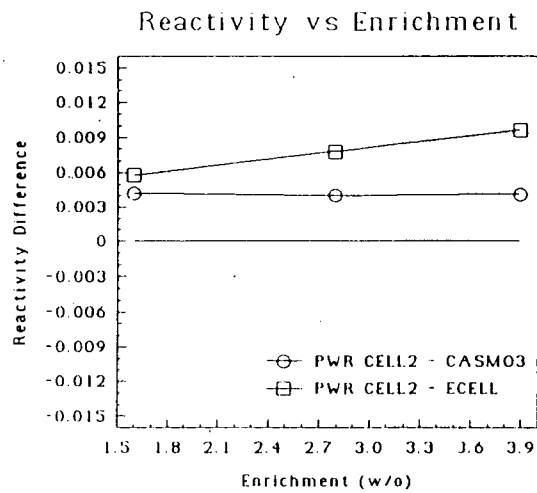


Figure 10. Significant Differences.

intended to cover all of the application areas of FREY. Preliminary results show good comparison between FREY calculated values and test data. The V&V effort is planned to be completed in the near future.

A utility FREY working group has been formed to participate in the V&V effort. Currently, Commonwealth Edison Company is taking the lead in establishing a FREY UGRA (Utility Group for Regulatory Application). A code design review followed by submittal of FREY to the NRC by FREY UGRA for a safety evaluation report (SER) are planned. Even though FREY has not been formally released, it has already been used by one utility in fuel procurement evaluation. Recently, the localized cladding corrosion has caused some BWR plants to reduce power ramp rate and operating power level. A BWR utility, using the unique characteristics of FREY, was able to model this asymmetric phenomenon and has analyzed fuel clad integrity under various ramp rates and operating conditions. Their FREY results, shown in figure 11, have provided them confidence in their power ascension maneuvering during the plant startup process.

### 3.3 A Qualified Core Thermal Hydraulics Code for Utility Applications

EPRI developed the VIPRE code in response to the utility industry's need for a publicly available, detailed thermal hydraulics code for the analysis of PWR and BWR cores. The code, based on specifications developed by a utility safety analysis working group drew from the strengths of the COBRA series of codes. After extensive prerelease testing, the utility group decided to use VIPRE for licensing submittals. EPRI set up a Design Review Committee of experts to review VIPRE code and documentation to ensure that it performed according to the original design specifications. The code was revised to incorporate the Design Review Committee's recommendations. Improvements include treatment of supercritical flows and iterations on the radial peaking factor for a specified minimum departure from nucleate boiling ratio. The VIPRE code has been extensively validated against data from rod bundle experiments, boiling heat transfer data, and critical heat flux tests. The code designated as VIPRE-01, MOD-01 is maintained under a quality assurance program in conformity with NRC regulations 10 CFR 50, App. B.

VIPRE-01, MOD-01 is widely used for the calculations of core safety limits such as minimum departure from nucleate boiling ratio, critical power ratio, fuel and clad temperatures and the coolant thermal-hydraulic state. Several utilities have prepared topical reports on thermal hydraulics analysis using VIPRE and two utilities (Northern States Power and Northeast Utilities Service Co.) have received safety evaluation reports from the NRC on their topicals.

Because of its large selection of two-phase correlations, VIPRE-01 can calculate flow behavior over a wide range of two-phase flow conditions in steady-state applications. In transient calculations, this empirical modeling of slip between phases and void quality relations can result in calculational instabilities in some applications. To overcome this shortcoming, a drift flux model option has been developed for VIPRE. In this drift flux, a fourth conservation equation for vapor mass continuity has been added, and the mixture momentum and energy equations have been modified to include drift

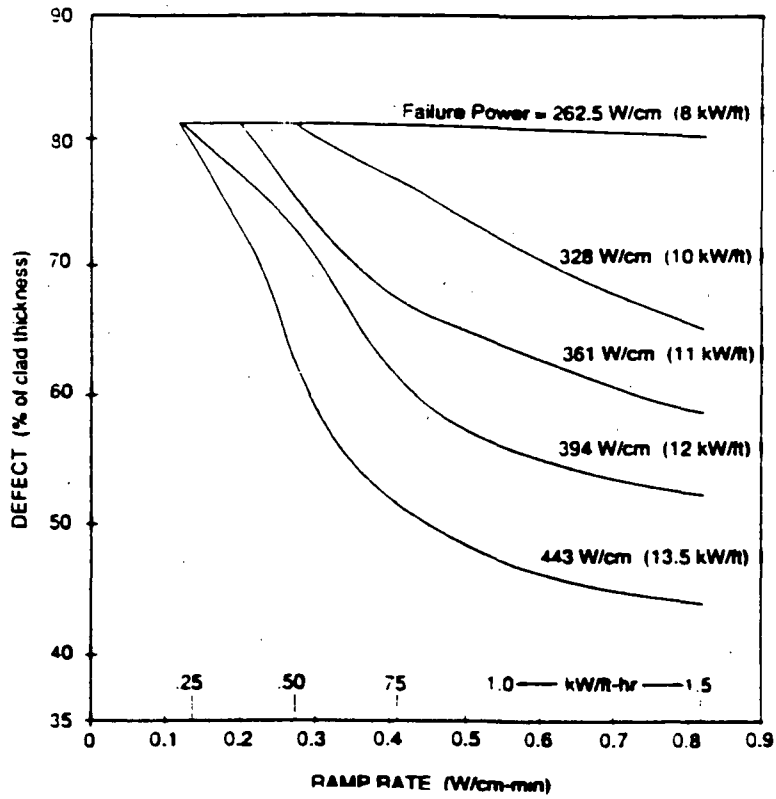


Figure 11. Defect Compared With Ramp Rate for Various Failure Powers.

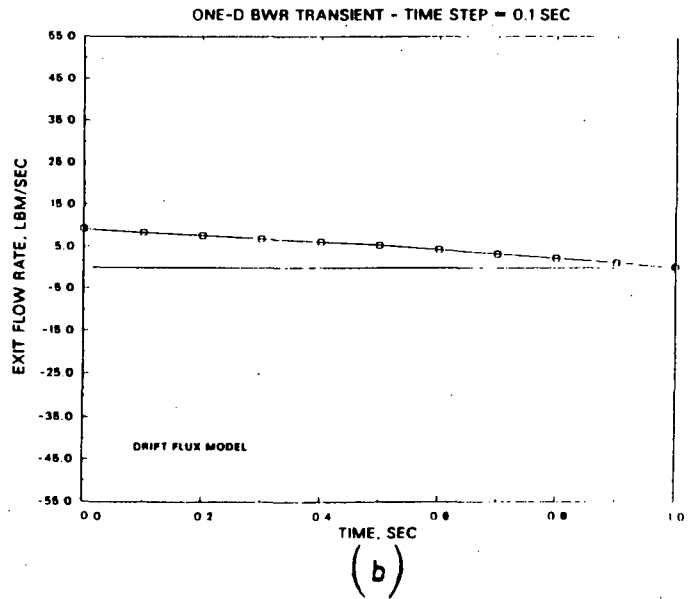
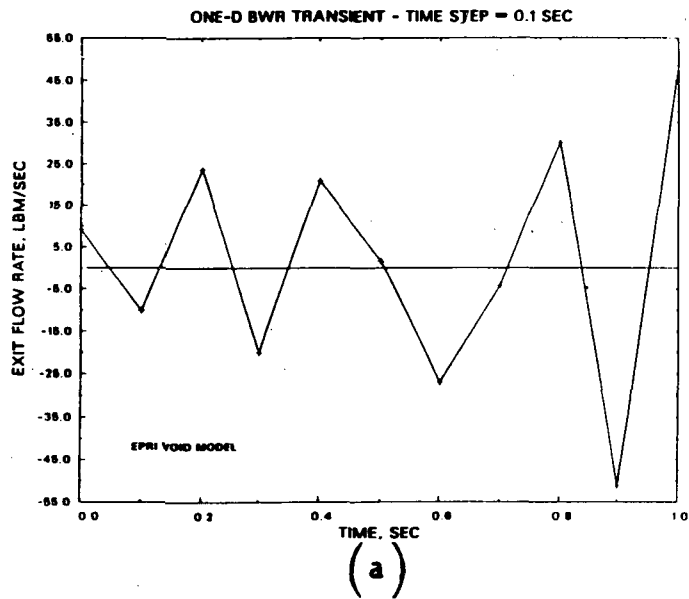


Figure 12. VIPRE Calculated Exit Flow Rate With (a) Homogeneous Model Using the EPRI Slip Model, (b) the Drift Flux Model.

terms (18). Two additional constitutive relations are needed to calculate the drift velocity and the vapor generation rate. The constitutive relations that have been selected in VIPRE are based on the work of Lellouche and Zolotar (19).

A test problem has been selected to demonstrate the effectiveness of the drift flux model in transient calculations. It consists of a one-dimensional representation of a BWR channel subjected to a loss of flow transient. The inlet flow is ramped down from 9.2 lbm/s to 0.92 lbm/s in 0.5 sec and the power goes down by a factor of ten in a corresponding manner. The results are shown in the form of exit flow vs. time in figure 12 for the VIPRE homogeneous model with slip and the VIPRE drift flux model. The homogeneous model with slip predicts an unphysical oscillation, whereas the drift flux model shows the expected behavior of flow decrease with time. The drift flux option in VIPRE has been validated against test data and will be available as VIPRE-01, MOD-02.

Further work in core thermal hydraulics is in the development of VIPRE-02 based on two-fluid modeling. A first version of the code capable of simulating PWR and BWR cores with a PWR vessel model will be available to the utility industry early next year.

### 3.4 Reactor Analysis Support Package (RASP); Validation for Simulator Qualification

The objective of the Reactor Analysis Support Package (RASP) was to give utilities an in-house calculational capability for doing fuel management calculations and plant transient/accident analysis. RASP consists of computer codes for neutronic and thermal-hydraulic analysis of core and plant behavior as well as a series of guidelines for the application of these codes, or similar codes. The major applications are the safety analysis for reload licensing and plant support analysis.

The availability of the RASP codes and linkage software makes it possible for utility users to perform their own analyses of nuclear steam supply system behavior and fuel performance. However, before embarking on a project to utilize these tools for plant support and/or reload licensing analysis, the utility should be aware of how these tools can be used to do event analysis, what requirements there are in terms of quality assurance and documentation, and what the procedure is for getting approval from the NRC to use the methodology for licensing analysis. Volume 1 of RASP, "Introduction and Overview," and Volume 10, "Guidelines for Developing a Reload Licensing Capability," give the utility analyst and manager the background needed to understand what must be done. The technical details, or how to apply the codes to do specific analysis, is explained in Volumes 2-9 of RASP. Taken together, they are invaluable to the analyst beginning to do analysis and a useful reference for the more experienced engineer.

One specific application of RASP is in simulator qualification. Following the TMI-2 accident, utilities have made increasing use of full-scope control-room simulators to train plant operators. Most simulators purchased by utilities

since then have possessed the technical capability required to represent abnormal events. EPRI and the nuclear utility industry continue to work to develop improved methods for qualifying nuclear control-room simulators. EPRI report NP-4243 presents guidelines for developing simulator evaluation criteria based on operator training objectives. Under RASP the development and testing of the engineering code RETRAN, which provides best-estimate response information to satisfy the NRC requirement for qualifying simulators, was documented.

The objective of the report (NP-5840) was to demonstrate the ability of the RETRAN code to provide best-estimate reference information for qualifying full-scope nuclear power plant training simulators.

The transient selection matrix documented in report NP-4243 shows the dynamic states important to the training environment. Existing RETRAN code transient analyses of 31 BWR and 50 PWR events were evaluated to determine the extent to which the RETRAN code experienced these dynamic states. A unique rating system, developed from an operator's point of view, noted when the RETRAN code predicted correct, incorrect, and incorrect but nonessential information, allowing investigators to measure the overall accuracy of RETRAN code predictions.

Evaluations of the 81 transient analyses cover essentially all the dynamic states, such as valve openings and control system actions, required for qualification of nuclear power plant full-scope simulators. Transient predictions made using the RETRAN code proved the code's ability to predict important system parameters--including reactor power, flow, and pressure--corresponding to plant instrumentation readings, with the fidelity required to qualify power plant training simulators.

The material in EPRI report NP-5840, along with the simulator qualification plan presented in EPRI report NP-5504, can help utilities qualify full-scope nuclear power plant control-room simulators. Composite ratings for the magnitude, timing, and trend measures indicate that utility engineers can use RETRAN event analysis with confidence.

### 3.5 ARROTTA Code Development

ARROTTA (20) is an advanced, state-of-the-art nodal code which performs three-dimensional calculations for steady-state and transient applications. It solves the two-group neutron diffusion equations with a coarse-mesh nodalization based on the QUANDRY methodology (21) and permits up to six families of delayed neutrons. Its thermal-hydraulic model, originally derived from the BEGAL-01 code (22), uses a single core pressure during a time step and is based on a three-equation model. Unlike most nodal codes, ARROTTA can perform calculations in which the core pressure changes from time step to time step. It permits two-phase flow, and its thermal-hydraulic model recently has been enhanced to perform calculations above the critical pressure based upon routines taken from the RETRAN-02 systems transient code (23).

The ARROTTA code has been well-exercised and validated against a variety of PWR static and slow transient calculations and experiments. It has been released for such slow transient analysis in IBM and CDC versions together with a substantially upgraded User's Manual and a preview of a Validation and Verification (V&V) document. Besides comparisons with standard advanced nodal static and transient benchmarks, the following core representations have been used for this V&V: Zion Unit 2, Catawba Unit 1, a generic CE core, and three Westinghouse three-loop plants. The following V&V has been performed:

- A. Power distribution, ITCs, and control rod worths have been compared with PDQ.
- B. Power distributions, including gamma scans, ITCs, and peak xenon calculation have been compared with assorted reactor measurements.
- C. A PWR natural circulation transient has been analyzed using static ARROTTA and RETRAN calculations in tandem and then was reanalyzed using ARROTTA in the transient mode driven by forcing functions edited from RETRAN. The results of the (ARROTTA) RETRAN analysis and the ARROTTA reanalysis are shown in figure 13 (derived from reference 24).

Furthermore, ARROTTA, with other codes, is being applied in a design basis accident project for both rod ejection accident and also steam line break transient studies in cooperative efforts with two utilities.

During its BoL testing (25), as part of the "below bank rod test," Duke Power's Catawaba-1 plant had a single asymmetric control rod inserted into the core long enough to excite upon removal a full-core xenon oscillation. Due to the placement of the external detectors on the diagonals in the Catawaba plant, it is most accurate to use the two assemblies straddling the diagonal which are closest to the detector location as a measure of the normalized detector response to this spatial transient. The analytic equivalent of the detector normalization is obtained by dividing the two edge assembly powers in the maximum power quadrant by the core average of these edge powers, thus the Maximum Edge Tilt (MET).

The ARROTTA-generated MET reproduced both the period and the amplitude of the data quite well as shown in figure 14. Not only do these calculations demonstrate the ARROTTA spatial xenon transient capability, but dramatically show the consistent correlation between edge assembly powers and ex-core detector response.

A standard PWR nodal code, NODE-P2 (26), was also used to calculate a MET for this event. NODE-P2 reproduced the time scale of this oscillation well, but did a poor job at matching experimental MET as shown in figure 14. The NODE-P2 predictions of MET were consistently low. NODE-P2 does accurate core follow analyses, including equilibrium xenon, upon proper normalization to higher order calculations. However, this type of extreme asymmetric oscillation is beyond its basic core-follow capability.

# Natural Circulation Transient

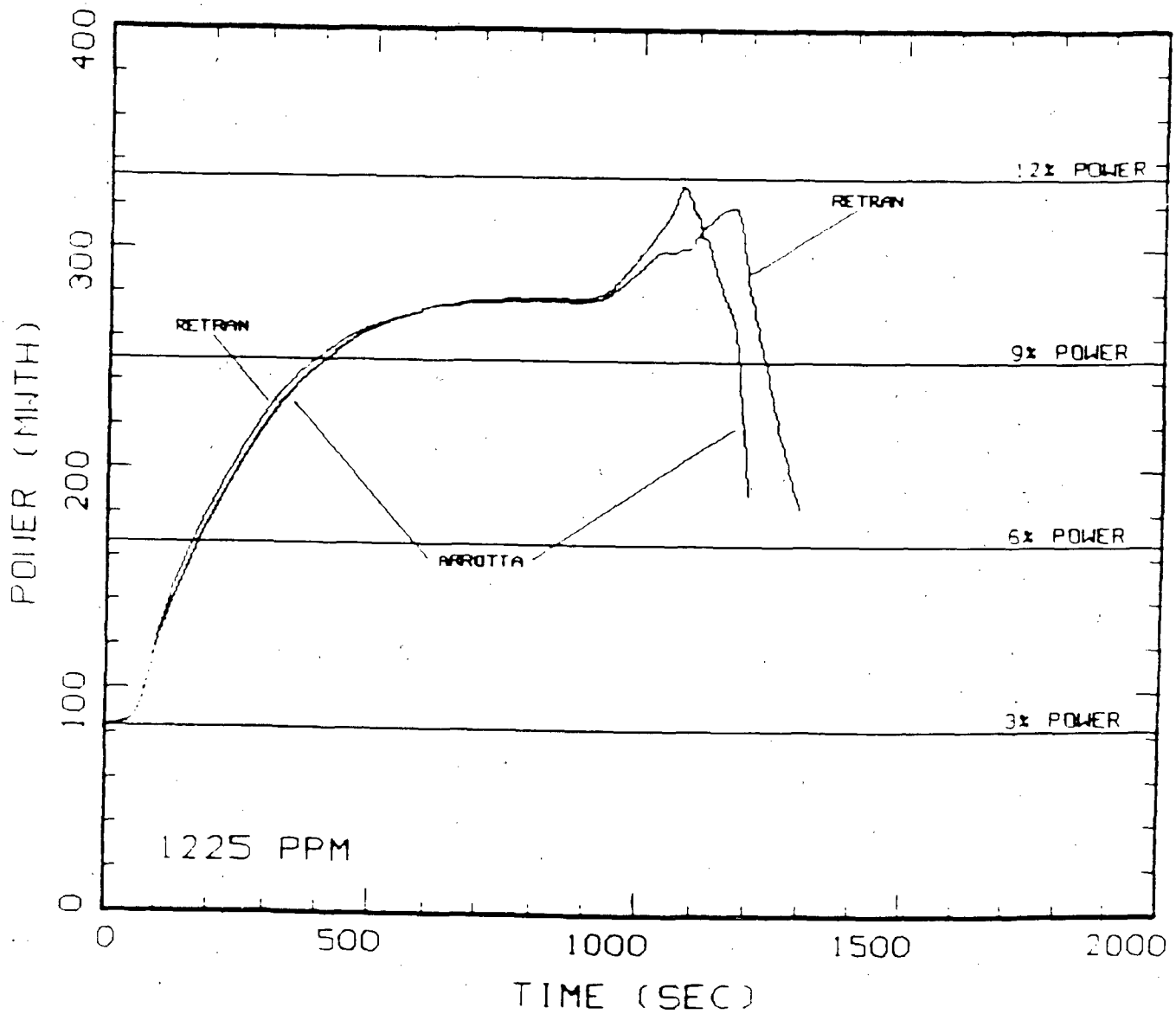


Figure 13. RETRAN vs. ARROTTA Power.

CATAWBA XENON OSCILLATION

ARROTTA & NODEP-2 MET vs. EXPERIMENT

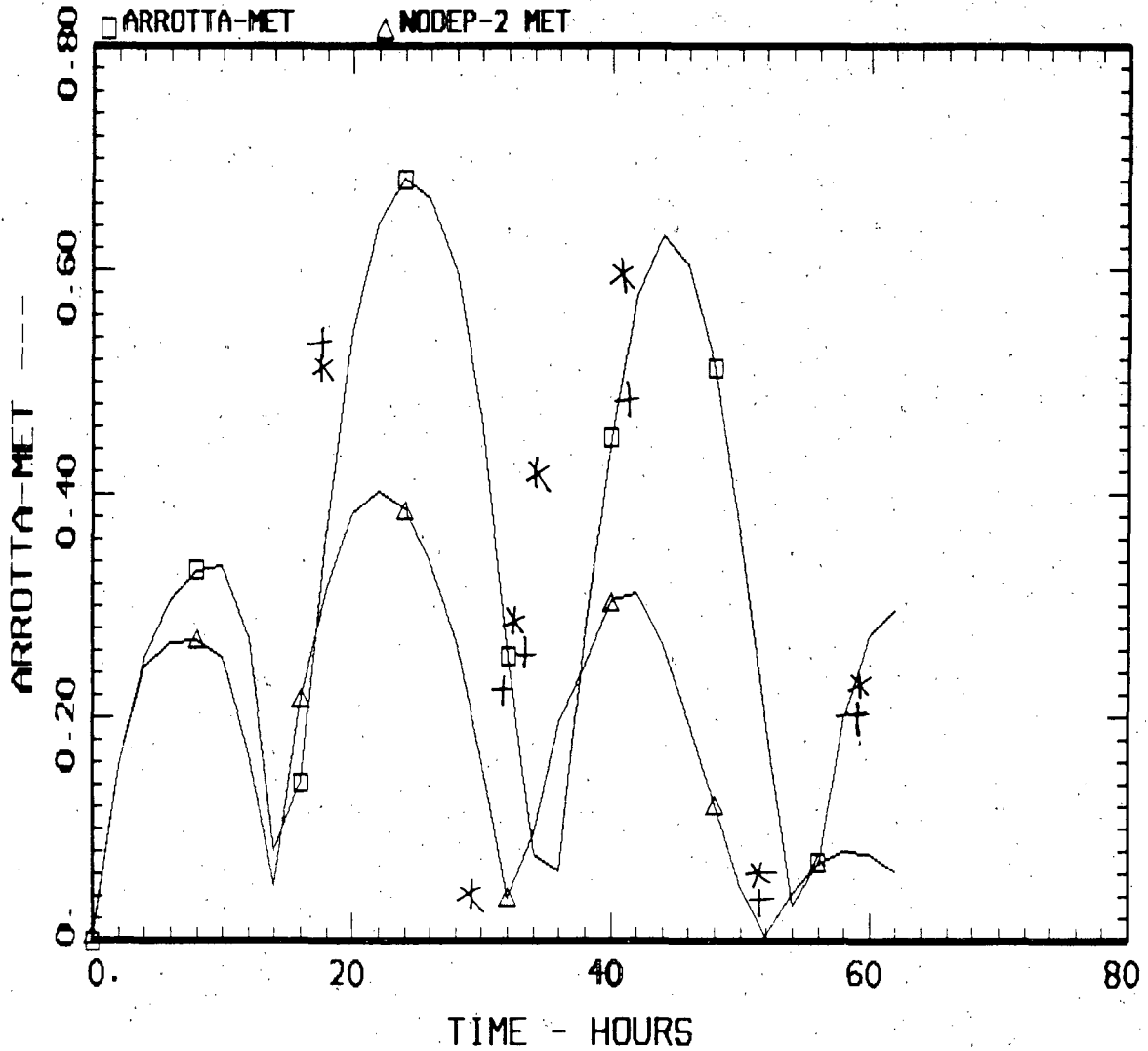


Figure 14. Catawba Unit I Xenon Oscillation.

The superiority of the advanced nodal methodology of ARROTTA versus the standard nodal methodology of NODE-P2 is based on the difference in the neutronic modeling inherent in the two programs. ARROTTA has a true two-group flux solution and an explicit spatial representation of the reflector regions while NODE-P2 simply uses leakage factors (albedo-like quantities) that are constant throughout the event. This approximation for the reflector tends to damp out the amplitude of such radial oscillations, that is, the reflector boundary conditions tend to enforce symmetry over the full core even when it is not appropriate.

### 3.6 LWR Set Point Methodology Demonstrations

Reactor instrument settings or set points are those instrument limits at which a system automatic or operator manual operation must take place to preserve the assumptions of the plant safety analysis. The specific process used to establish the set points is important because it is necessary to satisfy the applicable plant safety and licensing requirements without restricting plant capacity and operation flexibility. The output of set point methodology demonstrations is a set of verified instrument settings that optimally satisfy the plant safety analysis requirements. This is accomplished by identifying the uncertainties in key variables which affect the particular instrument setting, and combining these uncertainties by use of a statistical combination of uncertainties methodology to evaluate the optimal safety margin.

The primary objective of this effort is to document specific applications of the generic set point methodology guidelines developed under the Reactor Analysis Support Program (RASP). The use of different plant designs and utility participation are key factors in the selection of the demonstration projects. The emphasis in the demonstrations will be the use of statistical combinations of uncertainties (SCU). It is expected these applications will extend the existing capability to show how gains in operating margin, extensions in surveillance intervals, etc., can be made.

One of the initial applications of the RASP set-point methodology was in the modification of the high-pressure set points of GPUN's Oyster Creek plant to gain margin to compensate for the set-point drift experienced during plant operation. Concern was expressed over the plant's inability to accommodate instrument tolerances and drift without violating technical specifications or overlapping the high-pressure set points. In addition, there is a lack of documentation for the basis of existing high-pressure set points. Two potential approaches considered were: (i) replace existing pressure switches with costly analog instrumentation, and (ii) justify a modification of the current set points by doing a set-point analysis. GPUN chose the second alternative.

The generic set-point modification process is indicated in figure 15. The first task was to identify all set points that would be affected by a change in the high-pressure set point. The next main task was to identify all events that would be affected by the set-point change and develop event acceptance criteria. This process will establish all those events which are potentially limiting. A baseline analysis performed by using RETRAN with variation in the

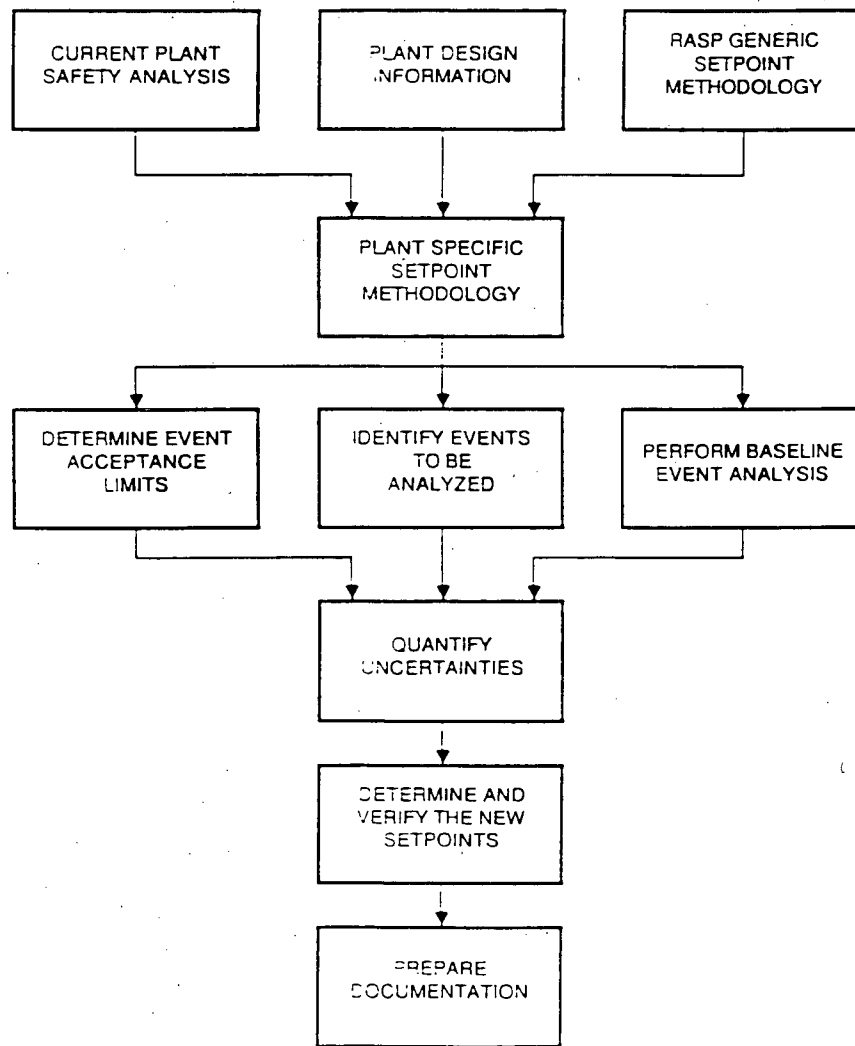


Figure 15. Set Point Modification Process.

input parameters identified the key parameters. The most important task is the uncertainty analysis which determines the total uncertainty in the set-point value by combining the uncertainties in the key parameters. The treatment of the uncertainties can be performed by deterministic, statistical or a mixed approach. In this case, a mixed approach was used. The final steps are to verify the acceptability of the proposed set-point changes from the plant operation viewpoint by means of a statistical assessment, and to verify the adequacy of the set-point changes from a regulatory standpoint by performing an analysis of the license base events.

This work is at the final stages of completion and a detailed report will be published in the near future.

#### 4.0 SYSTEMS RELIABILITY ANALYSIS AND ACCIDENT MANAGEMENT

##### 4.1 Operator Reliability Experiments

The importance of including operating crew actions in estimates of plant risk has become increasingly clear in the years since the TMI-2 accident. However, almost no data specific to nuclear plant accident situations was available. It appeared that plant simulators, with crews undergoing requalification training using realistic accident sequences, could offer a significant source of cost-effective data. Such data would enable a model or at least a correlation to be structured that could account for many of the ways operators could either cause accidents or recover from them.

Early research in previous EPRI projects produced ideas for correlating success of operating crew actions to the time taken and to the complexity of the cognitive processing required. Support for this human cognitive reliability correlation (HCR) was obtained in 1984 from small-scale tests and fragmentary simulator data. Greatly expanded simulator experiments using EPRI member utility facilities and crews during requalification training was expected to provide the necessary refinement of the approach and validation. The objectives of this project were therefore: (1) To develop models of operator reliability for control room decisions and actions, (2) to obtain data to validate the models mainly using plant simulators, and (3) to assist the evaluation of training, procedures and of other post-TMI benefits such as changes to control-room design.

Six U.S. utilities are cosponsoring the experimental work. The main thrust is to use simulator data to validate a model or correlation of crew success probability as a function of time for use in risk assessment. It was recognized that qualitative information would also be obtained that might be of value to training or other utility programs (e.g., improvements to EOPs). The current program has succeeded in acquiring a large database (>1,000 data points) of relevant quantitative performance information. Most of the hypotheses underlying the EPRI human reliability model (HCR model) have already been verified using the data; others are being refined according to the experimental results. The current status of data acquisition and HCR hypothesis testing is shown in tables 2 and 3. It is already clear, nine months before the end of project date, that the original objectives of

Table 2  
STATUS OF SIMULATOR DATA STATISTICS

<u>Simulator</u>	<u>Number of Scenarios</u>	<u>Number of Crews</u>	<u>Nof. of HIs</u>	<u>Total No. of Qualified Data Points</u>
PWR1	3	10	10	95
BWR1	2	18	10	137
BWR2	7	3-10*	13	125
PWR2	7	6	30	167
BWR3	8	5-7*	12	130
BWR3 II	6	9	15	125
PWR1 II	6	15	15**	200**

HI means "Human Interaction."  
 \*Scenario-dependent.  
 \*\*Estimates.

Table 3  
STATUS OF HCR HYPOTHESES TESTING ANALYSES

<u>Hypothesis</u>	<u>Status</u>
Time dependence	Valid
Single parameter does normalization	Valid
Median performs well	Valid
Discrete correlation groups appear	Valid
S,R,K characterize groups	?
Weibull and/or lognormal	Valid
PSFs impact quantifiable	Invalid thus far

S,R,K mean 'skill', 'rule', and 'knowledge', respectively.  
 PFSFs mean 'performance shaping factors'.

the project will be attained. Feedback of interim results, both quantitative and qualitative, to participating utilities has drawn strong support from training managers and PRA groups. The project is not far off its original schedule, a delay of three or four months being experienced due to the much larger quantity of data assembled than anticipated, a change of contracting organization by the key personnel and a burgeoning of the non-PRA uses of the qualitative information that has been developed so far from the data.

Figures 16 and 17 show the aggregated data from PWR and BWR plants respectively. Note that the ordinate scale reaches to probabilities of order  $10^{-3}$ .

The data and its comprehensive qualitative and statistical analysis has been issued, in proprietary form, for international peer review. It is expected to have a large impact on the quantification of human actions in a PRA or an IPE (individual plant evaluation).

Beyond the objectives of the original PRA, qualitative insights have been obtained that (1) identify crews with much larger than average variability in response, (2) identify sequences with much larger than average variability in crew response that may require more training or attention to procedures, (3) identify the existence of different strategies in interpreting a procedure, the degree of difference in performance between the strategies and which crews are following which strategy, and (4) identify where specific parts of an EOP are consistently causing performance problems, and by how much. These are just a few of the specific training uses already revealed. They have not yet been rigorously investigated using all the data available. Similarly, no work has yet been done on the number of operator errors, their types, causes, corrections and effects on performance. There is a good chance that additional planned work on these topics will reveal considerable benefits.

During 1988 and 1989 the project will focus on completing this analysis with only modest effort on increasing the amount of experimental data.

#### 4.2 Aid to Plant Operations

The project, entitled "Use of SRA Methods for Enhancing Plant Safety and Availability," is an important R&D endeavor at EPRI. It is intended to develop a practical software tool which combines key features of plant information management systems with applications of system reliability techniques and modern computer technology to relieve the work burden on plant personnel and engineering staff and assist plant management to make more accurate and timely decisions regarding plant safety and productivity. Specifically, this software, Reliability Assessment Program with Integral Data (RAPID) will: (1) resolve many technical difficulties of maintaining an up-to-date probabilistic risk assessment (PRA); (2) aid operators in complying with technical specifications; (3) provide equipment outage tags in consultation with technical specification requirements; and (4) reduce the number of unplanned scrams and, ultimately enhance availability.

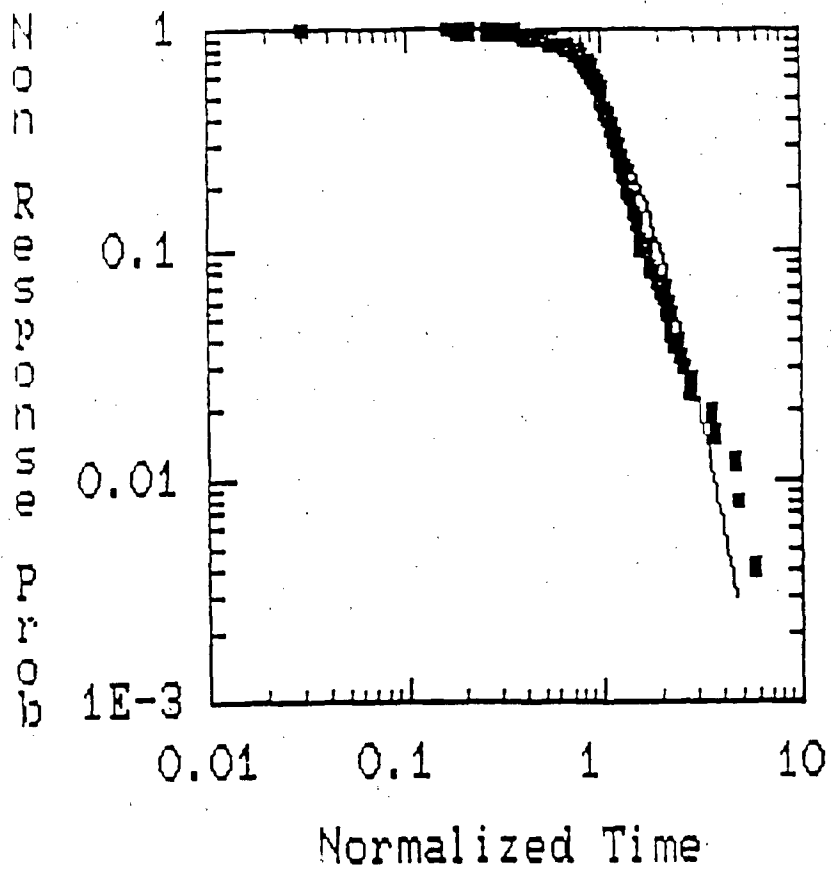


Figure 16. PWR Aggregate Time Reliability Curve.

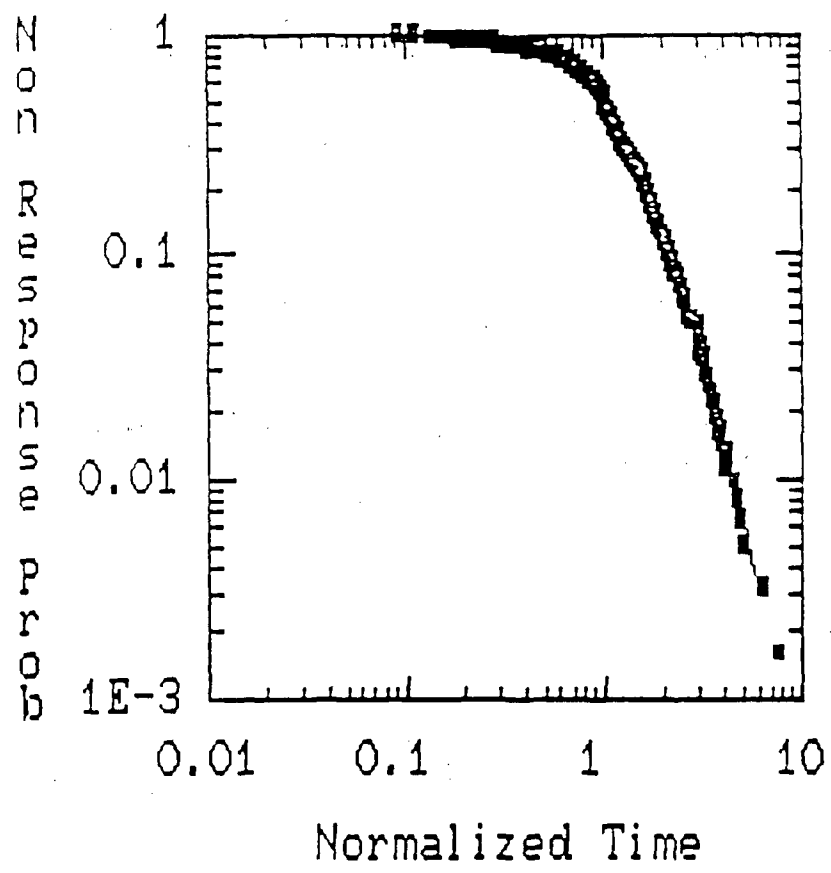


Figure 17. BWR Aggregate Time Reliability Curve.

The RAPID software performs a broad range of functions which include on-line activities for addressing plant O&M assistance and off-line for performing basic reliability engineering and data compilation tasks. Two major applications modules, plant status monitoring (PSM) and reliability assessment/utility modules (RAM/UM), are being demonstrated. The RAPID/PSM is a tool to aid plant management, operations and maintenance personnel in monitoring and assessing the operational status of their nuclear power plant. The reliability assessment module (RAM) has been developed to provide a computerized environment for performing a broad range of basic probabilistic system analysis functions. The utility module (UM) provides the interface between RAPID and automated or manual plant information management systems. The UM software acquires data from the plant information system, if any, and converts it, when necessary, for use in RAPID. The emphasis is to demonstrate that a "living" level I PRA study can be a reality without imposing an undue burden on the PRA staff. The core RAPID software has been operational since 1987.

The transfer of RAPID technology to EPRI member utilities has been conducted using a phased approach. Each phase has produced software with additional capabilities, and features, as well as enhanced maturity. The first phase, or demonstration phase, was conducted at two host utility sites to install the first working versions of RAPID modules. The Plant Status Module was developed as a stand-alone system and installed at GPUN's Oyster Creek Nuclear Generating Station. The RAM, UM and DBM modules were installed at Arizona Nuclear Power Project (ANPP).

Following the demonstration phase of the RAM/UM/DBM modules, a two-day workshop was held in April 1987 at ANPP for EPRI utility members. The second phase for these RAPID modules was then initiated from interest developed during the workshop. Southern California Edison, Carolina Power and Light, and Duke Power are hosting second round demonstrations of the RAM/UM/DBM modules. In addition to technology transfer, RAPID has been converted for use with state-of-the-art database management systems (DBMSs): IBM's DB2 and ORACLE's ORACLE. During this period, PSM has also been modified to run with DB2. It has been installed in a production mode at Oyster Creek. In addition, new features have been incorporated, including a tagging system and an interactive graphics interface for displaying system schematics. Presently, about a dozen additional EPRI member utility companies as well as foreign establishments such as EDF have requested RAPID software. The mainframe version of RAPID is ready to be released and will become available from EPRI's Electric Power Software Center in 1988. Technical enhancements are still being made to expand RAPID application modules. Most noticeable effort has been the activity to migrate the mainframe RAPID to IBM PS2/System 80 with AUTOCAD features activity. The microcomputer version of RAPID is scheduled to complete its Beta testing by 1989.

#### 4.3 PRA Software Development

Since the recognition by the utility industry of the potential value of PRA following the TMI accident, EPRI has taken leadership in developing analysis software and training for utility engineers.

The WAM-E and CAFTA software packages are available to solve, quantify, and use large fault tree and event tree models for nuclear plant systems analysis (27, 28).

The WAM-E package is an enhancement to the established WAM family of fault tree analysis codes. This mainframe suite of 7 codes (WAM3AM, WAMTAP, WAMCUT, WAMCUT II, WAMFM, WAMMRG, AND SPASM) provides accurate top-event failure probabilities, cutsets, uncertainty analyses, and accident sequence quantification by iterative use of the various codes.

The CAFTA code is PC workstation software that aids utility engineers to build, modify, quantify, and edit the cutset results of fault trees. The code was carefully designed to overcome the most serious inefficiencies encountered in previous PRA analyses. The code helps eliminate rework, modeling errors, data inconsistencies, and model inconsistencies that have previously plagued large PRA projects. Most importantly, CAFTA provides a structured environment for managing all the steps in the fault tree analysis process. The latest CAFTA version uses the power of the "386" PCs to solve large fault trees. CAFTA also prepares input and accepts output from the WAM-E codes.

#### 4.4 Accident Management

In addition to the above work on traditional elements of systems reliability and risk analysis, we have initiated the development of a strategy, and of both industry and related program objectives, in the subject of accident management. This issue has a high priority during 1988 and 1989 as a NUMARC undertaking and as a result of NRC's forthcoming requirements on accident management as an adjunct to utility disposition of IPE findings.

NUMARC's Severe Accident Working Group (SAWG) is defining an industry policy and position on Accident Management for presentation to the NRC. The SAWG initiative is anticipated to ensure a realistic approach for the industry program. EPRI's role, through the Systems Reliability Program, is to provide technical support to the SAWG effort. Our initial strategy is to propose definitions and concepts as the basis for an Industry Accident Management Program. Feedback from the SAWG, the Safety Technology Task Force, and from EPRI member utilities will help to revise and sharpen the focus of the framework. An EPRI utility and a contractor are currently evaluating the technical and organizational elements that will make up an operational definition of the industry's Accident Management Program. At the same time, EPRI is initiating work to review and compile results of previous industry technical work that can be useful to utilities in setting up their programs. This will also include guidelines for the development of coping plans. Coping plans will address the processes by which a utility, faced with a core threatening situation, will take action during and after the execution of Emergency Operating Procedures to prevent vessel and containment failure and to minimize the total release of radioactivity to the atmosphere. Clearly, coping plans will include activities of the Technical Support Center and must interface with existing Emergency Management actions.

The industry program is expected to reach the end of its definition phase by early in 1989. EPRI anticipates the need for increasing R&D support to the NUMARC initiative in this area during the next three years.

## 5.0 SEVERE ACCIDENT STUDIES

During the past year the Source Term Program has been active (1) in completing the LACE Program and in formulating the ACE Program, (2) in studying the PWR upper internal and primary system flow distribution and (3) in a number of activities related to the MAAP code. These activities are reported on below.

### 5.1 F. P. Behavior in RCB and PCS

**5.1.1 Marviken/DEMONA/LACE.** Extensive efforts have been made in recent years to understand aerosol behavior in nuclear reactors during severe accidents. In particular, there have been three large-scale experiments to study aerosol behavior in the primary systems and reactor containment buildings associated with water reactors. Formation, transport, and deposition of aerosols which simulate radioactive ones were studied in the Marviken-V Aerosol Transport Tests (MARVIKEN-V) in Sweden, the Demonstration of Nuclear Aerosol (DEMONA) Behavior Program in the Federal Republic of Germany, and the LWR Aerosol Containment Experiments (LACE) in the United States of America. Data were obtained for use in computer code development and testing. These experiments, representing an investment of more than \$30 million, were performed between 1981 and 1988 and were sponsored by three consortia consisting of up to 16 research organizations from countries in Europe, North America, and Asia, including EPRI (and NRC) who were cosponsors of each of these programs.

The cosponsoring parties recognized that further benefits could be gained by a workshop to review the results of the three projects collectively. The objectives of the workshop were to examine the main results from the experiments and the associated computer modeling and support studies and to compare the data from all three programs so that the state of knowledge of the relevant phenomena could be determined. The workshop took place from June 28 to July 1, 1988, at Montreux. About 90 experts from the sponsoring parties participated in the meeting, which was organized by the Paul Scherrer Institute, Villigen-Würenlingen, Switzerland.

A full report on the findings made during the workshop will be issued in the first part of 1989. The major conclusions of the workshop were as follows:

- Significant progress has been made in the last eight years and a sound technical basis now exists for understanding aerosol transport in the primary systems and reactor containment buildings of water-cooled nuclear reactors during major accidents.
- The MARVIKEN-V, DEMONA, and LACE projects were successful in establishing a technical basis on aerosol behavior and thermal hydraulics. As a result of these projects extensive databases on aerosol removal and related thermal hydraulics are now available.

- Many aspects of aerosol processes are much better understood today than they were even a few years ago.
- The programs greatly improved our ability to perform large-scale aerosol experiments and to analyze the results from such experiments.

The experts at the workshop discussed many aspects of aerosol physics, chemistry, and thermal hydraulics. A consensus was achieved among the experts on the following four technical points:

- Processes leading to aerosol removal from the atmosphere of containment buildings are well understood. Sedimentation is the dominant removal mechanism. Condensation of steam significantly enhances aerosol deposition in water reactors.
- Deposition of aerosols in pipes and other volumes characteristic of the primary system (such as pressurizers) was investigated. Although we believe that processes leading to deposition in pipes appear to be adequately understood, they have not yet been adequately modeled in all instances. An extensive amount of experimental data now exists which can serve as the basis of future modeling activities and the development of correlations.
- Major progress has also been made in the development of computer codes capable of predicting aerosol transport and removal. Computer codes have now been extensively tested over a broad range of conditions. In the LACE program, these efforts included the testing of the codes under so-called "blind" conditions. In particular, the aerosol code comparisons for the containment tests illustrated that the codes that included steam condensation effects gave reasonable representation of the results from the tests.
- The workshop identified that knowledge of thermal-hydraulic conditions is important in calculating aerosol transport. It appears that the major constraint is the ability to specify the details of the scenario to be calculated. An important result of the code comparison efforts was an improvement in the skill of the code users.

In summary, the workshop concluded that the MARVIKEN/DEMONA/LACE experimental programs were highly successful and resulted in an improved understanding of the behavior of radioactive particles during severe nuclear reactor accidents.

5.1.2 ACE Program. A new series of Advanced Containment Experiments (ACE) has been started at Argonne National Laboratory and in the Containment Systems Test Facility (CSTF) at Battelle-PNWL, Hanford Engineering Development Laboratory. Technical support and related experiments are being provided by the cosponsoring organizations. The ACE program will complement the recently completed LWR Aerosol Containment Experiments (LACE) Program by investigating additional fission-product production and deposition phenomena involved in degraded reactor containment building (RCB) conditions and means of controlling fission-product release using passive filtering devices. The objectives of the ACE program are: (1) to provide a comparative experimental basis for filtration techniques (e.g., submerged gravel beds, water pools, sand beds, etc.), (2) to provide data for modeling radioactive iodine species transport, (3) to determine fission-product releases from molten corium concrete reactions, and (4) to develop and validate the applicable computer codes and models. The work is being cosponsored by 16 organizations: VTT (Finland), CEA (France), PSI (Switzerland), ENEA (Italy), JAERI (Japan), AEA (UK), OH (Canada), GRS (FRG), UNESA (Spain), JEMA (The Netherlands), Kurchateo Inst. (USSR), ABBA (Sweden), and Westinghouse, NRC, DOE, and EPRI (USA).

The ACE Program is divided into three phases. Phase A seeks to compare filtration techniques for aerosol removal as in containment environment scrubbing systems. Six types of filtration systems (pools, submerged venturi, submerged gravel scrubber, fiber metal, heat sink gravel bend, and sand bed) are being studied in 18 separate tests. The tests study decontamination factors and other key parameters (spectrum size, etc.) for a mixed CsOH/CsI/MnO aerosol system. Ten experiments have been performed to date.

Phase B, still in its planning stage, will consist of large-scale experiments on iodine behavior to be performed at Hanford with related small-scale experiments planned at Whiteshell Laboratories and ORNL. The key issues being studied are:

- Behavior of CsI aerosol mixtures in moist atmospheres.
- Interaction of vapor species with aerosols.
- Effects of H<sub>2</sub> burning on iodine speciation.
- Accident control and recovery measures.

The experimental program has just been started and is scheduled to run through 1990.

Phase C is studying the interaction of molten corium with concrete. These tests involve ~300 kg of molten corium with simulated fission products and varying amounts of structural materials (e.g., Zr) and control materials (e.g., B<sub>4</sub>C, AgInCd). The objectives of these experiments are:

- To measure the release of semivolatile fission products (species of Ba, La, Sr, etc.).

- To characterize aerosols produced.
- To determine concrete ablation rates.
- To coordinate computer code validation efforts.

Recently, the first of the eight experiments in the test matrix was completed (along with experimental validation of the test apparatus). Ten smaller-scale tests involving ~30 kg of molten corium were completed in March 1988. These data are currently being analyzed. About one large-scale (300 kg) test per quarter will be performed through 1990.

## 5.2 PWR Upper Internal and Primary System Flow Distribution Testing

The general objective of the experimental part of this program is to provide pertinent data on flow patterns and velocity and temperature distributions for natural circulation flows in a PWR PCS during postulated high-pressure severe accidents.

5.2.1 Approach. A 1/7-scale model of a Westinghouse four-loop reactor system, shown in figure 18, was used to perform the experiments. The model is comprised of a one-half section of the reactor vessel (sliced through a vertical, nearly diametral plane), hot legs and two steam generators. The slice place is covered with a transparent window to permit flow visualization and use of a laser-doppler anemometer to measure velocities. The core is simulated with electrically heated rods placed in an "egg-crate" type structure, containing slots, that models the flow resistance of fuel assemblies. Water and sulfur hexafluoride ( $SF_6$ ) were used as analog fluids. Water tests enabled visualization of flow patterns through injection of a dye. Complete thermal-hydraulic similarity between the model and the prototype, for high-pressure severe accident conditions, can be achieved with moderately pressurized  $SF_6$  gas. However, in the initial phase of the program reported here, all tests were performed at 1 atm pressure. To accomplish the objectives, a number of steady-state tests with water and  $SF_6$  gas, and a few transient tests with  $SF_6$  gas, were performed. Fluid temperatures were measured at 132 locations in all tests. In several steady-state water tests, recirculation flow patterns were observed visually. Heat deposited by the recirculation flow in the cooler regions above the core was also measured. Based on the measured temperatures and rates of heat deposition in the cooler regions, recirculation flow rates and velocities were calculated. In some water and  $SF_6$  tests, flow velocities were also measured directly at several locations using a laser-doppler anemometer. By using the data from these atmospheric pressure tests and scaling laws, flow patterns, velocities and temperatures expected in the future high-pressure tests have been predicted.

A forty-nine tube model acrylic (transparent) steam generator was constructed and substituted for one of the simulation steam generators. It provided visual evidence of the natural recirculation in some tubes from the inlet to outlet plenas and return flow in the remainder of the tubes. Flow initiation from an unstable equilibrium was observed. The fluid dynamics of stratified hot leg flow, mixing in the inlet plenum and tube bundle of flow were correlated using simple models and the experimental results.

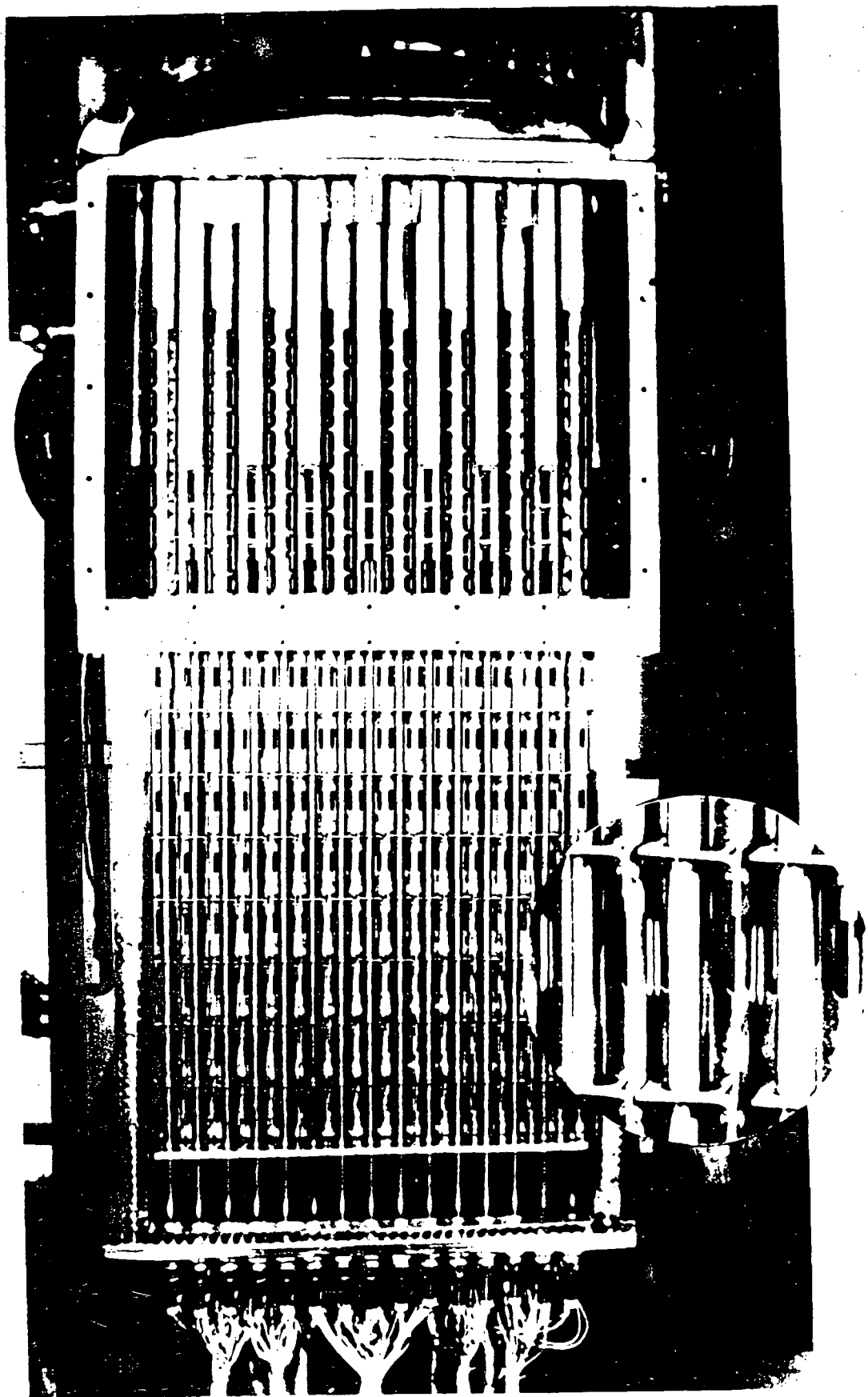


Figure 18. Front View of the Experimental Reactor Model.  
Inset Shows Core Construction.

5.2.2 Some Results. Water recirculation flows were observed visually in the vessel and the hot legs. The hot flow ascended in the middle and cold flow descended at the core periphery and moved across the heater rods to the middle of the core. The upper plenum was found to be quite well mixed. The upper plenum hot fluid was found to flow to the steam generators in the upper half of the hot legs. The lower half of the hot legs was occupied by the cold fluid returning from the simulated steam generators. A characteristic inclined separation plane was observed between the hot and cold flow streams. This configuration was found to maximize the flow to the steam generators.

The measured temperature distribution in one of the water tests is shown in figure 19. The measured temperatures conform to the visual flow observations. The corresponding velocities measured with LDA are shown in figure 20. Very similar results are obtained in the SF<sub>6</sub> steady-state experiments.

The 49-tube acrylic steam generator was connected to one of the hot legs and the flow patterns observed by adding a dye. A most interesting flow field was observed, namely, the hot flow entering the steam generator inlet plenum mixed with some of the cold fluid resident there; however, a thermal front was established in the tubes and some of the tubes (approximately one-third) carried the buoyant fluid to the cold plenum of the steam generator. Continuity considerations prompted cold plenum fluid to return to the hot plenum as a cold stream through the rest (approximately two-third) of the tubes. Thus, the steam generator mass participated in the heat exchange process that the hot fluid from the core undergoes with the the PCS. The measured temperature distributions in the steam generator plenum and tubes are shown in figure 21. Tests with the 49-tube steam generator were also performed with SF<sub>6</sub> as the simulant fluid.

The safety relief valve venting tests were performed with the 49-tube steam generator connected to the right hot leg in which the SF<sub>6</sub> venting took place. Changes in the thermocouple temperatures were observed. In the case of single vent tests (8% of SF<sub>6</sub> withdrawn rapidly; then vent closed), hot upflow, instead of cold downflow, resulted in the core periphery next to the right hot leg for the duration of the vent flow. The original flow patterns were reestablished soon after the vent was closed. The vessel temperatures showed very little change in regions away from the hot leg.

In the case of periodic venting, the steam generators transferred 50 to 75% more heat, since they were receiving a forced alternating flow through the tube bundle and the plenum.

In the tests with He addition and SF<sub>6</sub> withdrawal, heated (to same temperature as SF<sub>6</sub> at injection location), a large amount of He was introduced in approximately 40 seconds. The He concentration in the upper plenum was measured as a function of time. A temporary stratification was found to occur and the hot leg flow was disturbed. It was found, however, that He mixed reasonably fast and the natural circulation flow fields were reestablished.

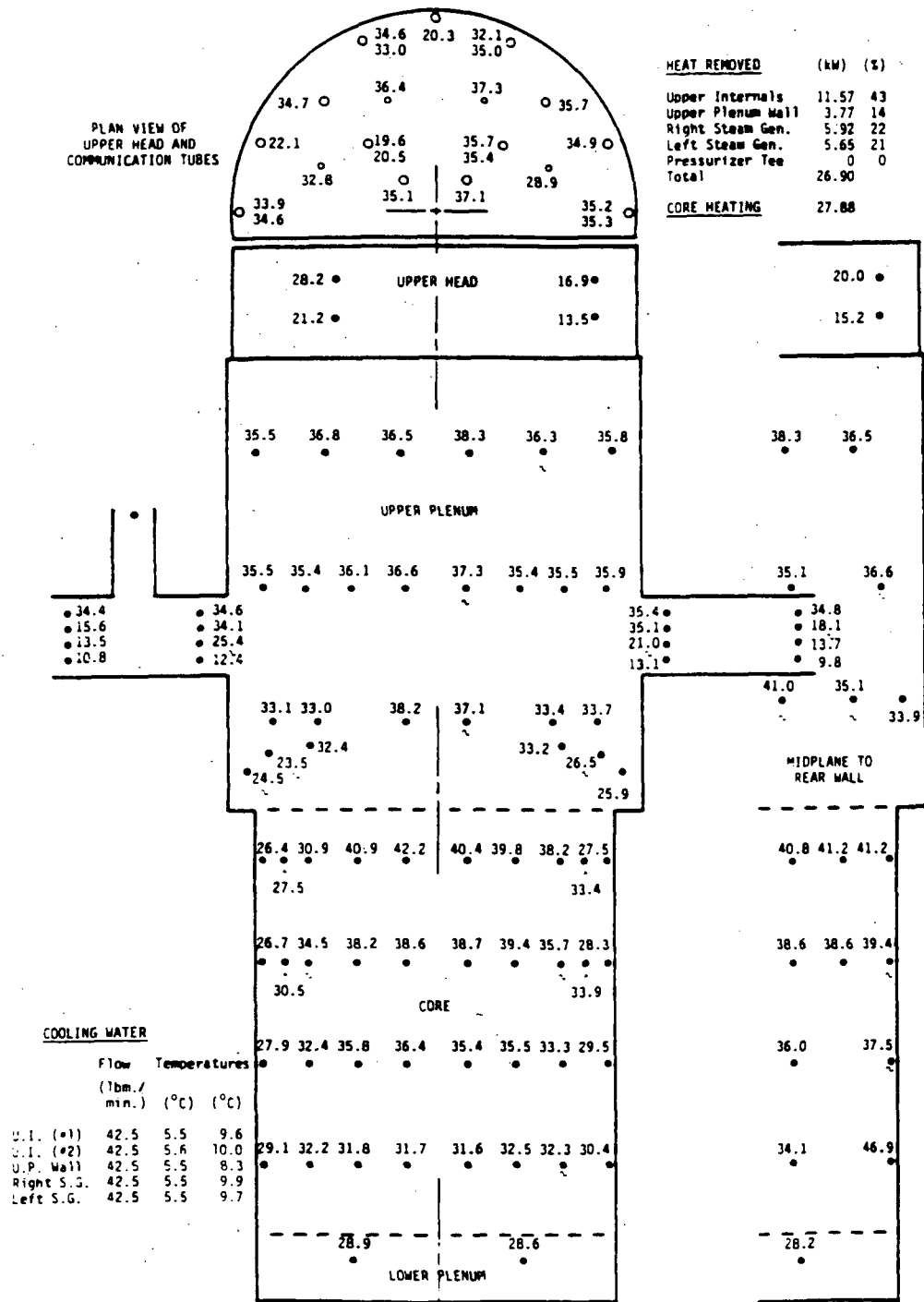


Figure 19. Test No. 5. Temperatures (°C) of Water in Reactor Model. High Cooling by Steam Generators.

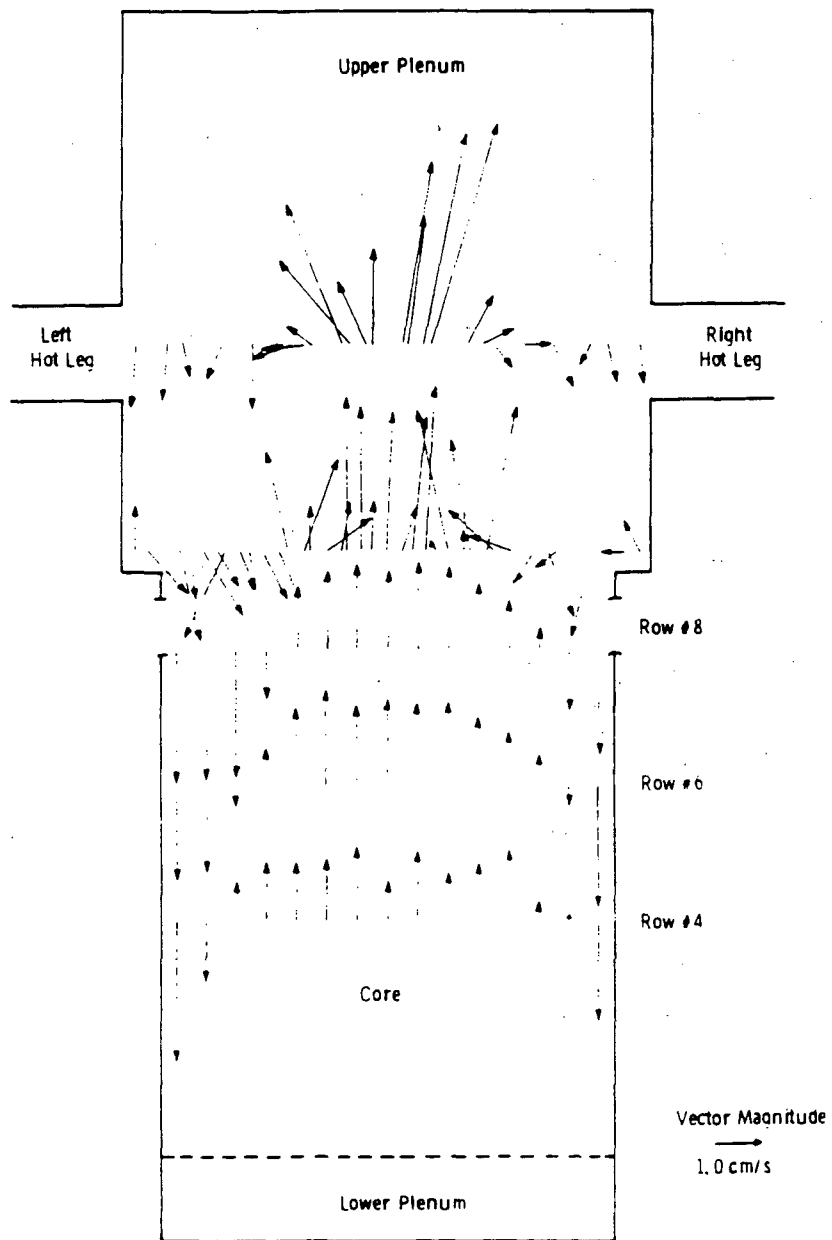


Figure 20. Velocity Vectors With 28-kW Input into Water and With Steam Generators Connected.

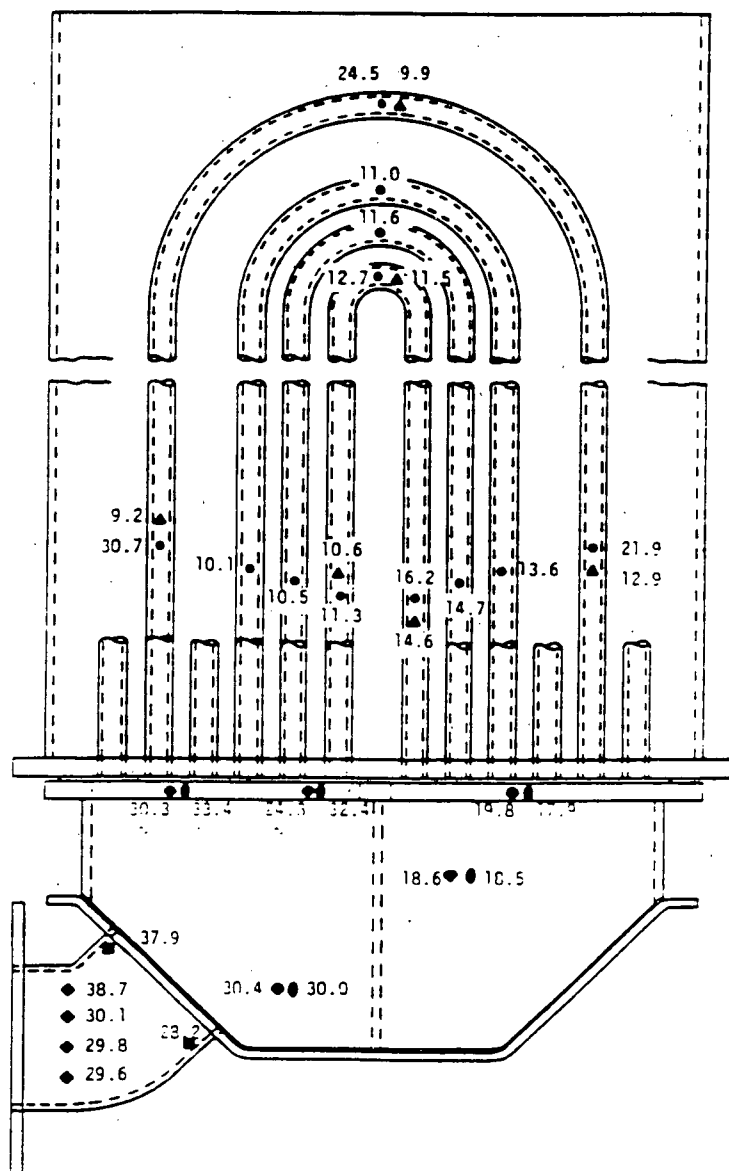


Figure 21. Test No. 20. Temperatures ( $^{\circ}\text{C}$ ) Water in Steam Generator Model on Right Side of Reactor.

Three tests were conducted with blockages of various porosities to restrict axial flow in 41 out of 104 fuel bundles. Measured temperature distributions showed that the effect of blockages was quite local; the buoyant flow fields, a little distance from the blockage, were not affected significantly.

Future work on this subject is to be cofunded by EPRI and NRC.

### 5.3 MAAP Development and Application

This topic has been discussed at each of the last two WSRI meetings, especially at the 1987 meeting when it was the subject of a separate comprehensive paper (29). The present discussion will summarize developments which have occurred since that time.

During the past year the ownership of MAAP (Modular Accident Analysis Program) was transferred from IDCOR to EPRI, which manages the activities related to its continued enhancement and use. The objective of the work is to provide all MAAP licensees with an efficient, stable, and qualified tool for performing necessary severe accident progression and management analysis of current generation LWR power plants. Current work has included installation of further code enhancements, continuation of the independent verification and validation studies, and an updating of the TMI-2 benchmark calculations. The results of each of these efforts are described in the following paragraphs.

5.3.1 Enhancement of MAAP. Two major modeling enhancements have been installed in the code during the past year. The first of these is the METOXA model. This is an equilibrium model for calculating fission-product releases during core-concrete interaction processes. It was developed to permit analysis of reactive vaporization of core debris components as well as simple congruent vaporization. The METOXA model assumes the metal and oxide phases are in equilibrium, which is determined by a Gibbs free energy minimization technique. A hard-wired compound list is used to maintain computational efficiency, and chemical equilibrium is calculated by solving the algebraic relations for mass action and element balances. The data required for the METOXA model are defined in terms of the fundamental chemical thermodynamic data available for individual elements and compounds. The six fission-product groups previously used in MAAP have also been expanded to twelve to accommodate the capabilities of the METOXA model.

The other major modeling improvement added to MAAP is the generalized auxiliary/reactor building model. A node-and-junction approach is used, enabling the user to construct a geometric representation appropriate for his auxiliary building (PWR) or reactor building (BWR). This model is significantly more sophisticated than those in previous MAAP versions. More computational volumes are allowed, which can either connect directly to each other or with a junction that has a specific failure pressure differential ( $\Delta p$ ). The new model also allows two kinds of flows to occur in a volume; normal flow between volumes through junctions (unidirectional flow) and a circulating flow inside a volume and through junctions (countercurrent flow). This countercurrent flow can be an important driving force for fission-product deposition onto building surfaces in some accident scenarios.

In addition to the above, several other modifications were made in the code to improve computational stability and efficiency and to upgrade selected models (steam generator analysis for PWRs) or subroutines (pool decontamination factor calculations for BWRs). The current version which contains all these additions is identified as the MAAP 3.0B version.

**5.3.2 Independent Verification and Validation.** The purpose of this effort is to enhance the credibility of MAAP by independently carrying out formal verification of the coding and by validating key models against relevant experiments. The verification procedure involves a line-by-line inspection of the coding as illustrated in previous reports (29). A continuous record is generated with potential errors or questions highlighted by numbered comments. Resolution of the comments either leads to correcting the code, educating the independent verifier, or both. Comments regarding the MAAP 3.0 version have now been resolved and verification work is underway on MAAP 3.0B. The PWR code is about 90% verified at this time while the BWR code is about 60% complete.

The recent model validation work has focused on comparison of MAAP predictions against the measured results from several large-scale experiments, specifically, the LA1, LA2, and LA4 tests from the LACE program (30). The models involved in the validation were those that calculate containment thermal-hydraulic conditions (pressure, gas and structure temperatures, species mass fraction, and steam condensation) and containment aerosol behavior characteristics (settling, wall deposition, and particle size distribution). Preliminary results show that MAAP is quite capable of predicting the proper thermal-hydraulic conditions in these tests. The principal uncertainty involves the analyst's ability to correctly represent the performance of the insulation as installed on the LACE test vessel. The aerosol behavior predictions are still being evaluated, but it appears that the MAAP correlations tend to predict somewhat broader particle size distributions than those recorded during the experiments. The LACE comparison effort should be completed by the end of the calendar year. Further model validation work is planned for the coming year.

**5.3.3 Simulation of the TMI-2 Accident.** The objective of this work is to provide an updated benchmarking analysis of the TMI-2 accident using the latest version of MAAP (i.e., MAAP 3.0B). The analysis used parameter and control card files based on optimum parameter files composed of both the EPRI-developed MAAP 2.0 and the OECD TMI-2 Analysis Exercise parameter files. Results from the analysis through Phases 1 and 2 (up to 174 minutes into the accident) showed that MAAP 3.0B could follow the TMI-2 primary system pressure history quite closely. MAAP 3.0B predicted peak core temperatures that closely matched the four time-temperature windows that have been identified in the OECD TMI-2 Analysis Package data package. The resulting production of hydrogen (about 155 kg) was also consistent with what should have occurred in this time. Finally, the core slumping predicted by MAAP 3.0B closely matched the approximate end state lower crust boundary that has been defined from TMI-2 core examination activities.

These results were presented to the OECD TMI-2 Analysis Exercise participants last May and a final report of the work should be issued soon.

## 6.0 SAFETY MARGINS AND TESTING

The objective of the Safety Margins and Testing Program are, on the one hand, to help utilities reduce operating and maintenance costs and, on the other hand, to help resolve safety concerns. Section 6.1 is an example of a project achieving the first objective while sections 6.2 and 6.3 address the second objective.

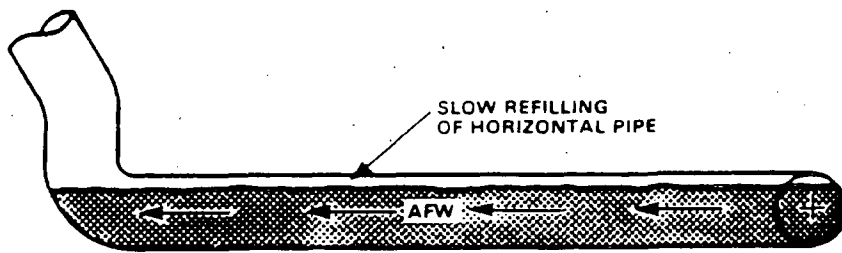
### 6.1 Water Hammer in Nuclear Power Plants

Water hammer damages plant safety components and impacts plant operations and availability due to forced outages of plants. Even though water hammer events have been investigated for years, they continue to be one of the main causes of costly financial losses in nuclear power plants. EPRI has initiated an R&D project to prevent water hammer events and to help utilities mitigate and accommodate their impact. For instance, the well-publicized water hammer event of Southern California Edison's SONGS-1 (31, 32) resulted in a multi-million dollar financial loss. Water hammer can happen in either single-phase or two-phase conditions although most of the severest water hammer events in nuclear power plants are largely due to two-phase mechanisms (33, 34). In a recent study, the following seven major potential mechanisms leading to water hammer have been identified (35):

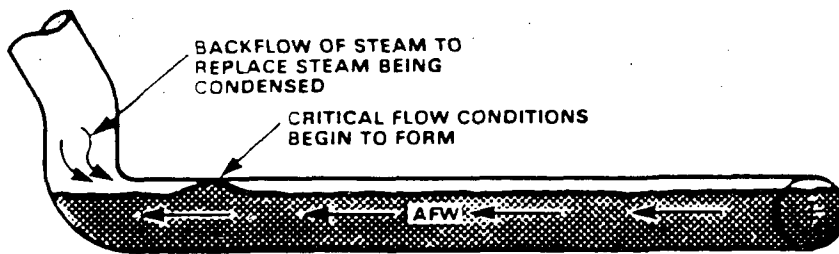
1. Water Cannon: Subcooled water in condensing steam in a vertical pipe.
2. Steam-Water Counterflow: Steam and water counterflow in a horizontal pipe.
3. Steam Bubble Collapse: Pressurized water entering a vertical steam-filled pipe.
4. Flashing-Collapsing Steam Bubble: Hot water entering lower pressure line.
5. Steam-propelled water slug.
6. Shock/pressure wave due to rapid valve actuation.
7. Water column separation and rejoining.

As an illustration, the steam-water counterflow mechanism, which is believed to have caused the SONGS-1 event (31), is depicted in figure 22.

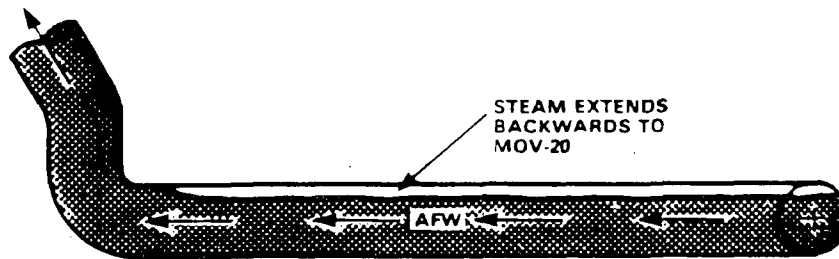
The identification of these physical mechanisms is essential in the development of improved design and operational procedures in nuclear power plants for prevention, mitigation, and accommodation of water hammer.



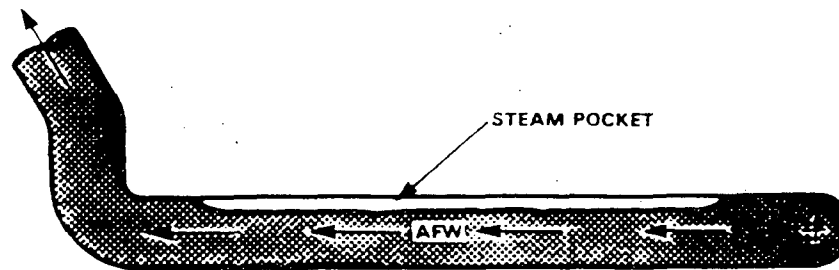
a. Pipe 90% Full When AFW Stopped



b. Wave Instabilities Being Formed Prior to Bridging of the Vertical Elbow



c. Elbow has Bridged and Vertical Leg Filled



d. Probable Steam Pocket Location Just Prior to Water Hammer

Figure 22. Refilling of a Horizontal Line With Auxiliary Feedwater (AFW) Leading to Water Hammer.

Various other tasks are also being performed whose results will be integrated into a handbook that can be routinely used by plant operators and engineers.

## 6.2 Steam Generator Tube Rupture Analysis Method

Steam generator tube rupture (SGTR) events which may occur in pressurized water reactors can lead to the release of radioactive species, such as iodine, to the environment. A fraction of the primary side coolant and radioactive species, which flow into the secondary side through the ruptured tubes, will be retained in the secondary side and the rest will be released in the form of vapor and entrained aerosols.

The Secondary-Side Transport and Retention of Radioactive Species (STARRS) computer code was developed to quantify the amount and composition of material released during an SGTR event. The STARRS code simulate a U-tube steam generator, and contains a reactivity transport/retention module, and while accepts the transient thermal-hydraulic parameters from general purpose thermal-hydraulic system codes, such as RETRAN and TRACE. This version of the code is called STARRS-TR.

STARRS-TR calculates the radionuclide transport and deposition phenomena on the secondary side of a U-tube steam generator provided that boundary conditions, such as the break flow and its thermodynamic conditions, system pressure, swell level height in the secondary side, etc., are known. To perform a transient analysis, the required thermal-hydraulic boundary conditions are input to the STARRS-TR code.

Figure 23 depicts a schematic of a U-tube steam generator. The important components of the system that participates significantly in the removal of radionuclides are the swollen pool (if it exists), the dryer, and the separator.

Following a tube rupture, the primary liquid partially flashes, creating bubbles, and partially mixes with the secondary-side fluid. A fraction of primary liquid forms liquid aerosols which are entrained by the rising bubbles. The rising bubbles, therefore, contain volatile radionuclides which are in the form of gas mixed with steam, or dissolved in the entrained liquid aerosols. The rising bubbles transfer mass and energy with the surrounding water pool continuously including scrubbing of the aerosols.

As the bubbles reach the pool surface, they shatter, release their vapor and aerosol contents into the steam volume on top of the water pool, and give rise to the entrainment of droplets of the water pool. The latter droplets also contain radionuclides as the scrubbed radionuclides gradually build up in the secondary-side coolant.

The liquid aerosols originating from the atomization of the primary coolant flowing through the break, as well as those originating from the entrainment of the secondary-side water, undergo further scrubbing in the separator and dryer.

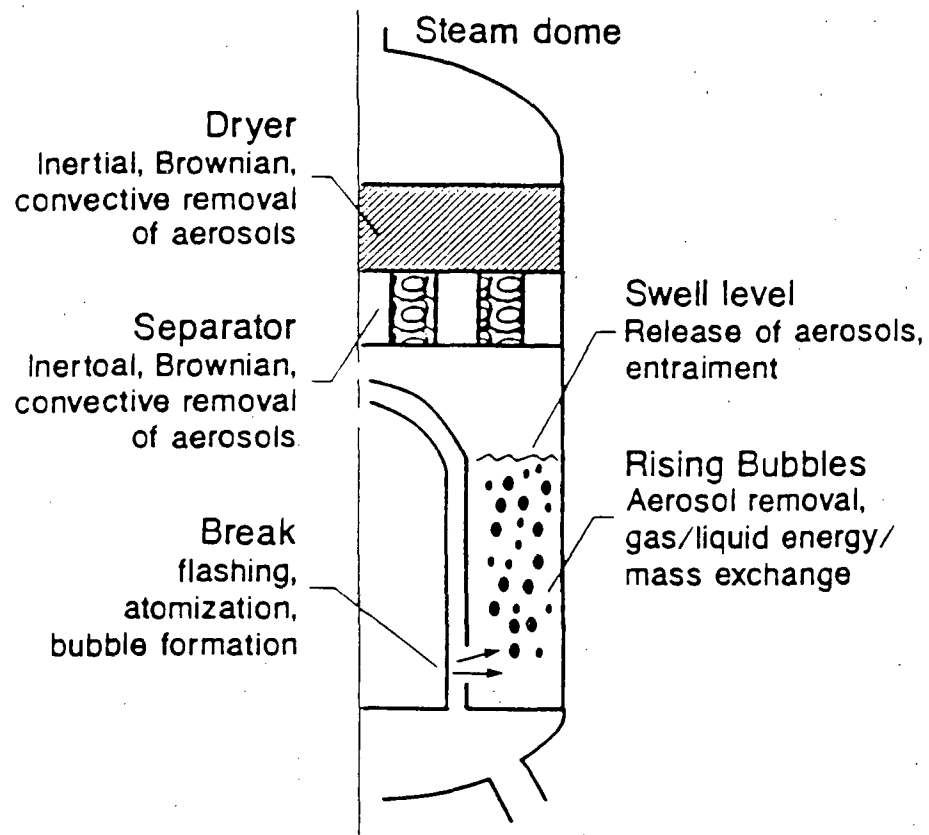


Figure 23. Schematic of the Secondary Side of a U-Tube Steam Generator in a Tube Rupture Incident.

If the break location is exposed during the transient, i.e., when the water level on the secondary side drops below the break location, the primary coolant partially atomizes. The liquid aerosols, which are too large to be carried over by the steam, fall back into the liquid pool, and the smaller droplets are carried over by the steam flow. Scrubbing mechanisms during the bubble rise do not exist in this case.

The STARRS-TR code includes detailed modeling of all of the phenomena: (i) flashing, atomization of bubble formation, (ii) transportation and deposition during bubble rise, and (iii) aerosol deposition in the stream volume separator and dryers, etc.

### 6.3 Stability Analysis Model for BWR Applications (SAMBA)

BWR core designers and operators must ensure that the plant has adequate operating margins so that its operating range (for example, flow-to-power ratio) does not approach a sustained oscillation mode or an instability mode. An understanding of the instability behavior resulting from perturbations in operating parameters, such as coolant flow rate, core inlet subcooling, or axial power distributions, is important for proper plant design, operations, and controls. Therefore, the objective is to develop stability models for predicting time-domain-coupled neutronics and thermal-hydraulic instabilities for BWRs and to validate the models using BWR plant and other simulation data.

A one-dimensional time domain analysis methodology to evaluate BWR stability has been developed. Modeled BWR systems include flow paths through heated core and bypass channels, recirculation and jet pumps, steam separators, and downcomers. The analytic approach uses four equations with slip hydrodynamic behavior, space-dependent neutron kinetics, and options for appropriate void and heat transfer correlations. The stability prediction models were validated with plant tests at four commercial reactors: The Pennsylvania Power and Light Peach Bottom-2 facility, the TVO-I and -II internal pump reactors in Finland, and the Forsmark-1 internal pump reactor in Sweden. The validation efforts also included separate hydrodynamic stability test data from the FRIGG test loop facility in Sweden.

The EPRI report (NP-5620-CCML, Vols. 1-4) describes the development and validation of BWR system behavior models (the SAMBA code) for predicting BWR stability. Predicted decay ratios agreed well with data from stability tests performed at the Peach Bottom-2 facility. At TVO-I and -II and at Forsmark-1, analysis of the limit cycle oscillation and stability tests revealed that the SAMBA code overestimated the stability of a high flow-to-power ratio at minimum pump speed and natural circulation. Evaluation of the hydrodynamic stability tests in the FRIGG loop revealed the accuracy of decay ratio and period-of-oscillation predictions at low pressure (30 bar). As pressure increased to 50 bar, the code underpredicted both values, although above 50 bar the code predictions reflected test data much more accurately. Overall, predictions agreed well with the extensive database of 31 tests used to qualify the SAMBA code.

The detailed documentation referenced above describes the equations and numerics used in developing the SAMBA methodology (vol. 1); user's manual (vol. 2); programming details (vol. 3); and all application and qualification efforts (vol. 4).

The examples of 'SAMBA' predictions of Peach Bottom stability tests and results are shown in figure 24a and 24b.

## 7.0 CONTROL AND DIAGNOSTICS

### 7.1 Goals and Near-Term Objectives

The mission of Control and Diagnostics Program R&D is to develop and deploy technology of control information systems for utility plant performance and safety enhancement. The key goals are outlined as follows:

1. To increase production of electricity. This includes the increase of availability and reduction of forced outages.
2. To reduce operations and maintenance costs. This includes the increase of productivity of utility personnel.
3. To improve safety and to meet regulatory challenges.

The near-term objectives of the program are:

1. To improve control and monitor system reliability and enhance human reliability of calibration and testing.
2. To improve diagnostics of operating events to decrease operations and maintenance costs.
3. To enhance emergency decision-making capability to reduce operation burden in control room.
4. To comply with NRC regulations on safety monitoring and simulator qualifications.

The tasks undertaken to achieve these goals and objectives are shown in table 4. Table 5 lists the industry strategic issues and needs in the control and diagnostics area and the corresponding EPRI R&D projects to address the industry needs.

The following are descriptions of two representative projects which are technological breakthroughs in the nuclear utility industry; one is the first Fault-Tolerant Digital Feedwater Control System for the BWRs in the United States and the other is an Advanced PWR Steam Generation Level Control System.

**7.1.1 BWR Fault-Tolerant Digital Feedwater Control System.** Feedwater control system (FCS) problems are the largest contributor to control-related plant outages in light water reactors. Current FCSs consist of analog control loops

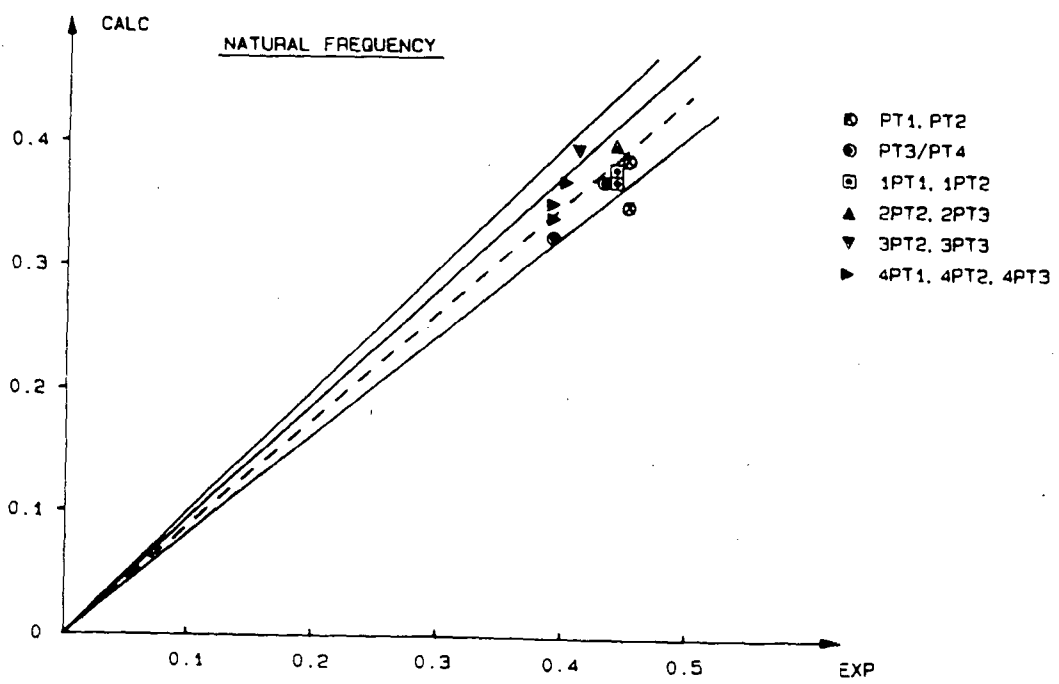
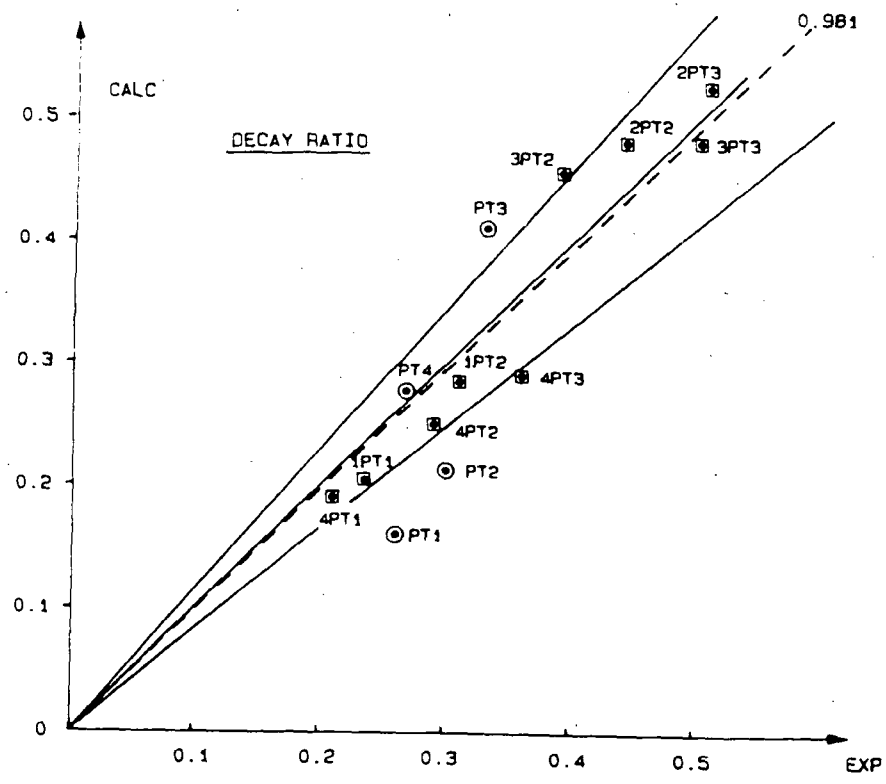


Figure 24. Calculated vs. Experimental Decay Ratio and Natural Frequency for Drift Velocity Model I (ISLIP=7).

Table 4

CONTROL & INFORMATION SYSTEMS

Goals	Tasks/Needs
<ul style="list-style-type: none"> <li>• Increase Production of Electricity                             <ul style="list-style-type: none"> <li>• Increase Availability</li> </ul> </li> </ul>	<ul style="list-style-type: none"> <li>• Reduction of Plant Trips</li> <li>• Tech Spec Management</li> <li>• Control Upgrade</li> <li>• Instrument Calibration</li> <li>• On-Line Testability</li> <li>• Core Shuffler Advisor</li> </ul>
<ul style="list-style-type: none"> <li>• Reduce Operations and Maintenance Cost                             <ul style="list-style-type: none"> <li>• Increase Personnel Productivity</li> </ul> </li> </ul>	<ul style="list-style-type: none"> <li>• Expert System Tools</li> <li>• Systems Simplification</li> <li>• Plant Communications</li> <li>• Station Information System</li> <li>• Diagnostics Aid</li> <li>• Maintenance and Repair Advisor</li> </ul>
<ul style="list-style-type: none"> <li>• Improve Safety and Meet Regulatory Challenges</li> </ul>	<ul style="list-style-type: none"> <li>• Emergency Decision Aid</li> <li>• Simulator Qualification</li> <li>• Alarm Processing</li> </ul>

Table 5

## CONTROL &amp; DIAGNOSTICS INDUSTRY STRATEGIC ISSUES

<u>Issues</u>	<u>Strategic Needs</u>	<u>Technical Objectives</u>
<ul style="list-style-type: none"> <li>• Increase production of electricity by reduction of forced outages and by increase availability.</li> </ul>	<ul style="list-style-type: none"> <li>• Reduction of plant trips.</li> <li>• Improvement of plant control and monitoring.</li> <li>• Increase reliability of on-line calibration and testing.</li> <li>• Improve outage management with core shuffler advisor.</li> </ul>	<ul style="list-style-type: none"> <li>• Provide digital feedwater controller for replacement of old analog controllers.</li> <li>• Provide technology justification for reduction of calibration for identification of faulty signals.</li> <li>• Provide automation for on-line testing to reduce human error related trips.</li> <li>• Provide core monitoring system for improving fuel utilization.</li> </ul>
<ul style="list-style-type: none"> <li>• Decrease operation and maintenance cost.</li> </ul>	<ul style="list-style-type: none"> <li>• Productivity increase.</li> <li>• Guidelines and methods for diagnostics, troubleshooting, and repairs.</li> <li>• Ease of system maintenance.</li> <li>• Integrated communications to facilitate transmission and management of data and information.</li> </ul>	<ul style="list-style-type: none"> <li>• Provide fuel insert shuffler expert system for reduction of refueling time.</li> <li>• Provide software tools for building application expert systems.</li> <li>• Develop moderate temperature coefficients using reactor noise diagnostics.</li> <li>• Provide methods to ease calibration burden.</li> <li>• Provide information on computer networking to reduce data management and maintenance cost.</li> <li>• Provide tagout expert system for streamlining maintenance work.</li> <li>• Provide on-line diagnostics of emergency diesel generators.</li> <li>• Provide method for development and maintenance of procedures.</li> </ul>

Table 5 (cont'd.)

Issues	Strategic Needs	Technical Objectives
<ul style="list-style-type: none"> <li>• Improve safety and meet regulatory challenges.</li> </ul>	<ul style="list-style-type: none"> <li>• Enhanced emergency decision making.</li> <li>• Simplification of systems to ease control-room operator's burden.</li> <li>• Utility compliance with NRC regulation.</li> </ul>	<ul style="list-style-type: none"> <li>• Provide emergency action level monitor expert system for reduction of errors in emergency classification.</li> <li>• Provide expert systems to automate tracking of emergency operating procedures.</li> <li>• Provide methodology for utilities to meet NRC regulations on qualification of training simulators.</li> <li>• Provide alarm processing and diagnostics capability for control-room operators.</li> </ul>

using 20-year old technology. Electrical component and sensor failures typically cause FCS failures, and utilities have difficulty obtaining analog controller spare parts. Northern States Power Company (NSP) engineers determined that analog controller component failures were a major cause of FCS-related outages at Monticello Nuclear Power Station.

Given the recent development in microprocessors and applications of fault-tolerant computer systems in other industries, NSP realized that digital technology could improve FCS reliability and operation.

Under EPRI projects, EPRI, NSP, and Science Applications International Corp. jointly funded the design, implementation, and testing of a prototype high-reliability digital FCS. This system replaced and upgraded the main and startup analog controllers at Monticello in 1986. It features automatic control, on-line signal validation, controller self-diagnostics, and fault tolerance. The dual-redundant hardware configuration minimizes spare parts availability problems. At a control room panel, operators select each feedwater valve's operating mode (one or three element control, manual, and so on) or set bias inputs for individual feedwater-valve demand. These and other features permit more exact FCS tuning, improving feedwater control in all modes of plant operation. During a recent recirculation pump trip at Monticello, the system precisely controlled the vessel water level. Parity space and analytic redundancy techniques isolate failed sensors and permit system switching to accurate sensors, thus avoid outages. The digital design also facilitates operator training. This microprocessor-based design improves the reliability of the old FCS by at least a factor of three.

**7.1.2 Advanced PWR Steam Generator Level Control System.** The objective of this project is to develop a steam generator feedwater control system prototype and demonstrate it on a utility simulator. This control system includes signal validation, single fault-tolerant hardware design and a color graphics man-machine interface.

The work consists of three phases. Phase I produced a preliminary design and algorithms which improved steam generator level response, detect sensor failures and equipment failures in the feedwater systems and the control system itself. Phase II finalized the design system. Phase III built the prototype system and produced system validation test specifications. The system then underwent factory testing and utility simulator testing. Two final reports will be written. The first will summarize the overall program and focus on guidelines which the utilities can use for design and installation of digital steam generator feedwater control system. The second will describe the software developed for signal validation and the man-machine interface. The system has been completed and tested by operation personnel at TVA Sequoyah plant simulator in June 1988.

## 8.0 ACKNOWLEDGMENTS

The authors wish to acknowledge the help of Robert Breen, Bill Sun, J. Carl Stepp, Jean-Pierre Surssock, Ian Wall, and David Worledge and their staffs.

## 9.0 REFERENCES

1. Stepp, J.C., 1988. "A Probabilistic Seismic Hazard Methodology for Critical Industrial Facilities". NRC/MITI Workshop, Tokyo, Japan.
2. "Earthquake Ground Motion Estimation in Eastern North America," 1988. EPRI NP-5875, Electric Power Research Institute.
3. Tagart, S.M., Tang, H.T., and Tang, Y.K., 1985. "Objectives for Piping Design Improvement--An Experimental Program". Society of Engineering Sciences Conferences.
4. Tagart, S.M., et al., 1988. "Seismic Analysis and Testing of Piping Systems and Components". ASME PVP Vol. 144.
5. Cloud, R.L., et al., 1986. "A Simplified Seismic Support System for Nuclear Power Plant Piping". Draft report submitted to EPRI by R.L. Cloud Associates.
6. Khalafallah, M.Z., et al., 1987. "A Study on Snubber Elimination Using Energy Absorbers". EPRI NP-5096, Electric Power Research Institute.
7. Singh, A., Kassawara, R.P., Wiedner, K., and Leung, J., 1987. "Large Shaker Experiments on Piping Response With Alternate Piping Support Systems". Proceedings of SMiRT-9, Lausanne, Switzerland.
8. Hadjian, A.H., 1988. "Piping System Damping Evaluation". Draft report submitted to EPRI by Bechtel Group, Inc.
9. Tang, H.T., Jaquay, K.R., and Larson, J., 1987. "Simplified Nonlinear Dynamic Piping Analysis Methodology Development". Proceedings of SMiRT-9, Lausanne, Switzerland.
10. Jaquay, K.R., Castle, W.R., and Larson, J.E., 1988. "Development and Evaluation of a Simplified Inelastic Seismic Analysis Method for Piping Systems". Draft report submitted to EPRI by Rockwell International.
11. Hansen, N.W., Roller, J.J., Schultz, D.M., Julien, J.T., and Weinmann, T.L., 1987. "Concrete Containment Tests, Phase 2: Structural Elements With Liner Plates." EPRI NP-4867M, Electric Power Research Institute.
12. Hansen, N.W., Roller, J.J., Schultz, D.M., and Azizinamini, A., 1988. "Concrete Containment Structural Element Tests, Phase 3: Structure Elements With Penetration Sleeves". To be published. Final report submitted to EPRI by Construction Technology Laboratories.
13. Hibbitt, H.D., Karlsson, B.I., and Sorenson, P., 1983. "ABAQUS-EPGEN: A General Purpose Finite-Element Code". EPRI NP-2709, Electric Power Research Institute.

14. Dunham, R.S., Rashid, Y.R., Yuan, D.A., and Lu, Y.M., 1985. "Methods for Ultimate Load Analysis of Concrete Containments." EPRI NP-4046, Electric Power Research Institute.
15. Dameron, R.A., Dunham, R.S., James, R.J., Lu, Y.M., Rashid, Y.R., and Yuan, K.A., 1987. "Methods for Ultimate Load Analysis of Concrete Containments: Second Phase". EPRI NP-4869M, Electric Power Research Institute.
16. Dameron, R.A., Dunham, R.S., James, R.J., Lu, Y.M., Rashid, Y.R., and Yuan, K.A., 1988. "Methods for Ultimate Load Analysis of Concrete Containments: Third Phase". To be published. Final report submitted to EPRI by Anatech International Corporation.
17. Clauss, D.B., 1987. "Round-Robin Pretest Analyses of a 1/6 Scale Reinforced Concrete Containment Model Subject to Static Internal Pressurization". SAND87-0891, NUREG/CR-4913.
18. Ishii, M. "One-Dimensional Drift Flux Model and Constitutive Equations for Relative Motion Between Phases in Various Two-Phase Flow Regimes." ANL-77-47, Argonne National Laboratory, Argonne, Illinois.
19. Lellouche, G. and Zolotar, B., 1982. "Mechanistic Model for Predicting Two-Phase Void Fraction for Water in Vertical Tubes, Channels, and Rod Bundles." EPRI NP-2246SR, Electric Power Research Institute.
20. Eisenhart, L.D. "ARROTTA Computer Code Documentation Package," to be published by EPRI.
21. Smith, K.S., 1979. "An Analytic Nodal Method for Solving the Two-Group, Multidimensional Static and Transient Neutron Diffusion Equations". Nuc. Eng. Thesis, Department of Nuclear Engineering, Massachusetts Institute of Technology.
22. Diamond, D.J., Chen, H.S., Eisenhart, L.D., and Aronson, A.L., 1984. "BEGAL-01: A Computer Code for Calculating Rapid LWR Core Transients." EPRI NP-3243-CCM, Electric Power Research Institute.
23. McFadden, J.H., et al., 1981. "RETRAN-02: A Program for Transient Thermal-Hydraulic Analysis of Complex Fluid Flow Systems". EPRI NP-1850, Electric Power Research Institute.
24. Mosteller, R.D., Anderson, M.J., Eisenhart, L.D., and Abdollahian, R. "Reactivity Calculations for Analysis of a PWR Natural-Circulation Transient". To be published by EPRI.
25. Catawba Nuclear Station Unit 1 - Startup Report. Duke Power Co., Docket 50-413, September 27, 1985.

26. Mosteller, R.D., and Anderson, M.J., 1986. "NODE-P2 Computer Code Manual". Part II, Chapter II, ARMP-02 Documentation, EPRI NP-4574, Electric Power Research Institute.
27. WAM-E User's Manual. EPRI NP-4460-CCM, Electric Power Research Institute, July 1986.
28. CAPTA Manual, Draft EPRI Report, January 1988.
29. Fuller, E.L., Ritzman, R.L., Mendoza, Z.T., Sherry, R.R., and Henry, R.E., 1987. "Recent MAAP Developments". 15th Water Reactor Safety Information Meeting, Gaithersburg, MD.
30. Rahn, F.J., 1987. "Summary of the LWR Aerosol Containment Experiments (LACE) Program". Interim Report LACE TR-012.
31. "Loss of Power and Water Hammer Event at San Onofre, Unit, on November 21, 1985". NUREG-1190, U.S. Nuclear Regulatory Commission, January 1986.
32. Ciu, C., Tuttle, D., and Serkiz, A.W., 1986. "Water Hammer in a PWR Horizontal Feedwater Line", Trans. ANS, Vol. 52, American Nuclear Society.
33. Kim, J.H., 1987. "Two-Phase Water Hammer in Nuclear Power Plants". Cavitation and Multiphase Flow Forum, ASME FED-Vol. 50.
34. Kim, J.H., 1987. "Water Hammer Prevention, Mitigation, and Accommodation: A Perspective". Trans ANS, Vol. 55, American Nuclear Society.
35. Van Duyne, D.A., 1988. "Water Hammer Prevention, Mitigation, and Accommodation". Presented at the Second EPRI Workshop on Water Hammer in Nuclear Power Plants, Boston.



## SCRUBBING OF AEROSOLS BY WATER POOLS

M. Merilo, Electric Power Research Institute  
J. A. Gieseke, Battelle Columbus Laboratories  
A.T. Wassel, Science Applications International Corporation

### ABSTRACT

During a severe core damage accident, the BWR suppression pool provides an important barrier to the release of radioactive fission product aerosols.

The experimental components of this program consisted of small, intermediate, and large scale tests which were performed at Battelle Columbus Laboratories under a variety of conditions representative of those expected to occur during severe accidents. The analysis work culminated in the development of the SUPRA (Suppression Pool Retention Analysis) Code. This code is based on an engineering approach in that, wherever possible, correlations were used to describe individual phenomena, rather than mathematical models based on first principles. The results of an extensive comparison effort between the calculated and the experimental results are described, as well as, indications of the implications of these results to severe accident analysis.

### INTRODUCTION

During reactor accidents involving severe core damage, gaseous fission products are released from the core and subsequently condense during transport through the reactor coolant system ( RCS ) to form aerosols. In boiling water reactors the steam-gas mixture which carries these fission products is constrained to pass through the suppression pool which is designed to condense steam released during a design basis accident. Depending on the details of the accident sequence, and the type of containment, injection into the suppression pool can occur through quenchers, downcomers, or side vents.

It has been known for some time that aerosols and vapors can be removed from a carrier gas by bubbling through water, though the extent to which this happens could not be accurately quantified. EPRI consequently initiated a research program on pool scrubbing to experimentally determine the fraction of aerosols retained in a water pool, and to develop a predictive capability which could describe this data and which could be used to determine pool scrubbing effectiveness for selected severe accident sequences.

## HYDRODYNAMIC EXPERIMENTS

The experimental program consisted of both hydrodynamic, and aerosol-removal tests. The purpose of the hydrodynamic tests was to determine parameters required for the mathematical modeling of the aerosol deposition. In particular, the gas-liquid interfacial area and the aerosol residence time in the pool are vital since they control the mass transfer effectiveness. This means that the bubble sizes and shapes are required, along with the absolute bubble rise velocity. This information was obtained photographically in the facilities shown in Figure 1.

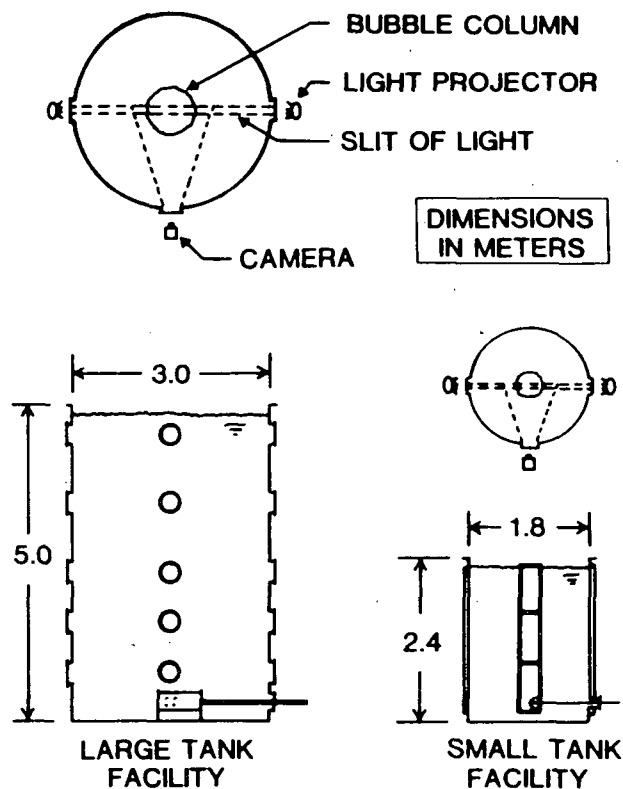


Figure 1. Scrubbing Test Facilities

Two tank sizes were used, one 1.8 m in diameter and 2.4 m high, and the other 3.0 m in diameter and 4.9 m high. In general, the smaller tank was used for the low flow rate tests and the larger one for the high flow rates. Hydrodynamic tests were performed for each injection configuration; representing spargers, for releases through the SRV discharge line, downcomers, for the Mark I and II containments, and side vents for the Mark

III . Both steam and non-condensable gases were injected. The type of phenomena observed is illustrated in Figure 2.

Even though the gas is injected at a constant flow rate, large gas bubbles are formed intermittently at the injector. The formation, growth and ultimate detachment of these large bubbles was studied photographically. The volume of the bubble at time of detachment was determined by measuring the major and minor axes, and assuming that the shape was an oblate spheroid. It was found possible to express the dimensionless bubble diameter at detachment uniquely as a function only of the injector Weber Number.

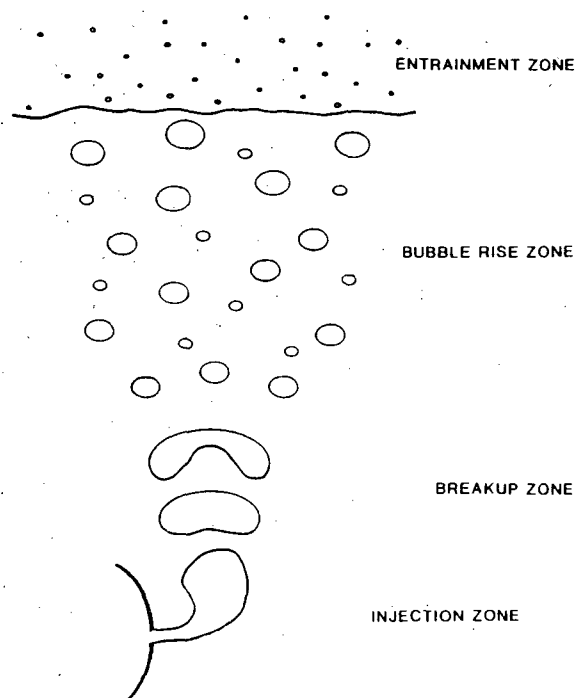


Figure 2. Hydrodynamic Phenomena

The large gas bubbles become unstable almost immediately after detachment and start to break up into smaller bubbles. Based on the flow visualization, the distance required for the bubbles to reach an equilibrium distribution corresponded to approximately 10 initial bubble diameters. The bubble size distribution and rise velocity in the bubble rise zone were studied photographically.

The equilibrium bubble size distribution turned out to be essentially independent of all the injector variables such as orientation, diameter, and gas flow rate. There was a slight dependence on the steam mass fraction when the steam mass fraction was over 90%, indicating that most of the

condensation occurred before the equilibrium bubble size was reached. This observation is consistent with previous studies appearing in the literature.

When the bubbles reach the surface, liquid droplets are formed, the smaller of which are carried away as entrainment, whereas the larger ones fall back into the pool.

### POOL SCRUBBING EXPERIMENTS

The major experimental objective of these tests was to determine the aerosol retention in the water pool over a range of conditions simulating those expected to occur during postulated severe core damage accidents. The most commonly used figure of merit is the Decontamination Factor, DF, which is defined as the ratio of the injected mass to the mass escaped. To measure this it is necessary to characterize the gas/aerosol mixture injected into the pool, and that leaving the pool. Figure 3 shows a schematic diagram of the test layout.

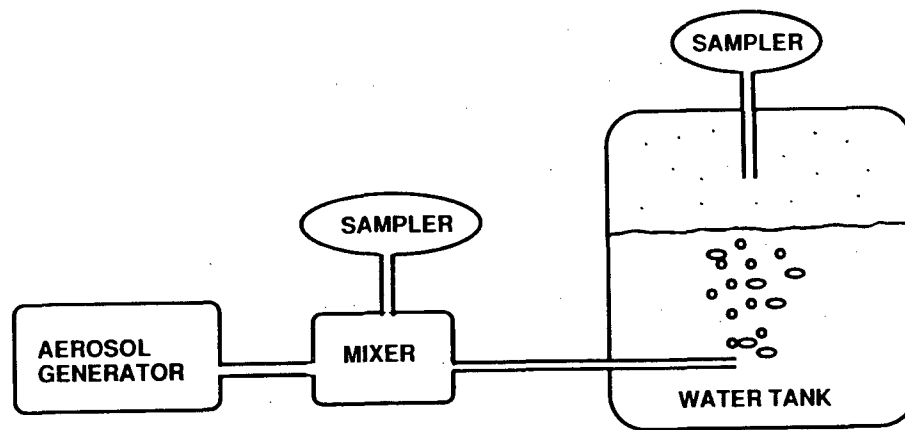


Figure 3. Scrubbing Test Layout

Depending on the type of aerosol and the quantities required, several different aerosol generation techniques were used. To generate aerosols of CsI, and TeO<sub>2</sub>, both of which are expected to be present during severe accidents, an evaporation-recondensation method was used. In this device, the aerosol material is vaporized by an RF field and is transported by a carrier gas into the mixing chamber. This method produces aerosols in the size range where the DF is expected to be a minimum, however, the quantity produced is low,

resulting in inadequate measurement sensitivity when used with a large facility.

Tin powder was selected for an aerosol in the larger size range because it is a constituent of structural materials in the reactor. The generation of the tin aerosol was accomplished by the mechanical dispersal of preformed powder into a gas stream. This method is suitable for producing large quantities of aerosols.

Another aerosol generation system that was used consisted of a 80 kW plasma torch and associated equipment. In this system a metered powder flow is carried by an inert carrier gas through a plasma generated by the torch. In the plasma both the carrier gas and the powder are heated rapidly, with vaporization of the material occurring in the plasma torch mixing chamber. Upon exiting the chamber the vapors are cooled and condense to form the desired aerosol. This method is good for generating large quantities of aerosols, however, the size distribution is quite broad and is hard to control.

To generate monodisperse polystyrene latex (PSL) aerosols, which were utilized in the separate effects, laboratory scale experiments, a Collision nebulizer was used. In this device a very fine mist of droplets of a liquid suspension carrying the solid particles is generated. The droplets are subsequently carried through a drying column where the water surrounding the particles is evaporated. The aerosol is then mixed with the main injection stream.

An accurate characterization of both the injected and escaping aerosols is required to determine the decontamination factor. The inlet aerosol was sampled by periodically diverting the total injected aerosol-gas mixture through a sampler. The stability of the aerosol generation is shown in Fig. 4, which gives the size distribution at three different times during a particular test. The exit flow did, of course, not have to be diverted but could be sampled at any time throughout the test.

The aerosol size distributions were measured by several techniques. This included cascade impactors, an Active Scattering Aerosol Spectrometer, and an Aerodynamic Particle Sizer. For aerosol mass concentration measurements the gas stream was sampled using Millipore filters. The size dependent DFs were obtained from the inlet and effluent size distributions, whereas the inlet and effluent mass concentrations were sufficient to determine the overall DF.

Table I provides a summary of all the scrubbing tests which were performed. As can readily be seen the majority of tests were performed with a single orifice injector in either the small tank or the bench scale facility. Only sixteen tests were performed in the large scale tank. This was primarily due to the difficulty and concomitant expense associated with the large scale tests.

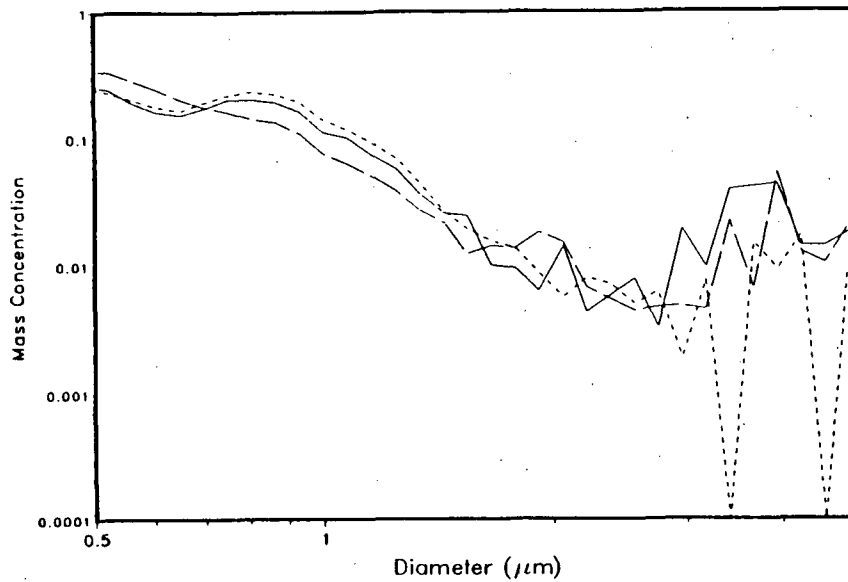


Figure 4. Typical Mass Distributions for Injected aerosols

Table I. Pool Scrubbing Test Summary

<u>INJECTOR</u>	<u>FACILITY</u>	<u>NO. OF TESTS</u>	<u>GAS</u>	<u>SUBMERG</u>	<u>AEROSOLS</u>
SINGLE ORIFICE	SMALL TANK	64	STEAM/AIR	0.3 - 2.8m	CsI, TeO <sub>2</sub> , SnO
SINGLE ORIFICE	BENCH TOP	48	AIR	.15 - 1.8m	PSL
MULTIPLE ORIFICE	LARGE TANK	5	AIR	1.7 - 3.4m	CsI
DOWNCOMER	LARGE TANK	6	STEAM/AIR	0.9 - 3.4m	CsI
HORIZONTAL VENT	LARGE TANK	6	AIR	1.2 - 2.4m	CsI, SnO <sub>2</sub>

Typical inlet and outlet size distributions are shown in Figure 5. The decontamination factor for a particular particle size can be obtained simply by evaluating the ratio of the inlet to outlet mass concentration for that diameter. This is appropriate when the aerosol particles do not grow while passing through the pool.

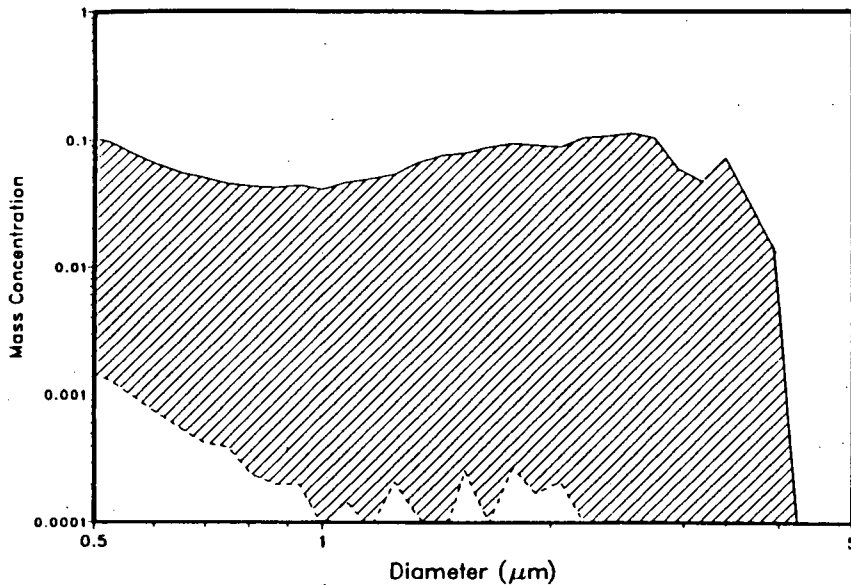


Figure 5. Typical Inlet and Outlet Size Distributions

In general, it was seen that particles larger than one micron are scrubbed very effectively and consequently do not escape from the pool.

### SUPPRESSION POOL RETENTION ANALYSIS

To analyze the scrubbing experiments and to be able to apply the results to severe accident sequences it is necessary to use mathematical models which account for all the important phenomena. The SUPRA code was developed for this purpose. The approach that was used was to develop models for the appropriate physical phenomena by utilizing data available in the open literature, and to only use the experimental scrubbing data for validation of the code.

Conceptually, the water pool is divided into three sequential zones, each of which has different heat and mass transfer characteristics. These zones are shown in Figure 6.

The injection zone is characterized by transfer that occurs during the formation of large bubbles or vapor jets at the injector. The bubble rise zone starts after the breakup of the large bubbles which leave the injector. The bubbles are assumed to be monodisperse and no interaction, such as coalescence, is assumed to occur. The bubbles can however grow due to the decrease in pressure during bubble rise, and due to evaporation of water into the bubbles. Breakup can subsequently occur if these bubbles reach a critical size.

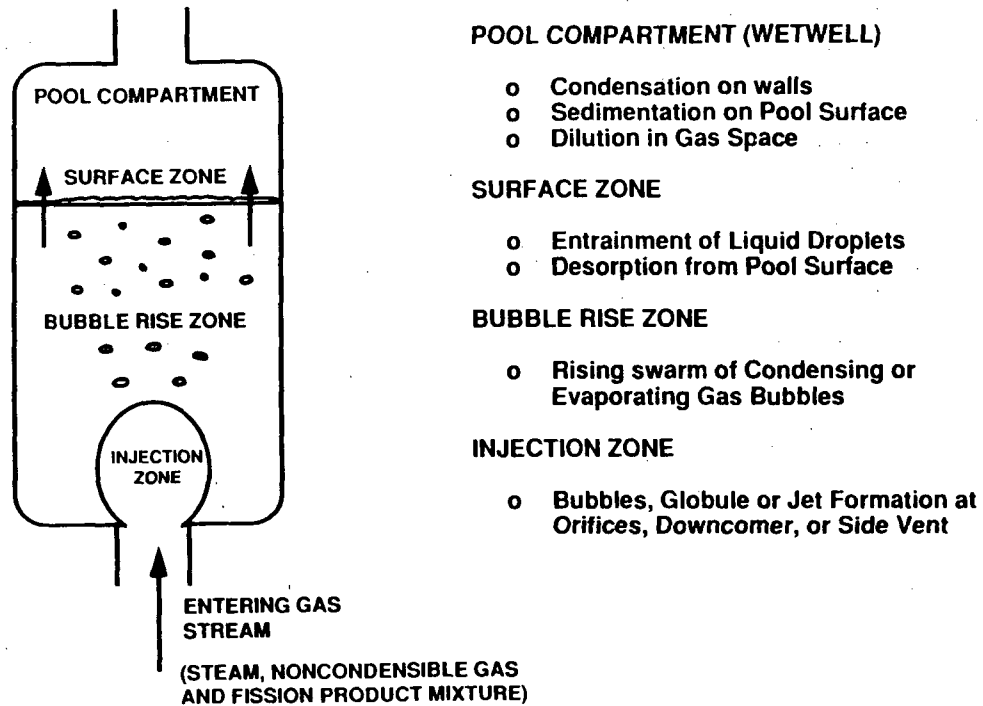


Figure 6. Pool Scrubbing Conceptual Model

The surface zone is characterized by transfer that can occur due to desorption of dissolved gases, or due to liquid entrainment. Gas bubbles which penetrate the pool surface can cause liquid droplets, which contain previously scrubbed material, to be entrained into the gas stream.

In addition to these three zones, it is necessary to account for the compartment above the pool to be able to interpret the experimental data.

The aerosol removal from the gas is calculated by including the well known mechanisms of sedimentation, inertial impaction, convective deposition, diffusiophoresis, thermophoresis, and Brownian diffusion. The hindering effect of evaporation into the bubble must also be accounted for. In the SUPRA code these removal mechanisms are calculated by using deposition velocities along with the appropriate interfacial areas, based on the two-phase flow conditions.

Extensive validation calculations have been performed to compare experimentally obtained data with computed results. In addition to data available in the open literature, numerous comparisons were made with the experimental scrubbing data obtained in the present experiments. Figure 7

illustrates the extent of agreement between calculated and experimental results for single orifice experiments utilizing steam/air mixtures and a subcooled pool. It is seen that the calculated DFs are generally within a factor of two of the experimental ones. This is generally considered to be good agreement.

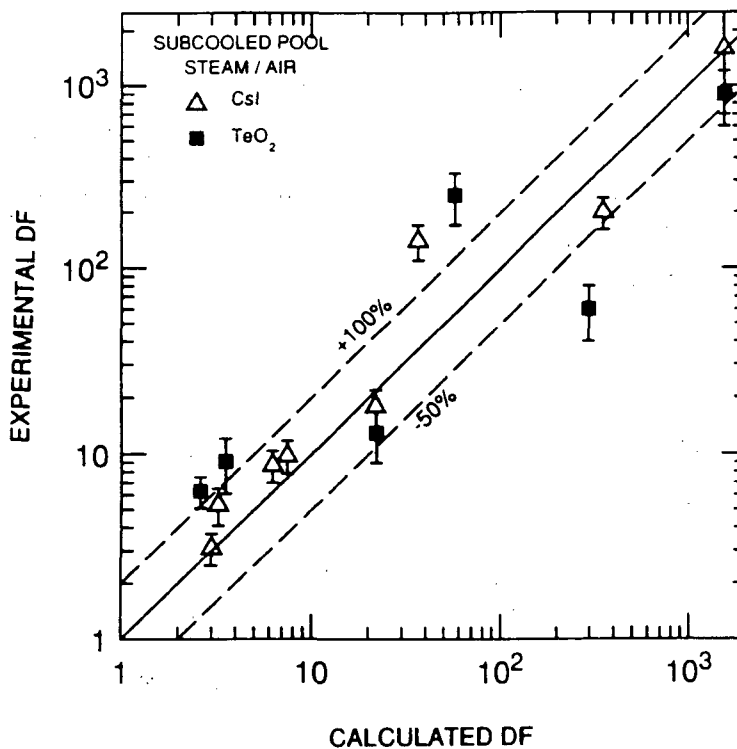


Figure 7. Single Orifice Scrubbing Comparison

Figure 8 provides a similar comparison, only this time the pool is nominally saturated. In fact, the pool is saturated only at the top surface since the increased hydrodynamic head at any location below the surface increases the local boiling temperature and renders the injection point subcooled. The agreement is similar to the subcooled pool, though there appears to be some underprediction of the DF.

To determine if single orifice data is applicable to the multiple orifice situation encountered in BWR suppression pools, experiments with multiple orifice injection were performed. As seen from the results in Figure 9, the agreement between experimental and calculated results is consistent with the single orifice results once the interaction of the bubble swarms is properly accounted for.

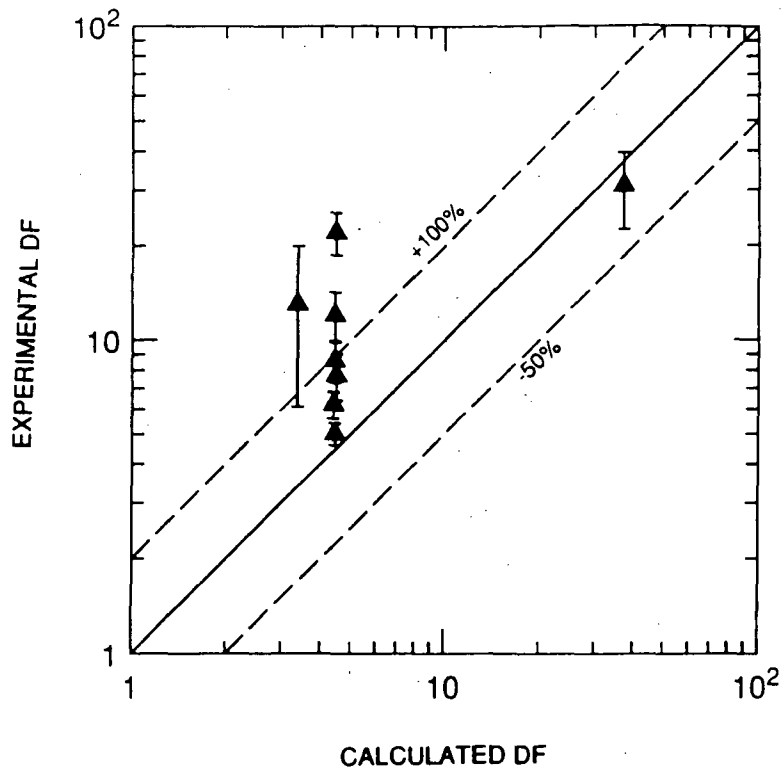


Figure 8. Scrubbing Comparison for a Saturated Pool

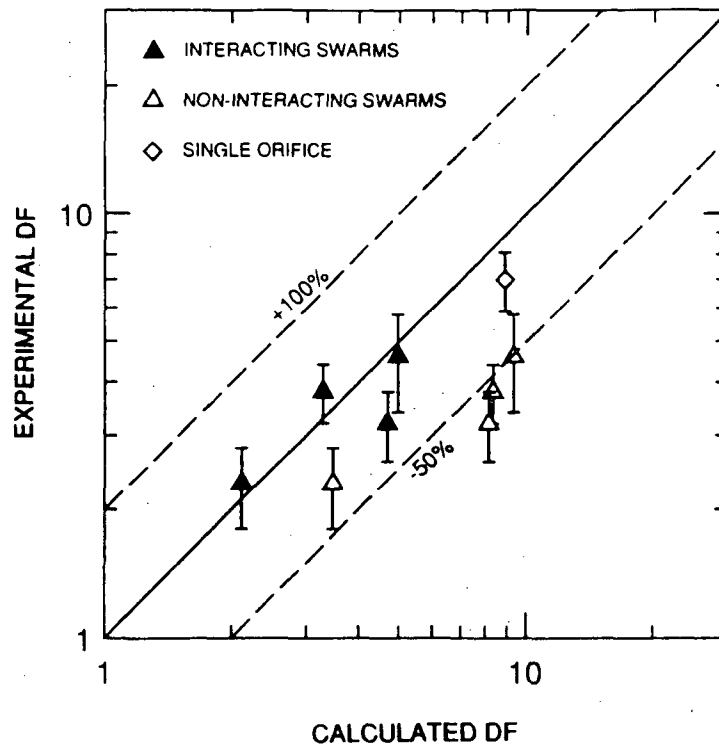


Figure 9. Multiple Orifice Injection Comparison

Similar results are shown for the downcomer injection and the side vent injection experiments in Figures 10 and 11 respectively.

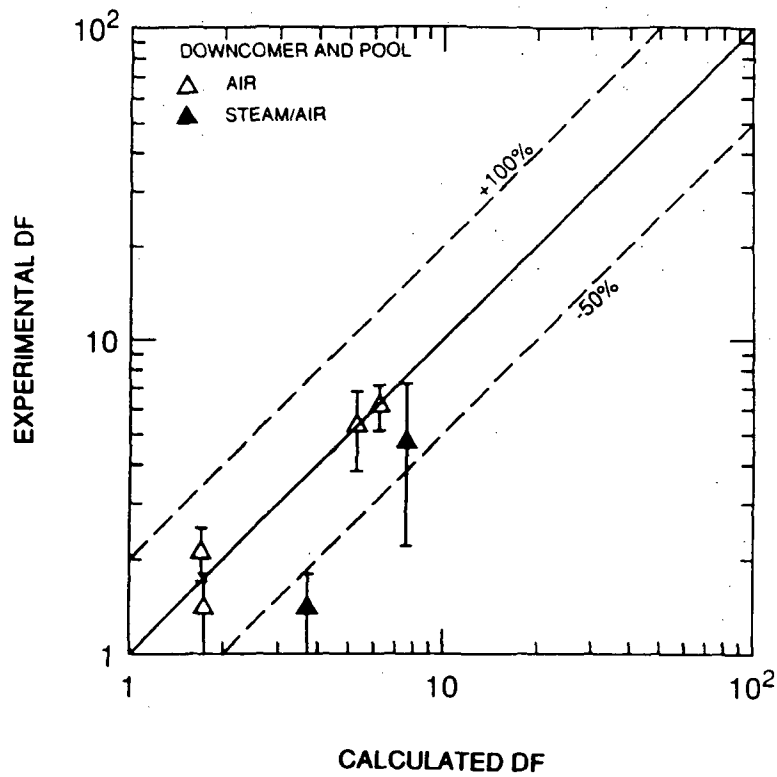


Figure 10. Downcomer Injection

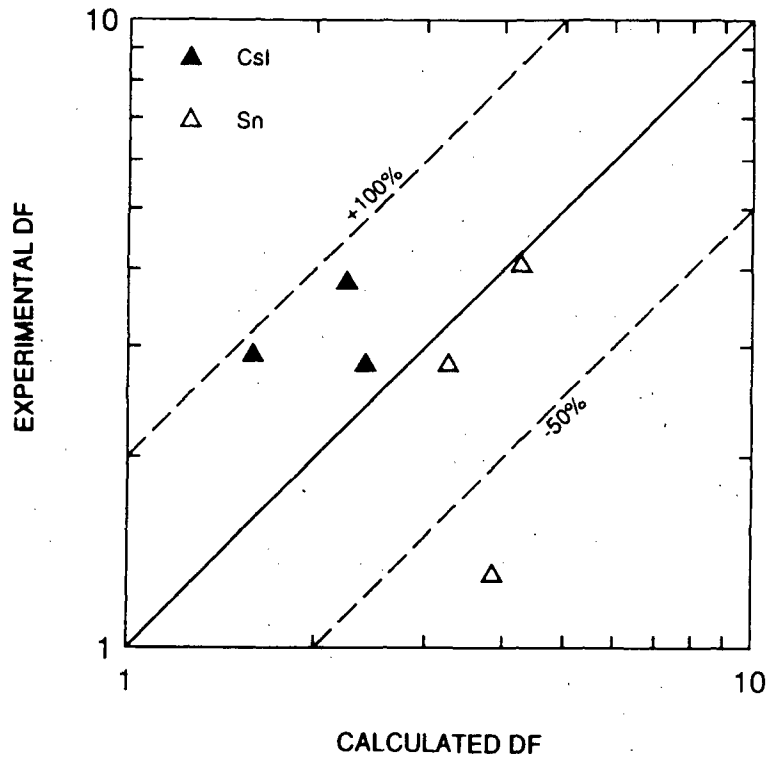


Figure 11. Side Vent Injection

Sensitivity studies and parametric calculations were also performed to determine the key parameters which affect the decontamination factors. The

results of a set of such calculations for a five meter deep pool are shown in Figure 12. It is clear that the two most important parameters are the aerosol particle size and the steam content of the carrier gas.

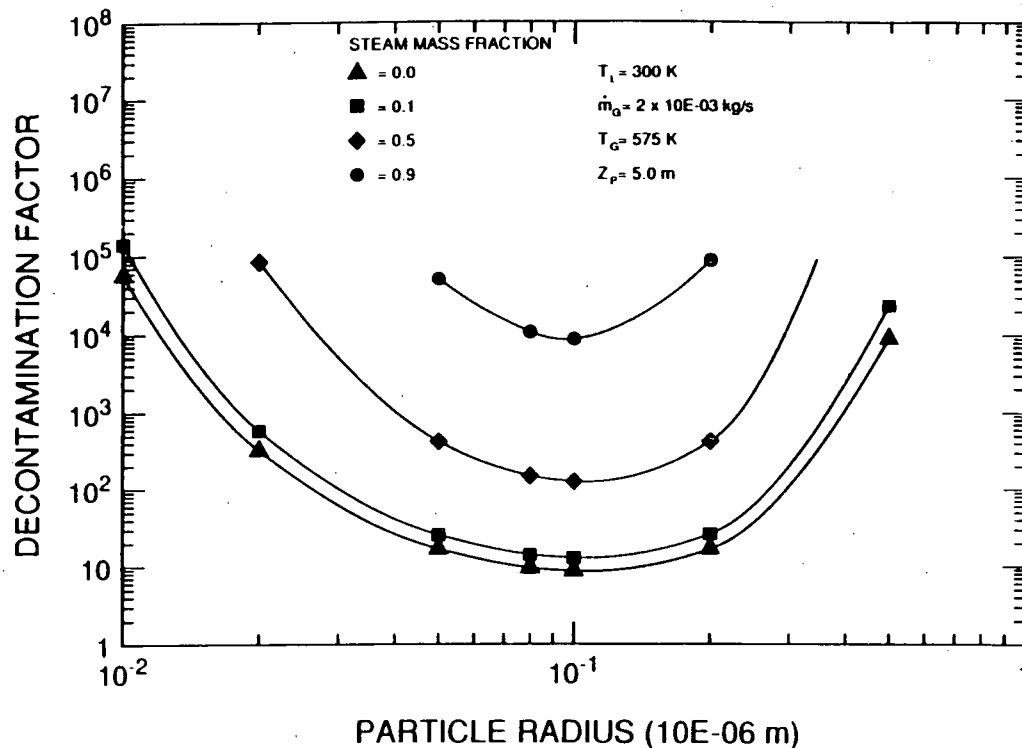


Figure 12. Effect of Particle Size and Steam Fraction on DF

### POOL SCRUBBING FOR A MARK I BWR TC SEQUENCE

In the BWR TC sequence chosen for this analysis, it is assumed that the control rods fail to insert during a reactor transient, but that the emergency core cooling systems function. The reactor power drops as a result of increased voidage, and heat is rejected from the reactor by the release of steam through the safety relief valves to the suppression pool. Makeup water is provided by the ECCS systems. Since the power level of the reactor exceeds, for the case considered, the heat removal capability from the suppression pool, the pool temperature rises, thereby pressurizing the containment. Before failure can occur, however, the wetwell is vented to relieve the containment pressure. At this point the water in the suppression pool boils and all injection systems are assumed to be lost. Since the core is no longer being adequately cooled it will heat up, melt, and ultimately lead to vessel failure.

Before vessel failure, fission product vapors and aerosols which are released from the core are transported to the suppression pool through the SRV lines

and injected through the quenchers. After vessel failure the path to the suppression pool leads through the downcomers.

Calculations for the fission product release and the thermalhydraulic conditions were performed with the MAAP code. The inlet conditions to the suppression pool included the gas mass flow rate, temperature, steam fraction, aerosol mass composition and size distribution. Other information provided by MAAP included the initial conditions in the pool and wetwell.

The main results of this illustrative calculation are shown in figure 13.

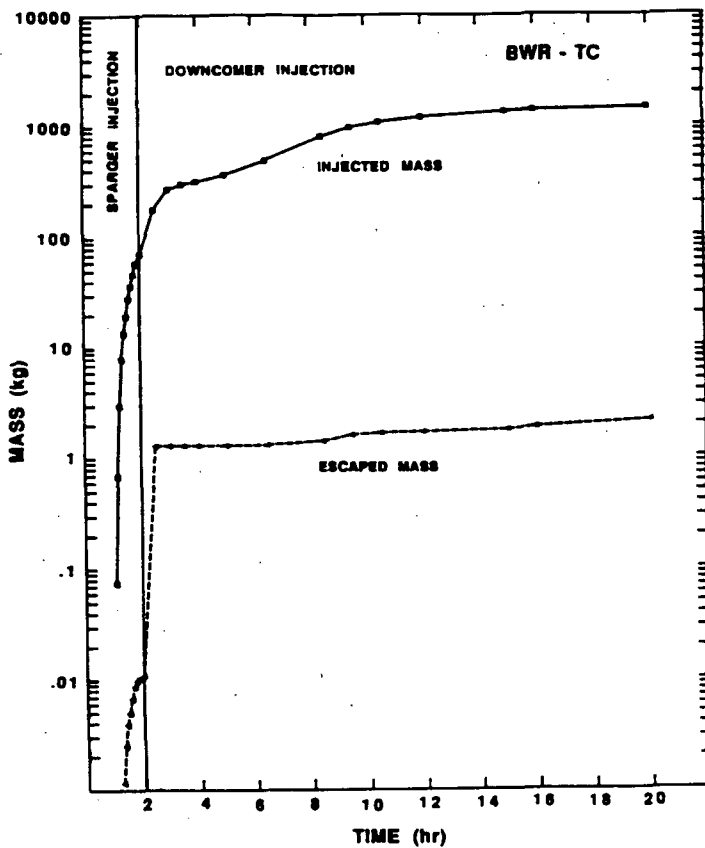


Figure 13. Injected and Escaped Aerosol Mass During the TC Sequence

This figure shows the integrated and escaped aerosol mass as a function of time. The material consists of tin-manganese, cesium iodide, tellurium oxide, and cesium hydroxide. Before vessel failure which occurs at about 2 hours, less than 100 kg of aerosol is injected into the pool through the spargers. By the end of the accident about 1500 kg has been injected, most of it through the downcomers. The overall decontamination factor for this calculation is 688. If we look at similar curves for the individual aerosol constituents we find that

each material has a different integral decontamination factor. These results are summarized in Table II.

Table II - Integral Decontamination Factors for the TC Sequence.

<u>Aerosol Material</u>	<u>Quencher Inj.</u>	<u>Downcomer Inj.</u>	<u>Total</u>
Sn-Mn	41,800	649	652
CsI	5,860	909	1455
TeO <sub>2</sub>	----	1935	1935
CsOH	5750	853	1601
Total	6780	657	688

The decontamination factors differ for each material because they are released from the core at different times and under different thermalhydraulic conditions. It is clear from this table that the DFs during quencher injection are substantially higher than during downcomer injection. The total DF does not provide an accurate indication of the fission product aerosol behavior because it is dominated by the structural, Sn-Mn, aerosol during downcomer injection. One should, therefore, differentiate between fission product DFs and structural material DFs in evaluating the results of particular accident sequences.

## SUMMARY AND CONCLUSIONS

The experimental program has shown that water pools can be very effective in separating aerosols from aerosol-gas mixtures. In particular, when the carrier gas steam fraction is high, or when the particle size is greater than one micron, the scrubbing effectiveness is very high.

The SUPRA code has been validated against an extensive set of scrubbing data and is capable of determining the decontamination factors within a factor of two to three. When applied to severe accident sequences the uncertainties in the knowledge of the particle size distribution dominate the uncertainties of the retention calculations.

## Validation of FREY for the Safety Analysis of LWR Fuel Using Transient Fuel Rod Experiments

R. O. Montgomery and Y.R. Rashid - ANATECH Research Corp.  
J. A. George and K. L. Peddicord - Texas A&M University  
C. L. Lin - Electric Power Research Institute

### ABSTRACT

The analysis and comparison of severe light water reactor transient experiments are presented from the FREY verification and validation effort. The methods used to model the fuel, cladding, and coolant geometry are discussed in addition to experimental data comparisons. The purpose of this study was to validate the predictive capabilities of the code for severe transient analysis. The FREY code has been developed, under the sponsorship of the Electric Power Research Institute, for the thermomechanical analysis of LWR fuel rods under steady state and transient conditions. A two-dimensional finite-element computational method is used to represent both symmetric (r-z) and plane (r- $\theta$ ) fuel geometries. The code can be used for both licensing and best estimate analyses.

A total of 10 test fuel rods from experimental programs conducted in both the Power Burst Facility (PBF) and the Transient Reactor Test Facility (TREAT) have been used in this study. The fuel rods were selected from the following test programs: Power Cooling Mismatch Tests, PCM-2 and PCM-4; Reactivity Initiated Accident Test, RIA 1-2; Loss-of-Coolant Accident Test, LOC-3; First Fuel Rod Failure Test, FRF-1; and Irradiation Effects Test, IE-3. The test programs used in this study cover a large range of code applications for severe transient analysis.

The results of the PCM-2, RIA 1-2, and FRF-1 analyses are presented to highlight the full two-dimensional modeling capabilities of FREY and to compare the thermal and mechanical measurements with FREY's prediction. The comparisons show good general agreement, with a tendency for FREY to overpredict the peak cladding surface temperature for a few cases where strong three-dimensional effects have been identified.

### INTRODUCTION

Under certain operational transients, fuel rods may be subjected to the film boiling heat transfer regime during which cladding surface temperatures could rise above the beta phase transformation temperature. An analysis of the fuel rod transient behavior in the post-DNB heat transfer regime requires the modeling of several interacting complex processes, namely, heat conduction in the fuel rod, heat flow to the coolant, thermal hydraulics of the flow channel, cladding deformations and possible cladding failure. Computer codes intended for this class of transients vary widely in their modeling approaches. For example, transient reactor simulation codes place much greater emphasis on thermal hydraulics modeling than on fuel rod thermal/mechanical modeling, utilizing thermal limits as evaluation criteria rather than mechanical limits [1,2]. Several fuel behavior codes, on the other hand, model the fuel and cladding behavior in detail, relying on input heat transfer coefficients obtained from separate thermal hydraulics

analysis [3]. This provides only passive coupling between the coolant and fuel models, introducing areas of uncertainty in the analysis. Full active coupling between the two types of models would be computationally prohibitive, particularly in multichannel or three-dimensional thermal hydraulics codes. An acceptable alternative would be to integrate a 1-dimensional coolant channel model with a fuel behavior code and then establish acceptance by validating the code against well characterized transient experiments. This approach was adopted for the FREY code [4]

## CODE DESCRIPTION

The FREY code has been developed as a Fuel Rod Evaluation sYstem for the transient and steady state analysis of light water reactor fuel. The code computes both the detailed thermal and mechanical behavior of the fuel rod during normal operation and transient events. The thermal boundary conditions are either calculated by the code using a closed channel coolant model to calculate the cladding surface-to-coolant heat transfer coefficient or the user can specify heat transfer coefficients and bulk temperatures as functions of spatial position and time. The later method extends the codes utility to a wide range of transients for which one-way coupling of thermal hydraulic and thermomechanical responses is valid. The computational structure of FREY is based on the two-dimensional finite element method combined with variable time and power stepping procedures. The two-dimensional finite element method is utilized to treat axi-symmetric (r-z) or plane (r- $\theta$ ) fuel rod geometries. A single compatible grid is used for both the thermal and deformation solution. The finite element models utilized by FREY incorporate all the necessary features required for the detailed representation of the fuel, cladding, gap, plenum, coolant channel, and pellet-cladding and pellet-pellet interface [4]

MATPRO-11 is used to determine the thermal and mechanical properties of the fuel, cladding, and internal gas [5]. In addition, the ANS5.4 fission gas release model is included for steady state fission gas release and the EPRI/CE model is used for transient gas release. Deterministic models for cladding integrity evaluation are available for design basis events as well as normal operation. In the operational range, the code uses a cladding failure criterion based on stress-corrosion cracking; for operational transients, the code produces all the necessary parameters needed for comparison with the specified acceptable fuel design limits and thermal margins. For safety evaluation under accident conditions, a cladding rupture and oxidation criteria are applied to the large deformation ballooning-type failures at high temperatures.

The temperature and deformation solutions are consistent in the time stepping iteration procedures. In each step, the heat transfer and deformation problems are solved in tandem with provisions for performing multiple iterations in both solutions independently and combined. The material constitutive relations rigorously account for the elastic-plastic-creep behavior of the fuel and cladding, fuel swelling, densification, relocation, and cracking. The Ross and Stoute gap conductance model is used to couple the fuel and cladding thermal response. The coolant flow model, which utilizes widely used heat transfer and critical heat flux correlations, is complemented by user-input of heat transfer coefficient and bulk temperature as functions of spatial position and time. An additional feature includes the option to specify the time and location at which specific axial positions depart from nucleate boiling and pass into post-DNB heat transfer.

The code's restart capabilities are versatile and highly user-oriented. Extensive pre- and post-processing features are provided for input simplification, data reduction and plotting. Prepared model libraries containing grid and geometric boundary conditions data for standard fuel rod

designs are incorporated into the code's pre-processor. This data can be easily retrieved and modified at will using only a few input parameters, which results in great time saving and convenience for the user. Typical models are modest in size and a large number of time steps can be economically computed.

## VERIFICATION AND VALIDATION

FREY is currently undergoing an extensive verification and validation effort for application to transient analysis of light water reactor fuel. The purpose of this study is to verify and validate the predictive capabilities of the code for severe transient analysis by evaluating fuel rods from different transient tests. In this study, both the predicted thermal and mechanical responses of the code were compared to in-reactor measurements and post-irradiation examinations to assess the applicability of the code.

Several accident conditions must be considered in the design and analysis of LWRs. The traditional loss-of-coolant accident (LOCA) and the reactivity initiated accident (RIA) are the two worst case conditions for the analysis of reactor transients. Complete or partial loss of coolant from the reactor core during a LOCA represents the extreme in loss of cooling capability. The severe power increase as a result of a control rod ejection from the core during an RIA represents the most critical overpower condition possible for a LWR transient. Resident between these two extreme transient conditions are several off-normal power or cooling conditions, normally referred to as power-cooling mismatch (PCM) transients. PCM type operational transients represent the less severe off-normal conditions which occur when the coolant cannot adequately remove the energy from the fuel rod. Numerous possible scenarios can be envisioned which are classified as PCM type transients, such as a loss of a primary coolant pump, flow blockage, or overpower condition during operation. In a majority of these transients, departure from nucleate boiling can take place, resulting in increased cladding surface temperatures and possible fuel rod failure.

Experimental data used in this verification and validation study encompassed a wide range of FREY applications. The tests selected include, LOCA, PCM, and RIA type of transient experiments to provide a comprehensive assessment of the capabilities of FREY. A total of 10 test fuel rods from experimental programs conducted in both the Power Burst Facility (PBF) and the Transient Reactor Test Facility (TREAT) have been used in this study. They were selected from the following test programs: Power Cooling Mismatch Tests, PCM-2 and PCM-4; Reactivity Initiated Accident Test, RIA 1-2; Loss-of-Coolant Accident Test, LOC-3; First Fuel Rod Failure Test, FRF-1; and Irradiation Effects Test, IE-3 [6-11]. The fuel rods used in this study are presented in Table 1.

The PCM and IE-3 tests utilized power increases and flow decreases to evaluate the effects of post-DNB operation on the fuel rod integrity. This type of behavior would be expected during either a loss-of-coolant flow event such as a locked rotor or loss of primary coolant pump transient or an overpower condition such as anomalous control rod movement. The large overpower effects of a control rod ejection accident were investigated in the RIA 1-2 test. Finally, the influence of the blowdown and heatup phase of a loss-of-coolant accident (LOCA) on the cladding behavior was studied in the LOC-3 and FRF-1 experiments conducted in the PBF and TREAT facilities.

All of the above test programs, except for the FRF-1 test, were conducted in the PBF reactor using the in-pile-tube (IPT). A schematic of the IPT geometry is shown in Figure 1. The test geometry consists of four fuel rods positioned radially in the IPT device. A separate flow shroud

Table 1  
 Fuel Rods Used in the FREY  
 Validation Study for Severe Transients

<u>Experiment</u>	<u>Rod</u>
PCM-2	UTA-008
PCM-4	UTA-015
IE-3	IE-017, IE-018
RIA 1-2	802-1, 802-2, 802-3
LOC-3	840, 932
FRF-1	Rod L

Table 2  
 Coolant and Geometry Parameters for Rod UTA-008

Coolant Pressure	13.53 MPa (1960 psia)
Inlet Mass Flux	1361 kg/sec-m <sup>2</sup> (1.0 Mlbm/hr-ft <sup>2</sup> )
Inlet Temperature	601 K (622 °F)
Hydraulic Diameter	5.6 mm (.22 in)
Fractional Density	93%
Enrichment	20%
Fuel Pellet Diameter	9.3 mm (.366 in)
Fuel-Cladding Dia. Gap	0.2 mm (7.9 mils)
Outer Cladding Diameter	10.72 mm (.422 in)
Initial Fill Pressure	2.58 MPa (374 psia)
Initial Fill Temperature	294 K (70 °F)
Initial Fill Gas Comp.	100% He
Initial Fuel Relocation	50%

was used to contain each test fuel rod, providing for thermal and hydraulic isolation. The coolant conditions in each of the flow shrouds were monitored during the test. These parameters included coolant pressure, coolant flow rate, inlet and outlet temperatures, axial neutron flux profiles, and fuel rod length changes. In-pile instrumentation was also carried out for a majority of the fuel rod parameters. Cladding thermocouples positioned at different axial and azimuthal locations, fuel centerline thermocouples, and bellows type pressure transducers were used to monitor the fuel rod behavior during the test.

The FRF-1 test was conducted in the TREAT facility using a seven-rod bundle of zircaloy-clad  $\text{UO}_2$  fuel rods in a flowing steam atmosphere. The bundle was contained in a zircaloy flow shroud. An equilateral triangular spacing was used to position the rods in the bundle. A schematic of the rod bundle used in TREAT is shown in Figure 2. Cladding surface temperature, fuel rod internal pressure, system pressure and steam flow rate were monitored during the duration of the test.

Extensive post-irradiation examinations (PIE) were conducted to characterize the mechanical and thermal performance of all the fuel rods. Diametral measurements were used to determine the cladding collapse or swelling during high temperature operation. Visual inspections were used to locate the regions of post-DNB operation and cladding oxide formation. Metallographic and metallurgical examinations were carried out on the cladding and fuel, respectively, to determine the thermal performance and to assess the interaction between fuel and cladding and between cladding and coolant.

The large amount of experimental data available from these tests provided for an extensive comparison between predicted and measured responses. However, a major effort and engineering judgement was required to interpret and apply the experimental data as a result of the 2-dimensional modeling of a 3-dimensional system. Several factors such as the stochastic nature of film boiling and the geometry changes caused by rod bowing lead to significant circumferentially varying effects not modeled in an r-z representation. Even with the amount of experimental data, either global parameters were monitored such as fuel rod internal pressure or a few local parameters were monitored at select positions, such as fuel centerline and cladding surface temperatures. PIE results yield a description of the fuel rod after the test has been completed and removed from the reactor. Therefore, some uncertainties exist in how accurate the experimental data illustrates the behavior of the fuel rod during the test. Secondly, limitations exist as to the ability of current state-of-the-art methods and correlations to account for all the phenomena occurring during severe fuel rod transients. These factors have an important impact on the comparison of code predictions to experimental results and must be acknowledged when assessments are made.

To highlight the results of the verification and validation study, a brief description of the PCM-2, RIA 1-2, and FRF-1 analyzes will be presented in the following sections. Each section will contain a review of the experimental test, the modeling procedures used, and a comparison of the predicted and experimental results.

### Power Cooling Mismatch Test 2 (PCM-2)

PCM-2 was simulated in the PBF reactor to characterize the behavior of unirradiated PWR type fuel rods under various normal and post departure from nucleate boiling (DNB) conditions. The test was performed using four unirradiated  $\text{UO}_2$ -fueled, zircaloy clad fuel rods. Departure

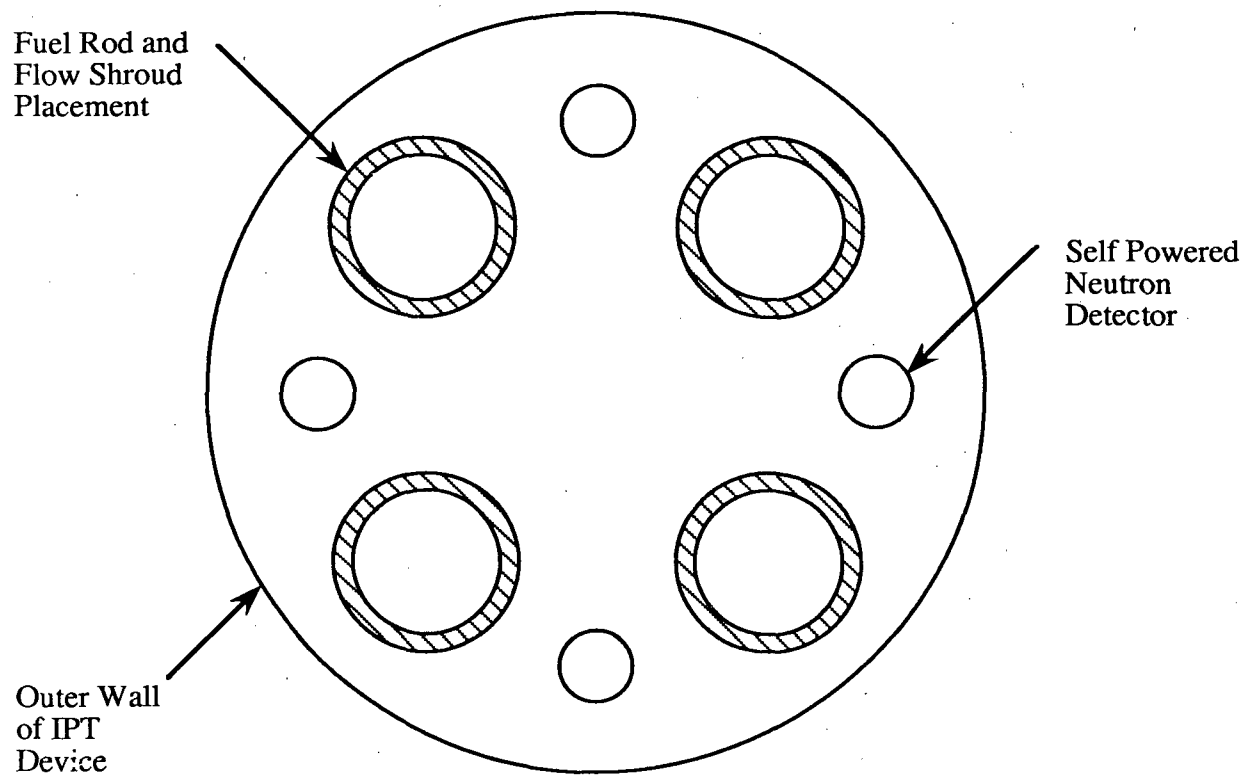


Figure 1. Fuel Rod and Flow Shroud Placement in the PBF In-Pile-Tube (IPT)

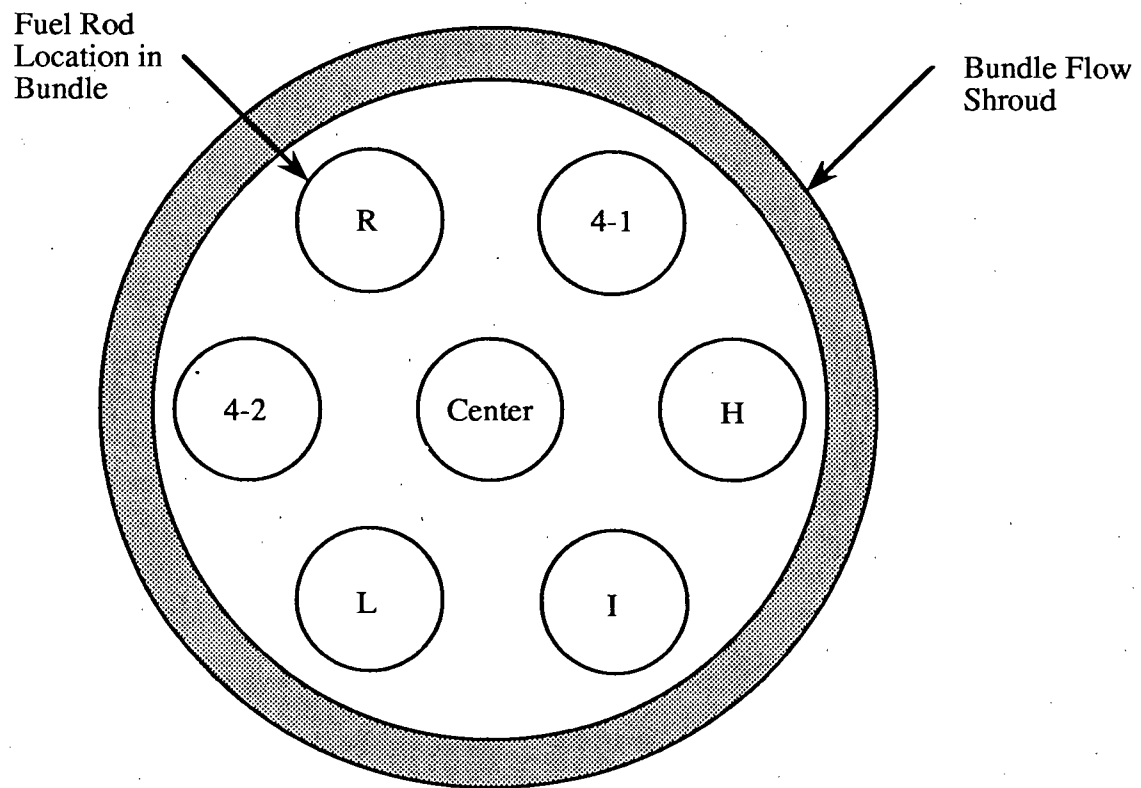


Figure 2. Fuel Rod and Flow Shroud Placement for FRF-1 in TREAT

from nucleate boiling (DNB) was achieved by decreasing the coolant flow rate while maintaining a constant fuel rod power. The specific parameters of interest during the test were: 1) the fuel rod power and coolant flow rate at which DNB occurred on the test fuel rods, and 2) the thermal and mechanical behavior of the test fuel rods following DNB.

The four fuel rods used in the PCM-2 test had a fueled length of .914 m (35.98 in) and a total length of .990 m (38.97 in). The UO<sub>2</sub> fuel pellets were 93% TD and 20% enriched. The nominal pellet diameter was 9.3 mm (.366 in). The pellets were contained in Zircaloy-4 cladding with a nominal 0.61 mm (24 mil) thickness and a nominal outside diameter of 10.7 mm (.421 in). Three of the rods were internally pressurized with He fill gas to 2.58 MPa (374 psia). The fourth rod was internally pressurized with He to 3.88 MPa (563 psia).

The PCM-2 experiment consisted of 4 phases; 1) power calibration, 2) preconditioning, 3) fuel rod aging, and 4) eight DNB cycles. The first three phases were used to calibrate the instrumentation and to prepare the fuel rods for DNB operation. The first 7 DNB cycles were used to determine the mass fluxes at which DNB was initiated. During the first set of DNB cycles, the fuel rod powers were reduced after DNB was indicated to prevent high cladding temperatures and possible fuel rod failure. Only during the eighth DNB cycle were the fuel rods left in post-DNB operation.

Rod UTA-008 during DNB cycle 8 was selected for examination and comparison with FREY. The coolant conditions during cycle 8 for rod UTA-008 consisted of a coolant flow reduction from 1361 kg/s-m<sup>2</sup> (1.00 Mlbm/hr-ft<sup>2</sup>) to 750 kg/s-m<sup>2</sup> (.55 Mlbm/hr-ft<sup>2</sup>) at a rate of 3 %/sec at a constant average fuel rod power of 46 kW/m (14 kW/ft). The axial peaking factor for this rod was 1.35. Film boiling conditions were terminated after 145 seconds of post-DNB operation by decreasing the average fuel rod power to 30 kW/m (9.1 kW/ft) and increasing the coolant mass flux. The measured peak cladding temperature was 1315 K (1908 °F). The measured fuel centerline temperature increased from 1685 to 2290 K (2574 to 3663 °F) after DNB occurred.

No fuel rod failures occurred as a result of 145 seconds of high temperature post-DNB operation. PIE conducted on the test fuel rods revealed cladding outer surface oxide formation on all the fuel rods. A region of cladding collapse was observed in the high temperature zone. Cladding temperatures were determined by metallographic examination of the cladding microstructures. The measured cladding temperature responses agreed well with the temperatures determined metallographically.

### FREY Analysis of PCM-2

Test PCM-2 rod UTA-008 was selected for analysis with FREY to determine the ability of the code to predict the cladding temperature, fuel centerline temperature, fuel rod internal pressure, and the mechanical response of the fuel rod. The behavior of rod UTA-008 was modeled during DNB cycle 8 when extended operation in high temperature film boiling occurred.

The finite element grid used to represent the rod UTA-008 is shown in Figure 3. An axisymmetric r-z representation was used to model the fuel, cladding, gap, upper and lower plena, and upper and lower end caps. A list of the important coolant and geometrical parameters are shown in Table 2. These values were determined from both test reports [6] and the EPRI/Utility Transient Fuel Behavior Data Information Source (ERUDITE) [13]. The Westinghouse (W-3)

critical heat flux correlation was used to determine the time and location of DNB. Adequate results were achieved with the W-3 correlation for this analysis. However, it is recognized that the prediction of DNB is strongly a statistical problem and it is recommended that the measured time and location of DNB be used to initiate DNB in future analysis.

The results of the PCM-2 analysis are shown in Figures 4 thru 7. Comparisons are made to the extent of film boiling along the cladding surface, the magnitude and response of the cladding surface temperature at the 0.686 m (27 in) axial location, the fuel centerline temperature, and the fuel rod internal pressure. Figure 4 shows the predicted axial profile of film boiling and the maximum achieved cladding surface temperatures for rod UTA-008. Both the metallographically determined temperatures and the maximum thermocouple readings are included for comparison. FREY slightly over predicts both the peak temperature and the extent of film boiling. Figure 5 shows the cladding surface temperature response at the 0.686 m (27 in) axial location for the thermocouple position. Using the W-3 critical heat flux correlation, FREY predicts DNB to occur approximately 10 seconds before the temperature excursions were indicated by the thermocouple responses. Good agreement is seen for the peak cladding temperatures and the trends between FREY and the thermocouple data. The slight overprediction of the peak cladding temperatures could be caused by the inability of a 2-dimensional representation of the fuel rod and coolant channel to account for the 3-dimensional effects associated with film boiling flow conditions and geometry changes due to rod bowing. Preliminary analysis indicates that these factors reduce the peak cladding temperatures. The calculated post-DNB heat transfer coefficients may also cause the high predicted temperatures. The correlations used were limited in their range of application and by applying these correlations near the limits of their range could lead to lower than actual heat transfer coefficients.

The fuel centerline temperature comparison at the location of the fuel thermocouple for rod UTA-008 is presented in Figure 6. FREY predicts the centerline temperature to be 120 K (216 °F) higher than the measured value. However, the predicted value resides within the uncertainty associated with the measured value. The predicted response shows good agreement with the measured response. FREY predicts the peak in the fuel temperature to be 150 K (270 °F) higher than the measured value. Overall, the predicted fuel temperature response agrees well with the measured values.

Lastly, the fuel rod internal pressure is shown in Figure 7 for rod UTA-008. The predicted value is approximately 0.6 MPa (87 psia) higher than the measured value. FREY also under predicted the initial internal volume as compared to the measured pre-irradiated volume. This difference could be attributed to the method used to model the external volume associated with the pressure transducers. However, the pressure response is consistent with the modeled internal volume. A slight increase in pressure is predicted when DNB occurs. The magnitude of the pressure increase is less than the measured value.

#### Reactivity Initiated Accident Test 1-2 (RIA 1-2)

The RIA 1-2 test was conducted to simulate the overpower effects of a reactivity initiated accident on fuel rod behavior. The main objectives of the test were to provide data on fuel rod failure mechanisms for previously irradiated PWR type fuel rods and its consequences during an RIA at enthalpy insertion values of 185 cal/g for radially averaged peak fuel enthalpy. Additionally, it was desired to study the effect of beginning-of-life (BOL) and end-of-life (EOL) rod internal pressures on the response of pre-irradiated fuel rods.

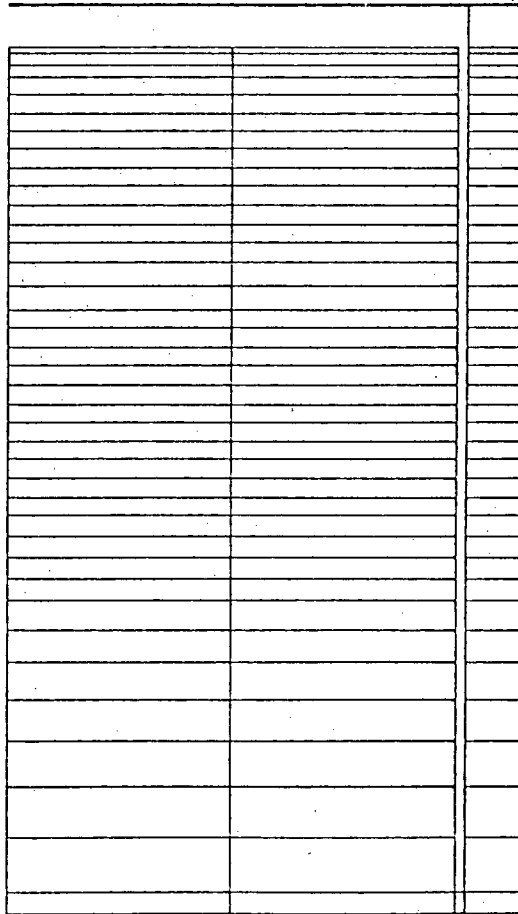


Figure 3. Finite Element Grid used in the PCM-2 Rod UTA-008 Analysis

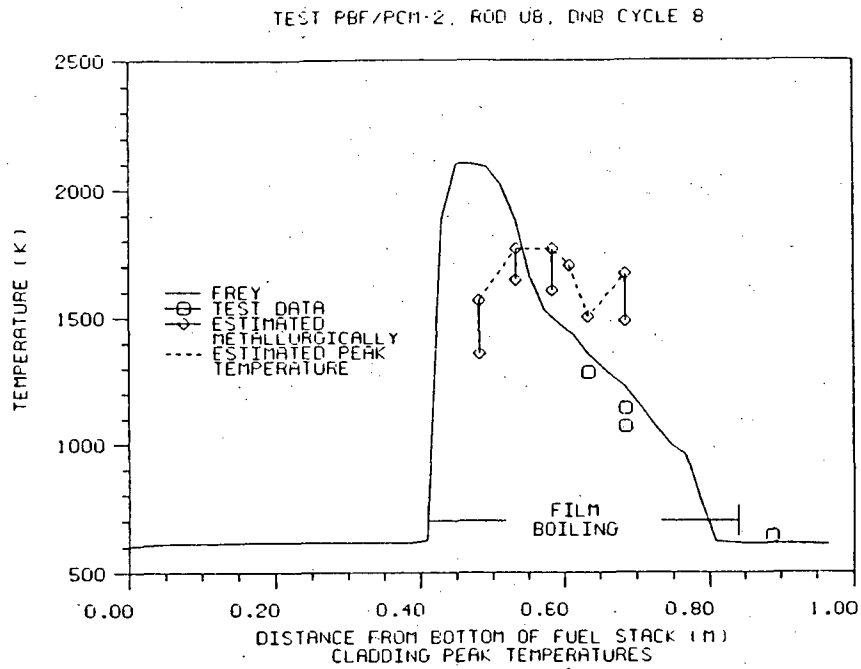


Figure 4. Axial Profile of the Maximum Cladding Surface Temperature for Rod UTA-008

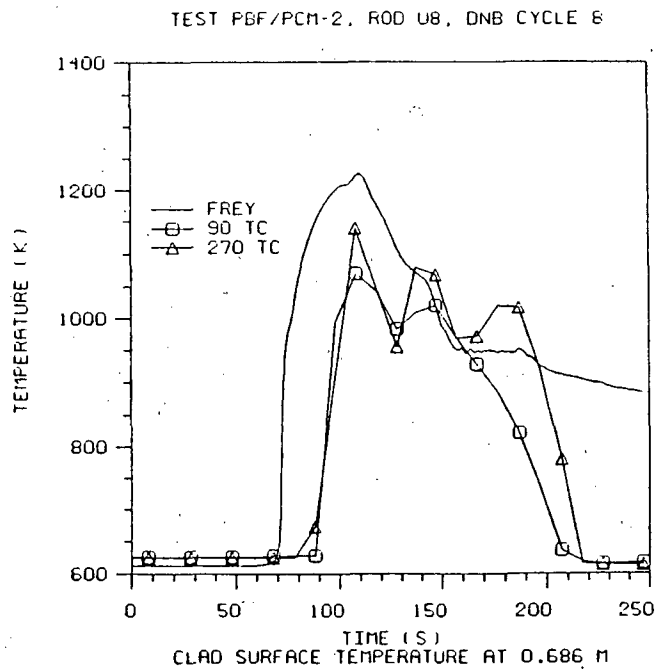


Figure 5. Thermocouple Response and FREY Prediction for the Cladding Surface Temperature at the 0.686 m Location for Rod UTA-008

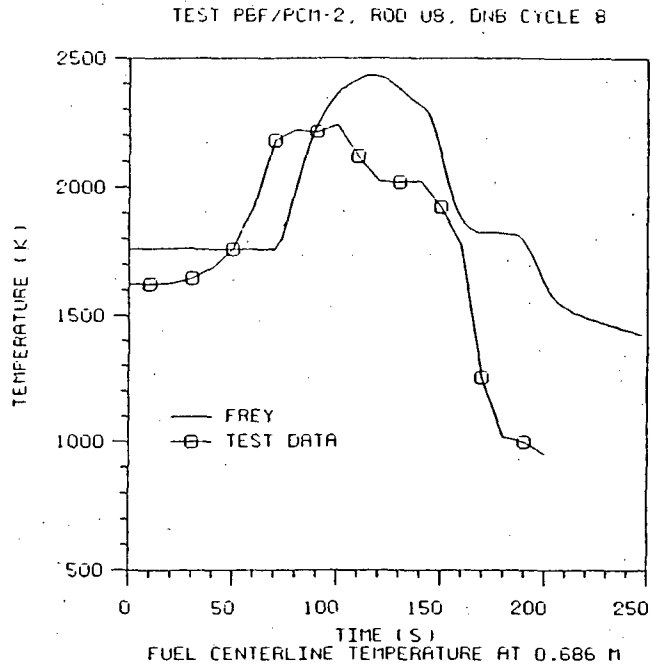


Figure 6. Thermocouple Response and FREY Prediction for the Fuel Centerline Temperature at the 0.686 m Location for Rod UTA-008

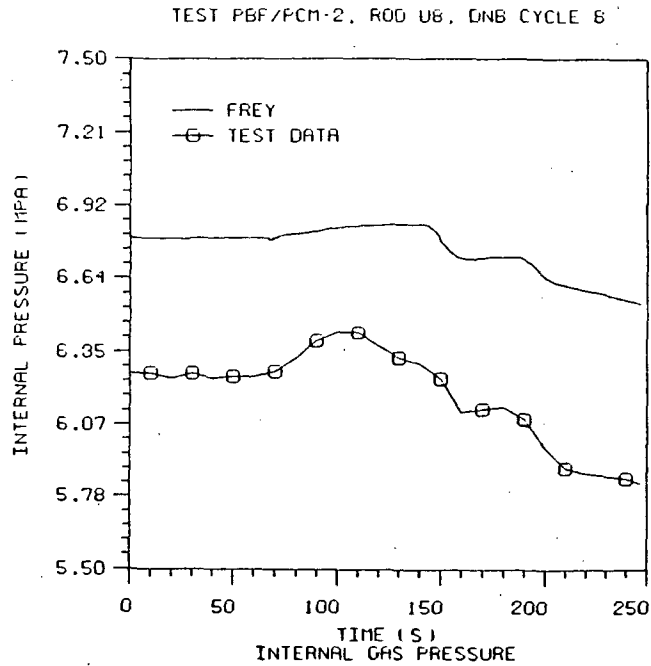


Figure 7. Measured and Predicted Fuel Rod Internal Pressure for Rod UTA-008

The test consisted of subjecting four individually shrouded PWR-type fuel rods at BWR hot-startup coolant conditions to a 24,000 kW/m (7300 kW/ft) peak transient power burst. The duration of the power burst was 60 ms. The four fuel rods had been previously irradiated in the Saxton reactor to burnups of approximately 4800 MWd/tU. Two of the fuel rods were backfilled to 2.41 MPa (350 psia) to represent end-of-life (EOL) conditions and a third rod was backfilled to 0.105 MPa (15 psia) to represent beginning-of-life (BOL) conditions to study the effects of different internal pressures.

The four fuel rods used in RIA 1-2 had a fueled length of .914 m (35.98 in) and a total length of 1.0 m (39.37 in). The UO<sub>2</sub> fuel pellets were 94% TD and 5.7% enriched. The nominal pellet diameter was 8.5 mm (.335 in). The pellets were contained in Zircaloy-4 cladding with a nominal 0.62 mm (24 mil) thickness and a nominal outside diameter of 9.9 mm (.39 in).

The RIA 1-2 experiment consisted of three phases: 1) power calibration, 2) preconditioning, and 3) power burst. Phases 1 and 2 were used to calibrate the instrumentation and to prepare the fuel rods for the test procedure. Phase 3 consisted of a single power burst of about 60 ms duration. This resulted in a peak fuel rod power of about 24,000 kW/m (7300 kW/ft) and the deposition of 185 cal/gm of energy for the radially averaged fuel enthalpy at the peak axial location.

One of the low pressure fuel rods failed as a result of the large deposition of energy during the power burst phase. The fuel rods operated in post-DNB heat transfer for 17 seconds after the power burst. Indicated peak cladding temperatures were above 1500 K (2240 °F) as determined from thermocouple response. Cladding collapse occurred due to the high temperature operation.

### FREY Analysis of RIA 1-2

RIA 1-2 rod 802-2 was selected for examination and comparison with FREY results to assess the capability of the code to calculate the thermal response of a fuel rod during a large power burst. The finite element grid used to represent rod 802-2 is shown in Figure 8. An axi-symmetric r-z representation was used to model the fuel, cladding, gap, upper and lower plena, and upper and lower end caps. A list of the important input and geometrical parameters are shown in Table 3. These values were determined from the test report [9]. The Babcock and Wilcox (B&W-2) critical heat flux correlation was used in the analysis to determine the time and location of DNB. However, the type of correlation used was not important in the analysis because DNB occurred at 0.1 second into the transient as a result of the large heat fluxes predicted to occur.

The results of the RIA 1-2 analysis are shown in Figures 9 thru 11 for rod 802-2. Comparisons were made to the experimental results for the fuel rod internal pressure and the magnitude and response of the cladding surface temperature at two axial locations. Figures 9 and 10 show the cladding surface temperature responses at 0.46 m (18.1 in), which is approximately the peak power location, and at 0.79 m (31 in) above the bottom of the fuel rod. At 0.46 m (18.1 in), FREY predicts much higher temperatures than the measured response for the temperature excursion associated with DNB. FREY predicts the decrease in temperature approximately 2 seconds after the initiation of the transient, however, the temperatures are still above the measured values. FREY does not predict the rewet of the fuel rod at 17 seconds due to the fact that the coolant channel analysis does not contain a rewet model. User specified boundary conditions can be used to analyze the thermomechanical response of a fuel rod during rewet. FREY shows

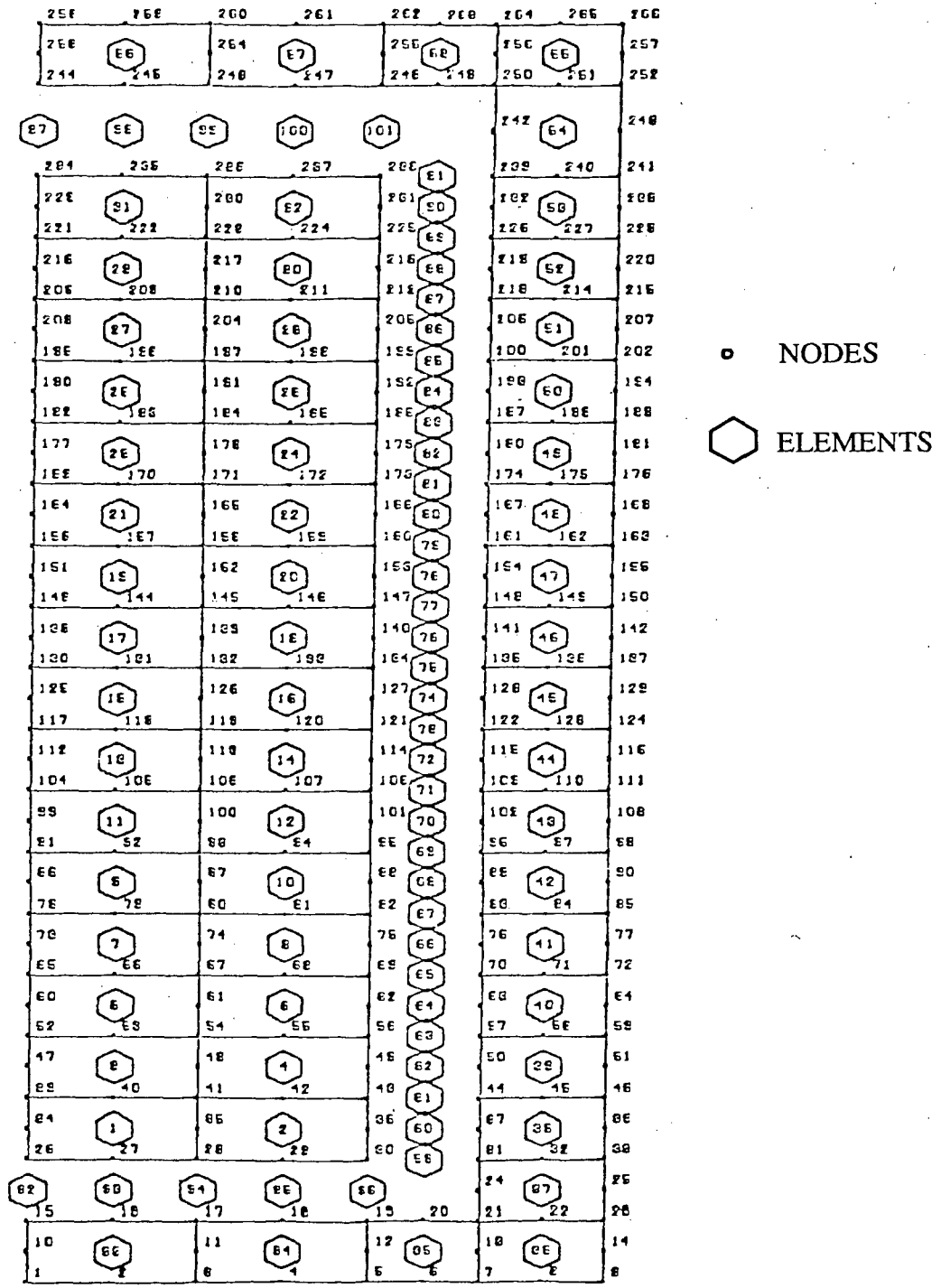


Figure 8. Library Model FULL-4 Used in the RIA 1-2 and FRF-1 Analysis

Table 3

## Coolant and Geometry Parameters for Rod 802-2

Coolant Pressure	6.45 MPa (935 psia)
Inlet Mass Flux	882 kg/sec-m <sup>2</sup> (.65 Mlbm/hr-ft <sup>2</sup> )
Inlet Temperature	538 K (509 °F)
Hydraulic Diameter	6.4 mm (.25 in)
Fractional Density	94%
Enrichment	5.7%
Fuel Pellet Diameter	8.58 mm (.337 in)
Fuel-Cladding Dia. Gap	0.17 mm (6.7 mils)
Outer Cladding Diameter	9.99 mm (0.393 in)
Initial Fill Pressure	2.41MPa (350 psia)
Initial Fill Temperature	294 K (70 °F)
Initial Fill Gas Comp.	77.7% He, 22.3% Ar
Initial Fuel Relocation	50%

Table 4

## Coolant and Geometry Parameters for Rod L

Coolant Pressure	0.149 MPa (21.6 psia)
Inlet Mass Flux	0.3408 kg/sec-m <sup>2</sup> (224 lbm/hr-ft <sup>2</sup> )
Inlet Temperature	457 K (363 °F)
Hydraulic Diameter	5.314 mm (.21 in)
Fractional Density	94.4%
Enrichment	2.5%
Fuel Pellet Diameter	12.49 mm (.49 in)
Fuel-Cladding Dia. Gap	0.22 mm (9 mils)
Outer Cladding Diameter	14.38 mm (.57 in)
Initial Fill Pressure	.979 MPa (142 psia)
Initial Fill Temperature	298 K (77 °F)
Initial Fill Gas Comp	100% He
Initial Fuel Relocation	0%

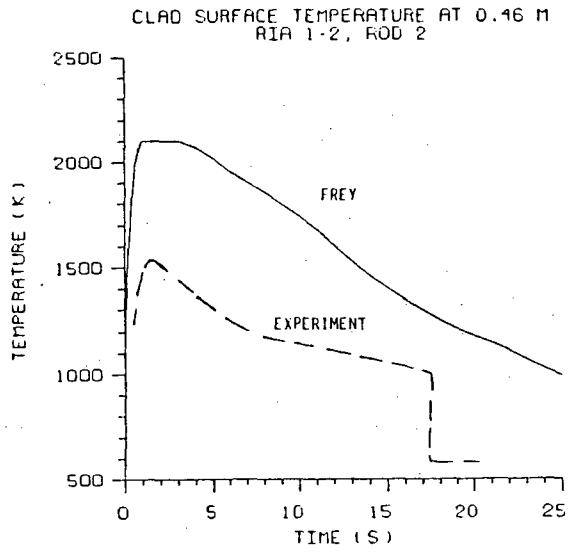


Figure 9. Thermocouple Response and the FREY Prediction for the Cladding Surface Temperature at the 0.46 Location for Rod 802-2

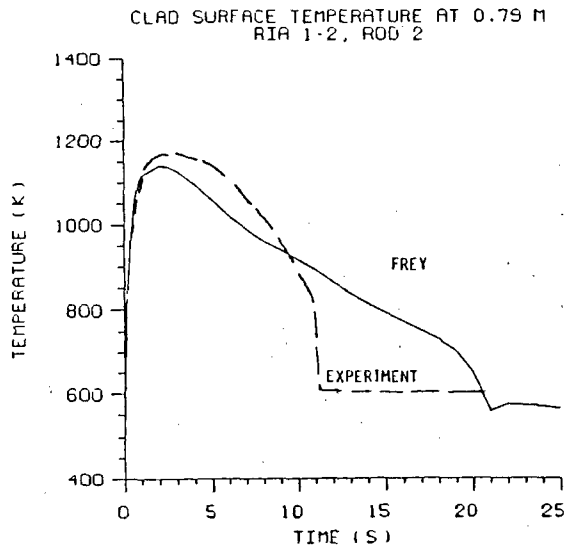


Figure 10. Thermocouple Response and the FREY Prediction for the Cladding Surface Temperature at the 0.79 Location for Rod 802-2

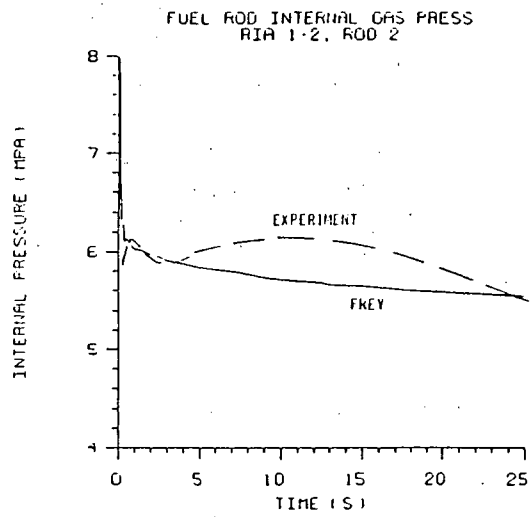


Figure 11. Measured and Predicted Fuel Rod Internal Pressure for Rod 802-2

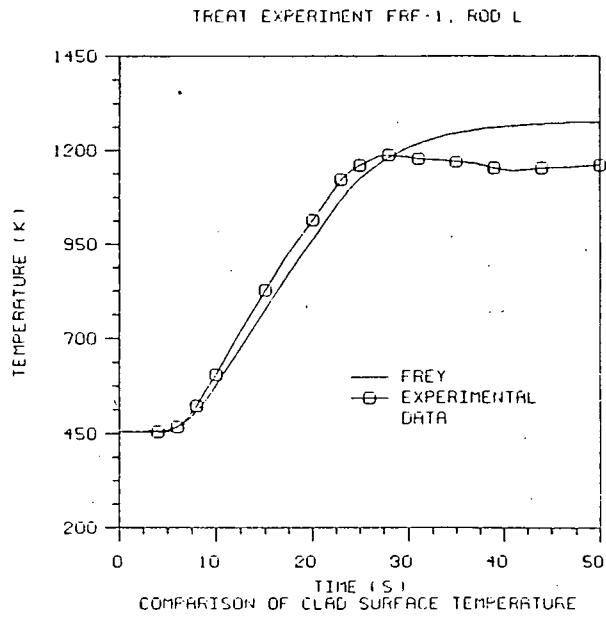


Figure 12. Thermocouple Response and FREY Prediction for the Cladding Surface Temperature for Rod L

excellent agreement with the measured cladding temperature response for Rod 802-2 at the 0.79 m (31 in) location. Again, FREY does not show rewet at about 12 seconds.

The overprediction of the cladding surface temperatures for FREY in the peak power location could be related to the post-DNB heat transfer correlations used in the analysis. Also, the analysis was carried out assuming all the energy generated was deposited in the fuel. Experimental evidence suggests that a significant fraction of the prompt gamma energy was deposited in the cladding, coolant, and structure. Coolant voiding was indicated at initiation of the power burst as a result of the deposition of gamma energy.

The predicted and measured internal fuel rod pressure responses are shown in Figure 11. FREY predicts a large pressure increase up to 7.8 MPa (1131 psia) during the first 0.5 seconds of the transient. The predicted pressure response quickly decreases to about 6 MPa (870 psia) and shows excellent agreement with the experimental data. The initial pressure increase for FREY is consistent with the predicted increases in the fuel surface temperature and subsequent increase in the average gas temperature. FREY assumes instant communication of the gas pressure from the gap to the upper plenum during the calculation. This communication may not have taken place in the experiment due to fuel-cladding mechanical interaction isolating the gap from the plenum or the instrumentation was not sensitive enough to measure the quick peak in internal fuel rod pressure. Both of these factors would tend to dampen the response measured by the pressure transducer. As a result, the measured values only show a small peak in the first second and then stabilizes at about 6 MPa (870 psia).

#### First Fuel Rod Failure Test (FRF-1)

The First Fuel Rod Failure Test (FRF-1) in the TREAT facility was performed to study the effects of steam flow on the cladding behavior of LWR fuel immediately following the blowdown portion of a LOCA. The test was conducted using a seven-rod bundle of 0.686 m (27 in) long zircaloy-clad UO<sub>2</sub> fuel rods in a flowing steam atmosphere. The TREAT reactor was operated at a constant power for 20 seconds resulting in a cladding surface temperature rise of 40 K/sec (72 °F/sec) to a maximum of 1255 K (1800 °F). The fuel rods were prepressurized with He which simulated end-of-life fission gas accumulation.

A seven rod bundle of 0.686 m (27 in) long zircaloy-clad fuel rods was used in the test. The fuel rods had a nominal fuel rod diameter of 14.33 mm (.564 in) and a wall thickness of .81 mm (32 mil). The fuel pellet diameter was 12.49 mm (.492 in) and the fuel material was 94.4% TD and enriched to 1.51% U<sup>235</sup>. Four of the fuel rods were clad with Zircaloy-2 and three were clad with Zircaloy-4. The rods were prepressurized with He at pressures ranging from 0.793 to 1.48 MPa (115 to 215 psia) to simulate end-of-life rod internal pressures. Two cladding surface thermocouples and two pressure transducers were located on rods designated L and H to monitor cladding surface temperature and fuel rod internal pressure responses. The seven rod bundle was contained in a 5.55 cm (2.18 in) zircaloy flow shroud. An equilateral triangular spacing of 1.905 cm (0.75 in) was used. A schematic of the rod bundle is shown in Figure 2.

Steam flow of 34 l/min (9 gal/min) through the test assembly was initiated prior to reactor startup. After equilibrium flow conditions were reached, the reactor power was increased in 8 seconds to 30 MW. The reactor power was held constant for 20 seconds, at which time the reactor was shutdown. The steam flow was continued for an additional 30 minutes. Cladding heating

rates of 40 K/sec (72 °F/sec) were achieved during the test, leading to fuel rod failures at about 28 seconds into the transient.

After completion of the test, post-test examinations were carried out to characterize the behavior of the cladding and fuel. PIE results showed that all seven rods experienced cladding ballooning and rupture. All ruptures occurred within a 5.1 cm (2 in) axial distance along the bundle. Rod-rod contact occurred as a result of the excessive cladding ballooning. Metallographic examinations of the ruptures indicate that the ruptures were ductile in nature. Internal volume increases were determined to be approximately 11 cm<sup>3</sup> (.67 in<sup>3</sup>) with initial internal volumes approximately 2.5 cm<sup>3</sup> (0.153 in<sup>3</sup>). The average rod maximum circumferential swelling was determined to be 36%.

### FREY Analysis of FRF-1

Rod L in test FRF-1 was analyzed with FREY to assess the capabilities of the code to calculate the extensive cladding deformation observed during FRF-1. A pressure transducer and cladding thermocouple were located on Rod L to monitor the fuel rod internal pressure and cladding temperature responses during the test. These two devices allowed for comparisons of both the thermal results (cladding temperature) and the mechanical results (volume increase) to experimental data. A single channel analysis was conducted using the specified inlet coolant conditions. The flow blockage and rod-rod contact were not modeled in this analysis. These two factors could have a small influence on the predicted results.

The finite element grid used in this analysis is shown in Figure 8. An axi-symmetric r-z analysis was conducted to accurately model the axial deformations observed in the test. The model shown in Figure 8 is resident in the models library included with the code. As a result, the grid is automatically generated from a single input parameter. The geometric parameters and inlet conditions are shown in Table 4. The values were obtained from the test description report [10]. The coolant boundary conditions were calculated by the coolant enthalpy model in FREY from the inlet conditions provided in the test report. Based on the cladding surface temperature predictions, this method adequately modeled the heat transfer from the fuel rod to the coolant.

The results of the FRF-1 analysis for Rod L are shown in Figures 12 thru 15. Comparisons are made between the predicted and measured results for cladding surface temperature, fuel rod internal pressure, and cladding deformations. The cladding surface temperature response, shown in Figure 12, indicates that the predicted heatup rate and peak temperature agree well with the measured values.

The fuel rod internal pressure history is shown in Figure 13. FREY slightly overpredicts the initial internal pressure. Again, this could be related to the method used to represent the pressure transducer volume. The pressure increase due to fuel rod heatup shows excellent agreement with the measured value. At approximately 23 seconds, extensive cladding ballooning occurs, causing an increase in the internal volume. This is indicated by the termination in internal pressure increase and the subsequent decrease in pressure. Fuel rod failure occurs at approximately 28 seconds as indicated by the significant drop in internal pressure to the coolant pressure for the measured response. The FREY prediction for cladding ballooning and subsequent volume increase agrees well with the experimental data. However, the predicted time to failure is at 46 seconds after the initiation of the test. This is 18 seconds after the indicated failure at 28 seconds.

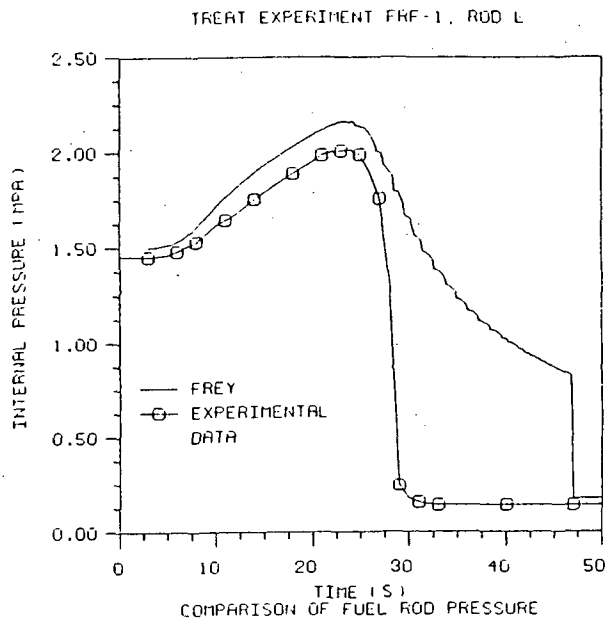


Figure 13. Measured and Predicted Fuel Rod Internal Pressure for Rod L.

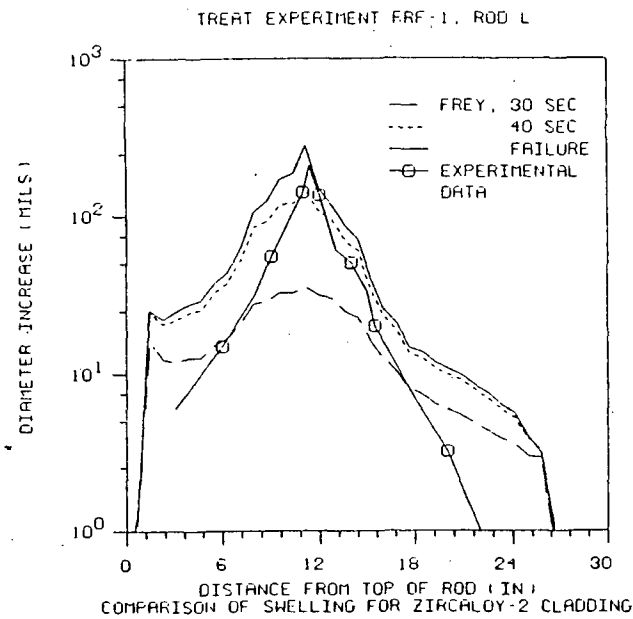


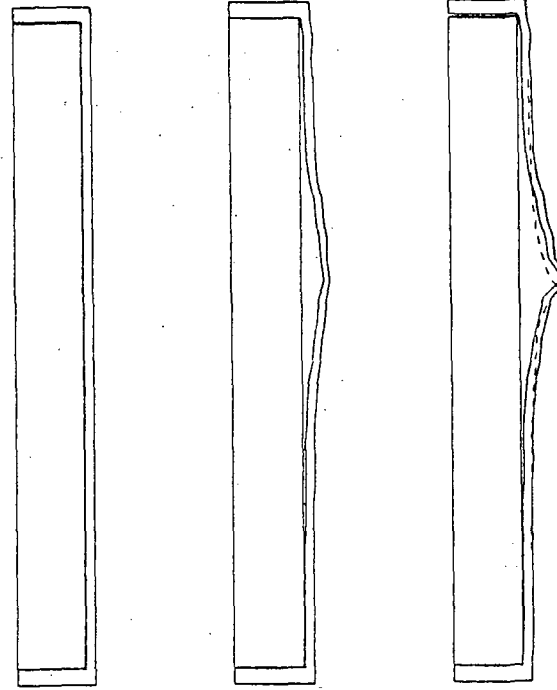
Figure 14. Axial Profile of the Measured Cladding Deformations and the FREY Predictions at 30 seconds, 40 seconds, and at the Time of Failure for Rod L

TREAT EXPERIMENT FRF-1, ROD L

0 SEC

40 SEC

FAILURE



FREY PREDICTION OF SWELLING FOR ZIRCALOY-2 CLADDING

Figure 15. A Histogram of the Predicted Cladding Ballooning for Rod L

The diametral increase as a function of axial position at 30 seconds, 40 seconds, and at time of predicted failure is shown in Figure 14. FREY overpredicts the amount of diametral expansion near the ends of the fuel rod. At 30 seconds, the fuel rod was measured to have failed. At that time, the FREY prediction shows only half of the localized deformations. However, the predicted internal volume, represented by the area under the large dashed curve in Figure 14, is approximately the same as the measured value as evident from the similar internal volumes shown in Figure 13. The localized deformations at 12 in (30.48 cm) are not predicted to form until 40 seconds into the transient. At the time of predicted failure, the localized diametral increase is similar for both the predicted and measured results. Lastly, Figure 15 depicts the cladding ballooning from initiation of the transient until predicted failure. The experimental results (dashed line) are also included for comparison. It is evident from this graph that the predicted mechanical response of FREY agrees well with the measure values.

## CONCLUSIONS

FREY is currently undergoing an extensive verification and validation effort for application to transient analysis of light water reactor fuel. The purpose of this study is to validate and verify the predictive capabilities of the code for severe transient analysis by evaluating fuel rods from different transient tests. In this study, both the predicted thermal and mechanical responses of the code were compared to in-reactor measurements and post-irradiation examinations to assess the applicability of the code.

A total of 10 test fuel rods from experimental programs conducted in both the Power Burst Facility (PBF) and the Transient Reactor Test Facility (TREAT) have been used in this study to provide a comprehensive assessment of the capabilities of FREY. Axi-symmetric, r-z finite element models were used to determine the cladding surface temperature, fuel centerline temperature, and cladding deformation for the 10 fuel rods. Where applicable, comparisons were made to in-pile test data measurements. PIE results for extent of film boiling, peak cladding temperature, and fuel rod deformation were compared to the predicted results.

FREY tends to overpredict the peak cladding temperatures for post-DNB operation. The high predicted cladding temperatures were located at the peak power position. However, the 2-dimensional r-z model representation and the 1-dimensional coolant model does not account for 3-dimensional effects associated with flow conditions during film boiling and geometry changes due to rod bowing. Significant circumferential temperature gradients were observed in the experimental data for several of the high temperature post-DNB tests. Preliminary analysis indicates that these factors could result in lower predicted cladding temperatures. A second area of uncertainty resides in the correlations used to calculate the post-DNB heat transfer coefficients. In some instances, these correlations were applied outside or near the limits for their range of application. The use of these correlations in this manner was manifested due to the lack of more appropriate models in the industry at the time of this analysis.

The thermal response of the fuel centerline temperatures agreed well with both the measured responses and PIE results. No significant differences were observed.

FREY predicted well both the cladding collapse associated with the high temperature PCM tests and the cladding ballooning during the FRF-1 and LOC-3 tests. The cladding deformations predicted by the code agreed well with the PIE determined values. Also, the internal pressure responses predicted by FREY showed good agreement with the in-pile measurements. Some

discrepancies were seen in the predicted time of cladding failure. This may be related to the large scatter in the failure strains characterizing zircaloy behavior in the alpha+beta phase during which experimental failure occurred

Overall, the verification and validation study has demonstrated the ability of the code to predict the thermal and mechanical response of fuel rods during severe transient tests. Several factors such as the stochastic nature of film boiling and the geometry changes caused by rod bowing lead to significant circumferentially varying effects not modeled in an r-z representation. Therefore, some uncertainties exist in how accurate the experimental data illustrates the behavior of the fuel rod during the test. Secondly, limitations exist as to the ability of current state-of-the-art methods and correlations to account for all the phenomena occurring during severe fuel rod transients. These factors have an important impact on the comparison of code predictions to experimental results and must be acknowledged when assessments are made. Lastly, due to the severity of several of the experiments used in this study, the results and conclusions can be extrapolated, in some cases, to the application of the code to licensing analysis which contain less severe forcing functions.

#### ACKNOWLEDGEMENTS

The analysis and experimental interpretation would not have been possible without the assistance of the staff from the Advanced Nuclear Fuels Laboratory of the Nuclear Engineering Department at Texas A&M University and Anthony Zangari of ANATECH Research Corp.. Their efforts are gratefully acknowledged. Funding for the verification and validation of the FREY code was provided by the Electric Power Research Institute.

#### REFERENCES

- [1] McFadden, J. H., et al., RETRAN-2: A Program for Transient Thermal Hydraulic Analysis of Complex Fluid Flow Systems, Vol. 1-3, Rep. EPRI-CCM-5, Electric Power Research Institute, CA (1982).
- [2] Stewart, C. W., et al., VIPRE-01: A Thermal-Hydraulic Code for Reactor Cores (Revision 2), Vol 1-3, Rep. EPRI-2511-CCM, Electric Power Research Institute, CA (1985).
- [3] Seifkin, L. J., et al., FRAP-T6: A Computer Code for the Transient Analysis of Oxide Fuel Rods, Rep. NUREG/CR-2148, Idaho Natl. Eng. Lab., ID (1981).
- [4] Rashid, Y. R. et al., FREY-01: Fuel Rod Evaluation System, Vol 1-3, EPRI NP-3277-CCM, Electric Power Research Institute, CA (1983).
- [5] Hagrman, D. L., MATPRO-Version 11 - A Handbook of Materials Properties for Use in the Analysis of Light Water Reactor Fuel Rod Behavior, Rep. NUREG/CR-0497, Idaho Natl. Eng. Lab., ID (1979).
- [6] Martinson, Z. R., Power-Cooling-Mismatch Test Series Test PCM-2 Test Results Report, Rep. TREE-NUREG-1038, Idaho Natl. Eng. Lab., ID (1977).
- [7] Peeler G.B., et al., Power-Cooling-Mismatch Test Series Test PCM-4 Test Results Report, Rep. TFBP-TR-190, Idaho Natl. Eng. Lab., ID (1977)
- [8] Yackle, T. R., et al., Test LOC-3 Quick Look Report, Rep. TFBP-Tr-328, Idaho Natl. Eng. Lab., ID (1979).

- [9] Cook, B.A., et al., Reactivity Initiated Accident Test Series Test RIA 1-2 Fuel Behavior Report, NUREG/CR-1842, Idaho Natl. Eng. Lab., ID (1981).
- [10] Lorenze, R. A., et al., Final Report on the First Fuel Rod Failure Transient Test of a Zircaloy-Clad Fuel Rod Cluster in TREAT, Rep. ORNL-4635, Oak Ridge Natl Lab., TN (1971).
- [11] Farrar, L. C., et al., Irradiation Effects Test Series Test IE-3 Test Results Report, Rep. TREE-NUREG-1106, Idaho Natl. Eng. Lab., ID (1977).
- [12] Ploger, S. A., Post Irradiation Examination Results for the Irradiation Effects Test IE-3, Rep. TREE-NUREG-1200, Idaho Natl. Eng. Lab., ID (1978).
- [13] Johnson, R. T., ERUDITE Users Guide EPRI/Utility Transient Fuel Behavior Data Information Source, NP-2755-CCM,R2, Electric Power Research Institute, CA (1986).

## EPRI OPERATOR RELIABILITY EXPERIMENTS PROGRAM

V. Joksimovich, A.J. Spurgin, D. D. Orvis, P. Moieni  
Accident Prevention Group, Inc.  
11545 West Bernardo Court, Ste. 100  
San Diego, CA 92127

D.H. Worledge  
Electric Power Research Institute  
Nuclear Power Division  
3412 Hillview Avenue  
Palo Alto, CA 94304

### ABSTRACT

The primary purpose of the EPRI Operator Reliability Experiments (ORE) Program is to collect data for use in reliability and safety studies of nuclear power plant operation to more realistically take credit for operator performance in preventing core damage. The two objectives for fulfilling this purpose are: (1) to obtain quantitative/qualitative performance data on operating crew responses in the control room for potential accident sequences by using plant simulators, and (2) to test the Human Cognitive Reliability (HCR) correlation.

This paper briefly discusses the background to this program, data collection and analysis, the results and quantitative/qualitative insights stemming from phase one which might be of interest to simulator operators and trainers.

### BACKGROUND AND INTRODUCTION

The comprehensive treatment of human interactions is deemed to be a key to the adequate understanding of various accident sequences and their relative importance in public safety considerations. There is an abundance of evidence to support the notion that humans play a dominant role in both causing and terminating accidents at various industrial facilities. Such evidence comes in the form of actuarial data (e.g, Chernobyl, TMI 2, numerous precursors) or results from various generic and plant-specific probabilistic risk assessment (PRA) studies.

In view of this importance of human interactions, EPRI has sponsored a series of research projects over the past six years to increase understanding and improve techniques for analyzing them. Although the principal aim of this research was to support PRA, the results and insights derived therefrom have proved to have applications in operator training, emergency operating procedures development and human factors considerations.

Human reliability analysis (HRA) is a complex subject that has not lent itself to relatively straightforward models like those for component and system reliability assessments. In order for this complexity to be amenable to modeling, EPRI perceived that a number of development steps were necessary:

1. Classify human interactions (HIs) into a limited number of classes. An HI covers the response of the crew from the detection of a critical change in plant state (e.g., an alarm), through diagnosis of that plant state, to the decision to take actions to return the plant to an acceptable state.
2. Introduce an acceptable framework to organize the application of HRA to PRA studies.
3. Survey available approaches to quantification.
4. Develop promising models.
5. Conduct experiments to establish an appropriate data base to validate the model(s) with regard to specific applications.

The EPRI human reliability projects have followed these steps as previously reported in the Nuclear Engineering International article (Joksimovich and Worledge, 1988). The latest project of the series is the principal topic of this paper. It should be pointed out that an NRC commissioner favorably commented on the program (Rogers, 1988). The paper describes the scope and interim (Phase I) results in the form of time-reliability curves of crew responses to key human interactions. In addition, the paper discusses how the use of complex scenarios and quantitative evaluation of crew responses can be applied to operator training.

#### ORE PROGRAM

The current program is divided into two phases. Phase I is mainly concerned with the testing of the human cognitive reliability (HCR) correlation (Spurgin, et. al., 1984). The HCR correlation is intended to represent the behavior of crews performing tasks in nuclear power plant control-rooms. The HCR correlation is a form of time-reliability curve which quantifies the probability of non-response of a control room crew within a specified time. Key features of the HCR correlation are reflected in the several hypotheses listed in Table 1. The testing of the HCR correlation entails carrying out experiments using large plant simulators, developing data collection and

analysis methodology and examining the analyses to see if the basic HCR hypotheses are confirmed and to suggest modifications to HCR if necessary. The status of HCR hypotheses testing is seen in Table 1. Phase II of the program comprises more simulator experiments, refined testing of the HCR and applications of the refined correlation.

Table 1  
STATUS OF HCR HYPOTHESIS TESTING

Hypothesis	Status
1. Time Dependence	Valid
2. Single Parameter Does Normalization	Valid
3. Median Performs Well	Valid
4. Discrete Correlation Groups Appear	Valid ?
5. S, R, K Characterize Groups	?
6. Weibull and/or Lognormal	Valid
7. PSFs impact quantifiable	Invalid Thus Far

#### Simulator Facilities Used For ORE

Modern control room training simulators provide a considerable potential for making measurement of operator performance to improve understanding of the basic models and to provide support for human reliability estimates. This was fully recognized during development of the HCR model; the use of simulators for validation purposes became an obvious choice. Furthermore, experiments on simulators can take advantage of requalification training sessions with only minor perturbations to the utility. Currently, six U.S. utilities are participating in the program: Commonwealth Edison (La Salle), Pacific Gas and Electric (Diablo Canyon), Wisconsin Public Service (Kewaunee), Philadelphia Electric (Limerick), Pennsylvania Power & Light (Susquehanna), and Duke Power (Oconee). Electricite de France (EDF) (Bugey and Paluel) and EPRI are collaborating closely in their respective programs of operator experiments including the design of the experimental method, statistical analysis of data and interpretation of qualitative observations.

It should be pointed out that EDF has pioneered the use of simulator experiments for emergency procedure and safety panel validation. A large number of experiments has been conducted since 1983 employing simulators at the three training centers: Bugey, Paluel and Caen. This background of experience provided a stepping stone for the EPRI project. The collaborative agreement provides cross-fertilization between the two programs. The two programs, if fully combined, would constitute the largest source of human reliability simulator data in the world, from which numerous nuclear safety insights could be derived.

The U.S. participants typically: a) make the full-scale plant simulators, with the associated equipment together with the operating crews, available for the conduct of experiments (typically in conjunction with scheduled requalifications sessions); b) have close involvement in defining accident scenarios; c) perform programming of scenarios and assist in the conduct of experiments; d) share the information and insights being generated; and e) provide guidance via a steering group. This process usually involves the close collaboration of utility PRA groups and training staff.

#### ORE Status

The status of EPRI ORE data collection is summarized in Table 2. Two or more scenarios were observed at each simulator with several crews being exposed to the same (or essentially the same) scenarios. Each scenario spans several pre-defined "key" human interactions for which timing data is collected and analyzed. Preliminary data are reviewed (qualified) to assure that each HI measurement is representative of the population of licensed control room operators and is unaffected by simulator problems or trainer interference. To date, nearly 1,000 qualified data points have been collected.

Data Collection . Data collected during simulator retraining sessions with control room-crews is performed by observer teams collecting response times of crews augmented by simulator records, such as data loggers, and video recordings. In addition to time data, post-transient interviews are also carried out to help define insights into operator decisions, such as which plant variables or alarms are used by the crews in given circumstances. This latter information is used along with information on operator experience and education to determine the influence of various performance shaping factors (PSFs).

Table 2  
STATUS OF SIMULATOR DATA COLLECTION

Simulator	Number Of Scenarios	Number Of Crews	Number Of HIs	Total Number Of Qualified Data Points
PWR 1	3	10	10	95
BWR 1	2	18	10	137
BWR 2	7	3-6*	13	125
PWR 2	7	6	30	167
PWR 3	8	5-7*	12	130
BWR 3 II	6	9	15	125
PWR 1 II	6	15	15**	200**

\* Scenario Dependent  
\*\* Estimates

Total - 1000

Data Analysis . Statistical measures are used to characterize crew responses to key interactions. Principal measures are; a central point estimate (mean or median response time) and an estimate of spread or variability (variance or standard deviation). Voluminous raw response time data are reduced to a small set of statistical measures and subjected to preliminary evaluation for consistency and trend.

The data was further organized and analyzed to test the HCR correlation. The seven hypotheses listed in Table 1 were examined using various analysis techniques. Later, data was aggregated in several ways to develop interim positions on the HCR correlation. These aggregated curves are discussed below.

## INTERIM RESULTS

### Hypotheses

For the HCR correlation to be valid, the seven hypotheses have to be confirmed. Table 1 shows the current state of investigation for each

hypothesis. The majority of the key hypotheses are confirmed. Hypotheses 1, 2, 3, and 6 are clearly confirmed. Hypothesis 4 can be viewed as partially confirmed.

The crew responses are clearly time dependant (Hypothesis 1) and are shown to fit either Weibull or lognormal distributions (Hypothesis 6). Hypotheses 2 and 3 relate to normalization by dividing actual response times of the crews by the median value ( $T_{1/2}$ ) of response times for all crews. This produces a set of dimensionless response times. This process can be illustrated by showing that very similar human interactions with different actual times can yield close standard deviations after normalization. Table 3 shows two examples from the results. The corresponding curves for the PWR results are shown in Figure 1. These results indicate that underlying cognitive behavior for these HIs is similar (i.e, the shape of the curves are very close) and despite the existing plant-specific differences among the two PWRs, the response curves moved closer together once normalized.

Table 3

COMPARISON OF RESPONSE TIME PARAMETERS FOR  
SIMILAR HUMAN INTERACTIONS FOR DIFFERENT PLANTS

HI	Plant	Median Response+ (Seconds)	Normalized Sigma Value*
B ATWS: Suppression	A	79	0.71
W Pool Cooling	B	145	0.74
R Initiation	C	138	0.85
P MSLB/SGTR: SG Isolation	A	323	0.24
W	B	766.5	0.30
R			

\* Median of measured response times for all crews at each plant.

\* Standard deviation of normalized response times for each plant where normalized times equal actual times divided by the median response.

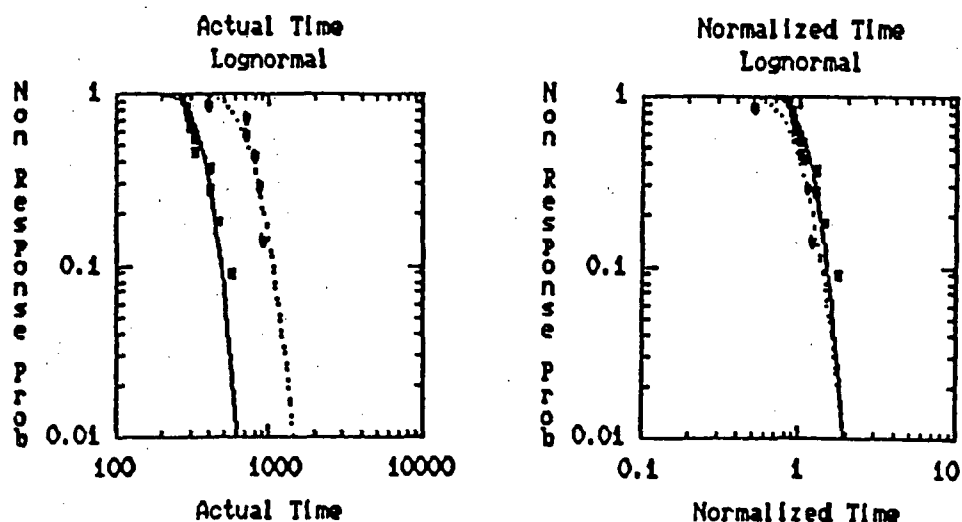


Figure 1. Time Reliability Curves of Non-Normalized and Normalized Data For Isolation of Faulty Steam Generator in a SGTR for Two PWRs.

Hypotheses 4 is partially verified because data do suggest the presence of groups, but they overlap considerably. It has been found that the preliminary interpretation of skill(s), rule (R) and knowledge (K) based attributes for the human interactions involved (hypothesis 5) do not map the interactions unambiguously into one of the observed interaction groups. Further work is underway in Phase II of the project to find good labels for these interaction groups. Testing of hypothesis 6 is not complete and is continuing in Phase II.

### Aggregated Curves

Data aggregation in the ORE program means that operator response times for individual HIs among various scenarios, various plants or types of plants are combined (pooled) in various ways. Data aggregation is performed to 1) enhance the statistical database and 2) provide bases for comparison of results, at different levels of aggregation, e.g., to compare results for all BWRs to results for all PWRs. Several forms of interim correlation curves were formed for various types of data aggregation. For example, aggregating all the data irrespective of plant type similar to the original HCR curves.

Figure 2, for example, shows the respective aggregate curves for all-BWR and all-PWR data. It also shows the aggregate of these two as the "all-data" curve. The results indicate that aggregated curves correspond roughly to "rule-based" behavior with the PWR curve to the left and the BWR curve to the right of the "all-data" curve.

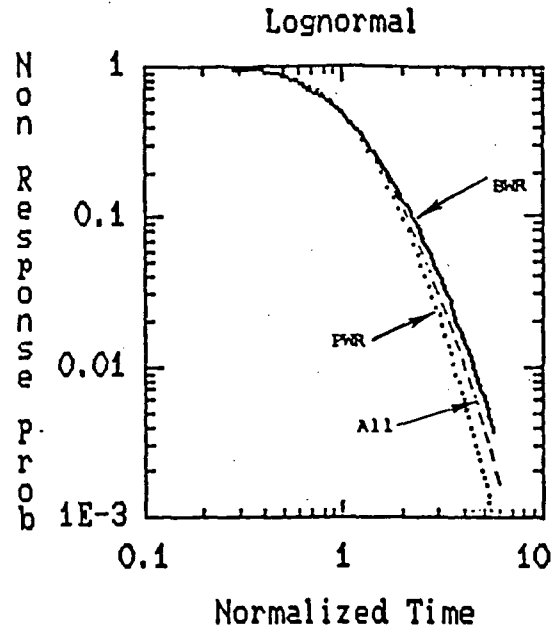


Figure 2. Aggregate Time Reliability Curves for all, PWR and BWR Data.

It should be remembered that, first, the coincidence of the grand aggregate curve with the original HCR "rule-based" curve is not surprising because in the majority of instances the HIs included corresponded roughly to rule-based situations. Second, the connection between this curve and the "rule-based" attribute is now considered tenuous as discussed above. At least, the decision framework for deciding what is rule-based needs to be revised. This is being done.

#### QUALITATIVE INSIGHTS

In the course of participating in the experiments, the observer teams made qualitative observations relative to the responses of the crews. Records taken during the experiments provide not only information for use in the program, but also provide a useful data base for trainers, operators, procedure developers and human factors personnel. Observations below are grouped into five categories; simulator validity, procedures, training, human factors, and crew structure and communications.

#### Simulator Validity

Areas which appear need attention in PWRs are mainly associated with thermal-hydraulic modeling. These cover modeling of void formation, hot leg behavior from "bubbly" flow to high void, and reflux cooling in the steam generator. Some generator models seem to be in need of improvement.

One area that seemed to be particularly deficient in the minds of the crews was the modelling of auxiliary operators by the trainers. There did not appear to be consistent criteria applied to the time taken by the auxiliary operators in performing tasks. Also there were no criteria for when they could be expected to be successful. EPRI expects to examine the potential for including actions of auxiliary operators and maintenance technicians outside the main control room in the same quantitative framework as the HCR model.

### Procedures

The emergency operating procedures (EOPs) provide the backbone of crew responses to accident scenarios. The current vintage of both BWR and PWR EOPs are considered to be "symptom based" so that crews may react as dictated by the EOPs to various symptoms indicated by displays and instrumentation. (It is noted, however, that the PWR procedures tend to be a hybrid of symptom-and-event based.) In general, these procedures, which help diagnose and make decisions, evoke "pure" rule-based cognitive behavior on the part of the crews. Preliminary analysis of the PSF influences on the data suggest the existence and forced use of the EOPs are responsible for smoothing out or leveling between crews the otherwise considerable influence on performance that psychologists have hereto expected from PSFs. If this is born out by further analysis, it can be considered to be a singularly valuable contribution by the industry to improving plant safety.

A number of problem areas surfaced with the procedures which affected the crews' performance. These areas were obscure logic, incorrect order of instruction and separation of warning advice from those areas in which the advice was required. For example, in the case of obscure logic, it was not quite clear what the crew should do, either go to the next step in the procedure or jump out of the procedure. Simpler statements would have prevented much confusion. Another area of confusion was associated with interlocks. During recovery actions it is necessary to defeat complicated interlocks. The order of how instructions are interpreted is important. If the order is wrong and the crew can not solve the logic quickly then they may have to forego the use of a crucial system which can terminate the accident progression.

The observer records quite clearly show where the crews have difficulties and how many of the crews suffer from these problems. Training staff and the procedure developers can help resolve these problems.

### Training Aspects

Use of Scenarios . The scenarios used in the operator experiments have been designed so as to pose varying levels of complexity to the crews. At some simulators the experiments were the first PRA-oriented scenarios experienced by the crews. These crews were unused to dealing with the more complex scenarios. However, the training staff noted that the crews became much more comfortable with complex scenarios over the course of the experimental program. On the whole, crews were generally favorable toward the challenges afforded by such scenarios.

Training Program Evaluation . By and large, training staffs evaluate the crews on qualitative performance measures such as application of correct procedures and intra-crew and extra-plant communications. It is believed that routine timing of crews on key human interactions in simulator scenarios along with commentary to characterize the crew response with respect to use of procedures, slip/errors made and recovered and other factors could provide a means under utility control to evaluate training effectiveness.

Such records and trending of the crew's performance would enable objective evaluations to be made of all of the crew's performance. The training group could then evaluate how to improve the training program or suggest what improvements should be made to the procedures or control-room displays.

### Human Factors

Control room design reviews and task analysis programs have, or seem to have, obviated most human factors deficiencies. During the EPRI experiments, however, observers noted several items that seemed to affect the crew response time and accuracy. In the same vein, utilities should encourage training and operating staffs to use simulator training as another means to identify potential problems. Typical human factor items identified by observers were as follows:

- o Instrument Location
- o Instrument/Panel Design
- o Control Handle Location and Labelling
- o Display Characteristics and Design
- o Alarms/Annunciator Design
- o SPDS Validity and Reliability

### Crew Structure and Communications

Organization . Training practices of augmenting crews and/or random personnel absences resulted in variability in crew structure during the respective experimental series, although the latter is viewed as representative of actual plant practice. Essentially constant across the plants is the use of at least two licensed reactor operators (RO) who manipulate controls; one PWR uses three RO's. Also constant is the assigned responsibility of one licensed Senior Reactor Operator (SRO) to be in charge of executing Emergency Operating Procedures. Beyond these two areas of responsibility, crew size and organization varies significantly from plant to plant.

The quality of the response seemed mainly to depend on the quality of the procedure reader (SRO) and his ability to see where the plant is headed and what the procedures say. It is not yet clear what crew size and organization is optimal.

Communications : During training at all simulators, intra-crew communications are emphasized and evaluated as part of the requalification exercises. What is observed, however, is that crews often do not communicate in the desired fashion during the first time back on the simulator; after being reminded in trainer critiques, most crews attempt to follow the desired style even while noting that to do so is "acting" for them. Those who express some resistance note that they know their crew members well and are able to communicate well in their "normal" mode.

The human factors form used during scenario observations asks to characterize the crew leadership style on a five-point scale ranging from "authoritarian" to "democratic". Qualitatively, it appears that the most efficient crews, in terms of response times, tend to be more "authoritarian" so long as the true leader understands the plant state and does not force the crew to make poor decisions. Most crews, however, are characterized as "participative" in which the ultimate decision maker is clearly understood but crew members feel free to challenge the SRO as a way of checking the diagnosis.

## QUANTITATIVE INSIGHTS

In general, the responses of crews are grouped close to specific HCR curves and large deviations from such a curve may indicate differences in the performances of groups of crews or individual crews. For example, crews may implement different strategies in response to an event and this shows in the shape of the curves. The differences in strategies could be due to differences in cues/indications that crews act upon or the order of tasks that they perform. Often the trainers are only peripherally aware of these different strategies and do not usually know the effects on performance. The operations group may wish to selectively modify how the crews carry out the tasks based on this information.

The average (or median) time spent by crews on various HIs differ significantly. This is usually principally due to differences in plant response to different transients although there are often marked differences between median response times for similar transients at different plants. The latter may be due to familiarity with the actions, degree of complexity of procedures, etc. The measured crew median response times on various HIs could be a useful perspective to trainers, procedure developers and human factors persons.

In general, a small number of operator errors (slips/mistakes) was observed. This will be further examined in Phase II of the program. The results suggest that various measures related to crew experience at a given plant do not have a significant effect on crew response. This could be due to the fact that all the operating crews undergo similar training/requalifications and use the same procedures.

## SUMMARY

The combination of a quantitative method for collecting performance data together with a systematic method for recording qualitative data relating to aspects of crew performance, such as communications, can build an information base to help utilities to refine plant operations. It can provide information on which parts of plant procedures cause difficulties and how they affect the crews. It can provide information on whether the training program is continuing to have an impact on crew performance, also it can provide information on the difficulties that individual crews have with some aspect of plant operation.

We expect the results of these experiments to have far reaching effects, not only on risk estimates, but also on how training is measured and monitored. Already, EPRI's research program is turning to these issues. It appears that the area of operator training can benefit greatly from focused R&D that has the goal of improving the operators ability to respond to accident situations. Further, the qualitative steps forward that the industry has taken in this technical area since the TMI-2 accident are now yielding quantitatively measurable performance improvements.

This development is a healthy sign that shows the continuing emphasis that the industry attaches to excellence in plant operations.

## REFERENCES

Joksimovich, V. and D. H. Worledge, 1988. "Using Simulator Experiments to Analyze Human Reliability for PRA Studies," Nuclear Engineering International, January 1988.

Rogers, K. C., 1988. "Nuclear Plant Simulators from a Regulatory Point of View," address to Power Simulation Users Conference, Anapolis, Maryland, March 1988.

Spurgin, A. J., G. W. Hannaman, Y. Lukic and D. H. Worledge, 1984. "Impact of a Behavior Model of the Control-Room Crew on Plant Transient Analysis," Paper Presented at the International Conference on Power Plant Simulation, Cuernavaca, Morelos-Mexico, November 19-21, 1984.

STARRS: A METHODOLOGY TO EVALUATE CONSEQUENCES OF STEAM  
GENERATOR TUBE RUPTURES

S. P. Kalra  
Electric Power Research Institute  
Nuclear Power  
P. O. Box 10412  
Palo Alto, CA 94303

ABSTRACT

Steam generator tube rupture (SGTR) events which may occur in pressurized water reactors can lead to the release of radioactive species, such as iodine, to the environment. A fraction of the primary-side coolant and radioactive species which flow into the secondary-side through the ruptured tubes, will be retained in the secondary-side and the rest will be released in the form of vapor and entrained aerosols.

A mechanistic approach was used to develop the Secondary-side Transport and Retention of Radioactive Species (STARRS) computer code to quantify the amount, and composition of radioactive species released during an SGTR event. The STARRS code which simulates a U-tube steam generator contains a reactivity transport/-retention module and thermal-hydraulic modules (which utilize the modular modeling system (MMS) routines).

A version of the code called STARRS-TR was also developed which contains only the transport/retention module and which accepts the transient thermal-hydraulic parameters from general-purpose thermal-hydraulic system codes, such as RETRAN and TRAC.

STARRS-TR calculates the radionuclide transport and deposition phenomena on the secondary-side of a U-tube steam generator, provided that boundary conditions such as the break flow and its thermodynamic conditions, system pressure, swell level height in the secondary side, etc., are known. To perform a transient radioactive transport analysis, the required thermal-hydraulic boundary conditions are input to the STARRS-TR code.

In addition the 'STARRS' code has been evaluated when coupled with a thermal-hydraulic MMS code, which provides required transient T/H conditions. Under this format, no separate thermal-hydraulic boundary conditions are needed as input.

Both thermal-hydraulic aspects and radioactive retention aspects have been assessed using experimental data. The code predictions are in good agreement with the data. In addition, STARR's applications have been extended for PWR plant simulation and sensitivity analysis have been completed.

## 1. Introduction

PWR steam generator tubes can be damaged in a variety of ways (e.g., corrosion, mechanical wear) during their normal operating life. Tube degradation can cause leaks or ruptures, which can result in venting of steam and direct release of radioactive fission products to the atmosphere. Therefore, NRC considers a full double-ended guillotine break of a single steam generator tube a design-basis fault and specifies activity release limits in regulation 10CFR100.

In any steam generator tube rupture (SGTR) fault, the amount of activity released will depend on both the degree of active species retention in the steam generator and the activity levels in the primary coolant. Retention levels for primary coolant that has mixed fully with the steam generator bulk water are assumed to be similar to those for normal operating conditions: no retention of noble gases, 1% by mass carryover of iodine and 0.1% by mass carryover of cesium and similar nonvolatile fission products.

In addition to the release of fission products from the bulk water, there is also the possibility of release of primary coolant that has not mixed with the bulk water. In such a case, it is postulated that the primary coolant will flash as it leaves the tube break, forming very fine droplets that may be carried in steam bubbles through the bulk water to the separators. A fraction of these droplets may be small enough to pass through the separators and be released to the atmosphere. Because of a lack of experimental data, such uncertainties have not been quantifiable - and it has been assumed that no active species retention occurs during SGTR faults.

The Secondary-side Transport and Retention of Radioactive Species (STARRS) computer code was developed to quantify the amount and composition of radioactive species released during an SGTR event. The STARRS-TR version simulates a U-tube

steam generator, and contains a transport/retention module, that accepts the transient thermal-hydraulic parameters from general purpose thermal-hydraulic system codes (e.g., MMS RETRAN and TRAC). In addition, simultaneous computation of transient thermal-hydraulic conditions using MMS code has also been performed to demonstrate coupled calculational capability of STARRS for SGTR event.

The details of the steam generator and thermal-hydraulic system codes are available in the open literature (e.g., See Ref. 1 and 2); therefore, this paper will mainly focus on the transport and retention aspects.

## 2. Analysis Approach

### 2.1 Radionuclide Transport/Removal Module

This module calculates the radionuclide transport and retention phenomena in the secondary side of the steam generator, provided that boundary conditions, such as the break flow and its thermodynamic conditions, system pressure, swell level height in the secondary side, etc., are known. In a transient analysis, the radionuclide transport and retention module is coupled to the thermal-hydraulic module and the required boundary conditions are calculated by the latter module.

A schematic of a U-tube steam generator for a SGTR event and associated physical phenomena are shown in Figure 1. The important components of the system that participates significantly in the removal of radionuclides are the two-phase pool, the dryer and separator. However, if rupture is in the steam space (or steam generator is dry), the removal process by the two-phase pool is absent.

A tube rupture can be of the guillotine-type or a fish-mouthed break. Upon rupture, the primary coolant liquid (which is normally under 150 atm pressure) flows into the secondary side. The primary liquid partially flashes, creating bubbles, and partially mixes with the secondary side liquid. A fraction of the primary liquid forms liquid aerosols which are entrained by the rising bubbles. The rising bubbles, therefore, contain volatile species which are in the form of gas mixed with steam, or liquid species which are dissolved in the entrained liquid aerosols. The flashing phenomenon is fast and partitioning of the volatile radionuclides between liquid and vapor phases is far from equilibrium. The rising bubbles transfer mass and energy with the surrounding water pool continuously. In addition, the liquid aerosols are scrubbed due to the many deposition mechanisms involved. As the bubbles reach the pool surface, they shatter, release their

vapor and aerosol contents into the steam volume on top of the water pool, and give rise to the entrainment of droplets. The latter droplets also contain radionuclides, as the scrubbed radionuclides gradually build up in the secondary side coolant. The liquid aerosols originating from atomization of the primary coolant flowing through the break, as well as those originating from entrainment of the secondary side water, undergo further removal in the separator and dryer.

If the break location is exposed during the transient, (when the water level on the secondary side drops below the break location), the primary coolant partially atomizes. The liquid aerosols which are too large to be entrained over by the steam fall back into the liquid pool, and the smaller droplets are carried over by the steam flow. Scrubbing mechanisms during the bubble rise do not exist in this case.

The phenomena explained above are briefly described below:

#### 2.1.1 Flashing, Atomization and Bubble Formation at a Break

The flashing model assumes that the superheated vapor, originating from the primary side, loses a fraction of its superheating with respect to secondary side pressure, before stable bubbles are formed. The non-evaporated primary liquid is assumed to be atomized and entrained in the bubbles. The entrained aerosols are assumed to have a log normal size distribution initially. The log normal distribution of droplets upon break-up of a jet is supported by the investigations of Reference (3). The mean droplet diameter is calculated from a critical Weber number of 12.5 and a hydrodynamic break-up criterion is used in the analysis (Ref. 4).

The radionuclides are assumed to distribute uniformly in the liquid aerosols and the steam content of the bubbles. In other words, upon the formation of stable flashing bubbles, the initial mass fraction of trace species in the steam is identical to that in the liquid aerosols suspended in the bubbles.

#### 2.1.2 Transport and Deposition During Bubble Rise

The flashing bubbles, upon formation, are assumed to be of uniform size and have the maximum stable bubble size according to Lehrer (Ref. 5). The bubble rise velocity is calculated using Harmathy's correlation (Ref. 6). The retarding effect of the surrounding pipes on the bubble rise velocity is included by using

correlations suggested by the same author. As they rise, the bubbles exchange energy and mass with the surrounding water. The energy, mass and radionuclide species conservation equations are, therefore, solved for the bubbles. These equations are cast in the form of ordinary differential equations representing the rate of variation of gas enthalpy, bubble total mass, and radionuclide species mass fraction, with respect to axial coordinate  $z$ . The resulting coupled ordinary differential equations are then numerically integrated up to the water surface.

As bubbles rise in the liquid, the entrained aerosols undergo different deposition mechanisms. Inertial deposition takes place because larger droplets cannot follow the gas stream lines (due to their inertia). The gas in the rising bubble undergoes circulatory motions (Hill's vortex), which results in inertial deposition of the aerosols on the liquid boundary of the bubble. This mechanism is most effective for the removal of larger droplets. Sedimentation takes place due to the effect of gravity. During the bubble's rise in the water pool, gravity imposes a retarding effect on the aerosols. As a result, some of the aerosols are deposited onto the liquid boundary of the bubble.

Brownian deposition arises from the random motion of the aerosol particles in the gas. Particles diffuse down their own concentration gradient. The Brownian diffusion is effective for smaller particles.

The convective flow of gas near the liquid-gas interface gives rise to the convective deposition mechanism. In the case of a superheated bubble rising in a liquid environment where evaporation takes place at the interface, the convective flow in the steam is away from the interface and towards the bubble center. In such a case, convection of gas has a retarding effect on the deposition of aerosols. In case of condensation at the interface, however, the opposite takes place and the deposition of aerosols is markedly augmented by the convective flow.

Thermophoretic deposition takes place because aerosols tend to move down the temperature gradient. The aerosols are therefore deposited on the cold interface.

Two different flow streams reach the water surface -- the steam produced by boiling, and in the steam carried by the bubbles formed at the break. The flashing bubbles entrain aerosols which have survived during bubble rise in the water. The steam content of these bubbles also has radionuclides dissolved in it.

When the bubbles, (whether produced by flashing or secondary side boiling), rupture at the surface, droplets are formed and carried by the steam flow into the separator. The surface entrainment is modeled following Kataoka and Ishii (Ref. 7). The semi-empirical correlations of Kataoka and Ishii are used for predicting the rate of entrainment, size distribution of the entrained droplets, and the initial velocity of the droplets at the water surface.

### 2.1.3 Aerosol Deposition in the Steam Volume, Separator and Dryer

When the water level in the secondary side falls below the separator, the aerosols have to pass through a volume of steam before reaching the separator. In this region, the aerosols undergo deposition due to sedimentation and Brownian diffusion. Brownian deposition takes place on available solid surfaces. For example, when the tubes are partially covered, the aerosols pass through the tube bundle while being suspended in the steam flow.

The dominant deposition mechanism in the separator is inertial deposition. The inertial deposition here is induced by the centrifugal force. Brownian diffusion is also significant because the steam flows through relatively narrow passages where Brownian deposition on existing solid surfaces can take place.

Mechanistic models have been developed for the inertial deposition in the separator. The curvilinear equation of motion of an aerosol in the separator passages is solved and the rate of deposition is calculated. The Brownian deposition rate is simulated by using analogy between aerosol deposition and heat and mass transfer.

The dryer in a PWR plant has the configuration of chevron plates. The removal mechanisms of significance are, again, inertia and Brownian motion. Both mechanisms have been modeled and are incorporated in the code. For the inertial deposition there are two options. One option uses a mechanistic model which is based on a solution of curvilinear equation of motion of aerosols in idealized chevron passages. The other option uses a semi-empirical correlation (Ref 8). The Brownian deposition is modeled using analogy between aerosol and heat and mass transfer processes.

#### 2.1.4 Material Properties

The radionuclide transport and deposition module includes a thermophysical and transport package. Thermophysical properties of liquid water and steam are calculated using the curve fits of TRAC (Ref 9) and RETRAN (Ref 10). Thermophysical and transport properties of iodine are also simulated in the module. It includes procedures for estimating the iodine partition coefficient based on the data of (Ref. 11), and iodine mass diffusivity in water and steam.

#### 2.2 Thermal-hydraulic Model

A schematic depicting the primary and secondary sides is shown in Figure 2. The primary side contains N U-tubes, hot and cold plena. Each tube is divided into two volumes representing the hot and cold legs. Each tube has its own characteristics -- length, cross-sectional area (diameters), heated perimeter and flow resistance. The user may specify the number of tubes in the model which would then behave independently during a transient. This approach differentiates between the broken and unbroken tubes. The broken and unbroken tubes may have different responses, and long tubes may reach saturation conditions (i.e., phase transition occurs) before short tubes. The pressure and enthalpy rate equations are derived from transient mass, energy conservation and state equations using the MMS two-phase flow model (Ref 12,13). For two-phase flow conditions, the mixture density depends on the void fraction and is calculated by the Zuber-Findlay correlation (Ref. 14). A tube break capability is included in the model. The user can specify the size of the break at an appropriate time during an SGTR transient, as well as, the break location, which can be in either the hot or cold leg. The break flow rate is determined from the RETRAN/MMS critical flow model (Ref. 15, 16) (if a choked condition exists) or quasi-steady state momentum equation (if a choked condition does not exist). Depending on the upstream flow conditions, a specific model is chosen as follows: when the upstream is subcooled, the extended Henry-Fauske model is used; when the upstream is saturated, the Moody model is used, and when the upstream is superheated, the isoenthalpic model is selected to evaluate the critical flow rate.

The secondary side of the steam generator is divided into five regions: down-comer, subcooled volume, saturated volume, two-phase mixing zone (riser) and steam dome region. During normal operation, vapor is at saturation and the two-phase mixture (swell) level is at the separator elevation. However, for some transient (e.g., loss of feedwater flow), the mixture level may drop below the U-bend, thus

causing vapor to be superheated. The coolant from the primary side can discharge into the subcooled volume, saturated volume or superheated steam region (if the mixture water level drops below the break location). The mixture level is tracked according to the Sun-Duffey model (Ref 17). The user can specify the carryover and carryunder fractions to define the separator performance. In summary, fourteen coupled conservation equations are needed to simulate the dynamic response of the secondary side. The boundary conditions for the secondary side are as follows: feedwater flow rate and enthalpy, auxiliary feedwater flow rate and enthalpy, and exit steam pressure and flow rate.

The logical flow diagram for 'STARRS' calculation with coupled thermal-hydraulic modules of MMS is shown in Fig. 3. As mentioned earlier the transient T/H conditions can be input at location (1) of this diagram. This process could be automated for a selected code.

### 3. Results and Application

The STARRS Code has been validated/applied using the following tests relevant to the following categories:

#### 1. Transport and Retention Model

##### 1.1 Model Boiler (MB-2) test series (Ref. 18)

- SORV with SGTR Quasi-Steady
- SORV with SGTR (Transient)
- SGTR in Dry Steam Generator

#### 2. Thermal-hydraulic Model

##### 2.1. Semi-scale (Mod 2B) Tests (Ref. 19)

- ADV Stuck Open Following a SGTR
- ADV cycling with SGTR

##### 2.2 - MB-2 Tests

- SORV with SGTR
- Blowdown with SGTR

### 3. Plant Applications

#### 3.1 Plant Simulation - Sensitivity Study

- Partition Coefficients
- Swell Level Variation
- Radioactivity Concentration (Primary and Secondary)

The details of these test results will be published in an EPRI (proprietary) report. Some examples of the 'STARRS' prediction results are described below.

The test conditions simulated in MB-2 facility are provided in Table 1. These tests were conducted under prototypical thermal hydraulic conditions. A typical comparison of estimated carryover and decontamination factors is given in Table 2. Also shown in Fig. 4, is the variation in mass fraction of primary species (simulated with KOH) mixed in the secondary side (simulated with LiOH) during the transients. Figure 5 compares predicted and measured K mass fraction at SORV exit. The agreements are in general good and within the experimental errors. The attenuation factor (decontamination) measured in the dry steam generators (for detail of test see Ref. 18) and model predictions are shown in Fig. 6).

Several sensitivity studies were performed with respect to partition coefficients, swell level, concentration, break location, etc. Fig. 6(a) indicates effects of submerged and nonsubmerged break for low power conditions, whereas Fig. 7(b) provides the sensitivity of activity retention on the partition coefficients.

The other analysis (in progress) includes comparing MB-2 results with prototypical plant and simulating specific plant conditions.

#### 4. Summary and Conclusions

Flashing, atomization and bubble formation, of primary fluid flowing through a break were modeled. Conservation equations for aqueous aerosols and gaseous species were solved for the rising bubbles. The bubble flow is one-dimensional and the conservation equations are represented in their Lagrangian form.

Entrainment of droplets at the swell level is modeled using semi-empirical aerosol size and modified velocity distribution correlations of Kataoka and Ishii. The trajectories of entrained droplets in the dry sections of the system, including the separators and dryers, are obtained by solving the momentum equations governing the motion of these droplets.

Overall species conservation equations governing the accumulation of radioactive species in the secondary side are also derived. The scrubbing models can therefore be used in conjunction with a system thermal-hydraulic model, where the transient species conservation equations for the secondary side can be integrated over time.

The transport/retention module of the STARRS Computer Code was validated using the MB-2 experimental data. The validation calculations included the dry secondary side, as well as the partially-full secondary side experiments (Phase II tests). The results indicate that, within the uncertainties associated with experimental conditions, the model agrees with the experimental data. Furthermore, the model correctly predicts all trends in the data.

Parametric calculations were also performed, using the geometry of a Westinghouse Model-F U-tube steam generator. The simulated cases included tube ruptures under full (100%) power, low (10%) power, and a partially full secondary side. Iodine was the species considered in the calculations. The parameters included the concentration of iodine in the primary and secondary side fluids, the iodine partition coefficient, the break height, and the size distribution of the aerosols generated at the break. Model predictions for the prototypical UTSG agree with the MB-2 experimental trends. The following are the major conclusions:

1. When the secondary-side is full up to the level corresponding to normal operation, or when the water level in the secondary side is low, but the break is submerged in the secondary side by a few meters:
  - a. The vapor iodine concentration in the steam leaving the swell level is at equilibrium with the secondary side water.
  - b. The bulk of the iodine leaving the system is in the volatile phase. The mass flow rate of the aqueous aerosols leaving the system is small.

- c. The iodine differential decontamination factor of the system is insensitive to the break height and size distribution of the generated aerosols at the break. It is, however, sensitive to the iodine concentration in the primary and secondary sides.
  - d. The differential decontamination factor is quite sensitive to the iodine partition coefficient. Large values of DDF in excess of 1000 are predicted.
2. When the water level in the secondary side is low and the break is not submerged:
- a. The volatile iodine introduced into the secondary side constitutes the bulk of iodine leaving the system. The contribution of the aqueous aerosols is relatively small in comparison with the volatile iodine.
  - b. The differential decontamination factor in a prototypical steam generator is of the order of 5-10, and is almost independent of break height. It is also relatively insensitive to the size distribution of aqueous aerosols generated at break flow.

#### Acknowledgements

This work was performed under EPRI Research Project RP2453-4 by A. T. Wassel, S. M. Ghiaasiaan and C. S. Lin of Science Application International Corporation (SAIC), Hermosa Beach, California.

#### Nomenclature

DDF differential decontamination factor  
 m mass fraction  
 p partition coefficient  
 R carry over ration defined as mass fraction at SORV divided by mass fraction in secondary-side liquid  
 Z height above lower tube support plate, m  
 B<sub>g</sub> geometric standard deviation for flashing aerosols

## Subscripts

I	iodine
K	potassium
Li	lithium
out	secondary-side exit (SORV)
P	primary-side
S	secondary-side liquid
SL	swell level

## 5. References

1. S. P. Kalra, "Modeling Transients in Power Steam Generator Units", Nuclear Safety Journal, Vol. 25, No. 1, pp. 33-52, 1984.
2. U. S. Rohatgi, P. Saha, "Realistic Evaluation Methodology for Advanced LWRs, NSAC/86, 1985
3. R. Brown and J. L. York, "Sprays Formed by Flashing Liquid Jets, " AIChE Journal, 8, pp. 149-153, 1962.
4. J. H. Lienhard and J. B. Day, "The Breakup of Superheated Liquid Jets," J. Basic Engineering, 88, pp. 515-522, 1970.
5. T. H. Lehrer, "On Bubble and Drop Formation and Breakup," Israel J. of Technology, 13, pp. 246-252, 1975.
6. T. Z. Harmathy, "Velocity of Large Drops and Bubbles in Media of Infinite or Restricted Extent," AIChE Journal, 6, p. 281, 1960.
7. I. Ktaoka and M. Ishii, "Mechanistic Modeling of Pool Entrainment Phenomenon," Int. J. Heat and Mass Transfer, 27, pp. 2000-2014, 1984.
8. M. Y. Young, K. Takeuchi, O. J. Mendler, and G. W. Hopkins, "Prototypical Steam Generator Transient Testing Program: Test Plan/Scaling Analysis," EPRI NPL-3494 (1984).

9. Staff Report, "TRAC-PD2, An advanced Best-Estimate Computer Program for Pressurized Water Reactor Loss of Coolant Accident Analysis," NUREG/CR-2054, LA-5709-MS, Los Alamos Scientific Laboratory, New Mexico (1981).
10. Staff Report, "RETRAIN-02 - A Program for Transient Thermal-Hydraulic Analysis of Complex Fluid Systems," EPRI NP-1850-CCM (1981).
11. C. C. Lin, "Volatility of Iodine in Dilute Aqueous Solutions," J. Inorg. Nucl. Chem., 131, pp. 1-10 (1981).
12. Staff Report, "Modular Modeling System (MMS): A Code for the Dynamic Simulation of Fossil and Nuclear Power Plants," EPRI CS/NP-3016-CCM (March 1983).
13. J. P. Sursock, "Description of MMS Two-Phase Modules," presented at MMS-01 Release Workshop, EPRI CS/NP-2099-LD (1983).
14. N. Zuber and J. A. Findlay, "Average Volumetric Concentration in Two-Phase Flow Systems," J. Heat Transfer (1965).
15. G. S. Duleba and B. R. Ummel, "MMS: A Code for the Dynamic Simulation of Fossil and Nuclear Power Plants, "MMS-2 User's Manual, Draft Report (1984).
16. S. Oh, "MMS Critical Flow Model and Edwards Pipe Test Simulation," presented at MMS-02 Release Seminar, New Orleans, Louisiana (1984).
17. K. H. Sun, R. B. Duffey and C. Peng, "The Prediction of Two-Phase Mixture Level and Hydrodynamically Controlled Dry-Out under Low Flow Conditions," Int. J. of Multiphase Flow, Vol. 7, p. 5 (1981).
18. K. Garbett, et al, "Tests of Steam Generator Transient Response to Scenarios Involving Steam Generator Tube Ruptures and Stuck Open Safety Relief Valves", EPRI NP4787, Vol 182, 1987.
19. C. S. Lin, A. T. Wassel, "MMS Analysis of the Semi-Scale Mod-2B SGTR Experiments", EPRI NP-4783, 1986.

Table 1  
 CONDITIONS OF MB-2 PHASE II EXPERIMENTS

Test Series	Test Run	Water† Level m	Break Location	Primary Pressure M Pa	Primary Temperature K	Secondary Pressure M Pa
2.2	T-1970	11.3	bottom**	3.84	493	2.0
	T-1982	11.24	"	"	517	2.1
	T-2067* Part I	11.24	"	"	"	"
	T-2067* Part II	2.54	"	"	"	"
2.3	T-1990	2.54	"	12.75	578	7.44
	T-1991	3.8	"	"	"	"
	T-1992	7.11	"	"	"	"
2.4	T-1976	1.47	top***	"	"	"
	T-1978	4.57	"	"	"	"
	T-1979	7.11	"	"	"	"
	T-2052	4.57	"	"	"	"
	T-2054	7.11	"	"	"	"

- Dryer was bypassed
- \*\* Break is at 0.152 m above lower tube support sheet
- \*\*\* Break is at 7.16 m above lower tube support sheet
- † Above lower tube support sheet.

Table 2  
 COMPARISONS BETWEEN DATA AND PREDICTIONS  
 Test 2.2 - Run T-1982 (submerged break)

Model Predictions

$\rho$	$S_K$	$DDF_K$	$R_K$	$R_{Li}$
$10^6$	$40 \times 10^{-6}$	$6.5 \times 10^3$	$8.2 \times 10^{-5}$	$8.2 \times 10^{-5}$
$10^7$	$40 \times 10^{-6}$	$4.8 \times 10^4$	$1.1 \times 10^{-5}$	$1.1 \times 10^{-5}$
$10^8$	$40 \times 10^{-6}$	$1.3 \times 10^5$	$4.0 \times 10^{-6}$	$3.9 \times 10^{-6}$

Experimental values

$$R_K \approx 2.3 \times 10^{-6}, \quad R_{Li} \approx 5. \times 10^{-6}$$

$$DDF_K \approx 1.25 \times 10^5 - 1.37 \times 10^5$$

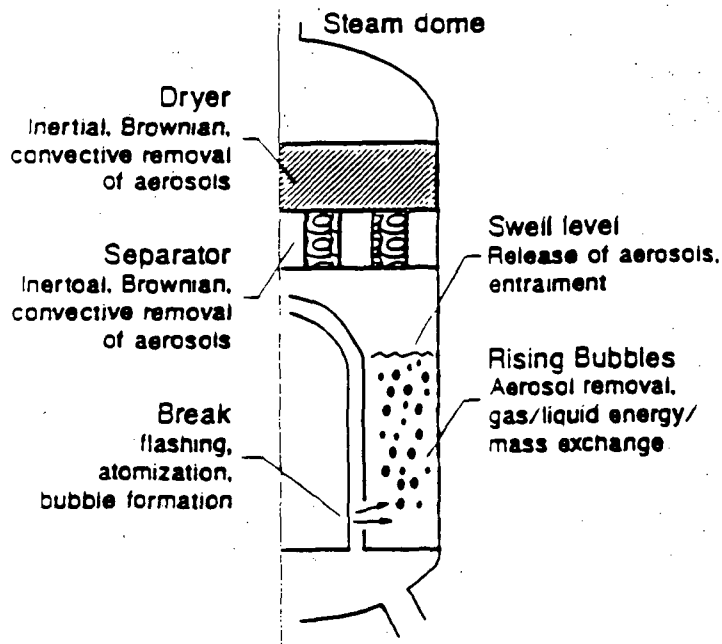


Figure 1. Schematic of the Secondary Side of a U-Tube Steam Generator in a Tube Rupture Incident

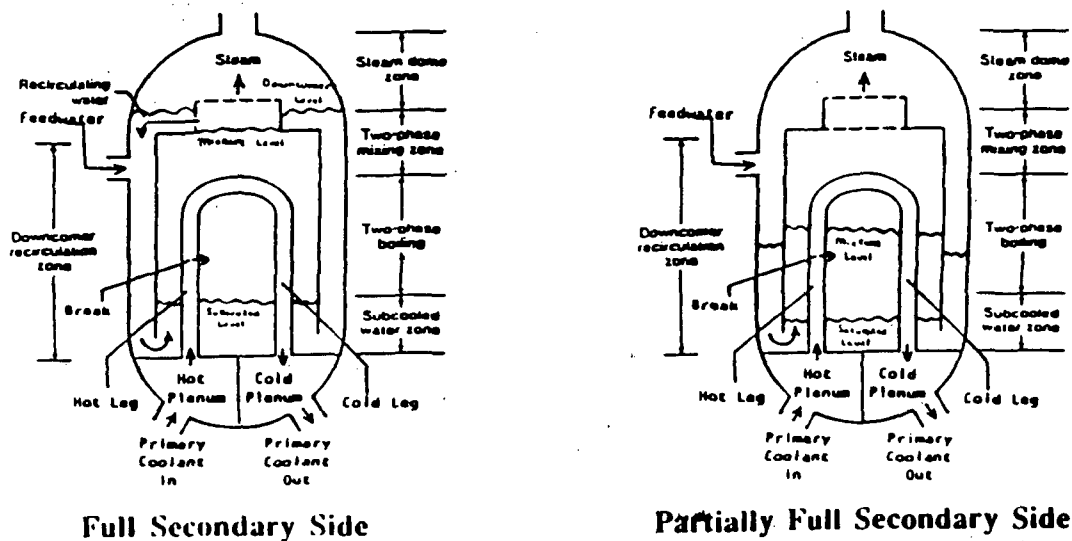


Figure 2. U-Tube Steam Generator Thermal Hydraulic Module.

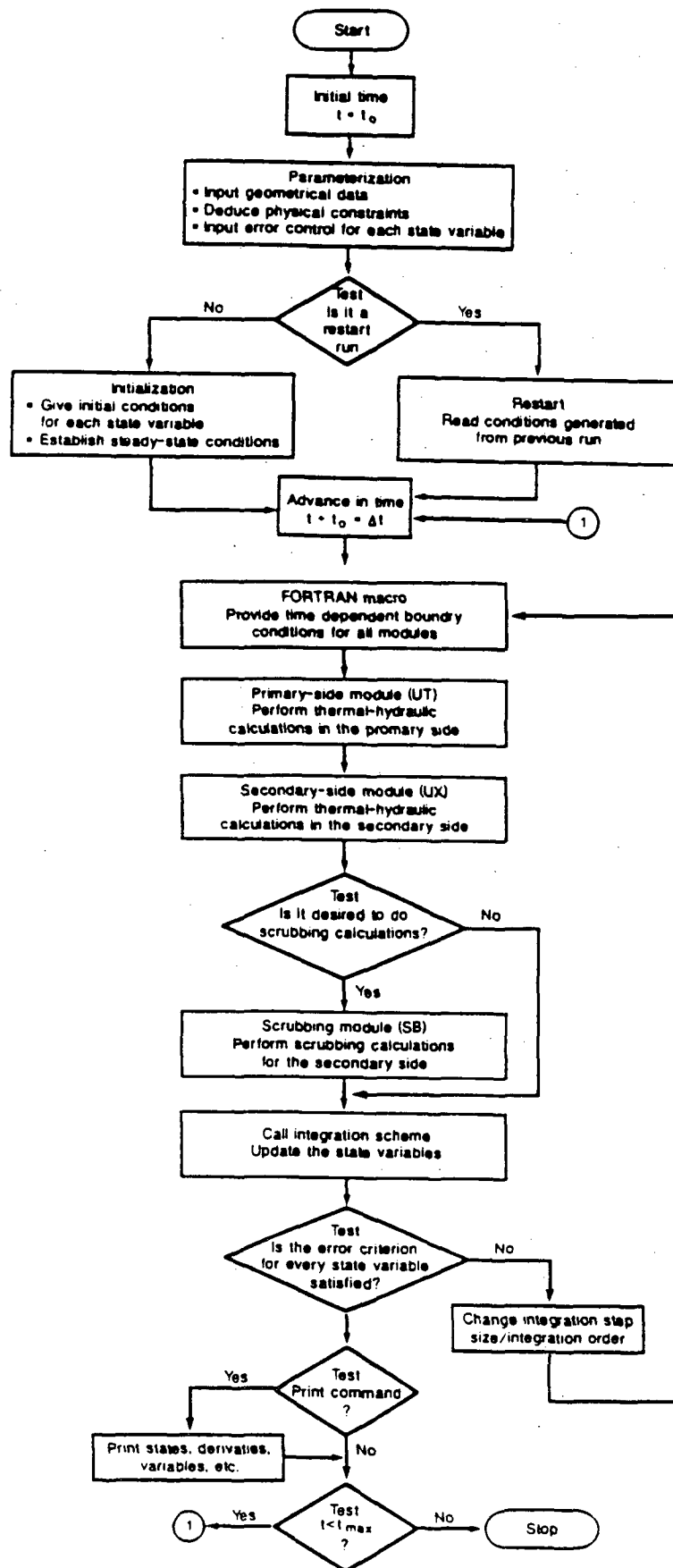


Figure 3 Flow Diagram of the STARRS Code

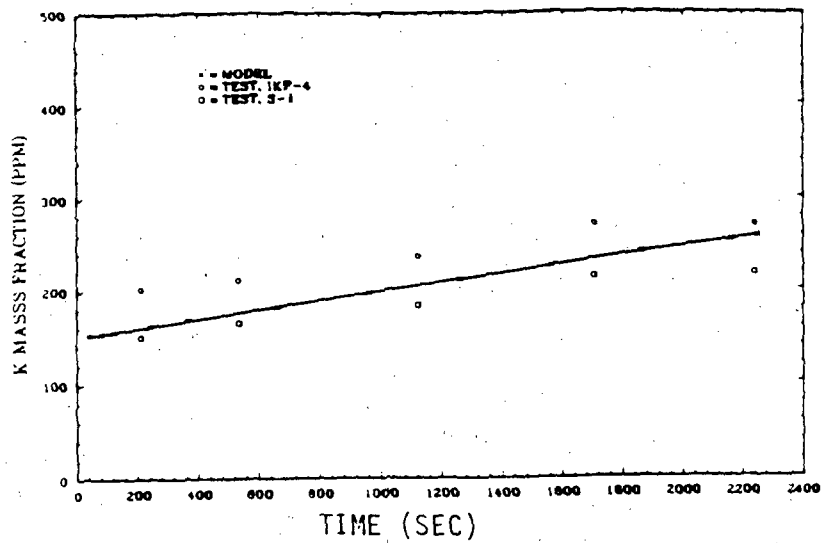


Fig. 4 MASS FRACTION OF K IN SECONDARY-SIDE WATER IN TEST 2054 MB2

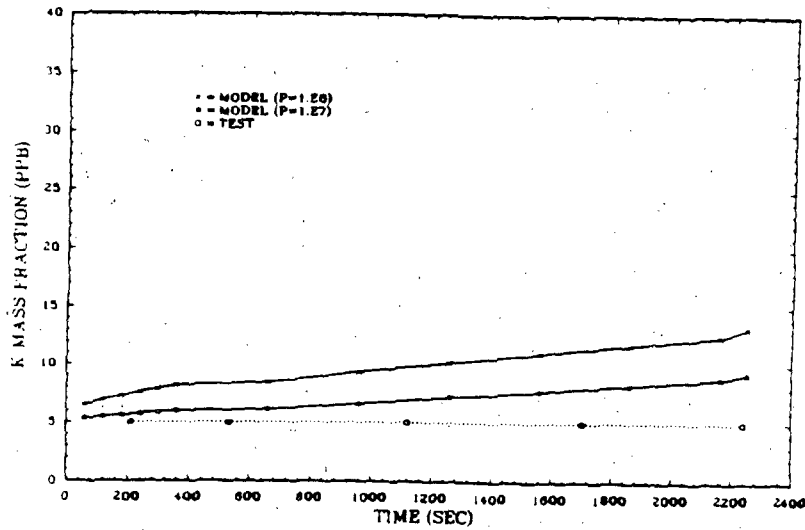


Fig. 5 K MASS FRACTION AT EXIT IN TEST 2054 OF MB2

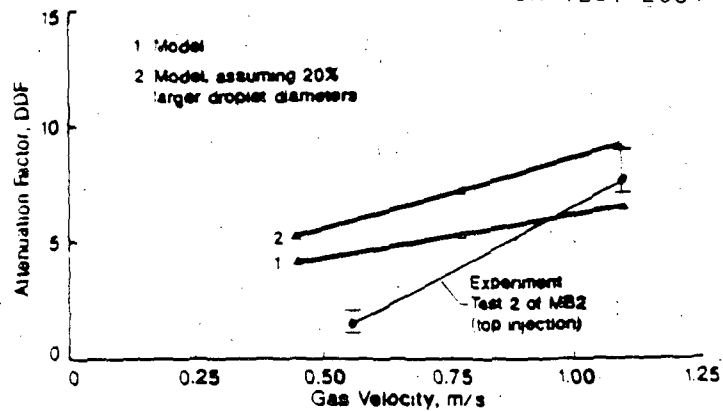
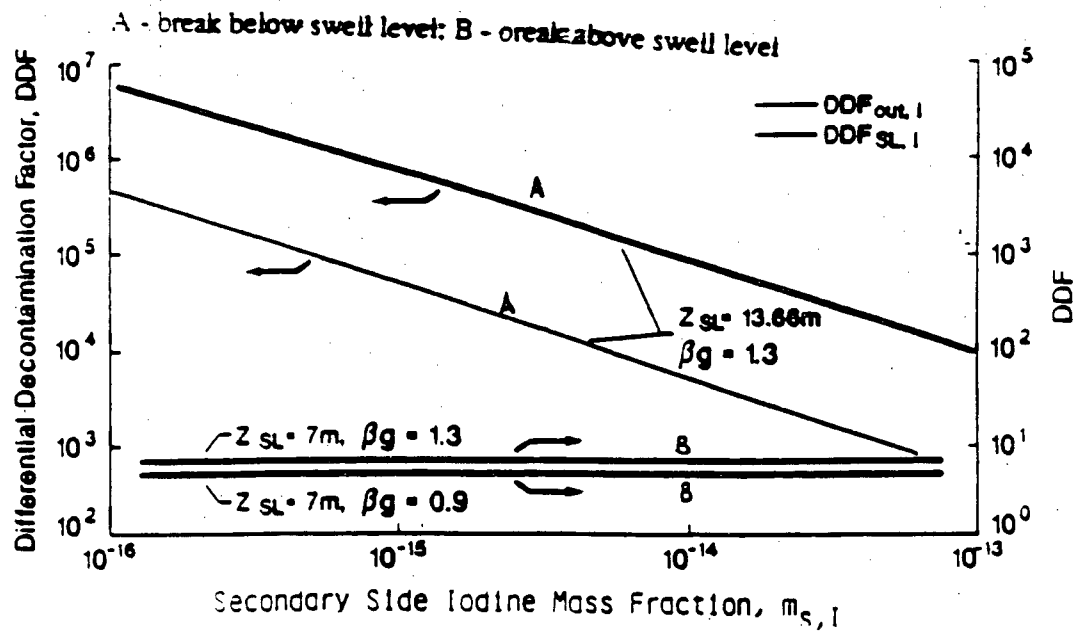
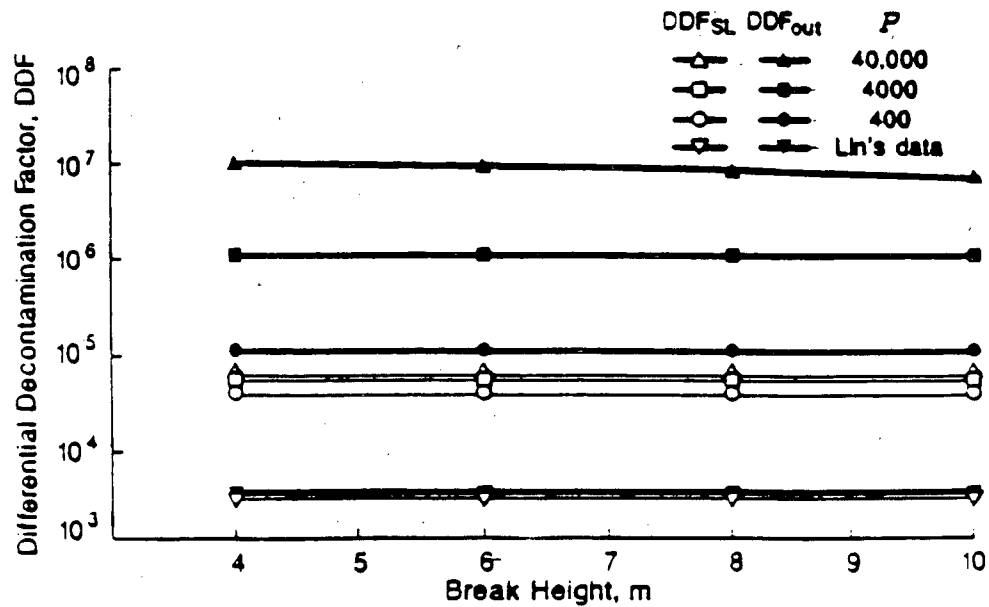


Fig. 6 ATTENUATION FACTOR IN MB-2 DRY SECONDARY-SIDE EXPERIMENTS



(a)



(b)

sl: Swell level  
out: Exit

Fig. 7 (a) DDF at Low Power (10%) for  $m_{p,I} = 10^{-11}$ ,  $Z_B = 8m$   $P = 4000$

Fig. 7 (b) Effect of Partition Coefficients on DDF  
( $m_{p,I} = 10^{-11}$ ,  $m_{s,I} = 10^{-16}$ ,  $Z_{S,L} = 13.6m$ )

## RISK MANAGEMENT FOR THE BWR PLANT

Robert A. Cushman,\* , Paul R. Hill,\* Herschel Specter\*  
Source Term Committee  
EPRI Safety Technology Task Force

Ian B. Wall  
Nuclear Power Division  
Electric Power Research Institute

### ABSTRACT

The operational risk from a BWR plant can be significantly reduced by implementing a program which incorporates the elements of:

- 1) Emergency operating procedures (i.e., accident management);
- 2) Operator training;
- 3) Transient analysis;
- 4) Risk analysis; and
- 5) Plant and operator performance monitoring.

Large reductions in the calculated core melt and containment failure frequencies, relative to more standard PRA numbers, appear to be justified by the methodology presented herein. The methodology is based on employing realistic, rather than "conservative" assumptions in analysis; maximizing the use of available plant equipment (safety and non-safety related); taking full credit for operator actions in carrying out well developed EOPs as a consequence of simulator training; and utilizing improved analytical techniques which more adequately describe core melt progression (thus helping to identify "success paths" and develop EOPs).

### Introduction

This paper presents the views of four persons associated with the Source Term Committee of the EPRI Safety Technology Task Force who are actively interested in the issue of risk management; it should not be inferred that it necessarily presents the views of their organizations.

The process of risk analysis described here has been applied to a BWR4 plant, and the use of the defense-in-depth criteria has resulted in the calculated low frequency of core damage. These results can be taken as illustrative, but not generic. The risk management process advocated, however, does have generic application.

---

\*Company affiliations, for identification only are:  
R. A. Cushman - Niagara Mohawk Power Corporation  
P. R. Hill - Pennsylvania Power & Light Company  
H. Specter - New York Power Authority

**THE THREE ELEMENTS  
OF  
NUCLEAR PLANT OPERATIONAL RISK**

° **RISK MANAGEMENT**

- A PROCESS WHICH MEASURES AND CONTROLS THE LEVEL OF PERFORMANCE OF EQUIPMENT AND OPERATORS AND WHICH EVALUATES THE EFFECTIVENESS OF EOPs TO ASSURE A SUFFICIENTLY LOW LEVEL OF PUBLIC RISK FROM NUCLEAR PLANT OPERATIONS.

° **ACCIDENT MANAGEMENT**

- A PROCESS WHICH DEFINES THE PROCEDURES WHICH ASSURE OPTIMAL USE OF ALL PLANT EQUIPMENT IN RESPONSE TO ANY CREDIBLE INITIATOR IN COMBINATION WITH ANY NUMBER OF INDEPENDENT EQUIPMENT FAILURES TO AVOID OR MINIMIZE THE LEVEL OF PLANT DAMAGE.

° **EMERGENCY MANAGEMENT**

- A PROCESS WHICH ASSURES ADEQUATE COMMUNICATIONS, RADIOLOGICAL MONITORING, AND ACCIDENT CONSEQUENCE PROJECTIONS TO ASSURE THE EFFECTIVENESS OF EMERGENCY PLANS TO MINIMIZE THE HEALTH EFFECTS WHICH COULD RESULT FROM A RELEASE OF RADIOACTIVE MATERIAL INTO THE ENVIRONMENT.

## Nuclear Plant Operational Risk

This view graph presents and describes the three program elements which are essential to a demonstrable level of control of the magnitude of nuclear plant operational risk and describes the objectives of each of the three elements. In the discussion which follows, only the BWR plant will be considered.

The three program elements described may be viewed as a "defense-in-depth" strategy for limiting the magnitude of BWR plant operational risk in that:

- 1) Risk Management is intended to assure the lowest level of public risk achievable with a given plant,
- 2) Accident Management is intended to assure a minimum level of plant damage given the occurrence of an initiating event and any combination of independent equipment failures, and
- 3) Emergency Management is intended to minimize the off-site health consequences if items 1) and 2) above fail to prevent a release of radioactive material to the environment.

This presentation shall focus attention on the approach to assure effectiveness of the first two of these three program elements. Previous and current evaluations of risk associated with nuclear plant operations have considered the third of these three elements by conservatively determining the magnitude of radioactive material release from severe accidents and the effectiveness of emergency procedures.

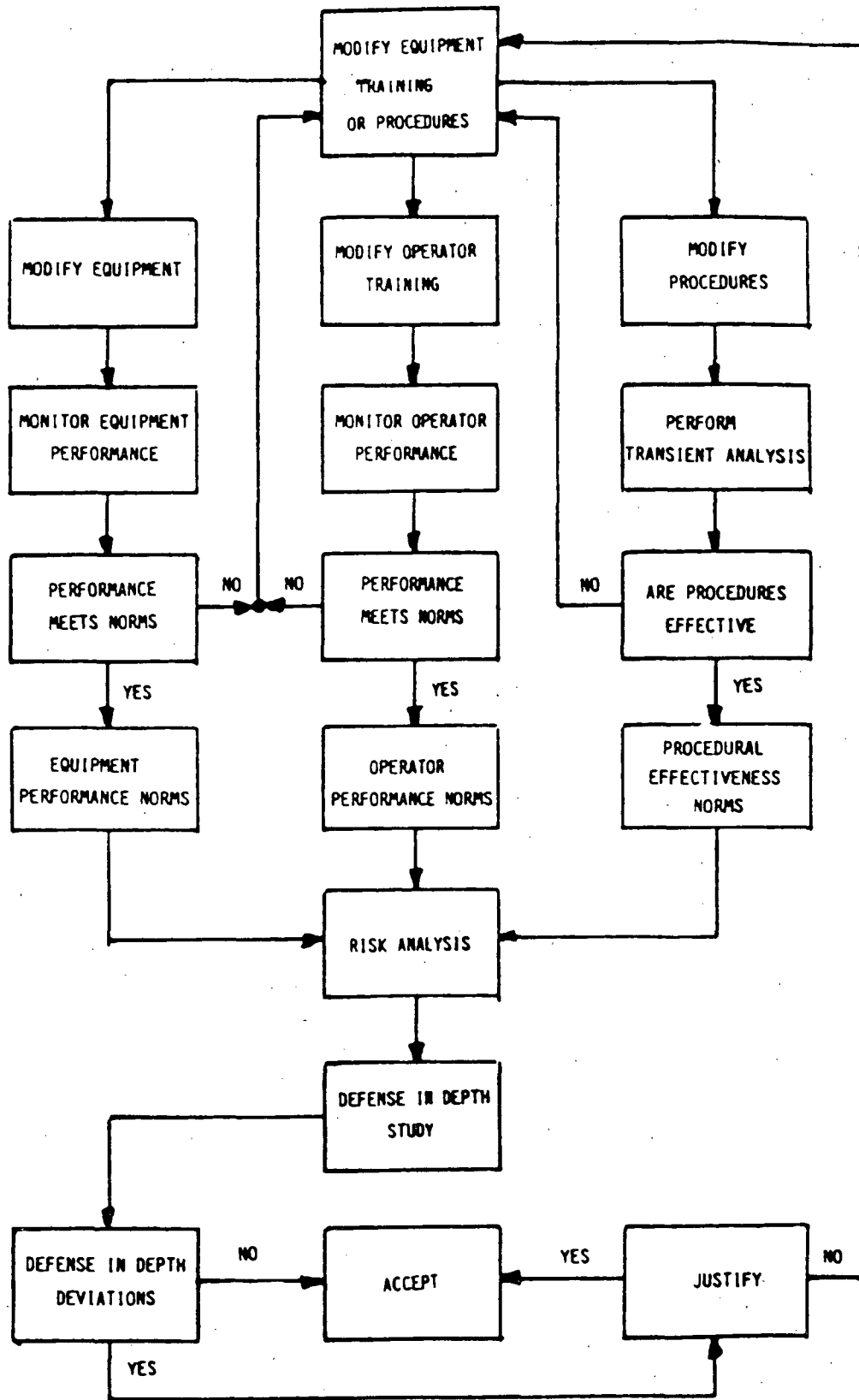
It should be noted that the risk to the public health and safety, represented by the release of radioactive material from severe accidents is consistently being calculated to be within the NRC's safety goals. Risk management is important in reducing that risk; it is also important in reducing the risk to plant investment, a risk that could remain even if no radioactive material were released in the event of a severe accident. Utility management should endorse and utilize operational risk management to reduce risk in both these areas.

The various requirements imposed by the NRC particularly since the TMI-2 accident have resulted in creating Emergency Plans for protection of the general public should a severe accident occur at an operating plant. The NRC requirements have also provided a considerable portion of what is required for Risk Management and Accident Management including:

- 1) control room enhancements,
- 2) implementation of symptom based Emergency Operating Procedures (EOPs), and
- 3) periodic operator training in use of EOPs.

The BWR Owner's Group development of Emergency Procedures Guidelines (EPGs) from which BWR plant EOPs are derived have been found to result in development of a near optimal set of EOPs to exploit all plant capability for avoiding or minimizing plant damage if the unique characteristics of a plant are considered in the development of the plant's EOPs.

# THE RISK MANAGEMENT PROCESS



## The Risk Management Process

This view graph is intended to represent the risk management process. This is a continuous, or cyclic process, which must be carried out to reflect,

- 1) changes in equipment or procedures,
- 2) the effectiveness of operator training,
- 3) changes in equipment or operator performance, and
- 4) new phenomenological data or improved analytical models.

Effective implementation of this process imposes new and more stringent requirements on the risk analysis process, and requires implementation of an accident management process.

The overall objectives of this process are to assure that:

- 1) the entire available capability of the plant will be effectively utilized to avoid or minimize plant damage that could result from any initiating event in combination with any number of independent equipment failures,
- 2) procedures will achieve a very high success rate in utilization of available plant capability,
- 3) operator training will result in a minor contribution to plant damage frequency due to operator failure to correctly follow and execute these procedures, and
- 4) changes in equipment, procedures, or training will not lead to degraded performance over a long period of time.

These objectives then imply a need to carry out the risk analysis process in the most realistic manner possible. The use of simplifying conservative assumptions is not acceptable. The use of realistic analyses is superior to simplified conservative analyses in identifying operator actions and their timing that could successfully terminate an accident. Each accident transient must be calculated as accurately and realistically as possible in order to determine the time available for operator response actions, the level of success to be expected from operator actions, and the availability of unambiguous symptoms to assure that operators will take the necessary actions. The purpose of the risk analysis is not to derive a conservative estimate of plant damage frequencies but is to determine the effectiveness of the plant Emergency Operating Procedures and the capability of the operators to successfully execute those procedures.

The most important aspect of this process is the measurement of actual performance of plant equipment and operator performance in execution of EOPs for comparison with target values established to control the calculated frequency of plant damage. Deviations from the target values would be used to identify where maintenance programs, procedures, or operator training need improvement.

REQUIRED CHARACTERISTICS  
OF THE  
RISK ANALYSIS

- o TRANSIENT ANALYSIS FOR EACH SEQUENCE TO DETERMINE:
  - TIME OF INITIAL CORE DAMAGE,
  - TIME LIMIT TO AVOID VESSEL FAILURE,
  - TIME LIMIT FOR VENT OPERATION,
  - TIME LIMIT FOR MASS ADDITION TO SUPPRESSION POOL, ETC.
  
- o EVENT TREES TO DETERMINE
  - AVOIDANCE OF PLANT DAMAGE
  - INITIATION OF CORE DAMAGE
  - CONTAINMENT OVERPRESSURE FAILURE
  
- o DISPOSITIONING OF EACH EVENT TREE ENDPOINT, INDIVIDUALLY, TO THE FULL SPECTRUM OF FINAL PLANT DAMAGE STATES.
  
- o REALISTIC CREDIT FOR ALL OPERATOR ACTIONS REQUIRED BY PLANT EOPs.
  
- o FULL TRACEABILITY OF EACH INDIVIDUAL ACCIDENT SEQUENCE.
  
- o FULL ACCOMMODATION OF ALL TECHNICAL SPECIFICATION CONSTRAINTS AND INFLUENCE OF THE ACTUAL SEQUENCE OF FAILURES.
  
- o CAPABILITY TO ISOLATE EACH SEQUENCE INVOLVING HIGH PHENOMENOLOGICAL UNCERTAINTY.

The Risk Management Process  
(Continued)

A set of defense-in-depth criteria governing both equipment and procedures is applied to each individual accident sequence. These criteria, in combination with the use of symptom based EOPs, provide a high level of assurance that the likelihood of severe consequences from any accident will be extremely low.

Required Characteristics  
of the  
Risk Analysis

For risk management purposes, the objective of risk analysis is not to derive an estimate of plant damage frequency or public risk. The purpose is to realistically test the adequacy of plant facilities, EOPs, and operator capability to respond to any combination of initiating events and equipment failures to minimize damage to the plant. This latter objective imposes far more stringent demands on the risk analysis process and the nature of accident transient calculations for accuracy and realism in the results.

Operator actions to respond to an accident, to recover failed equipment, and to prevent avoidable loss of essential equipment are extremely important in assuring that plant damage frequency and public risk been minimized. Full have exploitation of the operator's capability in this regard results in a two-decade reduction in plant damage frequency in comparison with traditional risk analysis models. The most important aspect of this reduction, however, is the influence on the conditional containment failure probability (given core damage) which is on the order of a one to two decade reduction.

To achieve this gain requires the development of a carefully prepared and thoroughly tested set of EOPs and comprehensive training of operators in their use. It may also be necessary to correct some deficiencies in plant equipment which degrade the capability for or prevent operator actions. Examples of such improvements might be:

- 1) provision of backup inventory to the condensate storage tank (CST), and
- 2) extension of DC power endurance in Station Blackout.

The ability to quantify the degree to which operators act successfully requires transient calculations which identify the plant symptoms, prompt the necessary operator response, and give realistic estimates of the time available for such action. Operator training in the use of these procedures is of fundamental importance in achieving the level of frequency reduction cited for core damage and containment failure. For example, in the case of ATWS, operator actions may be shown to be extremely effective at avoiding containment overpressure failure to a level determined almost entirely by equipment failure. If, however, the operator does not recognize ATWS or is unaware of the various action alternatives available to him and the associated time constraints, the rate of containment failure may be increased by as much as four to five decades.

## DEFENSE-IN-DEPTH CRITERIA

### (FREQUENCY AND EQUIPMENT)

- o ACCIDENT SEQUENCES HAVING HIGH CALCULATED FREQUENCIES ARE NOT ACCEPTABLE.
  
- o ACCIDENT SEQUENCES HAVING THE LOW CALCULATED FREQUENCIES MUST ALSO HAVE DEFENSE-IN-DEPTH BOTH IN THE FORM OF EQUIPMENT AND PROCEDURES. DEFENSE-IN-DEPTH IS DEFINED FOR EQUIPMENT AND PROCEDURES AS FOLLOWS:
  - o EQUIPMENT
    - CORE OR CONTAINMENT DAMAGE SHALL NOT OCCUR WITHOUT MULTIPLE FAILURES OF REDUNDANT OR DIVERSE EQUIPMENT.
    - VESSEL FAILURE SHALL NOT OCCUR FOLLOWING CORE DAMAGE UNLESS ADDITIONAL INDEPENDENT EQUIPMENT FAILURES OCCUR.
    - CONTAINMENT FAILURE SHALL NOT OCCUR FOLLOWING CORE DAMAGE UNLESS ADDITIONAL INDEPENDENT EQUIPMENT FAILURES OCCUR.
    - CONTAINMENT FAILURE SHALL NOT OCCUR FOLLOWING VESSEL FAILURE UNLESS ADDITIONAL INDEPENDENT EQUIPMENT FAILURES OCCUR.

Required Characteristics  
of the  
Risk Analysis  
(Continued)

For this reason, risk analysis must explicitly consider the quality and character of the plant EOPs, the level and quality of operator training, and the constraints imposed on plant operation by Technical Specifications. The Technical Specification constraints are important to specific event sequences and can have a decade or more influence on the resulting plant damage frequency.

There are currently a number of phenomenological issues which have very large uncertainties associated with them, for example the core-concrete interaction phenomena. If an effective risk management process is applied, however, the fraction of plant damage events which involve core-concrete interaction can be shown to be small. For this reason, the tabulation of results of the risk analysis must have the capability of segregating sequences which have such high impact, high uncertainty characteristics. This is important not only to avoid obscuring the effectiveness of plant equipment, procedures, and operator actions in responding to the great majority of plant accident sequences, but also to determining the impact of various response strategies on these high uncertainty sequences.

Defense-in-Depth Criteria  
(Frequency and Equipment)

This view graph presents recommended criteria for plant equipment defense-in-depth. If these criteria are satisfied for all accident sequences, a very low frequency of plant damage is calculated, as is an extremely low frequency of significant off-site consequence. The reasons for this are:

- 1) the frequency of initiators combined with sufficient equipment failures to lead to core damage will be on the order of  $3 \times 10^{-7}$ /Ry for all contributions combined,
- 2) given that core damage has occurred, the conditional probability of sufficient additional failures resulting in reactor vessel failure will be on the order of  $10^{-2}$ ,
- 3) given that reactor vessel failure has occurred, the conditional probability of containment failure will be on the order of  $10^{-1}$ ,
- 4) given that reactor vessel failure has not occurred, the conditional probability of containment failure will be on the order of  $10^{-3}$  or less, and
- 5) given that core damage does not occur, the conditional probability of containment overpressure failure will be on the order of  $3 \times 10^{-9}$ /Ry.

DEFENSE-IN-DEPTH CRITERIA  
(PROCEDURES AND INSTRUMENTATION)

o PROCEDURAL

- NO PROCEDURE SHALL HAVE ADVERSE CONSEQUENCES IN THE CASE OF ADDITIONAL EQUIPMENT FAILURES BEYOND THOSE OCCURRING INITIALLY.
- THE NECESSARY ANTICIPATORY ACTIONS SHALL BE PERFORMED TO AVOID LOSS OF ADDITIONAL EQUIPMENT BUT SHALL NOT DEGRADE THE EXISTING SITUATION.
- THE NECESSARY ANTICIPATORY ACTIONS SHALL BE PERFORMED TO PERMIT SUCCESSFUL RESPONSE TO POTENTIAL ADDITIONAL FAILURES, BUT, SHALL NOT DEGRADE THE EXISTING SITUATION.

o INTERFACE

THE NATURE AND TIMING OF INFORMATION TO THE OPERATOR SHALL BE SUFFICIENT TO ASSURE TIMELY EXECUTION OF ALL APPROPRIATE PROCEDURAL STEPS.

Defense-in-Depth Criteria  
(Frequency and Equipment)  
(Continued)

These results are a direct consequence of meeting the defense-in-depth criteria, the frequency of the initiators which can potentially lead to plant damage if sufficient equipment fails, and the inherent unavailability of the various systems which must fail to lead to one of the results listed above.

Procedural defense-in-depth criteria assure optimal use of all plant equipment in order to achieve these results, and operator training assures a minor contribution to plant damage frequency as a result of operator failure to follow procedures correctly. Overall, this approach to severe accident response results in a calculated core damage frequency on the order of  $3 \times 10^{-7} \text{ yr}^{-1}$  and a containment failure with core damage on the order of  $3 \times 10^{-9} \text{ yr}^{-1}$  for the BWR-4 plant. This result does depend on utilization of all available plant systems in response to an accident, execution of important anticipatory actions to avoid or accommodate additional equipment failures, and availability of a reliable wetwell vent. Lack of wetwell vent capability could increase the containment failure frequency by one to two decades. Absence of a wetwell vent capability, however, would be found to result in violation of the defense-in-depth criteria for important accident sequences. Both the core damage frequency and the containment failure frequency could be influenced by as much as one decade by differences in emergency service water system design, inability to backup CST inventory, inability to extend DC power availability, or inability to utilize unconventional vessel injection sources such as injection from the Fire Main System.

The checking of all accident sequences against defense-in-depth criteria, both procedural and equipment, clearly identifies any important contributions resulting from either procedural deficiencies or from inability to make unconventional use of plant equipment in severe accident situations. The EOPs can then be revised to correct any deficiencies.

Defense-in-Depth Criteria  
(Procedures and Instrumentation)

The defense-in-depth criteria for procedures are important to assure optimal use of plant equipment. For some accident sequences the consequences of the accident may lead to an unnecessary loss of equipment, for example, loss of HPCI due to high suppression pool temperature in ATWS. This loss may be prevented simply by not allowing the suction transfer from CST to suppression pool and backing up the CST inventory to avoid its depletion. The procedural criteria are important to assuring effectiveness of the equipment criteria.

The final criterion relating to instrumentation is important to assure that the actions called for by procedures will actually be executed. In the absence of a symptom requiring the action, it is unlikely that the action will be taken.

## SEVERE ACCIDENT MANAGEMENT

### o DEFINITION :

ACTIONS TAKEN TO AVOID OR MINIMIZE PLANT DAMAGE RESULTING FROM AN INITIATING EVENT AND ANY COMBINATION OF ADDITIONAL EQUIPMENT FAILURES.

### o APPLICABLE TIME PERIOD:

FROM THE TIME OF THE INITIATING EVENT UNTIL THE OPERATORS ACHIEVE A LONG TERM STABLE PLANT CONDITION OR UNTIL CONTROL ROOM ACTIONS CAN NO LONGER INFLUENCE THE PLANT CONDITION.

### o SOURCE OF GUIDANCE:

THE EMERGENCY OPERATING PROCEDURES AND SUPPLEMENTAL PROCEDURES REFERENCED BY THE EOPs.

### o ROLE OF RISK ASSESSMENT:

DETERMINE OPTIMAL RESPONSE STRATEGIES FOR STRUCTURING EOPs AND THE DEGREE AND NATURE OF PLANT DAMAGE TO BE EXPECTED IN EACH ACCIDENT SEQUENCE.

Defense-in-Depth Criteria  
(Frequency and Equipment)  
(Continued)

These defense-in-depth criteria in combination with the symptom based EOPs are believed to provide a high degree of protection against known accident sequences. While the calculated value of the frequency of these sequences may be optimistic as a consequence of a lack of completeness in the modeling of plant dependencies and interactions, the effectiveness of the operator actions is nevertheless valid. For this reason, the plant damage frequency and degree of public risk derived by this approach is believed to be the best assessment of the actual risk associated with the plant operations. The use of arbitrary conservatisms to attempt to compensate for a lack of completeness does not result in a more credible evaluation, may obscure the true nature of dominant risk contributor, and may obscure success paths available to the operator.

Severe Accident Management

If the risk management process previously described is implemented for a plant, an effective severe accident management program will result. The definition of severe accident management provided in this view graph states that the EOPs are the source of guidance for response to an accident. The risk management process assures that EOPs are developed that are comprehensive and provide the optimal response to any event sequence considered in the risk assessment.

The EOPs must provide the operators with complete directions on the actions necessary to stabilize the plant. Effective advice from outside the control room is not likely within the first hour or two of the accident since some time is required for staffing and Technical Support Center and Emergency Operations Facility and to bring the personnel up to speed on the plant status. In most BWR accident sequences the critical actions must all be taken within the first hour or so of the accident so that outside assistance should not be depended upon for accident mitigation.

The primary role of these external resources must be the implementation of the Emergency Plan and the planning and execution of recovery actions once the operators have stabilized the plant. In a case where the operators can no longer influence the plant from the control room, perhaps because of loss of habitability, these external resources may be used to develop and execute coping actions to bring the plant back to a safe condition.

Thus, the EOPs represent the severe accident management process in that they must be designed to make optimal use of the plant equipment to avoid or minimize damage to the plant. This definition is important since any less stringent definition will leave the plant vulnerable to improper response during the critical first hour or two of a severe accident sequence.



## Potential Accident Trajectories

There appears to be much confusion over the issue of severe accident management and what objectives should be set for it. The diagram on the view graph is intended to define the various phases which can occur in the accident sequences for a plant.

The limits on the definition for Severe Accident Management and EOP applicability are presented in the form of a time line for potential accident sequences in the view graph. The EOPs govern actions taken during those portions of potential accident sequences labeled AB and AC. In the case of the segment AC stabilization and control of the plant are eventually re-established by control room actions, although in some cases with varying degrees of plant damage up to, but not including, the point of containment failure. Venting could take place during the segment AC in order to avoid uncontrolled failure of the containment. Upon reaching point C, a period begins during which recovery actions are initiated. These are actions which would re-establish long term safe conditions in the plant. In a sequence where little or no plant damage is sustained recovery could involve refurbishing as needed for continued operation of the plant. In cases, such as for TMI-2, it could involve clean up of fission products and removal of fuel in preparation for decommissioning of the plant. In all cases, the EOPs completely govern the time segment AC, but do not apply over the time period, CD. There are currently no formal programs or procedures defined for the segment CD other than the Emergency Plan. That plan, however, primarily addresses communications, evacuation, and monitoring of radioactive material releases.

The alternative time line, AB, represents an accident sequence where control of the plant cannot be regained by application of the EOPs, usually as a consequence of massive levels of equipment failure. In those cases containment would fail, either with or without prior core damage, and control room habitability would be lost. In cases where no core damage had occurred, the possibility of core damage resulting from consequential loss of equipment would require consideration. In such cases, it is likely that control room occupancy and reactor building access would be lost so that further actions would be initiated from outside the control room. At the point where control room actions are no longer effective or cannot be taken, the EOPs are no longer applicable to defining the actions to be taken. Currently, we have defined the actions to be taken during the time segment BC to be coping actions. As in the case of recovery actions, no formal programs or procedures have been defined other than the general provisions for activation of the EOF and General Office support. By the nature of the situation in such cases, a formal definition of actions to be taken to bring about stabilization and control will be difficult to develop.

The view graph then defines the time period for Severe Accident Management (segments AC and AB only), and the EOPs fully define the actions to be taken during those time periods. The EOPs, therefore, are by definition the Severe Accident Management program, and it is essential that plant specific EOPs be developed.

## EMERGENCY OPERATING PROCEDURES

- o THE EOPs MUST COVER ALL ACTIONS REQUIRED TO REGAIN CONTROL OF THE PLANT AND TO STABILIZE IT.
- o THE EOPs MUST BE FUNDAMENTALLY BASED ON PLANT SYMPTOMS WHICH ARE RELIABLY INDICATED BY PLANT INSTRUMENTATION.
- o THE OPTIMAL FORM FOR THE EOPs IS A FLOW CHART FORMAT WHICH PERMITS TIMELY INDICATION OF ALL ACTIONS FOR WHICH TIME IS CRITICAL.
- o ACTIONS WHICH ARE NOT TIME CRITICAL MAY BE REFERENCED TO EXTERNAL SUPPLEMENTAL PROCEDURES.
- o THE PROCEDURES MUST AVOID COMPLEXITIES AND AMBIGUITIES.
- o THE PROCEDURES OR TRAINING MUST ADVISE THE OPERATOR OF TIME CONSTRAINTS AND PRIORITIES.
- o THE ACTIONS SPECIFIED MUST BE FEASIBLE.
- o THE PROCEDURES SHOULD REINFORCE BASIC OPERATOR TRAINING.
- o PROCEDURES AND TRAINING FOR THEM MUST EXIST IF OPERATOR ACTION IS TO BE CONSIDERED SUCCESSFUL AND EFFECTIVE.

## Emergency Operating Procedures

In order to fulfill the objectives of the Risk Management and Severe Accident Management process, it is necessary to impose a number of requirements on the EOPs. The view graph lists the requirements which are important to development of effective procedures.

The symptom based procedures have an important disadvantage--in most accident sequences it is necessary to follow through several branches of the procedures simultaneously. This process can be simplified by use of a flow diagram structure for the EOPs, but, even so, the wording and organization of the flow charts are critically important for effective use by operators.

Testing the effectiveness of the procedures by simulator exercises has been found to be an excellent means for discovering and eliminating ambiguities in the flow charts. Another helpful practice is to use supplemental procedures external to the flow charts for those actions which are not time constrained. This permits a considerable reduction of the volume of information which must be included on the flow charts and therefore enhances the ease of following the procedures involved.

In the best situation, however, the EOPs remain complex and challenging. For this reason rigorous operator training on the use of EOPs reinforced by periodic re-training is an essential element to assuring a high degree of reliability in operator performance in use of the EOPs.

### Summary

The Risk Management Process for the BWR imposes special requirements on EOPs, operator training, transient analysis, and risk analysis and, in addition, requires monitoring of unavailability of equipment and operator performance in execution of and knowledge of EOPs. The EOPs must consider all initiators in combination with any degree of equipment failure and assure utilization of all available plant facilities to minimize the degree of plant damage. In this process it is essential to account for operator recovery and repair actions. Realistic estimates of recovery and repair times must be used in combination with realistic estimates of available time for success.

The success criteria used in the risk analysis must distinguish a full range of plant damage states which must include:

- 1) core damage only,
- 2) core damage with reactor vessel failure only,
- 3) wetwell venting in combination with no core damage and 1) and 2) above,
- 4) Containment overpressure failure with no core damage and with 1) and 2) above, and
- 5) containment drywell overtemperature failure with 2) above.

## SUMMARY

- ° RISK MANAGEMENT ENCOMPASSES ACCIDENT MANAGEMENT
- ° THE RISK MANAGEMENT PROCESS IMPOSES SPECIAL REQUIREMENTS ON:
  - EMERGENCY OPERATING PROCEDURES
  - OPERATOR TRAINING
  - TRANSIENT ANALYSIS
  - RISK ANALYSIS
  - PLANT AND OPERATOR PERFORMANCE MONITORING
- ° THE BENEFITS OF THE PROCESS ARE:
  - A REDUCTION IN CALCULATED AND ACTUAL PLANT DAMAGE FREQUENCY
  - A REDUCTION IN CALCULATED AND ACTUAL PUBLIC RISK
  - SEGREGATION OF SEQUENCES INVOLVING MAJOR UNCERTAINTIES
- ° WE BELIEVE THAT THIS APPROACH OFFERS A MEANS OF CLOSURE OF THE SEVERE ACCIDENT ISSUE WHICH HAS CREDIBILITY AND AUDITABILITY.
- ° THE PROCESS RESULTS IN AN ASSESSMENT OF PLANT DAMAGE FREQUENCY WHICH IS PERIODICALLY UPDATED, REFLECTS ACTUAL PLANT AND OPERATOR PERFORMANCE, AND CAN READILY INCORPORATE THE INFLUENCE OF IMPROVED METHODS AND NEW PHENOMENOLOGICAL DATA.

Summary  
(Continued)

This degree of resolution in plant damage states permits events having very high uncertainty, or a controversial basis, to be segregated from the general array of plant damage sequences, but imposes more severe demands on the supporting transient analysis both in terms of the number of calculations and the realism of the calculations. It is particularly important to derive and apply criteria for halting the core damage progression before reactor vessel failure and for stabilizing core debris on the drywell floor before thermally induced failure of containment integrity. Application of these criteria in turn requires a higher degree of accuracy in describing the core degradation processes, the reactor vessel failure process, and the phenomena which govern the behavior of core debris falling into the under-pedestal region.

The benefits from this process are a very large reduction in the calculated and actual frequency of plant damage and public risk. This reduction far exceeds what can be achieved with even major plant equipment modifications with the exception of a wetwell vent. The actual value and risks associated with the wetwell vent have not yet been adequately quantified, but the results that are currently available indicate that it can sharply reduce the frequency of containment overpressure failure due to loss of decay heat removal systems. Such failures are of great concern since consequential loss of equipment could lead to inadequate core cooling and core damage.

The process can also be used to isolate and focus attention on those accident sequences which involve controversial phenomena or very high uncertainty. This is important because such sequences tend to be those having the most severe consequences, but also tend to be those having the lowest calculated frequencies. The proposed risk analysis process will permit such sequences to be placed in a much clearer perspective and permit a more accurate and effective assessment of the appropriate measures to be taken.

Finally, we see this Risk Management Process as a rational approach to resolution of the severe accident issue. It would utilize actual plant operating experience (supported by generic data only when needed) to characterize the calculated value of plant damage frequency and would clearly identify the important contributors to the calculated value. While we believe that calculated values are optimistic because of dependencies or interactions not known and considered, we believe the defense-in-depth concept in combination with comprehensive EOPs and thorough operator training offers the best possible defense against all accident sequences including those which may have been overlooked because of a missed dependency or interaction. Further, we believe that this approach is by far the most effective application of resources for true risk reduction.



EVALUATION AND IMPROVEMENT IN  
NONDESTRUCTIVE EXAMINATION (NDE) RELIABILITY FOR  
INSERVICE INSPECTION OF LIGHT WATER REACTORS<sup>(a)</sup>

S. R. Doctor, J. D. Deffenbaugh, M. S. Good, E. R. Green,  
P. G. Heasler, F. A. Simonen, J. C. Spanner, T. T. Taylor, T. Vo  
Pacific Northwest Laboratory  
Operated by Battelle Memorial Institute

ABSTRACT

The Evaluation and Improvement of NDE Reliability for Inservice Inspection of Light Water Reactors (NDE Reliability) program at the Pacific Northwest Laboratory was established by the NRC to determine the reliability of current inservice inspection (ISI) techniques and to develop recommendations that will ensure a suitably high inspection reliability. The objectives of this program include determining the reliability of ISI performed on the primary systems of commercial light-water reactors (LWRs); using probabilistic fracture mechanics analysis to determine the impact of NDE unreliability on system safety; and evaluating reliability improvements that can be achieved with improved and advanced technology. A final objective is to formulate recommended revisions to ASME Code and Regulatory requirements, based on material properties, service conditions, and NDE uncertainties. The program scope is limited to ISI of the primary systems including the piping, vessel, and other inspected components. This is a progress report covering the programmatic work from October 1987 through September 1988.

OBJECTIVE

The Evaluation and Improvement of NDE Reliability for Inservice Inspection of Light Water Reactors (NDE Reliability) program at Pacific Northwest Laboratory (PNL) was established to determine the reliability of current ISI techniques and to develop recommendations that will ensure a suitably high inspection reliability. The objectives of this NRC program are to:

- determine the reliability of ultrasonic ISI performed on commercial light-water reactor (LWR) primary systems
- using probabilistic fracture mechanics analysis, determine the impact of NDE unreliability on system safety and determine the level of inspection reliability required to ensure a suitably low failure probability

---

(a) Work supported by the U.S. Nuclear Regulatory Commission under Contract DE-AC06-76RLO 1830; Dr. J. Muscara, NRC Program Manager, FIN B2289

- evaluate the degree of reliability improvement that could be achieved using improved and advanced NDE techniques
- based on material properties, service conditions, and NDE uncertainties, recommend revisions to ASME Code, Section XI, and Regulatory Requirements that will ensure suitably low failure probabilities.

The scope of this program is limited to ISI of primary systems; the results and recommendations may also be applicable to Class II piping systems.

The program consists of three basic tasks: a Piping task, a Pressure Vessel task, and a New Inspection Criteria task. Because of the problems associated with the reliable detection, correct interpretation, and accurate characterization of defects during inservice inspection of piping, the major efforts were concentrated in the Piping task and the New Inspection Criteria task. However, work did begin this year on the Pressure Vessel Task.

This report is divided into six sections. The first section highlights the Management activity, the second section covers the ASME Code Activities, the third section covers work related to Inspection of Reactor Pressure Vessels, the fourth section covers New Inspection Criteria, the fifth section covers one fast response for Consulting on Field Problems, and the sixth section covers Piping Inspection activities.

## 1.0 NDE MANAGEMENT

During this past year, many task activities made significant progress towards reaching conclusions and in developing the technical basis needed to establish positions for ASME Code recommendations and regulatory recommendations.

## 2.0 ASME CODE ACTIVITIES

Proactive participation in ASME Section XI activities continued toward achieving Code acceptance of NRC-funded PNL research to improve the reliability of nondestructive examination/in-service inspection (NDE/ISI). The objective of this task is to develop upgraded criteria and requirements for qualifying ultrasonic testing/in-service inspection (UT/ISI) systems.

During the past year, PNL representatives attended four different series of meetings held in conjunction with the ASME Section XI Subcommittee on In-service Inspection of Nuclear Power Plant Components. PNL staff hold memberships on the Working Group on Volumetric Examination and Procedure Qualification, Working Group on Surface Examination and Personnel Qualification, chair a Task Group on Acoustic Emission Monitoring, and serve as Secretary and member of the Subgroup on Nondestructive Examination (SGNDE). In May, a joint meeting of the ASME Boiler and Pressure Vessel Code Committees and the National Board of Pressure Vessel Inspectors provided an opportunity to attend ASME Section

V Subcommittee meetings and serve as technical liaison between Section V and the SC-XI SGNDE. Following each SGNDE meeting, minutes were prepared and distributed to a mailing list of about 85 addressees, along with agenda materials for the next meeting.

A proposed revision to Code Case N-409 (N 409-1) received final approval from Section XI, the Main Committee, and the Board on Nuclear Codes and Standards. Code Case N 409-1 consists of an expansion of N-409 that describes a statistically designed performance demonstration to qualify the personnel, equipment, and procedures used for UT/ISI of all light-water reactor piping welds in accordance with Section XI requirements.

The proposed Appendix VII on Personnel Training and Qualification was formally approved by the Main Committee (M.C.), although two letter ballot negatives were received during second consideration of this item. A response to these two negatives was prepared, along with a proposed editorial revision to accommodate concerns expressed by the negators, resulting in withdrawal of one negative. Reaffirmation of the proposed Appendix VII, including the editorial change, was approved by the cognizant Working Group, the SGNDE, and the Section XI Subcommittee. This item was then submitted for consideration by the Board on Nuclear Codes and Standards (BNCS). Four negatives were received from the initial BNCS ballot on Appendix VII, and an extensive response was prepared to address concerns raised in these negative ballots. Two BNCS members were contacted regarding their ballots, and both tentatively agreed to withdraw their negative votes on this item. It is expected that the proposed Appendix VII will be approved by BNCS on a second consideration ballot to be issued in early October.

The proposed Appendix VIII on UT/ISI Performance Demonstrations was approved by the SGNDE and Section XI Subcommittee for submittal to the Main Committee. It is expected that this document will be considered by the M.C. during the December 1988 meeting. This document includes essentially all of the provisions of Code Case N 409-1, plus it extends the performance demonstration concept to other Section XI applications such as clad/base metal interface of pressure vessel shell welds, nozzle inner radius areas, pressure vessel shell welds other than the clad/base metal interface, nozzle-to-shell welds, and bolting and studs. When adopted, this Appendix will represent a significant enhancement in the performance demonstration requirements for all of the key Section XI UT applications.

A proposed rewrite (restructuring) of IWA-2300 was approved by the SGNDE and SC-XI and was included as an introductory element in the proposed Appendix VII package. PNL staff gave technical presentations on a) new inspection criteria, b) the SAFT technology, c) Surry steam generator program results, and d) acoustic emission technology overview to various SC-XI and/or SC-V groups. A document entitled "Qualification Process for Ultrasonic Testing on Nuclear Inservice Inspection Applications" (NUREG/CR-4882) was revised to accommodate NRC and PNL review comments. This document has now received PNL clearance and has been submitted for final NRC review.

### 3.0 PRESSURE VESSEL INSPECTION TASK

#### 3.1 ANALYSIS OF PISC II

PNL received a complete set of the Programme for the Inspection of Steel Components (PISC-II) round-robin data on the four plates from the Joint Research Centre, Ispra, Italy in June 1986. The initial objectives of this task were to review the data present and attempt to duplicate some of the results present in the PISC-II reports so that we can be sure that we understand the data and that it is correct. The specific tasks completed to date include:

- Assembling and computerizing complete information on the true-state data. The original computer data did not contain a complete description of the flaws or the blocks. We had to extract the relevant information from PISC reports and communications with Ispra.
- Duplicating selected defect detection probabilities from PISC-II Report No. 5. This was an attempt to identify exactly what set of data was used in the PISC-II reports and verify the procedures Ispra used to calculate defect detection frequency probability (DDF).
- Implementing a scoring procedure for PISC data. We want to utilize different scoring methods than those employed by PISC and also want to verify their results.

Review of PISC-II Scored Results in "CLEAN.PROC". After reviewing the data file "CLEAN.PROC" that was received from Ispra, we have determined the summary tables on pages 23-27 in Report No. 5 were developed as follows:

The best detection results from each team (the selection was normally made by computer program that compiled the results of several inspection reports) were compared with intended defects only. A list of intended defects for each specimen may be found in PISC II Report No. 2. Other defects such as unintended weld fabrication defects or implantation defects, etc. were not used in scoring. None of the inner radius cracks (which were intended defects) were used in scoring the data. Also, no false calls were reported in the tables.

The following three examples provide a comparison of our analysis vs. the results in Report No. 5. When reading the examples, remember PNL did not score any inspection results -- "CLEAN.PROC" contains scored results (i.e., PISC personnel have associated intended defects with each team's inspection results). All we have done is divide the total number of intended defects that should have been detected into the defects that "CLEAN.PROC" indicates were detected.

Example 1:

Team EC005499	Plate 1
PISC II Results	1.00
Our Results	1.00
Number of Defects	15

Team EC005499 is a computer-compiled selection of the best results of all procedures/techniques used by Team EC. PISC Report No. 2 indicates that Plate 1 had 15 intended defects. Reviewing data in "CLEAN.PROC" indicates that EC005499 did indeed detect all 15 flaws; therefore, its DDF is 1.00. In this example, our results and the results reported in Report No. 5 for Plate 1 are in agreement.

Example 2:

Team DB005599	Plate 1
PISC II Results	0.92
Our Results	0.93
Number of Defects	14

Note in this example that the number of defects is 14 instead of 15 for Plate 1. Fourteen defects were used in this instance because the inspection coverage coordinates in "CLEAN.PROC" indicate that team DB005599 (again a computer selection) did not entirely scan Plate 1 and an area where one defect was located was not scanned; therefore, only 14 defects were used in determining DDF.

Reviewing the detection data in "CLEAN.PROC" indicates that 13 of the 14 defects were detected. Our results and the PISC II results are in close agreement ( $13 \div 14 = 0.9286$ ) -- perhaps PISC II rounded down.

Example 3:

Team ES000799	Plate 1
PISC II Results	0.46
Our Results	0.40
Number of Defects	15

Team ES000799 illustrates an example where our results and PISC II do not agree and we cannot ascribe a logical reason for the disagreement. The data in "CLEAN.PROC" indicates that the entire block was scanned and that six flaws were detected.  $6 \div 15 = 0.40$  DDF, yet PISC II results indicate a DDF of 0.46.

If one assumes that only 13 flaws should be used, then a DDF of 0.46 is correct; however, using 13 flaws is inconsistent with the inspection coverage data. Perhaps the data in "CLEAN.PROC" is wrong -- who knows?

Scoring Algorithm. PNL has developed a software algorithm that will score data from the RAW.PROC. data file. The algorithm compares the dimensions of each indication for a specific inspection with flaw dimensions given in true-state data for the test plate that was examined. When all indication dimensions x, y, and z intersect with true-state flaw dimensions, the algorithm associates that specific indication with a specific flaw. This scoring algorithm will be applied to the PISC-II data base, an analysis performed, and reported next year.

### 3.2 EQUIPMENT INTERACTION MATRIX

The objective of this subtask is to evaluate the effects of frequency domain, UT/ISI equipment interactions, and determine equipment tolerance values for controlling inspection reliability. An integrated computer model for the entire inspection system including the pipe section and flaw has been developed to explore the effects of frequency interaction on flaw detection and sizing. Work in FY88 concentrated on the validation of the model for the acoustic components -- the perspex shoe and the flawed pipe section:

- Excellent agreement was found between the model predictions and measured single frequency beam patterns for through-transmission, 90° corner reflection, and tandem-probe scanning of strip flaws. The model is based on two-dimensional, elastodynamics physical optics (EPO) ray tracing theory.
- Comparisons between model predictions and frequency domain measurements of specular reflection signals from large, smooth flaws showed good agreement. An example is the frequency domain comparison shown in Figure 1 for specular reflection within a block with an end cut to 42° measured using a 45° SV transducer.
- Model calculations showed that flaws can have transfer functions that would produce decreased detection and sizing reliability due to frequency domain equipment interactions. Several worst-case flaws can be identified in the calculated transfer functions shown in Figure 2.
- The model results showed the primary cause of undesirable, flaw transfer functions to be phase cancellation at the receiving piezoelectric element face due to the wavefront and face not being parallel. Thus, frequency domain equipment interactions might be greatly reduced through the use of a phase-insensitive receiving probe. The worst-case flaws were selected based on placing nulls in the center of the equipment passband.
- Calculations for equipment center frequency and bandwidth sensitivity studies were completed using several worst-case flaw transfer functions calculated by the ray tracing model. It was found that the present equipment bandwidth tolerance of ±10% as given in ASME Code N 409-1 is acceptable and that it may be possible to relax this standard slightly. The results for the center frequency study have not been analyzed yet.

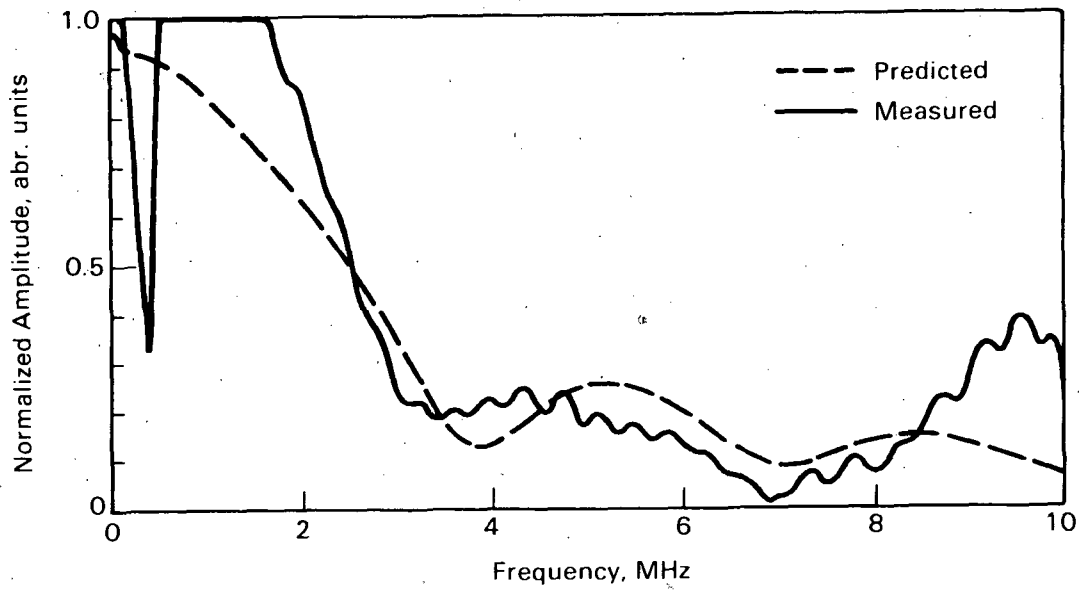


FIGURE 1. Measured vs. Predicted Transfer Functions for 42° Flaw Normalized with respect to 45° Flaw

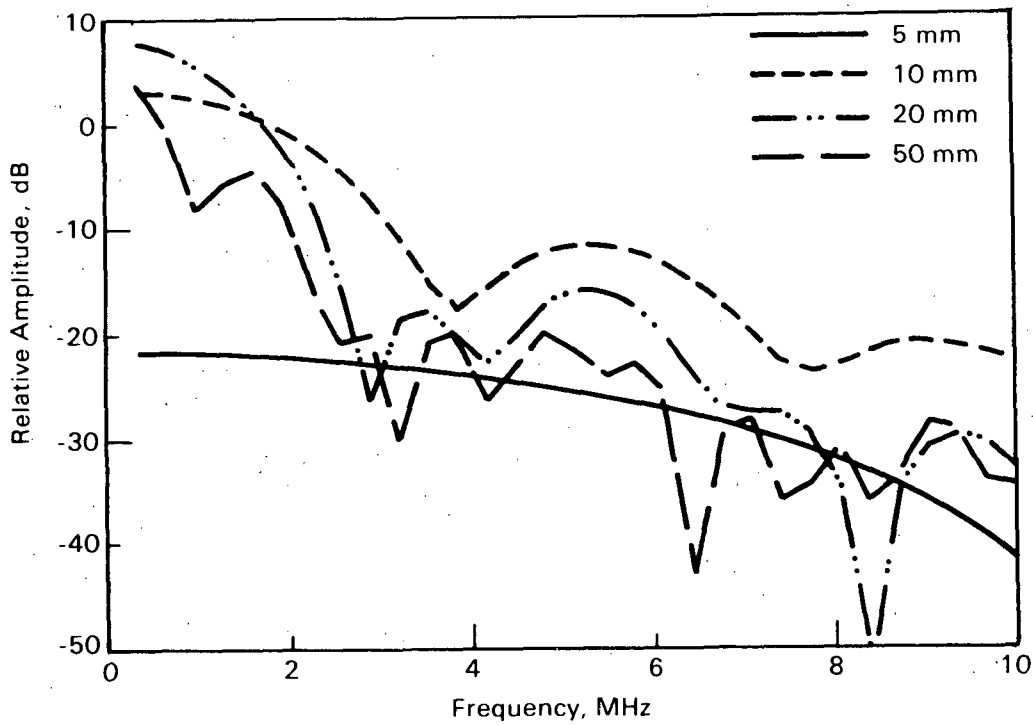


FIGURE 2. Frequency Responses of Various Sizes of 85° Flaws

It was concluded that the present equipment tolerances for things like pulser amplitude can be relaxed; however, tolerances that affect the frequency characteristics will need to be tightly controlled. It should be noted that ASME Code currently controls all operating characteristics at the  $\pm 10\%$  level.

#### 4.0 NEW INSPECTION CRITERIA

Work continued on the assessment of the adequacy of existing ASME Code requirements for ISI and on developing technical bases for improving these requirements to assure safe nuclear power plant operation. Several inter-related activities on this task have been directed to the development of probabilistically based inspection requirements. Particular attention has been directed to requirements for inspection intervals and weld inspection sampling plans.

#### DEVELOPMENT OF PROBABILISTIC APPROACHES

During this past year PNL has continued with the development and assessment of alternative approaches for probabilistically based inspection requirements. This activity has emphasized interaction with NRC staff, other laboratories, ASME groups, and industry efforts as performed by EPRI.

An overview document has been written that outlines a comprehensive probabilistic approach for the development of improved inspection requirements. This document provides a flow chart that relates inspection requirements to quantitative goals for improvements in systems safety. Computational methods and sources of data for quantifying the approach are described and are critically reviewed. The document will guide future efforts on the NDE Reliability program.

PNL has actively participated in the startup of an ASME Task Group on Risk-Based Inspection Guidelines, which is to be an ASME research activity. Participation in this group is expected to further the goals of the NDE Reliability program, and to lead eventually to specific recommendations for the introduction of probabilistic methods as a basis for ASME Section XI requirements. While the initial focus will be on nuclear power, the group will also be concerned with insights to be gained from applications in other industries such as aircraft, navel, petrochemical, and civil engineering structures. While a planning meeting was held on February 18, 1988 at Washington, D.C., further activities have been delayed as funding for the task group is being sought.

A one-day workshop was held at PNL on January 20, 1988 to permit an exchange of views between PNL and NRC staff on the topic of PRA methods and their potential use in establishing priorities for inservice inspection. Parallel applications to prioritize plant aging issues were noted. Also discussed was the approach to be taken by the proposed ASME Task Group on Risk-Based Inspection Guidelines.

## DATA BASE ON PLANT OPERATING HISTORIES

This activity responds to a recommendation from a 1987 workshop with NRC staff, which suggested that data bases and industry records be searched for information on piping failures and repairs, and also for information on findings of inservice inspections (effectiveness). During the past year, we established sources of such information and determined the potential usefulness of the types of information that is most readily available.

Contacts with utilities indicated that suitable records are maintained at plant sites, but that costs of on-site visits to extract the information was beyond the scope of the NDE Reliability program. Further discussions with NRC staff revealed two potentially useful data bases; namely, Licensing Event Reports (LERs) and an industry-maintained data base available through the Nuclear Power Plant Reliability System (NPRDS).

A trial search of the potentially more useful NPRDS data base was performed. It was determined that most of the information relates to "failures" of minor consequence (gasket leaks, cracks in small diameter fittings, etc.) and that these "failures" were typically found visually through evidence of leakage. Nevertheless, inservice inspection has in many cases been effective in detecting weld cracks. The NPRDS data were determined to be relatively accessible, and easy to interpret. Therefore, a complete evaluation of all the piping related failures (400 items) in the NPRDS data base was initiated. Useful trends will be extracted from this information and reported during the next year.

## OCONEE-3 PILOT STUDY

The objective of this study was to initially assess and demonstrate the feasibility of using data from existing Probabilistic Risk Assessments (PRA) to establish inspection priorities for pressure boundary systems and components. A pilot application of PRA methods to the Oconee-3 plant was completed during the past year. The study was based on PRA data from an EPRI study (NSAC-60) and on data for failure probabilities from NRC-funded evaluations of actual observed failure data (NUREG/CR-4407). Based on the results of the pilot study, the proposed use of PRA methods has been demonstrated to be a useful tool for identifying those systems and piping sections or welds that need to be inspected with the highest priority.

Table 1 lists a number of Oconee-3 systems and rankings that provide insight into which systems should be given the highest priority for inservice inspection. Two alternative ranking parameters were employed. The Birnbaum parameter addresses the consequences of failure, given that a failure does occur. This parameter focuses inspection towards the most safety critical systems (importance to preventing core melt), even if they have performed very reliably in the past. In contrast, the Weld Inspection Importance parameter makes use of estimates of system reliability to focus additional attention towards systems that are more likely to experience service failures. In general, the two parameters give similar priorities. However, there are notable

exceptions such as the steam generator, which moves up in priority when the relatively poor service performance of steam generator tubes is taken into consideration.

A further step in the pilot study involved a much more detailed assessment of the emergency feedwater system. Failure Modes and Effects Analysis (FMEA) was applied to identify and prioritize the most risk-important piping sections within this system. The results were then compared to the current inspection requirements specified by ASME Section XI.

**TABLE 1.** Rankings of Systems and Components for Inspection Priority as Based on Risk Considerations for Oconee-3

System (a)	Weld Inspection Importance		Birnbaum Importance	
	Rank	Value	Rank	Value
Low-Pressure Injection (b)	1	(5.9E-06)	2	(1.5E-02)
High-Pressure Injection	2	(5.1E-06)	5	(5.4E-03)
Reactor Pressure Vessel	3	(5.0E-06)	1	(1.0)
Steam Generators	4	(1.5E-06)	9	(1.5E-04)
Emergency Feedwater	5	(7.2E-07)	3	(1.5E-02)
Service Water	6	(3.6E-07)	4	(7.7E-03)
Reactor Coolant (c)	7	(1.7E-07)	6	(3.6E-03)
Power Conversion	8	(8.0E-08)	8	(2.1E-04)
Standby Shutdown Facility	9	(3.0E-08)	7	(6.9E-04)
Instrument Air	10	(7.0E-10)	10	(1.5E-05)

(a) Only systems of interest to Code-Type ISI are listed.

(b) Under normal conditions, the most frequently used function of the LPI system is decay-heat removal (DHR) after a shutdown.

(c) The PCS system consists of the following: main feedwater, main steam, condensate, condenser circulating water, and vacuum systems.

## 5.0 CONSULT ON FIELD PROBLEMS

This is a summary review of the round-robin studies that have been conducted to quantify the performance of ultrasonic procedures to detect, locate, and size defects in pressure vessel shells and nozzles. The results are examined in light of the inspection conditions and ultrasonic procedures in use in the United States.

In 1965, the U.S. Pressure Vessel Research Committee (PVRC) began an NDE program in which teams of trained inspectors conducted inspections on thick-section test blocks containing various welding defects. During the early stages of this program, it was found that the inspection procedures were not well defined and the published results revealed large differences in performance

between teams using nominally the same inspection procedure. A generally small defect detection probability was found which was worse when the inspections were performed through cladding. A new program was initiated in 1974 to test procedures related closely to those required by the 1974 ASME Code Section XI. This round robin study consisted of three unclad test blocks provided by PVRC and used in the aforementioned PVRC program (two butt-welded plates and one welded forged nozzle) and was under the guidance of the Plate Inspection Steering Committee (PISC I). The PISC I program was designed to investigate the capability of the 1974 ASME Section XI inspection requirements to detect, locate, and size defects. In addition, several European agencies applied alternative procedures, some of which were employed for ISI in Europe at that time. A total of 34 inspection agencies took part in the PISC I program, with 28 teams employing the ASME-based procedure.

In 1981, another round-robin testing program was started under the guidance of the Program for the Inspection of Steel Components (PISC II) and was completed in 1986. The PISC II program was designed to evaluate the capability of procedures to detect and locate defects as well as to accurately size the defects. The PISC II program had 50 inspection agencies involved in the inspection of the four plates (two butt-welded flat plates and two plates containing nozzles). The U.S. had five teams that employed manual inspections and several teams that employed advanced ultrasonic techniques.

The PISC I and II results can be summarized by the plot in Figure 3. The vertical axis is the probability that a defect will be detected and correctly sentenced, and the horizontal axis is the through-wall extent of the defect. The term "sentenced" pertains only to defects which were rejectable according to ASME Section XI IWB-3510 1974 Edition and include only those defects which were not undersized by more than 3 mm. The 50% DAC curve is the performance for ASME 1974 Code, while the 20% DAC is for the 1986 version of ASME Section XI Code. The error bars on the two curves show the range of variability of the teams employing procedures in the spirit of ASME at the respective DAC levels. These results clearly show the ineffectiveness of procedures based on early ASME Code. This point is further seen in Figure 4, where the detection probability (MDDF which is the mean value of the defect detection frequency for ASME procedure on all the defects in the specified plate) is plotted versus the DAC level for three of the plates. The trends are pretty similar for each plate, but show the improvement that can be achieved by the 10% and 20% DAC levels. Clearly, the 50% DAC level provides very low defect detection rates.

The results from the two PISC studies can be summarized by the plots shown in Figure 5. The two studies are consistent with one another and show a clear division of the defects into three categories. The data in Figure 5 is only for Plate 3 and for 50% DAC. The most difficult defects to detect are the smooth, sharp planar defects that would include cracks.

The smooth, sharp planar defects are detected by the lower crack tip response, and Figure 6 shows some PISC-II data that shows the DAC levels required to detect this lower tip signal for defects with a 10- to 25-mm

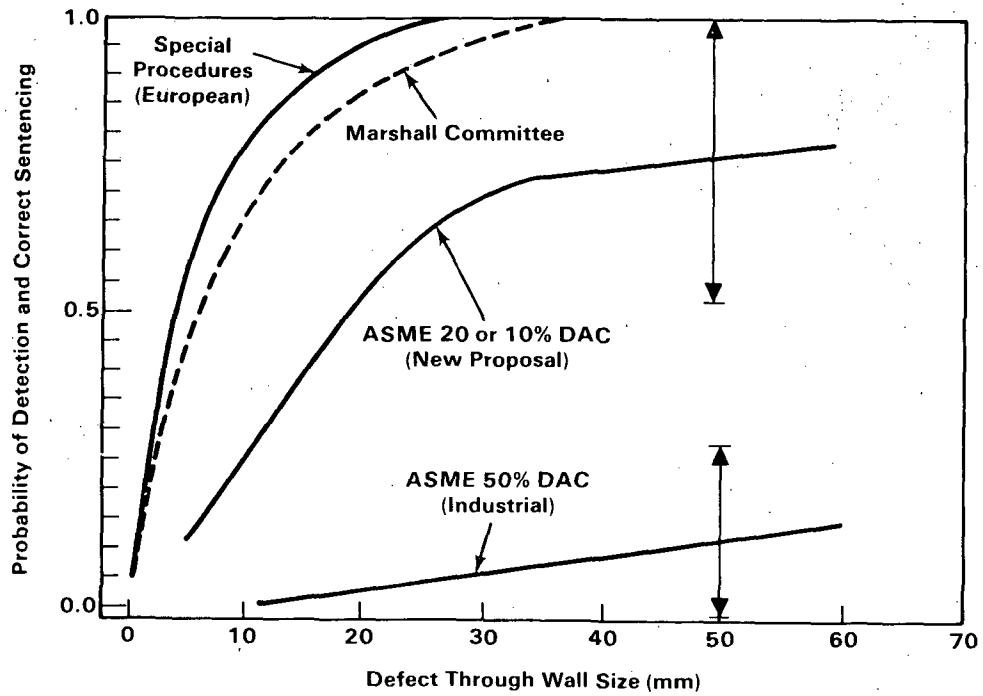


FIGURE 3. Plot of the Defect Detection and Correct Sentencing of Defects for Plate 3 for Various Inspection Procedures as a Function of Through-Wall Size

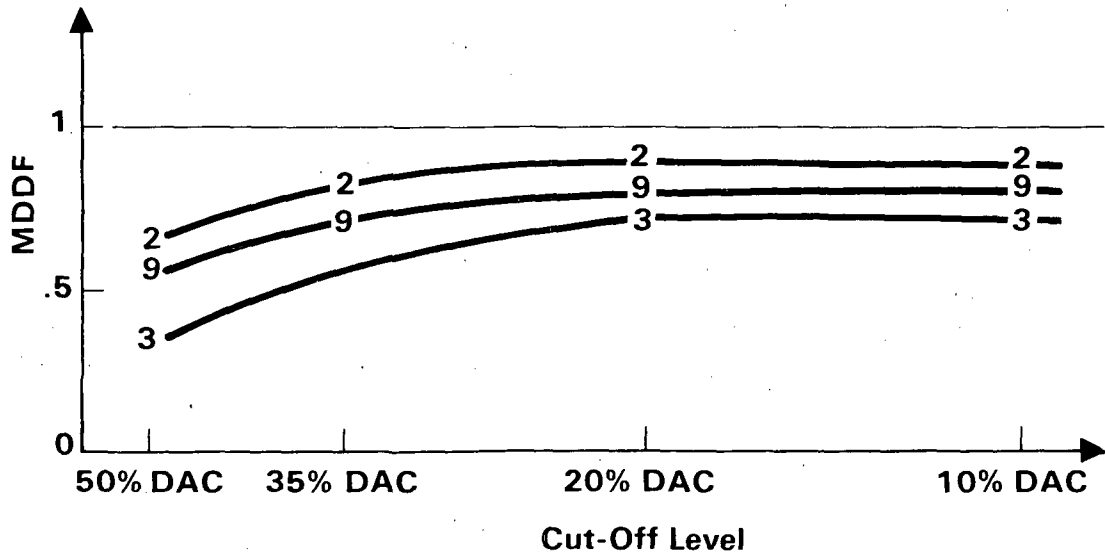
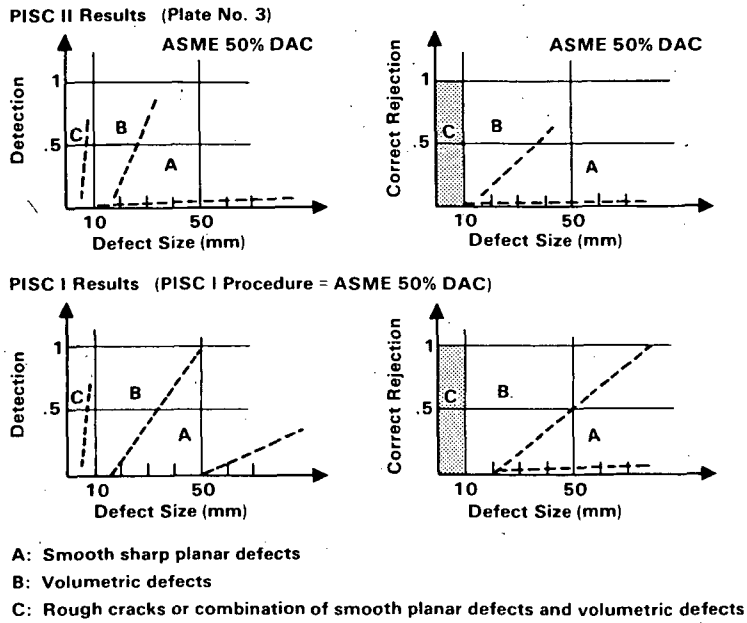
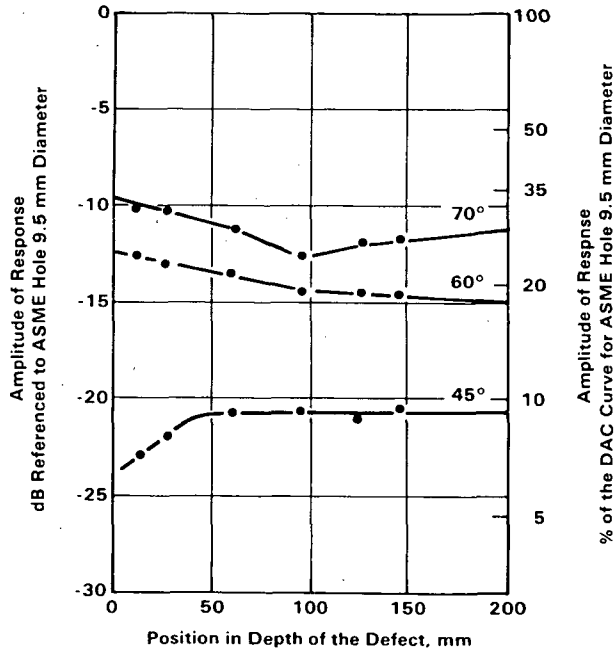


FIGURE 4. Mean Value of the Defect Detection Frequency for ASME Procedures for All the Defects in Each Specified Plate



**FIGURE 5.** Plot of Results from PISC I and PISC II for ASME 50% DAC Procedures of Defect Detection Probability Versus Defect Size when Classifying the Defects into Three Categories



**FIGURE 6.** Amplitude Response (DAC Level) from the Lower Tip of Smooth, Planar Defect that is used for Detecting this type of Defect showing that for the 45° Inspections, 5% DAC must be Employed

through-wall height. The response is plotted as a function of the defect location from very near the surface to 200-mm deep. These data show that if a 45° probe is to be used to detect this class of defect (i.e., cracks), then it will have to be performed at 5% DAC. These data clearly show the necessity for using a 60° and 70° inspection at 20% and 10% DAC, respectively.

The five U.S. teams (not all inspected each plate) which participated in the PISC-II round-robin exercise used a procedure that was developed by the PVRC and was called Procedure C. A comparison of ASME Code minimum requirements and the PVRC Procedure C is shown in Table 2. The significant difference noted is the inclusion of a near-surface technique, the increased scan sensitivity, and the lower recording level. The results for the U.S. teams are shown below in Table 3:

TABLE 2. Comparison of ASME Code Minimum Requirements Contrasted to the PVRC Procedure C that the U.S. Teams Employed in the PISC-II Program

<u>Code (Minimum)</u>	<u>Procedure C</u>
• <u>Techniques (Minimum)</u> 0°, 45°, 60°	0°, 45°, 60°, 70° RL Dual Element (Inner Near Surface)
• <u>Recording Level</u> 50% DAC	20% DAC
• <u>Scan Overlap</u> Overlap Minimum Beam Dimension, or 50%	50%, 1/4" Near Surface
• <u>Scan Sensitivity</u> 6 dB	14 dB and 12 dB (70°)

TABLE 3. Detection Performance

<u>Plate Number</u>	<u>Defect Detection Probability</u>	<u>Number of Teams</u>
#2	94-100%	5
#3	50-84%	3
#9	75-92%	3

Since the U.S. teams performed manual inspections, the results found in the PISC study may not be directly comparable to field ISI work because much of the field work is performed with mechanized scanning systems. However, the PISC-II data does show that the average inspection performance was nearly the same for both manual and mechanized inspections for the plates in this study. This was somewhat of a surprise, but probably is a result of the human being yielding high performance under the attention of an important international study. Thus, these data are useful and the U.S. teams' performances were found to be consistent with other teams using comparable procedures. The U.S. teams provided useful data in showing that reasonably effective examinations can be performed on vessels, but it also demonstrates that there will be a considerable variation in inspection results from teams using the same inspection procedure. These data indicate that considerable increase in inspection reliability could occur if the reasons for the variability in inspection performance were understood and corrective actions taken.

In the PISC-II round robin, it was found that the procedures employed had a lot to do with the performance that was achieved in the detection of defects. As an example, one team (denoted as EC) performed a number of inspections according to a variety of conditions. These results are summarized in the table below:

<u>Team</u>	<u>Procedure and Code</u>	<u>DDF</u>
EC005499	10% M,B,S,TD	1.0
EC000699	20% M,U	0.94
EC002599	20% M,C,TD	0.94
EC001699	20% M,U,S,TD	1.0
EC005399	20% M,B,S,TD	1.0
EC005099	35% M,B,S,TD	1.0
EC001199	50% M,U	0.56
EC003099	50% M,C	0.56
EC001299	50% M,U,S	0.61
EC005699	50% M,U,S,TD	0.78
EC005799	50% M,C,S,TD	0.83
EC004899	50% M,B,S,TD	0.83

The legend for this table is:

- M -- Manual examination
- B -- Examination from both sides of the plate
- 10-50% -- Percent DAC reporting level
- S -- Use of near-surface technique
- U -- Unclad-side inspection
- C -- Clad-side inspection
- TD -- Tandem technique
- DDF -- Defect Detection Frequency

These data clearly show the use of a 50% DAC level is unacceptable resulting in a defect detection frequency of 0.56. The utilization of a 20% DAC

with a tandem procedure resulted in a defect detection frequency of 0.94. These data are very useful since it was all obtained by a single team and, thus, allows one to focus on the effectiveness of various procedure parameters.

Conclusions. It is apparent from the PISC-I and PISC-II data bases that important conclusions can be drawn about defect detection performance. However, it must be remembered that the data have some qualifications that have to be recognized in order to keep the results in perspective.

1. The PISC round-robin tests were conducted in the laboratories of the teams and, thus, were conducted under optimum conditions. For this reason, these results represent an upper bound on performance.
2. The PISC round-robin tests were designed to measure procedure capability and, thus, are an upper bound of performance and should not be confused with procedure reliability.
3. Many of the inspections were conducted with teams having researchers and other highly qualified staff that do not normally conduct field ISI; thus, these results again form an upper bound for performance.
4. The condition of the cladded surfaces were to the high standards in use in Europe and are not typical of the conditions that exist in U.S. pressure vessels. Thus again, the results represent an upper bound for performance.

The significant conclusions that pertain to ISI as practiced in the U.S. are:

- Even under the most optimum conditions of the PISC exercises, the use of the 50% DAC and other minimum requirements from the 1974 Edition (including the Summer of 1975 addenda to ASME Section XI Code) clearly demonstrate that vessel examinations performed to these requirements will not be effective for detecting defects.
- The PISC-II round-robin data base indicates that significant improvement in the effectiveness of pressure vessel examinations can be achieved by working at 20% DAC and including an effective near-surface technique. Thus, pressure vessel examinations should be conducted, at a minimum, to the requirements of the 1986 ASME Code Edition (including the Winter 1987 addenda) since this code has been upgraded to contain these requirements.
- Given the caveats above, the performance of U.S. teams (using the upgraded requirements that are in the 1986 ASME Code Edition) during the PISC-II trials indicates that high levels of defect detection can be achieved. The data also shows large variability in the performance of the U.S. teams using the same procedure. If the reasons for the variability could be understood and corrective action were taken, then considerable improvement in pressure vessel inspection reliability would result.

## 6.0 PIPING TASK

### 6.1 MINI-ROUND ROBIN

A complete description and analysis of this study can be found in NUREG/CR-4908. The Mini-Round Robin (MRR) was conducted to provide an engineering data base for UT/ISI that would help:

- quantify the effect of training and performance demonstration testing that resulted from IEB 83-02,
- quantify the differences in capability between detecting long (greater than 3-in.) cracks versus short (less than 2-in.) cracks, and
- quantify the capability of UT/ISI technicians to determine length and depth of intergranular stress corrosion cracks (IGSCC).

Data from the depth sizing portion of the MRR was analyzed using both absolute and relative statistics. An overview of this analysis is presented below.

This section examines flaw sizing capability using absolute measurements. Table 4 presents a summary of the MRR sizing data expressed in absolute units.

TABLE 4. Summary of Absolute Sizing Performance

Destructive Depth, in.	UT Crack Depth Estimate (inches)							
	Team 1	Team 2	Team 3	Team 4	Team 5	Team 6	Team 7	Team 8
0.000	0.550	0.165	0.220	0.234	0.516	0.072	0.131	0.062
0.000	0.103	0.124	0.330	0.117	0.172	0.048	0.344	0.200
0.000	0.103	0.124	0.323	0.144	0.344	0.227	0.399	0.310
0.033	0.352	0.171	0.110	0.160	0.413	0.099	0.132	0.198
0.077	0.088	0.248	0.028	0.061	0.028	0.061	0.209	0.171
0.127	0.132	0.099	0.028	0.000	0.055	0.165	0.330	0.193
0.143	0.253	0.138	0.127	0.055	0.413	0.074	0.209	0.110
0.172	0.275	0.158	0.220	0.069	0.344	0.034	0.261	0.179
0.209	0.039	0.160	0.149	0.127	0.440	0.088	0.209	0.116
0.227	0.578	0.124	0.248	0.151	0.516	0.034	0.172	0.158
0.242	0.649	0.346	0.381	0.069	0.649	0.606	0.502	0.199
0.255	0.103	0.055	0.385	0.076	0.344	0.048	0.117	0.110
0.450	0.675	0.476	0.485	0.113	0.649	0.433	0.589	0.598

If all inspections were performed on material of the same thickness, both relative and absolute sizing measurements would give the same results. However, in the MRR specimens, two are constructed of thicker material (0.9 in. versus 0.6 in.); and furthermore, one of these thicker specimens also contains the largest crack in the data set, a circumstance that could cause

differences. It is also important to note that the regressions performed with the two types of measurements rest on different assumptions about measurement error variability. The absolute model assumes that variability remains the same as thickness changes; the relative model assumes that variability increases as wall thickness increases.

Consequently, the absolute model "weights" observations from the thick sections more heavily than the relative. In the current data set, absolute regression will weight the 0.45-in. and 0.242-in. cracks more heavily than the relative.

Another important difference between the two models occurs when results of a regression fit are used to predict sizing performance in other thicknesses of material, particularly thicker material. The absolute sizing model, when extrapolated to thicker material, produces a smaller variance for the measurements than the relative. Thus, extrapolations using the absolute model are less conservative than the relative.

In Table 5 regression parameters obtained from the absolute measurements are presented. These regressions utilized inspections on cracks larger than 0.04 in. From these results, we see that the slope, and more importantly, the  $R^2$  statistic is consistently larger for the absolute regressions, indicating a better fit to the data.

TABLE 5. Summary of Team Regression Fits for Absolute Sizing Data with Small Cracks (< 0.040-in.) Removed

	Absolute Results				Relative Results	
	Intercept, in.	Slope	Standard Deviation, in.	$R^2$	Slope	$R^{2*}$
Team 1	-0.02	1.57	0.21	0.43	0.96	0.12
Team 2	0.04	0.78	0.11	0.38	0.25	0.03
Team 3	-0.06	1.36	0.08	0.80	1.37	0.62
Team 4	0.03	0.22	0.04	0.27	0.27	0.18
Team 5	0.04	1.61	0.15	0.59	1.77	0.44
Team 6	-0.05	1.05	0.18	0.30	0.58	0.08
Team 7	0.10	0.91	0.13	0.38	0.27	0.03
Team 8	-0.03	1.12	0.10	0.62	0.73	0.25

\* $R^2$  = square of multiple correlation coefficient

The residuals of both sets of regressions were examined in an attempt to determine exactly why the absolute model fit the data better than the relative

model. We found the difference to be entirely attributable to a single crack (the crack with depth 0.45 in. in Table 5). When this crack was deleted from the regressions, both models fit equally well. As explained before, this crack is weighted more heavily in the absolute regression because it is in a thicker section. The absolute model does better because the teams can size this one crack better than the rest.

Selection of the superior model depends entirely on whether or not this particular crack is "anomalous." It so happens that the two cracks in the thick sections were manufactured with a different process than the others and were consequently much stronger reflectors. Because of this and the conservative nature of the relative model, we favor it in spite of the better fit shown by the absolute model.

## 6.2 INSPECTION OF CAST STAINLESS STEEL

The objective of this task is to evaluate the effectiveness and reliability of ultrasonic inspection of cast materials used within the primary pressure boundary of LWRs. Due to the coarse microstructure of this material, many inspection problems exist and are common to structures such as clad pipe, inner-surface cladding of pressure vessels, statically cast elbows, statically cast pump bowls, centrifugally cast stainless steel (CCSS) piping, dissimilar metal welds, and weld-overlay-repaired pipe joints. Far-side weld inspection is an inspection technique included in the work scope since the ultrasonic field passes through weld material. Activities included weld-overlay-repaired pipe joints and CCSS.

Weld-overlay repair is being used as a temporary repair mechanism for BWR piping weakened by IGSCC and is being sought as a longer-term repair mechanism. NUREG/CR-4484, Status of Activities for Inspecting Weld Overlaid Pipe Joints, was published in 1986. Activities thereafter were monitored and a status update provided in the form of a Research Information Letter (RIL).

The primary conclusion of the redrafted RIL (April 27, 1988) was that much work has been performed to demonstrate the effective ultrasonic inspection of weld-overlay-repaired pipe joints; however, insufficient data exists to classify this inspection as effective and reliable. The RIL also described an evaluation test that was recommended for providing sufficient data for determining if the technique is effective and reliable.

CCSS piping is used in the primary reactor coolant loop piping of 27 pressurized water reactors (PWRs) manufactured by the Westinghouse Electric Corporation. However, CCSS inspection procedures continue to perform unsatisfactorily due to the coarse microstructure that characterizes this material.

Past work began with an evaluation of distortion incurred by an ultrasonic field after it had propagated through the pipe wall thickness. A matrix of different wave modes (both longitudinal and vertically polarized shear waves) at different resolution settings (6, 3, and 1.5 mm) were passed through either a pure equiaxed or a pure columnar CCSS microstructure and the resulting ultra-

sonic field maps were collected [4,5]. To expand this work to the more complex microstructures that exist in CCSS, an upgrade to the data acquisition and analysis system was made. This was needed since the signal patterns of the complex material forms have numerous spurious signals that interfere with the data acquisition process of the previous system. Another factor was that the majority of field material was thought to be of a mixed microstructure.

Activities for the past work period included acquiring three additional CCSS pipe sections, acquiring a second scan matrix of ultrasonic field maps with the upgraded system, and submission of an article to the annual Review of Progress in Quantitative Nondestructive Evaluation [7].

Three CCSS pipe sections were on loan to PNL from Southwest Research Institute (SwRI) and reported at the last LWR meeting. The ultrasonic field map system upgrade was implemented by digitizing the RF signals and implementing a post-gating process. The data acquisition technique was also changed so that the field map of a 45° longitudinal-wave field was essentially not degraded by receiver directivity. This was accomplished by applying the microprobe to a 45° facet which increased reception uniformity about a broad angular zone centered about 45°. The previous technique (applying the microprobe normal to the sample) biased sensitivity toward 0°. Four maps were taken from material of each microstructural classification, each in unique material volumes (Figure 7); however, only one field map for each microstructural classification was displayed.

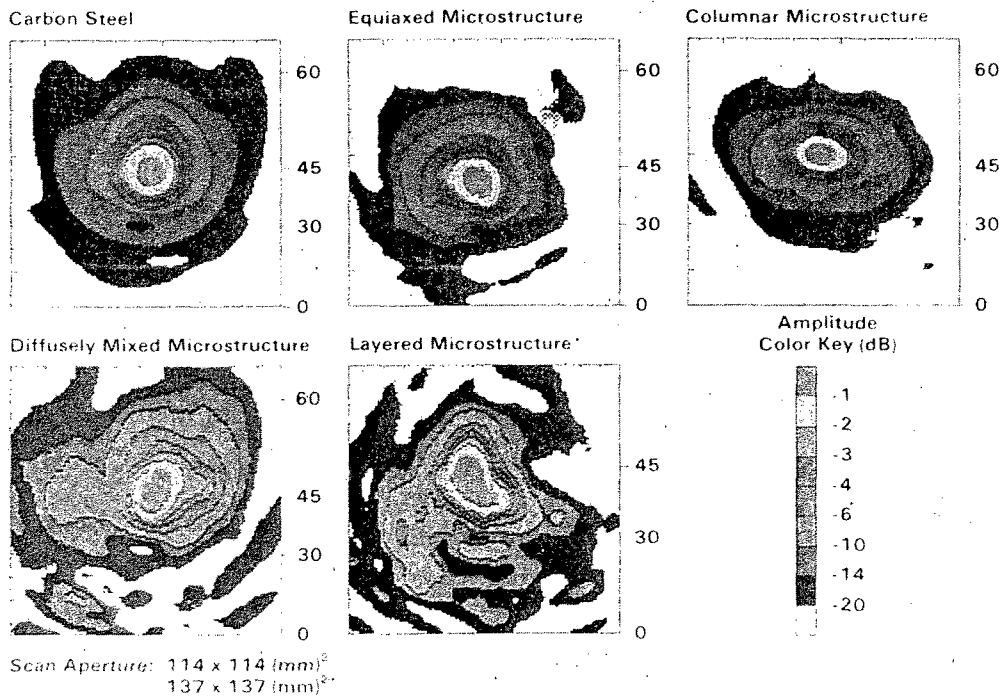


**FIGURE 7.** Ultrasonic Field Maps of 1-MHz, 45°, Longitudinal-Wave Fields

The objectives of this work were to determine if a 1-MHz, 45°, longitudinal field maintained spatial coherence in all the microstructural forms of CCSS, to quantify the degree of distortion incurred by the ultrasonic field, and to evaluate if an effective ultrasonic inspection could be performed in all the CCSS microstructures. Spatial coherency was evaluated by examining all 20 field maps. Each field map except one (from the diffusely mixed microstructural sample) displayed an ultrasonic field in which the 0 to -3 dB region was contiguous. Thus, the spatial coherency of the transmitted field was rated as high for the pure microstructural forms and as moderate for the mixed microstructural forms.

Field distortion was evaluated by measuring the refracted angle and the positional variation of the field (Figures 8 and 9). Significance of the refracted-angle results was the increased standard deviation of the equiaxed sample and the extremely large standard deviations of both materials having a mixed microstructure.

Another parameter selected to quantify field distortion was the field-position variation normalized to field width. When inspecting a selected material volume, sufficient field overlap is designed into the scan procedure to ensure detection sensitivity remains high for a defect anywhere within the material volume of interest. Obviously, if a small field width exists, then the allowable field displacement error must be small. Likewise, if a large field width exists, then the field-displacement error may be larger. Therefore,

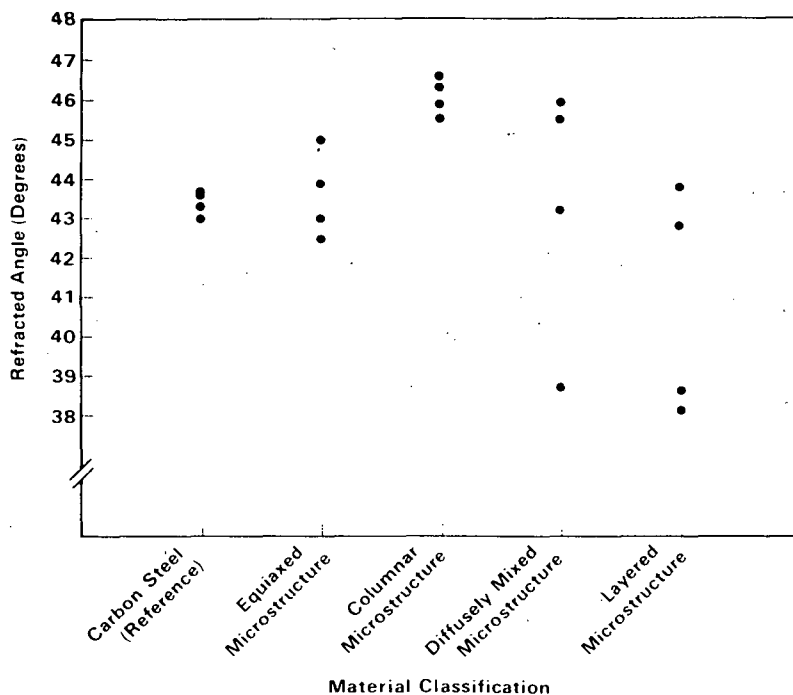
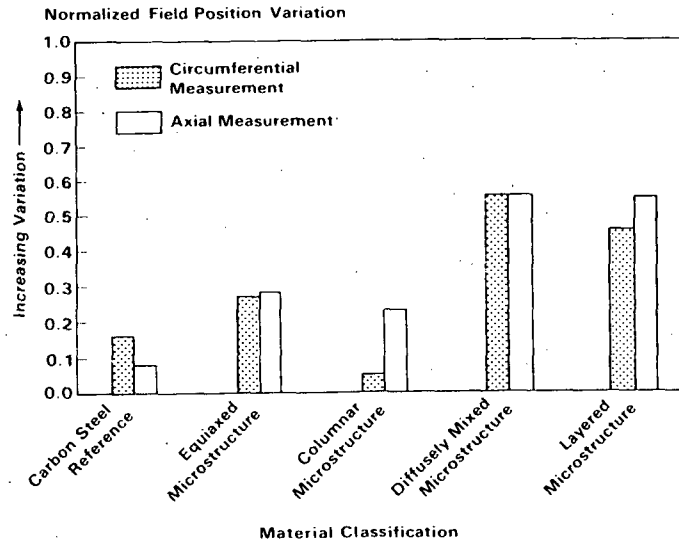


FIGURE 8. Effective Refracted Angles of 1-MHz, 45°, Longitudinal Wave

$$NFPV = \frac{RVFP}{MFW}, \text{ where}$$

MFW is the Minimum of Measured 3 dB Field Widths and

RVFP is the Range of Variation in Field Position



**FIGURE 9.** Positional Variation of Longitudinal-Wave Fields

the field-position variation was normalized to field width and are plotted in Figure 9. The variations associated with the reference samples are assumed to be indicative of set-up variation.

For CCSS material, increased variation was expected for the equiaxed material and ranged between 27% and 28% for values pertaining to measurement along both pipe axes. A low circumferential value of 5% was obtained for the columnar samples; however, the axial value was 23%. This latter value might initially seem high since the standard deviation of the refracted angle was small; however, the axial, -3 dB, field width of the columnar scans also is reduced and produces a higher normalized value. The two mixed microstructural forms had values ranging between 45% and 55%. This is alarming since scan patterns on a pipe may use circumferential increments as high as 50%. If two successive measurements are made and the field misdirection is outward from the two positions, then a material volume thought to be inspected by past procedures might be skipped.

Due to the difference in field distortion, the worst-case material classification (mixed equiaxed-columnar microstructure) should be assumed for an inspection. An alternative is to continuously determine the microstructure as a scan is performed and to interrupt the data acquisition process and implement an appropriate technique customized to the detected microstructure when the probe passes to a different microstructure. This latter choice assumes an effective microstructural classifier and that an effective inspection technique exists for each of the possible microstructures.

### 6.3 SURFACE ROUGHNESS CONDITIONS

The objective determined for this work was to establish specifications such that an effective and reliable ultrasonic inspection is not prevented by the condition of the exposed surface. Past efforts included an attempt to quantify the effect produced by an outer surface irregularity. This approach was then modified through coordination of the NRC with EPRI in establishing a mathematical model to be used as an engineering tool to derive guidelines for surface specifications. Activities for the past work period included the formulation of a coordination plan between EPRI, NRC, the Center for NDE (CNDE) at Ames Laboratory, and PNL; a visit by CNDE personnel at PNL; an exchange of data between CNDE and PNL; and development of better experimental procedures for obtaining quantitative data for comparing to the model predictions.

Both EPRI through the CNDE at Ames Laboratory and the Research Branch of the NRC through PNL have developed capabilities that are uniquely suited for establishing a validated model. First, CNDE has extensive experience in the computational modeling of ultrasonic wave propagation fields in solid materials. For this reason, EPRI and the NRC have established a three-year time frame in which the two organizations, through the referenced institutes, will cooperate in attempting to determine and validate an ultrasonic computer model. To facilitate the cooperation between CNDE and PNL, a coordination plan was formulated. This plan assigned individual and joint responsibilities to both CNDE and PNL.

The first exchange of data was completed in February, which involved an immersion scan with isotropic materials. The bottom line of this work was that the model and experimental results were in good agreement for the longitudinal mode except for low amplitudes (i.e.,  $\leq -14$  dB). There are still some discrepancies with the shear-wave data that are being studied further.

PNL began an effort of refining ultrasonic microprobes and data acquisition techniques so that the collected experimental data would accurately measure the parameters predicted by the model. This effort resulted in longitudinal-wave microprobe refinements, a presentation concerning the development of a shear-wave microprobe at the "Review of Progress in Quantitative Nondestructive Evaluation," and submittal of a manuscript for publication in the conference proceedings [8].

### 6.4 CHARACTERIZATION OF FIELD PIPE

The objective of this task is to provide pipe weld specimens that can be used to help determine the effectiveness and reliability of ultrasonic ISI that is being performed on BWR piping. This goal will be accomplished by obtaining BWR recirculating piping from a variety of power plants. These weld specimens will also serve to support PNL laboratory studies and such programs as PISC III.

Weld specimens were acquired from Monticello and Vermont Yankee BWR nuclear power plants. The welds were sectioned from the pipe remnants in FY 1986.

Due to high amounts of alpha contaminations on the Monticello specimens, it was decided to decontaminate only the 11 Vermont Yankee specimens and wait until FY 87 to have the 28 Monticello weld specimens decontaminated. A complete characterization of the 11 Vermont Yankee weld specimens was performed by PNL personnel; this included ultrasonic and penetrant examinations.

After the decontamination of the 28 Monticello weld specimens (14-12", 2-22", 12-28") PNL representatives performed a complete characterization on each individual weld specimen. This included penetrant testing on the ID of the weld region, ID and OD weld profiles, counterbore and penetrant pictures. In some cases, ultrasonic verification was performed on some of the specimens. After the evaluation was finished, the weld specimens were packaged and returned to PNL.

During FY88, a complete UT evaluation was performed on a selected number of weld specimens (20 welds) using manual ultrasonics and the PNL SAFT-UT field system. When the UT evaluation was completed, a thorough analysis was performed on the data that was gathered. A weld specimen summary report (which included PT and UT information, and specimen characteristics) was put together on 42 weld specimens. A selected number of these specimens will be sent to Europe to be used in the PISC III international round robin on austenitic steel. The remaining weld specimens will remain at PNL to be used to support other future NRC-related programs.

In FY88, five of the Monticello safe-end weld specimens were packaged in an overseas shipping container and are pending shipment to Europe. These will also be used in the PISC III exercises. The remaining five safe-ends were packaged and sent to a DOE burial site in Richland, Washington.

## 6.5 PISC III

Work continued in support of the Programme for the Inspection of Steel Components to ensure that the results will be useful and reflect the practice, conditions, and defects of interest to the U.S. light-water reactors. Specific thrusts were in the area of the round robin studies on austenitic stainless steels.

### REFERENCES

1. Plate Inspection Steering Committee (PISC). Full Reports, Euratom Report, EUR-6371-EN (Vol. I/VI, 1979).
2. Plate Inspection Steering Committee, "Analysis of the PISC Trials Results for Alternative Procedures," Euratom Report No. 6, EUR-6371-EN (1980).
3. Program for the Inspection of Steel Components (PISC II), Organization for Economic Cooperative and Development, Nuclear Energy Agency, Committee on the Safety of Nuclear Installations, CSNE No. 117-121, September 1986.

4. Crutzen, S., et. al, "The Major Results of the PISC II RRT," Preprint to be published in Nuclear Engineering and Design in 1988.
5. Good, M. S. and L. G. Van Fleet, "Ultrasonic Beam Profiles in Coarse Grained Materials," in 8th International Conference on NDE in the Nuclear Industry, edited by D. Stahl (American Society for Metals International, Metals Park, Ohio, 1987) pp. 657-666.
6. Good, M. S. and L. G. Van Fleet, "Mapping of Ultrasonic Fields in Solids," in Review of Progress in Quantitative Nondestructive Evaluation, edited by D. O. Thompson and D. E. Chimenti (Plenum Press, New York, 1988), Vol. 7A, pp. 637-646.
7. Good, M. S. and E. R. Green, "Mapping of 1-MHz, 45° Longitudinal Fields in Centrifugally Cast Stainless Steels," submitted for inclusion in Review of Progress in Quantitative Nondestructive Evaluation, edited by D. O. Thompson and D. E. Chimenti (Plenum Press, New York, 1989), Vol. 8.
8. Good, M. S. and E. R. Green, "A Shear-Wave Microprobe Utilizing Surface-Wave Mode Conversion," submitted for inclusion in Review of Progress in Quantitative Nondestructive Evaluation, edited by D. O. Thompson and D. E. Chimenti (Plenum Press, New York, 1989), Vol. 8.



FINAL DEVELOPMENTS, VALIDATION AND TECHNOLOGY TRANSFER  
FOR AE AND SAFT-UT

S. R. Doctor, P. H. Hutton, J. C. Spanner, L. D. Reid  
Pacific Northwest Laboratory  
Operated by Battelle Memorial Institute  
Richland, Washington 99352

ABSTRACT

The program for Validation and Technology Transfer for AE and SAFT-UT is designed to accomplish the final step of moving research results into beneficial application. Accomplishments for FY88 in the areas of Acoustic Emission (AE) and Synthetic Aperture Focusing of Ultrasonic Test data (SAFT-UT) under this program are discussed in this paper. The information is treated under the topics of Code Activities, Field Validation, and Seminars. Projected FY89 activities will continue to focus on these three areas.

INTRODUCTION

The program concerning Validation and Technology Transfer for AE and SAFT-UT has the objective of developing field procedures, performing field validation testing, and providing training for NRC headquarters and regional staff for the use of advanced NDE technology. The objective also includes ASME Section XI Code acceptance of the AE and SAFT-UT technologies to facilitate implementation of the methods by Regulatory staff and the utilities.

This program will benefit nuclear regulation in the following areas:

- Provides a mechanism for technology flow from PNL to the NRC staff.
- Supports the process of moving advanced technology into the ASME Code.
- Provides technology that can solve ISI problems and, thus, can aid the NRC staff in assuring the structural integrity of components.

The program for each of the technologies is structured under three general headings:

1. Code Activities. Establish the technologies as a recognized and approved part of the ASME Code through the appropriate instrument (Code Case, Code Appendix, Code modification, etc.).
2. Field Validation. Apply the technologies to problems on operating reactors to demonstrate validity for the intended applications of the technology.

3. Seminars. Present technical information and demonstrations to NRC Regulatory staff to acquaint them with the technologies and the application methodology.

FY88 results will be presented under the three headings described above.

## DISCUSSION

### ACOUSTIC EMISSION

#### Code Activities

A Nonmandatory Appendix to the ASME Section XI Code titled "Acoustic Emission Monitoring of Nuclear Reactor Pressure Boundaries During Operation" was approved by the Working Group on Volumetric Inspection and the Subgroup on Nondestructive Examination in the November 1987-January 1988 time frame. It was subsequently tabled by the Subcommittee on Nuclear Inservice Inspection with the recommendation that it should be resubmitted as a Code Case. A Code Case version of the material was approved by the Subcommittee in April 1988 and is on the Main Committee agenda for December 1988.

#### Field Validation

Most of the on-reactor demonstration of technology developed under the NRC AE program has taken place at the TVA Watts Bar Unit 1 Nuclear Power Plant. Selected areas of the reactor pressure boundary have been AE monitored during cold hydrostatic [1] and hot functional [2] testing of the reactor system with significant benefit to the AE technology. A third set of tests has been performed to evaluate the signal source location capability of the installed AE system.

It is important to evaluate the signal source location capability of the AE system on a reactor because of the large wall thickness used in pressure boundary components. AE signal source location algorithms available today for practical application locate in two dimensions. Many reactor pressure vessels have a wall thickness of 8 to 12 inches or more. This is particularly true of the vessel nozzle region. With a third dimension of this magnitude, there is a need to evaluate the accuracy of the two-dimensional source location. The Watts Bar Unit 1 vessel, being completely empty, offered an opportunity to evaluate the source location function using simulated AE signals injected on the inside of the vessel and nozzles.

Signal attenuation by the vessel cladding and the clad-to-base metal interface in the 400 to 500 kHz frequency range being used to monitor for AE precluded use of the normal pencil leak break signal source to inject signals at the inside of the vessel and nozzles. In real application of AE monitoring, this problem would not be present because one would be seeking to detect signals originating in the ferritic vessel wall. An electronic pulser with a transducer was used to inject acoustic signals at known points around the inside of the #2 inlet nozzle and on the inside surface of the vessel.

Figure 1 shows the location of the AE sensors on the #2 inlet nozzle and the location of the signal inputs on the inside surface of the nozzle. Source location for signals injected on the nozzle ID was accurate to the projected signal input location within about 3 to 5 inches in the circumferential direction in all cases. In the front-to-rear direction, the location was accurate to within about 5 to 7 inches for signals originating within the region under the AE sensor array. Figures 2 and 3 illustrate representative results obtained from input signals within the AE sensor array. The front-to-rear accuracy deteriorated progressively as the source point moved farther outside of the AE sensor array. There are methods of improving the front-to-rear location accuracy for signals outside of the sensor array by using additional sensors; however, since the signals are being detected and the radial location is reasonably accurate, it may be difficult to justify the additional hardware for the increase in source localization accuracy.

No usable data was obtained on the vessel wall. In its present operating mode, the AE monitor instrument requires that all four sensors in an array receive a signal before it will be processed for source location. Signal attenuation in the cladding and at the clad-to-vessel interface was large enough to prevent detection of the injected signals at all four AE sensors mounted on the vessel wall. Many of the signals were detected by two or three of the sensors which would be sufficient to perform a less-than-optimum source location. This suggests that the operating mode of the AE instrument needs to be changed to accept data from less than four sensors to give minimum source location information in such cases.

The fact that these test signals were not detected by all four sensors does not imply inability to detect AE signals originating from crack growth in the vessel wall belt-line region. That capability has been demonstrated separately in two previous tests [3,4].

In summary, the test results demonstrated that acceptable two-dimensional location of acoustic signal sources can be achieved on a reactor structure even in the relatively complex geometry of the nozzle-to-vessel joint.

### Seminars

Material describing the status of AE technology development and potential applications beneficial to regulatory needs was presented to NRC Region III in a technical workshop held in February 1988. A similar presentation will be made at NRC Region I, King of Prussia during a technical workshop scheduled for October 10-14, 1988. The workshop is being organized by Region I with attendance and participation by Regions II and IV plus NRR and RES staff members. These workshops provide an opportunity to discuss current regulatory needs vs. NDE technology capabilities.

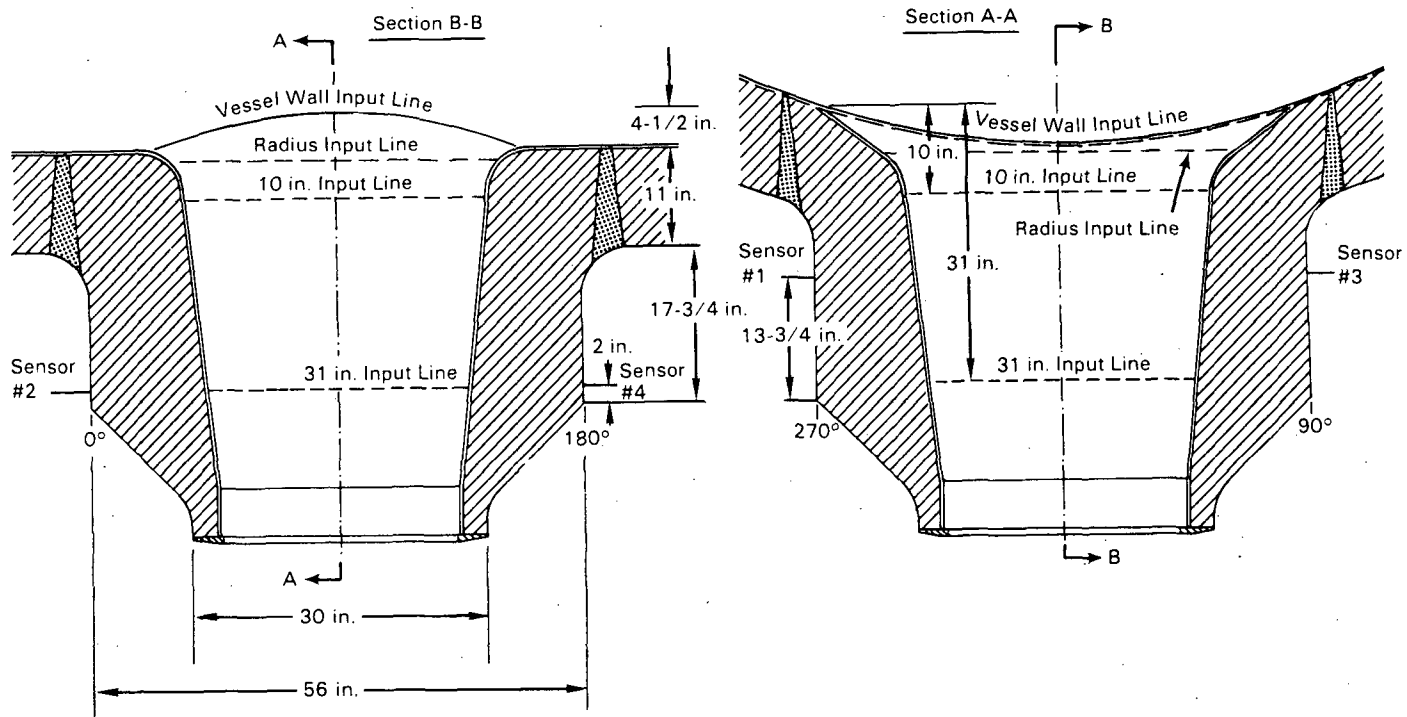


FIGURE 1. Signal Input Locations on #2 Inlet Nozzle, Watts Bar 1, for AE Source Location Calibration

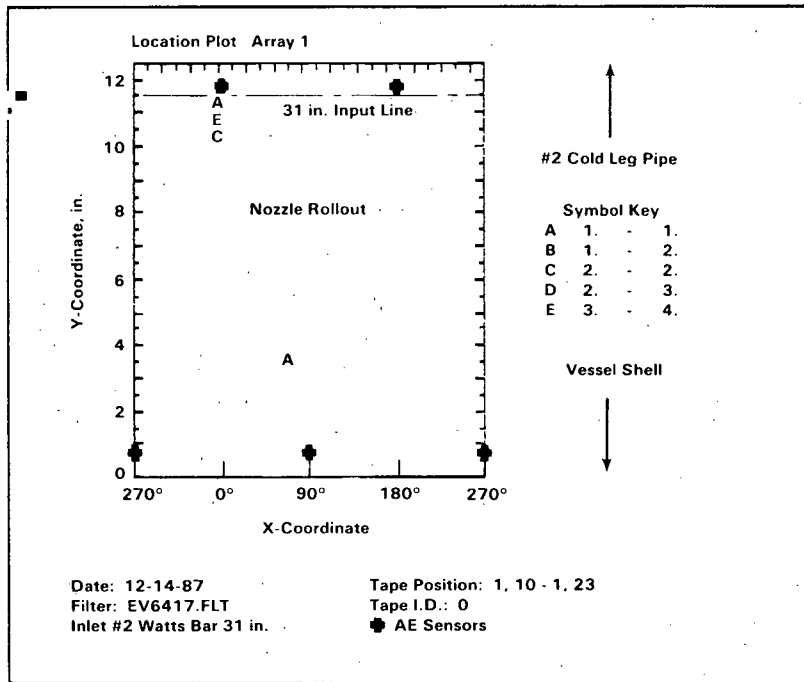


FIGURE 2. AE Source Location Indications - Input at 0° on 31" Input Line.

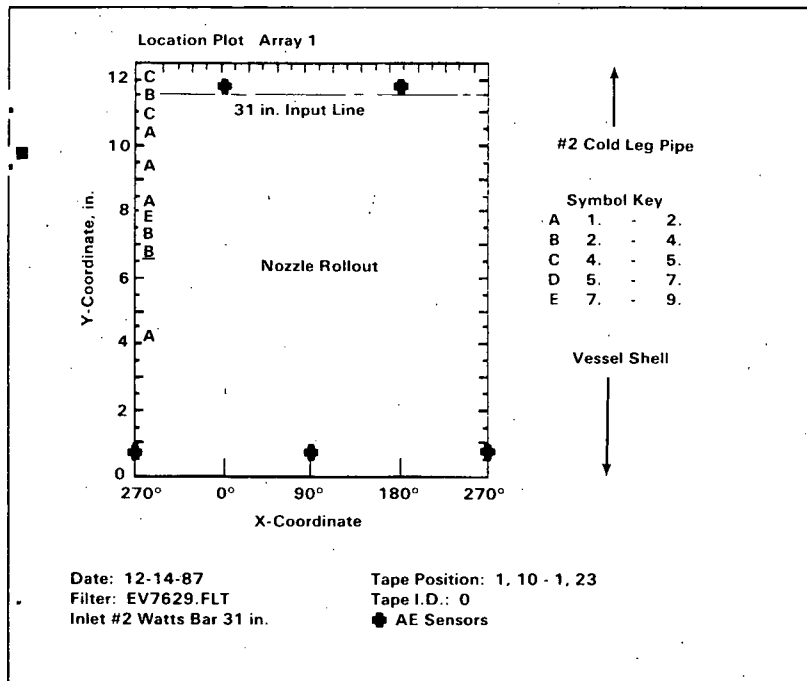


FIGURE 3. AE Source Location Indications - Input at 270° on 31" Input Line

## SAFT-UT

### Code Activities

The emphasis of this activity was to get the SAFT technology into ASME Section XI Code. The position of Section XI has been not to include prescriptive procedures in the Code because this has been found not to work. Section XI has taken the position that performance demonstrations will be used, and any system passing the demonstration requirements can be used for ISI. Hence, we have discussed where else would it be appropriate for the technology to be included in the Code. Section V was then approached and was receptive to including SAFT in a new appendix to Article 4 called "Computer Processed Imaging." This happened at the end of the fiscal year and no other progress can be reported.

### Field Validation

Two activities occurred this year that stand out with regard to field validation. The first was participating in the inspection of an O.D. indication in the belt line region of the reactor pressure vessel at Indian Point Unit No. 2. The second was the inspection of several defects in a cast elbow on the hot leg of the Trojan Nuclear Power Plant. In addition, a report was published detailing the operational principles and implementation of the SAFT-UT real-time inspection system (NUREG/CR-5075). This report provides a full description of the hardware and software used in the real-time SAFT-UT system, how it operates, how to use it, and where to go to find more information. A final report was drafted for the SAFT-UT program and was approved by the NRC program manager for publication once a new section is added based on the work to be performed on thick sections early next fiscal year. This final report pulls together all the relevant information on studies and documentation that completes the work performed at PNL to develop and engineer a fieldable SAFT-UT real-time system. This final report also contains the procedure that has been developed to conduct inspections for defect detection, characterization and sizing.

The inspection that was performed at Indian Point Unit No. 2 was conducted through the use and cooperation of Westinghouse and their vessel scanner and Dynacon and their data acquisition system. PNL provided the transducer to be used in conducting the examination, and the other companies conducted the examination and provided PNL with the digitized data for subsequent processing at PNL. Some problems were encountered with the equipment during the data acquisition and the number of scans was reduced to 2 and 1/2. The 1/2 was a scan with only 1/2 the aperture in the increment direction. The data turned out to be quite useful and provided some very good images. There were several limitations of the equipment that prevented us from doing all of the work that we wanted; for example, the scanner could not increment reliably in one wavelength intervals; and thus, we were limited to only doing 2-D or line-SAFT processing.

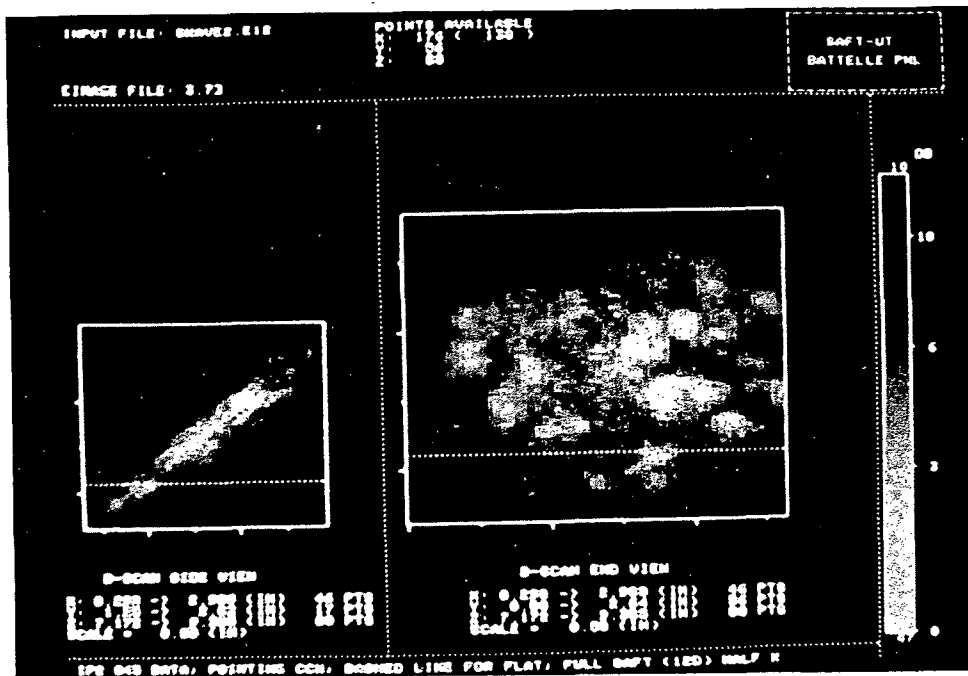


**FIGURE 4.** SAFT Processed Image of the Indication Located in the Belt Line Region Near the Outside of the Indian Point Unit 2 Nuclear Power Plant

The results obtained by SAFT processing are shown in Figure 4. If the indication was surface connected then the image in Figure 5 would be expected; and hence, it is concluded that the indication was not surface connected. This is extremely important and needed to be determined to aid in assessing the significance of the defect. The data supports the position that the indication was not parallel to the O.D. surface but was at a taper.

The inspection at Trojan was similar in that the data acquisition was handled by Amdata using their I-98 system. PNL provided a probe for the data acquisition, and the data was subsequently processed and analyzed at PNL. The results were rather dramatic and provided some very good images of the indications. The SAFT images had about a 10 dB increase in the signal-to-noise ratio versus the images collected and displayed with the conventional inspection using the I-98. This was a statically cast component, and it had a relatively fine grain structure that made it easy to image and to obtain good signal-to-noise ratios. The data was collected with a 500-kHz shear-wave probe at a 45° inspection angle.

The images of the defect areas shown in Figure 6 produced some very good results that made it possible to cluster the indications. The indications were disbursed; and through analysis, it was pretty apparent that there were a number of indications and we chose to combine them in a logical manner.

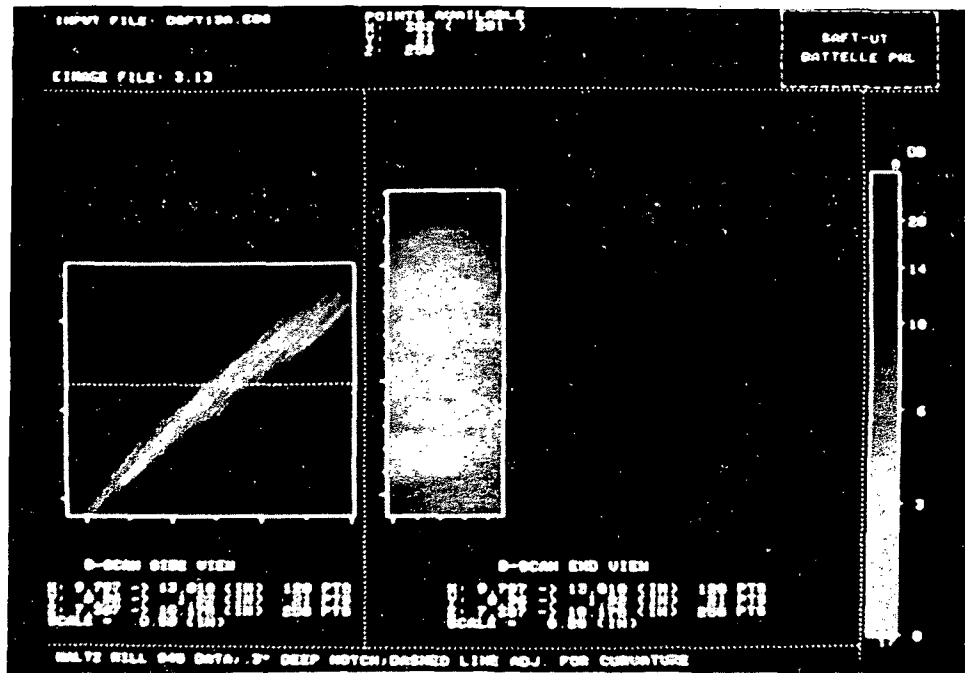


FIGURE 5. SAFT Image of a Surface-Connected Notch that is 0.3 Inches Deep that was Located in a Calibration Block and Used to Assess the Capability of the Westinghouse Scanner and the Dynacon Data Acquisition System with the PNL SAFT Technology

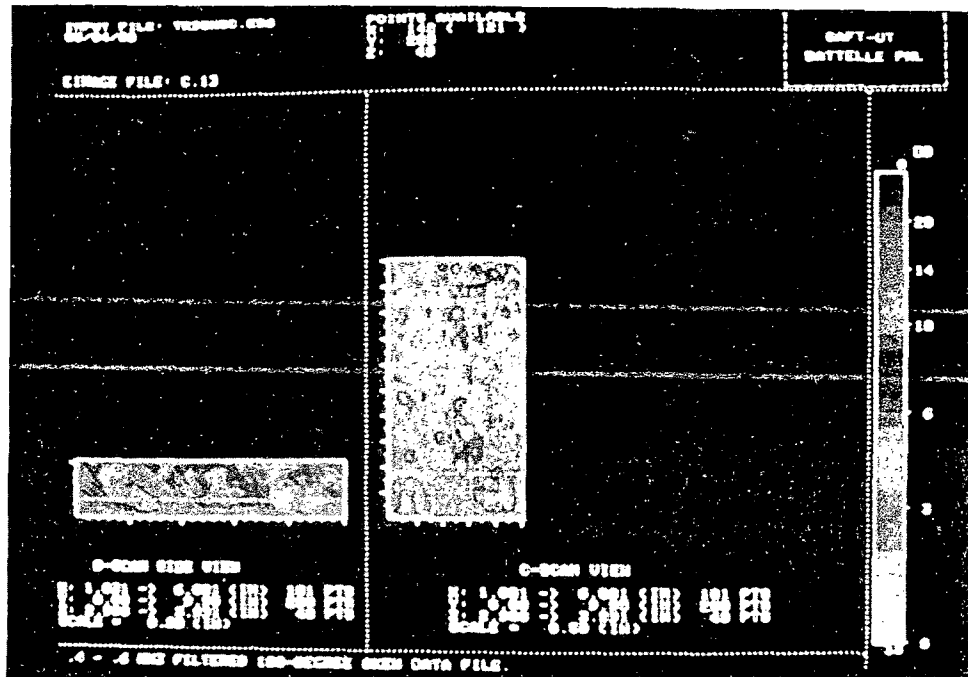


FIGURE 6. SAFT Image of One Zone Scanned on the Cast Elbow at the Trojan Nuclear Power Station showing the Clustering of the Indications and the High Signal-to-Noise Ratio

These two field trials illustrate that other commercial equipment can be used to collect SAFT-type data and can give very good results that help to resolve inspection problems. The results were very good, but there has not been any destructive correlation to ascertain the bottom-line effectiveness of the SAFT performance. These tests were very encouraging in the sense that the SAFT technology is compatible with many pieces of commercial equipment.

### Seminars

The participation in seminars includes all the activities already highlighted in the AE section and includes the SAFT field system demonstration at the October 1988 seminar. In addition, Region I personnel had some hands-on experience during June 1988 while they were at PNL to gain training on IGSCC in some field samples at PNL.

### SUMMARY

Significant progress has been made in obtaining ASME approval of a Code Case for inservice AE monitoring to be incorporated into the Section XI Code. Calibration of source location capability of the AE monitor system installed at Watts Bar Unit 1 reactor showed that good two-dimensional location of an acoustic signal source can be accomplished even on the complex nozzle-to-vessel geometry. Progress has been made in transferring AE technology to NRC Regional and NRR staff.

Substantial progress has been made in finalizing the SAFT field system documentation, initial field trials with other commercial UT equipment with extremely good resulting images, and finding a receptive audience for acceptance of the SAFT technology within the ASME Code.

### FY89 PLANS

Program plans for FY89 include:

- Complete ASME approval of AE Code Case.
- Follow up on expression of interest from Taiwan Power Company and Toledo-Edison Company in AE monitoring reactor components.
- Participate in technical workshop scheduled to be held at NRC Region I.
- Develop input for Appendix to ASME Section V Code to the SAFT technology.
- Participate in field trial of SAFT technology evaluation on thick-section steel at the EPRI NDE Center.
- Work to develop a means whereby the SAFT technology can be used in the PISC III program on the Full Scale Vessel.
- Publish the final report.

## PUBLICATIONS

Hutton, P. H., M. A. Friesel, J. F. Dawson, and J. C. Harris. 1988. Acoustic Emission System Calibration at Watts Bar Unit 1 Nuclear Reactor. NUREG/CR-5144. Pacific Northwest Laboratory, Richland, Washington.

Doctor, S. R., T. E. Hall, L. D. Reid, and G. A. Mart. 1988. "Synthetic Aperture Focusing Technique for Real-Time and Tandem Operation for Thick Section Steels," in Proceedings of 9th International Conference on NDE in the Nuclear Industry, Tokyo, Japan, April 25-28, 1988. American Society of Metals, pp. 411-416.

Hall, T. E., L. D. Reid, and S. R. Doctor. 1988. The SAFT-UT Real-Time Inspection System - Operational Principles and Implementation. NUREG/CR-5075. Pacific Northwest Laboratory, Richland, Washington.

## REFERENCES

1. Hutton, P. H. T. T. Taylor, J. F. Dawson, R. A. Pappas, and R. J. Kurtz. 1982. Acoustic Emission Monitoring of ASME Section III Hydrostatic Test, Watts Bar Unit 1 Nuclear Reactor, NUREG/CR-2880. Pacific Northwest Laboratory, Richland, Washington.
2. Hutton, P. H., J. F. Dawson, M. A. Friesel, J. C. Harris, and R. A. Pappas. 1984. Acoustic Emission Monitoring of Hot Functional Testing, Watts Bar Unit 1 Nuclear Reactor, NUREG/CR-3693. Pacific Northwest Laboratory, Richland, Washington.
3. Ibid, pp. 18-19.
4. Hutton, P. H., R. J. Kurtz, R. A. Pappas, J. F. Dawson, L. S. Dake, and J. R. Skorpik. 1985. Acoustic Emission Results Obtained from Testing the ZB-1 Intermediate Scale Pressure Vessel, NUREG/CR-3915. Pacific Northwest Laboratory, Richland, Washington.

# FINAL EVALUATION OF ADVANCED AND CURRENT LEAK DETECTION SYSTEMS\*

D. Kupperman, R. Carlson, R. Lanham, and W. Brewer  
Materials and Components Technology Division  
ARGONNE NATIONAL LABORATORY  
Argonne, Illinois 60439

## ABSTRACT

This report presents the results of a study to evaluate the adequacy of leak detection systems in light water reactors. The sources of numerous reported leaks and methods of detection have been documented. Research to advance the state of the art of acoustic leak detection is presented, and procedures for implementation are discussed.

### Current Practice

According to the Code of Federal Regulations 10CFR part 50, means must be provided for detecting and, to the extent practical, identifying the location and source of leakage. The safety significance of a leak can vary, and prompt and quantitative information is necessary to permit immediate action should a leak be detrimental to the safety of the facility. U.S. Nuclear Regulatory Commission Guide 1.45 [1] recommends the use of at least three different methods to detect leakage in reactors. Monitoring of both sump-flow and airborne-particulate radioactivity is recommended. A third method can involve either monitoring of condensate flow rate from air coolers or monitoring of airborne gaseous radioactivity. Although the current methods used for leak detection reflect the state of the art, other techniques may be developed and used. Regulatory Guide 1.45 also recommends that leak rates from identified and unidentified sources be monitored separately to an accuracy of  $3785 \text{ cm}^3/\text{min}$  (1 gal/min), and that indicators and alarms for leak detection be provided in the main control room.

Since the recommendations of Regulatory Guide 1.45 are not mandatory, the technical specifications for 74 operating plants including pressurized-water reactors (PWRs) and boiling-water reactors (BWRs) have previously been reviewed by the present author [2] to determine the types of leak detection methods employed, the range of limiting conditions for operation, and the surveillance requirements for the leak detection systems. The results are presented again here for completeness.

\*RSR FIN Budget No. A2250; RSR Contact: J. Muscara.

The submitted manuscript has been authored by a contractor of the U. S. Government under contract No. W-31-109-ENG-38. Accordingly, the U. S. Government retains a nonexclusive, royalty-free license to publish or reproduce the published form of this contribution, or allow others to do so, for U. S. Government purposes.

All plants use at least one of the two systems specified by Regulatory Guide 1.45. All but eight use sump monitoring, and all but three use particulate monitoring. Monitoring of condensate flow rate from containment air coolers and monitoring of atmospheric gaseous radioactivity are also used in many plants.

The limit on unidentified leakage ("identified" leakage is generally that collected from monitored valves) for all PWRs is  $3785 \text{ cm}^3/\text{min}$  (1 gal/min), whereas the limit for most BWRs is  $18930 \text{ cm}^3/\text{min}$  (5 gal/min). The limits on total leakage are generally  $37850 \text{ cm}^3/\text{min}$  (10 gal/min) for PWRs and  $94630 \text{ cm}^3/\text{min}$  (25 gal/min) for BWRs. (Regulatory Guide 1.45 does not specify leakage limits, but does suggest that the leakage detection system should be able to detect a  $3785\text{-cm}^3/\text{min}$  leak in 1 h.) In some cases, limits on rates of increase in leakage are also stated in the plant technical specifications. Two BWRs have a limit of  $379 \text{ cm}^3/\text{min/h}$  (0.1 gal/min/h); four have a limit of  $1893 \text{ cm}^3/\text{min/h}$  (0.5 gal/min/h).

Leakage is checked every 12 h in most PWRs, and every 4 or 24 h in most BWRs. One BWR specifies that a continuous monitor with control room alarm shall be operational. For BWRs, calibration is generally performed at 18-month intervals; functional tests are performed every month.

The estimated sensitivity of leakage monitoring systems is occasionally addressed in the technical specifications. For example, one specification indicates that air particulate monitoring can, in principle, detect a 0.013-gal/min leak in 20 min, that the sensitivity of gas radioactivity monitoring is 2-10 gal/min, and that the sensitivity of condensate flow monitoring is 0.5-10 gal/min. Continuous sump pump monitoring appears capable of detecting a 1-gal/min leak in 10-60 min.

The impact of Reactor Coolant Pressure Boundary leakage detection systems on safety was evaluated for eight reactors as part of the Integrated Plant Safety Assessment-Systematic Evaluation Program (SEP) and described in eight SEP reports (NUREG-0820 through -0827). In four of the eight reactors evaluated, a 1-gal/min leak could not be detected within 1 h; and four of the eight reactors did not have three leakage monitoring systems, contrary to the suggestions in Regulatory Guide 1.45. The fracture mechanics and leak rate calculations in the SEP reports are consistent with other studies, which indicate that (a) current leak detection systems will detect throughwall cracks 10-25 cm (4 to 10 in.) long in 12- to 28-in. piping within one day, and (b) current leakage limits will necessitate plant action after such a detection event. Since these cracks are much smaller than those required to produce failure in tough reactor piping, improved leak detection systems may offer little safety benefit for this particular class of flaws when crack growth occurs by a relatively slow mechanism. However, the SEP reports state that local leak detection systems may be necessary for some postulated leak locations where separation and/or restraint is not a practical way to mitigate the effects of a high-energy pipe break.

One other safety-related aspect of improved leak detection systems concerns radiation exposure of plant personnel. Improved systems with leak location capability could reduce the exposure of personnel inside the containment and could present an attractive alternative to augmented in-service inspection (ISI). Improved leak detection is consistent with the defense-in-depth philosophy of the Nuclear Regulatory Commission (NRC) and would lead to earlier detection of system degradation.

Unidentified leakage ultimately passes through the sump pump unless it is trapped in the system. In addition, condensate from the containment air cooling systems passes through a flowmeter and then the sump, adding to the unidentified leakage. Identified leakage, primarily that which is selectively collected from leaking valves, flows to a drain tank that is also pumped out. The total leakage is the combined unidentified and identified leakage. Estimates of leak rates are obtained from the cooling system flow meter, the level indicators, and the frequency of operation of the pumps.

There are no requirements for monitoring leakage outside the containment. These leaks are detected by a variety of methods such as temperature and pressure rises, changes in background radiation, and visual examination during routine maintenance.

Many methods can be used to detect a leak. These include radiation monitors, sump monitors, condensate flow monitors, coolant inventory, and variations in temperature, pressure, and dew point. Generally speaking, reactor operators rely on sump pump monitoring to establish the presence of leaks. Other methods appear to be less reliable or less convenient. In most reactors, the surveillance periods are too long to detect a 3785-cm<sup>3</sup>/min (1-gal/min) leak in 1 h, as is suggested by Regulatory Guide 1.45, but it appears that this sensitivity could be achieved if monitoring procedures were modified. Simply tightening the current leakage limits to improve sensitivity is not adequate, however, since this might produce an unacceptably high number of spurious shutdowns because of the inability of current leak detection systems to identify leak sources. None of the systems currently in use provides any information on leak location, and leaks must be located by visual examination after shutdown.

In order to help characterize more quantitatively the cause of leaks in reactors and to obtain information regarding the adequacy of leak detection technology, Licensee Event Report (LER) Compilations from June 1985 to March 1988 (e.g., LER Compilation for March 1986, NUREG/CR-2000, ORNL/NSIC-200) were reviewed. These compilations contain summaries of information submitted by the nuclear power plant licensees in accordance with federal regulations. Each summary includes the date of the incident; the reactor, component, and system involved; and, if a leak occurred, usually the leak rate and action taken. Of over 4000 reported events, a total of 91 were identified as relevant to the problem of detecting leaks in the primary systems of light water reactors (LWRs).

Differences between PWRs and BWRs, with regard to leak detection, have been analyzed. The primary source of leaks, accounting for 56% of reported leaks, is valves and pumps.[1] The sump monitor accounts for 46% of the detection methods reported. Events have been divided into those in PWR reactors and those in BWR reactors. PWRs account for about 71% of the reported leaks. This is slightly higher than the percentage of PWRs in the U.S (about 70%). Although pumps and valves are the main source of leaks regardless of the reactor type (58% occurs PWRs and 49% in BWRs), a greater percentage of small-line leaks occurs in BWRs than in PWRs (39% vs. 14%). With regard to detection methods, the greatest differences between reactor types are as follows: (a) The sump pump is reported as the detection method more frequently in BWRs than in PWRs (66% vs. 37%). (b) The radiation monitor is reported as the detection device (excluding false alarms) more frequently in PWRs. In fact, for the events studied, the radiation monitor never correctly detected a leak in a BWR (it did, however, initiate four BWR false alarms). Another point of interest is that inventory balance was reported as the method of detecting a leak in 16% of the PWR cases.

For both BWRs and PWRs, about one false alarm occurs for every three actual leaks. Anomalous signals from radiation monitors are the cause of these false alarms. Tables 1.1-1.3 summarize the analysis presented above.

Numerous questions arise in connection with an assessment of the adequacy of leak detection. One concern is whether the flow path for unidentified leakage to the sump pump is unimpeded. All indications are that fluid from a leak will pass directly to the sump pump if it is not absorbed by the environment or insulation. Levels in the containment are separated by gratings that permit the fluid to pass to the sump(s). Another concern is the time it takes to locate a leak. In general, leaks are located by visual examination, which is a slow process. (For this reason, an important benefit of improved leak location capability would be reduced personnel radiation exposure.) In addition, in the case of BWRs, the start of the examination can be delayed by up to six hours while the inert gas is removed from the drywell.

Table 1.1. Leak Sources for LWRs

Leak Source	PWR + BWR (% of total)	PWR (% of total)	BWR (% of total)	PWR (% of PWR)	BWR (% of BWR)
Valves	46	35	10	48	37
Pumps	10	6	3	10	12
Small Lines	20	10	10	14	39
IGSCC	3	2	2	2	6
Misc.	21	20	2	26	6
TOTAL	100	73	27	100	100

Table 1.2. Leak Detection Methods for LWRs

Detection Method	PWR + BWR (% of total)	PWR (% of total)	BWR (% of total)	PWR (% of PWR)	BWR (% of BWR)
Sump Pump	46	27	19	37	66
Radiation Monitor	19	19	0	26	0
Visual Inspection	14	7	6	11	20
Inventory Balance	12	12	0	16	0
Other	10	6	4	10	14
TOTAL	100	71	29	100	100

Table 1.3. False Alarms Obtained with Leak Detection Systems in LWRs (% of actual leaks)

PWR + BWR	PWR	BWR
31	23	8

The issue of whether a significant delay in leak detection could result from the absorption of leakage by the environment or insulation has also been addressed. A simple calculation based on the ideal gas law ( $PV = nRT$ ) has indicated that even in the worst case, i.e., with an ambient temperature of 120°F (323 K) and the cooling condenser off, a delay of only a few hours would result from the absorption of moisture by the environment. Assuming a containment volume of 500,000 ft<sup>3</sup> (14,000 m<sup>3</sup>) and a vapor pressure of 12 kPa, the maximum amount of water that can be absorbed by the air is about 300 gal. At a leak rate of 1 gal/min, saturation would be reached in about 5 h. With the condenser on, moisture from a leak would be collected at the sump in a much shorter time. The question of whether a significant amount of moisture could be held in the insulation is more difficult to answer and has not been addressed.

Although sump monitoring can be reliable if conscientious surveillance is maintained, the reliability of radiation monitors is questionable, primarily for two reasons: (a) The high background radiation level in some reactors forces the alarm trip point to be set so high that the monitor is potentially insensitive to a rise in radiation level due to a leak; in one case, the radiation alarm was not activated by the presence of a 25-gal/min leak. (b) Spurious electrical signals cause false alarms to occur at a relatively high rate.

Also addressed was the issue of whether action is taken before leaks exceed the flow rates recommended in the plant technical specifications. The answer to this question is "not necessarily," according to the LERs that were reviewed. Reported flow rates ranged from 0.3 gal/min to ">32 gal/min total"; sometimes, reports simply described leakage as "excessive."

#### Problems Associated with Current Leak Detection Technology

Although current leak detection systems are adequate to ensure a leak-before-break scenario in the great majority of situations, one must also consider the possibility that large cracks may initially produce only low leak rates. This situation could arise because of corrosion plugging or fouling of relatively slowly growing cracks or the relatively uniform growth of a long crack before penetration. In such cases, the time required for a small leak to become a significant leak or rupture could be short, depending on crack geometry, pipe loading, and transient loading (due to a seismic or water hammer event).

The shortcomings in existing leak detection systems are not simply a matter of conjecture. The Duane-Arnold safe-end cracking incident [2] indicates that the sensitivity and reliability of current leak detection systems are clearly inadequate in some cases. In the Duane-Arnold case, the plant was shut down on the basis of the operator's judgment when a leak rate of 11360 cm<sup>3</sup>/min (3 gal/min) was detected; however, this leakage rate is below the required shutdown limit for almost all BWRs. Examination of the leaking safe-end showed that cracking had occurred essentially completely around the circumference. The crack was throughwall over about 20% of the circumference and 50-75% throughwall in the nonleaking area.

The concern about potential problems with current leak detection technology extends beyond the U.S. borders. The experience with PWRs in France has been discussed in a paper [3] presented at an international conference on surveillance of reactor coolant boundaries. French regulations related to primary coolant systems are based on NRC Regulatory Guide 1.45. In practice, however, leak detection is largely based on the chemical and control volume tank level and (to a lesser extent) the sump level and flow monitor. Locating leakage is generally difficult and is done by local inspection after a leak is detected. The main components involved in leaks of primary coolant systems in France have been valves and, to a lesser extent, primary pump casing seals. During transient operation, the leak detection capability is reduced; as a result, the French Safety Authority has required that primary coolant leakage detection and quantification methods be improved. Otherwise, few problems have arisen in France from the primary coolant leakage detection system in the past few years.

#### Future Needs and Current Developments

It has become apparent that no single currently available leak-detection method for LWRs combines optimal leakage detection sensitivity, leak-locating ability, and the desired level of accuracy in leakage

measurement. For example, although quantitative leakage determination is possible with condensate flow monitors, sump monitors, and primary coolant inventory balance, these methods do not provide adequate location information and are not necessarily sensitive enough to meet regulatory-guide goals. Leak detection capability can be improved at specified sites by use of acoustic monitoring or MST.[1] However, current AEM techniques provide no source discrimination (e.g., to distinguish between leaks from pipe cracks and valves) and no leak rate information (a small leak may saturate the system). MST provides neither quantitative leak rate information nor specific location information other than the location of the tape; moreover, its usefulness with "soft" insulation needs to be demonstrated.

Since the issuance of NRC IE Bulletins 83-02 and 82-03 and the training of ultrasonic inspection personnel, the probability of detecting IGSCC under field conditions has increased. However, many cracks are missed during ultrasonic ISI and are detected only because of leakage, thereby raising doubts concerning the capability of ultrasonic ISI to detect cracks. The present ultrasonic testing procedures for ferritic weldments (ASME Code Sections V and XI) do not appear to be adequate for the detection and evaluation of IGSCC in austenitic stainless steel (SS) piping. The detection of IGSCC before the cracks have grown large enough to cause a leak, and the detection, location, and sizing of leaks once they occur, are very difficult technical goals to achieve. Leak detection techniques need further improvement in the following areas: (a) identifying leak sources through location information and leak characterization, so as to eliminate false alarms; (b) quantifying and monitoring leak rates; and (c) minimizing the number of installed transducers in a "complete" system through increased sensitivity.

Further motivation for work on leak detection systems comes from the report of the U.S. NRC Piping Review Committee [4], where the validation of leak detection systems and efforts to determine the reliability of methods to predict leak rates are recommended. This report points out that "Improved leak detection systems would permit more stringent requirements on unidentified leakage without increasing the occurrence of spurious shutdowns due to relatively benign leakage ..." The work described in our recent report [5] is directed toward achieving those stated goals. This report describes the development of a field-implementable acoustic leak detection system for the detection, location, and characterization of leaks in the primary piping of LWRs and guidance for the installation and operation of the system in a nuclear reactor.

#### Acoustic Leak Detection System

The first step in the implementation of an acoustic leak detection and location system is to identify acoustic receiver sites and determine the spacing between waveguides required to meet the sensitivity needs of the system. The spacing scheme will differ depending on whether a PWR or BWR is being monitored and will depend on the level of sensitivity required. Estimates of S/N ratios for IGSCC leaks as a function of distance and

acoustic background levels are presented in Ref. 5, Fig. 3.28, Section III.C.3. The level of background noise needs to be established for the various regions to be monitored in order to optimize the number of sensors used. The figure can be used to estimate the optimum sensor spacing once the desired sensitivity and background noise levels are established. While the figure is for 10-in. pipe, the data will be assumed to be valid for all piping systems unless alternate data are available. Attenuation measurements will have to be obtained for other piping systems in the field to obtain more precise sensor spacing information.

The results presented in Fig. 3.28, Ref. 5 are for BWR conditions. Because of the higher pressure in a PWR, the acoustic signals for a given leak rate are higher. Adding 6 dB of S/N to the results of the figure should provide a conservative estimate of acoustic signal vs. leak rate for a PWR. As an example, assume 100 m of monitored piping in a BWR (the approximate length of the primary pressure boundary), is divided into low, moderate, and high levels of acoustic background noise covering 40, 40, and 20 m of piping, respectively. Also assume that the desired detection sensitivity is 1 gal/min. For a 3-dB S/N ratio, the required sensor spacings (for a signal in the 300- to 400-kHz range) are approximately 10, 2, and 1 m. Four sensor locations are required to cover the low-acoustic-background area (40 m of piping), 20 sensors for the moderate-noise area (40 m of piping), and 20 sensors for the high-noise region (20 m of piping). For location analysis, three sensors are required at each site to carry out the correlation averaging routine. Therefore, 132 sensors are needed to adequately cover the reactor primary pressure boundary under the conditions proposed. For a PWR, assume that 150 m of piping has a 60-m/60-m/30-m set of piping lengths at low-, moderate-, and high-background levels. With an increase of 6 dB in signal intensity for a PWR compared to a BWR, one has sensor spacings of 12, 4, and 2 m for a 3-dB S/N ratio. Approximately 150 sensors will be required  $[3 \times (5 + 15 + 30)]$  to completely monitor the plant under this scenario. Obviously, the number of sensors can be significantly reduced if only isolated sections of the plant are monitored.

Sensors with a resonance frequency of 375 kHz but with good sensitivity down to 100 kHz were used by ANL. Other sensors may be selected. However, to take full advantage of the information in the acoustic signal, tests using these sensors on an ALD facility will be required to establish their response characteristics and develop curves of leak rate vs. acoustic signal intensity. The considerations in the selection of transducers are the center frequency, bandwidth, ruggedness, response to temperature and humidity, ability of cables and preamplifiers to withstand the reactor environment, and obtaining approval to place materials used to fabricate the equipment inside the reactor. A plan to bring out the electrical signals to the control room for analysis by a computer needs to be established. Feed-through cables can be minimized by use of a multiplexer inside the reactor.

The next step is the selection of waveguides and coupling schemes. Waveguides as described in this report will be satisfactory; however, others may be more appropriate. Considerations for waveguides are the length, diameter, material, and surface finish. Stainless steel is preferred. The long, thin waveguides minimize heat transfer from the pipe but reduce the acoustic energy transferred to the receiving transducer. Thus a compromise must be made. Waveguides ranging in diameter from 3 to 13 mm and up to 250 mm in length seem most effective. Two coupling schemes seem adequate. In the first, the waveguides are screwed into a plate to mechanically press the waveguide to the pipe outer wall. In the second, a spring loading device is used to press the waveguide to the pipe. Generally speaking, a rounded tip on the end of the waveguide in contact with the pipe is most effective. For averaging of correlograms, three waveguides with transducers will be required at each site, separated by a minimum of 10 cm around the circumference. This allows nine correlograms to be generated and averaged for each pair of detector locations.

The selection of electronic filters and amplifiers is important. High-gain, low-noise preamplifiers and amplifiers are desirable. Amplifiers built into the casing of the transducer housing are available though they have not been extensively evaluated in this program. Preamplifiers feeding a signal to a multiplexer followed by a quality linear amplifier in the control room seem most efficient. Selection of filters is also important. Filters should have variable adjustments so that the frequency of the window of operation can be manipulated as needed. Signals are filtered after amplification and then are transmitted to the analyzing computer.

Receivers should be calibrated by using a pencil-lead breaking scheme or electronically simulated ultrasonic waves.[5] Variations in sensitivity of the numerous transducer-waveguide systems can then be stored in the computer, and thus rms signal intensities can be normalized.

Computer hardware and interfaces similar to that described in Ref. 5 can be used. Modifications that include state-of-the-art computer hardware and software will be desirable along with upgrading the system to handle data from more than two waveguide-transducer systems. The system should include off-site monitoring of the rms signal from all sensors and proper interfacing between computer and acoustic signals. Computer programs must incorporate the correction for frequency-dependent attenuation if significant differences in attenuations between 100 and 400 kHz exist. This will assure that the analysis required to identify the leak source will be carried out correctly. The equations to be used are presented later in this section.

In addition to calibration of sensors, a permanent self-checking system may be installed. This could consist of a pulser generating an acoustic wave that can be detected by the various probes to check for system deterioration. If acoustic background noise levels are relatively constant, they may also be used to determine whether a probe is failing. Background noise data from each transducer should be stored for future reference.

The ALD system should be validated on a laboratory facility with leaking cracks such as the one ANL used for this investigation. The signal vs. leak rate and the frequency spectrum vs. leak type should be evaluated on the laboratory test loop. Calibration procedures could also be verified on the laboratory apparatus. Tests with field equipment must be carried out to account for differences in receivers.

Attenuation vs. frequency can be determined via pencil-lead breaking techniques or by use of a broadband or variable narrowband electronic source to simulate acoustic waves from 100-400 kHz. In order to determine the attenuation, the source should be placed 1 and 5 m from the sensor, and acoustic signals should be compared.

The equations used for the analysis of frequency-dependent sound waves are presented below. This information is important because it is a factor in making a decision regarding the source of the leak. Let

$s_{300}$  = Magnitude of signal for minimum leak rate in 300- to 400-kHz band (dB) ,

$n_{100}$  = Magnitude of acoustic background signal in 100- to 200-kHz band (dB) ,

$n_{300}$  = Magnitude of acoustic background signal in 300- to 400-kHz band (dB) ,

$S/N_{300min}$  =  $s_{300}/n_{300}$  ,

$\alpha_{100}$  = acoustic attenuation in 100- to 200-kHz band (dB/m) ,

$\alpha_{300}$  = acoustic attenuation in 300- to 400-kHz band (dB/m) ,

$Sig_{100*}$  = acoustic signal +  $n_{100}$  (dB) ,

$Sig_{300*}$  = acoustic signal +  $n_{300}$  (dB) ,

$Sig_{100}$  = acoustic signal minus acoustic background noise in 100- to 200-kHz band (dB) ,

$Sig_{300}$  = acoustic signal minus acoustic background noise in 300- to 400-kHz band (dB) ,

$Sig_{100} = [(Sig_{100*})^2 - (n_{100})^2]^{1/2}$  (dB) ,

$Sig_{300} = [(Sig_{300*})^2 - (n_{300})^2]^{1/2}$  (dB) ,

$D_{bwr}$  = transducer separation for 3 dB of  $S/N_{300min}$  (m) .

Then

$$D_{bwr} = [(\text{Sig}300 * 1 \text{ m from leak}) - 3 \text{ dB}] / \alpha_{300} \text{ (m)} .$$

Let

$$D_{pwr} = \text{transducer separation for 3 dB of S/N}_{300\text{min}} \text{ (m)} ,$$

$$D_{pwr} = [(\text{Sig}300 * 1 \text{ m from leak}) + 3 \text{ dB}] / \alpha_{300} \text{ (m)} .$$

For leak source discrimination, let

$$R = \text{leak source discrimination parameter.}$$

If  $\text{Sig}100/\text{Sig}300 > R$ , then the leak is not an IGSCC. If  $< R$ , the leak could be from an IGSCC. If  $\text{Sig}100/\text{Sig}300 > R$ , locate the leak through cross-correlation analysis [5] and see if the corrected ratio it is still  $> R$  after frequency-dependent attenuation is accounted for. If  $\text{Sig}100/\text{Sig}300 < R$ , no correction is required. Note that  $R$  is determined from leak tests with 1-m probe-to-source distance as described in Section III.C.3.

The correction to  $\text{Sig}100/\text{Sig}300$  is carried out by letting

$$R = (\text{Sig}100) / (\text{Sig}300)$$

for IGSCC at 1 m distance (e.g., at ANL,  $R = 2$ ). If  $\text{Sig}100/\text{Sig}300 < R$ , an IGSCC is indicated and frequency dependent attenuation calculations are not required. If  $\text{Sig}100/\text{Sig}300 > R$ , the calculation is required because, in general, the attenuation of higher frequencies is greater than that of lower frequencies. Thus, correcting  $\text{Sig}100/\text{Sig}300$  for frequency-dependent attenuation will only decrease the ratio.

Correct for frequency-dependent attenuation by calculating

$$R_{cor} = \frac{\text{Sig}100(\text{at } D) \cdot 10^{(\alpha_{100}(D-1)/20)}}{\text{Sig}300(\text{at } D) \cdot 10^{(\alpha_{300}(D-1)/20)}}$$

where  $D$  is the leak-to-acoustic-sensor distance. If  $R_{cor} > R$ , the leak is not an IGSCC.

Once the source of the leak is established the leak rate is estimated from the graph (or equivalent) in Section III.C.3, Fig. 3.29.[5] With the system installed as described in that report, and with the analysis carried out as indicated, an ALD system will be in place that can make low-level decisions and detect, locate, and characterize leaks in LWRs. This system can be set up to monitor the reactor continuously by means of a computer, alerting reactor personnel to problems, and automatically analyzing acoustic signals. The results of the ANL work on such a system is described completely in Ref. 5.

## Acknowledgments

The authors wish to thank R. Popper for his assistance in the design and data acquisition phases of this project.

## References

- [1] Reactor Coolant Pressure Boundary Leakage Detection Systems, U.S. Nuclear Regulatory Commission Guide 1.45 (May 1983).
- [2] D. S. Kupperman, T. N. Claytor, D. W. Prine, and T. A. Mathieson, "Evaluation of Methods for Leak Detection in Reactor Primary Systems and NDE of Cast Stainless Steel," in Proc. of U.S. Nuclear Regulatory Commission Twelfth Water Reactor Safety Research Information Meeting, Gaithersburg, Maryland, Oct. 22-26, 1984, NUREG/CP-0058, Vol. 4, pp. 342-362 (1985).
- [3] P. Cassette, C. Giroux, H. Roche, and J. J. Seveon, "Evaluation of Primary Coolant Leaks and Assessment of Detection Systems in Continuous Surveillance of Reactor Coolant Circuit Integrity," in Continuous Surveillance of Reactor Coolant Circuit Integrity, Proc. CSNI Specialist Mtg., London, England (August 1985), Nuclear Energy Agency, Paris, France, 1986, pp. 165-178.
- [4] Report of the U.S. Nuclear Regulatory Commission Piping Review Committee (Summary), NUREG-1061, Vol. 5, p. 33 (April 1985) and Vol. 1, pp. 4-52 (August 1984).
- [5] David S. Kupperman, David Prine, and Thomas Mathieson, Application of Acoustic Leak Detection Technology for the Detection and Location of Leaks in Light Water Reactors, Argonne National Laboratory Report NUREG/CR-5134, ANL-88-21 (October 1988).

EDDY-CURRENT INSPECTION FOR STEAM GENERATOR TUBING PROGRAM  
ANNUAL PROGRESS REPORT FOR PERIOD ENDING DECEMBER 31, 1988

C. V. Dodd, W. E. Deeds, and J. R. Pate

Metals and Ceramics Division  
OAK RIDGE NATIONAL LABORATORY  
Oak Ridge, Tennessee 37831

ABSTRACT

Reflection probes have demonstrated an improved capability to detect and size defects in degraded steam generators. We have been optimizing the reflection probes and the instrument operating parameters for steam generator inspections. We have developed programs that accurately calculate the changes in the eddy-current signals produced by the many possible property variations such as tube sheets, tube supports, copper deposits, magnetite deposits, denting, and defects. Other programs compute the accuracy and sensitivity of eddy-current measurements of defects in the presence of these property variations. These programs have been run to optimize reflection, pancake and circumferential coils. A comparison between the optimum of each type showed that the reflection coils are best, the pancake coils next and the circumferential coils are worst. We have designed both single reflection coil probes and an array of 16 reflection coils. We have also studied the accuracy of the defect theory for reflection, pancake and circumferential coils and experimentally verified the theory. The newest inversion technique shows good potential for a direct and accurate determination of defect size and depth.

INTRODUCTION

Among the many types of serious tubing degradation are long-known ones, such as wastage, pitting, and fretting, and recently discovered ones, such as intergranular attack (IGA), intergranular stress-corrosion cracking (IGSCC), and fatigue. However harmless artifacts, such as tube supports, tube sheets, small dents, and buildup of copper or magnetite, also affect eddy current signals and must be distinguished from the dangerous ones. This can be accomplished by taking eddy current readings at several different frequencies and using the additional information to eliminate the unwanted variables, provided the various artifacts affect the readings differently at the different test frequencies. To optimize the sensitivity to the properties of interest, we must find which combination of test frequencies is best able to determine any particular property and also which probe design is most sensitive to defects in the region of interest. These optimizations are performed by computer modelling, using programs developed at Oak Ridge National Laboratory (ORNL). When the appropriate hardware has been constructed, then the actual test equipment is calibrated, or "trained," by using it to measure an array of standards containing all combinations of expected property variations. Then the algorithms can be determined that will measure the desired properties and ignore the others.

Finally, the optimized hardware and computer algorithms are used to make measurements on actual steam generator (SG) tubes.

#### DEVELOPMENT OF BETTER PROBES

Figure 1 shows the three types of probes that have been investigated for

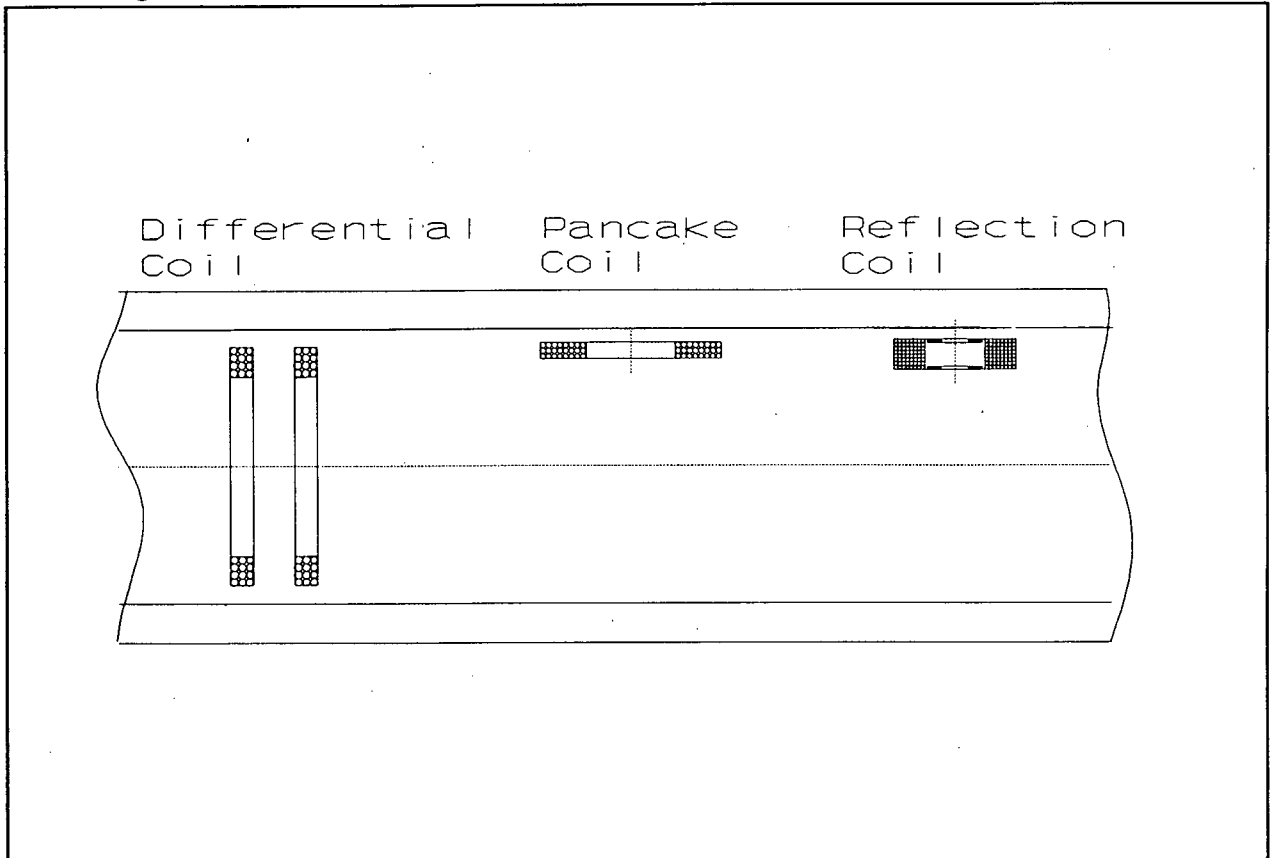


Figure 1 Coil types that have been analyzed

inspecting SG tubes. The differential coils are ideally coaxial with the tube. They must be made smaller than the tube inner diameter (ID) in order to pass dents or corrosion buildup. This decrease of fill factor limits their sensitivity and also allows probe wobble, which makes variable sensitivity around the circumference. Differential coils can detect changes in tube properties which occur in distances comparable to the coil separation, but are insensitive to slowly varying changes along the tube. The slow changes can be detected by monitoring the output of one of the coils, as an "absolute" coil. However, either type of circumferential coil arrangement averages the tube properties around the circumference of the tube and is therefore relatively insensitive to the effect of a small defect at some point around the circumference.

Small pancake probes can be pressed against the inner wall of the tube, minimizing liftoff problems while still being able to pass small dents and corrosion buildup. Since they interrogate a smaller volume of tube, they are much more sensitive to small localized tube variations and are also much less sensitive to artifacts outside the tube, such as tube supports. The penalties

are that either the inspection speed is decreased or the probe must have an array of pancake coils to cover the circumference of the tube in one pass. In addition there is more data to store and analyze.

A small reflection coil can also be pressed against the inner wall of the tube, like a pancake coil, but it has several additional advantages as well. For one thing, it can be made insensitive to liftoff over a finite range; this is useful if the probe has to slide over small dents or a buildup of corrosion products. For another thing, it can be "nulled," i.e., constructed to give zero reading, when the coil is in air, so that it measures only changes from nominal conditions, which can then be amplified more than the non-nulled signal from a single coil. Both theoretically and experimentally, reflection coils are an order of magnitude more sensitive to small defects than circumferential coils and have a better signal-to-noise ratio than pancake coils. They are also less sensitive to artifacts outside the tube.

The defect sensitivity factor at a given location in a conductor is a measure of the eddy current flow signal produced by an infinitesimal flaw located there. It is generally a maximum near the coil and falls off exponentially with distance into the conductor. Figure 2 shows a plot of the defect sensitivity factor for a pancake coil against a flat plate (this is approximated by a very small pancake coil against the inner wall of a much larger tube). Note that the defect sensitivity is spread over a wide area, making it less sensitive to a localized small flaw. Figure 3 shows the corresponding graph for a reflection coil. Note that the sensitive region is more sharply focussed under the coil, so that a defect located there will produce a larger signal change.

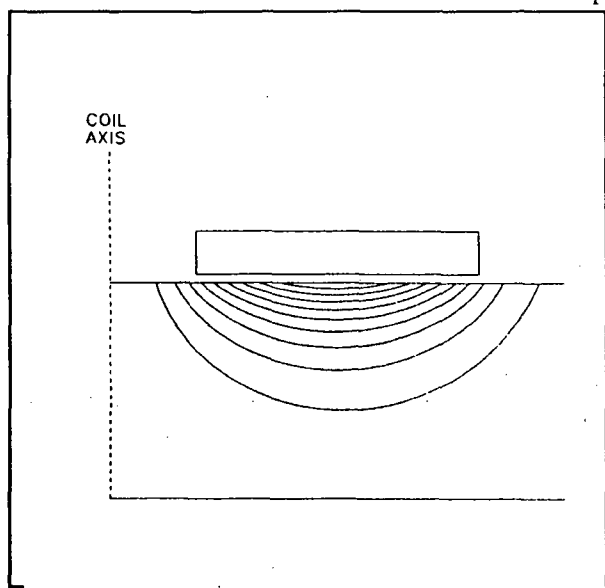


Figure 2 Defect sensitivity factor for a pancake coil above a plate

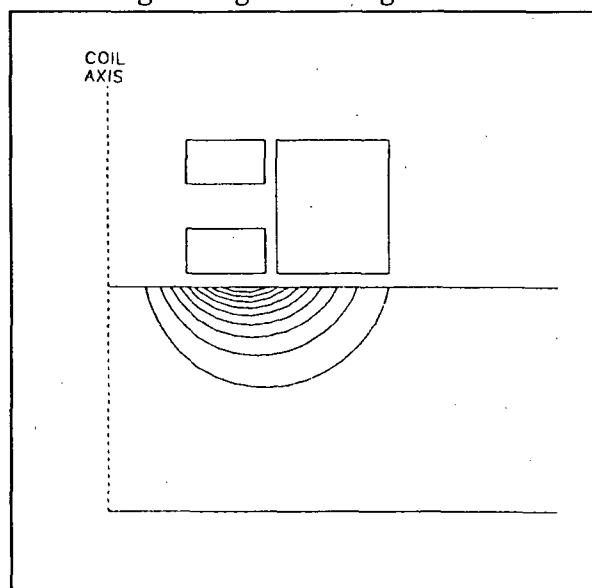


Figure 3 Defect sensitivity factor for a reflection probe above a plate

Figure 4 shows a comparison of the accuracy of depth measurements made with pancake and reflection coils for a set of property variations including defects, tube supports, copper coating, magnetite and wall thinning.

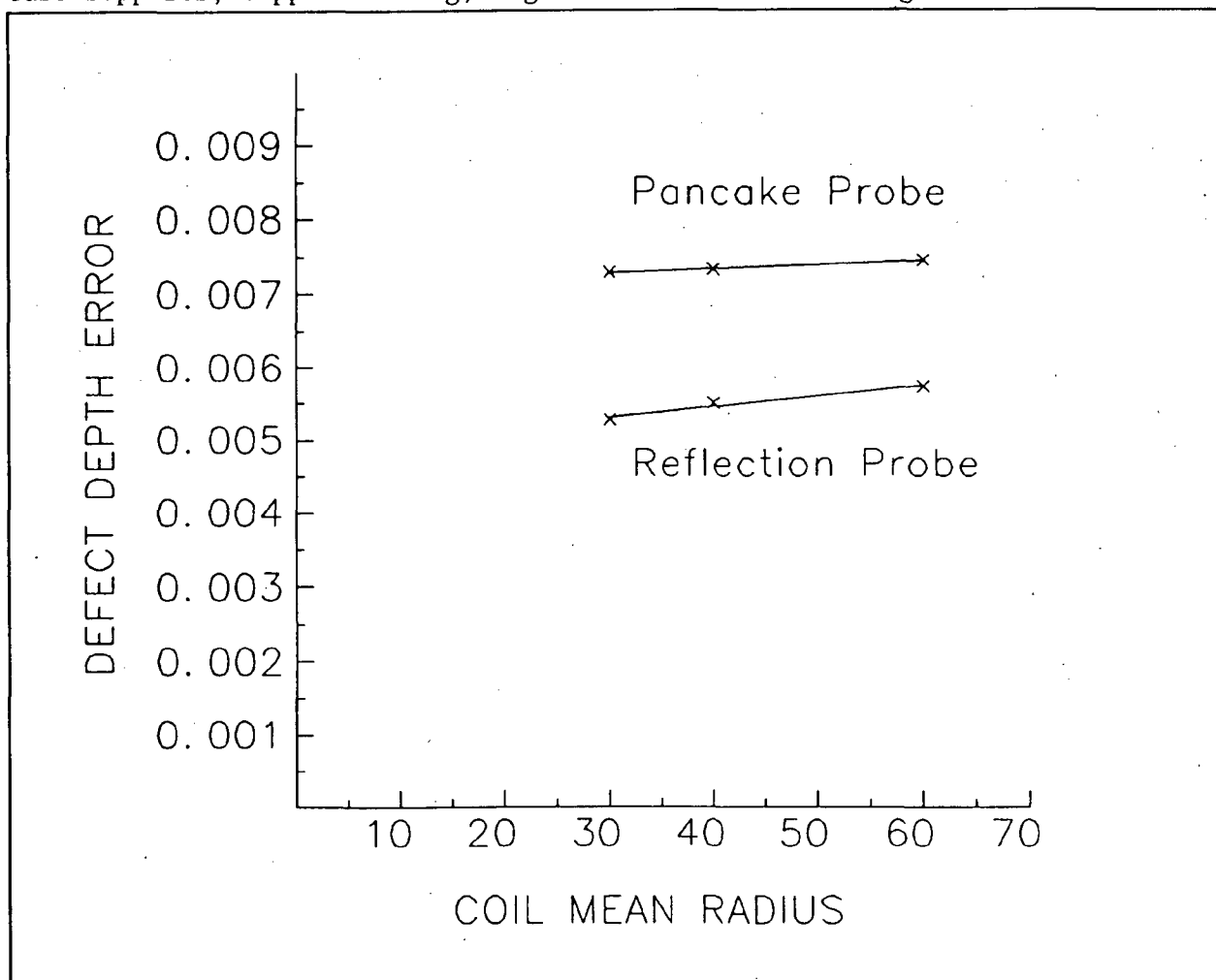


Figure 4 Comparison of defect depth measurement error for reflection probe and pancake probe with the same property variations

#### DEVELOPMENT OF REFLECTION COIL ARRAYS

Since reflection coils are superior to the pancake or circumferential coils, we have investigated several types of multi-coil arrays to make it possible to scan the entire circumference of a tube simultaneously. The size of reflection coil that has the best compromise between defect sensitivity and coverage ability is one with a mean driver coil radius of 1 mm (0.04 in.). However an array of sixteen of these coils is needed to cover the inner circumference of a SG tube in one pass with sufficient overlap to ensure detection of every flaw of detectable size. Actually, only eight such coils can be mounted in a single ring inside the tube, and the other eight must be mounted in another ring indexed 22.5 degrees around the axis. A sixteen-coil array was

made using pancake coils in Zetec mounts, but it proved too fragile for practical use. More rugged arrays of reflection coils have been made, using fewer than sixteen coils, and they have survived torture testing. But we have not yet been able to procure a sixteen-coil array of the more rugged design.

FLAW INVERSION, OR DETERMINING FLAW PROPERTIES FROM EDDY CURRENT SIGNALS

There are many ways to calculate the flaw properties from the eddy current signals. The most straightforward and elegant method is to make a Fourier-Bessel transform of the eddy current readings, which involve the flaw size and depth. By scanning across a flaw, multiplying the readings by the appropriate Bessel function and integrating the result, one can obtain a complex number from which the flaw size and depth can be extracted. Unfortunately, the method loses accuracy if the flaw has finite size (since the defect sensitivity factor varies appreciably over the flaw volume) or if the experimental data are noisy. Much effort has gone into various schemes for averaging the eddy currents over the flaw volume, with limited success. Figure 5 shows a plot of defect depth calculated by this inversion method from actual experimental measurements versus the actual flaw depth. Note that the agreement is better for small flaws (i.e., little depth) than for large flaws. Figure 6 shows the results of various methods of averaging the eddy current signal over a large flaw to try to reproduce the actual experimental signal, marked "EXP," as the probe is moved past the flaw. The curves marked S.P.T, DEP, and VOL respectively represent the results of using the eddy current at a Single Point at the center of the flaw, averaging the eddy current signals over the DEPTH of the flaw, and averaging over the VOLUME of the flaw.

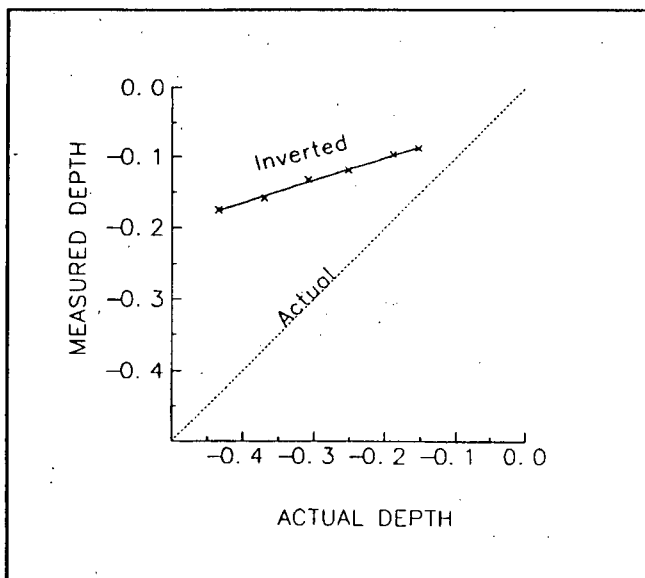


Figure 5 Defect depth determined by inversion plotted against actual defect depth

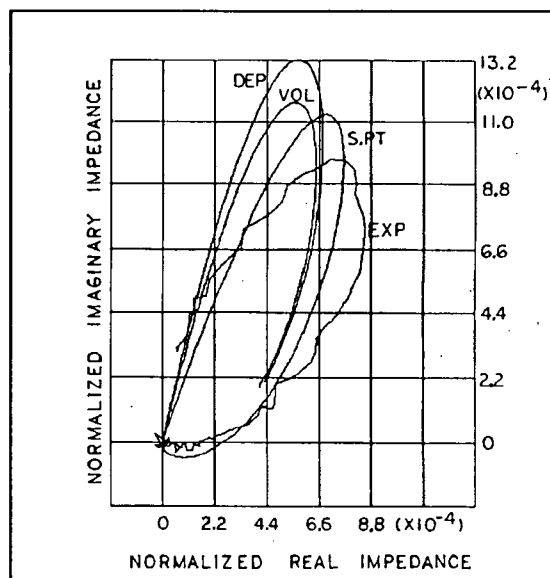


Figure 6 Normalized Impedance Change Due to a 60% Farside Flat Bottom Hole

Another method, which is less elegant, but faster and more satisfactory at present, is to build a lookup file containing the results of theoretical calculations at different depths throughout the wall of the tube. Then, when the tube is scanned by a reflection or pancake probe, the lookup file can be searched for a match with the signals measured by the probe, and the depth and volume of any defects can be found very quickly. Another advantage of this method is that we can choose to consider only the interval where the defect signal is strongest. Since this is the region with the highest signal-to-noise ratio, the effect of noise on the results is minimized.

Other flaw inversion techniques have been described and tried, but all of them so far are very sensitive to noise in the data, and some require inordinate amounts of computer time as well.

#### DEVELOPMENT OF TESTS FOR FATIGUE OF SG TUBES

It has recently become apparent that metal fatigue can contribute to failure of SG tubes in aging reactors, and it has been shown that fatigue can change the electrical and magnetic properties of materials. Therefore we have designed tests to measure these properties on samples of Inconel tubing subjected to repeated flexing. To measure the changes of conductivity and permeability most accurately, we have used through transmission measurements, as shown in Figure 7, with the transmitting and receiving coils on opposite sides of the tube wall.

Inconel tubes 0.46 m (18 in) long, clamped at one end, were flexed 0.63 cm (0.25 in) back and forth at the other end by a motor-driven eccentric cam as indicated in Figure 8. Two different tubes broke completely in two after each was flexed about 5.6 million cycles. Tube samples will be tested at different intervals to determine if a measurable change in the conductivity and permeability occurs in Inconel.

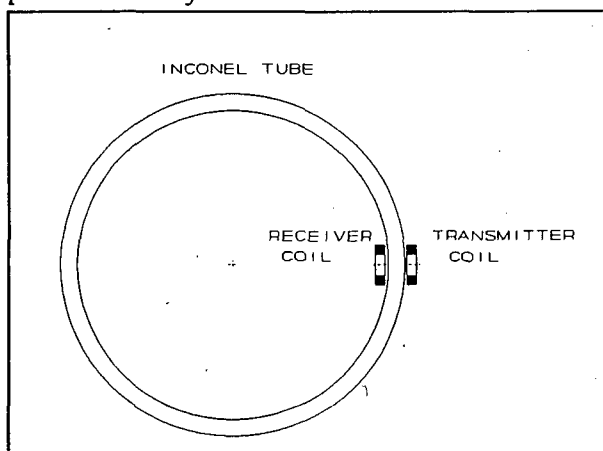


Figure 7 Measurement of conductivity and permeability using a through transmission eddy current test

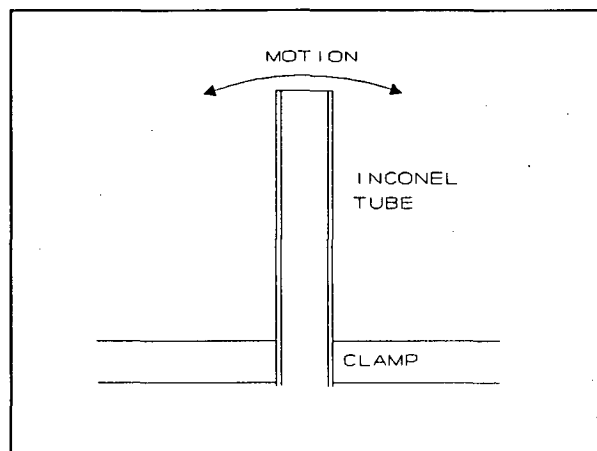


Figure 8 Diagram of Inconel Tube Fatigue Test

This kind of failure can lead to catastrophic SG failure, such as occurred at the North Anna reactor site.

#### SUMMARY AND CONCLUSIONS

The importance of reliable steam generator inspection has increased as the generators have aged. At the same time, the number and complexity of the known problems involved in steam generator inspections have also increased. The problems have become so complicated that conventional equipment is no longer capable of distinguishing many newly discovered types of defects from other artifacts that may be completely harmless. Therefore it is important to have equipment that can determine the critical properties reliably. Small reflection coils pressed against the inner wall of the tube have significant advantages over conventional bobbin coils or even small pancake coils in their ability to distinguish various tube properties and be relatively insensitive to harmless artifacts outside the tube. Although the reflection coils are more expensive and difficult to construct, they are the most accurate and sensitive eddy current probes available at this time. Finally, metal fatigue has now taken its place as one of the critical tube properties that should be monitored.



REVIEW OF THE STATUS OF NONDESTRUCTIVE MEASUREMENT TECHNIQUES  
TO QUANTIFY MATERIAL PROPERTY DEGRADATION DUE TO AGING  
AND PLANNING FOR FURTHER EVALUATION<sup>(a)</sup>

Program Manager  
S. R. Doctor

Principal Investigators  
D. M. Boyd, S. M. Bruemmer, E. R. Green, G. J. Schuster, E. P. Simonen

Pacific Northwest Laboratory  
Operated by Battelle Memorial Institute

ABSTRACT

The materials used in nuclear reactors are inspected periodically during the service life of the power plant to detect degradation that might occur. These inspections follow the rules specified in Section XI of the ASME Boiler and Pressure Vessel Code. These inspections are designed to detect service-induced failure mechanisms. This program is designed not to look at the detection of defects but the making of nondestructive measurements to quantify the material properties that a defect may reside in or the incipient condition(s) that may initiate a defect.

This program is intended to provide an assessment of the technologies that are available to quantify with nondestructive measurements material properties or material property changes related to degradation due to aging of structural components in light water reactors. In addition, a program plan will be developed that describes the work necessary to create adequate engineering data bases for demonstrating and validating prototypic systems for making these measurements.

The main thrust this year has been an extensive review of literature and an assessment of the technology. The second major activity was the planning of a workshop to bring together 30 leading experts in materials and NDE to discuss the state-of-the-art and to address where future work should go.

---

(a) Work supported by the U.S. Nuclear Regulatory Commission under Contract DE-AC06-76RLO 1830; Dr. J. Muscara, NRC Program Monitor, FIN B2921

## NDE METHODS FOR MEASUREMENT OF MATERIALS PROPERTIES AND PROPERTY CHANGES

### Introduction

The objective of this project has been to review the literature, current expertise, and related activities; and to prepare a plan for development of engineering data bases and validation of prototypic systems for nondestructively measuring material properties and property changes due to aging in structural components of light water reactors. In order to achieve this task, the scope of work for the program has been divided into the literature review, preparing a white paper on the nondestructive measurements (NDM) and materials evaluation of aging-induced microstructural changes, holding a workshop on the topic, and preparing a program plan for the next phases of the program. This report will review the status of the program and discuss the upcoming workshop to be held on October 27-29.

### State-of-the-Art NDM

The inservice inspection (ISI) role requires NDE measurements to detect and size flaws in order to provide input for fracture mechanics analysis. The present minimum flaw size is set by the fracture analysis performed on the initial reactor design. The fracture mechanics analysis requires assumptions about the material properties such as yield strength, fracture toughness, and fatigue parameters. The goal of improving the fracture mechanics information requires use of either destructive or nondestructive methods to assess the materials properties and materials properties changes. The destructive techniques of material properties measurements such as tensile testing, fatigue testing, and fracture toughness testing are not always practical or cost effective. Destructive methods also require making test coupons from either sections of the actual component or aging the coupons in a manner similar to the component loading conditions and service environment. Nondestructive testing methods have the potential for obtaining in-situ the needed material property data for input to the fracture mechanics analysis. The NRC has identified that additional information on fracture toughness and fatigue (remaining fatigue life) are two important areas for future development in support of power plant life extension.

As part of this program, a library search and literature review has been performed. The library data base system was used to locate references to nondestructive evaluation techniques to measure the materials properties of fatigue life and fracture toughness, when subjected to radiation embrittlement, fatigue and thermal embrittlement. From this data base, the abstracts were reviewed and pertinent papers were obtained for detailed review.

One of the papers reviewed was by R. Bruce Thompson and Donald O. Thompson, "Ultrasonics in Nondestructive Evaluation," Proc of the IEEE, Vol. 73, No. 12, December 1985, on the use of ultrasonic waves in NDE. One of the sections included a review of Material Property Measurements. They pointed out that the microstructure of materials such as grain, porosity, inclusions, microcracks, second phase content and morphology, and texture are important to

material performance and failure modes in a structure. They also pointed out that each of these microstructural properties affect the ultrasonic velocity and the attenuation. Their concluding statement was "... material property measurements are only possible in samples in which only a few of the metallurgical parameters are unknown." However, in the section on material property measurements, they provided a review of two NDE measurements that have made progress in quantitative property measurements. The first was a review of ultrasonic stress measurements using velocity and birefringence methods. One comment on the stress measurements was that "considerable work remains before high resolution images of spatially varying stress patterns can be obtained." The second material property technique discussed was grain size determination. Grain size measurements have been demonstrated using scattering of ultrasound and frequency-dependent attenuation measurements.

A paper by E. P. Papadakis, "Physical Acoustics and Microstructure of Iron Alloys," International Metals Reviews, Vol. 29, No. 1, 1984, is a review of ultrasonic grain scattering in iron alloys. The effect of microstructure on the frequency-dependent scattering is discussed. The three regions for ultrasonic scattering are reviewed: Rayleigh Region ( $\alpha F^4$  when  $\lambda \gg \bar{D}$ ), Stochastic Region ( $\alpha \bar{D} F^2$  when  $\lambda \simeq \bar{D}$ ), and Diffusion Region ( $\alpha F^2 / \bar{D}$  when  $\lambda \ll \bar{D}$ ). Scattering theory and experimental verification show that acoustic scattering is a function of frequency. He provides an excellent review of research in grain scattering with the salient points as follows:

Theory agrees with experiments for:

1. Homogenous bulk specimens
2. No preferred orientation
3. Equiaxed grains
4. No twins, intergranular transformation products or precipitates
5. Nodular graphite in ductile iron

Theory does not agree with experiments for:

1. inhomogeneous specimens
2. wires and thin sheets
3. preferred orientation
4. elongated grains
5. complex intergranular structure

The paper then provides a detailed review of specific frequency versus attenuation experimental data on the different scattering regimes and iron alloy specimens.

The literature review has looked at many NDE techniques which may have potential as a method for material property and property change measurements. The methods reviewed include acoustic elasticity, internal friction, acoustic emission, electrical resistivity, small angle neutron scattering, thermal, magnetic hysteresis, Barkhausen noise, eddy current, holographic interferometry, and micro hardness methods. This is not an all-inclusive review; however, an

attempt has been made to identify the initial techniques which have potential. Table 1 shows a summary list of potential techniques for NDM.

TABLE 1. Potential NDE Methods for NDM

	<u>Fracture Toughness</u>	<u>Hardness Radiation)</u>	<u>Fatigue</u>	<u>Yield Strength</u>
Magnetic Hysteresis		X	X	X
Eddy Current		X		X
Internal Friction	X	X	X	X
Holographic Interferometry		X		X
Acoustics	X	X	X	X
Acoustic Emission	X	X	X	X

This table identifies only that the NDE technique has potential as a method for material property measurements.

This information has been used to provide an understanding of the present "state-of-the-art" of NDE for material property measurements. This information will be used to help guide the workshop and discussion sessions on the future direction for the program.

#### MATERIAL AGING MECHANISMS

A literature review was conducted to assemble relevant reports and documents related to the aging that occurs in light water reactor materials. The best reference uncovered was a report by the Idaho Nuclear Engineering Laboratory for the NRC Aging Program (NUREG/CR-4731, Vol. 1). This report dealt in great detail with the materials and environmental aging factors that are present in light water reactors. A summary of the ranking and three major degradation drivers are shown in Table 2. The components that are highlighted with two asterisks are the ones of more structural significance because of the implication to operational functionality. It is very evident that the reactor pressure vessel is by far the most important reactor component. The second ranked component is the cast stainless steel piping.

TABLE 2. Primary LWR Degradation Mechanisms  
(Condensed from NUREG/CR-4731, Vol. 1)

- Radiation Embrittlement
  - \*\* Reactor Pressure Vessel  
RPV Supports  
Neutron Shield Tank  
Internal Reactor Components
- Thermal Embrittlement
  - \*\* Cast Stainless Steel Piping  
Pump Bodies and Elbows  
Ferritic Stainless Steels
- Fatigue (Mechanical, Thermal, and Corrosion)
  - \*\* Reactor Pressure Vessel  
Piping and Nozzles  
Pumps  
Steam Generator

#### WORKSHOP

The scheduled workshop is designed to bring together a cross-section of NDE and material experts to discuss the work and knowledge with regard to the changes in material microstructure and material property changes that result from the light water reactor aging environment. The NDE experts are to be present to provide them with a basic understanding of the problem, to place into perspective the work that has been conducted, and to see where the future work should be performed. It was also hoped that material specimens which have already been aged can be identified. This is extremely important because one of the major costs with this kind of program will be the development of a series of well-characterized specimens with known material properties and aging history.

The workshop is by invitation only and is to be held from October 27 through noon on October 29, 1988 at the National Institute of Standards and Technology (formerly NBS). The plan is to have one day on materials, one day on NDM, and the third day on integration and getting out things that attendees had not had a chance to say before.

#### FUTURE WORK

The workshop will be held and then the major work to be performed next fiscal year will be to write the report containing an assessment of the NDM technology and a program plan to conduct the needed work to develop and validate techniques to nondestructively measure material properties.



Progress in Research and Standards Activities in the  
Materials Engineering Branch for 1988

C. Z. Serpan, Jr.

16th Water Reactor Safety Research Information Meeting

Rules, Guides and Codes

The achievements this year in publication of rules, guides and code documents have been so significant that they deserve prominent mention at the beginning of this report.

First, successful culmination of over a decade's work was reached this summer in publication on June 27 of the "General Requirements for Decommissioning Nuclear Facilities" contained in 10 CFR Parts 30, 40, 50, 51, 70 and 72. This "Decommissioning Rule" will ultimately affect every licensed nuclear facility in the country. The revised regulations address decommissioning planning needs, timing, funding methods, and environmental review requirements. The intent is to assure that all licensed facilities will be decommissioned in a timely, safe manner and that adequate funds will be available. Backing up the rule is the "Final Generic Environmental Impact Statement on Decommissioning of Nuclear Facilities," NUREG-0586, dated August 1988. Promulgation of the rule was not possible without this massive and comprehensive study which included analysis of the comments from 143 different organizations and individuals.

Another important rule published this summer, on August 19, was the "Licensing Requirements for the Independent Storage of Spent Nuclear Fuel and High-Level Radioactive Waste," 10 CFR Parts 2, 19, 20, 21, 51, 70, 72, 73, 75 and 150. This rule provides for licensing the storage of spent nuclear fuel and high level waste in MRS (monitored retrievable storage) facilities. This is important because the Nuclear Waste Policy Act of 1982 requires that monitored retrievable storage facilities for spent nuclear fuel and high level radioactive waste be subject to licensing by NRC.

Notable success in publication of guides and code documents has also been achieved in the Materials area as well. First is publication in May 1988 of Revision 2 to Regulatory Guide 1.99, "Radiation Embrittlement of Reactor Vessel Materials." This guide is very important to the safe licensing and regulation process because it describes general procedures considered acceptable for calculation and prediction of the effects of neutron embrittlement of the low-alloy steel currently used for light water reactor pressure vessels.

It is thus a key element in assuring compliance with General Design Criterion 31, "Fracture Prevention of Reactor Coolant Pressure Boundary." Turning next to non-destructive examination, a number of achievements have been recorded. ASME Code Case N-409-1, "Procedure and Personnel Qualification Requirements for Ultrasonic Detection and Sizing of Flaws in Piping Welds," Section XI, Division 1, was published on December 7, 1987. This important code case sets forth procedures for inspection of all piping welds, not just for stainless steel. Following in this same track will be the Mandatory Appendix VII "Training, Qualification and Certification of NDE Personnel that Perform Ultrasonic Examinations under Section XI, Division 1." This appendix is currently before the Board of Nuclear Codes and Standards, and is expected to be passed for inclusion in the Winter 1989 Addendum. Also following this track is the proposed Mandatory Appendix VIII, "Ultrasonic Examination Performance Demonstration" which is in the Main Committee agenda for December 1988. This appendix combines requirements for personnel, procedures and equipment with a statistically designed set of samples in a performance test to demonstrate an acceptable level of flaw detection and sizing. Details have been set out for piping, vessels, bolting and other exams. Finally, a new code case, "Acoustic Emission for Successive Inspections Required by Section XI, Division 1" is also at the Main Committee for their consideration. This Code case provides a procedure for monitoring a suspected flaw indication region continuously during reactor operation using acoustic emission techniques to detect flaw growth.

### Research and Application

The priority effort in the Heavy Section Steel Technology (HSST) program this year was evaluation of the implications of low temperature low flux embrittlement on reactor vessel support structures. This issue arose from findings of higher than expected embrittlement in the High Flux Isotope Reactor at Oak Ridge. The HSST staff studied and categorized all LWRs into support structure types, and then selected two specific plants for more detailed review. The results showed that the effect of the higher than expected embrittlement was significant in reducing the lifetime structural integrity of the supports for postulated accident conditions. While the HSST analysis relied on extrapolation of embrittlement data from the HFIR to LWR support systems, independent confirmation of the effect was obtained by testing of the Shippingport reactor neutron shield tank material by researchers at Argonne National Lab. Working in cooperation with PNL and the Shippingport decommissioning team, ANL secured samples of the tank material and has tested Charpy-V specimens machined therefrom. These specimens showed very low toughness for the inner surface of the tank --5-7 ft-lbs at room temperature -- and a substantial increase in NDT. Further results are expected, and plans are being made to obtain similar data from the decommissioned Belgian BR-3 reactor.

Results are now available from the 5th HSST irradiation program which was designed to show the effect of neutron irradiation on high copper welds for LWR pressure vessels, specifically regarding their performance relative to the ASME  $K_{IC}$  curve shift procedure. The shift in fracture toughness was slightly greater than the shift measured by Charpy-V specimens, a result on the non-conservative side, but not much. However, in one of the rare experiments

measuring the radiation effect on drop weight specimens at realistic reactor operating temperatures, the drop-weight shift was matched by the Charpy-V specimen shift. Additional work is underway on low upper shelf (LUSE) materials to determine any difference between the current practice "good" material and the LUSE material. Closely related to this issue is that of how to measure the J-integral fracture toughness from small surveillance or lab specimens which only provide a small amount of crack growth, and then apply it to large amounts of crack growth possible in real structures. This is called the  $J_m$ - $J_d$  controversy. A great deal of information has been presented to expose facets of the problem, and much experimental work is underway to resolve the issue. A new effort that addresses the over LUSE issue involves removing LUSE weld metal from the cancelled Midland plant, and use that as starting material to determine initial properties of these materials and for irradiations of large specimens to produce data that can help answer the LUSE questions.

Many interesting results have been produced this year in piping research. The Battelle Degraded Piping Program staff has completed bend tests of a 12-in. cast stainless steel surge line from a cancelled PWR and a 14-in. centrifugally cast stainless steel pipe supplied by Framatome, both of which had been artificially aged to simulate end of life conditions. The results of these tests relative to margins and to the possibility of modifying ASME-XI IWB-3640 rules for flaw evaluation to include these materials are being studied carefully. Another test result receiving close scrutiny is that from the bend test of a submerged arc weld in a 37-inch diameter carbon steel PWR cold leg. The fracture was highlighted by many dynamic crack jumps which had the effect of lowering the overall fracture toughness. The International Piping Integrity Research Group (IPIRG) Program also being conducted at Battelle has conducted some 10 tests of 6-inch diameter pipe, including carbon and stainless steel under both inertial and dynamic displacement control loading conditions. Tests in IPIRG are conducted under operating temperature and internal pressure conditions. These results also show that the toughness is lowered, apparently due to the effect of cyclic loading.

Most work to confirm the "fixes" for IGSC cracks in BWR stainless steel piping welds has been completed. Some highlights of work done at ANL include fracture mechanics data to show that the Type 308L weld overlay material does have a strong inherent resistance to stress corrosion cracking, and that modified Type 347 stainless steel has somewhat superior resistance to SCC than Type 316 NG stainless steel. ANL has also completed two reports covering a review of erosion/corrosion in single phase flows, and a survey of experience in PWR feedwater piping. (Ref. 1 and 2) Finally, ANL has completed preparation of reports on both PWR and BWR water chemistry which should be published by the end of this year.

All research work has been completed on the Steam Generator Tube Integrity Group Program, and drafts have been prepared of updates of the pertinent Regulatory Guides 1.83 and 1.121, ISI of PWR SG Tubes, and Bases for Plugging Degraded PWR Steam Generator Tubes, respectively.

Ultrasonic inspection of primary system components and materials continues to be a very important aspect of reactor safety. This year, we have begun a cooperative study with EPRI on the effect of surface conditions on inspection reliability; the NRC-PNL experimental work has already begun to confirm some of the EPRI-Ames Laboratory models for longitudinal waves. PISC-III cooperative studies on UT inspection of stainless steel are starting up with completion of the test matrix and preparation of samples. Meanwhile, round robins are already underway on carbon steel samples, featuring use of the most advanced techniques to demonstrate upgraded inspection methods. Calibration studies for continuous acoustic emission (AE) monitoring at the Watts Bar I plant have been completed, and the system is now ready for monitoring the plant once it starts up. AE characteristics for slow crack growth have been shown to follow the same trend as fast crack growth.

- Ref. 1 Review of Erosion-Corrosion in Single Phase Flows  
G. Cragnolino, C. Czajkowski and W. J. Shack,  
NUREG/CR-5156, ANL-88-25, Argonne National Lab.  
April 1988.
- Ref. 2 Erosion-Corrosion of PWR Feedwater Piping Survey of Experience,  
Design, Water Chemistry and Materials, Otakar Jonas, NUREG/CR-5149,  
ANL-88-23, Argonne National Laboratory, March 1988.

IMPACT OF RADIATION EMBRITTLEMENT ON INTEGRITY OF  
PRESSURE VESSEL SUPPORTS FOR TWO PWR PLANTS\*

R. D. Cheverton      G. C. Robinson  
W. E. Pennell        R. K. Nanstad

Oak Ridge National Laboratory  
P.O. Box 2009  
Oak Ridge, Tennessee 37831-8056

ABSTRACT

Recent pressure-vessel surveillance data from the High Flux Isotope Reactor (HFIR) indicate an embrittlement fluence-rate effect that is applicable to the evaluation of the integrity of light-water reactor (LWR) pressure vessel supports. A preliminary evaluation using the HFIR data indicated increases in the nil ductility transition temperature at 32 effective full-power years (EFPY) of 100 to 130°C for pressurized-water-reactor (PWR) vessel supports located in the cavity at midheight of the core. This result indicated a potential problem with regard to life expectancy. However, an accurate assessment required a detailed, specific-plant, fracture-mechanics analysis. After a survey and cursory evaluation of all LWR plants, two PWR plants that appeared to have a potential problem were selected. Results of the analyses indicate minimum critical flaw sizes small enough to be of concern before 32 EFPY.

INTRODUCTION AND SUMMARY

Structural supports for most pressurized-water-reactor (PWR) pressure vessels are located in the cavity between the vessel and the biological shield (Fig. 1). Within the cavity the fast neutron flux  $\phi$  for energies  $E > 1.0$  MeV is  $\leq 2 \times 10^9$  neutrons/cm<sup>2</sup>·s, and temperatures are  $< 65^\circ\text{C}$ . The corresponding calculated increase in the nil ductility transition temperature (NDTT) by 32 effective full-power years (EFPY), based on the radiation embrittlement data<sup>1,2</sup> available from materials testing reactors (MTRs) before 1987, is quite small, if the difference in the MTR and the PWR cavity fast neutron energy spectra is neglected.

Early in 1978 it became apparent that the fast neutron spectrum above 0.1 MeV was much softer in the PWR cavity than in the MTRs (the result of

---

\*Research sponsored by the Office of Nuclear Regulatory Research, U.S. Nuclear Regulatory Commission under Interagency Agreement 1886-8011-9B with the U.S. Department of Energy under Contract No. DE-AC05-84OR21400 with Martin Marietta Energy Systems, Inc.

"The submitted manuscript has been authored by a contractor of the U.S. Government under contract No. DE-AC05-84OR21400. Accordingly, the U.S. Government retains a nonexclusive, royalty-free license to publish or reproduce the published form of this contribution, or allow others to do so, for U.S. Government purposes."

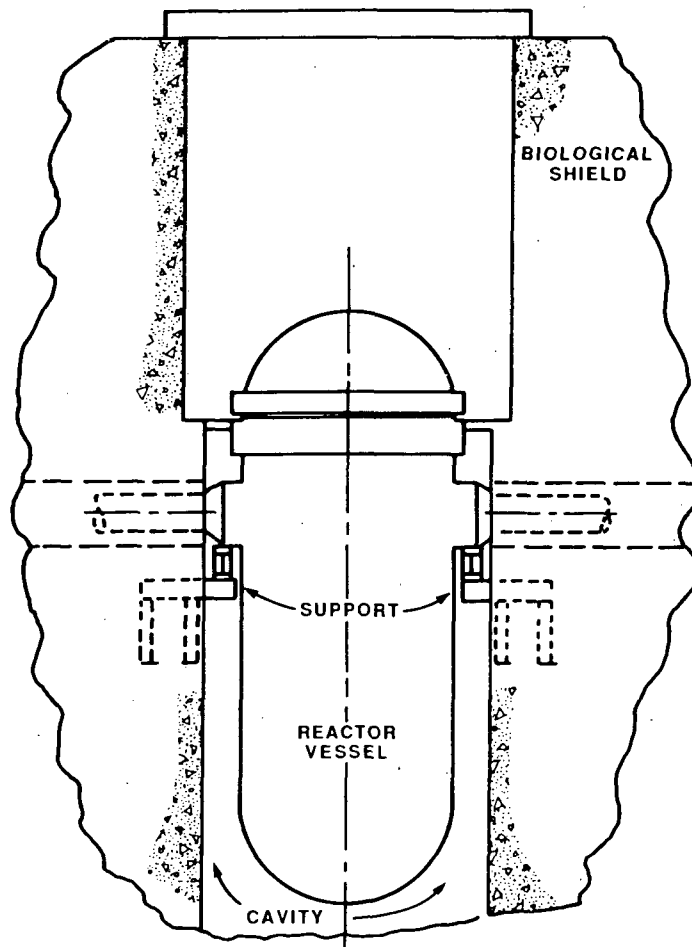


Fig. 1. PWR vessel support located in cavity between the vessel and biological shield.

inelastic scattering in the PWR vessel wall); thus, correlating the MTR embrittlement data with fast neutron fluence  $\phi$  for  $E > 1.0$  MeV resulted in an underestimation of  $\Delta$ NDTT for supports in the cavity. As a part of the more recent study discussed here, the MTR data were correlated with displacements per atom (dpa) for  $E > 0.1$  MeV, and  $\Delta$ NDTT values of  $\leq 40^\circ\text{C}$  were calculated for 32 EFY for supports located in the cavity at midheight of the core.

Several studies pertaining to radiation damage of PWR vessel supports<sup>3-6</sup> were conducted between 1978 and 1987, and during this period, presumably there was no reason to believe that low-temperature ( $<100^\circ\text{C}$ ) MTR embrittlement data, correlated with dpa ( $E > 0.1$  MeV), were not appropriate for evaluating embrittlement of PWR vessel supports. However, late in 1986, data from the High Flux Isotope Reactor (HFIR)<sup>7</sup> vessel surveillance program<sup>8,9</sup> indicated that the embrittlement rates of the several vessel materials (A212-B, A350-LF3, A105-II) were substantially greater than anticipated on the basis of MTR data.<sup>9</sup> Further evaluation of the HFIR data suggested that a fluence rate effect was responsible for the apparent discrepancy because the fast neutron

flux in the MTR that provided the design data<sup>1</sup> was  $\sim 10^5$  times that in the HFIR vessel, while the small differences in the fast neutron energy spectra were accounted for by correlating the data with dpa ( $E > 0.1$  MeV), and the irradiation temperatures were nearly the same (50 to 100°C). As a result of this new information, the Nuclear Regulatory Commission (NRC) requested that the Oak Ridge National Laboratory (ORNL) evaluate the impact of the apparent embrittlement rate effect on the integrity of light-water-reactor (LWR) vessel supports.

The purpose of the initial study was to provide a preliminary indication of whether the integrity of reactor vessel supports is likely to be challenged by radiation-induced embrittlement before 32 EFPY. Because of the diversity in support designs, specific-plant evaluations were undertaken; because of the urgency associated with the preliminary study, only readily available data for these plants were used. This factor and others have resulted in some inconsistencies in the evaluations of the plants considered. Even so, the study satisfies its intended purpose.

The scope of the ORNL evaluation included

1. correlation of the HFIR data for application to the evaluation of LWR vessel supports,
2. a survey and cursory evaluation of all U.S. LWR vessel support designs,
3. selection of two plants for specific-plant evaluation, and
4. a specific-plant evaluation of both plants to determine critical flaw sizes for their vessel supports.

The two plants selected for specific-plant evaluation were Trojan (Portland General Electric) and Turkey Point Unit 3 (Florida Power and Light); both are PWR plants and have vessel supports similar to that shown in Fig. 1. Westinghouse was the nuclear-steam-supply-system (NSSS) designer and Bechtel the architect-engineer for both plants. The utilities and their contractors have been very cooperative in providing, where possible, design data required for the ORNL study.

Over the course of several months, two sets of radiation damage trend curves ( $\Delta$ NDTT vs dpa), based on the HFIR vessel surveillance data, were developed. Also 32-EFPY  $\Delta$ NDTT values were calculated for "typical" General Electric (GE), Babcock and Wilcox (B&W), Westinghouse (W), and Combustion Engineering (CE) plants, assuming that a critical portion of a support existed in the cavity at midheight of the core. The results, presented in Table 1, indicate much larger shifts in NDTT based on the HFIR data than on the MTR data.

Many vessel supports are not located at midheight of the core and thus experience smaller shifts in NDTT than those indicated in Table 1. For instance, all but one of the GE boiling-water-reactor (BWR) vessels and all but one of the B&W PWR vessels are supported by a skirt at the bottom of the vessel where the fluxes are much less. However,  $\sim 25\%$  of the PWR vessel supports are exposed to the peak flux, and many others are exposed to fluxes within a factor of one-half of the peak.

Radiation embrittlement is of concern because it increases the potential for propagation of flaws in the support structures. In this study the potential for propagation of flaws was evaluated using linear-elastic fracture mechanics, which requires knowledge of the stresses in the structure and the

Table 1. Vessel support ANDTT values corresponding to 32 EFPY and midheight of core ("typical" LWR plants)

NSSS designer (type reactor)	$\phi$ (E > 1 MeV) (neutrons/cm <sup>2</sup> ·s)	dpa rate (E > 0.1 MeV) (s <sup>-1</sup> )	dpa	ANDTT (°C)		
				MTR data	HFIR data	
					A <sup>a</sup>	B <sup>a</sup>
GE (BWR)	$2.9 \times 10^7$	$5.8 \times 10^{-14}$	$5.8 \times 10^{-5}$	0	b	b
B&W (PWR)	$2.0 \times 10^8$	$6.1 \times 10^{-13}$	$6.1 \times 10^{-4}$	11	100	72
W (PWR)	$5.9 \times 10^8$	$3.9 \times 10^{-12}$	$3.9 \times 10^{-3}$	28	133	122
CE (PWR)	$1.8 \times 10^9$	$4.5 \times 10^{-12}$	$4.5 \times 10^{-3}$	39	139	122

<sup>a</sup>ANDTT vs dpa (E > 0.1 MeV) correlations A (Fig. 8) and B (Fig. 9).

<sup>b</sup>ANDTT not estimated for dpa < 10<sup>-4</sup>.

fracture toughness of the material. The output of the fracture-mechanics analysis for this study is the critical flaw size, that is, the size of the smallest flaw that will propagate under a given set of assumed conditions and result in failure of the support. If the critical flaw size is small enough that the critical flaw is likely to exist, then the frequency of failure is equal to the frequency of application of the assumed load. A determination of the probability of the existence of flaws was not, however, included in the scope of this study.

Loading conditions were provided by the utilities and included large- and small-break loss-of-coolant accidents (LBLOCA and SBLOCA), seismic loading, thermal loading, and deadweight loading. Dynamic loading data were available for Trojan but not for Turkey Point.

Several uncertainties exist in the analysis. Those judged to be the most significant are the radiation-damage trend curve deduced from the HFIR surveillance data, the fracture toughness of the unirradiated material, the initial NDTT of the material, and the normal operating temperature of the structure at the critical location. These uncertainties result in a wide variation in calculated critical flaw size. The critical flaw size is, of course, also dependent on the applied load and the flaw location and type. Critical flaw sizes (depth/surface length) were calculated for a reasonable range of conditions, and 32-EFPY "best-estimate" values for the most sensitive flaw location and type and for the most severe credible loading conditions are 10/64 mm for Trojan and 8/15 mm for Turkey Point (Table 2). Corresponding values for late 1988 are 23/406 and 8/15 mm, respectively.

For both plants the flaw locations resulting in the smallest critical flaw depths were on the upper flange of the horizontal cantilever beam at points within the concrete biological shield. The best-estimate values of T - NDTT at these locations are -7 and -14°C for 32 EFPY and -7 and 16°C for late 1988 for Trojan and Turkey Point, respectively. (The indicated invariance with time of the value for Trojan is the result of a shift in the critical location of the flaw to a position of lower neutron flux.)

Table 2. Summary of best-estimate minimum critical  
 flaw sizes and values of T - NDTT for  
 Trojan and Turkey Point vessel  
 supports (cantilever beam)

Plant	EFPY	T - NDTT (°C)		Critical flaw size (depth x surface length) (mm)		
		a	b	LBLOCA	SBLOCA	Seismic (SSE)
Trojan	7.5 <sup>c</sup>	-7	-7		23 x 406	27 x 406
	32	-7	-66		11 x 64	30 x 64
Turkey Point	11.8 <sup>c</sup>	16	6	8 x 15		25 x 51
	32	-14	-14	8 x 15		23 x 46

<sup>a</sup>At location of minimum-depth critical flaw.

<sup>b</sup>At inner surface of biological shield.

<sup>c</sup>Late 1988.

The propagation of flaws by low-cycle fatigue was calculated to be negligible. Thus, if corrosion is not a viable means of growing flaws to critical size or larger, flaws of critical size or larger would have to be present at the time of fabrication.

#### HFIR VESSEL SURVEILLANCE DATA

HFIR<sup>7</sup> is a high-performance, light-water-cooled, low-temperature (50 to 70°C), research reactor at ORNL that began operation in 1965. Its stainless-steel-clad, carbon-steel, pressure vessel (Fig. 2) was designed for 20 EFPY, and a surveillance program was maintained to monitor the actual radiation-induced embrittlement.<sup>8</sup> Late in 1986, a reevaluation of the integrity of the vessel was commenced in an effort to extend the permissible life.<sup>9</sup> The surveillance data, which had not been carefully examined since 1974, indicated that the embrittlement rate was significantly greater than had been anticipated on the basis of data obtained in the early 1960s from MTRs.<sup>10</sup> The neutron energy spectra and the irradiation temperatures for the HFIR surveillance specimens and for MTR specimens were believed to be essentially the same, and the materials were similar; however, the fast neutron flux ( $\phi$ ) in the MTRs was  $\sim 10^5$  times that in the HFIR specimens. Thus, it appeared that the lower flux in HFIR was responsible for the relatively large amount of embrittlement per neutron; that is, there appeared to be a negative fluence-rate effect.

The portions of the HFIR vessel that are subjected to the highest fast-neutron fluxes are close to the beam tubes (Fig. 2) because the beam tubes displace beryllium (reflector) and water that otherwise constitute shielding for the vessel wall. Thus, both shell material (A212-B) and beam-tube nozzle

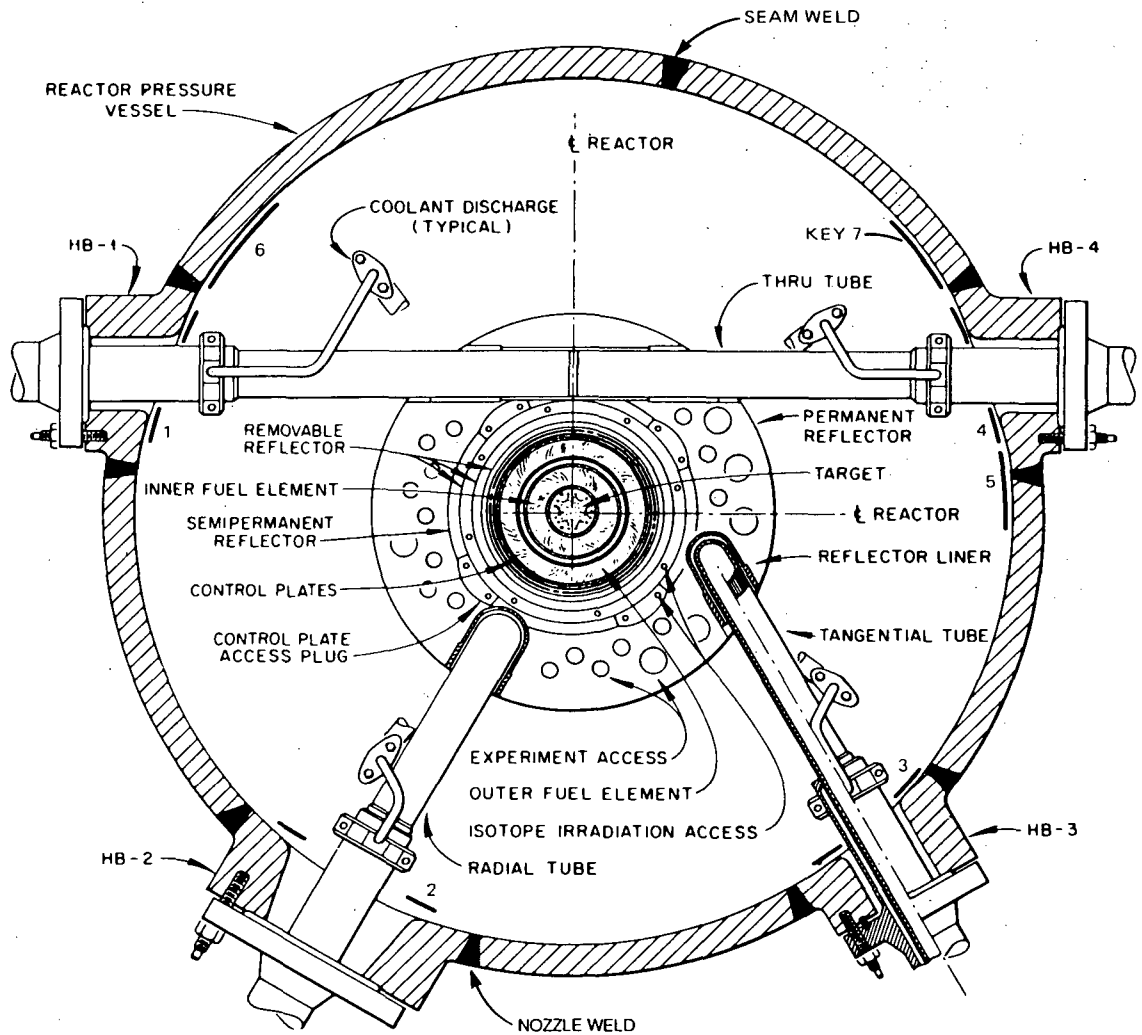


Fig. 2. Cross section of HFIR vessel and core at midheight of core, indicating locations of vessel surveillance specimens (keys 1-7).

materials (A105-II and A350-LF3) were included in the HFIR vessel materials surveillance program, and the surveillance capsules, each containing three Charpy V-notch (CVN) specimens and a flux monitor, were located close to the beam tubes (keys 1-7, Fig. 2).

Surveillance specimens of A212-B were removed for testing after 15.0 and 17.5 EFPY, and A105-II and A350-LF3 specimens were removed after 2.3, 6.5, 15.0, and 17.5 EFPY. The corresponding  $\Delta$ NDTT data are presented in Table 3;<sup>10</sup> in Figs. 3 and 4 [ $\Delta$ NDTT vs  $\phi$  ( $E > 1.0$  MeV)] these data are compared with the MTR data<sup>1</sup> available at the time the vessel was designed. If it is assumed that spectrum and chemistry effects are not responsible for the incongruity of the several sets of data, the comparison indicates a fluence-rate effect.

To evaluate the effects of possible differences in chemistry and fast spectrum, HFIR archive A212-B material was recently irradiated in the Oak Ridge Research Reactor (ORR), a typical high-flux, low-temperature MTR, and

Table 3. Summary of irradiation effect for selected HFIR pressure vessel materials.

Material	Unirradiated NDT [°C (°F)]	EPFY	$\Delta$ NDT [°C (°F)]	$\phi$ (neutrons/cm <sup>2</sup> ·s) <sup>a</sup>	dpa/s	$\phi$ (neutrons/cm <sup>2</sup> ) <sup>a</sup>	dpa
<i>ORR irradiations</i>							
A212-B (LT)	-21 (-5)		56 (101)	$9.59 \times 10^{12}$	$1.34 \times 10^{-8}$	$2.43 \times 10^{18}$	$3.39 \times 10^{-3}$
A212-B (TL)	-12 (10)		47 (85)	$9.59 \times 10^{12}$	$1.34 \times 10^{-8}$	$2.43 \times 10^{18}$	$3.39 \times 10^{-3}$
A212-B (TS)	-21 (-5)		56 (101)	$9.59 \times 10^{12}$	$1.34 \times 10^{-8}$	$2.43 \times 10^{18}$	$3.39 \times 10^{-3}$
A212-B (EGCR) <sup>b</sup>	0 (32)		10 (18)	$1.05 \times 10^{13}$	$1.46 \times 10^{-8}$	$1.54 \times 10^{17}$	$2.14 \times 10^{-4}$
A212-B (EGCR) <sup>b</sup>	0 (32)		103 (185)	$2 \times 10^{12}$	$4.8 \times 10^{-9}$	$9.8 \times 10^{18}$	$2.4 \times 10^{-2}$
<i>HFIR surveillance</i>							
A212-B (LT)	-21 (-5)	15.01	11 (20)	$4 \times 10^7$		$1.89 \times 10^{16}$	
		15.01	29 (52)	$2.43 \times 10^8$	$3.66 \times 10^{-13}$	$1.15 \times 10^{17}$	$1.73 \times 10^{-4}$
		17.53	42 (75)	$2.43 \times 10^8$	$3.66 \times 10^{-13}$	$1.34 \times 10^{17}$	$2.02 \times 10^{-4}$
A105-II	-62 (-80)	2.34	10 (18)	$4.66 \times 10^8$	$6.92 \times 10^{-13}$	$3.44 \times 10^{16}$	$5.12 \times 10^{-5}$
		6.45	17 (30)	$4.89 \times 10^8$	$7.26 \times 10^{-13}$	$9.9 \times 10^{16}$	$1.48 \times 10^{-4}$
		15.01	33 (60)	$4.89 \times 10^8$	$7.26 \times 10^{-13}$	$2.31 \times 10^{17}$	$3.44 \times 10^{-4}$
		15.01	33 (60)	$3.35 \times 10^8$	$4.89 \times 10^{-13}$	$1.85 \times 10^{17}$	$2.70 \times 10^{-4}$
		17.53	35 (63)	$7.27 \times 10^8$	$1.08 \times 10^{-12}$	$4.01 \times 10^{17}$	$5.97 \times 10^{-4}$
A350-LF3 (key 2)	-79 (-110)	2.34	14 (26)	$1.1 \times 10^9$	$1.58 \times 10^{-12}$	$8.20 \times 10^{16}$	$1.16 \times 10^{-4}$
		6.45	29 (52)	$1.1 \times 10^9$	$1.58 \times 10^{-12}$	$2.26 \times 10^{17}$	$3.21 \times 10^{-4}$
		15.01	56 (100)	$1.1 \times 10^9$	$1.58 \times 10^{-12}$	$5.26 \times 10^{17}$	$7.47 \times 10^{-4}$
		17.53	66 (118)	$1.1 \times 10^9$	$1.58 \times 10^{-12}$	$6.14 \times 10^{17}$	$8.73 \times 10^{-4}$
A350-LF3 (key 3)	-62 (-80)	2.34	19 (34)	$1.29 \times 10^9$	$1.85 \times 10^{-12}$	$9.55 \times 10^{16}$	$1.36 \times 10^{-4}$
		6.45	33 (60)	$1.40 \times 10^9$	$2.01 \times 10^{-12}$	$2.84 \times 10^{17}$	$4.09 \times 10^{-4}$
		15.01	54 (97)	$1.03 \times 10^9$	$1.48 \times 10^{-12}$	$4.88 \times 10^{17}$	$7.01 \times 10^{-4}$
		17.53	64 (115)	$1.29 \times 10^9$	$1.85 \times 10^{-12}$	$7.12 \times 10^{17}$	$1.02 \times 10^{-3}$

<sup>a</sup>E > 1 MeV.

<sup>b</sup>Material from previous ORNL EGCR study.

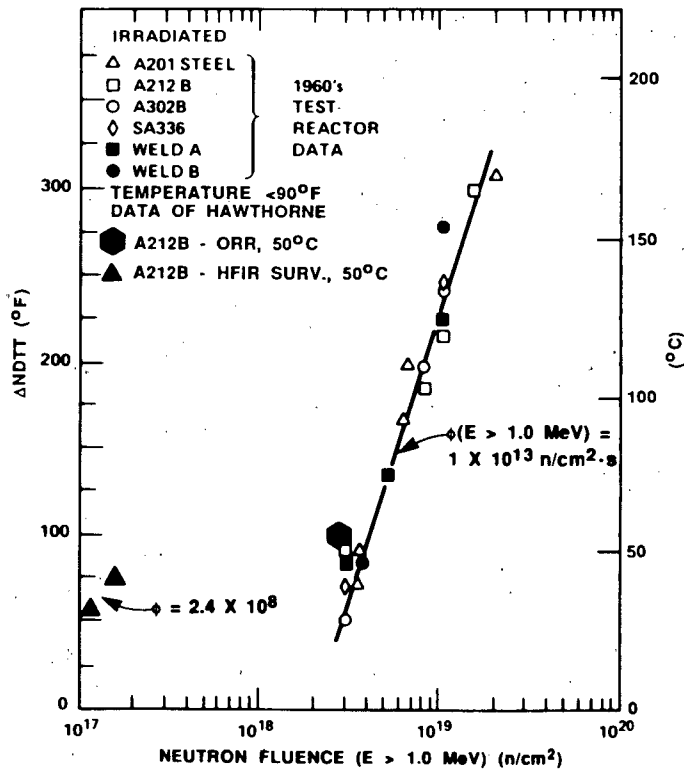


Fig. 3. Increase in NDTT with fluence (E > 1.0 MeV) for A212-B irradiated in HFIR (vessel surveillance positions) and ORR, and for several similar materials irradiated in MTR (Hawthorne).

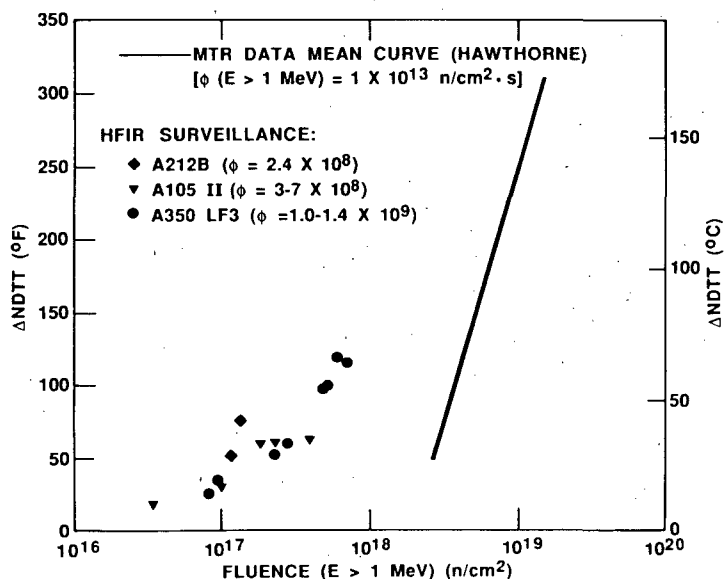


Fig. 4. Increase in NDTT with fluence ( $E > 1$  MeV) for irradiations in HFIR (vessel surveillance positions) and MTR (Hawthorne).

the HFIR and ORR A212-B data were plotted as a function of dpa for  $E > 0.1$  MeV (Fig. 5)\* as well as a function of  $\phi$  for  $E > 1.0$  MeV (Figs. 3 and 4). (The ORR data and values of dpa corresponding to both the HFIR and ORR data are included in Table 3.) Figure 3 shows the A212-B archive material (irradiated

\*To obtain the MTR curve, it was assumed that the calculated spectrum for the ORR was appropriate for the "MTR" data.

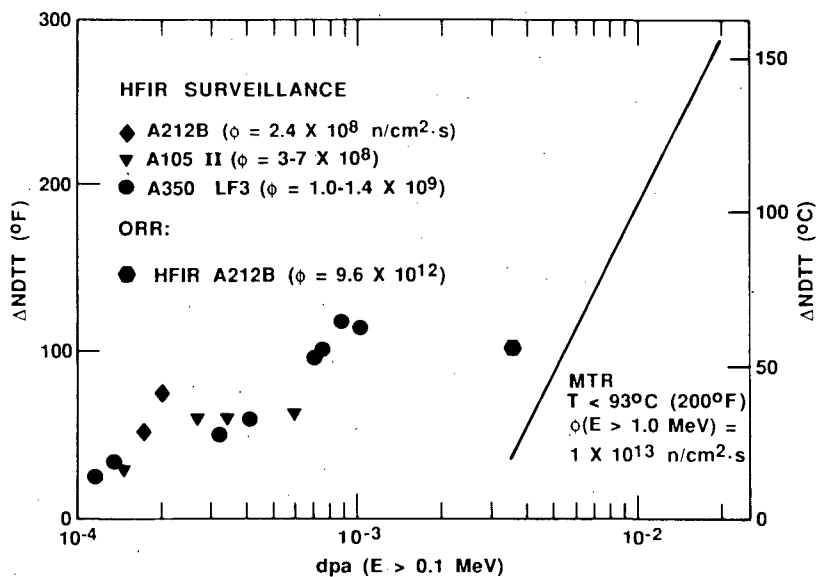


Fig. 5. Increase in NDTT with dpa for irradiations in HFIR (vessel surveillance positions), ORR, and MTR (Hawthorne).

in the ORR) to be consistent with the MTR data, implying that the chemistry of the HFIR A212-B material is not significantly different from that corresponding to the MTR data (assuming that a difference in spectrum does not compensate for a difference in chemistry).

Figure 5 shows that when the HFIR and MTR data are plotted as a function of dpa ( $E > 0.1$  MeV), there is still evidence of a significant rate effect. Thus, the small differences in the HFIR and MTR fast spectra are not responsible for the incongruity in Figs. 3 and 4.

If an embrittlement rate effect exists, the total reaction rate associated with embrittlement should probably be accounted for when applying the HFIR data to a situation involving a different fast spectrum. This can be accomplished by correlating NDTT with dpa rate rather than  $\phi$ , integrating the dpa rate over all energies that contribute significantly to embrittlement.

In the previous discussion, the only spectral variations considered were those above 0.1 MeV. However, Nanstad et al.<sup>11</sup> have suggested that lower energy neutrons may be making a significant contribution and that there might be significant differences in the low-energy spectra of HFIR and the MTRs. Multigroup transport calculations performed at ORNL<sup>12</sup> indicate that the HFIR spectrum above 1.0 MeV is somewhat harder than that in the ORR; the epithermal flux is a smaller fraction of the total nonthermal flux; and  $\phi_{th}/\phi_f$ , the ratio of the thermal-to-fast ( $E > 1.0$  MeV), is greater in HFIR (~50) than in ORR (~8). Thus, the trends in Figs. 3 and 4 are not the result of differences in the epithermal fluxes, but the comparison of  $\phi_{th}/\phi_f$  suggests a possible thermal-flux effect. In addition, Alberman et al.<sup>13</sup> irradiated A537 at 60°C in a spectrum with  $\phi_{th}/\phi_f \cong 1000$  and found that >70% of the embrittlement was due to thermal neutrons. Thus, perhaps thermal-neutron embrittlement is at least in part responsible for what was otherwise believed to be a rate effect.<sup>14</sup> At this time, however, there are not enough data to support this contention.

#### APPLICATION OF HFIR DATA TO VESSEL SUPPORT EVALUATION

Soon after the HFIR surveillance data were evaluated in late 1986, it became apparent that the indicated embrittlement rate effect might apply to the supports of some LWR vessels because fast neutron fluxes, irradiation temperatures, and materials were thought to be similar. Temperatures of the supports range from ~250°C at the point of contact with the vessel to <65°C at a point of contact with the biological shield (65°C is the normal maximum permissible operating temperature of the concrete biological shield). The temperature of the HFIR vessel and surveillance specimens is ~50°C. Thus, presumably a portion of the support operates at a temperature close to that of the HFIR vessel.

Multigroup neutron transport calculations were performed recently for the vessel wall and the cavity of one BWR and three PWRs,<sup>15,16</sup> and Table 4 summarizes the fast fluxes ( $E > 1.0$  MeV) [as well as dpa rate ( $E > 0.1$  MeV)] for the LWR cavities and the HFIR surveillance specimens (also, see Table 3). It is apparent that  $\phi$  ( $E > 1.0$  MeV) values for the PWR cavities is similar to those for the HFIR surveillance specimens ( $10^8$  to  $10^9$  neutrons/cm<sup>2</sup>·s), while that for the BWR is much less.

Table 4. Summary of fast neutron fluxes ( $E > 0.1$  MeV) for LWR cavities and HFIR surveillance specimens

Reactor	$\phi(E > 1.0 \text{ MeV})$ (neutrons/cm <sup>2</sup> ·s)	dpa rate ( $E > 0.1 \text{ MeV}$ ) (s <sup>-1</sup> )
HFIR	$2.4 \times 10^8 - 1.4 \times 10^9$	$3.7 \times 10^{-13} - 2.0 \times 10^{-12}$
GE (BWR)	$2.8 \times 10^7$	$6.3 \times 10^{-14}$
B&W (PWR)	$2.1 \times 10^8$	$6.8 \times 10^{-13}$
W (PWR)	$6.1 \times 10^8$	$4.7 \times 10^{-12}$
CE (PWR)	$1.8 \times 10^9$	$5.0 \times 10^{-12}$

Table 5 summarizes LWR fast-flux data for  $E > 1.0$  MeV (group A) and  $0.1 \leq E \leq 1.0$  MeV (group B). These data indicate that the ratio of group A to group B fluxes is much less in the cavity than it is at the inner surface of the vessel wall (the result of inelastic scattering in the vessel wall). Thus, the fast flux ( $E > 0.1$  MeV) in the LWR cavity is much softer than that at the location of the HFIR surveillance specimens. As suggested in the last section, to account for this difference in energy spectrum when applying the HFIR data to the evaluation of the supports in the cavity, the  $\Delta$ NDTT data can be correlated with dpa rate and dpa for  $E > 0.1$  MeV instead of  $\phi$  and  $\Phi$  for  $E > 1.0$  MeV, the assumption being made that most of the neutrons contributing to embrittlement have energies  $> 0.1$  MeV. A comparison of dpa rate ( $E > 0.1$  MeV) for HFIR and the LWR cavities (Table 4) indicates that the maximum cavity dpa rate ( $5.0 \times 10^{-12} \text{ s}^{-1}$ ) is about twice the maximum HFIR dpa rate ( $2.0 \times 10^{-12} \text{ s}^{-1}$ ), while the maximum fast-flux values ( $E > 1.0$  MeV) are about the same. This result indicates that some extrapolation of the HFIR data is necessary.

Application of the HFIR data to the LWR vessel supports requires extrapolation with regard to both dpa rate and dpa. Thus, correlations between  $\Delta$ NDTT, dpa rate, and dpa are required. Two different correlations between  $\Delta$ NDTT and dpa are proposed and are shown in Figs. 6 and 7. Figure 6 was

Table 5. Summary of calculated fluxes for "typical" BWR and PWR vessels and cavities

NSSS designer (type reactor)	Neutron flux (neutrons/cm <sup>2</sup> ·s)					
	Vessel inner surface			Cavity		
	A <sup>a</sup>	B <sup>a</sup>	A/B	A	B	A/B
GE (BWR)	$6.3 \times 10^8$	$3.5 \times 10^8$	1.8	$2.8 \times 10^7$	$1.1 \times 10^8$	0.3
B&W (PWR)	$5.8 \times 10^9$	$7.4 \times 10^9$	0.8	$2.1 \times 10^8$	$1.6 \times 10^9$	0.1
W (PWR)	$2.6 \times 10^{10}$	$2.7 \times 10^{10}$	1.0	$6.1 \times 10^8$	$1.3 \times 10^{10}$	0.5
CE (PWR)	$4.6 \times 10^{10}$	$5.6 \times 10^{10}$	0.8	$1.8 \times 10^9$	$1.0 \times 10^{10}$	0.2

<sup>a</sup>A:  $E > 1.0$  MeV  
<sup>a</sup>B:  $0.1 \leq E \leq 1.0$  MeV

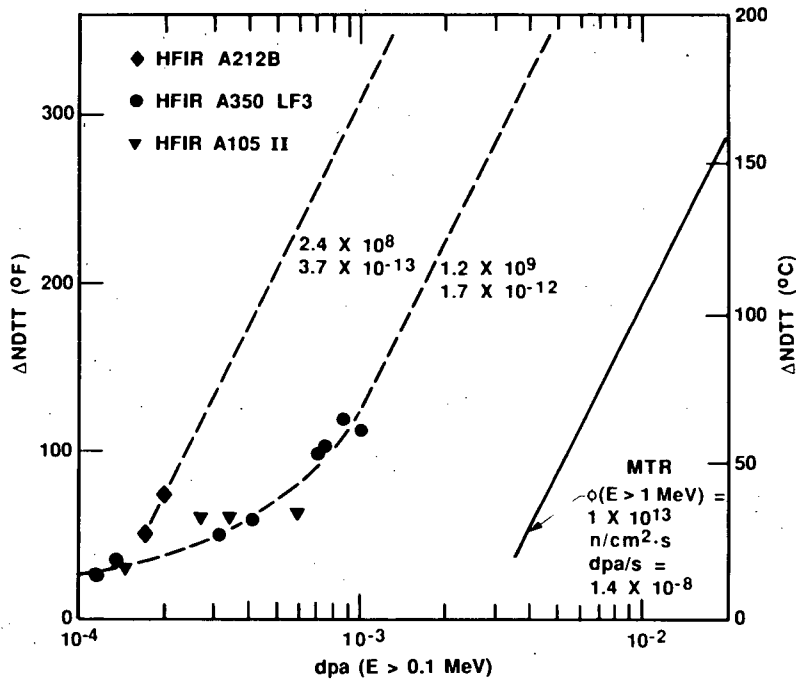


Fig. 6. Method for extrapolating HFIR vessel surveillance  $\Delta$ NDTT vs dpa ( $E > 0.1$  MeV) data, assuming  $\Delta$ NDTT =  $81 \ln(dpa/dpa_0)$ , °C, for  $\Delta$ NDTT  $> 30$  °C.

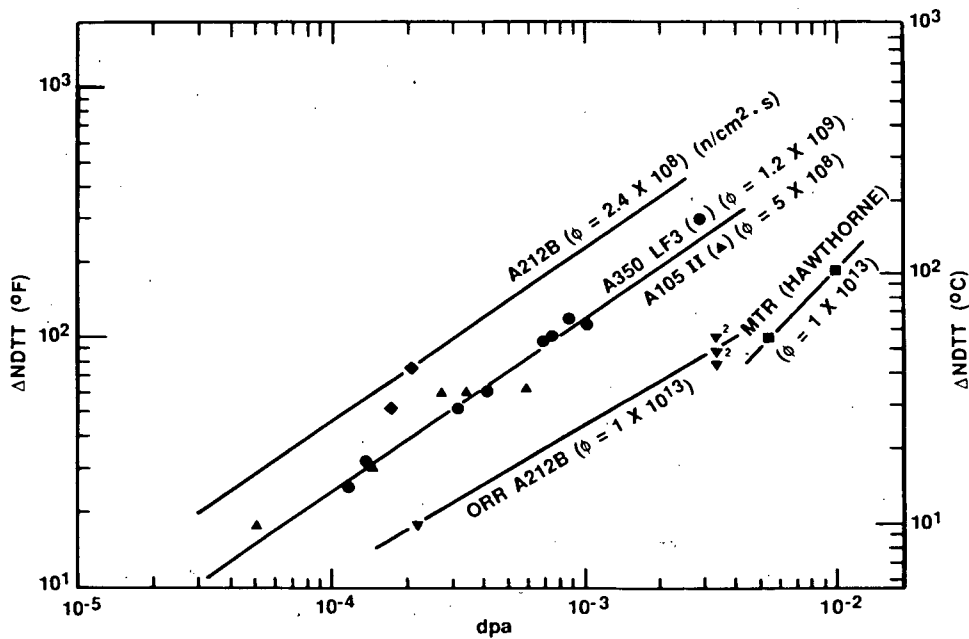


Fig. 7. Method for extrapolating HFIR vessel surveillance  $\Delta$ NDTT vs dpa ( $E > 0.1$  MeV) data, assuming  $\Delta$ NDTT  $\propto dpa^{0.688}$  for  $10 \leq \Delta$ NDTT  $\leq 150$  °C.

created by drawing separate straight-line curves through the maximum  $\Delta$ NDTT data points, for the A212-B and A350-LF3 HFIR surveillance materials, parallel to the MTR curve, which Hawthorne constructed as a straight line on semilog paper.<sup>1</sup>

The other correlation (Fig. 7) was obtained by first plotting the HFIR A350-LF3 data on log-log paper and constructing a best-fit, straight-line curve. Next, the ORR A212-B data obtained in connection with the recent HFIR vessel study<sup>9</sup> and a much earlier study<sup>17</sup> (Table 3) of the vessel for the experimental gas-cooled reactor (EGCR) at ORNL were plotted, and a straight line was constructed. Finally, the MTR data<sup>1</sup> above  $\Delta$ NDTT = 40°C were plotted and a straight line was constructed. The indication is that the relatively high fast-flux data (ORR and MTR) are essentially parallel to the HFIR A350-LF3 data. This finding was used as justification for constructing a curve through the HFIR A212-B data points parallel to the A350-LF3 curve. The upper A212-B point was used as a conservative measure.

A comparison of the correlations represented by Figs. 6 and 7 (upper two curves) shows that Fig. 7 predicts less of a rate effect between  $\phi(E > 1.0 \text{ MeV}) = 2.4 \times 10^8$  and  $1.2 \times 10^9$  neutrons/cm<sup>2</sup>·s. In this study, the authors have considered the correlation implied by Fig. 7 to provide the more accurate estimate of  $\Delta$ NDTT for the LWR vessel supports.

One might argue that the small difference in fast fluxes corresponding to the HFIR A212-B and A350-LF3 irradiations ( $2.4 \times 10^8$  and  $1.2 \times 10^9$  neutrons/cm<sup>2</sup>·s) relative to the factor of  $\sim 10^5$  between HFIR and the MTRs ( $\sim 10^8$  and  $10^{13}$  neutrons/cm<sup>2</sup>·s) would not permit distinguishing between the two HFIR fluxes with regard to establishing a rate effect. However, Hamilton<sup>18</sup> recently presented data indicating that, for an irradiation temperature at 100°C, there was essentially no rate effect in the fast flux ( $E > 1.0 \text{ MeV}$ ) range of  $1 \times 10^{10}$  to  $3 \times 10^{13}$  neutrons/cm<sup>2</sup>·s. This finding indicates that the  $\Delta$ NDTT differences observed between HFIR and the MTRs are associated with a rate effect below a fluence rate of  $\sim 1 \times 10^{10}$  neutrons/cm<sup>2</sup>·s. Thus, for this study, the observed differences in  $\Delta$ NDTT for fluxes of  $2.4 \times 10^8$  and  $1.2 \times 10^9$  neutrons/cm<sup>2</sup>·s were considered to be real. There is, however, an inconsistency with regard to the A105-II data: although these data correspond to an intermediate flux level ( $3\text{--}7 \times 10^8$  neutrons/cm<sup>2</sup>·s), they tend to coincide with the A350-LF3 data, which correspond to a higher flux ( $1.2 \times 10^9$  neutrons/cm<sup>2</sup>·s). Perhaps this implies that a rate effect is not discernible within the flux range of  $2.4 \times 10^8$  to  $1.2 \times 10^9$  neutrons/cm<sup>2</sup>·s. However, for this study, the A105-II data were discounted insofar as establishing a rate effect.

Extrapolation and interpolation of the HFIR data for application to the support study were accomplished by assuming  $\text{dpa} \propto (\text{dpa rate})^\eta$  for a given value of  $\Delta$ NDTT. Corresponding values of dpa, dpa rate, and  $\Delta$ NDTT were taken from Figs. 6 and 7 to obtain the log-log plots in Figs. 8 and 9, respectively. As mentioned above, Fig. 7 and thus Fig. 9 are believed to be the more accurate representation of the trends. However, it must also be emphasized that in either case the values of  $\Delta$ NDTT > 40°C and values of dpa rate outside the range  $3.7 \times 10^{-13}$  to  $1.7 \times 10^{-12} \text{ s}^{-1}$  represent extrapolations of the HFIR data.

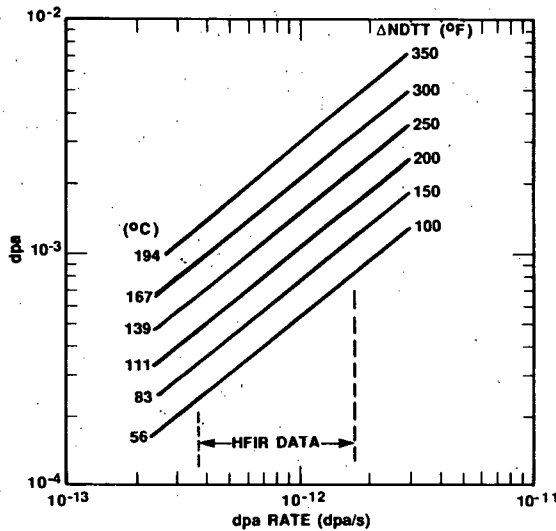


Fig. 8. dpa ( $E > 0.1$  MeV) vs dpa rate for specific values of  $\Delta$ NDTT (correlation A).

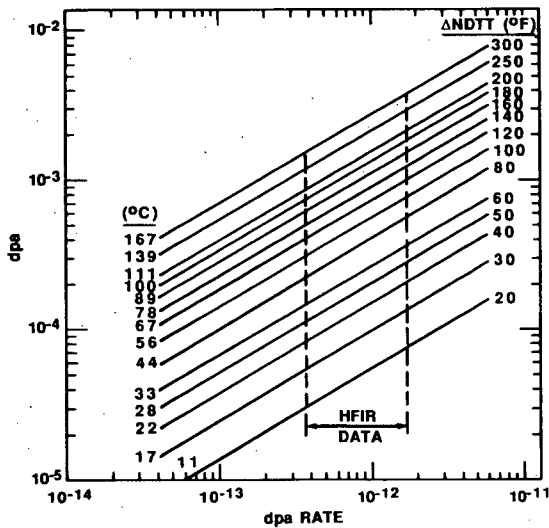


Fig. 9. dpa ( $E > 0.1$  MeV) vs dpa rate for specific values of  $\Delta$ NDTT (correlation B).

#### SELECTION OF LWR PLANTS FOR SPECIFIC-PLANT ANALYSIS

A survey and cursory evaluation was made of all LWR vessel supports using final safety analysis reports (FSARs) and information provided in two previous related studies by Hopkins<sup>5</sup> and Knorovski et al.<sup>3</sup> This information was then used in the selection of two LWR plants that would be subjected to specific-plant evaluation of the impact of radiation-induced embrittlement on the

integrity of the reactor vessel supports. Criteria established for selection of the two plants follow.

The plants should be among those having a relatively high potential for failure of vessel supports as a result of radiation-enhanced propagation of flaws. Compliance with this condition was judged on the basis of the following considerations:

1. A potentially critical portion of the support should be exposed to the relatively high-neutron-flux regions of the cavity (from midheight to the end of the core).
2. The support material should have a relatively high potential for radiation embrittlement.
3. The portion of the support within the high-flux region should be subjected to relatively high tensile stress. Primary-load tensile stresses are of particular concern, but secondary tensile stresses (thermal and residual) can also have a significant effect.
4. The potentially critical portion of the support should have a relatively high potential for flaws of critical size.

Information in Table 4 indicates that the cavity fluxes for the BWRs are much less than those for PWRs, and BWR vessels are supported on skirts that are far removed from the bottom end of the core. (Big Rock Point is an exception but was not considered because of its small size.) Thus, BWRs were excluded from consideration. All but one of the B&W PWRs are supported on skirts, and they also were excluded from consideration.

About 10% of the PWR vessels are supported on long columns and another 10% on shield tanks that extend the length of the core and thus are exposed to the maximum fluence. At the outset of this study the PWR NSSS vendors and the Electric Power Research Institute (EPRI) were contacted informally and given the opportunity to contribute to the study. CE and EPRI responded (informally) with updated analyses of the long columns (CE) and shield tanks (EPRI, Stone and Webster), considering the HFIR surveillance data. The preliminary indication was that critical flaw sizes corresponding to 32 EPY were "acceptably" large. Thus, these supports also were excluded from consideration in this study.

The remaining PWR vessel supports fall in a category referred to as "short column" that includes, as one extreme, very short, stubby supports (columns) that rest directly on the concrete biological shield at an elevation above the upper end of the core, where the flux is relatively low (Fig. 10); the other extreme includes columns that extend to about midheight of the core and rest on steel cantilever beams. Only Trojan and perhaps Davis Besse are of this latter type, while Turkey Point Units 3 and 4 (identical supports) are similar to Trojan but with the steel cantilever beam located closer to the top of the core, where the flux is somewhat less. It appeared that of all those plants in the short-column category, Trojan and Turkey Point have the greatest potential for fracture-related failure of the vessel supports. Both designs include cantilever beams in high-flux regions of the cavity, and both cantilevers are stressed in tension by primary loads.

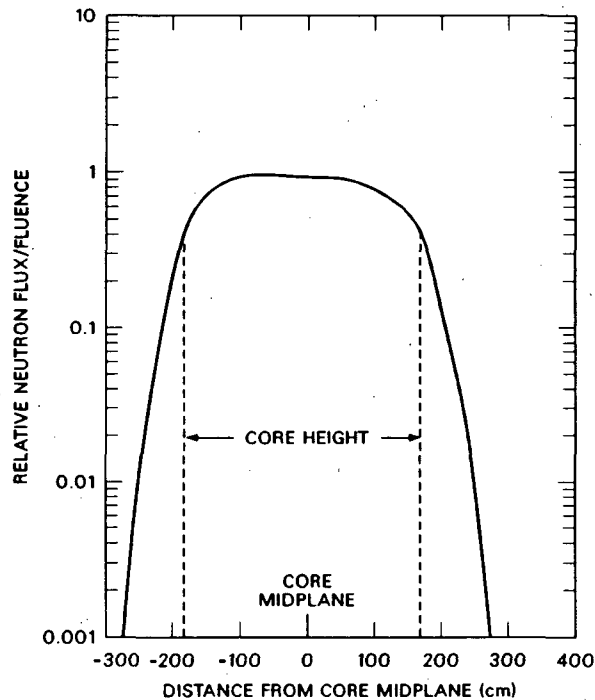


Fig. 10. "Typical" relative axial variation of fast neutron ( $E > 1.0$  MeV) flux and fluence within pressure vessel wall.

## EVALUATION OF VESSEL SUPPORTS FOR TROJAN AND TURKEY POINT

### Scope

The scope of the specific-plant evaluation consisted of (1) acquisition of design and operating data, including loads and loading rates, from the utilities; (2) a detailed stress analysis of the beam; (3) a determination of fracture properties based on published data and HFIR surveillance data; and (4) a parametric fracture analysis to determine a range of critical flaw sizes.

### Support Design

The Trojan vessel is supported at four main coolant-line nozzle locations. Each support structure is comprised of an upper component (shear frame) that resists horizontal loads, a lower component (two cantilever beams) that resists vertical loads, and two pinned columns that transfer vertical loads from a vessel nozzle to the lower component, which is located at an elevation just below midheight of the core (Fig. 11). The Turkey Point vessel is supported at six nozzle locations. At each of these locations horizontal and vertical loads are transferred through rollers and a lateral restraint device to a girder that is bolted to the ends of three cantilever beams, which are at an elevation equal to the upper end of the core (Fig. 11). For both

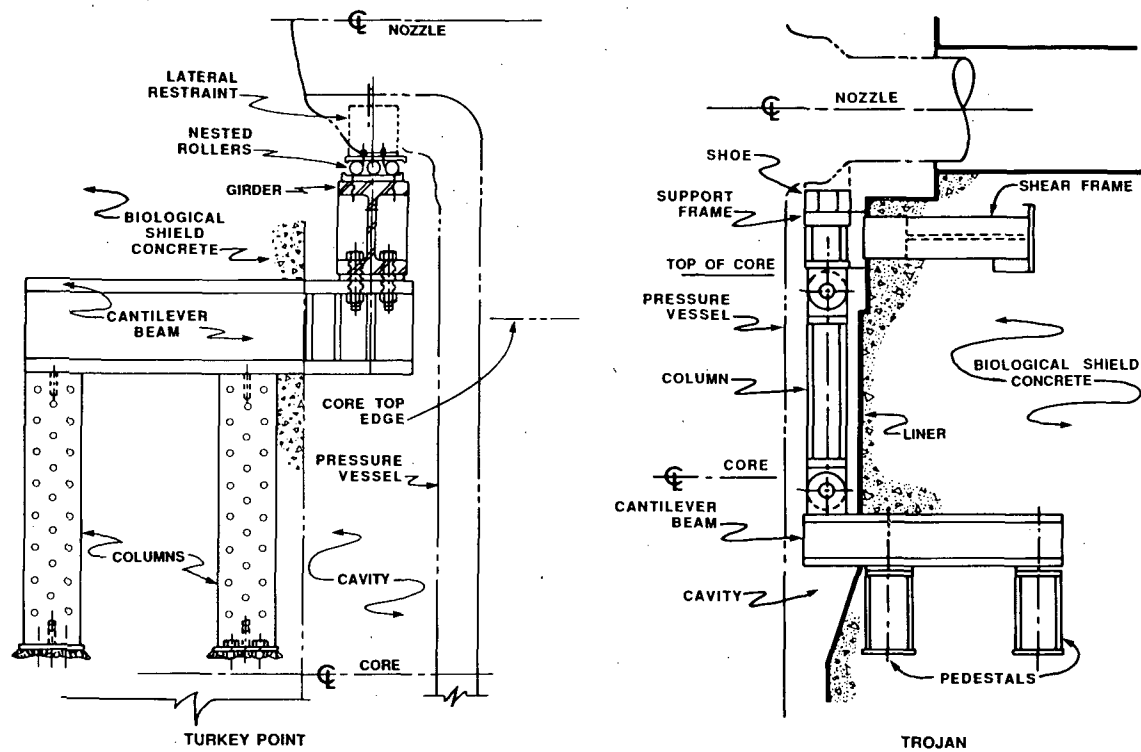


Fig. 11. Reactor vessel support for Turkey Point and Trojan.

reactors, the cantilever beams extend radially from the cavity into the concrete biological shield, where they are attached to two steel pedestals that are also embedded in the concrete (Figs. 11 and 12). The beam materials are A36 for Trojan and A588 for Turkey Point, both of which are commonly used bridge steels. The Trojan beam is a double-webbed weldment, while the other

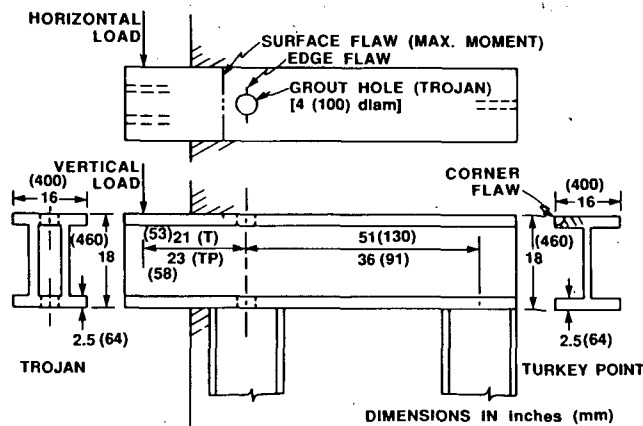


Fig. 12. Details of vessel support cantilever beam for Trojan and Turkey Point.

is a standard wide-flanged beam. An unusual feature in the Trojan beam is a 100-mm-diam grout hole in the top and bottom flanges directly above the pedestals (Fig. 12).

### Loads

All loads applied to the vessel supports were supplied by the utilities. Individual loads include the vessel deadweight and contents (DW), thermal loads resulting from differential expansion (T), the operating basis earthquake (OBE), the safe shutdown earthquake (SSE), and small- and large-break loss-of-coolant accidents (SBLOCA and LBLOCA). Suitable maximum credible loads for this study were specified by the utilities as DW + T + SBLOCA for Trojan and DW + T + LBLOCA for Turkey Point. The Trojan SBLOCA was a bounding case involving failure of auxiliary coolant lines.

The rate of loading is important because the fracture toughness of the beam material is load-rate sensitive. A loading rate corresponding to the maximum credible load was provided by the utility for Trojan but not for Turkey Point.

### Temperature

Operating temperatures of the supports for Trojan and Turkey Point range from  $\sim 250^{\circ}\text{C}$  at the point of contact with the nozzles to  $< 65^{\circ}\text{C}$  at the biological shield. Information from the utilities indicates that the temperature of the cantilever beam is  $\sim 32^{\circ}\text{C}$  for Trojan and  $\sim 50^{\circ}\text{C}$  for Turkey Point.

### Neutron Fluxes

The neutron fluxes and dpa rates used in this study were obtained from multigroup transport calculations performed by the utility and/or the utility contractor. Actual and postulated future changes in the fuel-loading schemes to reduce fast-neutron leakage were considered so that estimated values of fluence and dpa would be reasonably accurate.

### Material Properties

The material properties of primary concern for the cantilever beams are the fracture toughness, the initial value of NDTT, and the increase in NDTT as a function of dpa. A few dynamic fracture-toughness data  $K_{Id}$  are available for the Trojan beam material (A36), and they span the appropriate strain rate for the beam, thus permitting interpolation.<sup>19</sup> Corrections were made to the interpolated curve for lack of plane strain in the beam, where appropriate, in accordance with Ref. 20. A lower-bound curve was constructed by shifting the modified interpolated curve by  $\sim 28^{\circ}\text{C}$ , consistent with the assumption that  $K_{Id} \rightarrow \infty$  as  $T \rightarrow \text{NDTT} + 40^{\circ}\text{C}$  (Ref. 21). These curves are shown in Fig. 13, where they are compared with the  $K_{IR}$  curve.<sup>22</sup>

Fracture-toughness data ( $K_{IC}$ ,  $K_{Id}$ ) and loading rate were not available for the Turkey Point cantilever beam. As a conservative measure, the ASME  $K_{IR}$  curve was used in the analysis (Fig. 13).

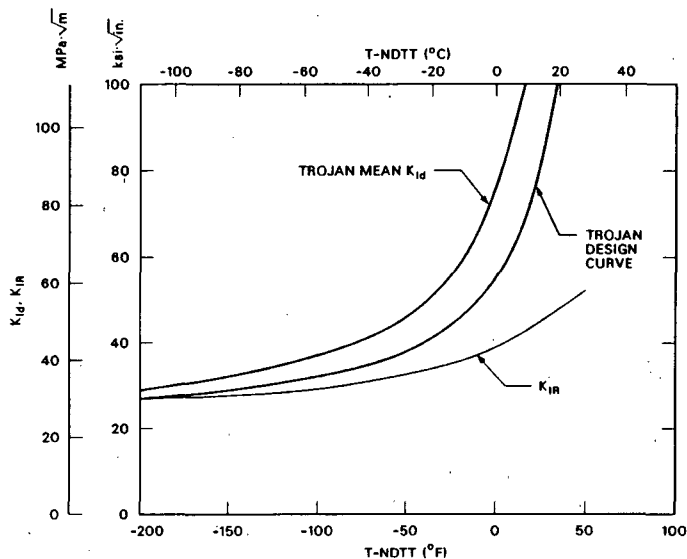


Fig. 13. Fracture-toughness curves used in Trojan and Turkey Point vessel support evaluations.

Initial values of NDTT were not available for the specific heats of material used for the beams. Best-estimate values were obtained from Ref. 19 for Trojan ( $-2^{\circ}\text{C}$ ) and from Refs. 23 and 24 for Turkey Point ( $18^{\circ}\text{C}$ ).

The radiation-induced increase in NDTT was assumed to be in accordance with the trends provided in Fig. 9.

#### Stress and Fracture Analyses

Because the cantilever beam rests on pedestals and the pedestals and a portion of the beam are embedded in concrete, a beam-on-elastic-foundation type of stress analysis was appropriate and was used for Trojan. Calculations of this type were made with and without the concrete between the shield liner and the inner face of the inboard pedestal because of concerns that this section of concrete would not carry load as a result of not actually being in contact with the underside of the beam. Calculations were also made with and without the reinforcing steel present. Results of these calculations indicate that the reinforcing steel has a negligible effect and that removal of the innermost section of concrete increases the maximum bending moment by 15% and the moment at the grout hole by 21% (Fig. 14). Without the innermost section of concrete present, the moment at the inner surface of the inboard pedestal, where the remaining concrete has no effect whatsoever, is only 11% less than the maximum moment. For this reason, the maximum bending moment for Turkey Point was simply taken as the load multiplied by the distance to the inner surface of the inboard pedestal.

The fracture analysis considered several radial locations for assumed flaws because the increasing moment (up to the point of the maximum moment) and the attenuation of the neutron flux tend to compensate each other in terms of potential for propagation of flaws. Also, the existence of the grout hole

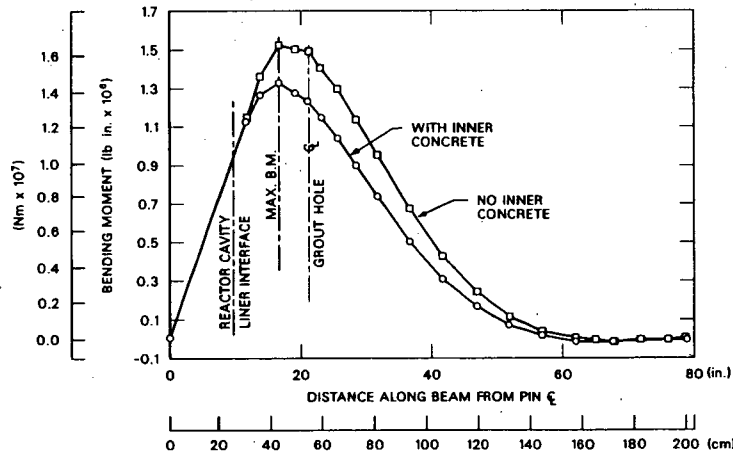


Fig. 14. Bending moment in Trojan reactor vessel support beam produced by a 100-kip (445-kN) load.

in the Trojan beam introduced another radial location of interest because of the resulting reduced section and the stress concentration at the sides of the hole. For Trojan, semielliptical surface flaws on the top flange were considered at the inner surface of the shield and at the location of maximum moment, while through-thickness edge cracks were considered in the grout hole (Fig. 12). For Turkey Point, which has both horizontal and vertical loads applied to the cantilever beam, corner flaws on the upper flange at radial locations between the inner surface of the shield and the inner surface of the inboard pedestal are of greatest concern.

Stress-intensity factors  $K_I$  were calculated assuming the beam flange to be a detached finite-width plate. Only  $K_I$  values at the deepest point of the semielliptical flaws were considered, and, of course, the full-width (uniform-depth) flaw had the largest  $K_I$  value and thus the shallowest critical depth. For the grout hole, the two loading conditions illustrated in Fig. 15 were considered. One assumes uniform loading on the end of a finite-length plate containing the hole, and the other attempts to simulate the actual shear load between the two webs and the flange by including two line loads in the two-dimensional model.  $K_I$  values were calculated using a finite-element analysis,

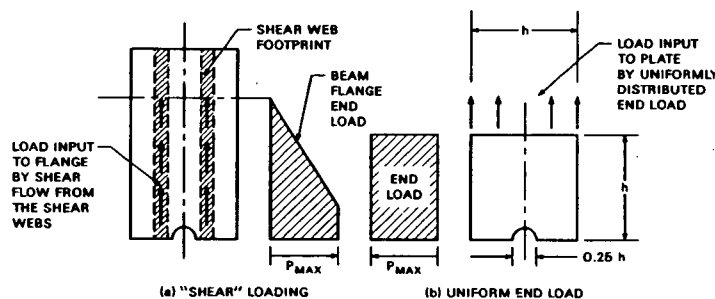


Fig. 15. Two two-dimensional models used for Trojan beam with grout hole.

and the results indicated an 11% higher  $K_I$  value, for two symmetrical and opposite edge cracks, with the latter model. (Critical flaw sizes reported here were calculated using the uniform-load model and thus tend to represent nonconservative values.)

$K_I$  values for the corner cracks (Turkey Point) were calculated considering the bending moments resulting from both the horizontal and vertical loads, and critical flaw sizes (radii) were based on the maximum  $K_I$  values along the crack front.

## Results

Calculated critical flaw sizes are given in Tables 6 and 7 for Trojan and Turkey Point, respectively. Values are listed for each loading condition considered, for operating times corresponding to the present (late 1988) and 32 EFY, and for different locations on the cantilever beam upper flange. The effect of the inner concrete was not considered, the uniform-end-load model was used for the grout hole (Fig. 15, Trojan), and values of  $\Delta NDTT$  were taken from Fig. 9.

At 32 EFY the minimum critical flaw sizes (10 × 64 mm for Trojan and 8-m radius for Turkey Point) are small enough to be of concern.

For deeper cracks than those included in Tables 6 and 7, the stress-intensity factors are greater. Thus, crack initiation (onset of propagation) results in failure of the beam; that is, crack arrest does not take place as long as the load is applied.

Table 6. Summary of critical flaw depths for Trojan, assuming that the innermost section of concrete is not present

Location on beam	Loading condition <sup>a</sup>	Flaw type	Critical flaw depth (mm)					
			7.48 EFY <sup>b</sup>			32 EFY		
			$a/l^c$		$a/l$			
			0	0.1	0	0.1	0.2	0.3
Shield inner surface	A	Surface	29	>32	21	>32		
	B	semi-	27	>32	20	32	>32	
	C	ellipse	23	>32	17	25	>32	
Maximum bending moment	A	Surface	29	>32	19	30	>32	
	B	semi-	27	>32	18	26	>32	
	C	ellipse	22	>32	15	20	28	>32
Flange grout hole	A	Twin	>50		41			
	B	edge	>50		30			
	C	cracks	>50		11			

<sup>a</sup>A = DW + T + OBE, B = DW + T + SSE, and C = DW + T + SBLOCA.

<sup>b</sup>Corresponds to late 1988.

<sup>c</sup>Ratio of maximum depth (a) to surface length (l).

Table 7. Summary of critical flaw depths for Turkey Point

Location on beam	Loading condition <sup>a</sup>	Critical flaw depth (mm)					
		11.8 EFPY			32 EFPY		
		Flaw <sup>b</sup>			Flaw		
		E	F	G	E	F	G
Shield inner surface	B	>64	>64	43	>64	>64	30
	D	41	33	10	30	25	8
Maximum bending moment	B	53	>64	25	48	>64	23
	D	28	23	8	20	18	8

<sup>a</sup>A = DW + T + OBE, B = DW + T + SSE, and D = DW + T + LBLOCA.

<sup>b</sup>E = edge crack, F = full-width surface crack, and G = circular corner crack.

The sensitivity of critical flaw size to T - NDT and thus to operating temperature,  $NDTT_0$  and  $\Delta NDTT$ , for the case of no inner concrete is indicated in Fig. 16 for Trojan. By way of illustration, at 32 EFPY the best-estimate critical flaw size is 10 mm (Table 6) and T - NDT =  $-7^\circ\text{C}$ . If T - NDT were increased by  $6^\circ\text{C}$ , the critical flaw size would increase by  $\sim 5$  mm (50%); if

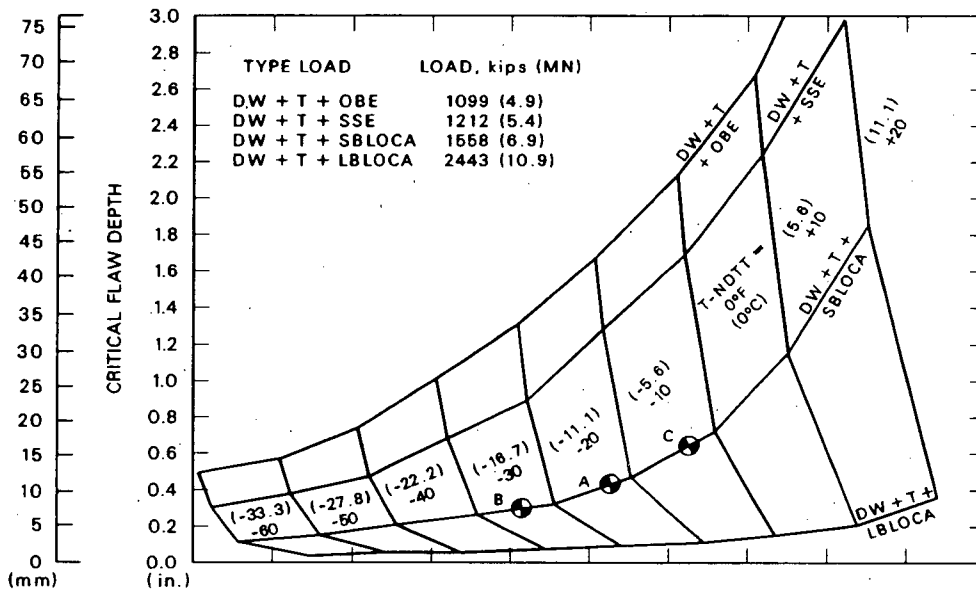


Fig. 16. Trojan grout hole critical flaw size vs load and T-NDTT.

T - NDT were decreased by 6°C, the critical flaw size would be reduced by ~3 mm (25%).

An estimation of the probability of the existence of flaws was not included in the scope of this study. However, an analysis was conducted that indicates no significant fatigue growth of flaws in the beams during the 32-EFPY period. Thus, if corrosion is not a viable mechanism for flaw growth, the flaws included in Tables 6 and 7 would have existed at the time of construction, at which time they might have been detected by a careful inspection.

### Discussion of Results

A comparison of the calculated critical flaw sizes for Trojan and Turkey Point (Tables 6 and 7) indicates smaller values for Turkey Point, and yet (1) the Turkey Point beam is farther from the neutron source, (2) it was assumed to operate at a higher temperature, and (3) it does not contain the grout hole or other discontinuity. There are two reasons for the apparent inconsistency. First, at the time of this study, Turkey Point was not exempt from consideration of dynamic loads associated with the LBLOCA, and thus the LBLOCA loads were considered as a component of the maximum credible loading condition. For Trojan, which is exempt, the maximum credible loading condition is an SBLOCA (auxiliary coolant-line break), which is much less severe. Secondly, because appropriate  $K_{Ic}$  data were not available for Turkey Point, the  $K_{IR}$  curve was used, and it was used without corrections for lack of plane-strain conditions. If one is concerned about the effect of low-toughness sites on the effective fracture toughness, then perhaps a lower bound  $K_{Ia}$  curve should be used for Trojan as well.

Residual stresses exist in the beams, particularly around the Trojan grout hole, but they were not included in the calculation of the critical flaw depths listed in Tables 6 and 7 because they are too uncertain for general consideration. However, to obtain some indication of the sensitivity of critical flaw size to residual stress around the grout hole, it was assumed that the bending stress plus the residual stress was equal to the yield stress. For this condition, the 32-EFPY critical flaw size was reduced by ~50%. If nothing more, the localized residual stress effectively introduces a "low-toughness" site that reduces the effective initiation toughness to  $K_{Ia}$ . That is, if a localized residual stress is not used directly in the analysis, it would probably be reasonable to use  $K_{Ia}$  rather than  $K_{Ic}$  to account for the possible existence of a residual stress.

### CONCLUSIONS

1. The calculated minimum critical flaw sizes are small enough to be of concern for both Trojan and Turkey Point.
2. Inspection for flaws at the critical locations probably is not possible because that portion of the beam is embedded in concrete.
3. The probability that the critical flaw sizes are smaller than indicated is fairly high because the values in Tables 6 and 7 are best-estimate values assuming no residual stresses, and the uncertainty in several input

parameters (radiation-damage trend curve, fracture toughness, operating temperature, and loading conditions) is large.

4. For Turkey Point, significant unequal horizontal forces associated with variations in sliding friction in the components that accommodate radial thermal expansion may exist and could decrease the critical flaw size relative to the best-estimate values.

5. Based on information that became available after the study was completed, presumably the most severe loading condition considered for Turkey Point (LBLOCA) is no longer considered credible. Thus, in this regard, best-estimate critical flaw sizes should be larger than those indicated.

6. Low-cycle fatigue is not a mechanism for creating flaws of critical size.

#### REFERENCES

1. J. R. Hawthorne, *Studies of Radiation Effects and Recovery of Notch Ductility of Pressure Vessel Steels*, British Nuclear Energy Conference, Iron and Steel Institute, London, England, November 30, 1960.
2. L. E. Steele et al., *Irradiated Materials Evaluation and Reactor Pressure Vessel Surveillance for the Army Nuclear Power Program*, NRL Memorandum Report 1644, September 1, 1965.
3. G. A. Knorovski, R. D. Krieg, and G. C. Allen, Jr., *Fracture Toughness of PWR Components Supports*, NUREG/CR-3009 (SAND78-2347), Sandia National Laboratory, February 1983.
4. *Requirements and Guidelines for Evaluating Component Support Materials Under Unresolved Safety Issue A-12*, EPRI NP-3528, Electric Power Research Institute, June 1984.
5. W. G. Hopkins and W. L. Grove, *A Study of the Embrittlement of Reactor Vessel Steel Supports*, *Reactor Dosimetry*, Vol. 2, ed., J. P. Genthon and H. Rottger, Dordrecht, Netherlands: D. Reidel Publishing Company, 1985, pp. 621-28.
6. W. G. Hopkins, *Reactor Pressure Vessel Supports for Pressurized Water Reactors and Boiling Water Reactors, Residual Life Assessment of Major Light Water Reactor Components - Overview, Volume 1*, NUREG/CR-4731 (EGG-2469), Vol. 1, Idaho National Engineering Laboratory, June 1987.
7. R. D. Cheverton and T. M. Sims, *HFIR Core Nuclear Design*, ORNL-4621, Union Carbide Corp. Nucl. Div., Oak Ridge Natl. Lab., July 1971.
8. J. R. McWherter, R. E. Schappel, and J. R. McGuffey, *HFIR Pressure Vessel and Structural Components Material Surveillance Program*, ORNL/TM-1372, Union Carbide Corp. Nucl. Div., Oak Ridge Natl. Lab., January 1966.

9. R. D. Cheverton, J. G. Merkle, and R. K. Nanstad, eds., *Evaluation of HFIR Pressure-Vessel Integrity Considering Radiation Embrittlement*, ORNL/TM-10444, Martin Marietta Energy Systems, Inc., Oak Ridge Natl. Lab., April 1988.
10. R. K. Nanstad et al., *Effects of 50°C Surveillance and Test Reactor Irradiation on Ferritic Pressure Vessel Steel Embrittlement*, presented at 14th International Symposium on the Effects of Radiation on Materials, Andover, Massachusetts, June 27, 1988 (to be published in ASTM STP).
11. R. K. Nanstad et al., "Accelerated Neutron Embrittlement of Ferritic Steels at Low Fluence: Flux and Spectrum Effects," submitted to *J. of Nuc. Matls.*, April 1988.
12. R. L. Childs, Oak Ridge Natl. Lab., personal communication to R. K. Nanstad, Oak Ridge Natl. Lab., August 10, 1988.
13. A. Alberman et al., "Influence of Thermal Neutrons on the Brittleness of High-Temperature Gas-Cooled Reactor Liner Steel," *Nucl. Technol.* 66, 639-46, September 1984.
14. L. K. Mansur and N. K. Farrell, Oak Ridge Natl. Lab., private communication to R. D. Cheverton and R. K. Nanstad, Oak Ridge Natl. Lab., September 1988.
15. N. Tsoulfanidis et al., "Neutron Energy Spectrum Calculations in Three PWR's," pp. 693-701 in *Proceedings of the Fifth ASTM-EURATOMS Symposium on Reactor Dosimetry* (1985).
16. M. L. Williams, Oak Ridge Natl. Lab., personal communication to F. Kam, Oak Ridge Natl. Lab.
17. M. S. Wechsler et al., *Radiation Hardening and Embrittlement in a Low-Carbon Pressure Vessel Steel, Irradiation Effects in Structural Alloys for Thermal and Fast Reactors*, STP 457, pp. 242-60, American Society for Testing and Material, Philadelphia, 1969.
18. M. L. Hamilton and H. L. Heinesch, "Tensile Properties of Neutron Irradiated A212-B Pressure Vessel Material," ASTM 14th International Symposium on Effects of Radiation on Materials, Andover, Massachusetts, June 27-29, 1988.
19. *Structural Alloys Handbook*, 1987 ed., Vol. 3, Battelle Columbus Laboratory, Columbus, Ohio.
20. S. T. Rolfe and J. M. Barsom, *Fracture and Fatigue Control in Structures: Applications of Fracture Mechanics*, Prentice Hall, Inc., Englewood Cliffs, New Jersey, 1977.
21. *The American Society of Mechanical Engineers Boiler and Pressure Vessel Code*, Sect. III, Subsect. NF.

22. ASME Boiler and Pressure Vessel Code, Sect. XI, "Rules for Inservice Inspection of Nuclear Power Plant Components," Article A-4000, Material Properties, 1986 ed., The American Society of Mechanical Engineers, New York.
23. R. Roberts et al., *Fracture Toughness of Bridge Steels - Phase II Report*, FHWA-RD-74-59, Lehigh University, Department of Transportation, Federal Highway Administration (National Technical Information Service PB-239-188), September 1974.
24. G. J. Buragino, S. S. Hansen, and D. C. Krouse, "Metallurgical Characterization of Jumbo Sizes," AISC National Engineering Conference, June 10, 1988.



## FRACTURE RESISTANCE CHARACTERIZATION FOR LWR MATERIALS

E.M. Hackett  
David Taylor Research Center  
Annapolis, Maryland 21402

J.A. Joyce  
United States Naval Academy  
Annapolis, Maryland 21402

### ABSTRACT

The objectives of this investigation were to; (1) present experimental results and development of an experimental analysis which attempt to define the limits of the J singularity controlled region of crack extension in bend type laboratory fracture mechanics specimens; and (2) develop and examine a J-R curve extrapolation technique. Current limitations on J-controlled crack growth as described in ASTM E1152-87 are highly restrictive (crack extension is required to be less than 10% of the initial specimen remaining ligament). This is particularly limiting in fracture analyses of nuclear plant structures which require development of J-R curves with large amounts of crack extension for use in instability analyses. Moreover, the E1152 limitations have not corresponded to observed experimental phenomena that could be taken to identify the loss of the singularity in a bend type fracture mechanics specimen. Additionally, an extension of the valid region of crack extension for a J-R curve from a laboratory specimen, does not often provide crack growth resistance information at large amounts of crack growth. In such cases, extrapolations may be required. There are, at present, no standardized approaches for extrapolating J-R curves obtained from small specimens to predict the crack growth resistance of larger specimens or structures.

The experimental test matrix included J-R curve tests on 1/2T, 1T and 2T compact [C(T)] and three-point-bend [SE(B)] specimens of several medium to high strength steels (ASTM A710, A516, A106, and A533B steels and a high yield strength, 3%Ni steel). The J-R curve tests were conducted in accordance with ASTM E1152-87 with the exception that crack extensions on the order of 60% of the initial remaining ligament were achieved. The data were analyzed both in terms of the deformation theory J integral and the modified J integral ( $J_M$ ). Tests of blunt-notched C(T) specimens were also performed to examine the accuracy of deformation plasticity assumptions at large deformations and crack extensions.

Results of the J-R curve and blunt-notched specimen tests indicate experimental support for extension of the E1152 crack growth validity limits to approximately 30% of the initial remaining ligament. An analysis, based on a plot of specimen bend angle versus crack extension, was developed to define the engineering limit to the J-controlled singularity region. In the majority of the cases examined, this analysis indicates loss of the controlling singularity at approximately 30% crack growth.

A J-R curve extrapolation technique is described which is based on a simple power law fit to J-R curve data in the above-defined singularity region. While this approach is not verified in a general sense, it does correspond to measured data in most cases for which data is presently available.

## INTRODUCTION

The J-integral [1-5] is widely accepted as a measure of elastic-plastic fracture toughness for engineering alloys. Assessment of the fracture safety of engineering structures can be performed utilizing J-integral resistance (J-R) curves for the material of interest, as the basis for resistance to ductile crack growth [6]. Questions of specimen size and geometry dependence for the deformation theory J-integral [7,8], coupled with development of a modified J-integral ( $J_M$ ) [9], have raised a controversy over which parameter more properly addresses the crack growth resistance of a flawed structure. Whether J or  $J_M$  is used to characterize the materials' crack growth resistance, structural integrity assessments of nuclear piping systems require resistance curve information to large amounts of crack growth (often in excess of 0.6 inches). For available surveillance specimens, this crack extension far exceeds the allowable ASTM limits as defined in E1152-87. Moreover, even extension of the validity limits will not often yield the large crack extensions required from small specimens without using extrapolations. The David Taylor Research Center (DTRC) is presently performing a research task to address the issues of parameter selection, extension of R-curve validity limits and extrapolation techniques for R-curves.

The results of this investigation are expected to significantly influence policy/standards decisions presently being undertaken by the Nuclear Regulatory Commission (NRC), the American Society of Mechanical Engineers (ASME) and the American Society for Testing and Materials (ASTM). The NRC is currently faced with decisions regarding the the appropriate fracture parameters and analyses required to assess the fracture safety of commercial nuclear plants with low upper shelf pressure vessel toughness. This topic is presently being addressed by the ASME Section XI Working Group on Flaw Evaluation. The working group is preparing an A-11 Support Document entitled "Development of Criteria for Assessment of Reactor Vessels with Low Upper Shelf Toughness". A reactor vessel is deemed to have low upper shelf toughness when tests of surveillance Charpy V-Notch (CVN) specimens result in

less than 50 ft-lbs absorbed energy. The A-11 document describes a fracture safety analysis based on characterization of the material fracture resistance by the J-integral fracture parameter. Key issues remaining to be resolved include: (1) Whether the deformation theory J-integral or the Ernst [9] modified J ( $J_M$ ) provides the more appropriate fracture resistance characterization; (2) Definition and extension of validity limits for J-R or  $J_M$ -R curves and; (3) Extrapolations of J-R or  $J_M$ -R curves from small specimen data to obtain fracture toughness information at the large crack extensions required for nuclear vessel analysis. The ASTM J-R curve standard (E1152-87) currently limits valid ductile crack growth to 10% of the remaining ligament in a bend-type fracture mechanics specimen and does not address possible extrapolation techniques. The crack growth validity limitation is highly restrictive for nuclear vessel analyses and extension of this validity limit, coupled with examination of a proposed extrapolation technique are the primary focus of this investigation.

#### APPROACH

J-R curve tests were conducted using the ASTM E1152-87 procedure with the exception that the tests were continued to large crack extensions, typically in excess of 60% of the initial specimen remaining ligament. These tests were conducted using 1/2T, 1T and 2T compact and three-point bend specimens to assess effects of specimen size and geometry and to provide large specimens (2T) to verify extrapolation techniques used on the smaller specimens. Only compact specimen results will be presented in this paper. A series of blunt notched calibration tests were performed, using 1T compact specimens, to assess the accuracy of the deformation plasticity assumptions on which the J-integral is based. Using the above generated data, and data available from ASME and ASTM committee sources, an analysis was developed to allow an assessment of the extent of the J-controlled singularity region for a laboratory specimen from a single plot. Lastly, a simple power law technique for extrapolating J-R curves from small specimens was evaluated for two materials.

#### MATERIALS

The alloys used in this investigation include ASTM designations A710, A533B, A516, and A106 steels, and a 3%Ni, high strength steel. These materials were chosen due to their use in nuclear steam systems and/or to provide a wide range of fracture toughnesses to assess the dependence of the fracture parameter on the level of toughness. Mechanical property data for these alloys are shown in Table 1.

#### RESULTS and DISCUSSION

##### J-R Curve Tests

Due to the extensive nature of the J-R curve testing performed for this investigation, only specific cases will be described herein. A matrix for the

entire test series is provided in Table 2. All J-R curve testing was performed using the crack growth corrected J equations found in ASTM E1152-87. Equations for  $J_M$  were taken from reference 9. Figures 1 and 2 provide J-R curves for different scale compact specimens of A533B and A710, respectively. The corresponding  $J_M$ -R curves are provided in Figures 3 and 4. A key feature of these data sets are the consistency of the J-R curves for both A533B and A710 to crack extensions far exceeding the ASTM E1152 allowable limits. This consistency was also noted for the A710  $J_M$ -R curves, but not however, for the A533B  $J_M$ -R curves, where a distinct upward sweep to the R curves was observed. This upward sweep trend has been observed for the  $J_M$ -R curves of specimens of the other materials that have been investigated. The data presented in Figures 1 through 4 have been presented previously [10], and were the cause of the continued investigation described herein. Development of the singularity zone analysis described in a later section indicates that the upward sweep in the  $J_M$ -R curves is indicative of the loss of the controlling singularity for the J-integral and the continued consistency of the J-R curves beyond this point is fortuitous.

Accuracy of the elastic compliance system in measuring the large crack extensions achieved in this test program was assessed and the results are presented in Table 3 for three of the alloys investigated. The agreement was generally good (less than 15% difference between estimated and measured values) with the largest errors occurring for the A710 steel. The tests of the highly ductile A710 alloy resulted in much larger deformations than either the 3%-Ni steel or the A533B steel at similar amounts of crack extension.

#### Blunt Notch Tests

Blunt notch tests of 1T compact specimens were conducted and the final loads and J values were compared with results from corresponding elastic compliance J-R curve tests. The general procedure for these tests is illustrated in Figure 5, and is described in detail in reference 11. For deformation plasticity conditions to prevail, the final loads and J values between the blunt notch and J-R curve tests should be in good agreement. A comparison of the load-displacement records for several A533B and A710 blunt notch and J-R curve tests are presented in Figures 6 and 7. A summary of the comparisons performed with A533B, A710 and the 3%-Ni steel is presented in Table 4. This comparison shows good agreement for the A533B and 3%-Ni steels and poor agreement for the A710 steel. The percentage differences for the final load and J values for the A710 alloy were found to increase progressively with crack extension. These specimens were characterized by larger deformations than either the A533B or 3%-Ni steels at similar amounts of crack growth. The blunt notch tests for materials other than the highly ductile A710 alloy indicate that deformation theory is applicable for elastic-plastic materials of the type described herein, even when large crack extensions and corresponding material unloading has occurred. This provides support for extension of J-R curve crack growth validity limits beyond that currently provided in ASTM E1152-87.

## Singularity Zone Analysis

To follow-up the blunt notch tests, an analysis, aimed at quantifying the extent of the J-singularity controlled region of crack growth in a laboratory specimen, was developed. It was observed that real (engineering) limits to the applicability of the J-integral were apparent in a plot of the plastic component of crack opening displacement versus crack extension. Such a plot is shown for a 3%Ni steel 1/2T compact specimen in Figure 8. This plot shows a region of initial crack blunting, a region of singularity controlled crack growth, and finally, a gradual return to crack blunting. While the presence of a singularity is difficult to verify experimentally, it is known that it should produce the most intense conditions for crack growth. The plot in Figure 8 shows the most intense crack growth occurring in the central linear region. The presence of blunting in the beginning of the test and the weakening of the singularity as the test progresses are reflected by the fact that the increment of crack growth per increment of plastic displacement is greatly reduced in these regions. The delineations between these zones are much more apparent on this plot than on a standard J-R curve. The limit of the singularity controlled crack growth region is taken to be at a 5% deviation from the linear region shown on the plot. Application of this type of analysis to the materials investigated, has shown the loss of singularity controlled growth to be at approximately 30% of the remaining specimen ligament. This loss of singularity region has also been found to be consistent with the beginning of the upward sweep observed in the  $J_M$ -R curves. The specimen size dependence demonstrated by the modified J, therefore, appears to be a clear indicator of a loss of singularity in these specimens.

## J-R Curve Extrapolations

The experimental singularity zone defined above extends the applicable region of the J resistance curve well beyond the present limits of ASTM E1152-87. As shown above, the results indicate that crack extensions of 30% of the initial remaining ligament can be justified by the singularity limit defined directly from experimental data.

When even this extended J-R curve data is not adequate to address crack growth resistance, it is proposed that an extrapolation can be made in the following manner. First, only small specimen data in the singularity zone should be utilized. Second, a simple power law of the form

$$J = C(\Delta a)^m \quad [1]$$

where C and m are fitting parameters and  $\Delta a$  is the amount of crack extension, should be fit to the small specimen singularity zone data for purposes of extrapolation. Such an analysis can be applied to either deformation theory J-R curves or to  $J_M$ -R curves.

Typical results are shown in Figure 9 for an A533B steel. The smooth power law curves have been fit to the 1/2T CT specimens in the region  $0.015 < \Delta a < 0.150$ . This region was determined to be the singularity zone using the

analysis described previously. The power law was then extended and compared with 1T CT data as shown in Figure 9. The comparison is excellent to a crack extension of 0.500 inches on the 1T specimen. Use of  $J_M$  for this alloy also gives good results as shown in Figure 10. In this case fitting data only in the singularity zone effectively avoids the upward sweep of the  $1/2T J_M$  resistance curves and produces an extrapolation function which is in good agreement with the 1T CT specimen results.

The same analysis was applied to J-R curve data on low upper shelf toughness, Linde 80 weld material from Babcock & Wilcox [12] as shown in Figures 11 through 14. This is the material that is the subject of the ASME A-11 support document referred to previously. Extrapolations based on the deformation J-R curves seem to be preferable for this material. On first examination, the small specimen data of Figure 11 appears to be grossly conservative in comparison with the 2T CT result. Utilizing only the data in the singularity zone for each small specimen, however and fitting the power law form of equation [1], provides the comparison shown in Figure 13. Repeating the process with the  $J_M$ -R curves produces the much less conservative results shown in Figure 14.

Application of this type of analysis to all materials and geometries studied in this program has supported the extrapolation procedure described above as being generally accurate to conservative if deformation J-R curves are used and generally accurate to non-conservative if  $J_M$ -R curves are used. The non-conservative extrapolations observed thus far using  $J_M$ -R curves indicate that use of J-R curves is preferred in the analysis of the Linde 80 material. Further analysis of the Linde 80 material from the Oak Ridge National Laboratory (ORNL) V8A test is in progress and should provide more conclusive information on selection of the appropriate fracture parameter for analysis of pressure vessels with low upper shelf toughness.

#### CONCLUSIONS

- (1) Blunt notch test results on several alloys indicate that J-R curves are generally useful well beyond the present crack extension validity limits in E1152-87.
- (2) An analysis was developed to define an engineering limit to the extent of J-singularity controlled crack growth in the alloys examined. This analysis indicates loss of the controlling singularity at approximately 30% of the initial specimen remaining ligament for a majority of the materials investigated.
- (3) J-R curve extrapolations based on fitting a simple power law to the data in the extended validity region provide accurate to conservative estimates of large specimen behavior in the case of deformation theory J, and accurate to non-conservative estimates of large specimen behavior in the case of  $J_M$ .

#### ACKNOWLEDGMENTS

The authors wish to acknowledge the support and guidance of Mr. Michael Mayfield (USNRC) and the technical support of Mr. Stan Womack, whose assistance in completing the test program was invaluable.

## REFERENCES

- (1) Hutchinson, J.W., "Singular Behavior at the End of a Tensile Crack in Hardening Material", JOURNAL OF THE MECHANICS AND PHYSICS OF SOLIDS, Vol. 16, 1968, pp. 13-31.
- (2) Rice, J.R. and Rosengren, G.F., "Plane Strain Deformation Near a Crack Tip In a Power-Law Hardening Material", JOURNAL OF THE MECHANICS AND PHYSICS OF SOLIDS, Vol. 16, 1968, pp. 1-12.
- (3) Rice, J.R., Paris, P.C., and Merkle, J.G. in PROGRESS OF FLAW GROWTH AND FRACTURE TOUGHNESS TESTING, ASTM STP 536, 1973, pp. 231-245.
- (4) Merkle, J.G. and Corten, H.T., in TRANSACTIONS, ASME, JOURNAL OF PRESSURE VESSEL TECHNOLOGY, 1974, pp. 286-292.
- (5) Ernst, H.A., Paris, P.C. and Landes, J.D. in FRACTURE MECHANICS, ASTM STP 743, 1981, pp. 476-502.
- (6) Vassilaros, M.G., Gudas, J.P., and J.A. Joyce, "Experimental Investigation of Tearing Instability Phenomena for Structural Materials", USNRC NUREG/CR-2570, April, 1982.
- (7) McCabe, D.E. and Landes, J.D. in ELASTIC-PLASTIC FRACTURE, ASTM STP 803, Vol. 2, 1983, pp. 353-371.
- (8) Davis, D.A., Vassilaros, M.G. and Gudas, J.P. in ELASTIC-PLASTIC FRACTURE, ASTM STP 803, Vol. 2, 1983, pp. 582-610.
- (9) Ernst, H.A. in ELASTIC-PLASTIC FRACTURE, ASTM STP 803, Vol. 1, 1983, pp. 191-213.
- (10) Davis, D.A., Hays, R.A., Hackett, E.M. and J.A. Joyce, "On The Use of The J-Integral and Modified J-Integral as Measures of Elastic-Plastic Fracture Toughness", Proceedings of the 15th WRSN, NUREG CP-0091, 1987.
- (11) Joyce, J.A., Davis, D.A., Hackett, E.M., and R.A. Hays, "Application of the J-integral and Modified J-Integral to Cases of Large Crack Extension", USNRC NUREG CR/5238.
- (12) Yoon, K., " $J_M/J_D$  Resistance Curve Issues - Linde 80 Welds", ASME Section XI Working Group on Flaw Evaluation, Colorado Springs, CO, August 30, 1988

TABLE 1 - MECHANICAL PROPERTIES FOR MATERIALS INVESTIGATED

MATERIAL	0.2% OFFSET YIELD STRENGTH (ksi)	ULTIMATE TENSILE STRENGTH (ksi)	ELONGATION % IN TWO INCHES (%)	REDUCTION IN AREA (%)
A710	74	87	32	80
A533B-02	65	90	19	60
A533B-H13	64	87	26	68
A516	70	45	36	60
A106	47	81	32	67
3%-Ni	89	106	23	80

TABLE 2 - J-R CURVE TEST MATRIX  
NUMBER OF SPECIMENS PER CONDITION

MATERIAL	COMPACT C(T)			THREE-POINT BEND SE(B)		
	1/2T	1T	2T	1/2T	1T	2T
A710	3	8	3	3	3	3
A533B-02	3	3		3	3	
A533B-H13		8				
A516	3	3	3	3	3	3
A106		8				
3%-Ni	3	8		3	3	

TABLE 3 - CRACK LENGTH MEASUREMENT TABULATION

SPECIMEN I.D.	SPECIMEN TYPE	ESTIMATED CRACK EXTENSION (inches)	MEASURED CRACK EXTENSION (inches)	PERCENT ERROR (%)
A710				
GFF-3	1/2T	0.135	0.158	-14.6
GFF-4	1/2T	0.130	0.155	-16.1
GFF-30	1T	0.279	0.322	-13.4
GFF-31	1T	0.287	0.311	-7.7
GFF-32	1T	0.198	0.219	-9.6
GFF-L8	2T	0.201	0.222	-9.5
GFF-L9	2T	0.392	0.451	-13.1
3-Ni STEEL				
S-1	1/2T	0.301	0.316	-4.7
S-2	1/2T	0.246	0.249	-1.2
A-1	1T	0.534	0.543	-1.7
A-2	1T	0.543	0.559	-2.9
A533B				
GT-25	1/2T	0.242	0.270	-10.4
GT-29	1/2T	0.271	0.297	-8.8
GAA-14	1T	0.533	0.569	-6.3
GAA-15	1T	0.526	0.569	-7.6

TABLE 4 - BLUNT NOTCH TEST SUMMARY

MATERIAL/ SPECIMEN	TEST TYPE	FINAL LOAD (pounds)	FINAL J (lbs/in)	% DIFF LOAD (%)	%DIFF J (%)	CRACK EXTENSION (inches)
3-Ni STEEL						
FYB-A3	BLUNT-NOTCHED	8100	1700	-4	-2	
FYB-A12	J-R CURVE	8400	1667			0.107
FYB-A7	BLUNT-NOTCHED	6000	2205	-5	0	
FYB-A11	J-R CURVE	6300	2216			0.202
FYB-A6	BLUNT-NOTCHED	4000	2435	-13	-1	
FYB-A10	J-R CURVE	4500	2405			0.3
A533B						
E74	BLUNT-NOTCHED	6880	2907	0	-6	
E71	J-R CURVE	6870	2749			0.096
E72	BLUNT-NOTCHED	5130	4463	-1	-1	
E75	J-R CURVE	5190	4401			0.209
E73	BLUNT-NOTCHED	3900	4278	-8	-2	
E76	J-R CURVE	4200	4208			0.274
A710						
GFF-J13	BLUNT-NOTCHED	8150	7150	-7	1	
GFF-J11	J-R CURVE	8700	7210			0.1
GFF-J14	BLUNT-NOTCHED	5800	9512	-17	6	
GFF-J10	J-R CURVE	6800	10170			0.207
GFF-J12	BLUNT-NOTCHED	3600	9450	-39	16	
GFF-J9	J-R CURVE	5000	11204			0.298
GFF-J6	BLUNT-NOTCHED	2400	10750	-50	19	
GFF-J5	J-R CURVE	3600	13250			0.387

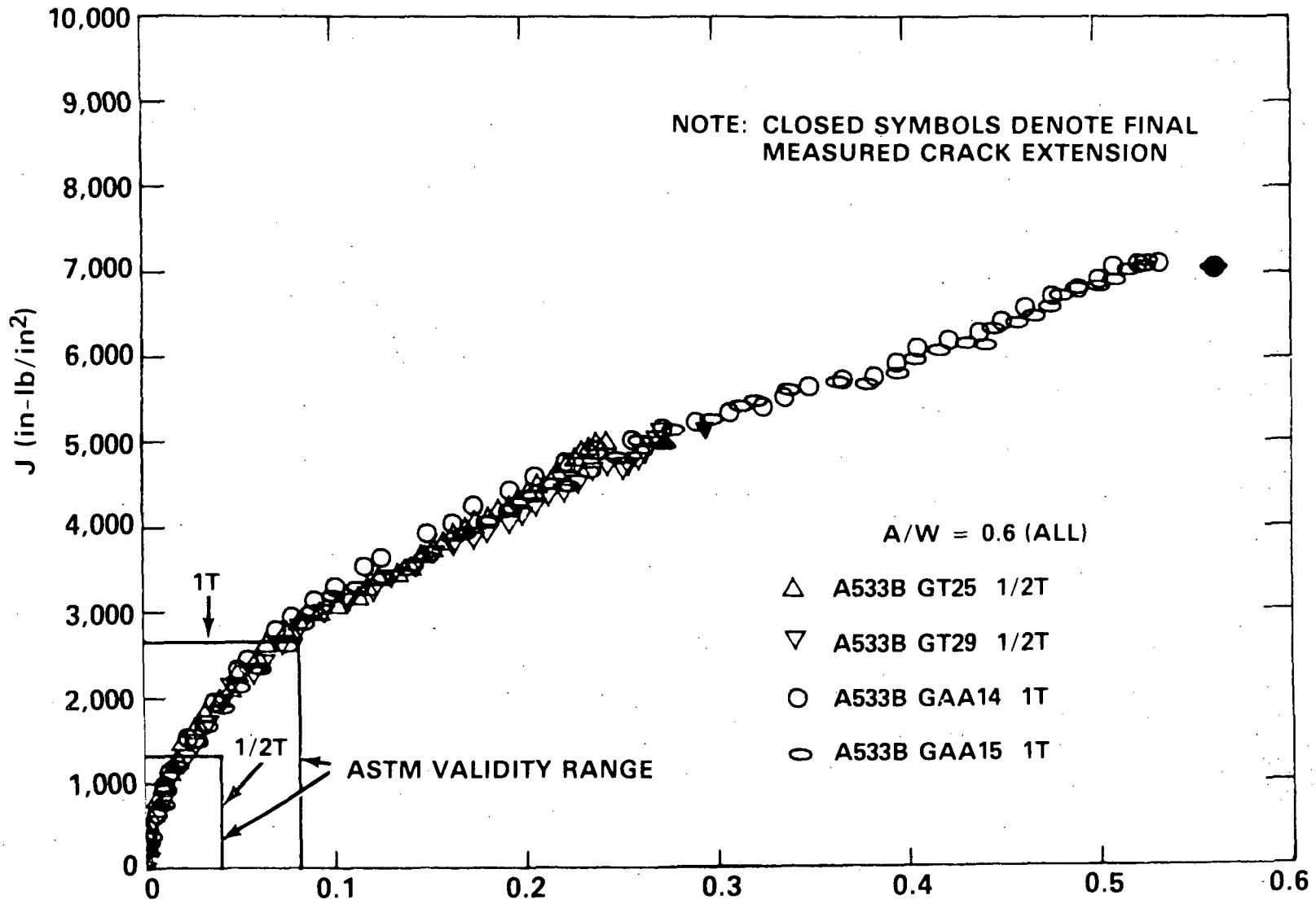


Figure 1 - J-R Curves for A533B Steel

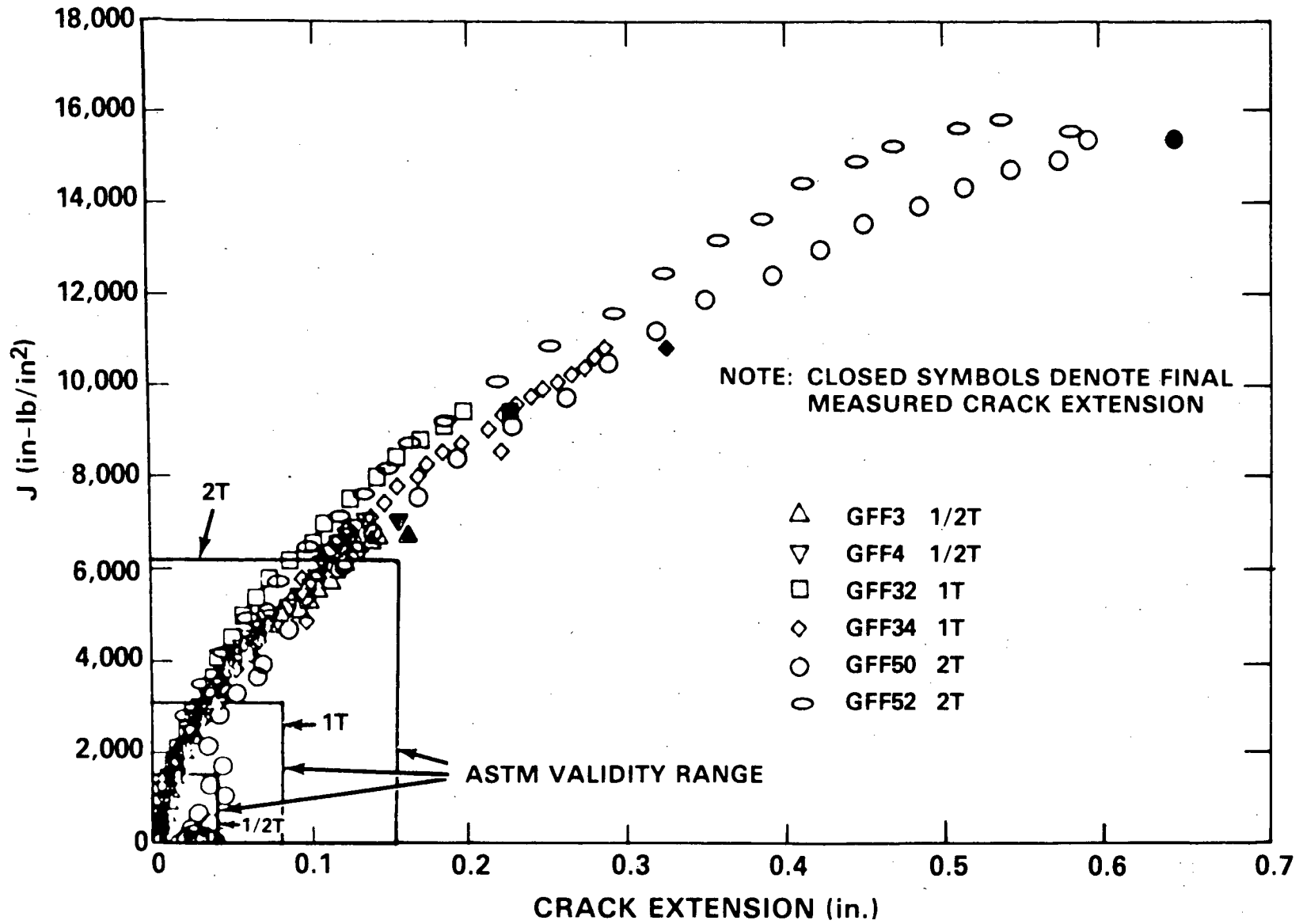


Figure 2 - J-R Curves for A710 Steel

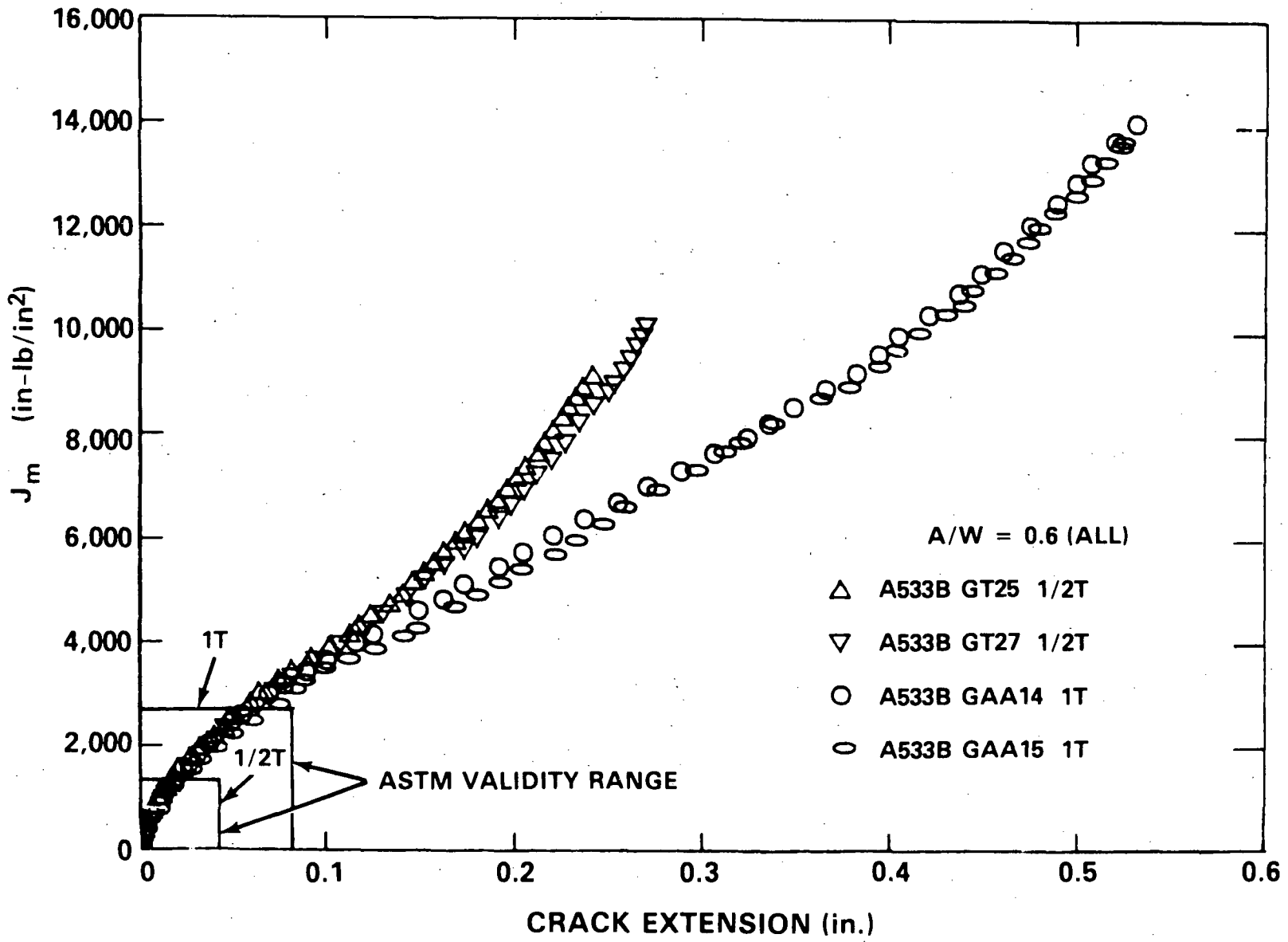


Figure 3 -  $J_m$ -R Curves for A533B Steel

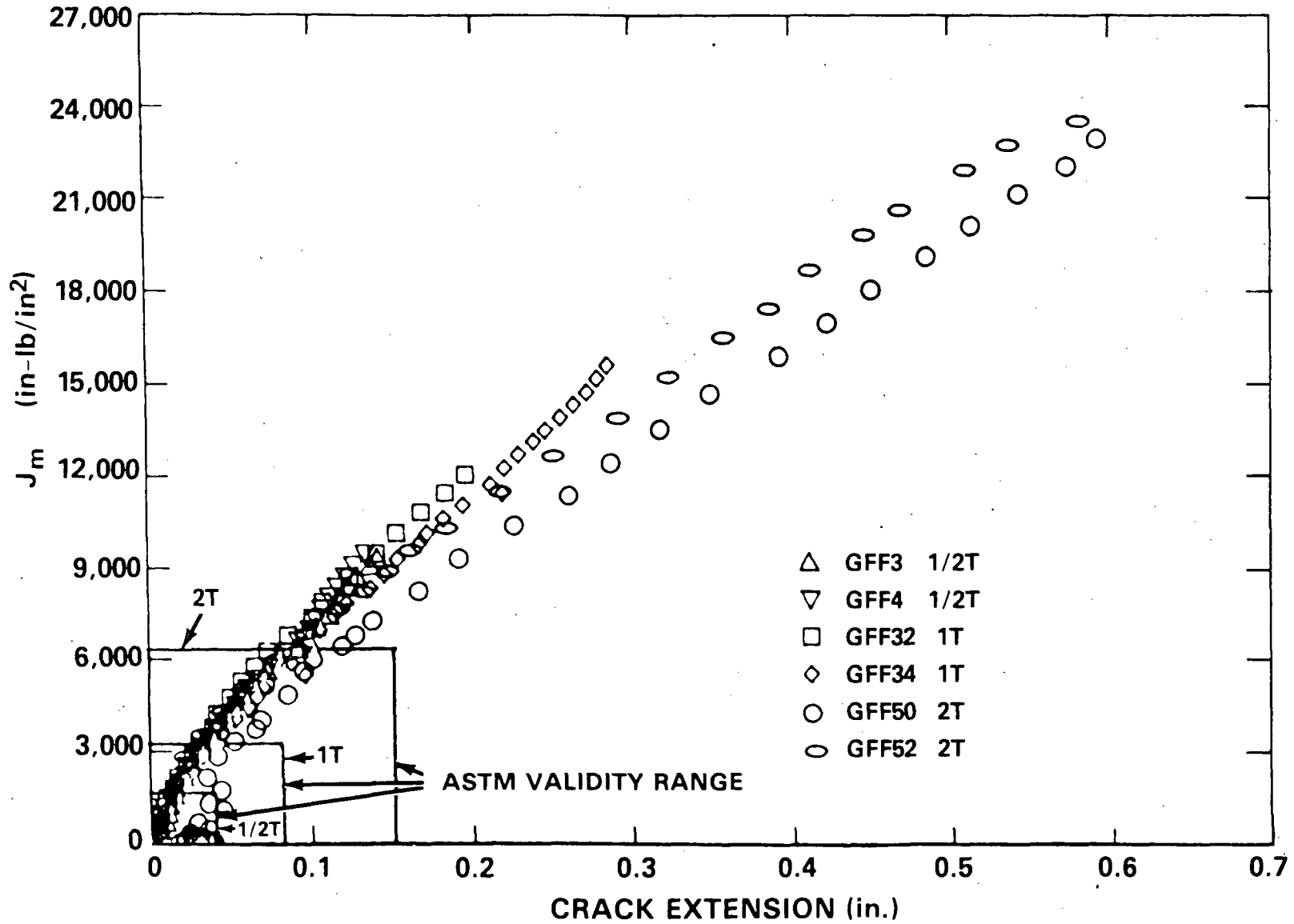
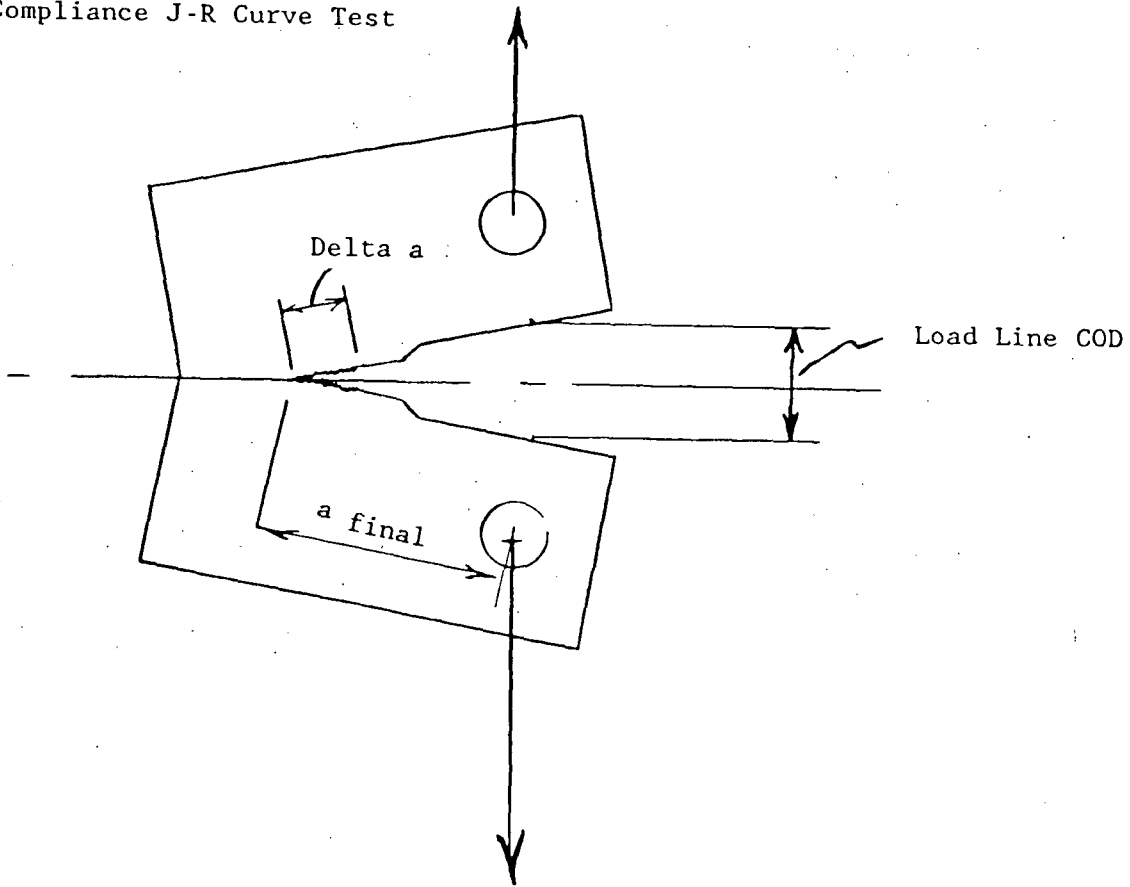
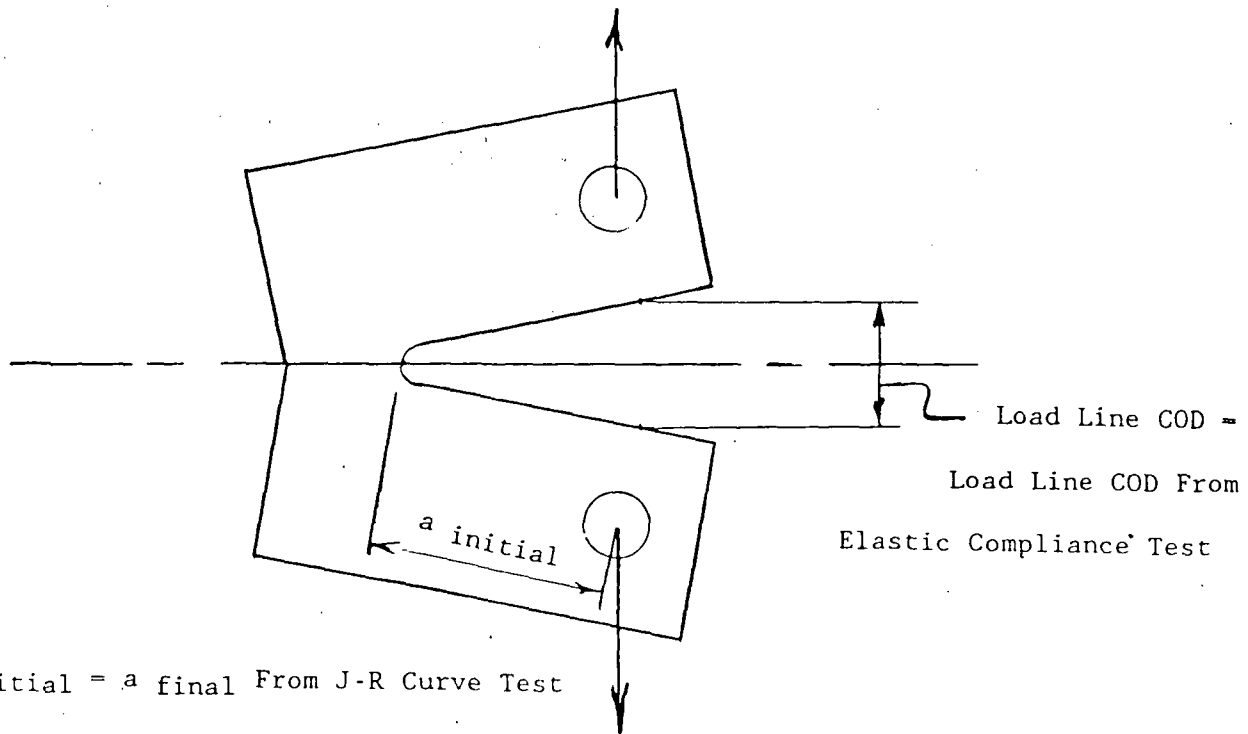


Figure 4 -  $J_M$ -R Curves for A710 Steel

Elastic Compliance J-R Curve Test



Blunt Notch Test



$a_{initial} = a_{final}$  From J-R Curve Test

Figure 5 - Schematic for Blunt Notch Tests

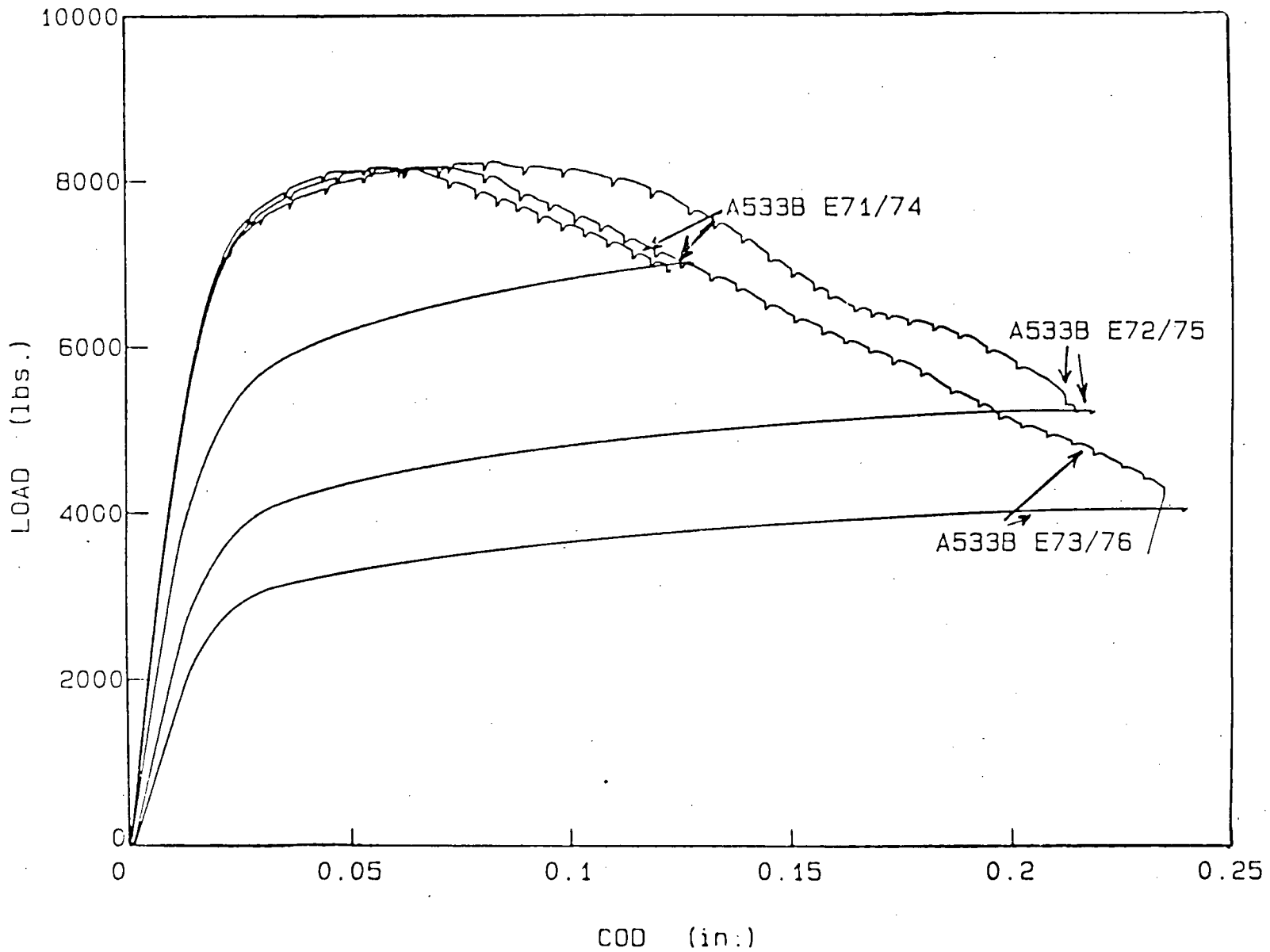


Figure 6 - Blunt Notch and Elastic Compliance Tests for A533B Steel

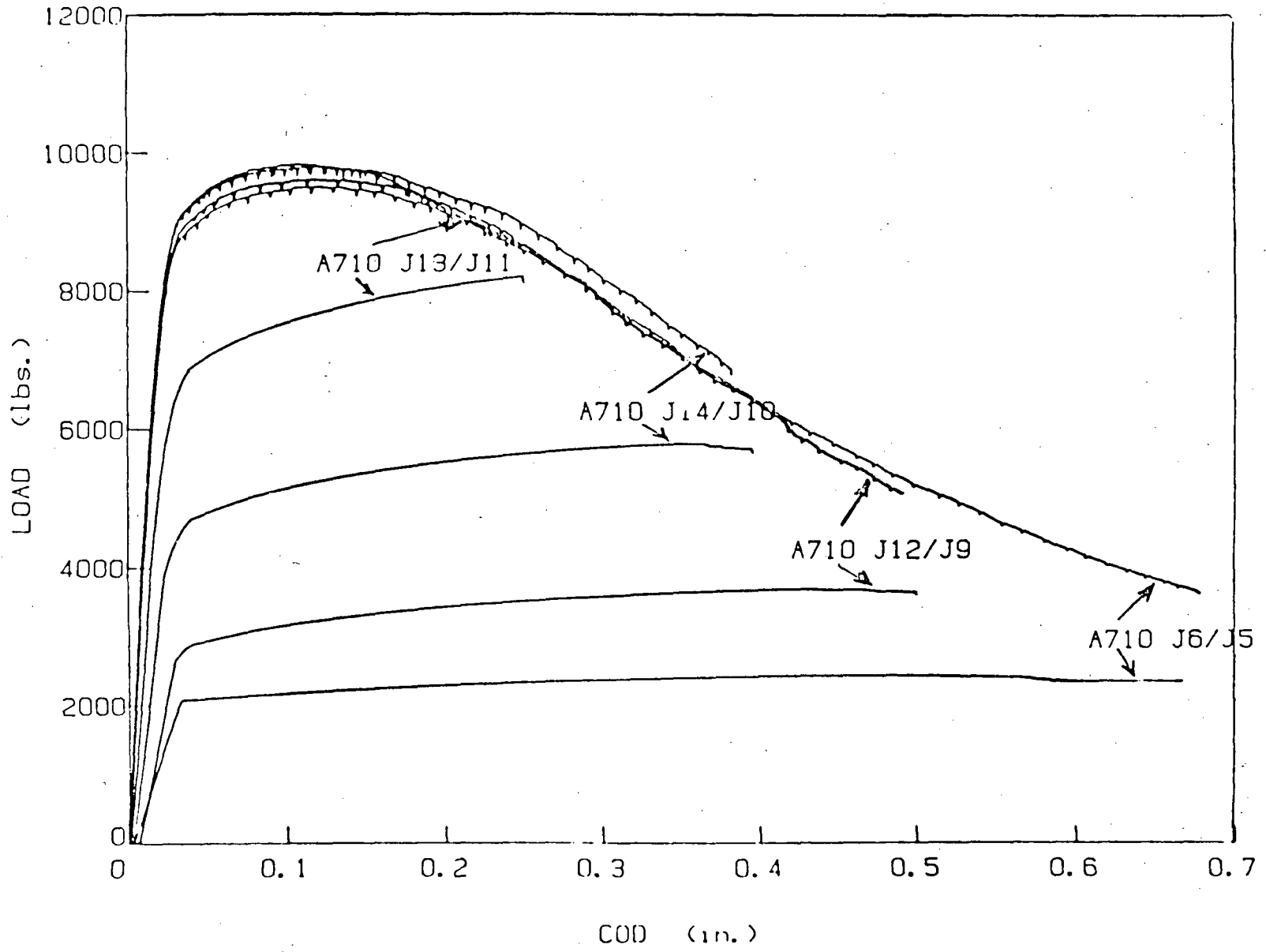


Figure 7 - Blunt Notch and Elastic Compliance Tests for A710 Steel

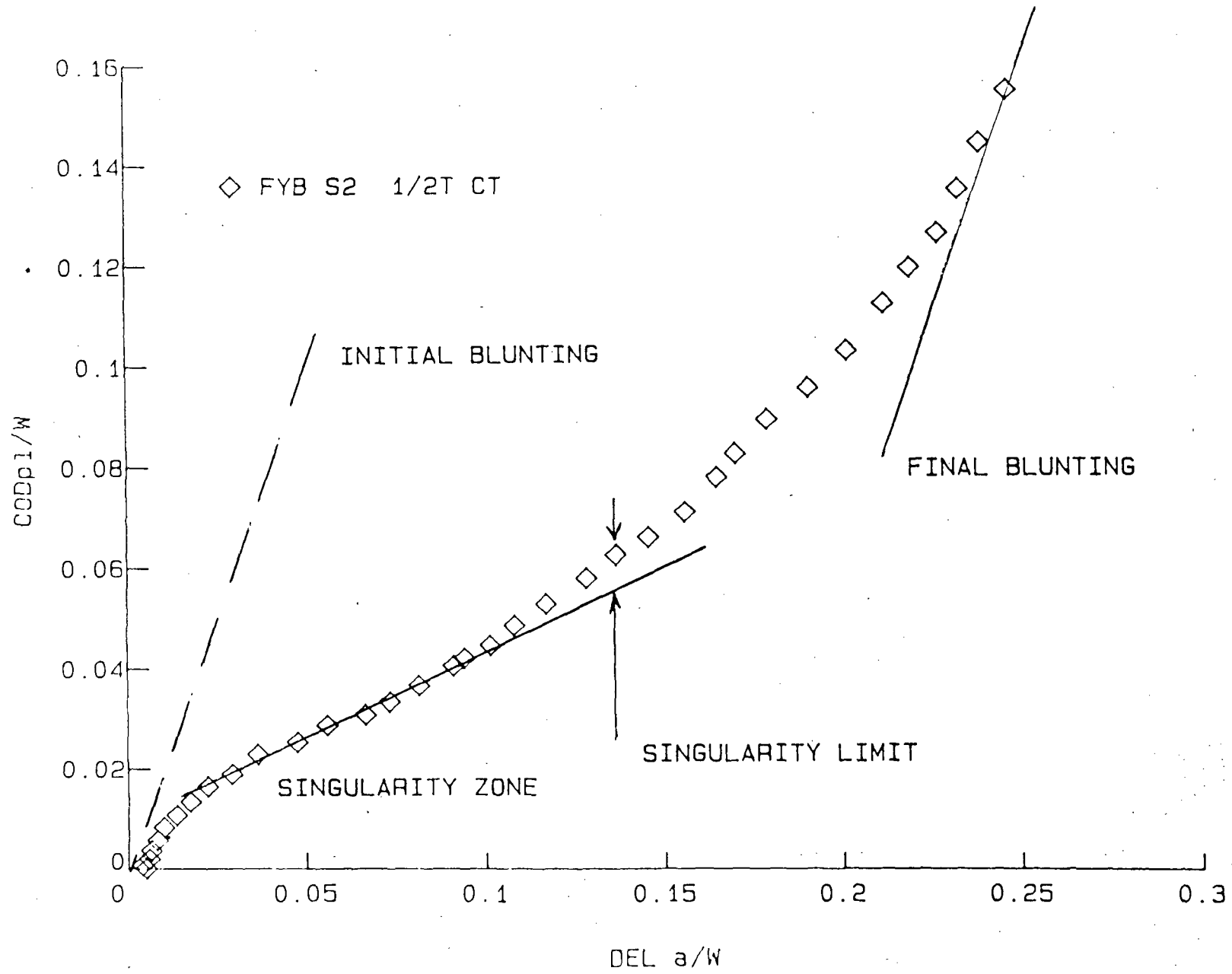


Figure 8 - Singularity Zone Analysis

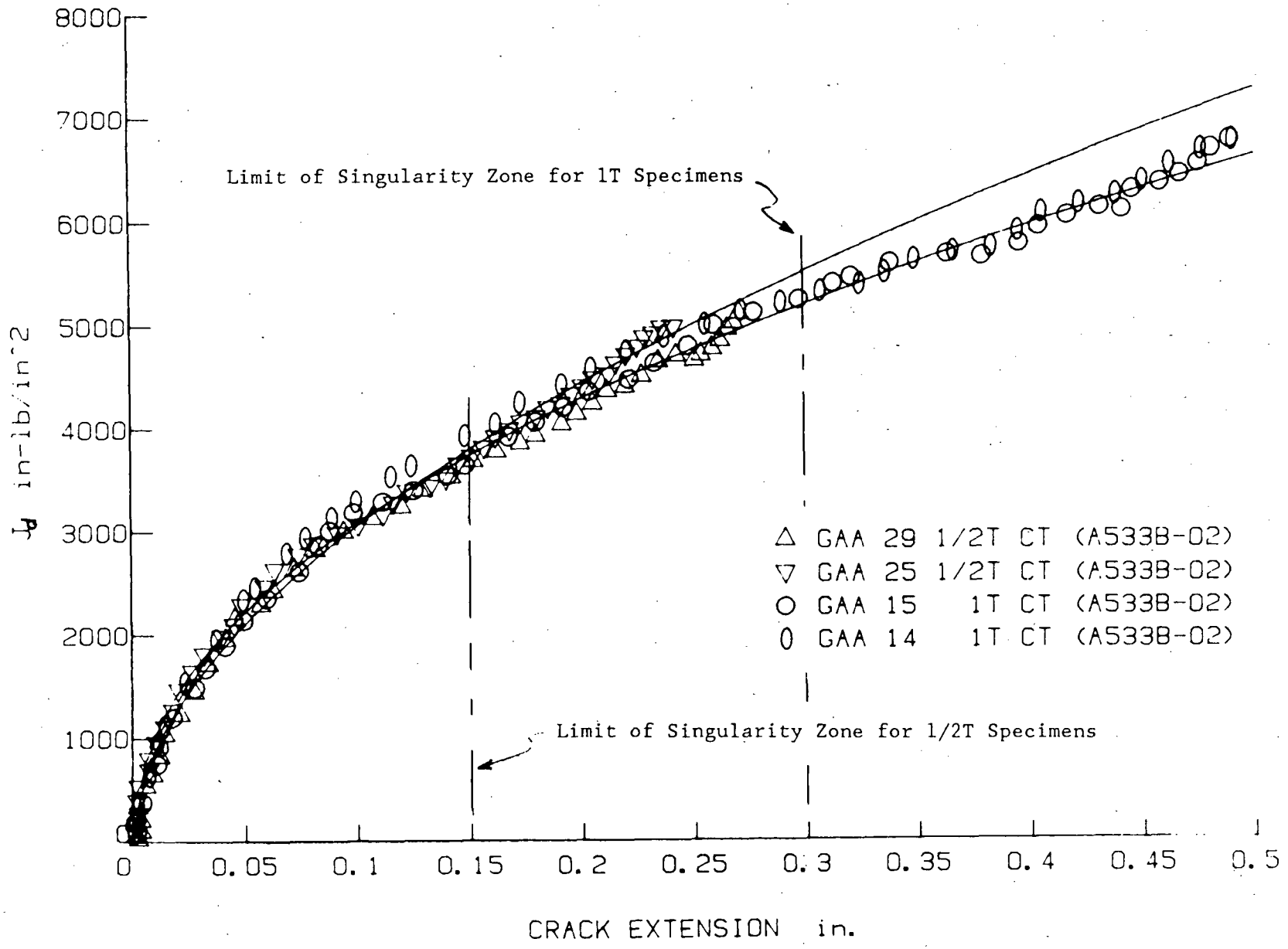


Figure 9 - Extrapolations on 1/2T C(T) J-R Curves for A533B Steel

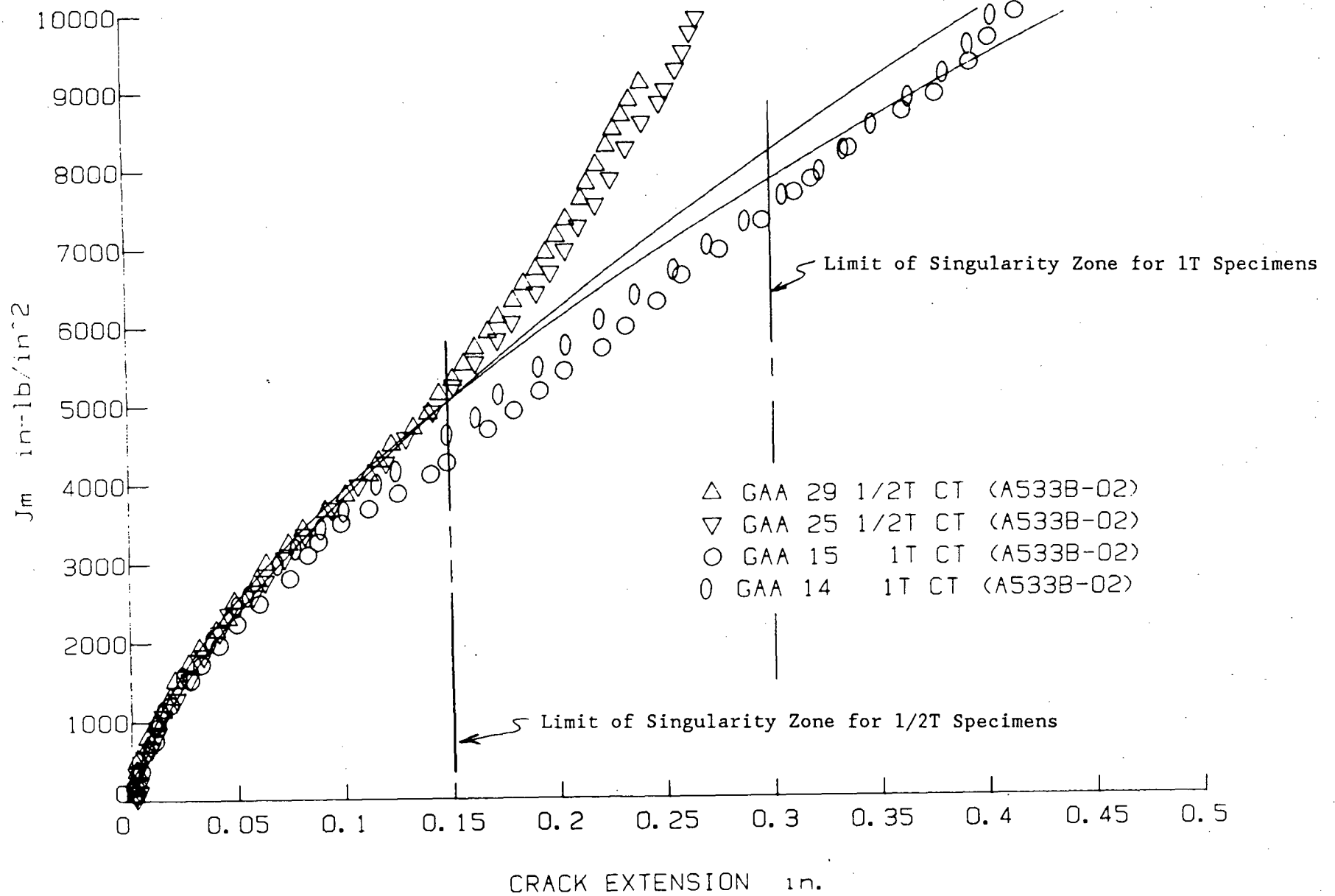


Figure 10 - Extrapolations on 1/2T C(T)  $J_M$ -R curves for A533B Steel

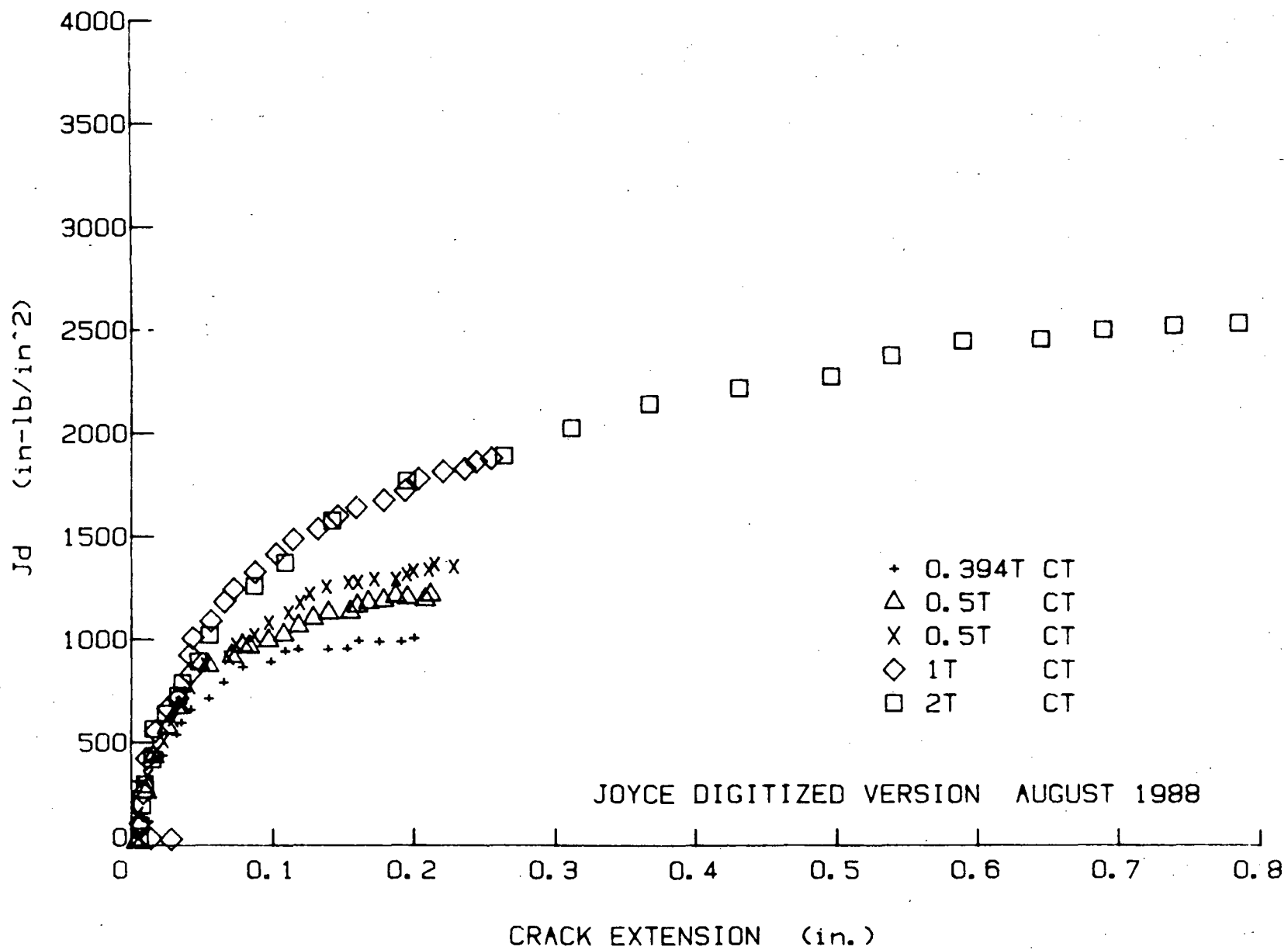


Figure 11 - J-R Curves for Linde-80 Welds (Reference 12)

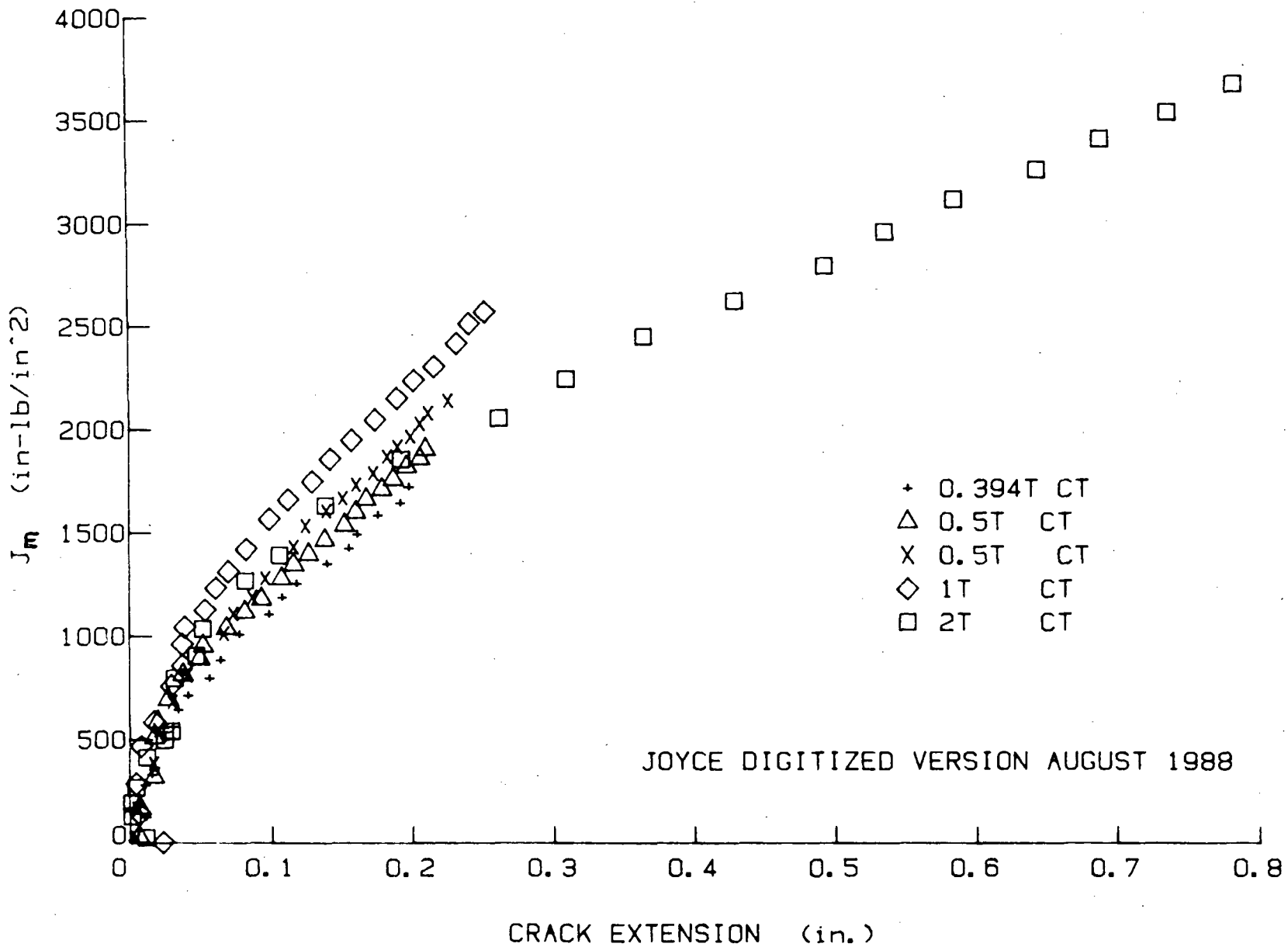


Figure 12 - J<sub>M</sub>-R Curves for Linde-80 Welds (Reference 12)

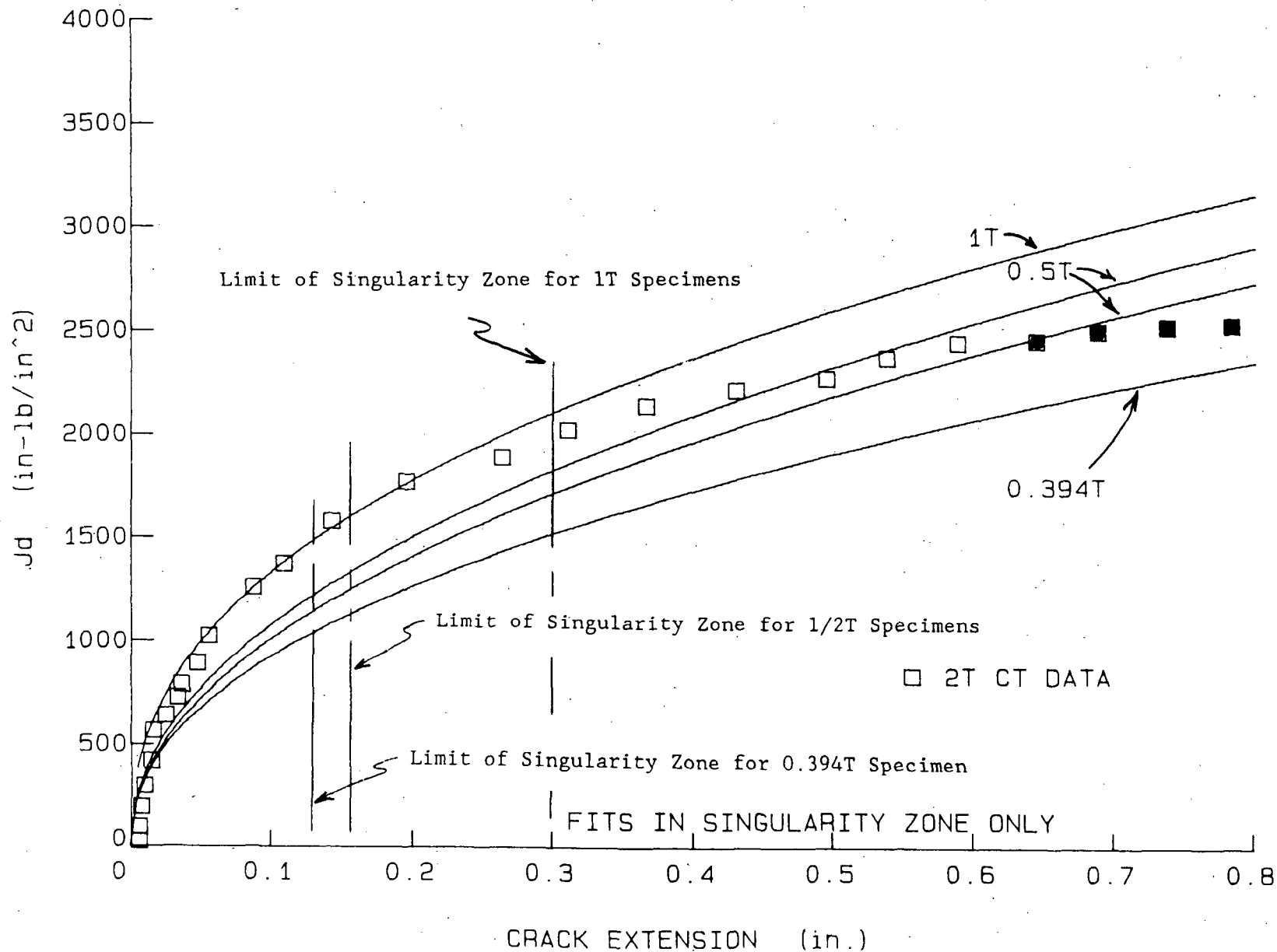


Figure 13 - Extrapolations on Small Specimen J-R Curves - Linde-80 Welds

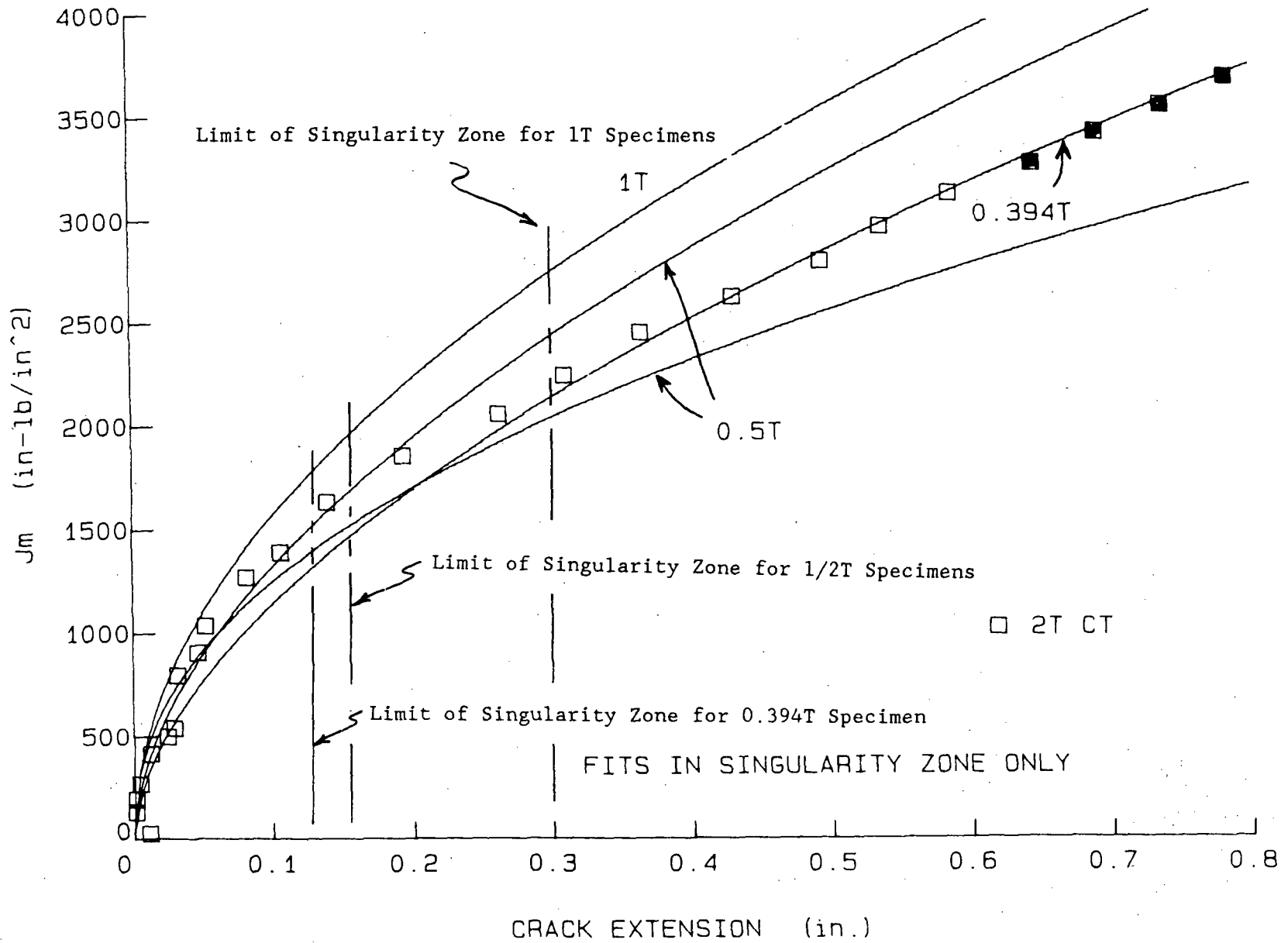


Figure 14 - Extrapolations on Small Specimen J<sub>M</sub>-R Curves - Linde-80 Welds

ADVANCES IN CRACK-ARREST TECHNOLOGY FOR  
REACTOR PRESSURE VESSELS\*

B. R. Bass and C. E. Pugh  
HEAVY SECTION STEEL TECHNOLOGY PROGRAM  
OAK RIDGE NATIONAL LABORATORY  
Oak Ridge, TN 37831

ABSTRACT

The Heavy-Section Steel Technology (HSST) Program at the Oak Ridge National Laboratory (ORNL) under the sponsorship of the U.S. Nuclear Regulatory Commission is continuing to improve the understanding of conditions that govern the initiation, rapid propagation, arrest, and ductile tearing of cracks in reactor pressure vessel (RPV) steels. This paper describes recent advances in a coordinated effort being conducted under the HSST Program by ORNL and several subcontracting groups to develop the crack-arrest data base and the analytical tools required to construct inelastic dynamic fracture models for RPV steels. Large-scale tests are being carried out to generate crack-arrest toughness data at temperatures approaching and above the onset of Charpy upper-shelf behavior. Small- and intermediate-size specimens subjected to static and dynamic loading are being developed and tested to provide additional fracture data for RPV steels. Viscoplastic effects are being included in dynamic fracture models and computer programs and their utility validated through analyses of data from carefully controlled experiments. Recent studies are described that examine convergence problems associated with energy-based fracture parameters in viscoplastic-dynamic fracture applications. Alternative techniques that have potential for achieving convergent solutions for fracture parameters in the context of viscoplastic-dynamic models are discussed.

1. INTRODUCTION

The Heavy-Section Steel Technology (HSST) Program at the Oak Ridge National Laboratory (ORNL) under the sponsorship of the U.S. Nuclear Regulatory Commission is continuing to improve the understanding of conditions that govern the initiation, rapid propagation, arrest, and ductile tearing of cracks in reactor pressure vessel (RPV) steels. In pressurized-thermal-shock (PTS) scenarios, inner surface cracks in an RPV have the greatest propensity to propagate because they are located in the region of highest thermal stress,

---

\*Research sponsored by the Office of Nuclear Regulatory Research, U.S. Nuclear Regulatory Commission under Interagency Agreement 1886-8011-9B with the U.S. Department of Energy under Contract DE-AC05-84OR21400 with Martin Marietta Energy Systems, Inc.

"The submitted manuscript has been authored by a contractor of the U.S. Government under contract No. DE-AC05-84OR21400. Accordingly, the U.S. Government retains a nonexclusive, royalty-free license to publish or reproduce the published form of this contribution, or allow others to do so, for U.S. Government purposes."

lowest temperature and greatest irradiation damage. If such a crack begins to propagate radially through the vessel wall, it will extend into a region of higher fracture toughness due to the higher temperatures and less irradiation damage. Because crack initiation is a credible event in a PTS transient, assessment of vessel integrity requires the ability to predict all phases of a fracture event. These phases included crack initiation, nonisothermal propagation, arrest, stable or unstable ductile tearing, and structural instability. Through the integrated efforts of several laboratory and university research groups, the HSST Program is developing various components of the technology required to treat these phases of a fracture event. The technology includes fracture models, analysis methods, criteria and data curves and is being developed and validated through small- and large-specimen experiments.

This comprehensive fracture technology development is addressing several important technical aspects: dynamic fracture-toughness models; rate-dependent data and constitutive models; crack-arrest data and interpretation; transferability of fracture models (e.g., from small to large specimens); cleavage/tearing transition data and modelling guidelines; and least-upper-bound temperature for cleavage behavior. Several of these issues must be studied in the context of inelastic-dynamic fracture models. Until recently, linear-elastic fracture mechanics (LEFM) concepts have been dominant in applications of dynamic analysis techniques [1]. However, except for very short crack jumps, LEFM assumptions may not be strictly valid characterizations of rapid crack propagation [2]. An indication that LEFM conditions are not satisfied occurs when elastodynamic analyses of crack run-arrest data lead to geometry-dependent fracture toughness relations. Recent studies [3] have demonstrated that this geometry dependence can be removed through application of viscoplastic fracture models that incorporate plasticity and strain-rate effects. The importance of viscoplastic effects in dynamic fracture analysis is a key component of the technology under development.

This paper describes recent advances in the coordinated effort being conducted under the HSST Program by ORNL and several subcontracting groups to develop the crack-arrest data base and the analytical tools required to construct inelastic-dynamic fracture models for RPV steels. Experimentally, large-scale tests [4-8] are being carried out to generate crack-arrest toughness data at temperatures approaching and above the onset of Charpy upper-shelf behavior. These tests involve large thermally-shocked cylinders [4], pressurized-thermally-shocked vessels [5,6], and wide-plate specimens [7,8]. The highest number of data points are being generated in these studies by the wide-plate tests [7,8] which are performed at the National Institute of Standards and Technology (NIST) for the HSST Program. These tests are extending the crack-arrest data base for ductile steels to temperatures that are higher than those capable of being imposed in conventional small-specimen tests. It is within the range of this higher temperature data that crack arrest is most likely to occur in a PTS scenario. To substantially augment the data base, crack-arrest toughness data from small- and intermediate-size specimens [9-12] subjected to static and dynamic loading are being generated at Battelle Columbus Division (BCD), ORNL, Southwest Research Institute (SwRI), and the University of Maryland (UM).

Analytically, viscoplastic effects are being included in the dynamic fracture models and computer programs and their utility validated through analyses of carefully controlled experiments. Material properties characterization testing has been performed on A533 grade B class 1 (A533B) steel by Ohio State University (OSU Ref. [13]), SwRI (Ref. [14]), and SRI International (Ref. [15]) using tensile and split-Hopkinson bar techniques. These data have been used to derive material constants for the Bodner-Partom [16], the Perzyna [17] and the Robinson [18] viscoplastic models. These constitutive models, along with crack propagation techniques and several proposed nonlinear fracture parameters, have been installed in HSST-developed finite-element computer programs. Two computer programs [ADINA/VPF (Refs. [19-20]) from ORNL and VISCRK (Ref. [11]) from SwRI] have been developed independently to evaluate different analysis techniques and to insure high-quality dynamic solutions. The capabilities of these nonlinear techniques are being compared and evaluated, in part, through applications to the small- and large-specimen crack run-arrest experiments.

Recent studies indicate that convergence of the leading energy-based fracture parameters ( $T^*$ , etc.) has not been established for viscoplastic-dynamic fracture applications [21]. Two parallel studies are under way to address the issue of convergence. SwRI is performing studies of the geometry independence of a two-component parameter ( $T^*$ ,  $\epsilon$ ) based on a process zone of height  $2\epsilon$  that extends with the moving crack tip [22]. ORNL is studying a crack propagation model based on a variable-order singular element formulation [23]. Other contributions include asymptotic crack-tip studies being conducted by OSU [24,25]. Additionally, ORNL and UM are determining preliminary relations of crack-tip velocity vs pseudo-K vs temperature for nonlinear fracture conditions. Some details of these recent developments in crack-arrest technology under the HSST Program are described in the following sections.

## 2. DYNAMIC FRACTURE TESTING PROGRAM

### 2.1 Wide-Plate Tests

A vital component of the HSST crack-arrest studies is the wide-plate tests which are conducted at NIST. A total of sixteen wide-plate experiments have been performed using two steels. Objectives of these tests are to: (1) extend the existing  $K_{Ia}$  data bases to values above the limit in the ASME Code, (2) clearly establish that crack arrest does occur prior to fracture-mode conversion, (3) provide data to improve and validate elastic and viscoplastic-dynamic fracture models, and (4) develop improved experimental dynamic fracture methods. The initial series of wide-plate crack-arrest specimens (WP-1) is taken from a plate of A533B steel that is in a quenched and tempered condition [7]. Drop-weight and Charpy V-notch test data indicate that  $RT_{NDT} = -23^\circ\text{C}$ , and Charpy upper-shelf energy is 160 J with its onset occurring at about  $55^\circ\text{C}$ . The WP-2 series of wide-plate specimens is taken from a plate of 2 1/4 Cr-1 Mo steel that has been heat treated to produce a low upper-shelf Charpy impact energy [8]. Based on a limited number of tests, the tentative



In each wide-plate test, a fracture toughness gradient was achieved across the plate by LN<sub>2</sub> cooling of the notched edge while heating the other edge. Liquid nitrogen flow and power to the heaters were continuously adjusted to obtain the desired thermal gradient. Tensile load was then applied at a rate of 11 to 25 kN/s until fracture occurred.

### 2.1.2. Summary of posttest analysis results

A summary of conditions for each test in the WP-1 and the WP-2 series is given in Ref. [8]. Posttest elastodynamic fracture analyses were conducted for each wide-plate test to investigate the interaction of parameters that affect the crack run-arrest events. Figure 2 summarizes crack-arrest toughness values for the WP-1 and WP-2 series which were computed in fixed-load, generation-mode dynamic finite-element analyses. (In the generation-mode analysis, the crack tip is propagated according to a prescribed crack position vs time relation obtained from measured data.) Results for both test series exhibit a significant increase in toughness at temperatures near and above the onset of Charpy upper shelf ( $T - RT_{NDT} = 78^\circ\text{C}$  for WP-1;  $T - DW_{NDT} = 90^\circ\text{C}$  for WP-2). Crack-arrest toughness values obtained from this series of tests extend consistently above the ASME reference fracture-toughness curve. The increase in arrest-toughness values which occurs at an accelerating rate with temperature near and above the onset of Charpy upper shelf suggests that a

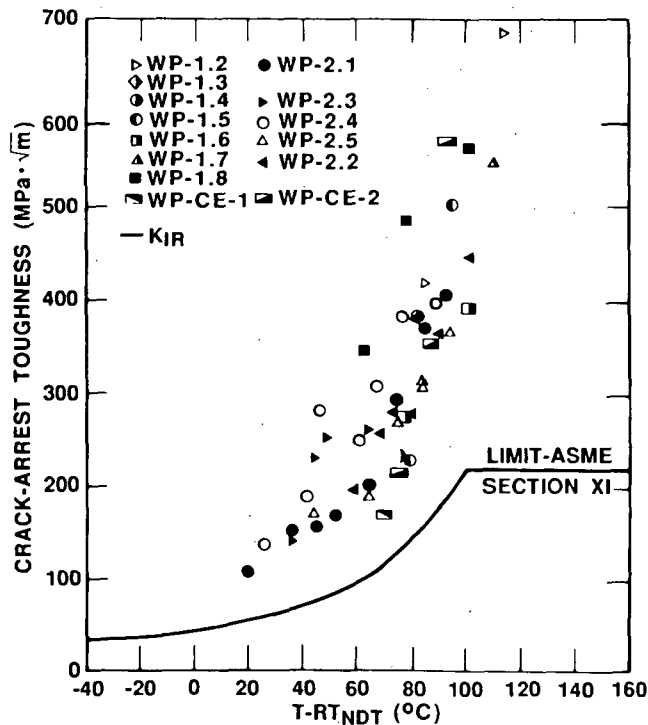


Fig. 2. Generation-mode (fixed load) crack-arrest toughness data versus temperature ( $T - RT_{NDT}$ ) for HSST wide-plate tests.

temperature limit exists at or below which cleavage crack propagation will arrest, no matter how high the applied driving force. Results presented in Fig. 2 also show that arrest of cleavage crack propagation can and does occur at temperatures above the onset of Charpy upper shelf.

The importance of the analysis method (static vs dynamic) and boundary conditions (fixed load or fixed load-pin displacement) utilized to interpret the wide-plate crack-arrest tests is demonstrated by comparing the values given in Fig. 3 for specimen WP-2.4. Values of  $K_{Ia}$  determined using the secant equation [26] and the Tada fixed load condition [27] represent approximate lower and upper bounds, respectively, to the dynamic results in Fig. 3. For long-duration crack run-arrest events (>20 ms), such as could occur for the low Charpy upper-shelf material, considerable load adjustment can take place as a result of specimen/pull-plate compliance. Therefore, the most meaningful values of  $K_{Ia}$  under such conditions must reflect this occurrence and involve a dynamic finite-element analysis. The dynamic generation-mode (fixed load) analysis results represent one such calculation.

Predictions of crack propagation and arrest in dynamic fracture problems requires specification of the relation among instantaneous crack-tip velocity,  $a$ , dynamic fracture toughness,  $K_{ID}$ , and temperature,  $T$ , for the fracturing material. This relation is a primary input for predictive application-mode dynamic fracture analyses. [In an application-mode analysis, the crack tip is propagated incrementally when the relation  $K_{applied} = K_{ID}(a, T)$  is satisfied.] At UM, Schwartz [28] has used data from the WP-1 series of

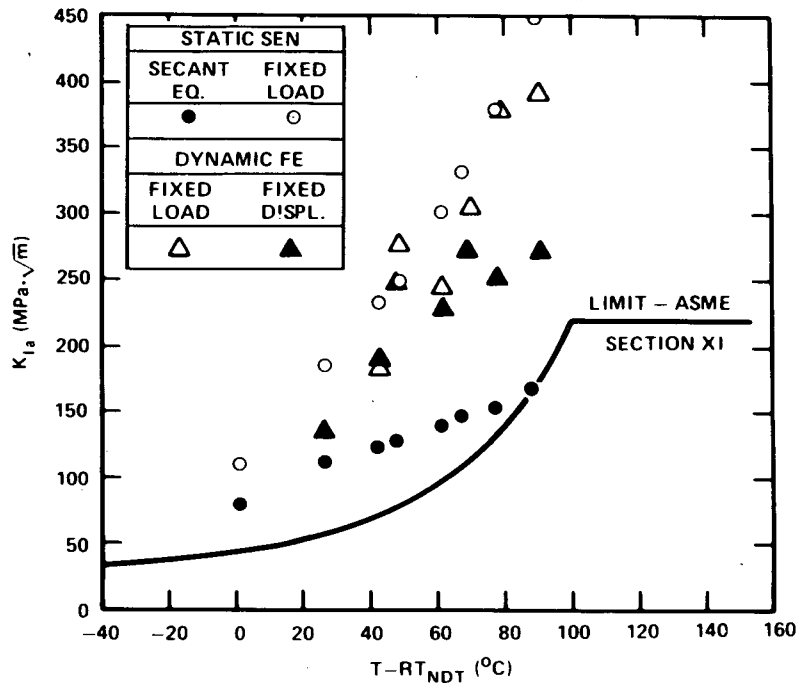


Fig. 3. Static and dynamic crack-arrest toughness determination vs temperature ( $T - RT_{NDT}$ ) for specimen WP-2.4.

wide-plate tests to estimate the  $\dot{a}$  vs  $K_{ID}$  vs T relation for A533B steel given in Fig. 4. The toughness relation in Fig. 4 has been used by ORNL for pretest analysis of intermediate-size crack-arrest specimens [10] of A533B steel.

Topographic analyses of selected wide-plate fracture surfaces are being performed at UM using stereo-SEM and relative-height measurement techniques. In Ref. [12], these techniques were applied to regions of fracture surfaces (from WP-1.7 and WP-CE-1) where cleavage arrest was followed by fibrous-tearing reinitiation. Estimates of crack-tip opening displacement (CTOD) obtained from relative-height measurements were used to calculate  $K_I$ -values at reinitiation. These studies indicated that high  $K_I$ -values ( $>350 \text{ MPa}\sqrt{\text{m}}$ ) were necessary to initiate fibrous tearing from an arrested cleavage crack in the upper transition temperature range. It is anticipated that large uncertainties in these topographic estimates of  $K_I$  at reinitiation can be reduced substantially by improving the topographic mapping of the regions of interest.

More refined analyses of the wide-plate test data will be performed by ORNL and UM to determine the influence of tunneling on computed crack-arrest toughness values. To address this issue, the relevant experimental and analytical literature on crack tunneling will be reviewed and a series of

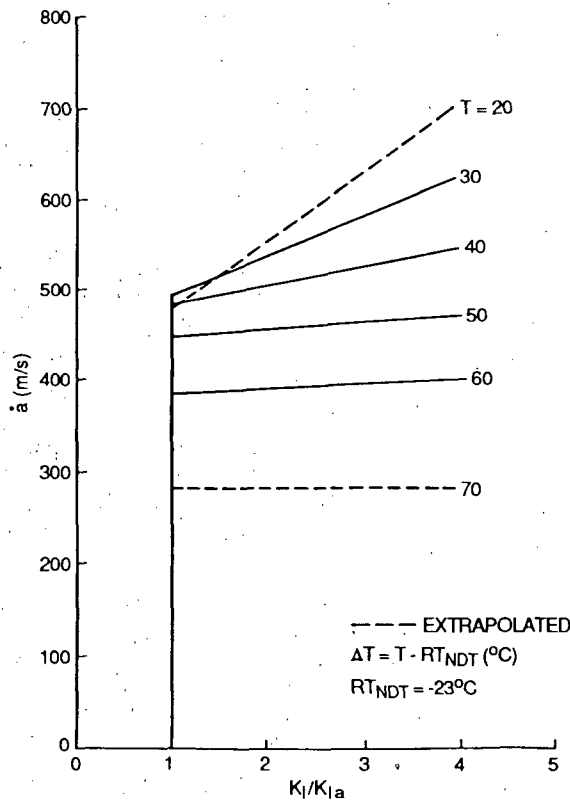


Fig. 4. Crack-tip velocity vs dynamic stress-intensity factor vs temperature inferred from A533B steel.

three-dimensional studies of crack tunneling will be performed under quasi-static conditions. The major thrusts of these investigations will be to develop a more refined analytical model for tunneling and to determine any necessary corrections to the wide-plate test results to account for the influence of tunneling.

## 2.2 Pressurized-Thermal-Shock Experiment (PTSE-2)

The HSST Program is obtaining additional crack-arrest data through pressurized-thermal-shock tests [5,6] that provide validation data under multi-axial transient conditions. The PTS experiments are the most recent of a long succession of validation experiments that are on a sufficiently large scale to allow important aspects of the fracture behavior of nuclear reactor pressure vessels to be simulated. Elastodynamic finite-element analyses [29] were previously carried out for the two cleavage crack run-arrest events that occurred in the second and third phases of the PTSE-1 test [5]. The dynamic results showed good agreement between data and predictions for the short crack runs of that experiment, and quasi-static and dynamic analyses showed little difference. These same dynamic fracture analysis techniques have been applied now to the analysis of the two crack run-arrest events of PTSE-2 [6].

### 2.2.1 Test conditions for PTSE-2

Dimensions of the test vessel and flaw geometry are given in Table 1 for the PTSE-2 test [6]. An HSST Intermediate Test Vessel (ITV) was used as a tough carrier vessel and prepared with a plug of test steel welded into the vessel. The test material was a specially heat treated 2 1/4 Cr-1 Mo plate with a low Charpy upper-shelf energy (~50 to 70 J) and low ductile-tearing resistance. The 1-m-long sharp flaw was implanted in the outside surface of the plug by cracking a shallow electron-beam weld under the influence of hydrogen charging. For each test, the ITV was extensively instrumented to give direct measurements of crack-mouth opening displacement, temperature profiles through the vessel wall, and internal pressure during the transient. In the experiment, the flawed vessel was enclosed in an outer vessel that was electrically heated to bring it to the desired uniform initial temperature of about 290°C. A thermal transient is initiated by suddenly injecting chilled

Table 1. Geometric parameters of PTSE-2 vessel

Inside radius	=	343 mm
Wall thickness. (w)	=	147.6 mm
Flaw length	=	1000 mm
Flaw depth (a)	=	14.5 mm
a/w	=	0.098 mm

water (or a methanol-water mixture) through an annulus between the test vessel and the outer vessel. Extensive material properties testing of the vessel insert material preceded the PTS experiment. The tensile strength was undesirably low, but other properties, although somewhat uncertain, were satisfactory. Some of the properties determined prior to the experiment are summarized in Table 2.

Table 2. Properties of PTSE-2 vessel insert material

Yield strength	= 255 MPa
Ultimate strength	= 518 MPa
NDT temperature	= 49°C
Onset of Charpy upper shelf (100% shear fracture appearance)	= 150°C
Charpy upper-shelf energy	= 50-75J <sup>a</sup>

<sup>a</sup>Range for all depths in plate. The average at 1/4 depth is 68 J.

The experiment was planned to consist of two transients, of which the first would induce warm prestressing ( $K_I < 0$ ) followed by reloading ( $K_I > 0$ ) until the crack propagated by cleavage. The second transient was planned to produce a deep cleavage crack jump with an arrest or mode conversion occurring only after conditions conducive to unstable tearing were attained. In the first transient PTSE-2A, ductile tearing occurred in three separate phases: (1) prior to warm prestressing; (2) during reloading; and (3) after the cleavage arrest. The crack propagated both axially and radially by cleavage. In the second transient PTSE-2B,  $K_I$  increased monotonically, while the crack tore stably, propagated radially in cleavage, and then tore unstably.

### 2.2.2 Summary of posttest analysis results

In the elastodynamic analyses of the transient observed in PTSE-2, a 2-D plane strain finite-element formulation was utilized to model the test vessel. The finite-element model and the material properties utilized in this analysis are described in Ref. [30]. Measured values of the radial temperature distribution and internal pressure at the time of cleavage crack propagation in the transient of PTSE-2 are given in Ref. [6]; the boundary conditions are assumed constant during the run-arrest event.

Results from application-mode elastodynamic analyses of the A and B transients are depicted in Figs. 5 and 6 and in Table 3. Figure 5 gives the computed crack-depth ratio,  $a/w$ , as a function of time for each of the two transients and compares computed values with measured data at crack arrest.

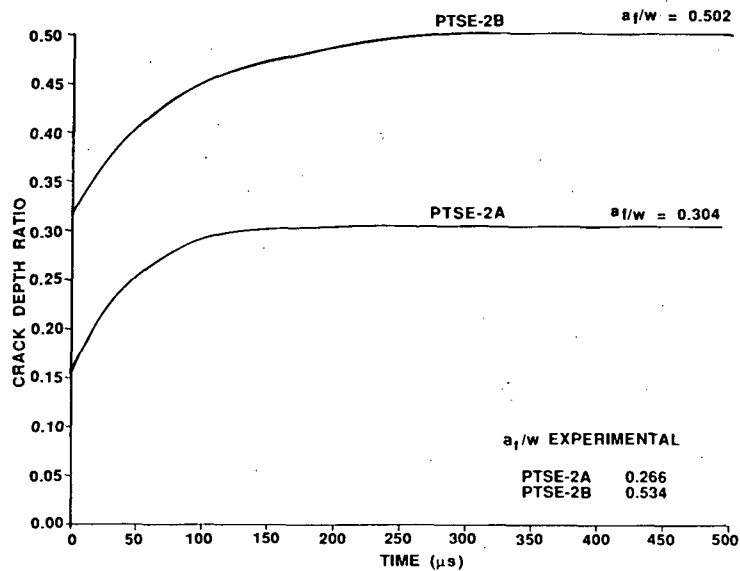


Fig. 5. Crack-depth ratio versus time for posttest elastodynamic analysis of PTSE-2.

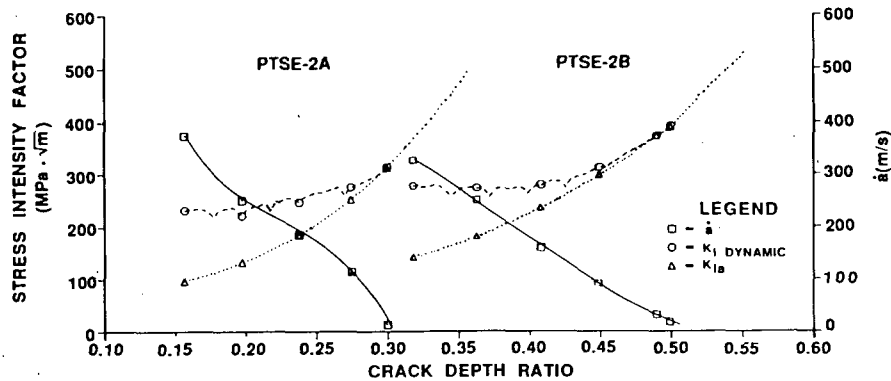


Fig. 6. Stress-intensity factor, crack-velocity, and static crack-arrest toughness versus crack-depth ratio for posttest elastodynamic analysis of PTSE-2.

Figure 6 depicts the dynamic stress-intensity factor,  $K_I$ , the crack velocity,  $a$ , and the static crack-arrest toughness,  $K_{Ia}$ , vs  $a/w$  relations for the transients, and it indicates that the crack propagates into a rising  $K_I$  field for both run-arrest events. Table 3 compares selected results from previously reported 2-D quasi-static elastoplastic analyses [6] based on measured crack depths and from the quasi-static elastic and elastodynamic analyses of the present study. The differences in computed  $K_I$  values at initiation in the two transients are due primarily to plasticity effects that are not modelled in this study.

Table 3. Initiation and arrest parameters from posttest elastoplastic and elastodynamic analyses of PTSE-2

Experiment phase	a/w	a (m)	Temperature (°C)	$K_{Ia}$ (MPa√m)	Event
PTSE-2A					
S <sup>a</sup>	0.1524	0.0225	80.7	198.9	Initiation
ES <sup>b</sup>	0.1524	0.0225	80.7	238.4	Initiation
S	0.2663	0.0393	130.6	261.4	Arrest
ED <sup>c</sup>	0.3040	0.0449	145.6	313.8	Arrest
PTSE-2B					
S	0.3123	0.0461	102.4	248.1	Initiation
ES	0.3123	0.0461	102.4	284.5	Initiation
S	0.5339	0.0788	162.9	419.3	Arrest
ED	0.5016	0.0740	155.4	393.2	Arrest

<sup>a</sup>S = quasi-static elastoplastic analyses (Ref. [6]) based on measured crack depth.

<sup>b</sup>ES = quasi-static elastic analysis (Ref. [30]).

<sup>c</sup>ED = application-mode elastodynamic analysis (Ref. [30]).

The computed results presented in Figs. 5 and 6 represent contrasts in the predicted kinematic behavior of the crack tip during the two transients of PTSE-2. In the A transient, the computed crack-tip velocity falls rapidly to zero at time  $t \approx 150 \mu\text{s}$  following initiation of the cleavage event. Calculations for the B transient indicate that the crack velocity was non-zero for a longer period of time, at least  $300 \mu\text{s}$ . The cleavage event observed in the B transient was interrupted by a narrow band of ductile tearing at  $a/w \approx 0.47$  that extended the entire length of the crack. Posttest studies of the fracture surface indicate that cleavage was still occurring over short discontinuous segments of the tearing band, and that the crack eventually reinitiated in cleavage and arrested at  $a/w = 0.534$ . Although the complex interactions of these fracture modes are not modelled in the present study, results in Fig. 6 show that a small increase in the  $K_{Ia}$  curve could produce an arrest at the approximate location of the ductile tearing band. No such interruption of the A transient cleavage event by tearing was detected, and the computed results in Fig. 6 are consistent with that observation.

Results presented in Fig. 3 show that the wide-plate  $K_{Ia}$  test results exhibit an accelerating increase in arrest-toughness values with increasing temperature. The trend for  $K_{Ia}$  values to extend consistently above the limit provided in ASME Section XI is further substantiated in Fig. 7 which presents data from the PTS and wide-plate experiments and from other large-scale tests summarized in Ref. [8].

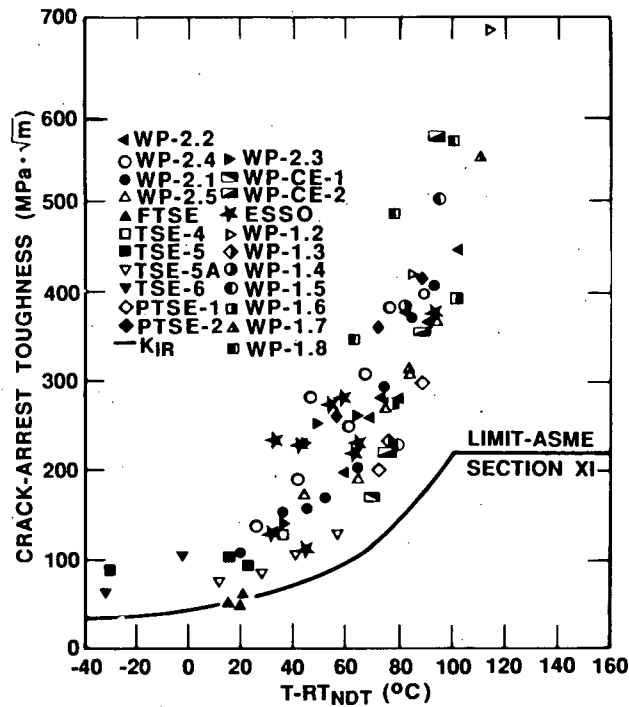


Fig. 7. High-temperature crack-arrest toughness data vs temperature ( $T - RT_{NDT}$ ) for wide-plate, PTS, and large-specimen tests.

## 2.3 Intermediate- and Small-Scale Specimen Tests

### 2.3.1 Stub-panel crack-arrest specimen

Studies [10] have been conducted by the HSST Program at ORNL to evaluate the usefulness of crack-arrest experiments that employ a relatively small panel specimen whose size is between conventional crack-arrest specimens and the wide-plate specimens. For the design of the specimen geometry, the following requirements were adopted:

1. measurement of crack-arrest toughness values  $>200 \text{ MPa}\cdot\sqrt{\text{m}}$ ,
2. measurement of toughness values in a rising field of stress-intensity factor, and
3. a limit capacity of 2.5 MN for the available testing machines.

The stub-panel specimen ( $45.1 \times 99.1 \times 3.39 \text{ cm}$ ) depicted in Fig. 8 was proposed to meet the above requirements. The plate is side-grooved to a depth of 12.5% of the thickness, resulting in a net thickness of 2.54 cm at the crack plane. A gradient in fracture toughness is achieved by cooling the stub region and heating the panel edge to produce a nonuniform steady-state temperature distribution across the plate. A tensile load is applied to the panel to produce a rising driving force. The stub is mechanically loaded to provide

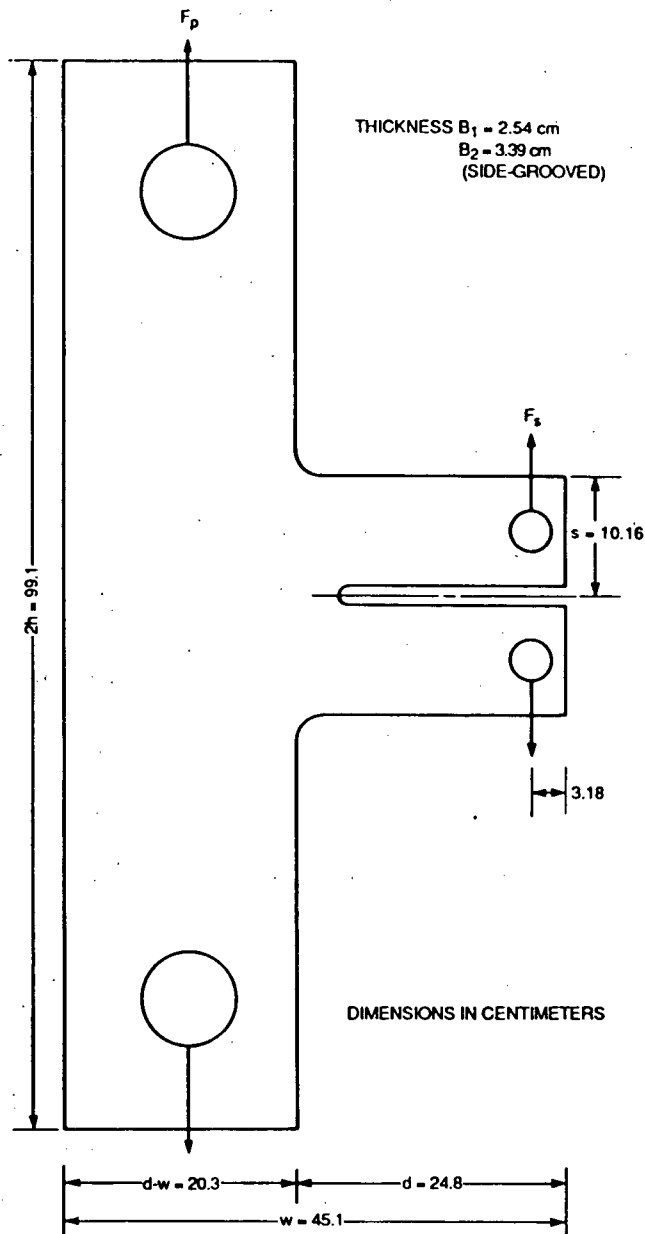


Fig. 8. Geometry and loading system of stub-panel crack-arrest specimen.

$K_I$  levels that are high enough for initiation of the chilled crack in cleavage. Arrest of the fast-running crack then occurs in the ductile high-temperature region of the panel. Static and dynamic analyses [10] were carried out for the stub-panel configuration to assess its utility for producing  $K_{Ia}$  data in the temperature regime of upper-shelf material behavior. These analyses indicated that crack-arrest toughness values  $>200$  MPa $\cdot\sqrt{m}$  could be measured in a rising  $K_I$  field by using available testing machines and appropriate thermal boundary conditions.

Plans have been formulated at ORNL for fabricating, instrumenting, and testing the stub-panel specimen in Fig. 8. The first specimen was fabricated from the same plate (HSST plate 13-A) of A533B steel as that used in the WP-1 series of wide-plate tests. Material properties for the test plates have been described previously in Ref. [10]. To record pertinent data during the test, the specimen will be instrumented with thermocouples, strain gages, and displacement gages, using a placement configuration and instrumentation chain similar to that employed for the wide-plate specimens [7]. The first specimen will be tested early in FY 1989.

### 2.3.2 Small dynamic-fracture specimens

Crack-arrest toughness data applicable to PTS conditions is being developed through small-scale specimen testing programs by several HSST subcontracting institutions. At SwRI, experimental research [31] has been directed toward obtaining dynamic crack-propagation data in A533B steel using small-scale specimens supplied by ORNL. For this purpose, a series of duplex A533B/4340 steel specimens of effective width,  $w = 127$  mm, were instrumented and tested at 23°C. Crack growth was monitored on both surfaces of each specimen using crack gages, whereas crack-line displacement was measured using an eddy-current transducer. Dynamic-strain measurements were also obtained and used to examine the detailed interaction between stress-wave propagation and crack-growth response. Results from dynamic analyses performed with the SwRI code VISCRK have been reported for two duplex experiments (SD2 and SD6) in Ref. [31]. Figure 9 shows the  $K_{Ia}$  values from these analyses plotted with the ORNL equation for  $K_{Ia}$  and the ASME  $K_{IR}$  curve. Similarly, the  $K_{Ia}$  values for SwRI analyses of the first crack-extension event in several of the WP-1 series of wide-plate experiments are shown in Fig. 9.

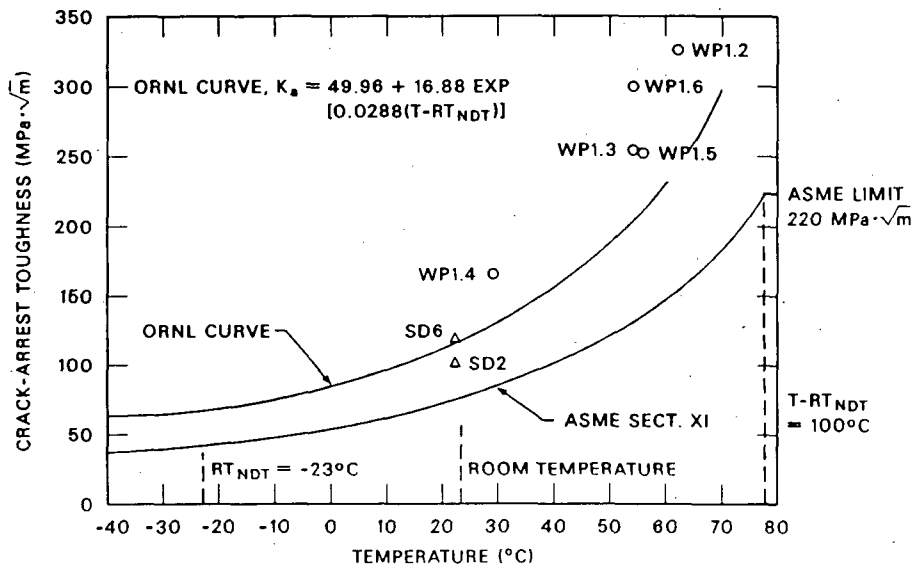


Fig. 9. Crack-arrest toughness data vs temperature for SwRI duplex specimen tests and HSST wide-plate tests.

A new technique developed at SwRI enables two relatively small specimens to be tested simultaneously using stress-wave loading from Hopkinson-type pressure bars [31]. Precracked compact-type A533B steel specimens, without side grooves and having an effective width  $w = 44$  mm, have been tested at 23 and 37°C. Crack growth of ~15 mm was achieved. Two A533B specimens with side grooves and a modified fastening mechanism to the pressure bars are being prepared for testing at temperatures ranging from 37 to 50°C.

At UM, efforts have focused on the development of two different rapid loading fracture experiments [12]. The goal of one of these studies is to determine the limits of approximating the crack-arrest toughness,  $K_{Ia}$ , by the dynamic initiation-toughness,  $K_{Id}$ . In the latter case, explosively-loaded notched short-bars are being tested and the  $K_{Id}$  values so obtained are compared with  $K_{Ia}$  values for the same material. In the other study, a method is being developed to measure "lower bound" cleavage initiation-toughness in the transition temperature range using a small specimen. A notched round-bar subjected to impact loading is being used for the latter study.

Feasibility studies demonstrated that photoelastic and strain-gage techniques could be employed to measure  $K_{Id}$  in the notched short-bar specimens. The loading of the short bar with its integral dog-bone ends is accomplished with four explosive charges that are detonated simultaneously. Tensile stress waves produced at each end of the bar propagate to the central region of the bar, where they combine to produce a rapidly increasing  $K_I$  field that initiates a stationary crack.

The first two notched short-bar specimens were fabricated from 12.7-mm-thick 4340 steel hardened to  $R_c = 51$ , with a fatigue-sharpened crack 17.5 mm deep used as an initiator. The first test indicated that symmetric loading was achieved and the central crack extended straight across the midsection of the bar. Strain gage records were successfully obtained in the second test, and indicate a dynamic initiation-toughness  $K_{Id} = 53.0$  MPa $\cdot\sqrt{m}$ . The next series of tests will focus on specimens of A533B steel subjected to very high rates of loading. These specimens will be extended to a length of 400 mm in the straight-bar region to move the crack-tip strain gages away from the explosive charges and to allow more time for the loading wave to propagate to the center notch.

The impact-loaded notched round-bar experiment was developed by UM in an attempt to simulate the effects of constraint of a very thick specimen with a relatively small round bar. The cylindrical shape of the bar should increase the effective thickness of the specimen by a factor of ~3. The specimen configuration used in testing consists of a notched bar with outside diameter of 38.1 mm and a machined notch of diameter 19.1 mm. The notch is machined with an overly sharp Charpy notch-cutting tool with a notch tip radius of 0.127 mm. The loading system designed to apply impact loading to these specimens is capable of delivering 1051 J of energy when the weight of 58.8 kg drops through a distance of 1.83 m. Initial experiments made with strain-gaged specimens indicate that nominal strain rates approach 20 s<sup>-1</sup> with this system. However, the actual strain rate at the notch is much higher because

of the 4/1 area ratio and because of the large strain concentration that occurs at the tip of the root radius.

In the first test series, five specimens of A508 steel were tested under axial impact loading applied by dropping the 58.6 kg weight a distance of 1.78 m. All five specimen failed, and data obtained for the determination of  $K_{Id}$  were found to be consistent and repeatable, yielding an average value of  $K_{Id} = 54 \text{ MPa}\sqrt{\text{m}}$ . For the next series of tests, twenty notched round-bar specimens are being machined from A533B steel. These specimens will be tested under impact loading for a range of temperatures to determine the change in initiation toughness from the lower to the upper shelf.

### 3. INELASTIC FRACTURE MODEL DEVELOPMENT

The basic postulate of LEFM requires that the inelastic deformation surrounding the crack tip be contained within the  $K_I$ -dominant region. Furthermore, it is assumed that rapid crack propagation is governed by a unique geometry-independent material property, the dynamic fracture toughness,  $K_{ID}$ . Propagation of a running crack occurs under the condition that the applied dynamic stress-intensity factor,  $K_I$ , satisfies  $K_I = K_{ID}(a, T)$ , where  $K_{ID}$  is taken to be a function of the crack-tip velocity,  $a$ , and the temperature,  $T$ . However, except for very short crack jumps, LEFM assumptions may not be strictly valid characterizations of rapid crack propagation [2]. In particular, a wake of residual plasticity left behind the moving crack tip can violate the  $K_I$ -dominance requirement of LEFM. An indication that LEFM conditions are not satisfied occurs when elastodynamic analyses of crack run-arrest data lead to geometry-dependent fracture toughness relations. Dahlberg, et al. [32] performed elastodynamic fracture analyses using crack run-arrest data from tests of single-edge-notched (SEN) tension panel specimens of different lengths. Their results for different panel lengths coincide for low crack velocities, but show a definite geometry dependence at higher velocities where non-linear effects are more pronounced. However, Brickstad [3] has demonstrated that this geometry dependence can be removed through application of an inelastic fracture model that incorporates plasticity and strain-rate effects (i.e., viscoplasticity).

These studies indicate that strain-rate effects ( $\sim 10^4 \text{ s}^{-1}$ ) can be important for rapid loading situations such as cleavage crack propagation events in ductile RPV steels. The HSST Program research efforts at ORNL and several subcontracting groups are supporting the development of viscoplastic-dynamic finite-element analysis techniques and validating their utility through analyses of carefully controlled experiments. Various viscoplastic constitutive models and several proposed nonlinear fracture criteria have been installed in general purpose (ADINA/VPF) [19,20] and special purpose (VISCRK) [11] finite element computer programs. The constitutive models include the Bodner-Partom [16], the Perzyna [17] and the Robinson [18] viscoplastic formulations; the proposed fracture criteria include three parameters,  $\{T^*$  from Ref. [33],  $J$  from Ref. [34], and  $\gamma$  from Ref. [3]\}, that are based on energy principles.

### 3.1 Viscoplastic Material Model Characterization

Research efforts at ORNL and several subcontracting groups are directed toward developing strain-rate and temperature-dependent constitutive models for A533B steel. These models will be used in dynamic fracture analyses to assess the effect of viscoplastic material behavior on cleavage crack propagation and arrest in RPV steels. As part of this effort, dynamic stress-strain data have been generated by OSU, SwRI, and SRI for A533B steel for use in deriving constants for proposed constitutive models. Kanninen et al. [14] obtained dynamic stress-strain data from tensile and split-Hopkinson bar tests for strain rates ranging from 0.001 to 550 s<sup>-1</sup> and for temperatures ranging from -60 to 175°C. To augment this data base, Giovanola and Klopp [15] recently performed 15 split-Hopkinson torsion-bar experiments at engineering shear-strain rates ranging from 400 to 3000 s<sup>-1</sup> and at temperatures of -60 to 150°C. Using similar test procedures, Gilat [13] has conducted tests at strain rates of ~800 and 5000 s<sup>-1</sup> and at temperatures of -150 to 20°C. (All specimens for these tests were taken from HSST Plate 13-A, which is the same source plate for the wide-plate crack-arrest specimens). Results for these tests show that both temperature and strain rate have a significant effect on the material response of A533B steel.

Kanninen et al. [14] used dynamic stress-strain data to derive constants for the Bodner-Parton constitutive model appropriate for A533B steel at test temperatures ranging from -60 to 150°C. At ORNL, Chang [35] has employed stress-strain data from Refs. [14-15] and an extended version of the Robinson model to represent the viscoplastic behavior of A533B steel. The extended Robinson model was originally developed to describe strain-aging effects [36] as exhibited by the phenomena of yield drop for Inconel 617 at 950°C and the reverse strain-rate effect for type 304 stainless steel at 550°C. As illustrated in Fig. 10, the Robinson model effectively models the yield drop

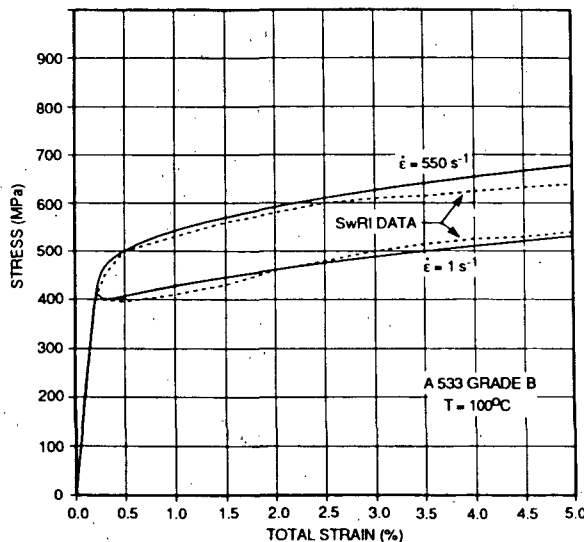


Fig. 10. Comparison of extended Robinson constitutive model predictions with measured stress-strain data for A533B steel at a temperature of 100°C and strain rates of 1 and 550 s<sup>-1</sup>.

and strain-rate sensitivity of the A533B steel at 100°C. Numerical implementation of the extended Robinson model into ADINA/VPF following a technique due to Hornberger [37] is currently under way at ORNL. Also, the SwRI stress-strain data for A533B steel has been employed by Brickstad [38] to characterize a Perzyna viscoplastic formulation based on the von Mises yield criterion with linear strain hardening.

### 3.2 Applications of Viscoplastic Analysis Methods

The predictive capabilities of the nonlinear techniques described in the previous section are being evaluated through applications of the ADINA/VPF and VISCRK computer programs to analyses of HSST crack-arrest experiments. Recently, viscoplastic-dynamic fracture analyses [39] of wide-plate tests WP-1.2 to WP-1.7 were conducted with the ADINA/VPF program at ORNL using finite-element models having improved mesh refinement near the plane of crack propagation. The finite-element model used to analyze tests WP-1.2 to 1.6 is shown in Fig. 11(a); the model used for test WP-1.7 is shown in Fig. 11(b). Both models consist of 2258 nodes and 715 eight-noded isoparametric elements. The dimensions of the elements along the crack path in Fig. 11 are 20 by 20 mm.

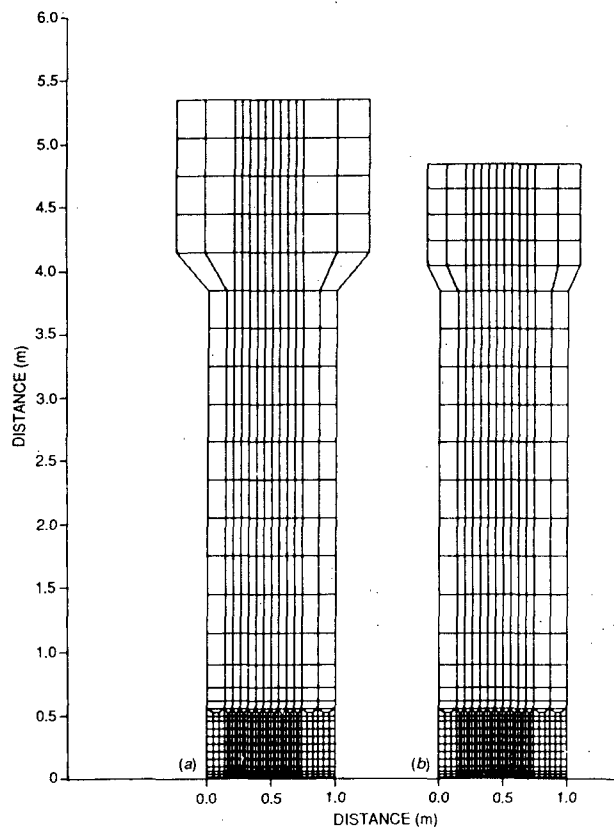


Fig. 11. Finite-element models used in dynamic analyses of tests WP-1.2 through WP-1.7: (a) model of WP-1.2 through WP-1.6, and (b) model of WP-1.7.

From Ref. [39], a generation-mode analysis of wide-plate test WP-1.2 was performed utilizing the estimate of crack position vs time from Fig. 12 and the Bodner-Partom model from Ref. [14]. The crack position vs. time relation in Fig. 12 was constructed in part from strain-gage data recorded at the crack-line strain-gage locations identified in Fig. 1. Figure 12 shows the two measured crack arrests at  $a_{fm1} = 0.55$  m and at  $a_{fm2} = 0.65$  m which occurred at times  $t_{m1} = 0.96$  ms and at  $t_{m2} = 2.7$  ms after crack initiation, respectively.

Figure 13 compares results from this analysis with those obtained from other models having different mesh refinements along the crack plane. The

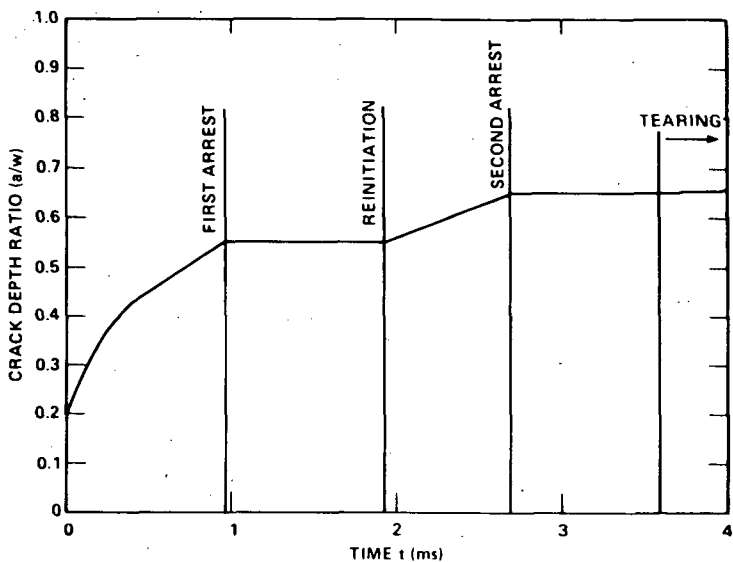


Fig. 12. Crack-depth history derived from strain-gage data for wide-plate test WP-1.2.

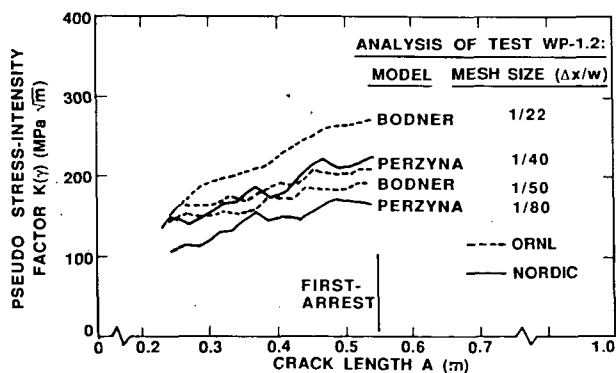


Fig. 13. Comparison of results [ $K_I(\gamma)$  vs crack depth] from generation-mode viscoplastic-dynamic analyses of test WP-1.2 for four crack-path mesh refinements.

results are expressed in terms of pseudo- $K_I$  values computed from the rate-of-work function  $\gamma$  (Ref. [3]) and plotted vs. crack length for the first run/arrest event. The characteristic mesh size is defined as the ratio of the crack-path element width to the plate width. The ORNL analysis results shown in Fig. 13 for mesh sizes 1/22, 1/40 and 1/50 were obtained from ADINA analyses described in Refs. [21], [20] and [39], respectively. Also shown in Fig. 13 are results obtained by Brickstad [38] at the Swedish Plant Inspectorate (SA) using mesh sizes 1/40 and 1/80 and the Perzyna viscoplastic model. These combined results indicate that the viscoplastic-dynamic solutions of the wide-plate test expressed in terms of the inelastic fracture parameters ( $T^*$ ,  $\hat{J}$ , and  $\gamma$ ) have not yet converged for the mesh refinements employed thus far in these studies.

Insight into the difficulties associated with modeling rapid crack propagation events in RPV steels exhibiting viscoplastic behavior are provided by several recent studies. Ahmad [40] employed an asymptotic analysis by Freund and Hutchinson [41] for steady-state crack growth in an elastic-viscoplastic material under small scale yielding to study an HSST wide-plate test specimen. To accurately model the high-strain-rate zone, Ahmad [40] estimates that the element size in the crack-tip region of the wide-plate model should be approximately 1 mm, or  $\sim 10^{-3}$  of the planar specimen dimensions. (Thus far, HSST wide-plate analyses have been limited to elements with dimensions greater than 10 mm.) More recent studies by Sheu [24] and by Popelar [25] indicate that the high-strain-rate zone is even smaller. Sheu [24] studied the mode I plane strain problem of dynamic steady-state crack growth in A533B steel using the Bodner-Partom model characterized in Ref. [14] and the assumption of small-scale yielding. Focusing on the immediate area surrounding the elastic-plastic boundary, Sheu [24] resolved the near crack-tip singular fields using a finite-element model with element dimensions approximately  $10^{-3}$  of the elastic-plastic zone size. (For the Bodner-Partom model, the stress field is  $r^{-1/2}$  singular and the elastic strain rates dominate the plastic strain rates near the crack tip.) In Fig. 14, Popelar [25] has elaborated further on the study of Sheu [24] by estimating the size of the zone-of-dominance of the

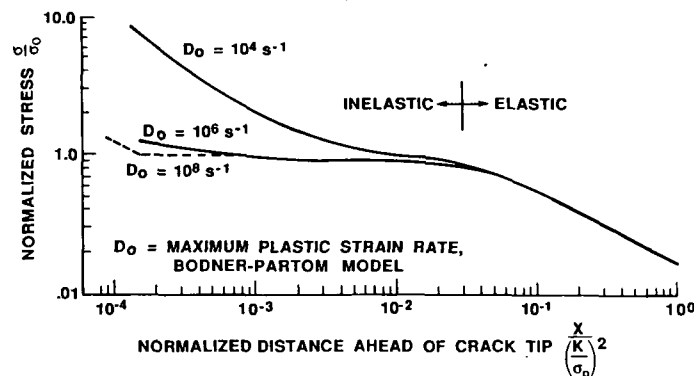


Fig. 14. Variation of effective stress ahead of crack tip as a function of limiting plastic strain rate,  $D_0$ , in Bodner-Partom model.

near-tip fields for values of the limiting plastic strain rate as high as  $D_0 = 10^8 \text{ s}^{-1}$ . The zone-of-dominance becomes smaller for increasing values of  $D_0$  and is approximately  $10^{-3}$  of the plastic zone size for  $D_0 = 10^8 \text{ s}^{-1}$ . Furthermore, for A533B steel over a temperature range from  $-60$  to  $100^\circ\text{C}$  and a crack speed of one-half the Rayleigh wave speed, Popelar [25] estimates that the zone-of-dominance extends from  $\sim 5$  to  $55 \mu\text{m}$  compared to an inelastic region with dimensions  $0.1$  to  $15 \text{ mm}$ . Representative data for A533B wide-plate material lists grain sizes at ASTM 7-8 corresponding to average diameters from  $\sim 27.5 \mu\text{m}$  to  $19.8 \mu\text{m}$ , respectively [7]. Given that the computational capacity were available to resolve such a small region using finite elements, it is clear that elements of this size invade the micro-heterogeneity of the material and broach the limits of isotropic continuum analysis.

Several techniques are being explored to circumvent these stringent requirements on crack-tip mesh refinement and related difficulties associated with possible violations of continuum assumptions. Motivated by the objective of computing a convergent non-zero value of  $T^*$ -integral for viscoplastic models, Nishioka [22] has proposed an exclusion zone technique that obviates the need for highly-refined crack-tip elements. In the viscoplastic calculations, a small rectangular domain of height  $2 \epsilon$  is defined around the crack tip to approximate a finite fracture process zone. Typically this zone is chosen such that  $\epsilon$  equals the height of one or two rows of elements along the plane of crack propagation in the finite-element model. During the dynamic analysis, this rectangle is extended in length (but not in height) to include a portion of the plastic wake behind the advancing crack. Nishioka [22] advocates excluding the integration of the volume term of the  $T^*$ -integral (see Ref. [33]) from this extending exclusion zone. According to a study by Nishioka [22], the  $T^*$ -integral should be essentially invariant with respect to the size of this extending domain provided  $\epsilon$  is sufficiently small.

To investigate the potential of the foregoing technique for characterizing fracture behavior, O'Donoghue [42] has performed studies of the geometry independence of the two-component parameter  $(T^*, \epsilon)$  using a center-crack panel problem (Fig. 15). The panel had dimensions  $2 w \times 2 h \times t$  ( $w = 40 \text{ mm}$ ,  $h = 20 \text{ mm}$  and  $t = 25.4 \text{ mm}$ ) with an initial crack length of  $a/w = 0.25$ . A fixed load was applied that produced a nominal stress of  $300 \text{ MPa}$  and an initial stress-intensity factor of  $K_I(T^*) = 77 \text{ MPa}\sqrt{\text{m}}$ . The panel was analyzed dynamically as a plane stress problem using the Bodner-Partom model [14] for a constant crack velocity of  $a = 1000 \text{ m/s}$  and a series of increasingly refined meshes. Results of these analyses presented in Fig. 15 indicate that the time history of  $T^*$  was relatively insensitive to mesh refinement for a given height of the exclusion zone. Based on these preliminary calculations, further studies will be conducted in the HSST program on the geometry independence of the  $(T^*, \epsilon)$  parameter when applied to small- and large-specimen crack run-arrest data.

Moving singular element formulations represent an alternative technique for achieving convergent solutions for fracture parameters in the context of viscoplastic-dynamic fracture analysis. A review of the various computational methods that have employed singular elements in elastodynamic fracture applications is given by Nishioka and Atluri [43]. Two aspects associated with

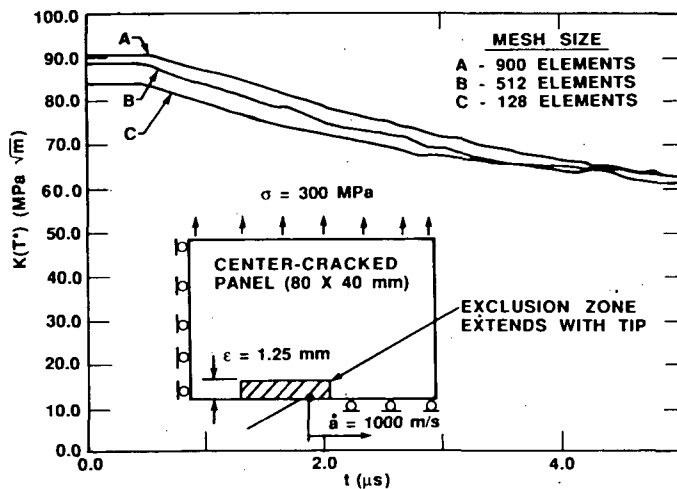


Fig. 15. Comparison of results  $[K_I(T^*) \text{ vs time}]$  from generation-mode viscoplastic-dynamic analyses of center-cracked panel for three mesh refinements and fixed exclusion zone ( $\epsilon = 1.25 \text{ mm}$ ).

moving singular element formulations may improve convergence characteristics in inelastic fracture applications. The first is the influence of including singular functions in the solution space of the Ritz-Galerkin approximation. The second, possibly more subtle, aspect is the capability of maintaining a node positioned precisely at the moving discontinuity. (Current nodal relaxation techniques do not specify the exact position of the crack-tip except when the tip is located at an interelement boundary.) In preliminary work, Thesken and Gudmundsson [23] have implemented a variable-order singular element proposed by Akin [44] into an elastodynamic finite-element formulation and have illustrated its advantages in modeling stationary cracks subjected to dynamic loading. More recently, Thesken and Gudmundsson [45] have incorporated a moving element formulation which allows an adjustable region of convecting elements to be embedded at the crack tip within a finite body. The latter technique permits the order of the crack-tip singularity to be specified by an adjustable parameter for dynamic crack growth problems. Applications [45] of this technique have shown good agreement with known analytic solutions of elastodynamic crack growth problems. Work is currently under way in the HSST Program to update the moving element formulation of Thesken and Gudmundsson [45] to accommodate viscoplastic material behavior. The resultant formulation will be investigated for its potential in resolving the near crack-tip singular fields of the Bodner-Partom constitutive model while remaining in the size regime of a continuum element.

### 3.3 Three-Dimensional Constraint Effects

The finite-element calculations carried out for the wide-plate tests thus far have assumed plane stress conditions over the entire plate. However, in the vicinity of the crack tip, there must be a transition from this plane stress field to a zone dominated by three-dimensional effects. Within this

region, the most significant of the three-dimensional effects may be transverse constraint. Insight into the importance of the plane stress vs plane strain issue is found in results reported by Freund and Hutchinson [46] for the extension of their asymptotic analysis of Ref. [41] to plane stress. In that study, the plastic dissipation under plane stress was found to be about two times that under plane strain, all other factors being equal.

Studies being performed by UM on three-dimensional constraint effects are focusing on center-cracked panels, SEN and bend-bar geometries. The SEN and bend-bar analyses have the same specimen geometries and differ only in the applied loading. These studies should provide additional insight into the differences between tensile and moment loading of the crack-tip region. A portion of these results will be employed in the development of techniques for incorporating 3-D constrain effects into 2-D finite element formulations for inelastic-dynamic fracture analysis.

#### 4. CONCLUSION

This paper has summarized recent developments in a coordinated effort being conducted under the HSST Program to develop the crack-arrest data base and the analytical tools required to construct a more comprehensive fracture technology for RPV steels. Because crack initiation is a credible event in a PTS transient, the technology must be available to treat all phases of fracture events. These phases include crack initiation, nonisothermal propagation, arrest, and stable or unstable ductile tearing. The discussion here has focused on analyzing initiation, propagation and arrest of cleavage-fracture behavior.

Experimentally, the crack-arrest data base continues to be enlarged through small- and large-scale experiments performed under the HSST Program. The large-scale wide-plate and PTS experiments are being analyzed using state-of-the-art dynamic analysis techniques. These analyses continue to produce arrest-toughness values that increase at an accelerating rate with temperature near and above the onset of the Charpy upper shelf. In order to construct valid dynamic fracture models for RPV steels, crack run-arrest data corresponding to higher temperature and toughness levels must be generated in greater quantities than can be achieved with large specimens such as wide plates. The intermediate-size stub-panel specimen being developed and tested at ORNL represents a promising technique for substantially augmenting the crack-arrest data base at an affordable cost.

A key component of the fracture technology under development in the HSST Program is evaluating the importance of viscoplastic effects in dynamic fracture analysis. To this end, additional high-strain-rate testing (up to  $5000 \text{ s}^{-1}$  in shear) has been performed on A533B steel and used to update material constants for the various viscoplastic constitutive models installed in HSST computer programs. The capabilities of these nonlinear techniques are being evaluated, in part, through applications to small- and large-specimen tests, including wide plates. Viscoplastic-dynamic fracture analyses of the

wide-plate tests, when expressed in terms of the fracture parameters ( $T^*$ , etc.), were found to exhibit a strong dependence on mesh refinement. From asymptotic studies of Sheu [24] and Popelar [25], resolution of the crack-tip singular fields in viscoplastic models of engineering structures using conventional finite-element formulations is apparently not within reach currently for practical mesh sizes, even in a supercomputer environment. Even if this resolution were achieved, questions still remain concerning the possible violation of continuum assumptions and the relevance of the proposed parameters ( $T^*$ , etc.) to predictions of fracture behavior in ductile RPV steel.

Alternative techniques are being investigated in the HSST program to deal with difficulties associated with the small dimensions of the high-strain-rate zones in viscoplastic models. These techniques include a two-component parameter ( $T^*$ ,  $\epsilon$ ) to exclude the high-strain-rate region from a portion of the calculations and a moving variable-order singular element formulation to build the crack-tip singularity into the finite-element approximation. These techniques will be evaluated separately through analyses of dynamic fracture data from small- and large-specimen crack-arrest experiments.

#### References

1. B. R. Bass et al., "Fracture Analyses of Heavy-Section Steel Technology Wide-Plate Crack-Arrest Experiments," *Fracture Mechanics: Nineteenth Symposium*, ASTM STP-969, T. A. Cruse (Ed.), pp. 691-733 (1987).
2. M. F. Kanninen and C. H. Popelar, *Advanced Fracture Mechanics*, Oxford University Press, New York, 1985, pp. 214-230.
3. B. Brickstad, "A Viscoplastic Analysis of Rapid Crack Propagation Experiments in Steel," *J. Mech. Phys. Solids*, Vol. 31, pp. 307-27 (1983).
4. R. D. Cheverton et al., "Fracture Mechanics Data Deduced from Thermal-Shock and Related Experiments with LWR Pressure Vessel Material," *Journal of Pressure Vessel Technology*, Vol. 105, pp. 102-110, May 1983.
5. R. H. Bryan et al., "The Heavy-Section Steel Technology Pressurized-Thermal Shock Experiment, PTSE-1," *Eng. Fract. Mech.*, Vol 23(1), pp. 81-97, 1986.
6. R. H. Bryan et al., *Pressurized-Thermal-Shock Test of 6-in. Thick Pressure Vessels. PTSE-2: Investigation of Low Tearing Resistance and Warm Prestressing*, NUREG/CR-4888 (ORNL-6377), Martin Marietta Energy Systems, Inc., Oak Ridge Natl. Lab., January 1988.
7. D. J. Naus et al., *Crack Arrest Behavior in SEN Wide Plates of Quenched and Tempered A533B Steel Tested under Nonisothermal Conditions*, NUREG/CR-4930 (ORNL-6388), Martin Marietta Energy Systems, Inc., Oak Ridge Natl. Lab., September 1987.

8. D. J. Naus et al., "HSST Wide-Plate Test Results and Analysis," *Proceeding of the Sixteenth Water Reactor Safety Research Information Meeting, October 23-27, 1988*, National Bureau of Standards, Gaithersburg, MD (to be published).
9. A. R. Rosenfield et al., "Crack-Arrest Studies at Battelle Columbus," in *HSST Semiannual Progress Report April-September 1984*, NUREG/CR-3744, Vol. 2, (ORNL/TM-9154/V2), pp. 102-109, Martin Marietta Energy Systems, Inc., Oak Ridge National Laboratory, December 1984.
10. J. Keeney-Walker and B. R. Bass, "Analysis of a Stubbed Panel Crack-Arrest Specimen," in *Heavy-Section Steel Technology Program Semiann. Prog. Rep. for April-September 1987*, NUREG/CR-4219, Vol. 4, No. 2 (ORNL/TM-9593/V4&N2), Martin Marietta Energy Systems, Inc., Oak Ridge Natl. Lab., April 1988.
11. R. J. Dexter et al., "Dynamic-Viscoplastic Analysis and Small-Specimen Experimental Methods for the Study of Fracture in A533B Steel," in *Proceedings of the Fourth International Conference on Numerical Methods in Fracture Mechanics, March 23-27, 1987, San Antonio, TX*.
12. W. L. Fournery et al., "Investigation of Damping and Cleavage-Fibrous Transition in Reactor-Grade Steel at the University of Maryland," in *Heavy-Section Steel Technology Program Semiann. Prog. Rep. October 1987-March 1988*, NUREG/CR-4219, Vol. 5, No. 1 (ORNL/TM-9593/V5&N1), Martin Marietta Energy Systems, Inc., Oak Ridge Natl. Lab., August 1988.
13. A. Gilat, "High Strain Rate Testing of A533 Grade B Class 1 Steel at Various Temperatures," in *Heavy-Section Steel Technology Program Semiann. Prog. Rep. October 1987-March 1988*, NUREG/CR-4219, Vol. 5, No. 1 (ORNL/TM-9593/V5&N1), Martin Marietta Energy Systems, Inc., Oak Ridge Natl. Lab., August 1988.
14. M. F. Kanninen et al., "Viscoplastic Characterization of A533B Steel," in *Heavy-Section Steel Technology Program Semiann. Prog. Rep. April-September 1986*, NUREG/CR-4219, Vol. 3, No. 2 (ORNL/TM-9593/V3&N2), Martin Marietta Energy Systems, Inc., Oak Ridge Natl. Lab., December 1986.
15. J. H. Giovanola and R. W. Klopp, *Viscoplastic Stress-Strain Characterization of A533B Class 1 Steel*, NUREG/CR-5066 (ORNL/Sub/87-SA193/1), SRI International Menlo Park, CA (to be published).
16. S. R. Bodner and Y. Partom, "Constitutive Equations for Elastic-Viscoplastic Strain Hardening Materials," *J. Appl. Mech.*, 42, 385-389, 1975.
17. P. Perzyna, "Fundamental Problems in Visco-Plasticity," pp. 244-368 in *Recent Advances in Applied Mechanics*, Academic Press, New York, 1966.

18. C. E. Pugh and D. N. Robinson, "Some Trends in Constitutive Equation Model Development for High-Temperature Behavior of Fast-Reactor Structural Alloys," *J. Nucl. Eng. Design*, Vol. 48, No. 1, June 1978, pp. 269-276.
19. K. J. Bathe, *ADINA - A Finite Element Program for Automatic Dynamic Incremental Nonlinear Analysis*, Report AE 84-1, Massachusetts Institute of Technology, Cambridge, MA (December 1984).
20. B. R. Bass et al., "Late-Event Viscoplasticity in Wide-Plate Crack-Arrest Tests," *International Journal of Pressure Vessels and Piping*, Vol. 31, pp. 325-348 (1988).
21. B. R. Bass et al., "Computational Methods for Viscoplastic Dynamic Fracture Mechanics Analysis," *Computers in Engineering 1988*, Vol. 3, (Eds.) V. A. Tipnis and E. M. Patton, ASME, New York (1988).
22. T. Nishioka, "Finite Element Analysis of the T\*-Integral in Nonlinear Dynamic Fracture Problems," Proceedings of International Conference on Computational Engineering Science, April 10-14, 1988, Atlanta, GA, pp. 9, V.1-4.
23. J. C. Thesken and P. Gudmundsson, "Application of a Variable Order Singular Element to Dynamic Fracture Mechanics," *Computational Mechanics*, Vol. 2, pp. 307-316 (1987).
24. J. C. Sheu, "Dynamic Elastic-Viscoplastic Crack Growth," Ph.D. Dissertation, School of Engineering, Ohio State University, 1988.
25. C. H. Popelar, "A Viscoplastic Analysis for Predicting the Dynamic Fracture Toughness of A533B Steel," submitted for publication.
26. C. F. Feddersen, *Current Status of Plane Strain Crack Toughness Testing of High-Strength Metallic Materials*, Crack Arrest Methodology and Applications, ASTM STP-410, American Society for Testing and Materials, Philadelphia, PA, 1967.
27. R. Tada, P. C. Paris, and G. R. Irwin, *The Stress Analysis of Cracks Handbook*, Del Research Corp., Hellertown, PA.
28. C. W. Schwartz, "Dynamic Fracture Propagation Relations Inferred from WP-1 Test Series," in *Heavy-Section Steel Technology Program Semiann. Prog. Rep. for April-September 1987*, NUREG/CR-4219, Vol. 4, No. 2 (ONRL/TM-9593/V4&N2), Martin Marietta Energy Systems, Inc., Oak Ridge Natl. Lab., April 1988.
29. B. R. Bass, C. E. Pugh, and J. K. Walker, "Elastodynamic Fracture Analysis of Large Crack-Arrest Experiments," *Nuclear Engineering and Design*, Vol. 98, 157-169, 1987.

30. C. E. Pugh et al., "Evaluation of Crack-Arrest Toughness through Dynamic Fracture Analysis of Large Vessel Tests," *Proceedings of the Seventh International Conference on Fracture, March 20-24, 1989, Houston, TX*, to be published.
31. M. F. Kanninen, "Elastodynamic and Viscoplastic-Dynamic Fracture Mechanics," in *Heavy-Section Steel Technology Program Semiann. Prog. Rep. October 1987-March 1988*, NUREG/CR-4219, Vol. 5, No. 1 (ORNL/TM-9593/V5&N1), Martin Marietta Energy Systems, Inc., Oak Ridge Natl. Lab., August 1988.
32. L. Dahlberg et al., "Influence of Specimen Geometry on Crack Propagation and Arrest Toughness," *Crack Arrest Methodology and Applications*, ASTM STP-711, G. T. Hahn and M. F. Kanninen (Eds.), pp. 89-108 (1980).
33. S. N. Atluri, T. Nishioka, and M. Nakagaki, "Incremental Path Independent Integrals in Inelastic and Dynamic Fracture Mechanics," *Eng. Fract. Mech.*, Vol. 20-2, pp. 209-244 (1984).
34. K. Kishimoto, S. Aoki, and M. Sakata, "On the Path-Independent Integral  $-\dot{J}$ ," *Eng. Fract. Mech.*, Vol. 13, pp. 841-50 (1980).
35. S.-J. Chang, "ORNL Unified Inelastic Deformation Model," in *Heavy-Section Steel Technology Program Semiann. Prog. Rep. October 1987-March 1988*, NUREG/CR-4219, Vol. 5, No. 1 (ORNL/TM-9593/V5&N1), Martin Marietta Energy Systems, Inc., Oak Ridge Natl. Lab., August 1988.
36. S.-J. Chang, *Inelastic Analysis and Testing of SUS 304 Stainless Steel*, by J. J. Blass et al., EPRI 2658-21, pp. 38-43, EPRI, Palo Alto, Calif., 1988.
37. K. Hornberger et al., "Numerical Integration and Implementation of Viscoplastic Models into Finite Element Codes," pp. 477-90, *Proc. of Third International Conference on Computational Plasticity, Barcelona, Spain, April 6-10, 1987*, Pineridge Press, Swansea, U.K.
38. B. Brickstad, *Wide-Plate Analysis of WP-1.2 and WP-1.5*, presented at the Third Annual HSST Workshop on Crack Arrest Technology, National Bureau of Standards, Gaithersburg, MD, May 1987.
39. B. R. Bass et al., *Viscoplastic Dynamic Fracture Analyses of the WP-1 Series of Wide Plate Crack-Arrest Tests*, ORNL/TM- , Martin Marietta Energy Systems, Inc., Oak Ridge Natl. Lab., to be published.
40. J. Ahmad, "Elastic-Viscoplastic Analysis of Rapidly Running Cracks," *Proc. of Fourth International Conference Numerical Methods in Fracture Mechanics*, March 23-27, 1987, San Antonio, TX.
41. L. B. Freund and J. W. Hutchinson, "High Strain-Rate Crack Growth in Rate-Dependent Plastic Solids," *J. Mech. Phys. Solids*, Vol. 33, No. 2, pp. 169-191 (1985).

42. P. O'Donoghue, "Crack-Tip Characterizing Parameters in Dynamic Visco-plastic Fracture Mechanics", *Fourth Annual HSST Program Workshop on Dynamic Fracture and Crack Arrest Technology, June 2-3, 1988, National Bureau of Standards, Gaithersburg, MD.*
43. T. Nishioka and S. N. Atluri, "Computational Methods in Dynamic Fracture," in *Computational Methods in the Mechanics of Fracture*, (Ed.) S. N. Atluri, North Holland, Amsterdam (1986).
44. J. E. Akin, "The Generation of Elements with Singularities," *Int. J. Num. Meth. Eng.*, Vol. 10, pp. 1249-1259 (1976).
45. J. C. Thesken and P. Gudmundsson, "Application of a Moving Variable Order Singular Element to Dynamic Fracture Mechanics," to be published.
46. J. W. Hutchinson, Letter Report on the 3rd HSST Workshop on Dynamic Fracture and Crack Arrest, to C. E. Pugh, Heavy-Section Steel Technology Program, Oak Ridge Natl. Lab., July 1, 1987.

## HSST WIDE-PLATE TEST RESULTS AND ANALYSIS\*

D. J. Naus, B. R. Bass and J. Keeney-Walker  
Oak Ridge National Laboratory (ORNL)  
Oak Ridge, Tennessee 37831

and

R. J. Fields, R. deWit and S. R. Low III  
National Institute of Standards and Technology (NIST)  
Gaithersburg, Maryland 20899

### ABSTRACT

Fifteen wide-plate crack-arrest tests have been completed to date, ten utilizing specimens fabricated from A533B class 1 material (WP-1 and WP-CE series), and five fabricated from a low upper-shelf base material (WP-2 series). Each test utilized a single-edge notched specimen that was subjected to a linear thermal gradient along the plane of crack propagation. Test results exhibit an increase in crack-arrest toughness with temperature, with the rate of increase becoming greater as the temperature increases. When the wide-plate test results are combined with other large-specimen results the data show a consistent trend in which the  $K_{Ia}$  data extends above the limit provided in ASME Section XI.

### 1. INTRODUCTION

Current light-water reactor (LWR) pressure-vessel safety assessment methods are based in large measure on Sects. III and XI of the *American Society of Mechanical Engineers (ASME) Boiler and Pressure Vessel Code (B&PVC)*. In pressurized-thermal-shock (PTS) scenarios, flaws on the inner surface of a reactor pressure vessel (RPV) have the greatest propensity to propagate because they are in the region of highest thermal stress, lowest temperature, and greatest irradiation damage. If such a flaw begins to propagate radially through the vessel wall, it will extend into a region of higher fracture toughness due to the higher temperatures and less irradiation damage. Although the thermal stresses may decrease with propagation depth, the stress-intensity factor caused by the elevated-pressure loading will be increasing.

The fracture toughness correlations contained in the *ASME B&PVC* embody the position that one cannot assume a crack-arrest toughness value ( $K_{Ia}$ ) above  $220 \text{ MPa}\cdot\sqrt{\text{m}}$  for LWR pressure-vessel steels. The imposition of this limit is

---

\*Research sponsored by the Office of Nuclear Regulatory Research, U.S. Nuclear Regulatory Commission under Interagency Agreement 1886-8011-9B with the U.S. Department of Energy under Contract DE-AC05-84OR21400 with Martin Marietta Energy Systems, inc.

"The submitted manuscript has been authored by a contractor of the U.S. Government under contract No. DE-AC05-84OR21400. Accordingly, the U.S. Government retains a nonexclusive, royalty-free license to publish or reproduce the published form of this contribution, or allow others to do so, for U.S. Government purposes."

based in part on the fact that no  $K_{Ia}$  data existed at or above this level and because Charpy tests showed that impact energy levels exhibit an upper-shelf behavior. Therefore, the nature of crack-arrest behavior and  $K_{Ia}$  extrapolations to temperatures higher than that at which this limit occurred could not be presumed.

The ASME limit does not impose difficulties in making assessments for LWR pressure vessels undergoing thermal shock transients with low accompanying pressure levels. However, PTS scenarios could lead to conditions where the driving force on a propagating crack increases to levels well in excess of the current ASME limit. Thus, safety assessment methods for this type of condition would require an understanding of the following points.

1. If the driving force on a crack exceeds  $220 \text{ MPa}\cdot\sqrt{\text{m}}$  by a significant margin, can the material exhibit crack-arrest behavior?
2. If the materials do exhibit high  $K_{Ia}$  values with increasing temperature, what is the relationship between  $K_{Ia}$  and temperature? That is, does a temperature limit exist above which cleavage crack propagation cannot continue regardless of how high the driving force?
3. If crack arrest does occur at high temperatures where the material behavior is typically dominated by ductile behavior, then what interactions exist between the various fracture modes, including arrest, stable crack growth, unstable crack growth, and tensile instability?

## 2. PROGRAM OBJECTIVE AND GOALS

The primary objective of the wide-plate crack-arrest studies is to generate data and associated analysis methods for understanding the crack-arrest behavior of prototypical RPV steels at temperatures near and above the onset of the Charpy upper-shelf region. Program goals include (1) extending the existing  $K_{Ia}$  data bases to values above those associated with the upper limit in the *ASME B&PVC*; (2) clearly establishing that crack arrest occurs prior to fracture-mode conversion; and (3) validating the predictability of crack arrest, stable tearing, and/or unstable tearing sequences for ductile materials. The wide-plate tests and analyses provide bases for obtaining and interpreting dynamic-fracture data (with relatively long crack runs) and bases for validation of viscoplastic fracture models and analysis methods.

## 3. MATERIAL PROPERTIES

### 3.1 WP-1 Test Series (A533B Material)

The initial series of wide-plate crack-arrest specimens is taken from the central portion of a 18.73-cm-thick plate of A533 grade B class 1 steel that is in a quenched and tempered condition. Properties of the plate include Young's modulus ( $E$ ) = 206.9 GPa, Poisson's ratio ( $\nu$ ) = 0.3, coefficient of thermal expansion ( $\alpha$ ) =  $11 \times 10^{-6} / ^\circ\text{C}$ , and density ( $\rho$ ) = 7850  $\text{kg}/\text{m}^3$ . The

temperature-dependent yield stress for the material is given by

$$\sigma_y = 374.87 + 59.89e^{-0.00793T} \quad (1)$$

where  $\sigma_y$  and  $T$  have units in megapascals and degrees Celcius, respectively. The ultimate strength of the material, for use in tensile instability calculations, is based on the average stress in the remaining ligament ( $\sigma_u$ ) equal to 550 MPa, which represents the lowest value determined for the temperature range of interest. For tearing instability calculations, the material tearing resistance is assumed to be given in the form of a power-law J-resistance curve

$$J_R = c(\Delta a)^m \quad (2)$$

where  $c = 0.3539$ ,  $m = 0.4708$ , and the units of  $J_R$  and  $\Delta a$  are MJ/m<sup>2</sup> and mm, respectively. Temperature-dependent fracture-toughness relations for initiation and arrest, based on small-specimen data, are given by

$$K_{Ic} = 51.28 + 51.90e^{0.036(T - RT_{NDT})} \quad (3)$$

$$K_{Ia} = 49.96 + 16.88e^{0.029(T - RT_{NDT})} \quad (4)$$

with units for  $K$  and  $T$  being MPa $\cdot\sqrt{m}$  and °C, respectively. Drop-weight and Charpy V-notch test data indicate that  $RT_{NDT} = -23^\circ\text{C}$ , and Charpy upper-shelf energy is 160 J with its onset occurring at  $55^\circ\text{C}$ .

Analytical studies have used a dynamic fracture toughness relation in the following form:

$$K_{ID} = K_{Ia} + A(T) \dot{a}^2, \quad (5)$$

where  $K_{Ia}$  is given by Eq. (4) and

$$A(T) = [329.7 + 16.25 (T - RT_{NDT})] \times 10^{-6}, \quad (6)$$

or

$$A(T) = [121.71 + 1.296 (T - RT_{NDT})] \times 10^{-6}, \quad (7)$$

if  $(T - RT_{NDT})$  is greater or less than  $-13.9^\circ\text{C}$ , respectively. Units for  $K_{ID}$ ,  $A$ ,  $\dot{a}$ , and  $T$  are megapascals times root meters, megapascals times square seconds times meters to the  $-3/2$ , meters per second, and degrees Celcius, respectively. The form of the  $K_{ID}$  expression in Eq. (5) and relations for

A(T) [Eqs. (6) and (7)] are derived from Ref. [1] by estimating that  $RT_{NDT} = -6.1^\circ\text{C}$  for the material used in that study.

### 3.2 WP-CE Test Series (A533B Material)

The WP-CE specimens were made from a second heat of A 533 grade B class 1 material that was provided to ORNL by Combustion Engineering (CE), Inc. The material was characterized by CE, and the detailed results are presented in Ref. [2]. Pertinent material properties include:

1. an ultimate tensile strength ranging from  $\approx 580$  MPa at room temperature to  $\approx 560$  MPa at  $66^\circ\text{C}$  to  $\approx 520$  MPa at  $120^\circ\text{C}$ ,
2. a nil-ductility transition temperature from  $\approx -34$  to  $\approx -23^\circ\text{C}$ ,
3. a Charpy upper-shelf energy of  $\approx 180$  to  $\approx 203$  J, and
4. the minimum temperature for fully ductile behavior occurring at  $\approx 43$  to  $\approx 49^\circ\text{C}$ .

Temperature-dependent fracture-toughness relations for the WP-CE material used for pretest planning were the same as Eqs. (3) and (4) with the  $RT_{NDT}$  changed to the appropriate value for the WP-CE material.

### 3.3 WP-2 Test Series (Low Upper-Shelf Material)

The WP-2 series of wide-plate crack-arrest specimens is taken from a 15.88-cm thick plate of 2 1/4 Cr-1 Mo steel. The material was supplied by Babcock and Wilcox after being heat treated in an effort to obtain a Charpy upper-shelf energy of 68 joules (50 ft-lb), or less.

Based on a limited number of tests, the tentative drop-weight nil-ductility temperature for the material is  $\sim 60^\circ\text{C}$ , and the Charpy upper-shelf energy is about 60 J with its onset occurring at about  $150^\circ\text{C}$ . The ultimate strength of the material, for use in tensile instability calculations, is based on the average stress in the remaining ligament ( $\sigma_u$ ) equal to 500 MPa. For tearing instability conditions, the values of  $c$  and  $m$  in Eq. (2) are 0.1114 and 0.3832, respectively. Tentative temperature-dependent fracture-toughness relations for initiation and arrest, which have been used for planning the WP-2 series tests are given by:

$$K_{Ic} = 39.53 + 93.47e^{0.036(T - DW_{NDT})} \quad (8)$$

$$K_{Ia} = 22.31 + 62.69e^{0.0177(T - DW_{NDT})} \quad (9)$$

with units of  $K$  and  $T$  being  $\text{MPa}\cdot\sqrt{\text{m}}$  and  $^\circ\text{C}$ , respectively, and the material  $DW_{NDT} = 60^\circ\text{C}$ . The dynamic fracture toughness relation is presented in Eq. (5) with  $60^\circ\text{C}$  used as the material  $RT_{NDT}$ .

#### 4. SPECIMEN PREPARATION, INSTRUMENTATION AND TESTING PROCEDURE

##### 4.1 Specimen Preparation

The  $1 \times 1 \times 0.1$  m, or  $1 \times 1 \times 0.15$  m, specimens such as shown in Fig. 1, were machined and precracked by ORNL. The precracking was done by hydrogen charging an electron-beam (EB) weld located at the base of a premachined notch in the plate. The total crack length, notch depth plus EB weld, for each specimen was nominally 0.2 m ( $a/W \sim 0.2$ ) and the flaw was oriented perpendicular to the rolling direction. Each side of a specimen was side grooved to a depth equal to 12.5% of the plate thickness. Starting with the third specimen in test series WP-1 (WP-1.3), the crack front of each specimen, with the exception of specimen WP-2.3, was machined into a truncated chevron configuration to reduce the tensile load required to achieve crack initiation. Upon completion of the machining operations each specimen was shipped to NIST where it was welded to pull plates nominally having the same cross-section geometry as the specimen. A specimen pin-to-pin length of approximately 9.6 m was selected to minimize stress wave effects. Tables 1, 2 and 3 present dimensions for each of the specimens in the WP-1, WP-CE and WP-2 test series, respectively, which have been tested to date.

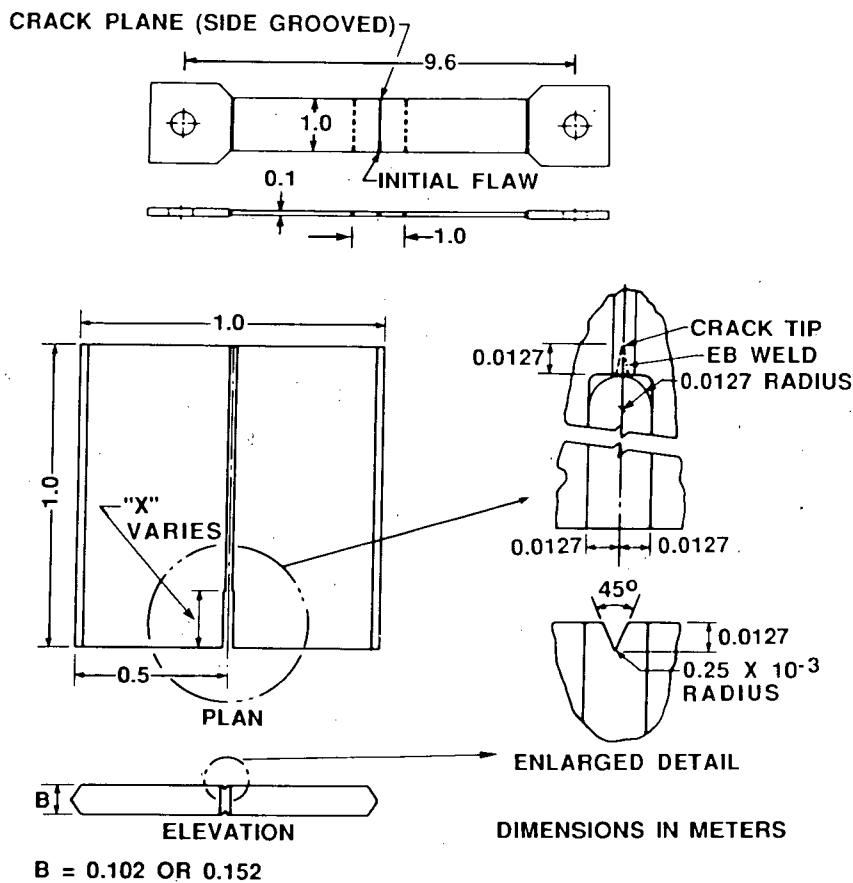


Fig. 1. Schematic of HSST wide-plate crack-arrest specimen.

TABLE 1  
WP-1 SERIES TEST SPECIMEN DIMENSIONS

Dimension	Symbol	Dimension (mm)							
		Specimen designation							
		WP-1.1	WP-1.2	WP-1.3	WP-1.4	WP-1.5	WP-1.6	WP-1.7	WP-1.8
Initial crack length	$a_o$	196.9	199	197	207.5	200	200	202	198
Thickness	B	101	101.8	99.5	99.6	101.7	101.8	152.4	152.4
Notched thickness	$B_N$	76.3	77.5	75.4	76.9	76.4	75.5	114.3	115.1
Chevron thickness (thickness at $a_o$ )	$B_C$	NA <sup>a</sup>	NA <sup>a</sup>	47.5	33.8	41.2	40.0	61.0	56.2
Width	W	997	998	1000	1000	1000	1000	1000	1000

<sup>a</sup>Not applicable.

TABLE 2

## WP-CE SERIES TEST SPECIMEN DIMENSIONS

Dimension	Symbol	Dimension (mm)	
		Specimen designation	
		WP-CE-1	WP-CE-2
Initial crack length	$a_o$	200	201
Thickness	B	101.7	101.8
Notch thickness	$B_N$	76.3	76.2
Chevron thickness (thickness at $a_o$ )	$B_C$	40.0	40.4
Width	W	1000	999.5

TABLE 3

## WP-2 SERIES TEST SPECIMEN DIMENSIONS

Dimension	Symbol	Dimension (mm)				
		Specimen designation				
		WP-2.4	WP-2.1	WP-2.5	WP-2.3	WP-2.2
Initial crack length	$a_o$	203	202.6	199	200	213
Thickness	B	101.7	152.3	101.6	152.4	152.4
Notch thickness	$B_N$	76.3	113.9	76.2	113.8	113.8
Chevron thickness (thickness at $a_o$ )	$B_C$	40.5	61.5	40.7	$b$	71.9
Width	W	1000	1000	999	1000	1000
Pop-in crack length	$a'_o$	251	NA <sup>a</sup>	264	NA <sup>a</sup>	NA <sup>a</sup>
Chevron thickness (thickness at $a'_o$ )	$B'_C$	75.5	NA <sup>a</sup>	NA <sup>a</sup>	$b$	$b$

<sup>a</sup>Not applicable because either a pop-in did not occur (WP-2.1, WP-2.2 and WP-2.3) or the crack length after pop-in ( $a'_o$ ) was past the region of the plate where the crack front had been chevroned (WP-2.5).

<sup>b</sup>Specimen non-chevroned.

## 4.2 Instrumentation

Up to 40 thermocouples were positioned on each specimen as shown in Fig. 2. During the heating-cooling processes, the 20 thermocouples adjacent to the crack plane were displayed graphically in real time to indicate the relationship between the actual and desired thermal gradient across the specimen width. The 20 additional thermocouples indicated the temperature distribution at other positions on the specimen and pull plates and were used primarily for post-test analyses.

Although the number of strain gages has varied from test to test, up to a total of 25 gages have been utilized to provide dynamic strain-field measurements for determination of crack velocity and assessing boundary conditions. Strain gage locations utilized for tests WP-1.7 and WP-CE-1 are shown in Fig. 3. The crack-line gages (numbers 1 through 20 in Fig. 3) were two-element, 90° stacked, 350-ohm Karma alloy (nickel-chromium alloy) gages on a polyimide backing. Near and far field gages were either uniaxial or three-element 350-ohm constantan alloy gages. The strain gage signals were recorded either by a transient digital oscilloscope or a combination of oscilloscopes and a multichannel, wide band, frequency modulated, magnetic tape recorder. Operations of the oscilloscopes and recorder during a test were controlled by the microcomputer-based system shown schematically in Fig. 4.

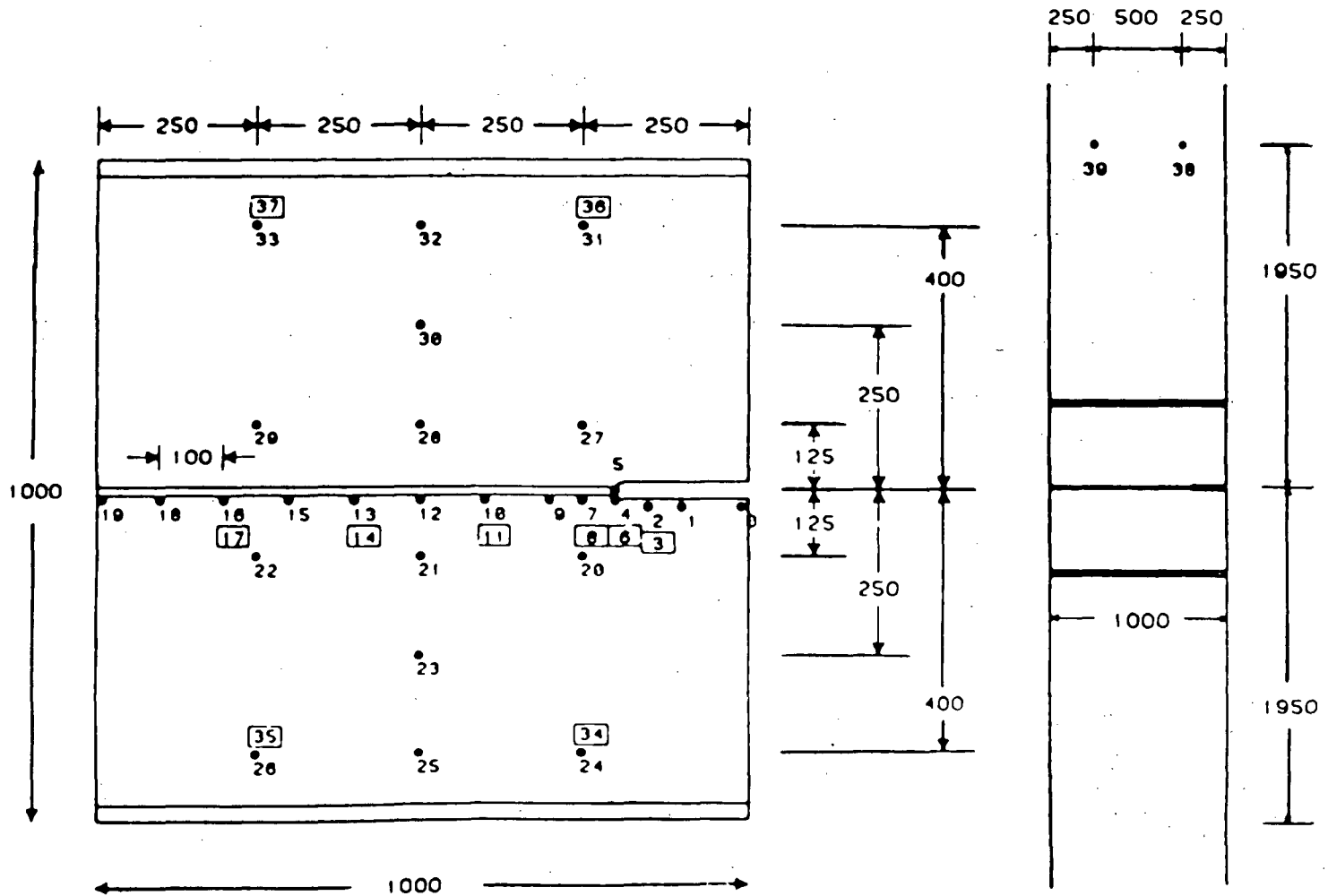
Additional instrumentation that have been used in selected tests include: (1) capacitance-based crack-opening-displacement gages mounted on the front and back plate faces at an  $a/W$  that varied from 0.120 to 0.175, (2) an acoustic emission transducer located on the specimen lower pull tab, (3) a displacement gage mounted on the specimen centerline approximately 3.5 m below the crack plane, and (4) accelerometers mounted on the specimen centerline approximately 3.5 m below and 3.5 m above the crack plane. More detailed information on the instrumentation systems can be obtained from Ref. [3].

## 4.3 Heating-Cooling-Insulation Systems

After being instrumented, the specimen was placed into the NIST testing machine and individual electric-resistance strip heaters attached to the back edge of the plate. The primary heating zone was formed by two pairs of heaters attached to the specimen edge above and below the fracture plane. The second heating zone, consisting of two areas on either side of the first zone, was heated by two outward pairs of heaters. Temperature levels in the two zones were independently controlled to better achieve and maintain a linear thermal gradient.

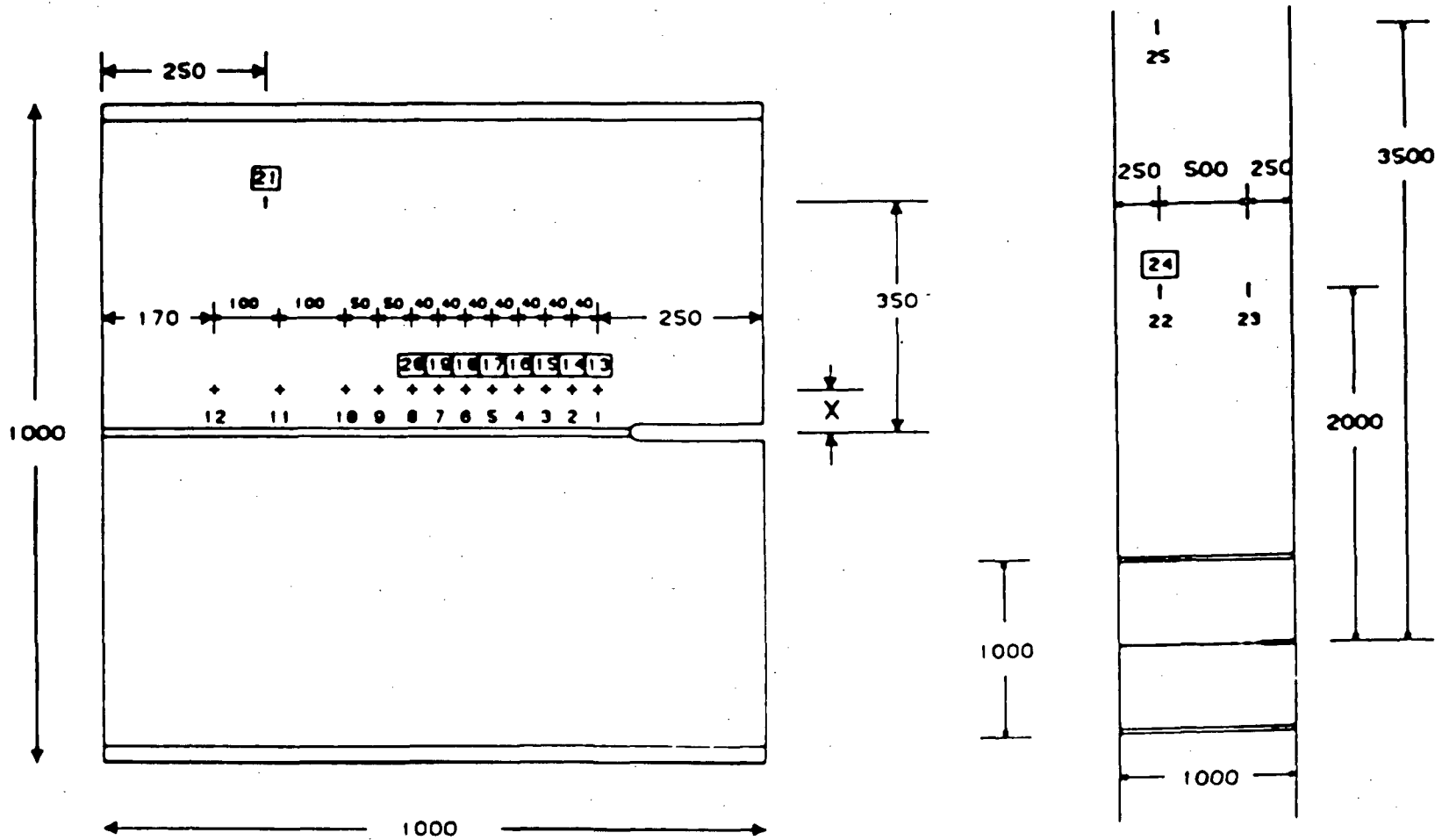
The cold edge of the specimen (notch) was cooled by spraying liquid nitrogen ( $LN_2$ ) directly onto the specimen surface using a copper-tube manifold system. The specimen cooling level could be controlled by manually setting a hand valve and with an on/off temperature controller interfaced with a thermocouple at the cold edge of the specimen.

● THERMOCOUPLE LOCATION  
 BOXED NUMBER INDICATES THERMOCOUPLE ON BACK OF SPECIMEN



ALL DIMENSIONS IN MILLIMETERS

Fig. 2. Thermocouple locations for a typical HSST wide-plate crack-arrest specimen.



x = 97.5 FOR WP-1.7    x = 65 FOR WP-CE-1

ALL DIMENSIONS IN MILLIMETERS

Fig. 3. Strain gage locations for a typical HSST wide-plate crack-arrest specimen.

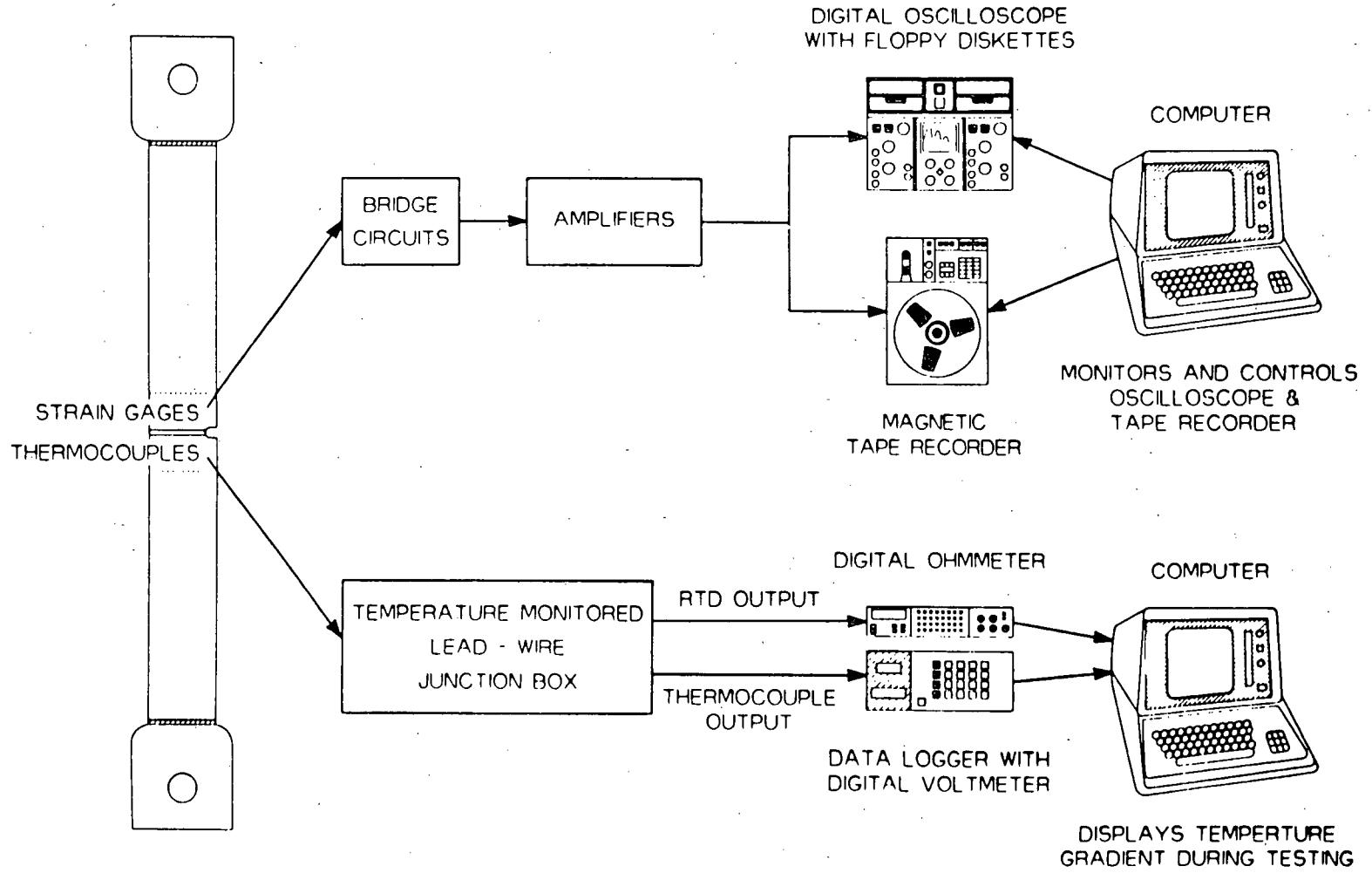


Fig. 4. Schematic of HSST wide-plate crack-arrest data acquisition system.

Two types of thermal insulation were used to insulate the hot and cold edges of the specimen. On the hot edge of the plate mineral wool bats were positioned on the specimen face at the vertical center line and extended beyond the heated edge and the strip heaters. The cold side of the plate was insulated with styrofoam sheets which butt up against the mineral wool at the specimen center and extend beyond the cooled edge.

#### 4.4 Testing Procedure

After completion of specimen insulation, all instrumentation was attached to the data acquisition system and a checkout conducted to demonstrate operability. A temperature gradient was imposed across the plate by LN<sub>2</sub> cooling of the notched edge while heating the other edge. Liquid nitrogen flow and power to the heaters were continuously adjusted to obtain the desired thermal gradient. Generally, the mid-plate ( $a/w = 0.5$ ) temperature was selected to correspond to that of the onset of Charpy upper-shelf energy for the material being tested and the crack-tip temperature was varied to provide the desired initiation load. Final calibration of the strain gages, COD gages and the load cell were completed just prior to initiation of specimen loading. Tensile load was then applied (Fig. 5) to the specimen at a rate of 11 to 312 kN/s until fracture occurred. Four exceptions to this procedure occurred during the fifteen tests conducted to date. Specimens WP-1.1, WP-CE-2 and WP-2.2 were initially warm prestressed to guard against initiation at a low load, and specimen WP-1.4 utilized a pillow jack device to initiate crack propagation at a prescribed tensile load.

### 5. TEST SUMMARY

#### 5.1 WP-1 Test Series

Table 4 presents a summary of conditions for each test in the WP-1 test series. The fracture surfaces for specimens WP-1.1 through WP-1.6 are presented in Fig. 6, and Fig. 7 presents the fracture surfaces for specimens WP-1.7 and WP-1.8. Since a description of tests WP-1.1 through WP-1.7 has been presented in a previous paper [4], it will not be repeated. Only a summary of test WP-1.8 will be provided.

Test WP-1.8 was the seventh test in the WP-1 series and the second which utilized a 152-mm-thick specimen. After obtaining a satisfactory thermal gradient, the specimen was loaded at an average rate of 20 kN/s until 24.5 MN was reached. Since a crack run-arrest event did not occur, the specimen was rapidly unloaded in an effort to sharpen the crack tip prior to application of a second load cycle. Two changes were then made in the testing procedure prior to application of a second load cycle: the crack tip temperature was lowered about 11°C to -47°C, and the specimen loading rate was increased to 312 kN/s. At a load of 26.5 MN, the crack run-arrest events initiated and lasted ~34 ms (cleavage crack propagation plus ductile tearing). Examination of the fracture surface and strain gage records indicated that three cleavage crack run-arrest events had occurred.

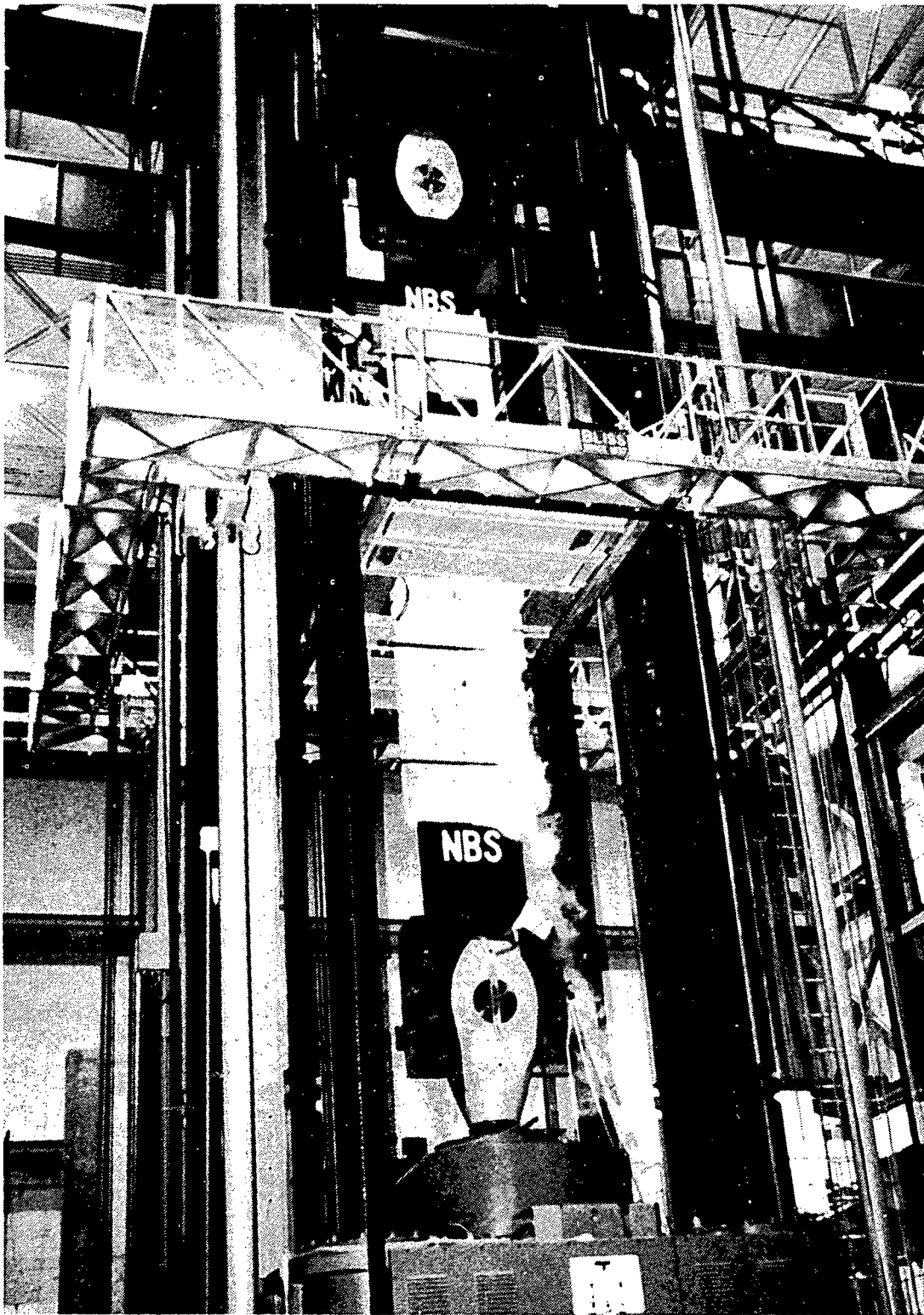


Fig. 5. Wide-plate crack-arrest specimen under test.

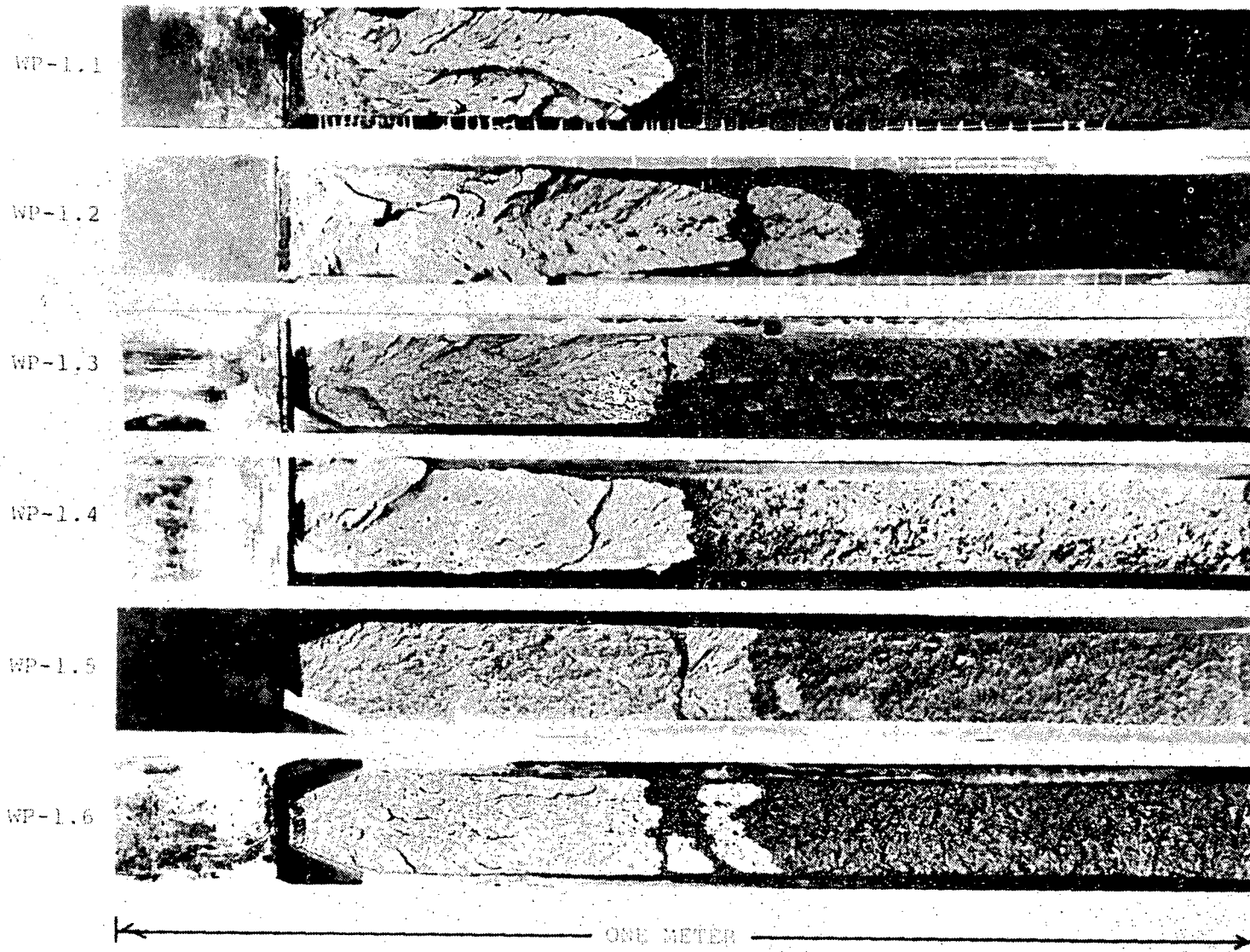


Fig. 6. Fracture surfaces of specimens WP-1.1 through WP-1.6.

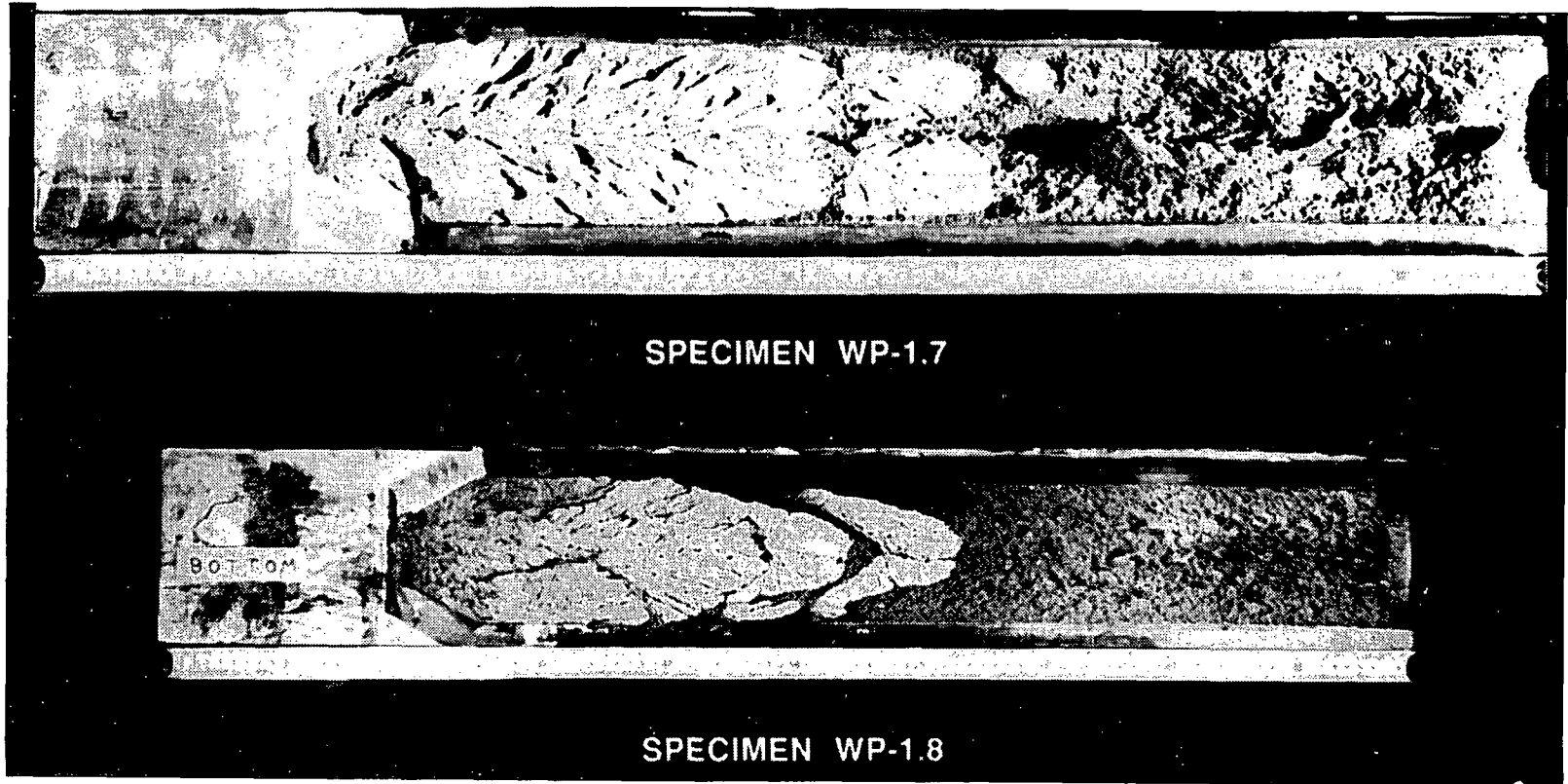


Fig. 7. Fracture surfaces of 152-mm-thick specimens WP-1.7 and WP-1.8.

TABLE 4

SUMMARY OF HSST WIDE-PLATE CRACK-ARREST TEST CONDITIONS  
FOR A533 GRADE B CLASS 1 STEEL: WP-1 AND WP-CE SERIES

Test No.	Crack location (cm)	Crack temperature (°C)	Initiation load (MN)	Arrest location (cm)	Arrest temperature (°C)	Arrest T - RT <sub>NDT</sub> (°C)
WP-1.1 <sup>a</sup>	20	-60	20.1	50.2	51	74
WP-1.2A	20	-33	18.9	55.5	62	85
WP-1.2B	55.5	62	18.9	64.5	92	115
WP-1.3	20 <sup>b</sup>	-51	11.25	48.5	54	77
WP-1.4A	20.7 <sup>b,c</sup>	-63	7.95	44.1	29	52
WP-1.4B	44.1	29	9.72	52.7	60	83
WP-1.5A	20 <sup>b</sup>	-30	11.03	52.1	56	79
WP-1.5B	52.1	56	11.03	58.0	72	95
WP-1.6A	20 <sup>b</sup>	-19	14.50	49.3	54	77
WP-1.6B	49.3	54	14.50	59.3	80	103
WP-1.7A	20.2 <sup>b</sup>	-24	26.2	52.8	61	84
WP-1.7B	52.8	61	26.2	63.5	88	111
WP-1.8A	19.8 <sup>b</sup>	-47	26.5	44.9	40	63
WP-1.8B	44.9	40	26.5	50.4	55	78
WP-1.8C	50.4	55	26.5	59.4	79	102
WP-CE-1	20.0 <sup>b</sup>	-34	10.14	42.0	36	70
WP-CE-2A <sup>d</sup>	20.0 <sup>b</sup>	-40	14.60	46.6	42	76
WP-CE-2B	46.6	42	14.60	50.4	53	88
WP-CE-2C	50.4	51	14.60	52.5	60	95

<sup>a</sup>Specimen was warm prestressed by loading to 10 MN at 70°C. Specimen was also preloaded to 19 MN.

<sup>b</sup>Crack front cut to truncated chevron configuration.

<sup>c</sup>Pillow jack utilized to apply pressure load to specimen's machined notch.

<sup>d</sup>Specimen was warm prestressed to 14 MN at 25°C.

## 5.2 WP-CE Test Series

Table 4 presents a summary of the conditions for the two tests in the WP-CE test series. The fracture surfaces for the two specimens comprising this test series are presented in Fig. 8.

Test WP-CE-1 was the first wide-plate crack-arrest test which used the A 533 grade B class 1 material provided by Combustion Engineering, Inc. After

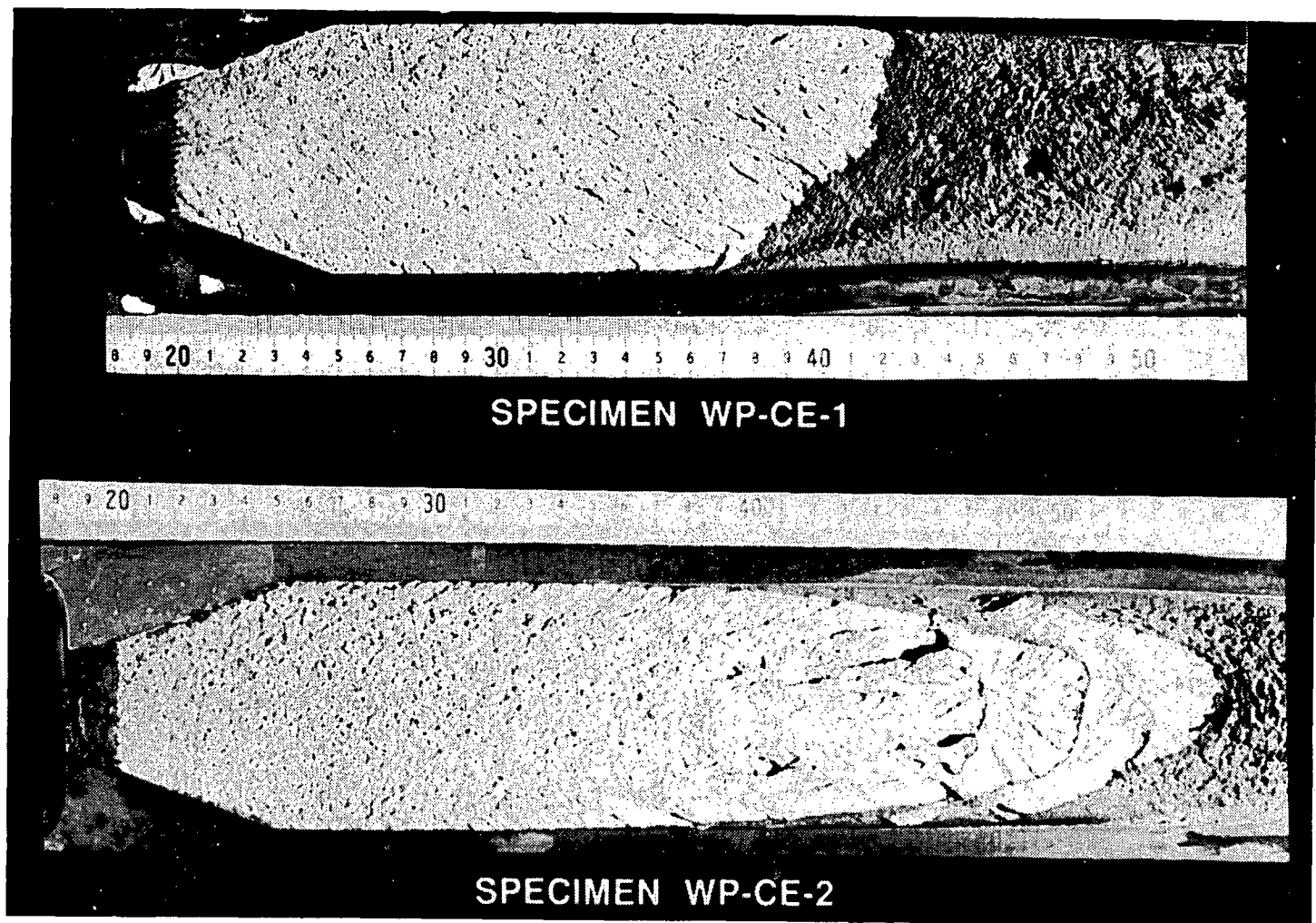


Fig. 8. Fracture surfaces of specimens WP-CE-1 and WP-CE-2.

obtaining a satisfactory thermal gradient, the specimen was loaded at an average rate of 24 kN/s. At a load of 10.14 MN, cleavage crack propagation initiated with a stable arrest occurring at  $a/w = 0.37$  on the plate front face and at  $a/w = 0.42$  on the plate back face. After holding the load constant for 150 s, loading was reinitiated at 24 kN/s. At a load of 15.26 MN, fibrous crack propagation began and was followed by a rapid drop in load to about 4.4 MN. After maintaining the load at this value for about 30 s, loading was reinitiated at 24 kN/s until at a load of 6.34 MN, complete separation of the plate occurred.

Prior to testing, specimen WP-CE-2 was warm prestressed at room temperature ( $\sim 25^\circ\text{C}$ ) by loading it to 14 MN, holding the load for 5 minutes, and slowly reducing the load to 5 MN. While maintaining the load at 5 MN, the temperature gradient was developed. Having established a satisfactory thermal gradient, the specimen was loaded at a rate of 9.6 kN/s. At a load of 14.6 MN, the crack run-arrest events initiated. Examination of the fracture surface and strain gage records indicated that three cleavage crack run-arrest events occurred.

### 5.3 WP-2 Test Series

Table 5 presents a summary of the conditions for the tests in the WP-2 series that have been conducted to date. The fracture surfaces for the five specimens that have been tested are presented in Fig. 9. Since a description of tests WP-2.4, WP-2.1, WP-2.5 and WP-2.3 have been presented in a previous paper [4,5], it will not be repeated. Only a summary of test WP-2.2 will be provided.

Prior to testing, specimen WP-2.2 was warm prestressed at  $120^\circ\text{C}$  by loading it to 16 MN, holding the load for 5 minutes, and slowly reducing the load to 3 MN. While maintaining the load at 3 MN, the temperature gradient was developed. The specimen was loaded at a rate of 16.2 kN/s. At a load of 17 MN, the crack run-arrest events initiated. Examination of the fracture surface and strain gage records indicated that six to seven cleavage crack run-arrest events occurred.

## 6. POSTTEST ANALYSES AND COMPARISON OF DATA WITH OTHER LARGE-SCALE TEST RESULTS

### 6.1 Posttest Analyses

Posttest analyses were conducted for each wide-plate crack-arrest test to investigate the interaction of parameters (plate geometry, material properties, temperature profile and mechanical loading) that affect the crack run arrest events. Three-dimensional (3-D), static, finite-element analyses were performed to determine the stress-intensity factor at the time of crack initiation using the ORMGEN/ORVIRT [6,7] fracture analysis system in conjunction with the ADINA-84 [8] finite-element code. Quasistatic analyses utilized the ORNL computer code WPSTAT [9] to evaluate the static stress-intensity factors as a function of crack length and temperature differential across the plate. WPSTAT also categorizes arrested crack lengths in terms of three types of

TABLE 5

SUMMARY OF HSST WIDE-PLATE CRACK-ARREST TEST CONDITIONS FOR  
SPECIALLY HEAT TREATED 2 1/4 Cr-1 Mo STEEL: WP-2 SERIES

Test No.	Crack location (cm)	Crack temperature (°C)	Initiation load (MN)	Arrest location (cm)	Arrest temperature (°C)	Arrest T - RT <sub>NDT</sub> (°C)
WP-2.4A <sup>a</sup>	20.3	45	7.52	25.1	61	1
WP-2.4B	25.1 <sup>b</sup>	61	8.85	33.8	86	26
WP-2.4C	33.8	86	8.85	39.7	102	42
WP-2.4D	39.7	102	8.85	41.3	107	47
WP-2.4E	41.3	107	8.85	46.2	121	61
WP-2.4F	46.2	121	8.85	48.4	127	67
WP-2.4G	48.4	127	8.85	51.5	137	77
WP-2.4H	51.5	137	8.85	55.5	149	89
WP-2.1A <sup>a</sup>	19.9	55	11.90	27.5	80	20
WP-2.1B	27.5	80	11.90	33.5	96	36
WP-2.1D	33.5	96	11.90	37.0	105	45
WP-2.1E	37.0	105	11.90	40.0	112	52
WP-2.1F	40.0	112	11.90	45.0	125	65
WP-2.1H	45.0	125	11.90	49.0	135	75
WP-2.1I	49.0	135	11.90	52.7	145	85
WP-2.1J	52.7	145	11.90	55.5	152	92
WP-2.5A <sup>a</sup>	19.9	66	7.53	27.2	86	26
WP-2.5B	27.2 <sup>b</sup>	86	8.90	35.0	104	44
WP-2.5C	35.0	104	8.90	43.5	124	64
WP-2.5D	43.5	124	8.90	47.8	135	75
WP-2.5E	47.8	135	8.90	51.6	144	84
WP-2.5F	51.6	144	8.90	56.0	154	94
WP-2.3A	20.0	66	15.3	34.0	97	37
WP-2.3B	34.0	97	15.3	37.5	106	46
WP-2.3D	37.5	106	15.3	39.7	111	51
WP-2.3F	39.7	111	15.3	45.7	126	66
WP-2.2A <sup>a</sup>	21.1	58	17.0	43.5	120	60
WP-2.2B	43.5	120	17.0	46.5	129	69
WP-2.2C	46.5	129	17.0	47.8	133	73
WP-2.2D	47.8	133	17.0	49.9	139	79
WP-2.2E	49.9	139	17.0	51.0	142	82
WP-2.2F	51.0	142	17.0	53.8	150	90
WP-2.2G	53.8	150	17.0	58.2	162	102

<sup>a</sup>Crack front cut to chevron configuration.<sup>b</sup>After pop-in.

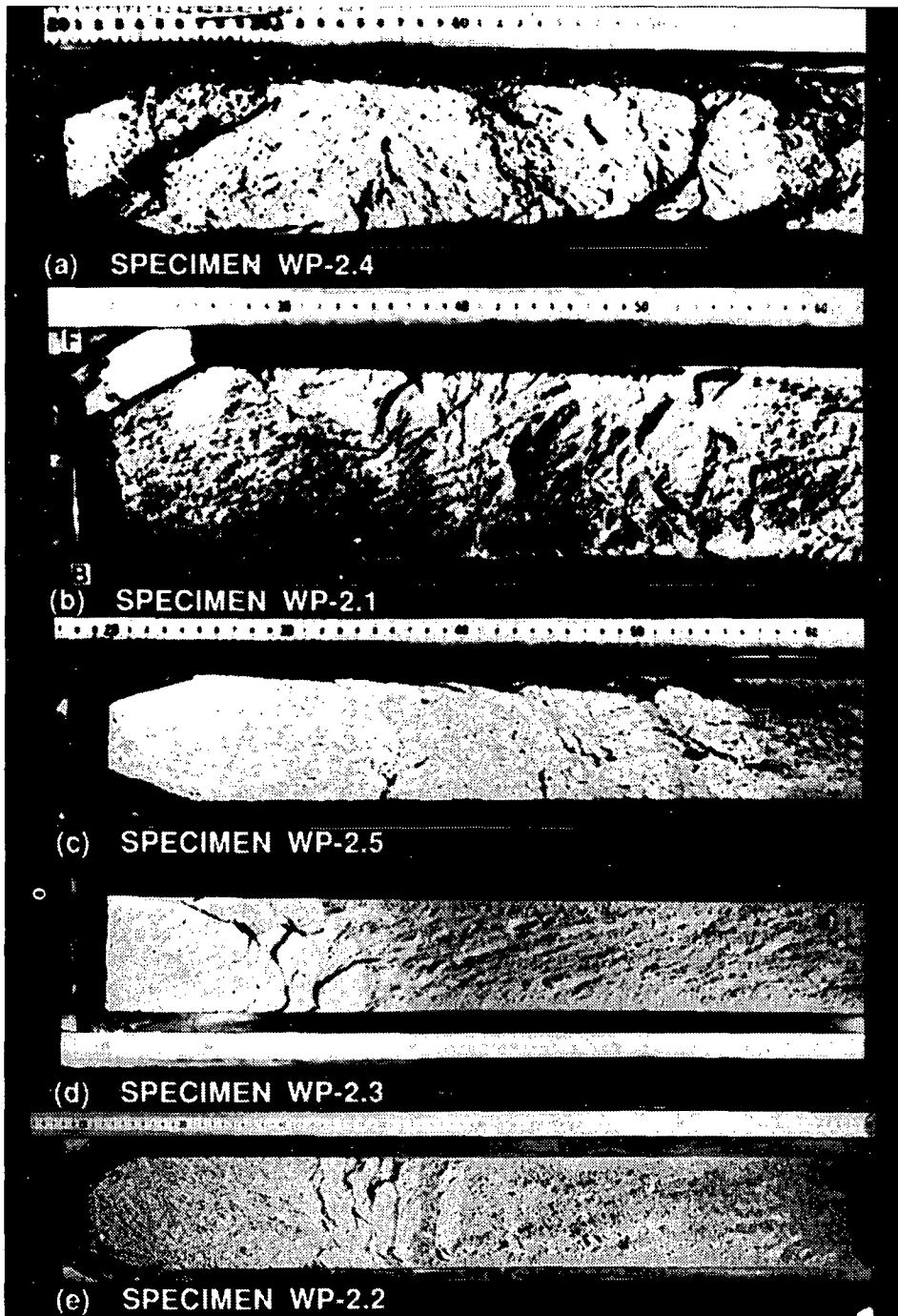


Fig. 9. Fracture surfaces of specimens WP-2.4, -2.1, -2.5, -2.3 and -2.2.

instability limits; i.e., reinitiation, tearing instability and tensile instability. Elastodynamic analyses are carried out using the ADINA/VPF [8] dynamic crack analysis code. The code is capable of performing both application-mode (crack tip is propagated incrementally when  $K_I$ , the dynamically computed stress-intensity factor, equals the specified dynamic fracture toughness value,  $K_{ID}$ ) and generation-mode (crack tip is propagated incrementally according to a prescribed crack position vs time relationship with the values of fracture toughness determined from the dynamically computed  $K_I$ ) analyses. For both modes of analysis, the dynamic stress-intensity factor is determined in each time step from the dynamic J-integral containing the appropriate inertial and thermal terms.

Tables 6 and 7 summarize crack-arrest toughness values for the WP-1, WP-CE and WP-2 series, which were computed by both static and dynamic analyses as well as those determined using handbook techniques [11,12]. The dynamic generation-mode (fixed-load) crack-arrest toughness results, presented in Fig. 10, extend consistently above the limit provided in ASME Sect. XI and exhibit a significant increase in toughness with temperature ( $T - RT_{NDT}$ ). This increase in arrest toughness with temperature occurs at an accelerating rate suggesting that a temperature limit exists at or below which a cleavage crack propagation will arrest, no matter how high the applied driving force.

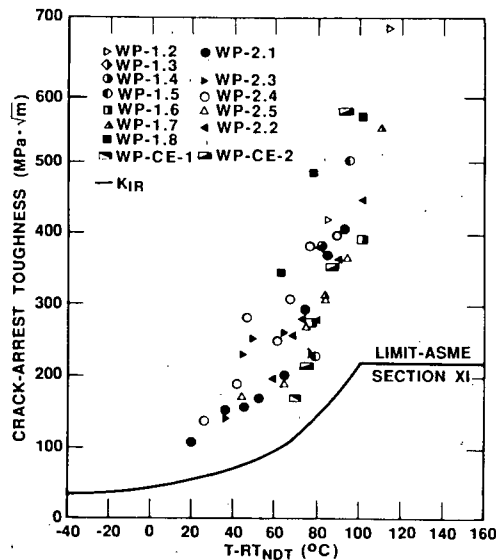


Fig. 10. Generation-mode (fixed load) crack-arrest toughness data versus temperature ( $T - RT_{NDT}$ ) for HSS wide-plate tests.

## 6.2 Comparison of Data with Other Large-Scale Test Results

The trend for  $K_{Ia}$  values to extend consistently above the limit provided in ASME Sect. XI is further substantiated in Fig. 11, which presents data from several large-scale tests [13-24] plus the wide-plate test results.

TABLE 6

SUMMARY OF CRACK-ARREST TOUGHNESS VALUES  
FOR A533 GRADE B CLASS 1 STEEL: WP-1 AND WP-CE SERIES

Test No.	Crack-arrest toughness values (MPa·√m)			
	Tada static SEN formulas		Fedderson alternate secant formula <sup>c</sup>	Dynamic FE <sup>d</sup>
	Displ. control <sup>a</sup>	Load control <sup>b</sup>		Generation mode
WP-1.1	391	813	340	NA
WP-1.2A	384	942	349	424
WP-1.2B	416	1489	419	685
WP-1.3	215	424	185	235
WP-1.4A	145	248	120	NA
WP-1.4B	331	433	170	387
WP-1.5A	217	472	191	231
WP-1.5B	229	616	213	509
WP-1.6A	279	565	242	275
WP-1.6B	306	881	290	397
WP-1.7A	351	793	311	319
WP-1.7B	385	1312	381	555
WP-1.8A	325	576	273	345
WP-1.8B	344	723	301	484
WP-1.8C	374	1083	356	563
WP-CE-1	180	293	148	170
WP-CE-2A	274	509	232	218
WP-CE-2B	285	597	249	354
WP-CE-2C	291	653	258	576

<sup>a</sup> From Ref. [11] (pp. 2.10-2.11) while assuming  $a = a_f$  and no further bending occurs due to propagation of the crack.

<sup>b</sup> From Ref. [11] (pp. 2.10-2.11) while assuming  $a = a_f$  and full bending according to SEN formula when the final crack depth is used.

<sup>c</sup>  $K_I = \sigma \left\{ \pi a \sec\left(\frac{\pi a}{2w}\right) \right\}^{1/2}$  with  $\sigma$  = far-field tensile stress,  $a = a_f$  = final crack length, and  $w$  = full plate width (Ref. [12]).

<sup>d</sup> Dynamic finite element analyses (fixed load) using ORNL program ADINA/VPF (Ref. [10]).

TABLE 7  
SUMMARY OF CRACK-ARREST TOUGHNESS VALUES  
FOR THE WP-2 TEST SERIES

Test No.	Crack-arrest toughness values (MPa·√m)			
	Tada static SEN formulas		Fedderson alternate secant formula <sup>c</sup>	Dynamic FED <sup>d</sup>
	Displ. control <sup>a</sup>	Load control <sup>b</sup>		Generation mode
WP-2.4A	104	113	79	---
WP-2.4B	155	186	111	137
WP-2.4C	168	234	124	188
WP-2.4D	171	249	128	281
WP-2.4E	181	303	140	249
WP-2.4F	185	332	145	307
WP-2.4G	191	378	153	381
WP-2.4H	198	451	165	397
-----				
WP-2.1A	114	132	88	106
WP-2.1B	126	166	100	153
WP-2.1D	133	190	106	158
WP-2.1E	138	213	112	170
WP-2.1F	146	260	123	201
WP-2.1H	153	306	132	293
WP-2.1I	158	359	141	371
WP-2.1J	163	406	149	406
-----				
WP-2.5A	108	123	83	---
WP-2.5B	165	196	114	171
WP-2.5C	184	273	134	190
WP-2.5D	193	326	144	268
WP-2.5E	200	382	155	306
WP-2.5F	209	464	167	366
-----				
WP-2.3A	164	217	129	144
WP-2.3B	172	249	138	232
WP-2.3D	177	271	144	255
WP-2.3F	190	344	160	258
-----				
WP-2.2A	210	350	171	201
WP-2.2B	217	395	180	259
WP-2.2C	220	416	185	281
WP-2.2D	225	454	192	299
WP-2.2E	227	476	195	380
WP-2.2F	233	538	206	364
WP-2.2G	242	656	223	446

<sup>a</sup>From Ref. [11] (pp. 2.10-2.11) while assuming  $a = a_f$  and no further bending occurs due to propagation of the crack.

<sup>b</sup>From Ref. [11] (pp. 2.10-2.11) while assuming  $a = a_f$  and full bending according to SEN formula when the final crack depth is used.

$$cK_I = \sigma \left\{ \pi a \sec\left(\frac{\pi a}{2w}\right) \right\}^{1/2}$$
 with  $\sigma$  = far-field tensile stress,  $a = a_f$  = final crack length, and  $w$  = full plate width (Ref. [12]).

<sup>d</sup>Dynamic finite element analyses (fixed load) using ORNL program ADINA/VPF (Ref. [10]).

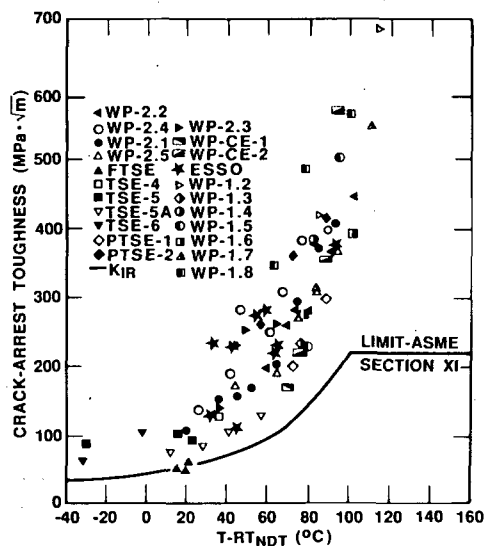


Fig. 11. High temperature crack-arrest toughness data versus temperature ( $T - RT_{NDT}$ ) for wide-plate and other large specimen tests.

## 7. CONCLUSIONS

In conclusion, the HSST program has an integrated effort underway to extend the range of applicability of current state-of-the-art crack-arrest practices and to develop alternatives where improvements are needed. Fractographic examinations confirm that the crack propagation in the wide-plate tests occurred by a predominately cleavage mode and that the arrest events were not preceded by conversion to ductile tearing. Arrest may be followed by stable or unstable ductile crack growth, but these modes of fracture may be analyzed independent of the cleavage run-arrest events. A consistent trend is formed when the crack-arrest data from the three types of HSST large-specimen tests are combined on a plot of  $K_{Ia}$  vs  $T - RT_{NDT}$  with other large-specimen data. Collectively these data show that arrest can and does occur at temperatures up to and above that which corresponds to the onset of Charpy upper-shelf behavior, and the measured  $K_{Ia}$  values extend above the limit included in Section XI of the ASME code. Further, the data suggest the existence of a limiting temperature above which a cleavage crack cannot propagate no matter how high the applied driving force. In summary, the data being obtained under the HSST wide-plate crack-arrest program support: (1) the use of fracture-mechanics concepts to analyze cleavage run-arrest events, (2) the treatment of cleavage- and ductile-fracture modes as separate events, and (3) the fact that cleavage arrest can occur at toughness levels well above the ASME limit.

## REFERENCES

1. M. F. Kanninen et al., *Preliminary Analysis of Japanese Wide-Plate Dynamic Crack Propagation Arrest Experiments*, Subcontract report from Battelle Columbus Laboratories to Oak Ridge National Laboratory, December 1983.
2. D. J. Ayres et al., *Appendix G, Material Characterization in Tests and Analyses of Crack Arrest in Reactor Vessel Materials*, EPRI NP-5121-SP, prepared by Combustion Engineering, Inc., Windsor, Conn., for Electric Power Research Institute, Palo Alto, Calif., April 1987.
3. G. A. Danko et al., *Wide-Plate Crack-Arrest Tests: Instrumentation for Dynamic Strain Measurements*, NBSIR 85-3289, National Bureau of Standards, Gaithersburg, Maryland, December 1985.
4. D. J. Naus et al., "Summary of HSST Wide-Plate Crack Arrest Tests and Analyses," *Proc. of the U.S. Nuclear Regulatory Commission Fifteenth Water Reactor Safety Information Meeting held at National Bureau of Standards, Gaithersburg, Maryland*, NUREG/CP-0091, pp. 17-40, February 1988.
5. C. E. Pugh and D. J. Naus, "Integration of Wide-Plate Crack-Arrest Test Results," *Proc. of U.S. Nuclear Regulatory Commission Fourteenth Water Reactor Safety Information Meeting held at National Bureau of Standards, Gaithersburg, Maryland*, NUREG/CP-0082, pp. 195-225, February 1987.
6. B. R. Bass and J. W. Bryson, *Applications of Energy Release Rate Technique to Part-Through Cracks in Plates and Cylinders, Volume 1, ORMGEN-3D: A Finite Element Mesh Generator for 3-Dimensional Crack Geometries*, NUREG/CR-2997, Vol. 1 (ORNL/TM-8527/V1), Union Carbide Corp. Nuclear Div., Oak Ridge Natl. Lab., December 1982.
7. B. R. Bass and J. W. Bryson, *Applications of Energy Release Rate Technique to Part-Through Cracks in Plates and Cylinders, Volume 2, ORVIRT: A Finite Element Program for Energy Release Rate Calculations for 2-D and 3-D Crack Models*, NUREG/CR-2997, Vol. 2 (ORNL/TM-8527/V2), Union Carbide Corp., Nuclear Div., Oak Ridge Natl. Lab., February 1983.
8. K. J. Bathe, *ADINA - A Finite Element Program for Automatic Dynamic Incremental Nonlinear Analyses*, Report A-1, Massachusetts Institute of Technology, Cambridge, Mass., 1984.
9. B. R. Bass, C. E. Pugh, and H. K. Stamm, "Dynamic Analyses of a Crack Run-Arrest Experiment in a Nonisothermal Plate," *Pressure Vessel Components Design and Analysis*, ASME Publication PVP, 98-2, 175-84, 1985.
10. B. R. Bass and J. Keeney-Walker, "Computer Program Development for Dynamic Fracture Analysis," pp. 5-12 in *Heavy-Section Steel Technology Program Semiann. Prog. Rep. April-September 1985*, NUREG/CR-4219, Vol. 2 (ORNL/TM-9593/V2), Martin Marietta Energy Systems, Inc., Oak Ridge Natl. Lab., January 1986.

11. R. Tada, P. C. Paris, and G. R. Irwin, *The Stress Analysis of Cracks Handbook*, Del Research Corp., Hellertown, Pa., 1973.
12. C. F. Feddersen, *Current Status of Plain Strain Crack Toughness Testing of High-Strength Metallic Materials*, Crack Arrest Methodology and Applications, ASTM STP-410, American Society for Testing and Materials, Philadelphia, Pa., 1967.
13. R. D. Cheverton et al., *Pressure Vessel Fracture Studies Pertaining to the PWR Thermal-Shock Issue: Experiments TSE-5, TSE-5A, and TSE-6*, NUREG/CR-4249 (ORNL-6163), Martin Marietta Energy Systems, Inc., Oak Ridge Natl. Lab., June 1985.
14. R. D. Cheverton et al., *Pressure Vessel Fracture Studies Pertaining to the PWR Thermal-Shock Issue: Experiment TSE-7*, NUREG/CR-4304 (ORNL-6177), Martin Marietta Energy System, Inc., Oak Ridge Natl. Lab., August 1985.
15. R. H. Bryan et al., *Pressurized-Thermal-Shock Test of 6-in.-Thick Pressure Vessels. PTSE-1: Investigation of Warm Prestressing and Upper-Shelf Arrest*, NUREG/CR-4106 (ORNL-6135), Martin Marietta Energy Systems, Inc., Oak Ridge Natl. Lab., April 1985.
16. R. H. Bryan et al., *Pressurized-Thermal-Shock Test of 6-in.-Thick Pressure Vessels. PTSE-2: Investigation of Low Tearing Resistance and Warm Prestressing*, NUREG/CR-4888 (ORNL-6377), Martin Marietta Energy Systems, Inc., Oak Ridge Natl. Lab., December 1987.
17. Japan Welding Council, *Structural Integrity of Very Thick Steel Plate for Nuclear Reactor Pressure Vessels*, JWES-AE-7806, 1977 (in Japanese).
18. T. Kanazawa, S. Machida, and T. Teramoto, "Preliminary Approaches to Experimental and Numerical Study of Fast Crack Propagation and Crack Arrest," pp. 39-58 in *Fast Fracture and Crack Arrest*, ASTM STP 627, American Society for Testing and Materials, Philadelphia, Pa., 1977.
19. N. Ohashi et al., "Fracture Toughness of Heavy Section LWR Pressure Vessel Steel Plate Produced by Basic Oxygen Furnace and Ladle Refining Process," *Proceedings of the Fourth International Conference on Pressure Vessel Technology*, Vol. 1, pp. 391-96, *I. Mech. E.*, 1980.
20. T. Kanazawa et al., "Study on Fast Fracture and Crack Arrest," *Experimental Mechanics* 21(2), 77-88 (February 1981).
21. S. Machida, Y. Kawaguchi, and M. Tsukamoto, "An Evaluation of the Crack Arrestability of 9% Ni Steel Plate to an Extremely Long Brittle Crack," *Journal of the Society of Naval Architect of Japan* 150, 511-17 (1981), translation ORNL-tr-5052.

22. T. Kanazawa, S. Machida, and H. Yajima, "Recent Studies on Brittle Crack Propagation and Arrest in Japan," pp. 81-100 in *Fracture Mechanics Technology Applied to Material and Structure Design*, G. C. Sih, N. E. Ryan, and R. Jones (eds.), Martinus Nijhoff, The Hague, 1983.
23. Y. Nakano, "Stress Intensity Factor During Brittle Crack Propagation and Arrest in ESSO Specimens," *18th National Symposium on X-Ray Study on Deformation and Fracture Solids*, The Soc. of Materials Science, Japan, July 13-14, 1981.
24. A. Pellissier-Tanon, P. Sollogoub, and B. Houssin, "Crack Initiation and Arrest in an SA 508 Class-3 Cylinder Under Liquid Nitrogen Thermal-Shock," Paper G/F 1/8, *Transactions of the 7th International Conference on Structural Mechanics in Reactor Technology*, Vol. G/H, pp. 137-42 (August 1983).



**SUMMARY OF THE HEAVY-SECTION STEEL TECHNOLOGY PROGRAM**  
**IRRADIATION SERIES\***

Randy K. Nanstad

Metals and Ceramics Division  
Oak Ridge National Laboratory  
P.O. Box 2008  
Oak Ridge, Tennessee 37831

**ABSTRACT**

The Heavy-Section Steel Technology (HSST) Program has considered the effects of radiation on pressure vessel steels since its inception in 1967. Research has focused on the conduct of experiments in test reactors to investigate the fracture toughness of both base metals and welds as a consequence of neutron irradiation under conditions similar (with the exception of irradiation rate) to those experienced by commercial power reactor vessels. The materials used for all the studies have been prototypic of commercial practice. The welds and plates are procured from commercial nuclear fabricators and fabricated using the same procedures used for reactor vessels.

The HSST irradiation task currently includes ten separate series; four have been completed, three are active, and three are under planning. This paper briefly summarizes the results from the completed series, discusses the results from Series 5 on the  $K_{Ic}$  curve shift and shape in some detail, and briefly summarizes the remaining series. The first four series dealt with dynamic fracture, ductile tearing resistance of low upper-shelf welds, and fracture toughness of current welding practice, low copper/nickel welds. Series 5 incorporates a large number of small and large specimens (up to 203-mm-thick compact specimens) of two welds to provide a basis for statistical analyses used to determine the temperature shift and shape of the postirradiation  $K_{Ic}$  curve. The testing is completed and preliminary analyses indicate that the fracture toughness shift can be greater than the Charpy impact shift and the  $K_{Ic}$  curve can change shape. Series 6 on crack-arrest toughness is well under way, while Series 7 on stainless steel cladding is virtually completed. Series 8 on the  $K_{Ic}$  curve shift and shape for low upper-shelf welds, Series 9 on the effects of thermal annealing in thick sections, and Series 10 on fracture toughness of the low upper-shelf weld in the Midland Unit 1 reactor vessel are in various stages of planning.

---

\*Research sponsored by the Office of Nuclear Regulatory Research, Division of Engineering, U.S. Nuclear Regulatory Commission under Interagency Agreement DOE 1886-8011-9B with the U.S. Department of Energy under contract DE-AC05-84OR21400 with Martin Marietta Energy Systems, Inc.

## INTRODUCTION

The degrading effects of neutron irradiation on carbon and low-alloy pressure vessel steels have been recognized and investigated since the early 1950s. In those steels at light-water-reactor (LWR) operating temperature (~288°C), radiation damage is produced when neutrons of sufficient energy displace atoms from their lattice sites. The defects formed in the steel as a result of those displacements typically cause hardening and a decrease in toughness. Tensile behavior exhibits an increase in yield strength, a decrease in the ultimate to yield strength ratio, and a loss of ductility as measured by specimen elongation. The decrease in toughness is most commonly represented by an increase in the ductile-brittle transition temperature and a decrease of the ductile shelf energy as measured by the Charpy V-Notch (CVN) impact test. When the Heavy-Section Steel Technology (HSST) Program was initiated in 1967, irradiation effects was one of the designated major topics of investigation. It was well recognized that the effects of irradiation could degrade the materials, but definitive effects on fracture properties, especially in thick sections, were not available. At that time, the field of fracture mechanics was in the early stages and even the amount of data on other material properties under LWR conditions was deficient. The United States Atomic Energy Commission (USAEC) had, in fact, already sponsored two irradiation effects projects, and the HSST Program assumed managerial responsibility for them. That role included the formulation of plans for extensions of those projects. During the intervening time, Title 10, Part 50 of the Code of Federal Regulations (10CFR50)<sup>1</sup> evolved to include requirements for fracture toughness of reactor pressure vessels. Those requirements include surveillance testing; CVN specimens are required, tensile specimens are recommended, and fracture toughness specimens are required if the surveillance materials are predicted to exhibit marginal properties. Furthermore, 10CFR50 requires prediction of radiation effects using Regulatory Guide 1.99 (Rev. 2)<sup>2</sup> and, if those predictions indicate unacceptable end-of-life toughness, the vessel must be designed to accommodate thermal annealing. Additionally, criteria are specified for toughness transition temperatures which, if attained by the surveillance tests, require plant-specific analyses to demonstrate adequate protection against pressurized thermal shock. As part of those requirements, 10CFR50 refers to the *ASME Boiler and Pressure Vessel Code*, Sections III and XI<sup>3</sup> for fracture toughness requirements and ASTM E-185 for surveillance testing and analysis as well as application of the test results. This paper summarizes the early irradiation projects as well as the resultant series of investigations which embody the HSST Program irradiation series.

## EARLY IRRADIATION PROJECTS

When the HSST Program was initiated in 1967, the USAEC transferred managerial responsibility for two ongoing irradiation projects to the HSST Program. The U.S.-Euratom Joint Research and Development Program was then being coordinated by Westinghouse Electric Corporation while the Irradiation Effects to Heavy-Section Pressure Vessel Steels Program was coordinated by Battelle Pacific Northwest Laboratories (PNL). Both of those programs were

directed toward fracture toughness using developmental specimens of limited size. The largest specimens used were 50.8-mm (2-in.) thick. Prior irradiation effects research demonstrated clearly that neutron irradiation could severely degrade the CVN impact toughness of ferritic steels, but the effects on initiation fracture toughness,  $K_{IC}$ , had not been demonstrated. It is also important to note that the ASTM standard for fracture toughness testing was in the early stages of development. The results from those early programs, however, were important in that they showed irradiation-induced degradation of fracture toughness, a strong temperature dependence of postirradiation fracture toughness, and a need for larger specimens.<sup>4</sup> Figure 1 shows some results from the Westinghouse program.<sup>5</sup> As with all the irradiation experiments, the target irradiation temperature was 288°C (550°F), considered the nominal operating temperature for commercial light-water reactor pressure vessels. The highest fracture toughness values measured which satisfied the suggested ASTM criteria were about 82 MPa $\sqrt{m}$  (75 ksi $\sqrt{in.}$ ).

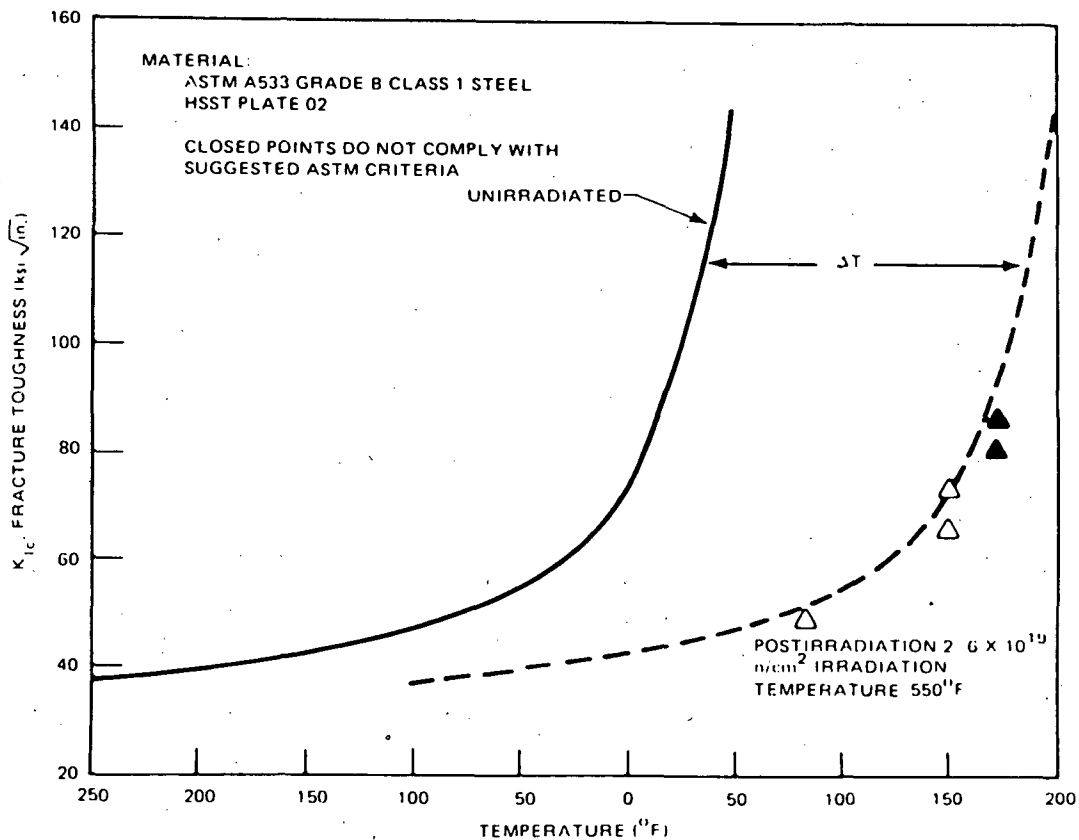


Fig. 1. Pre- and postirradiation temperature dependence of the fracture toughness  $K_{IC}$  of A533 grade B class 1 steel (HSST plate 02). Source: T. R. Mager, *Post-Irradiation Testing of 2T Compact Tension Specimens*, Heavy Section Steel Technology Program Technical Report No. 9, Westinghouse Nuclear Energy Systems, Pittsburgh, Pa., August 1970.

The PNL program determined that the double-cantilever beam specimen offered no advantage over the compact specimen geometry in terms of irradiation experiments and, more importantly, that the measuring capacity of the compact specimen was higher for a given thickness. It also showed that the  $K_{Ic}$  temperature shift was about the same as the CVN 41-J (30 ft-lb) shift and that postirradiation annealing of tensile specimens at 385°C (725°F) resulted in significant recovery of properties.<sup>4</sup> References 6, 7, and 8 provide more detailed descriptions of those programs. Additionally, ORNL produced irradiation effects data on CVN and tensile properties for HSST plates 01 and 02, submerged-arc weldments, and electroslag weldments irradiated at the poolside facility of the Oak Ridge Research Reactor.<sup>9</sup>

### SERIES 1 - DYNAMIC FRACTURE TOUGHNESS USING LARGE SPECIMENS

The irradiation of large fracture mechanics specimens represents a major factor in the HSST irradiation series. In terms of linear elastic fracture mechanics, the  $K_{Ic}$  measuring capacity increases with increasing specimen thickness with the actual value dependent on the material yield strength at test temperature. If the maximum  $K_{Ic}$  value for a 50.8-mm-thick (2-in.) specimen of a given material is  $75 \text{ MPa}\sqrt{\text{m}}$ , for example, a 101.6-mm-thick (4-in.) specimen can measure a value of  $106 \text{ MPa}\sqrt{\text{m}}$ . Size effects are also important in elastic-plastic fracture mechanics as will be discussed in subsequent sections. The largest practical size for irradiation experiments was determined to be 101.6 mm (4 in.) in thickness; for HSST Series 1, the newly developed ASTM compact tension (CT) specimen was used. Thus, the designation 4TCT was often used to designate the size (in English units) of the compact tension specimen. That specimen is now designated the compact specimen (CS) and, thus, the size designation commonly used is 4TCS. The objective of Series 1 was to verify that high values of fracture toughness under dynamic (high loading rate) conditions could be achieved in material irradiated to typical reactor vessel end-of-life neutron fluence [ $\sim 2 \times 10^{19}$  neutrons/cm<sup>2</sup> (>1 MeV)].

A critical factor in the performance of these 4TCS irradiations was the development of a capsule for encapsulating the specimens that would minimize temperature and neutron fluence gradients in the specimens. The internal generation of heat due to gamma ray absorption was overcome by incorporation of flowing gas through gas gaps to reject heat and electric heaters to control the temperature gradient through the specimen thickness. Later improvements in capsule design incorporated a separate gamma shield and controllable zoned heaters to provide excellent temperature control.

Specimens were fabricated from HSST Plate 02 and submerged-arc weldment with irradiations conducted in the Battelle Research Reactor in Columbus, Ohio, from October 1972 to December 1973. Specimen testing was performed by ORNL, Hanford Engineering Development Laboratory (HEDL), and Westinghouse. The static and dynamic tests showed that fracture toughness of irradiated large specimens reached high values. Figure 2 shows the results of dynamic testing with various specimen types, including 4TCS. The fracture toughness values were calculated using the equivalent energy method<sup>10</sup> (now an ASTM practice, E992). Indications were that the CVN energy shifts conservatively predicted the fracture toughness shifts but statistical analyses were not

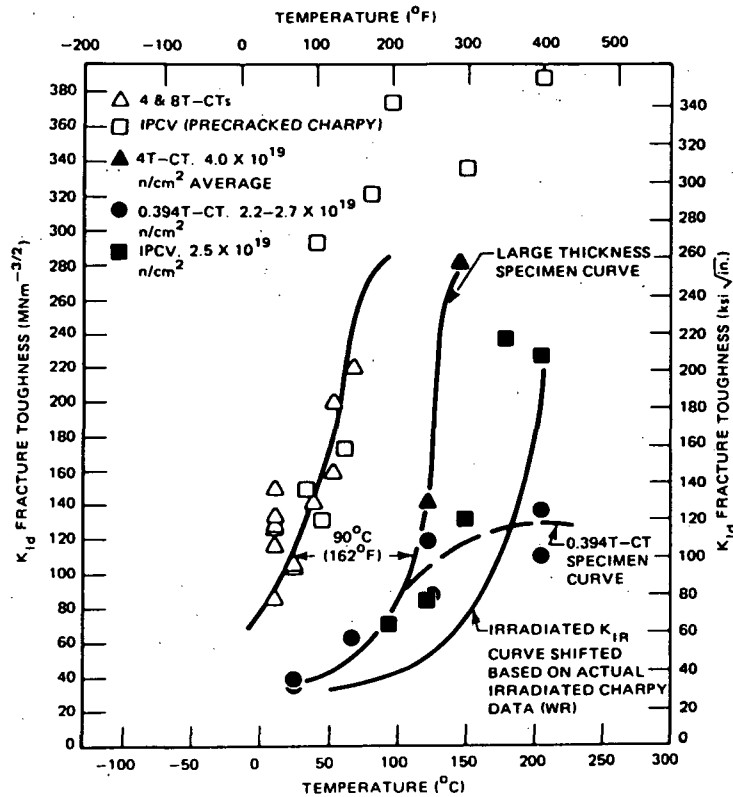


Fig. 2. Dynamic irradiated and unirradiated fracture-toughness,  $K_{I_d}$  (calculated using equivalent energy method), results for A533 grade B class 1 (HSST plate 02). The 4TCS data lie well above the shifted  $K_{I_R}$  curve and attained relatively high values of fracture toughness. Source: J. A. Davidson et al., *The Irradiated Dynamic Fracture Toughness of ASTM A533, Grade B, Class 1 Steel Plate and Submerged Arc Weldment*, Heavy Section Steel Technology Program Technical Report No. 41, Westinghouse Nuclear Energy Systems, Pittsburgh, Pa., October 1976.

feasible due to the limited data. This series also demonstrated that large specimens could be irradiated to reactor vessel end-of-life fluences in a practical manner and with acceptable control of temperature and fluence gradients. The smaller specimens, contained in regions of the capsules far from the 4TCS crack-line, were of limited usefulness because of substantial temperature and fluence variability. Detailed results from this series are discussed in refs. 11, 12, and 13.

#### SERIES 2 AND 3 - DUCTILE SHELF FRACTURE TOUGHNESS WITH 4TCS

In November 1975, the Nuclear Regulatory Commission (NRC) initiated an investigation of ductile fracture toughness of submerged-arc welds which

exhibited low CVN upper-shelf toughness and which contained high copper contents. Studies at the Naval Research Laboratory (NRL), reported in late 1968, revealed that certain residual elements, especially copper, substantially increased sensitivity of ferritic pressure vessel steels to neutron irradiation.<sup>14</sup> A number of reactor vessels had been fabricated with weld wire having copper flashing (to increase conductivity and corrosion resistance) and with Linde 80 welding flux. Use of that flux produced welds with a uniform dispersion of fine inclusions which resulted in CVN energies in the upper-shelf region ranging approximately from 68 to 95 J (50 to 70 ft-lb) in the unirradiated condition. Combined with sensitive radiation response due to relatively high copper contents, the postirradiation upper-shelf toughness of these "low upper-shelf" welds was predicted by Regulatory Guide 1.99 to go below the 68-J (50 ft-lb) minimum allowed in 10CFR50. By that time, 10CFR50 referred to the ASME Code, Section III, which had incorporated a reference fracture toughness curve,  $K_{IR}$ , for protection against nonductile failure. The curve was indexed to a normalized temperature scale which required determination of a reference nil-ductility transition temperature ( $RT_{NDT}$ ). The  $RT_{NDT}$  is determined through testing of drop-weight specimens to determine the NDT and CVN specimens to establish the temperature at which 68 J (50 ft-lb) is attained. Thus, if 68 J is not achieved with CVN specimens, the  $RT_{NDT}$  is infinite according to the definition, and the reference fracture toughness would be very low [ $30 \text{ MPa}\sqrt{\text{m}}$  ( $27 \text{ ksi}\sqrt{\text{in.}}$ )] at all temperatures.

The HSST Irradiation Series 2 and 3 were conceived to investigate the postirradiation ductile fracture toughness of these low upper-shelf welds to include the use of large fracture mechanics specimens, 4TCS. Six submerged-arc welds were supplied by Babcock and Wilcox Company and one weld was supplied by Westinghouse, all fabricated with copper-coated wire and Linde 80 flux. Mean copper contents ranged from 0.21 to 0.42 wt %. In addition to the capsule fabrication and irradiation requirements, a separate and complicated objective was the development of experimental procedures for obtaining as much data as practicable from each specimen to facilitate ductile instability analyses. Considerable effort was expended by many organizations in concluding that the single specimen unloading compliance procedure should be used to obtain J-integral resistance (J-R) curves.<sup>4</sup> The irradiation and testing program included CVN, tensile, precracked CVN, 0.5TCS, 0.8TCS, 1.6TCS, and 4TCS. The irradiations were performed in the Bulk Shielding Reactor (BSR) at ORNL from October 1976 to March 1978. The irradiation temperature at the crack-tip region on the 4TCS was controlled at 288°C, while the temperatures for the smaller specimens, located in the notches and pinholes of the large specimens, varied from 233°C to 343°C. Fluences varied from 0.4 to  $2.1 \times 10^{19}$  neutrons/cm<sup>2</sup>. ORNL tested all of the CVN specimens and the Series 3 tensile specimens.<sup>15</sup> Tensile specimens from Series 2 were tested by HEDL<sup>16</sup> while initial compact specimen tests were performed by HEDL and NRL. Most of the compact specimen tests were performed by NRL and Materials Engineering Associates (MEA).

Figures 3 and 4 show the effects of irradiation on the CVN toughness of weld 63W and the J-R curve for weld 61W, tested at 200°C. As Fig. 4 indicates, side-grooves were incorporated in the compact specimens to minimize crack front curvature during stable ductile tearing. It is obvious that irradiation substantially reduced the J-R curve and CVN upper-shelf toughness and increased the CVN transition temperature. Those are typical results for

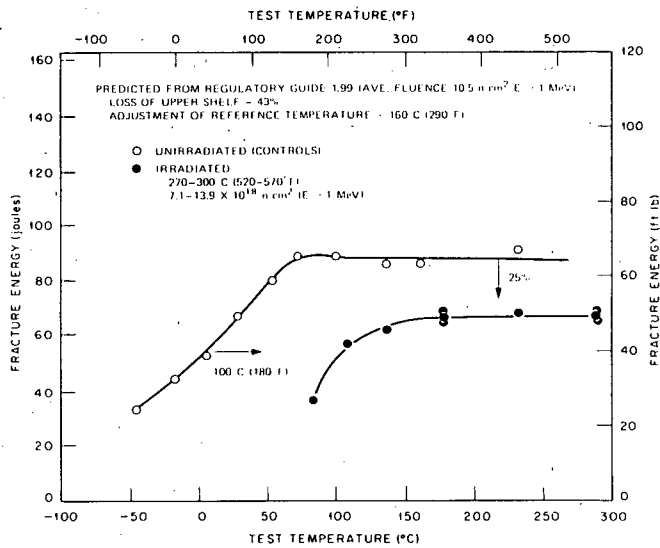


Fig. 3. Charpy impact energy vs test temperature for HSST weld 63W, unirradiated and irradiated. Irradiation temperatures varied from 270 to 300°C while the neutron fluence (>1 MeV) varied from 0.7 to  $1.4 \times 10^{19}$  neutrons/cm<sup>2</sup>. The upper-shelf energy has degraded considerably and the transition temperature has significantly shifted following irradiation.

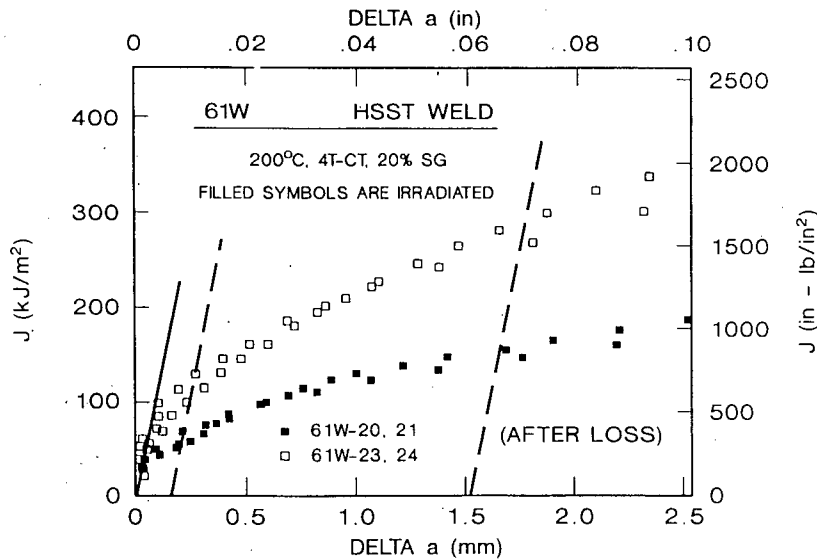


Fig. 4. J-integral vs crack extension for 4TCS specimens of HSST weld 61W tested at 200°C, unirradiated and irradiated. The ductile tearing resistance of this low upper-shelf weld has been substantially reduced by irradiation at ~288°C to a fluence (>1 MeV) of  $\sim 1.2 \times 10^{19}$  neutrons/cm<sup>2</sup>. Source: A. L. Hiser, F. J. Loss, and B. H. Menke, *J-R Curve Characterization of Irradiated Low Upper-Shelf Welds*, NUREG/CR-3506 (MEA-2028), Materials Engineering Associates, Inc., Lanham, Maryland, April 1984.

all the welds tested in these two series, with the results varying dependent on copper content, etc. Results of the fracture toughness tests are described in ref. 17. Figure 5 presents the correlation between the ductile fracture toughness (modified J-integral vs material tearing modulus) and CVN upper-shelf energy results developed in that study.<sup>17</sup> The two test series produced very valuable data directly related to structural integrity analyses of reactor pressure vessels containing low upper-shelf welds in regions of high neutron flux. The results from Series 2 and 3 can be summarized as follows:

1. A data base of J-R curves for irradiated low upper-shelf welds was established for use in elastic-plastic fracture mechanics analyses of reactor pressure vessels.
2. Irradiation to  $\sim 1 \times 10^{19}$  neutrons/cm<sup>2</sup> substantially decreased both the ductile initiation toughness,  $J_{Ic}$ , and tearing modulus.
3. The tearing modulus is a more discriminating indicator of degradation than  $J_{Ic}$ .
4. No specimen size effects were observed for irradiated low upper-shelf welds.
5. A correlation was developed between J-R curve parameters and CVN upper-shelf energy which offers potential for use in interpretation of surveillance data from CVN specimens
6. The CVN results showed Regulatory Guide 1.99 to be generally conservative for these test reactor irradiations.

#### SERIES 4 - FRACTURE TOUGHNESS OF STATE-OF-THE-ART WELDS

As a natural sequel to Series 2 and 3 on low upper-shelf welds, Series 4 was conceived to investigate submerged-arc welds fabricated with modern techniques and materials. Much previous work had demonstrated that relatively low contents of copper and nickel provided high resistance to neutron irradiation as measured by CVN and tensile tests. The objective of Series 4 was to validate those observations relative to fracture toughness, especially in the ductile shelf region. Studies of the effects of irradiation on fracture toughness properties of steels have generally included a minimum number of tests for each material condition. A secondary objective of Series 4 was to apply statistical analyses with multiple testing at selected temperatures to assess the accuracy and reliability of the results. The plan provided for at least half the specimens to be tested in the ductile shelf region using elastic-plastic fracture mechanics techniques. This series took advantage of the results from Series 2 and 3 regarding a lack of specimen size effects, and used 1TCS for all fracture toughness testing. Additionally, a large number of CVN specimens were also tested to allow for a statistical comparison of results from those tests. The testing was divided between ORNL and MEA which provided an interlaboratory comparison, except for the tensile testing which was performed only by ORNL.

The materials used for Series 4 were four commercially fabricated submerged-arc welds with copper contents from 0.04 to 0.12 wt %, nickel contents from 0.10 to 0.63 wt %, and one of three different welding fluxes, Linde 80, 91, and 124. The Electric Power Research Institute supplied the two welds fabricated by Combustion Engineering, Inc., while the other two welds

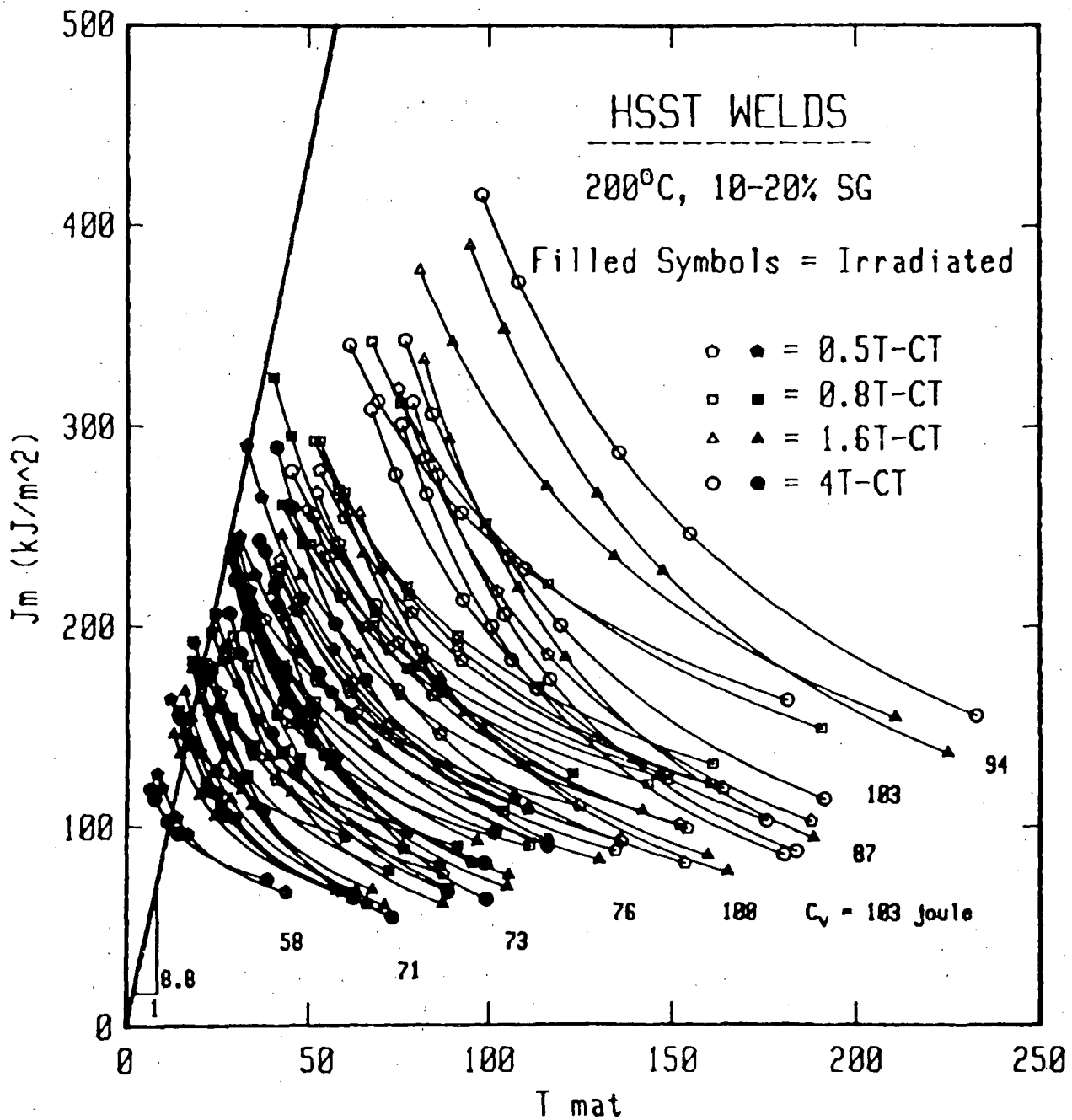


Fig. 5. Relationship between Charpy impact upper-shelf energy and J-R curve results at 200°C for unirradiated and irradiated low upper-shelf, high copper welds tested in HSST Irradiation Series 2 and 3. Source: A. L. Hiser, F. J. Loss, and B. H. Menke, *J-R Curve Characterization of Irradiated Low Upper-Shelf Welds*, NUREG/CR-3506 (MEA-2028), Materials Engineering Associates, Inc., Lanham, Maryland, April 1984.

were fabricated and supplied by Babcock and Wilcox Company. Additionally, an A533 grade B class 1 plate (HSST plate 02), with a copper content of 0.14 wt % and nickel content of 0.67 wt %, was used for comparison. The irradiations were performed in the BSR at 288°C to fluences from about 1.2 to  $2.0 \times 10^{19}$  neutrons/cm<sup>2</sup> (>1 MeV). Three different capsules were designed and fabricated and the irradiations were conducted from December 1979 to July 1982. The improved capsule designs resulted in much improved temperature control which facilitated the analysis of results.

The results of tensile tests showed average irradiation-induced yield strength increases (over the range 22 to 288°C) ranging from 12 to 19% for the welds and 31% for the plate. The flow strength (average of yield and ultimate strength) increases ranged from 10 to 12% for the welds and 24% for the plate. The flow strength is used in analysis of J-R curves to calculate the blunting line and the tearing modulus.

The results of CVN testing showed 41-J temperature increases ranging from 10 to 27°C for the welds and 68°C for the plate. The observed shifts for the welds are all within the predictions of Regulatory Guide 1.99 (Rev. 2) while that for the plate is 3°C greater than the Regulatory Guide without the margin discussed in that guide. The greatest CVN upper-shelf decrease for the welds was only 10%, while the decrease for the plate was 16%. Agreement in results between ORNL and MEA was very good. Figure 6 shows the CVN results for weld 71W with 0.046 wt % copper and 0.63 wt % nickel. At a fluence of  $1.6 \times 10^{19}$  neutrons/cm<sup>2</sup>, the 41-J shift is only 23°C, and the upper-shelf actually shows an increase of 10%.

All fracture toughness tests were conducted with computer-controlled single-specimen compliance techniques by both ORNL and MEA. Specimens which cleaved were analyzed by determining the J-integral ( $J_c$ ) at the point of cleavage and calculating a  $K_{Jc}$  from  $(E \times J_c)^{1/2}$ . For specimens which exhibited a J-R curve,  $J_{Ic}$  was determined from the J-R curve and used to calculate  $K_{Jc}$ . Figure 7 shows the fracture toughness results for weld 70W with 0.056 wt % copper and 0.63 wt % nickel. At a fluence of  $1.7 \times 10^{19}$  neutrons/cm<sup>2</sup>, the  $K_{Jc}$  shift (at a value of 125 MPa/m) is 25°C while the ductile shelf fracture toughness increased 3%. For test temperatures above 0°C, the fracture toughnesses were calculated from  $J_{Ic}$  results. Table 1 summarizes the effects of irradiation on the tensile, CVN, and fracture toughness properties of all five materials tested in Series 4. The  $K_{\beta c}$  parameter listed is the result of an adjustment to the  $K_{Jc}$  value to account for lack of constraint due to small specimen size.<sup>18,19</sup> The largest shift of  $K_{Jc}$  in the transition region for the welds was 47°C, and the greatest drop in fracture toughness on the ductile shelf was 3%. Thus, the results validated that welds with relatively low concentrations of copper and nickel would exhibit relatively low sensitivity to irradiation.

Regarding statistical analyses, the coefficients of variation were somewhat greater for the postirradiation condition than the unirradiated condition. Even though temperature control and fluence differences were considered good for this type of experiment, the differences among specimens were enough to cloud a conclusion regarding those variations. It was also observed that the variations for both CVN energy and fracture toughness were greater in the transition region than on the ductile shelf. Finally, predictions of transition temperature shifts show larger 95% confidence

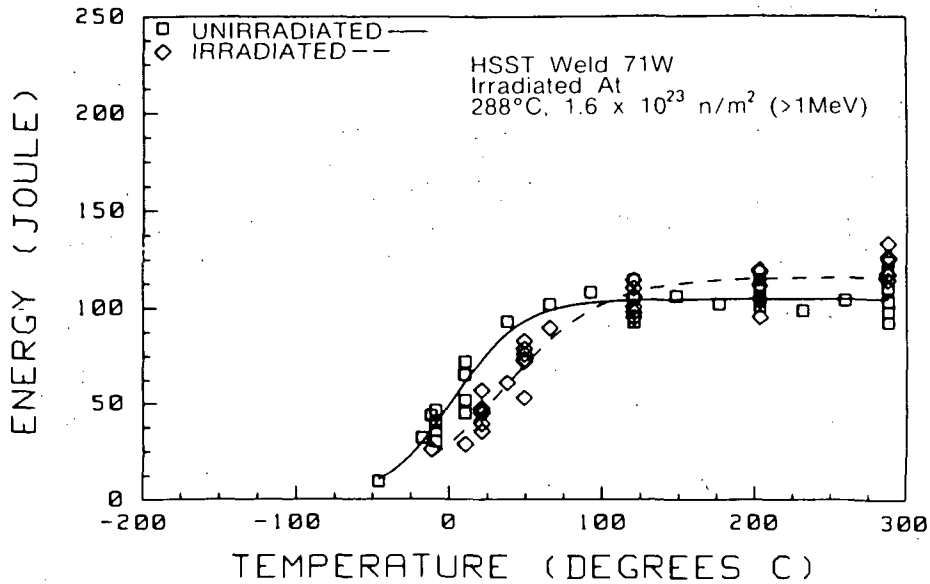


Fig. 6. Charpy impact energy vs test temperature for HSST weld 71W before and after irradiation at  $-288^{\circ}\text{C}$  to an average fluence ( $>1\text{ MeV}$ ) of  $1.6 \times 10^{19}$  neutrons/cm<sup>2</sup>. The effects of irradiation on this low-copper, typical-nickel weld are relatively small.

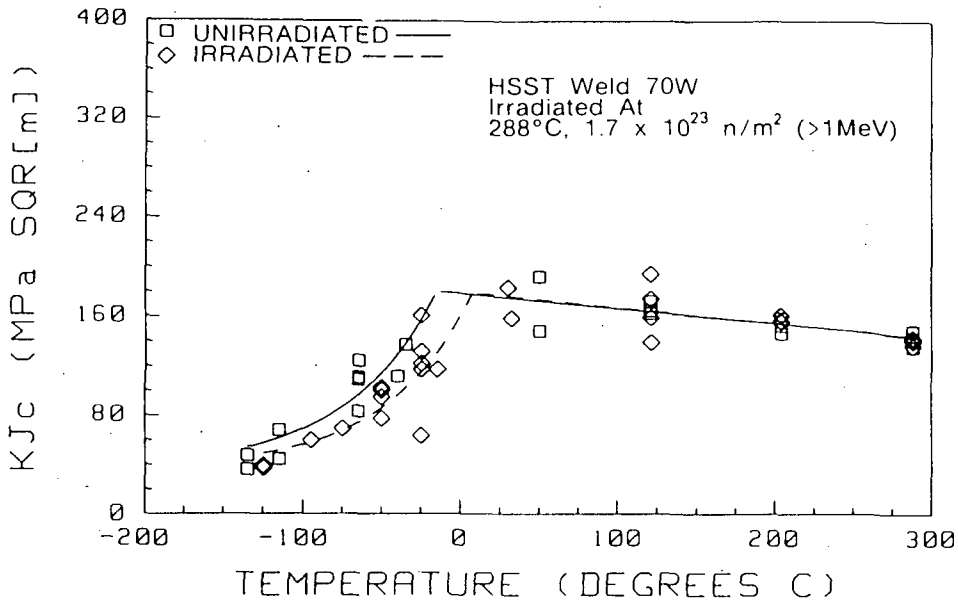


Fig. 7. Fracture toughness,  $K_{Jc}$ , vs test temperature for HSST weld 70W before and after irradiation at  $-288^{\circ}\text{C}$  to an average fluence ( $>1\text{ MeV}$ ) of  $1.8 \times 10^{19}$  neutrons/cm<sup>2</sup>. The effects of irradiation on this low-copper, typical-nickel weld are relatively small.

Table 1. Summary of irradiation-induced changes in material properties for HSST Irradiation Series 4

Material	Mean fluence [n/m <sup>2</sup> × 10 <sup>23</sup> (>1 MeV)]	Flow strength increase <sup>a</sup> (%)	Transition temperature increase (°C)			Ductile-shelf change (%)		Tearing modulus change <sup>b</sup> (%)
			CVN at 41 J	K <sub>Jc</sub> at 125 MPa√m	K <sub>βc</sub> at 90 MPa√m	CVN	K <sub>Jc</sub> <sup>b</sup>	
Plate 02, 0.14% Cu, 0.67% Ni	1.9	24	68	81	66	-14	-6	-46
Weld 68W, 0.04% Cu, 0.13% Ni	1.3	10	10	-6	-2	9	-3	-17
Weld 69W, 0.12% Cu, 0.10% Ni	1.2	12	27	47	39	-1	-2	-22
Weld 70W, 0.056% Cu, 0.63% Ni	1.7	10	23	25	21	-2	3	-29
Weld 71W, 0.046% Cu, 0.63% Ni	1.7	10	23	-1	16	10	2	-12

<sup>a</sup>Average change from 22 to 288°C.

<sup>b</sup>Average at 204°C.

intervals for fracture toughness than for CVN tests. More detailed presentations of Series 4 are available in refs. 20, 21, and 22. The results of Series 4 can be summarized as follows.

1. The degradation of fracture toughness due to irradiation is relatively slight for "current practice" welds with low copper and nickel contents.
2. Generally good agreement was observed between CVN and fracture toughness results from the two laboratories, ORNL and MEA.
3. Variations of both CVN and fracture toughness are greater in the transition region than on the ductile shelf.
4. Qualitative agreement was generally observed between transition temperature shifts determined from CVN and fracture toughness results for welds that exhibit CVN 41-J shifts from 10 to 27°C.
5. For materials which exhibit relatively low sensitivity to irradiation, caution must be applied in quantitatively correlating fracture toughness behavior from CVN and tensile results.

### SERIES 5 - $K_{Ic}$ CURVE SHIFT AND SHAPE

The primary objective of Series 5 is to validate the temperature shift and shape of the ASME Code Section XI  $K_{Ic}$  curve for irradiated reactor vessel materials. As mentioned earlier, 10CFR50, Appendix G, requires determination of the unirradiated  $RT_{NDT}$  using CVN and drop-weight specimens as specified in Section III of the ASME Code. Appendix A of Section XI contains the  $K_{Ic}$  curve which is normalized on the temperature scale to the  $RT_{NDT}$ . For determination of the adjusted  $RT_{NDT}$ , 10CFR50 refers to ASTM E185 which specifies the method for using surveillance test results. Standard E185 specifies that a minimum of 12 CVN specimens be used to obtain a "full" Charpy energy vs test temperature curve and to determine the transition temperature shift at an energy value of 41 J using the average curve fits to both the unirradiated and irradiated results. The 41-J shift is then added to the unirradiated  $RT_{NDT}$  to obtain the adjusted  $RT_{NDT}$ . Thus, the  $K_{Ic}$  curve for irradiated material would simply be shifted to higher temperatures by an amount equal to the CVN 41-J shift. The implicit assumptions in this procedure are that: (1) the CVN 41-J temperature shift represents the  $RT_{NDT}$  shift, (2) the  $K_{Ic}$  shift is the same as the CVN shift, and (3) the shape of the  $K_{Ic}$  curve does not change for irradiated materials. Furthermore, E185 does not contain any distribution requirements (in terms of test temperature) for testing of the CVN surveillance specimens, nor does it discuss statistical variation in test results.

Series 5 was conceived to verify the postirradiation  $K_{Ic}$  curve to as high a fracture toughness level as practicable. Additionally, a comparison of the  $K_{Ic}$ , CVN, and drop-weight (DWT) NDT shifts are supporting objectives within a framework of multiple tests for statistical analyses. The materials of choice are two submerged-arc welds with relatively high but different copper contents. The weld wire was specially produced with copper in the melt to minimize copper variability in the fabricated welds. The welds were fabricated by Combustion Engineering, Inc., in 216-mm-thick (8.5-in.) plate using Linde 124 welding flux; Fig. 8 shows a typical cross-sectional view of one of the welds. Table 2 gives the chemical composition of the two welds, designated HSST 72W and 73W, and shows they have virtually identical composition

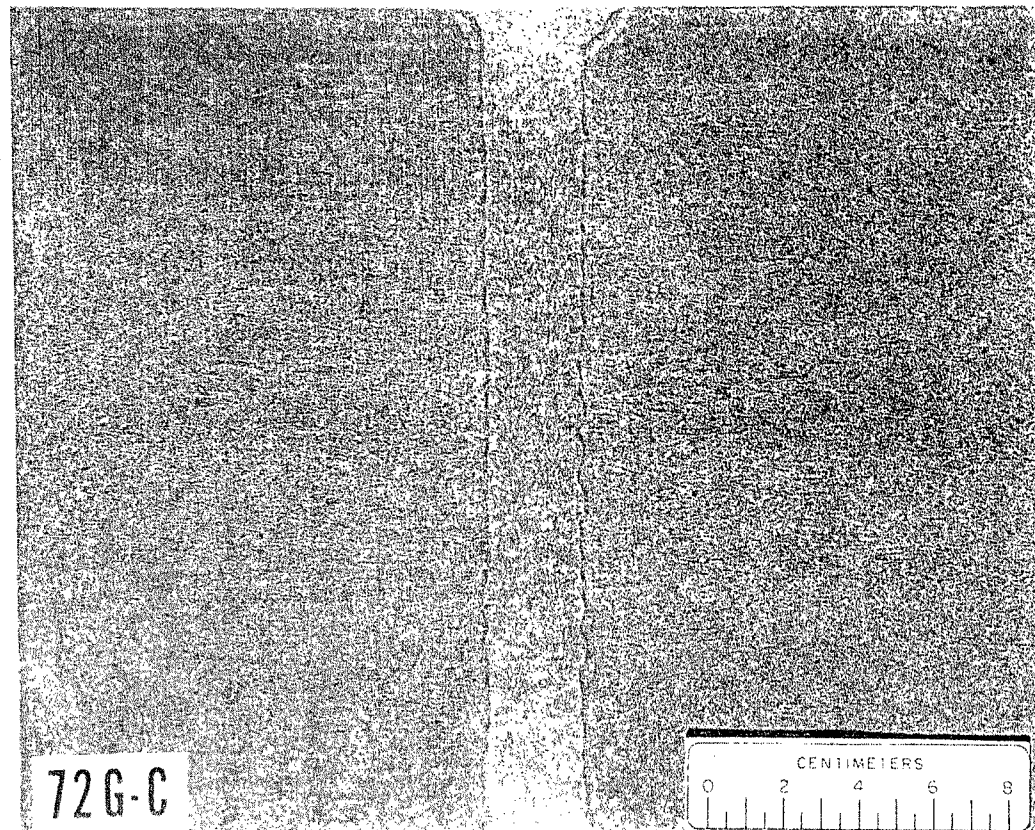


Fig. 8. Cross-sectional view of HSST weld 72W, a submerged-arc weld fabricated using Linde 124 flux and specially produced weld wire, with copper added to melt, in 216-mm-thick A533 grade B plate.

Table 2. Chemical compositions of the two submerged-arc welds in HSST Irradiation Series 5

Material	Composition, wt %									
	C	Mn	P	S	Si	Cr	Ni	Mo	Cu	V
72W	0.093	1.60	0.006	0.006	0.44	0.27	0.60	0.58	0.23	0.003
73W	0.098	1.56	0.005	0.005	0.45	0.25	0.60	0.58	0.31	0.003

except for copper contents of 0.23 and 0.31 wt %, respectively. About 14 lin m of each weldment were fabricated in ~1.3-m (4-ft) lengths and postweld heat treated at 621°C for 40 h.

As discussed earlier, the largest practical specimen for irradiation is a 4TCS and, given the yield strength of the materials and the expected increase due to irradiation, the maximum expected valid (according to ASTM E399)  $K_{Ic}$  was about 130 MPa m. Thus, to obtain similar measuring capacity in the unirradiated condition (lower yield strength than in the irradiated condition), 6TCS AND 8TCS were tested in Series 5. Figure 9 provides a visual comparison of the compact specimens ranging from 1TCS to 8TCS.

The irradiations were conducted at the poolside facility of the ORR from May 1984 to December 1985. Twelve separate capsules were designed and fabricated and were irradiated two at a time in a mobile structure which allowed the capsules to be inserted into the irradiation area after the reactor was stabilized at full power. A gamma shield was also designed and inserted in front of the capsules to minimize gamma heating inside the capsules. The design, fabrication, and operation of the capsules are discussed in a separate report.<sup>23</sup> Irradiation temperatures were controlled at 288°C and the target neutron fluence (>1 MeV) was  $1.75 \times 10^{19}$  neutrons/cm<sup>2</sup>. The temperature control was excellent considering the large numbers of specimens in the capsules contained in the small specimen capsules. Greater than 90% of the CVN, tensile, and 1TCS were  $288 \pm 9^\circ\text{C}$ , while the 4TCS were  $288 \pm 4^\circ\text{C}$ . The tensile and CVN specimens show an average fluence of about  $1.75 \times 10^{19}$  neutrons/cm<sup>2</sup>, while the compact specimens show an average of about  $1.6 \times 10^{19}$  neutrons/cm<sup>2</sup>. Two groups of DWT specimens were used and designated primary and scoping. The scoping groups had an average irradiation temperature and fluence of about 276°C and  $1.5 \times 10^{19}$  neutrons/cm<sup>2</sup>, respectively. The primary groups had averages of 291°C and  $1.0 \times 10^{19}$  neutrons/cm<sup>2</sup>, respectively. The primary groups were so designated because they were irradiated at about the target temperature. Due to placement in the capsules, however, they received less exposure than the CVN specimens and fluence adjustments are discussed later. Dosimetry, neutronics, etc. are discussed in refs. 24, 25, and 26.

The effects of irradiation on yield and ultimate tensile strength are summarized in Fig. 10. As seen in the figure, the yield strength increases range from about 22 to 30%, depending on test temperature, and weld 73W

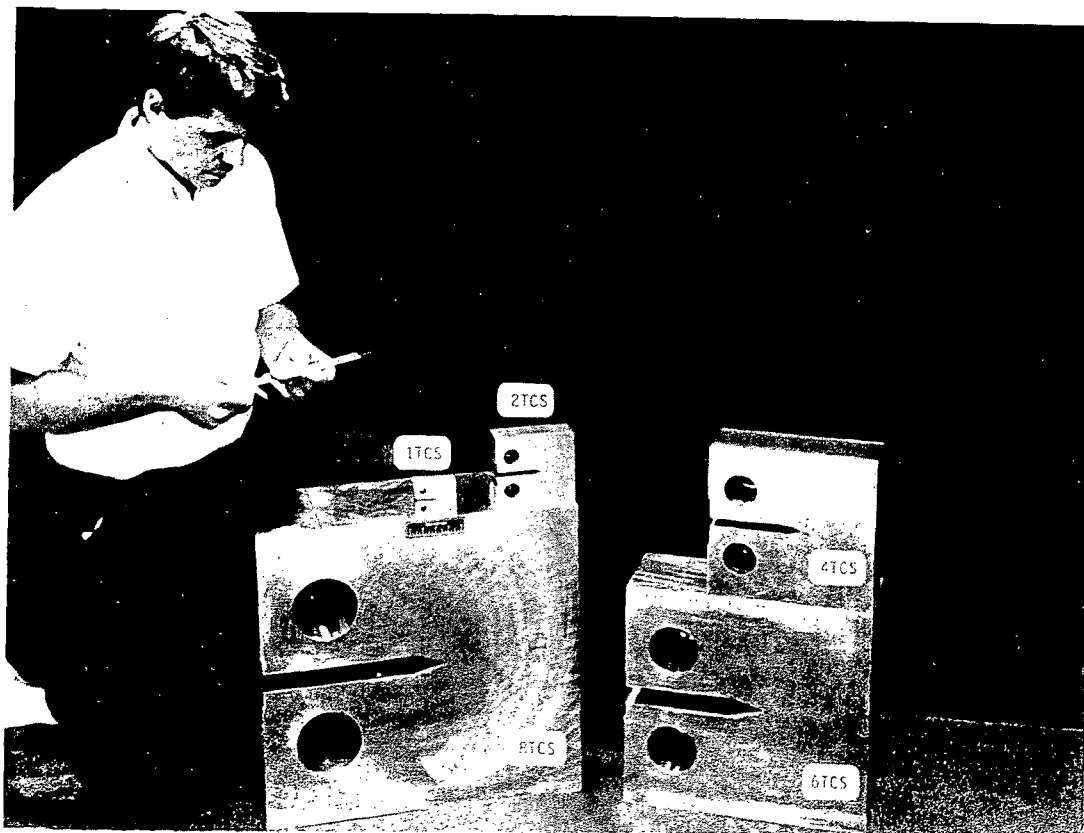


Fig. 9. Photograph of the various compact specimens tested in HSST Irradiation Series 5. All the specimen sizes were tested in the unirradiated condition while only the 1TCS, 2TCS, and 4TCS were irradiated.

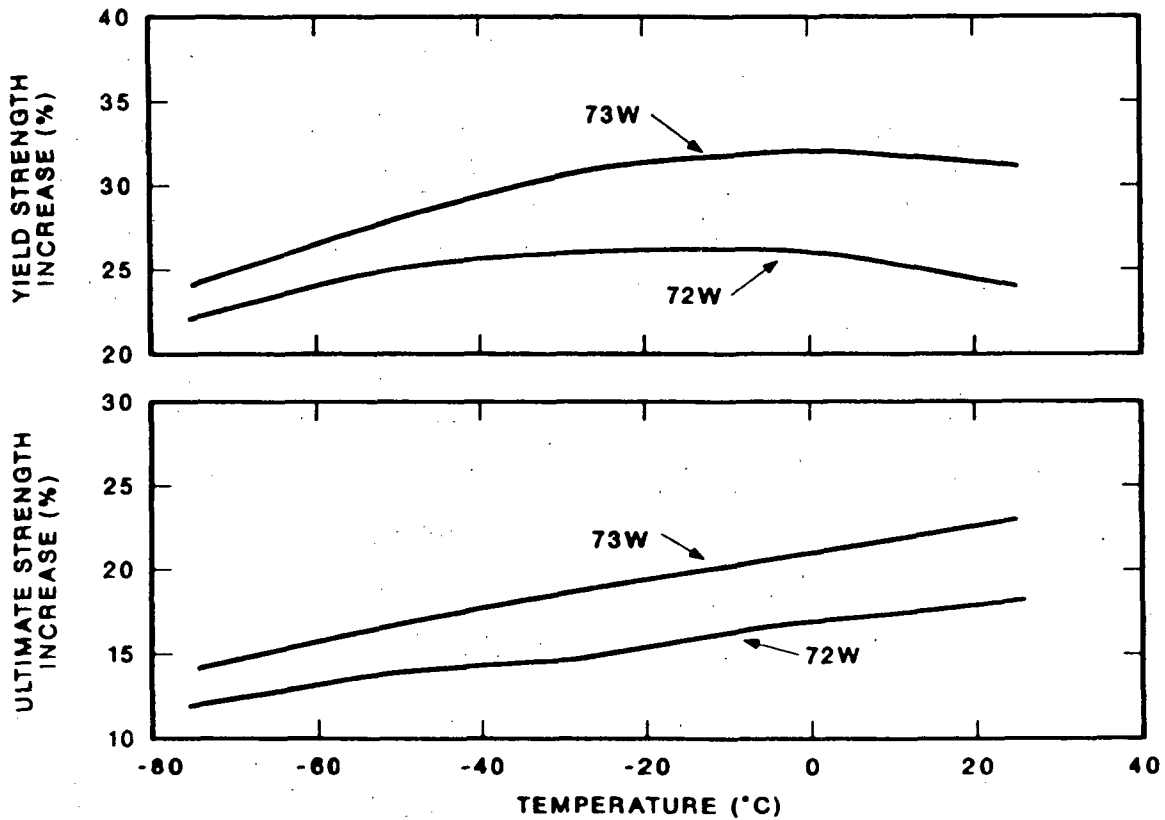


Fig. 10. Comparison of yield and ultimate strength increases due to irradiation at  $-288^{\circ}\text{C}$  to an average fluence ( $>1$  MeV) of  $1.75 \times 10^{19}$  neutrons/cm<sup>2</sup> for HSST welds 72W and 73W. Weld 73W has a higher copper content (0.31 wt %) than that of weld 72W (0.23 wt %) and shows greater strength increases.

experienced greater strengthening, as expected, due to its higher copper concentration. Figures 11 and 12 show the CVN energy results for welds 72W and 73W, respectively. The 41-J transition temperature shifts were 72 and 82°C, respectively, and, again, reflect the difference in copper contents. The shifts were determined using hyperbolic tangent curve fits to the data for each weld. Statistical analyses have not yet been performed. The results of CVN and DWT testing are summarized in Table 3. The actual 41-J shifts for both welds were substantially less than the predictions of Regulatory Guide 1.99 (Rev. 2) and a model developed by Metal Properties Council Subcommittee 6.<sup>27</sup> It is also noted that the 68-J shifts for the two welds show greater difference than do the 41-J shifts; this will be discussed later. The primary group of DWT specimens showed somewhat lesser NDT shifts but, as mentioned earlier, the fluence of those specimens was much less than that of the CVN specimens. The scoping group of DWT specimens showed greater shifts than those of the primary groups, but a comparison is difficult because the fluences and, especially, irradiation temperatures are significantly different. Table 4 shows the results of applying a linear adjustment scheme to the primary DWT data. The adjustment is made by normalizing the actual observations to the Regulatory Guide 1.99 predictions and accounting for the fluence differences assuming a linear material sensitivity to irradiation over the relatively small fluence range from 1.0 to  $1.75 \times 10^{19}$  neutrons/cm<sup>2</sup>. As shown in the table, the adjusted NDT shifts of 70 and 83°C are very close to the observed CVN shifts of 72 and 82°C for welds 72W and 73W, respectively. Thus, the conclusion from these tests is that the CVN 41-J shifts represent the DWT NDT shifts for these materials. This conclusion is in agreement with results shown previously by experiments at the NRL.<sup>28</sup>

The fracture toughness results for unirradiated specimens are shown in Figs. 13 and 14. All of the  $K_{Jc}$  values shown were calculated from the J-integral value at the onset of cleavage as previously described for Series 2 and 3. The dashed lines delineate the maximum  $K_{Ic}$  which can be measured by the indicated specimen size according to ASTM E399, and valid  $K_{Ic}$  results are indicated by filled symbols. The ASME  $K_{Ic}$  curve was constructed relative to the unirradiated  $RT_{NDT}$  for the specific material. It is notable that no data fall below the ASME curve. It is also notable that the 6TCS and 8TCS results do not always define the lowest fracture toughness results at their test temperatures as would be expected based on considerations of constraint in larger specimens. It is recognized, from a statistical perspective, that the number of large specimens is limited; however, at the highest test temperature for 72W, for example, the 8TCS scatter much higher above the 4TCS results than would be expected given statistical variation and further examinations of those results are warranted.

The results of tests with irradiated specimens are shown in Figs. 15 and 16. The unirradiated data are depicted by range bars and the irradiated  $K_{Ic}$  curves were constructed by shifting the unirradiated curves upward in temperature according to the CVN 41-J shifts as specified by E185. Both figures note "pop-in" values which represent cleavage events which occurred but did not fracture the specimen. The two results which fall below the  $K_{Ic}$  curve for 72W are both pop-ins, while the five results which fall below the curve for 73W are represented by two pop-ins and three specimen failures. As with the unirradiated results, the large specimens (4TCS) do not always define the lowest results at a given test temperature. The shift of the  $K_{Ic}$  curve

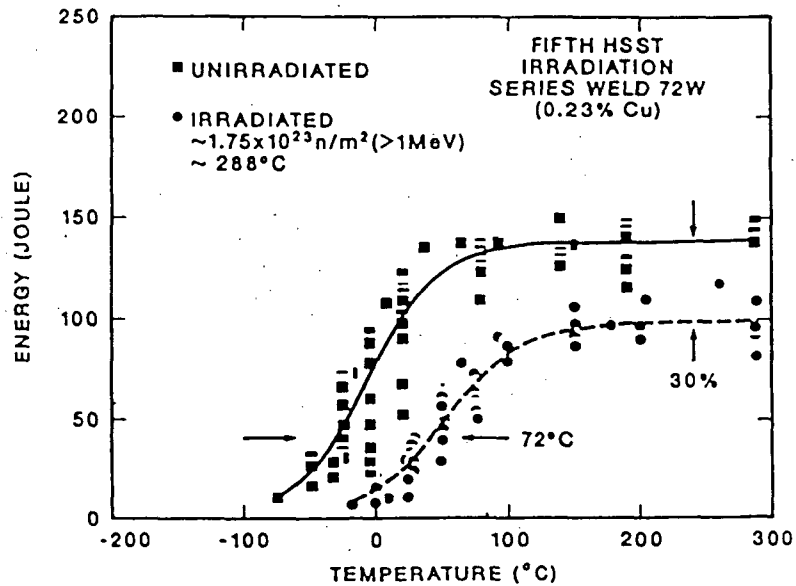


Fig. 11. Charpy impact energy vs test temperature for HSST weld 72W before and after irradiation at  $\sim 288^\circ\text{C}$  to an average fluence ( $>1\text{ MeV}$ ) of  $1.75 \times 10^{19}$  neutrons/cm $^2$ . The slope of the curve appears to have changed only slightly as a consequence of irradiation.

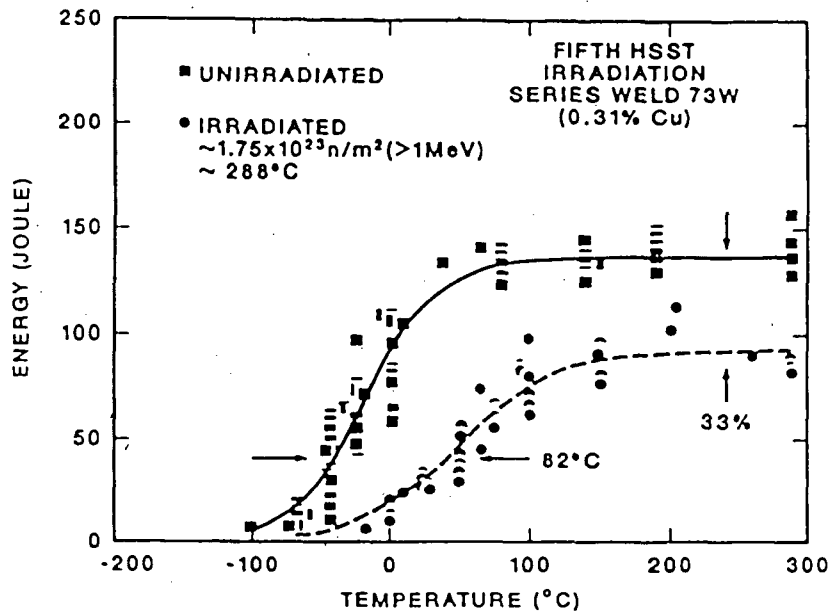


Fig. 12. Charpy impact energy vs test temperature for HSST weld 73W before and after irradiation at  $\sim 288^\circ\text{C}$  to an average fluence ( $>1\text{ MeV}$ ) of  $1.75 \times 10^{19}$  neutrons/cm $^2$ . The slope of the curve has substantially decreased after irradiation compared to that for weld 72W.

Table 3. Effects of irradiation on Charpy V-notch and drop-weight transition temperatures for welds 72W and 73W

Charpy transition temperature shift (°C)					Drop-weight NDT <sup>a</sup> temperature shift (°C)			
41 J					Primary <sup>b</sup>		Scoping <sup>c</sup>	
Actual	MPC-6 <sup>d</sup>	Draft RG 1.99 Rev. 2 <sup>e</sup>	0.89 mm	Fracture appearance	Actual	Draft RG 1.99 Rev. 2 <sup>e</sup>	Actual	Draft RG 1.99 Rev. 2 <sup>e</sup>
<i>Weld 72W, 0.23% Cu, 0.60% Ni</i>								
72	90	107	92	59	61	93	72	105
<i>Weld 73W, 0.31% Cu, 0.60% Ni</i>								
82	123	127	115	70	72	110	94	123

<sup>a</sup>Nil-ductility temperature.

<sup>b</sup>Average irradiation temperature of 291°C, fluence (>1 MeV) =  $1 \times 10^{19}$  neutrons/cm<sup>2</sup>.

<sup>c</sup>Average irradiation temperature of 275°C, fluence (>1 MeV) =  $1.5 \times 10^{19}$  neutrons/cm<sup>2</sup>.

<sup>d</sup>Metal Properties Council Subcommittee 6 on Nuclear Materials.

<sup>e</sup>Regulatory Guide 1.99 (Rev. 2).

Table 4. Charpy impact  $\Delta T_{41}$  and drop-weight  $\Delta NDT$  for HSST Irradiation Series 5 welds after adjusting for fluence differences

Charpy impact			Drop-weight				
Fluence (n/cm <sup>2</sup> )	$\Delta T_{41}$ (°C)	Draft RG 1.99 Rev. 2 <sup>b</sup> (°C)	Actual fluence (n/cm <sup>2</sup> )	Actual $\Delta NDT$ (°C)	Draft RG 1.99 Rev. 2 <sup>b</sup> (°C)	Adjusted fluence (n/cm <sup>2</sup> )	Adjusted $\Delta NDT$ (°C)
Weld 72W, 0.23% Cu, 0.60% Ni							
$1.75 \times 10^{19}$	72	107	$1.0 \times 10^{19}$	61	93	$1.75 \times 10^{19}$	70
Weld 73W, 0.31% Cu, 0.60% Ni <sup>a</sup>							
$1.75 \times 10^{19}$	82	127	$1.0 \times 10^{19}$	72	110	$1.75 \times 10^{19}$	83

<sup>a</sup>Weld 73W adjustment:  $\Delta RG 1.99 (1.75 - 1.0) = 17^\circ C$   
 $(72/110) * 17 = 11^\circ C$   
 $72 + 11 = 83^\circ C$   
Adjusted  $\Delta NDT = 83^\circ C$

<sup>b</sup>Regulatory Guide 1.99 (Rev. 2).

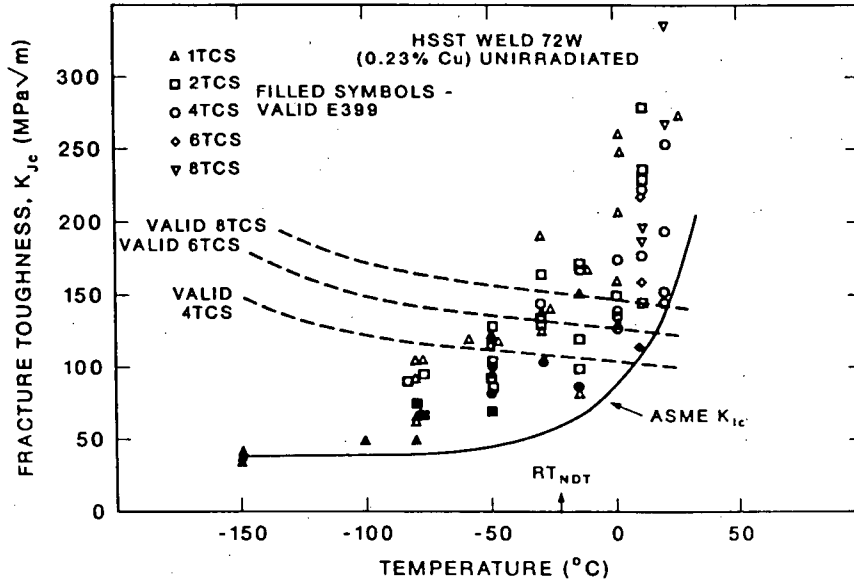


Fig. 13. Fracture toughness,  $K_{Jc}$ , vs test temperature for HSST weld 72W in the unirradiated condition. The ASME  $K_{Ic}$  curve is indexed to the  $RT_{NDT}$  and the figure shows that all data lie above the curve and that the curve is a good lower bound representation for this material.

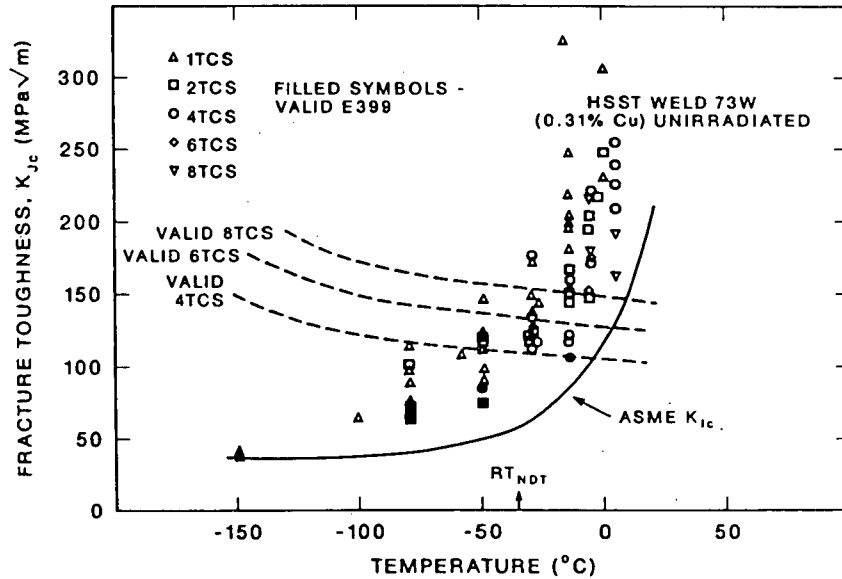


Fig. 14. Fracture toughness,  $K_{Jc}$ , vs test temperature for HSST weld 73W in the unirradiated condition. The ASME  $K_{Ic}$  curve is indexed to the  $RT_{NDT}$  and the figure shows that all data lie above the curve. A curve constructed as a lower bound representation of the data would lie about 5°C lower than the  $K_{Ic}$  curve.

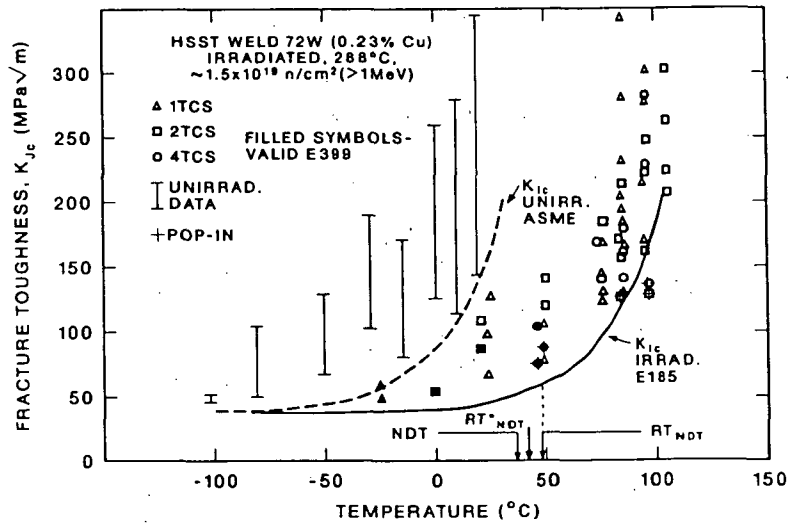


Fig. 15. Fracture toughness,  $K_{Jc}$ , vs test temperature for HSST weld 72W irradiated at  $\sim 288^\circ\text{C}$  to an average fluence ( $>1\text{ MeV}$ ) of  $1.5 \times 10^{19}$  neutrons/cm $^2$ . The  $K_{Ic}$  curve has been shifted  $72^\circ\text{C}$ , equal to the Charpy 41-J shift, as required by ASTM E185. Two  $K_{Jc}$  values determined at the onset of cleavage pop-ins lie below the shifted curve.

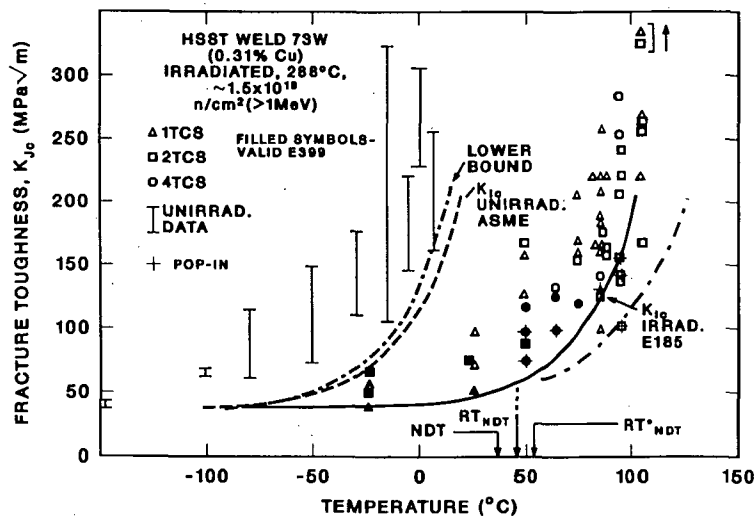


Fig. 16. Fracture toughness,  $K_{Jc}$ , vs test temperature for HSST weld 73W irradiated at  $\sim 288^\circ\text{C}$  to an average fluence ( $>1\text{ MeV}$ ) of  $1.5 \times 10^{19}$  neutrons/cm $^2$ . The  $K_{Ic}$  curve has been shifted  $82^\circ\text{C}$ , equal to the Charpy 41-J shift, as required by ASTM E185. Five  $K_{Jc}$  values lie below the curve, three results which fractured the specimens and two values determined at the onset of cleavage pop-ins. The dashed line drawn to the right of the  $K_{Ic}$  curve was constructed as a preliminary lower bound curve to the irradiated data and indicate a change in the shape of the curve.

for weld 72W is similar to that of the CVN 41-J shift, but that for weld 73W appears to be substantially greater than the CVN shift. For this purpose, a  $K_{Ic}$  value of  $125 \text{ MPa}\sqrt{\text{m}}$  was chosen for the comparison and was determined to be  $101^\circ\text{C}$  for weld 73W. That compares to a CVN 41-J shift of  $82^\circ\text{C}$  and, interestingly, a CVN 68-J shift of  $104^\circ\text{C}$ . The better comparison with the 68-J shift is reflective of the previously noted shape change of the CVN curve for the irradiated weld 73W.

It is clear that the interpretation of the significance of cleavage pop-ins to conclusions regarding the shift and shape of the postirradiation  $K_{Ic}$  curve is crucial. Various schemes for such an interpretation have been discussed within the technical community but have not yet been applied to these results. In that context, it is noted that a total of about 12 pop-ins were observed in the irradiated tests while only one was observed in the unirradiated tests. Thus, an investigation of such a preponderance of pop-ins in the irradiated condition is certainly warranted. It is also clear that a reasonable construction of postirradiation curves will involve the use of fracture toughness data outside the range of linear elastic fracture mechanics as defined by E399. The use of fracture toughness data determined by elastic-plastic fracture mechanics techniques in the transition temperature region will involve consideration of specimen size effects, stable ductile tearing preceding cleavage, and statistical analyses such as the Weibull method.

The preliminary observations from Series 5 are summarized as follows:

1. The scatter in fracture toughness and CVN results is large; statistical analyses and elastic-plastic fracture mechanics are required for interpretation.
2. The irradiated CVN shifts are about the same as the DWT NDT temperature shifts.
3. The  $K_{Ic}$  (at  $125 \text{ MPa}\sqrt{\text{m}}$ ) curve shift for weld 73W is greater than that of the CVN 41-J shift, about  $101^\circ\text{C}$  compared to  $82^\circ\text{C}$ . It is similar, however, to the CVN 68-J shift of  $104^\circ\text{C}$ .
4. The shape of the  $K_{Ic}$  curve changed for weld 73W, but the change is similar to that for the CVN curve.
5. The evaluation of cleavage pop-ins is significant to conclusions regarding the  $K_{Ic}$  curve shift and shape.

#### SERIES 6 - $K_{Ia}$ CURVE SHIFT AND SHAPE

The primary objective of Series 6 is to validate the temperature shift and shape of the ASME Section XI crack-arrest toughness,  $K_{Ia}$ , curve for irradiated reactor vessel materials. Because the  $K_{Ia}$  curve also describes the reference fracture toughness,  $K_{IR}$ , curve in Section III of the ASME Code, Series 6 is directly applicable to the shift and shape of the  $K_{IR}$  curve. The available data base for crack-arrest toughness of reactor vessel steels is very limited compared to that for initiation fracture toughness. Thus, an important supporting objective of Series 6 is to expand both the unirradiated and irradiated data bases for prototypic reactor vessel steels. The current known available data base for irradiated crack-arrest toughness consists of 19 data points for base metal and 17 data points for weldments.

The materials for this series are the same welds as used for Series 5, 72W and 73W. The irradiations were conducted at the poolside facility of the

ORR from December 1985 to May 1986 using the same capsule irradiation facilities and with the same target irradiation temperature and fluence as described for Series 5. Two capsules, each containing 30 crack-arrest specimens of various types, were irradiated. To account for any unexpected differences in irradiation temperature and fluence relative to Series 5, CVN specimens were placed in the notches of some of the crack-arrest specimens. Given the current validity limits of ASTM E1221 on crack-arrest testing, a 33-mm-thick compact crack-arrest (CCA) specimen (1.3TCCA) of 73W can measure a valid  $K_{Ia}$  value of about  $150 \text{ MPa}\sqrt{\text{m}}$ . In the unirradiated condition, a 2TCCA specimen is required to achieve the same measuring capacity. In addition to the standard CCA specimen which uses a starter notch located in a brittle weld material, duplex specimens are included in this series. The duplex specimen consists of a crack starter hole located in a section of hardened 4340 steel which has been electron beam welded to a section of the test material. For both types of specimens, the crack starter only serves to provide the driving force necessary to drive the crack well into the test material prior to arrest. The use of the duplex design allows tests to be conducted at higher temperatures than with weld-embrittled specimens of the same thickness. Thus, the plan is to perform multiple tests at each of several temperatures within about  $50^\circ\text{C}$  below and above the  $RT_{NDT}$ . Weld-embrittled specimens would be primarily used in the lower part of that range while duplex specimens would be primarily used at the higher temperatures. Both 1TCCA and 1.3TCCA weld-embrittled specimens were included in the irradiation capsules while only 1.3TCCA duplex specimens were included. The unirradiated specimen complement is similar but includes 2TCCA specimens of both types.

Most of the unirradiated  $K_{Ia}$  tests have been completed for both welds. Figure 17 shows those results for weld 72W relative to the ASME  $K_{Ia}$  curve which is indexed to the  $RT_{NDT}$ . The open symbols represent data which are valid according to E1221. The half-filled symbols representing "marginally invalid" results are noted because they failed one or more of the criteria by very small margins (i.e., a few percent) and may be used to interpret the results in addition to the strictly valid values. It is interesting to note that the lowest  $K_{Ia}$  data fall further above the curve than did the corresponding  $K_{Ic}$  data above the  $K_{Ic}$  curve. It is encouraging that, at comparable test temperatures, the weld-embrittled and duplex specimens provide about the same results.

A special fixture has been designed, fabricated, and evaluated for remote testing of irradiated CCA specimens in the hot cell. It is an enclosed environmental chamber which allows for cooling with cold nitrogen gas, heating with resistance heaters, self-alignment of the specimen and loading wedge, and specimen temperature measurement with a contact thermocouple. Testing of irradiated specimens will commence during 1989.

#### SERIES 7 - REACTOR VESSEL STAINLESS STEEL CLADDING

The objective of Series 7 is to evaluate the postirradiation mechanical properties, including fracture toughness, of the stainless steel cladding applied to the inside surfaces of LWR vessels. Cladding is applied to reactor vessels primarily to protect the coolant from contamination by corrosion products. Analyses of certain thermal shock scenarios have been

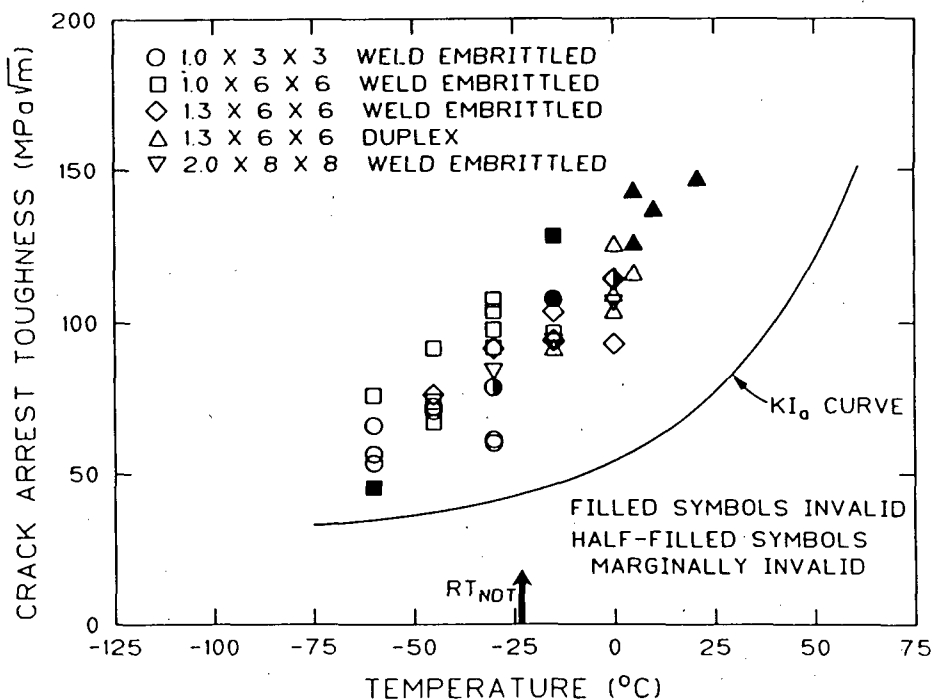


Fig. 17. Crack-arrest toughness,  $K_{Ia}$ , vs test temperature for HSST weld 72W in the unirradiated condition. Various size duplex and weld embrittled compact crack-arrest specimens were tested and the results lie substantially above the ASME  $K_{Ia}$  curve.

inhibited by a lack of information regarding the fracture resistance of the cladding, but the little information available in the literature indicated that austenitic stainless steel cladding may undergo severe embrittlement as a consequence of neutron irradiation.<sup>29</sup> Series 7 was conceived to investigate irradiation effects on stainless steel claddings representative of those used in early pressurized water reactors that are being examined for their fracture resistance under overcooling situations. The series was conducted in two phases with the phases being distinguished primarily by the cladding fabrication method.

The materials were austenitic stainless steel claddings deposited on A533 grade B class 1 steel plate using two weld cladding procedures. The fabrication techniques and postweld heat treatments duplicate commercial procedures as closely as possible. However, to permit fabrication of mechanical test specimens of the cladding, multilayer depositions were utilized to provide a cladding thickness of ~15 mm. This is thicker than the usual reactor vessel cladding (4 to 6 mm), but it should represent multilayer cladding, and test specimens were machined with due regard to location within the cladding. The two weld cladding procedures chosen for Series 7 are the single-wire oscillating submerged-arc procedure (Phase 1) and the three-wire series-arc procedure (Phase 2).

In Phase 1, the first layer of cladding was deposited using type 309 weld wire and subsequent layers using type 308. The materials were given a postweld heat treatment equivalent to 40 h at 621°C. Very high heat input during application of the first layer resulted in substantial base metal dilution (up to 50%), and the effects on properties were significant. Specimens for unirradiated characterization and irradiation testing were carefully machined from the different layers. CVN and tensile specimens were irradiated by MEA in the core of the 2-MW University of Buffalo Reactor (UBR) from June to July 1985 at a nominal temperature of 288°C to a fluence of about  $2 \times 10^{19}$  neutrons/cm<sup>2</sup> (>1 MeV). All testing was conducted at ORNL. CVN and tensile tests showed that the highly diluted cladding layer (adjacent to the base metal) experienced substantial radiation damage, while the cladding layers not diluted with base metal showed almost no effects of irradiation.<sup>30,31</sup> Significant observations were reported in this study regarding the ductile-brittle transition behavior exhibited by the stainless steel cladding, and detailed discussions have been presented concerning the important role of the delta-ferrite phase to the fracture process in the weld metal.<sup>32</sup>

In Phase 2, a three-wire series-arc procedure was used in which weld wires of types 308, 309, and 304 stainless steels were independently fed into the welding arc to obtain the desired cladding composition. Combustion Engineering, Inc., developed the procedure and produced a characterization block with three layers of cladding which was fabricated in such a way that all three layers had nominally the same mechanical properties. Furthermore, the three-wire series-arc process resulted in very little base metal dilution. Following fabrication, the material was given a postweld heat treatment equivalent to 40 h at 621°C. All irradiations were performed by MEA in the core of the UBR from September to December 1985 at a nominal temperature of 288°C. Tensile and CVN specimens were irradiated to fluences of about 2 and  $5 \times 10^{19}$  neutrons/cm<sup>2</sup>. Compact specimens (0.5TCS) were machined from both the three-wire and single-wire cladding. Specimens from the single-wire cladding were machined from the highly diluted type 309 layer and from the type 308 layer. The 0.5TCS were all irradiated to about  $2 \times 10^{19}$  neutrons/cm<sup>2</sup> (>1 MeV).

Tensile and CVN specimens of the three-wire cladding were tested from -125 to 288°C and showed that yield strength increased about 20% (about the same for both fluences) at room temperature, while ultimate strength and tensile elongation were essentially unaffected by irradiation. As shown in Fig. 18, the CVN energy of the three-wire cladding exhibited transition temperature shifts of 13 and 28°C at 2 and  $5 \times 10^{19}$ , respectively. The CVN upper-shelf energy decreased by 15 and 20% at the low and high fluences, respectively. Figure 19 shows the effect of irradiation of the CVN lateral expansion was substantial both on the ductile upper shelf, the transition region, and the brittle lower shelf. The 0.5TCS were tested from -75 to 288°C and showed consistent irradiation-induced decreases in both the  $J_{IC}$  and the tearing modulus. The results of Phase 2 are discussed in more detail in a separate paper by Haggag and Iskander in these proceedings.<sup>33</sup>

The results of Series 7 can be summarized as follows:

1. Yield strength of both single-wire and three-wire series-arc stainless claddings were increased by irradiation at prototypic LWR conditions.

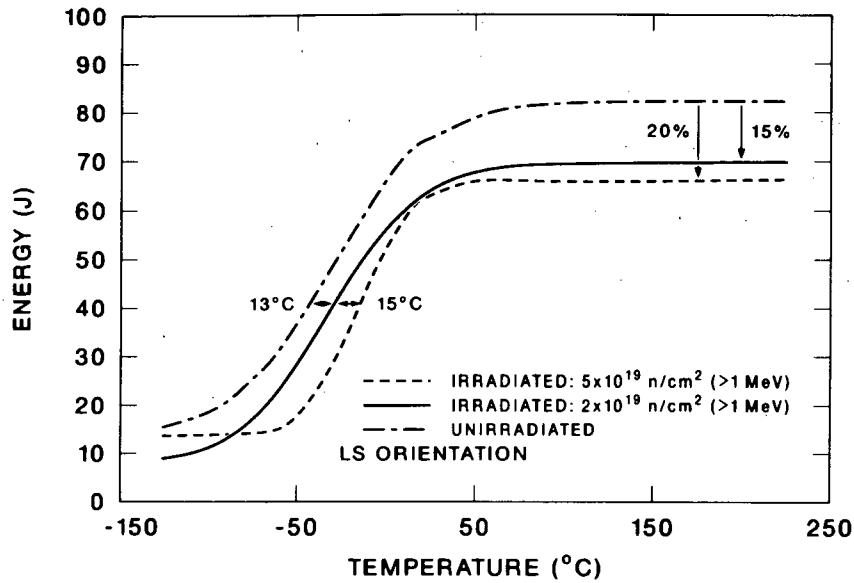


Fig. 18. Charpy impact energy vs test temperature for three-wire series-arc stainless steel weld overlay cladding, unirradiated and irradiated at  $\sim 288^\circ\text{C}$  to average fluences ( $>1$  MeV) of  $\sim 2$  and  $5 \times 10^{19}$  neutrons/cm $^2$ . The decreases in Charpy energy due to irradiation are relatively modest.

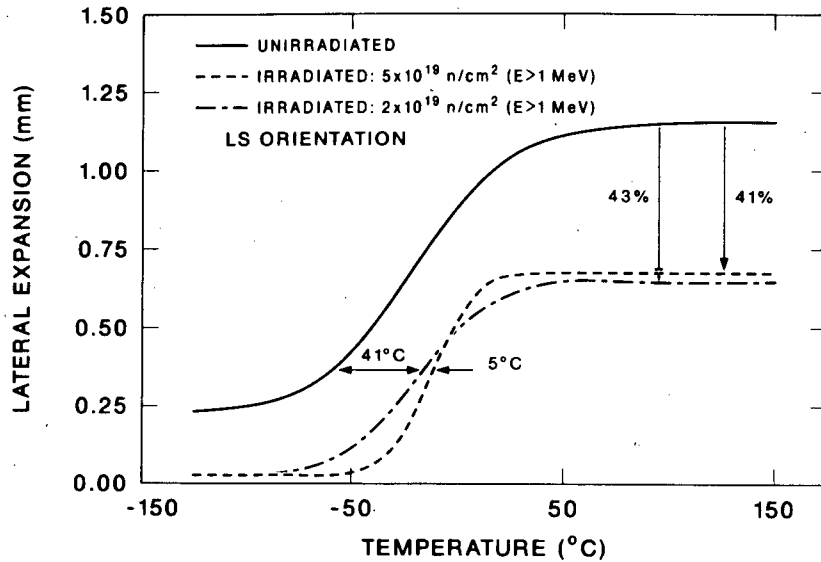


Fig. 19. Charpy impact lateral expansion vs test temperature for three-wire series-arc stainless steel weld overlay cladding, unirradiated and irradiated at  $\sim 288^\circ\text{C}$  to average fluences ( $>1$  MeV) of  $\sim 2$  and  $5 \times 10^{19}$  neutrons/cm $^2$ . Irradiation substantially degraded the lateral expansion of this cladding.

2. The CVN toughness of good quality stainless claddings is somewhat degraded by irradiation while highly diluted cladding exhibits very poor toughness and is significantly degraded by irradiation.

3. Irradiation exposure reduced both the  $J_{Ic}$  and the tearing modulus of both single-wire and three-wire cladding.

### **SERIES 8 - $K_{Ic}$ , $K_{Ia}$ CURVE SHIFT AND SHAPE, LOW UPPER-SHELF WELDS**

The primary objective of Series 8 is to validate the postirradiation temperature shift and shape of the ASME Code Section XI  $K_{Ic}$  and  $K_{Ia}$  curves for low upper-shelf, high copper welds. Considerable testing was performed with prototypic low upper-shelf welds in Series 2 and 3, but only CVN tests were performed in the transition temperature region. All fracture toughness tests were performed on the ductile-shelf and no crack-arrest tests were performed. This series is closely related to Series 5 and 6 in its objectives except for the specific material of interest. The existing data base for  $K_{Ic}$  and  $K_{Ia}$  data of low upper-shelf welds is sparse and inadequate for determining the postirradiation temperature shift and shape of the fracture toughness and crack-arrest toughness curves. The high concentration of inclusions which promote void formation and coalition leading to low energy tearing on the ductile shelf will likely result in different behavior in the ductile-brittle transition region as well. It is the effects of irradiation on the transition region fracture behavior of these materials which is of concern in Series 8, and direct comparisons will be made with the results of Series 5 and 6.

Series 8 is currently in the planning stage; thus, specific materials and irradiation conditions cannot be reported. However, because the materials of concern in commercial LWRs are the low upper-shelf welds with high copper contents, it is anticipated that one or more weldments with copper content in the range 0.20 to 0.40 wt % will be utilized. The possibility of obtaining welds from existing reactor vessels (see discussion of Series 10) has been investigated but, because the known low upper-shelf, high copper welds which might be appropriate in terms of properties and chemical composition were fabricated with copper-coated welding wire, they are probably not acceptable for this research project. The range of copper concentration reported in typical welds fabricated with copper flashing on the welding wire, even when only one lot of wire is used, is very wide. Because the irradiation sensitivity of these materials is strongly dependent on copper content, and the scatter of fracture toughness is high in the transition region, a wide specimen to specimen copper variation would exacerbate the variations and confound the results relative to determinations of curve shifts and shapes. Thus, it is likely that high-copper weld wire would be manufactured for this series as it was for Series 5 and 6, with welding flux and procedures used to commercially fabricate low upper-shelf welds. The specimen complement will be similar to that for Series 5 and 6 with the possible exception of 4TCS. The results of Series 5, which provide a direct comparison of irradiated 2TCS and 4TCS, will be used as the basis for a determination of the need for the larger specimens. Because only two 4TCS will fit in a capsule compared to 18 2TCS, the economic and statistical advantages are obvious. However, because this series will likely use the same material as Series 9, some 4TCS will be irradiated; it is the number of specimens which is yet to be determined.

The irradiation conditions for this series will be similar to those of Series 5 and 6; an irradiation temperature of 288°C and a target fluence of 1.5 to 2.0 × 10<sup>19</sup> neutrons/cm<sup>2</sup> (>1 MeV). Because the ORR has been permanently closed and the operating future of the BSR is uncertain, other irradiation facilities are under review. Although there are no firm schedules established, this series will probably begin about 1992.

#### SERIES 9 - THERMAL ANNEALING IN THICK SECTIONS WITH 4TCS

The primary objective of Series 9 is to validate the effectiveness of thermal annealing in restoring irradiation-induced degradation of thick-section reactor vessel steels to include reirradiation response. It has been well established that postirradiation thermal annealing at temperatures in excess of the irradiation temperature can result in significant recovery of mechanical properties. Thermal annealing is being examined in specific cases as a means to restore reactor vessel safety margins and, in fact, 10CFR50 requires that PWRs predicted to reach the pressurized-thermal-shock (PTS) screening criteria before design end-of-life be designed for incorporation of a thermal annealing procedure. Guidelines for in-service annealing of LWR vessels are contained in ASTM E509. Furthermore, annealing is one potential factor in plant life extension considerations. Annealing studies reported to date have used small specimens, e.g., CVN, 0.5TCS, and 1TCS. There are concerns that the larger amount of constraint in thick sections may affect the operative micromechanisms controlling fracture in postirradiation annealed microstructures. Series 9 would, therefore, directly compare the annealing response of small and large fracture mechanics specimens. An important aspect of the study would be a direct comparison of the reirradiation behavior of small and large specimens. Fracture toughness in the transition temperature and ductile-shelf regions will be investigated.

Series 9 is currently in the planning stages; thus, specific materials and irradiation conditions cannot be reported. The materials likely to result in decisions to thermally anneal a reactor vessel are the low upper-shelf, high copper welds. Thus, such a weld would be the primary candidate material for this series. Furthermore, if sufficient material were procured for Series 8, the same weld could be used for Series 9 with considerable savings in that unirradiated characterization and initial irradiations would have been performed. If that were the case, specimens would only be needed for the annealing and reirradiation phases. The specimen complement has not been planned for this series but would, of course, include CVN, tensile, and fracture toughness specimens up to 4TCS.

The initial irradiation conditions for Series 9 will probably be the same as for Series 5, 6, and 8, with an irradiation temperature of 288°C and a target fluence from 1.5 to 2.0 × 10<sup>19</sup> neutrons/cm<sup>2</sup> (>1 MeV). The thermal annealing temperature will likely be in the range 399 to 454°C (750 to 850°F). Reirradiation would be performed at 288°C with the target fluence dependent on annealing results. The irradiation facility will probably be the same as that for Series 8. Although there is no established schedule for Series 9, it is not likely that annealing studies would commence before 1995.

## SERIES 10 - LOW UPPER-SHELF WELD FROM MIDLAND REACTOR VESSEL

The primary objective of Series 10 is to investigate the postirradiation fracture toughness of the submerged-arc weld from the beltline region of the Midland Unit 1 reactor vessel. The reactor is a PWR owned by Consumers Power Company and was cancelled prior to start-up. The weld from that vessel is of considerable interest because it carries the Babcock and Wilcox designation WF-70, a submerged-arc weld fabricated with a specific heat of weld wire and specific lot of flux. Welds with the WF-70 designation are the controlling materials (regarding irradiation effects) in five operating nuclear plants. The WF-70 weld was fabricated using copper-coated wire and Linde 80 flux and is known to be a low upper-shelf, high copper weld. The fact that this particular weld exists in numerous operating reactors is the driving force for this series. The material from the Midland reactor was initially considered for Series 8, but concerns about the copper variability resulted in its inclusion in a separate irradiation series. An important supporting objective is the determination of local and global copper variation. The results of that study could conceivably lead to use of the Midland weld for Series 8, but that is considered unlikely. Another specific supporting objective is a complete unirradiated characterization to include determination of the  $RT_{NDT}$  and the CVN upper-shelf energy. Fracture toughness specimens will be used to examine size effects in J-R curve testing with this material. A long-term irradiation capsule will also be included to investigate irradiation rate effects.

The planning for Series 10 is not complete, but will probably include irradiation of CVN, tensile, DWT, and fracture toughness specimens up to 2TCS. All those specimens would be irradiated at 288°C to a fluence of about  $5 \times 10^{18}$  neutrons/cm<sup>2</sup> (>1 MeV). A similar complement, less the 2TCS, would be irradiated to  $5 \times 10^{19}$  to investigate irradiation saturation. Both of those irradiations would be performed under usual test reactor conditions. Additionally, a complement of tensile, CVN, and 1TCS would be irradiated at a relatively low neutron flux to investigate irradiation rate effects. The results of those studies would be used to determine the need for inclusion of 4TCS and the possibility of thermal annealing studies. It is not yet known which irradiation facility will be used for this series. Activities are now under way to procure about 11 m of weld from the Midland vessel. Unirradiated characterization will begin upon receipt of material in 1989 and irradiations will begin in 1990.

### SUMMARY

The HSST irradiation effects studies now span two decades of investigations which have sought to validate irradiated reactor vessel behavior. All of the investigations have contributed results having significance to the integrity analyses of reactor vessels. The observations are summarized as follows:

1. Crack initiation fracture toughness can attain high values even after irradiation.

2. Fracture toughness vs temperature curves are shifted to higher temperatures by irradiation; the amount of shift is a function of chemical composition (e.g., Cu, Ni, P).
3. Irradiation can markedly reduce resistance to ductile tearing, even for welds with unirradiated low tearing resistance.
4. Irradiation-induced decreases in ductile toughness and tearing resistance are roughly related to those from Charpy impact toughness.
5. The use of current welding practices and materials with low copper and nickel contents significantly reduces the irradiated fracture toughness degradation.
6. Some stainless steel weld overlay cladding procedures can result in cladding that is significantly embrittled by irradiation.
7. Based on irradiation of two different claddings, type 308 weld overlay cladding fabricated with low base metal dilution exhibits relatively high resistance to irradiation.
8. Preliminary analyses show that the  $K_{Ic}$  curve shift can be greater than the CVN 41-J shift and can change shape.
9. Irradiation series are either under way or planned to validate the shift and shape of the  $K_{Ia}$  curve, the shift and shape of the  $K_{Ic}$  and  $K_{Ia}$  curves for low upper-shelf welds, the response of thick sections to thermal annealing, and the fracture behavior of an actual weld removed from an unoperated commercial PWR.

#### REFERENCES

1. Title 10, Code of Federal Regulations, Parts 0 to 199, U.S. Government Printing Office, Washington, D.C., January 1987.
2. Radiation Embrittlement of Reactor Vessel Materials, Regulatory Guide 1.99 (Rev. 2), U.S. Nuclear Regulatory Commission, Washington, D.C., May 1988.
3. ASME Boiler and Pressure Vessel Code, An American National Standard, American Society of Mechanical Engineers, New York, 1986.
4. G. D. Whitman, *Historical Summary of the Heavy-Section Steel Technology Program and Some Related Activities in Light-Water Reactor Pressure Vessel Safety Research*, NUREG/CR-4489 (ORNL-6259), Oak Ridge National Laboratory, Oak Ridge, Tennessee, March 1986.
5. T. R. Mager, *Post-Irradiation Testing of 2T Compact Tension Specimens, Heavy-Section Steel Technology Program Technical Report No. 9*, Westinghouse Nuclear Energy Systems, Pittsburgh, August 1970.
6. T. R. Mager and F. O. Thomas, *Evaluation by Linear Elastic Fracture Mechanics of Radiation Damage to Pressure Vessel Steels*, WCAP-7328 (Rev.), Westinghouse Electric Corporation, PWR Systems Division, Pittsburgh, October 1969.

7. T. R. Mager, *Post-Irradiation Testing of 2T Compact Tension Specimens*, WCAP-7561, Westinghouse Electric Corporation, PWR Systems Division, Pittsburgh, August 1970.

8. C. W. Hunter and J. A. Williams, *Fracture and Tensile Behavior of Neutron-Irradiated A533-B Pressure Vessel Steel*, HEDL-TME 71-76, Hanford Engineering Development Laboratory, Richland, Washington, February 1971.

9. W. J. Stelzman and R. G. Berggren, *Radiation Strengthening and Embrittlement in Heavy Section Steel Plates and Welds*, ORNL-4871, Oak Ridge National Laboratory, Oak Ridge, Tennessee, June 1973.

10. *Standard Practice for Determination of a Fracture Toughness of Steels Using Equivalent Energy Methodology, E992-84*, 1986 Annual Book of ASTM Standards, Vol. 03.01, American Society for Testing and Materials, Philadelphia, 1986.

11. J. A. Williams, *The Irradiated Fracture Toughness of ASTM A533, Grade B, Class 1 Steel Measured with a Four-Inch-Thick Compact Tension Specimens*, HEDL-TME 75-10, Hanford Engineering Development Laboratory, Richland, Washington, January 1975.

12. J. A. Davidson et al., *The Irradiated Dynamic Fracture Toughness of ASTM A533, Grade B, Class 1 Steel Plate and Submerged Arc Weldment*, WCAP-8775, Westinghouse Electric Corporation, Pittsburgh, October 1976.

13. R. G. Berggren and T. N. Jones, "Toughness Investigation of Irradiated Materials," pp. 37-41 in *Quarterly Progress Report on Reactor Safety Programs Sponsored by the Division of Reactor Safety Research for July-September 1974. II. Heavy-Section Steel Technology Program*, ORNL-TM-4729, Vol. II, Oak Ridge National Laboratory, Oak Ridge, Tennessee, November 1974.

14. U. Potapovs and J. R. Hawthorne, *The Effects of Residual Elements on 550°F Irradiation Reponse of Selected Pressure Vessel Steels and Weldment*, NRL Report 6803, Naval Research Laboratory, Washington, D.C., November 1968; *Nucl. Appl.* 6, 27 (June 1969).

15. J. J. McGowan, *Tensile Properties of Irradiated Nuclear Grade Pressure Vessel Welds for the Third HSST Irradiation Series*, NUREG/CR-4086 (ORNL/TM-9477), Oak Ridge National Laboratory, Oak Ridge, Tennessee, March 1985.

16. J. A. Williams, *Tensile Properties of Irradiated and Unirradiated Welds of A533 Steel Plate and A508 Forgings*, NUREG/CR-1158 (ORNL/Sub-79/50917/2), Hanford Engineering Development Laboratory, Richland, Washington, July 1979.

17. A. L. Hiser, F. J. Loss, and B. H. Menke, *J-R Curve Characterization of Irradiated Low Upper-Shelf Welds*, NUREG/CR-3506

(MEA-2028), Materials Engineering Associates, Inc., Lanham, Maryland, April 1984.

18. G. R. Irwin, "Fracture Mode Transition for a Crack Traversing a Plate," *J. Basic Eng.*, ASME 82(2), 417-25 (June 1960)

19. J. G. Merkle, *An Examination of the Size Effect Data Scatter Observed in Small Specimens Cleavage Fracture Toughness Testing*, NUREG/CR-3672 (ORNL/TM-9088), Oak Ridge National Laboratory, Oak Ridge, Tennessee, April 1984.

20. J. J. McGowan, R. K. Nanstad, and K. R. Thoms, *Characterization of Irradiated Current-Practice Welds and A533 Grade B Class 1 Plate for Nuclear Pressure Vessel Service*, NUREG/CR-4880, Vol. 1 (ORNL-6484/V1), Oak Ridge National Laboratory, Oak Ridge, Tennessee, July 1988.

21. R. G. Berggren, J. R. Hawthorne, and R. K. Nanstad, "Analysis of Charpy V-Notch Impact Toughness of Irradiated A533-B Class 1 Plate and Four Submerged-Arc Welds," pp. 1094-110 in *Effects of Radiation on Materials: Twelfth International Symposium*, ASTM STP 870, American Society for Testing and Materials, Philadelphia, 1985.

22. J. J. McGowan and R. K. Nanstad, "A Statistical Analysis of Fracture Toughness of Irradiated Low-Alloy Steel Plate and Welds," pp. 569-89 in *Influence of Radiation on Material Properties: 13th International Symposium (Part II)*, ASTM STP 956, American Society for Testing and Materials, Philadelphia, 1987.

23. B. H. Montgomery and K. R. Thoms, *Design, Assembly, and Operating History of Capsules for the Fifth and Sixth Heavy-Section Steel Technology Irradiation Series*, TM report, Oak Ridge National Laboratory, Oak Ridge, Tennessee (to be published).

24. M. L. Williams, I. Remec, and F. B. K. Kam, *Neutron Spectral Characterization for the Fifth Heavy-Section Steel Technology (HSST) Irradiation Series, "Neutronics Calculations,"* NUREG/CR-4031, Vol. 2 (ORNL/TM-9423/V2), Oak Ridge National Laboratory, Oak Ridge, Tennessee, March 1985.

25. I. Remec, F. W. Stallman, and F. B. K. Kam, *Neutron Spectral Characterization for the Fifth Heavy-Section Steel Technology (HSST) Irradiation Series, "Neutronics Exposure Parameters,"* NUREG/CR-4031, Vol. 3 (ORNL/TM-9423/V3), Oak Ridge National Laboratory, Oak Ridge, Tennessee, March 1985.

26. L. F. Miller, C. A. Baldwin, F. W. Stallman, and F. B. K. Kam, *Neutron Exposure Parameters for the Metallurgical Test Specimens in the Fifth Heavy-Section Steel Technology Irradiation Series Capsules*, NUREG/CR-5019 (ORNL/TM-10582), Oak Ridge National Laboratory, Oak Ridge, Tennessee, March 1988.

27. Metal Properties Council Subcommittee 6 on Nuclear Materials, "Prediction of the Shift in the Brittle-Ductile Transition Temperature of Light-Water Reactor (LWR) Pressure Vessel Materials," *J. Test. Eval.* 11(4), 237-60 (July 1983).

28. J. R. Hawthorne and L. E. Steele, *The Effect of Neutron Irradiation on the Charpy V and Drop Weight Test Transition Temperatures of Various Steels and Weld Metals*, NRL Report 5479, Naval Research Laboratory, Washington, D.C., May 1960.

29. W. R. Corwin, *Assessment of Radiation Effects Relating to Reactor Pressure Vessel Cladding*, NUREG/CR-3671 (ORNL-6047), Oak Ridge National Laboratory, Oak Ridge, Tennessee, July 1984.

30. W. R. Corwin, R. G. Berggren, and R. K. Nanstad, *Charpy Toughness and Tensile Properties of a Neutron-Irradiated Stainless Steel Submerged Arc Weld Cladding Overlay*, NUREG/CR-3927 (ORNL/TM-9309), Oak Ridge National Laboratory, Oak Ridge, Tennessee, September 1984.

31. W. R. Corwin, R. G. Berggren, and R. K. Nanstad, "Charpy Toughness and Tensile Properties of a Neutron-Irradiated Stainless Steel Submerged-Arc Weld Cladding Overlay," pp. 951-71 in *Effects of Radiation on Materials: Twelfth International Symposium*, ASTM STP 870, American Society for Testing and Materials, Philadelphia, 1985.

32. W. R. Corwin, R. G. Berggren, R. K. Nanstad, and R. J. Gray, "Fracture Behavior of a Neutron-Irradiated Stainless Steel Submerged Arc Welding Cladding Overlay," *Nucl. Eng. Design* 89, 199-221 (1985).

33. F. M. Haggag and S. K. Iskander, "Results of Irradiated Cladding Tests and Clad Plate Experiments," submitted for publication in *Proceedings of 16th Water Reactor Safety Information Meeting*, Gaithersburg, Maryland, October 24-27, 1988.



**RESULTS OF IRRADIATED CLADDING TESTS**  
**AND CLAD PLATE EXPERIMENTS\***

F. M. Haggag and S. K. Iskander

Oak Ridge National Laboratory  
P.O. Box 2008  
Oak Ridge, Tennessee 37831

**ABSTRACT**

Two aspects critical to the fracture behavior of three-wire stainless steel cladding were investigated by the Heavy-Section Steel Technology (HSST) Program: (1) radiation effects on cladding strength and toughness, and (2) the response of mechanically loaded, flawed structures in the presence of cladding (clad plate experiments).

Postirradiation testing results show that, in the test temperature range from -125 to 288°C, the yield strength increased, and ductility insignificantly increased, while there was almost no change in ultimate tensile strength. All cladding exhibited ductile-to-brittle transition behavior during Charpy impact testing. Radiation damage decreased the Charpy upper-shelf energy by 15 to 20% and resulted in up to 28°C shifts of the Charpy impact transition temperature. Results of irradiated 12.5-mm-thick compact specimens (0.5TCS) show consistent decreases in the ductile fracture toughness,  $J_{IC}$ , and the tearing modulus. Results from clad plate tests have shown that (1) a tough surface layer composed of cladding and/or heat-affected zone has arrested running flaws under conditions where unclad plates have ruptured, and (2) the residual load-bearing capacity of clad plates with large subclad flaws significantly exceeded that of an unclad plate.

**INTRODUCTION**

The ability of stainless steel cladding to enhance the fracture resistance of an operating nuclear reactor pressure vessel, particularly during certain overcooling transients, depends greatly on the properties of the irradiated cladding. Therefore, weld overlay cladding irradiated at temperatures and to fluences relevant to power reactor operation was examined. Two weld cladding procedures were chosen for the two phases of this study, namely, the single-wire oscillating submerged-arc and the three-wire series arc. The primary differences between these procedures are in the heat input and the

---

\*Research sponsored by the Office of Nuclear Regulatory Research, Division of Engineering, U.S. Nuclear Regulatory Commission under Interagency Agreement DOE 1886-8011-9B with the U.S. Department of Energy under contract DE-AC05-84OR21400 with Martin Marietta Energy Systems, Inc.

resulting amounts of base metal dilution of the stainless steel cladding. In the first phase, reported previously in Refs. 1-3, Charpy V-notch (CVN) impact and tensile specimens from a three-layer stainless steel weld overlay fabricated using the single-wire procedure were irradiated to  $2 \times 10^{19}$  neutrons/cm<sup>2</sup> (>1 MeV) at 288°C. Cladding from the upper weldment layers, typical of good quality pressure vessel cladding, exhibited very little irradiation-induced degradation. However, ductile-to-brittle transition behavior, caused by temperature-dependent failure of the residual delta-ferrite, was observed during impact testing. In contrast, specimens from the first weldment layer, which also exhibited transition type behavior, were markedly embrittled. The cause of the embrittlement was determined to be high radiation sensitivity of the atypical microstructure resulting from excessive base metal dilution of the first weldment layer.

In the second phase, the first subject of this paper, a commercially produced three-wire series-arc stainless steel cladding was evaluated under similar irradiation (except for the high fluence specimens) and testing conditions as in the first phase. The results of tensile and CVN tests were reported earlier;<sup>4</sup> however, a summary is provided here together with the results of irradiated and unirradiated 12.5-mm-thick compact specimens (0.5TCS).

The objective of the clad plate program, the second subject of this paper, is to determine the effect of three-wire stainless steel cladding upon the propagation of small surface cracks subjected to stress states similar to those occurring during a pressurized thermal shock (PTS) scenario. The potential benefit to the U.S. Nuclear Regulatory Commission is an improved predictive capability of the fracture strength of a reactor pressure vessel (RPV) with hypothetical flaws. The objectives of this research were achieved by comparing the load-bearing capacity of clad and unclad flawed plates and the results are presented and discussed below.

## I. RADIATION EFFECTS ON CLADDING

### MATERIALS

The specimens were taken from commercially produced stainless steel cladding overlaid on a pressure vessel steel plate. Three layers of cladding were applied to provide adequate thickness (~20 mm) to fabricate the test specimens. The three-wire series-arc procedure, developed by Combustion Engineering, Inc., Chattanooga, Tennessee, produced highly controlled weld chemistry, microstructure, and fracture properties in all three layers of the weld. Various combinations of types 308, 309, and 304 stainless steel wires were used in the three layers of cladding. The cladding was given a postweld heat treatment (PWHT) equivalent to 40 h at 621°C. During cladding, the delta-ferrite content was monitored with a Fischer Ferritescope. The ferrite numbers (which correspond roughly to percentages of ferrite) varied from 7.5 to 10 throughout the three layers of the cladding. The photomicrograph of this cladding (Fig. 1) shows a distribution of delta-ferrite in an austenitic matrix quite typical of microstructures seen in good practice commercial weld overlay cladding in reactor pressure vessels.<sup>1-3</sup>

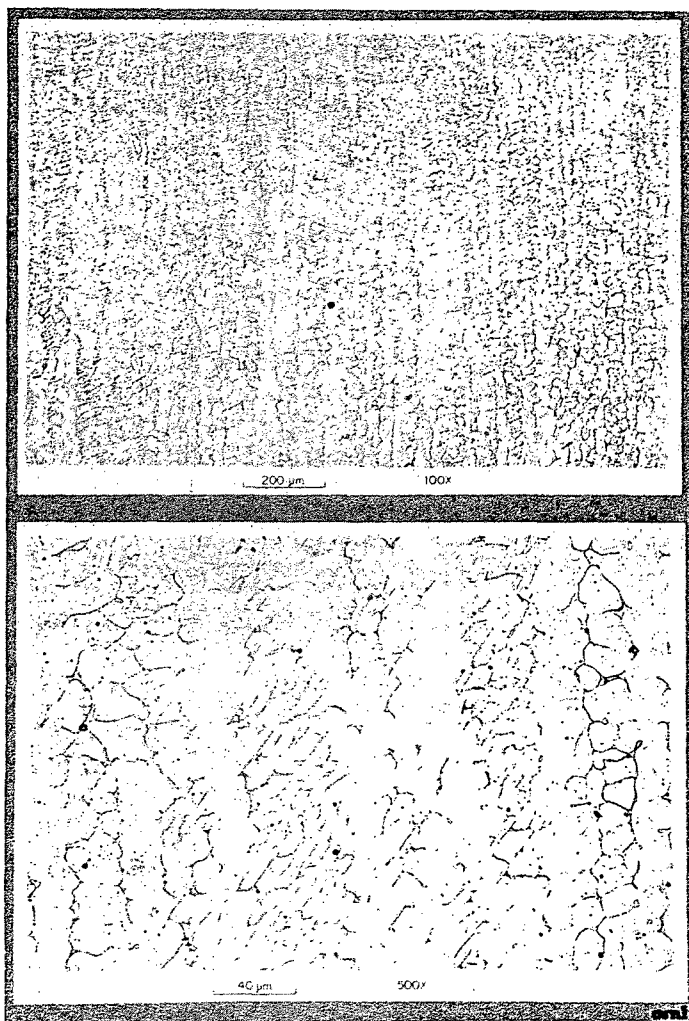


Fig. 1. Microstructure of three-wire stainless steel cladding weld overlay is typical of reactor pressure vessel cladding with delta-ferrite in austenitic matrix, good quality commercial cladding.

#### IRRADIATION HISTORY

The specimens were irradiated in three capsules by Materials Engineering Associates in the core of the 2-MW pool reactor (UBR) at the Nuclear Science and Technology Facility in Buffalo, New York. Each of the first two capsules contained 20 CVN and six miniature tensile (MT) specimens. The third capsule contained 24 0.5TCS specimens, of which eight specimens were fabricated from the three-wire cladding, while the remaining specimens were from single-wire cladding. All capsules were instrumented with thermocouples and dosimeters and the specimens resided in a mixed helium and air environment during the irradiation. Each capsule was rotated 180° at least once during its

irradiation exposure for side-to-side fluence balancing. Irradiation temperatures were maintained at  $288 \pm 11^\circ\text{C}$ . The average fluences for the three capsules were  $2.14 \pm 8\%$ ,  $5.56 \pm 5\%$ , and  $2.36 \pm 6\% \times 10^{19}$  neutrons/cm<sup>2</sup> (>1 MeV), respectively. These fluences are for a calculated spectrum based on Fe, Ni, and Co dosimetry wires.

## RESULTS AND DISCUSSION

**Effect of Irradiation on Tensile Properties:** The yield strength of three-wire stainless steel cladding increased due to radiation exposure. The effects were greater at room temperature and below (Fig. 2); e.g., at the fluence of  $2 \times 10^{19}$  neutrons/cm<sup>2</sup> the yield strength increased by 9, 20, and 28% at test temperatures of  $288^\circ\text{C}$ , room temperature, and  $-125^\circ\text{C}$ , respectively. At the higher fluence level of  $5 \times 10^{19}$  neutrons/cm<sup>2</sup>, the yield strength increased by 6, 16, and 34% at the test temperatures of  $288^\circ\text{C}$ , room temperature, and  $-125^\circ\text{C}$ , respectively. Hence, it can be seen that most of the radiation damage occurred at the first fluence level; increasing the fluence by a factor of 2.5 did result in a relatively smaller radiation damage increase. The effects of irradiation on the ultimate strength and ductility were insignificant or very small (Fig. 3).

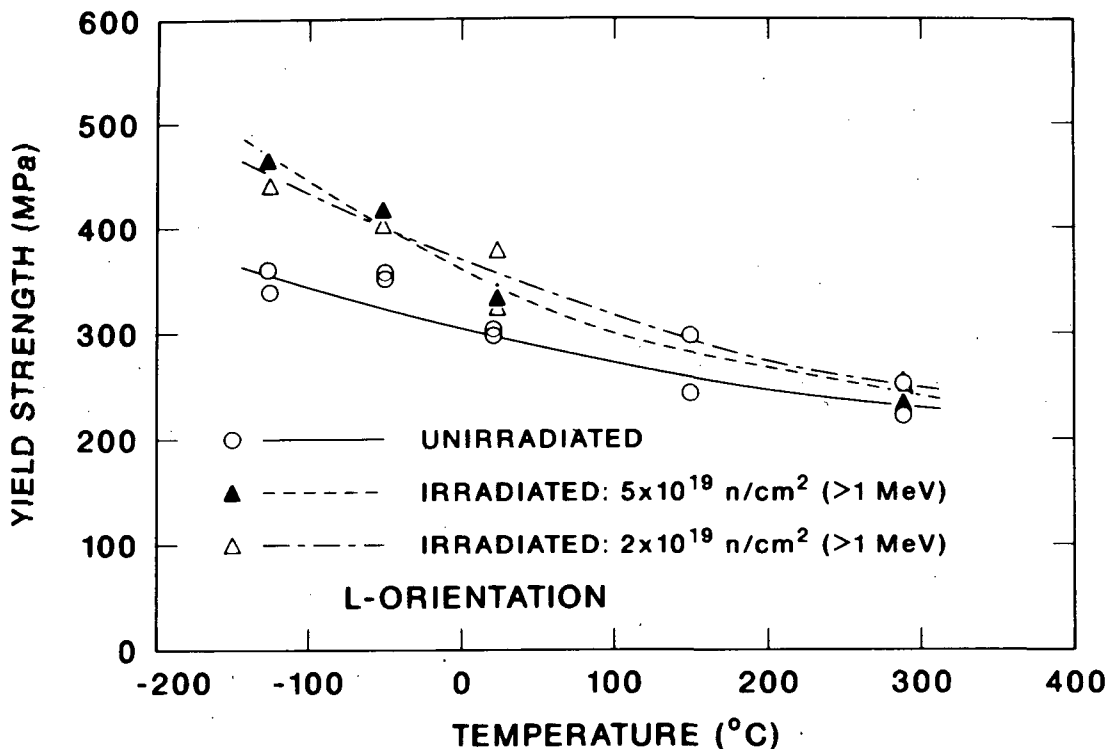
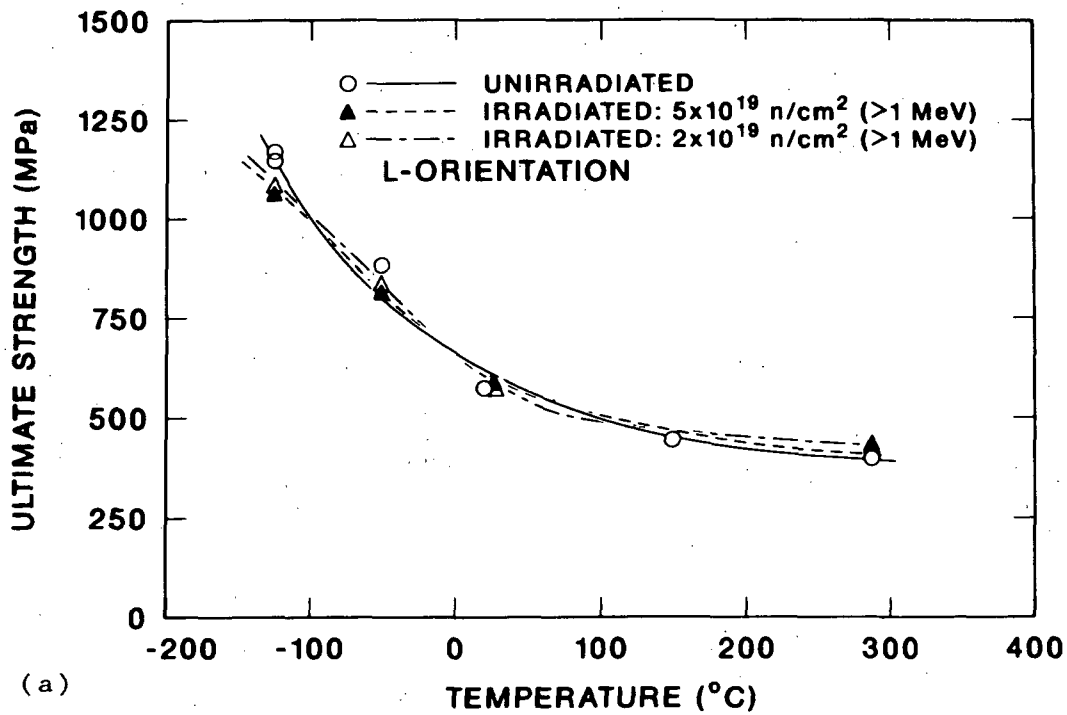
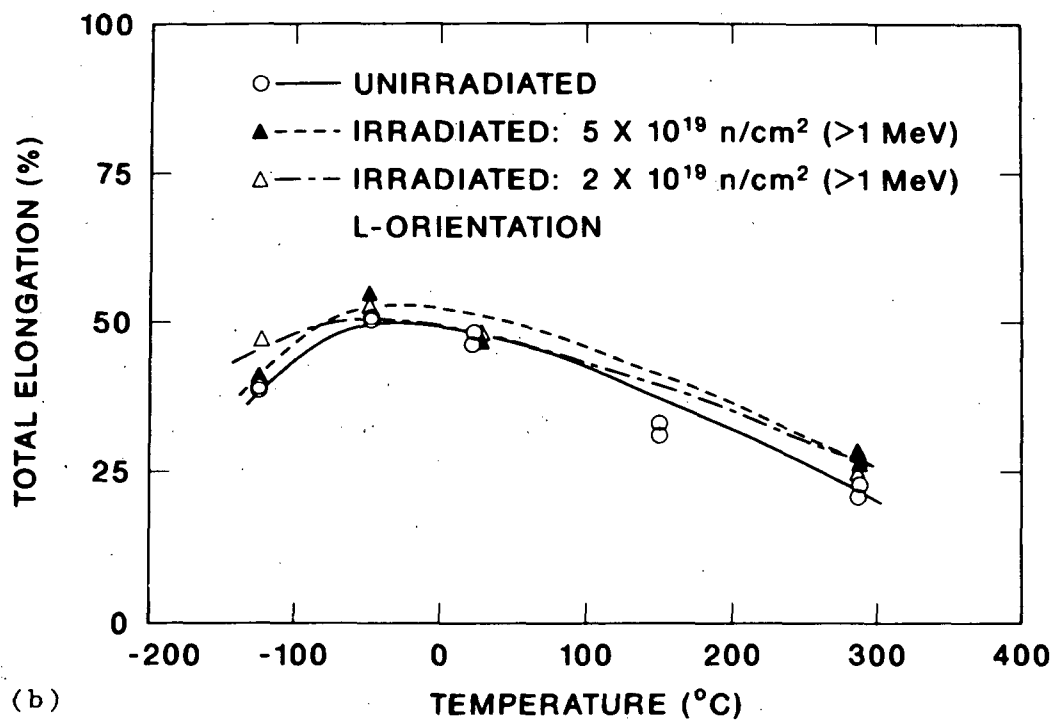


Fig. 2. Effect of neutron irradiation at  $288^\circ\text{C}$  on the yield strength of three-wire stainless steel cladding (yield strength vs test temperature).



(a)



(b)

Fig. 3. Effect of irradiation on the ultimate strength and elongation of three-wire stainless steel cladding: (a) ultimate strength vs temperature; (b) total elongation vs temperature.

**Effect of Irradiation on Charpy Impact Properties:** Irradiation of the three-wire stainless steel cladding specimens at 288°C to fluence levels of 2 and  $5 \times 10^{19}$  neutrons/cm<sup>2</sup> (>1 MeV) resulted in decreases of the CVN upper-shelf energy by 15 and 20% and increases of the 41-J transition temperature by 13 and 28°C, respectively (Fig. 4). Figure 4 shows that increasing irradiation from 2 to  $5 \times 10^{19}$  neutrons/cm<sup>2</sup> further degraded the three-wire stainless steel cladding. Irradiation also degraded the CVN lateral expansion significantly (Fig. 5). The upper-shelf lateral expansion was reduced by 43 and 41% at the low and high fluences, respectively. Furthermore, the 0.38-mm (0.015-in.) transition temperature shifts were 41 and 46°C for the low and high fluences, respectively. Table 1 also provides the curve fit results for the unirradiated and irradiated CVN test results. These results are in general agreement with those for the single-wire cladding produced with good welding practice.<sup>1-3</sup>

**Effect of Irradiation on Ductile Fracture Toughness and Tearing Modulus:** Results of the 0.5TCS fracture toughness specimens fabricated from three-wire series-arc stainless steel cladding shows the following. Irradiation exposure to an average fluence of  $2.41 \times 10^{19}$  neutrons/cm<sup>2</sup> (>1 MeV) resulted in a consistent decrease in the initiation ductile fracture toughness,  $J_{IC}$ , at test temperatures of -75°C, room temperature, 120°C, and 288°C (Fig. 6). This is in agreement with the reduction in both the CVN upper-shelf energy and lateral expansion discussed above. However, the percent reduction in initiation toughness of the 0.5TCS specimens is greater than that of the CVN impact energy but closer to that percent reduction of the CVN lateral expansion. Figure 6 also shows that the initiation toughness,  $J_{IC}$ , of both unirradiated and irradiated specimens increased from high temperature to a peak at about ambient temperature and then decreased at low temperatures similar to the ductile behavior shown in Fig. 3. Radiation exposure at 288°C has also resulted in a consistent decrease in the tearing modulus at test temperatures from -75°C to 288°C. An example of the J-integral vs crack extension of two specimens tested at 120°C is shown in Fig. 7.

## CONCLUSIONS AND DESCRIPTION OF FUTURE WORK

The effects of neutron irradiation on three-wire stainless steel weld cladding, prototypical of commercial light water reactor (LWR) materials, were evaluated at a wide range of test temperatures for conditions similar to those at the end of life of an LWR. The yield strength of this cladding increased with irradiation exposure; the increase rate was appreciably higher at low temperatures (room temperature and below). However, the effects of irradiation on the ultimate tensile strength and ductility (both uniform and total elongation) were insignificant.

All the unirradiated and irradiated three-wire cladding specimens exhibited ductile-to-brittle transition behavior similar to that seen earlier for the single-wire cladding. Again, this was also attributed to the dominance of failure of delta-ferrite at lower temperatures. The upper-shelf energy was reduced by 15 and 20%, while the upper-shelf lateral expansion was reduced 43 and 41%, at 2.14 and  $5.56 \times 10^{19}$  neutrons/cm<sup>2</sup> (>1 MeV), respectively. The 41-J transition temperature shifts were 13 and 28°C for the low and high levels of fluence, respectively.

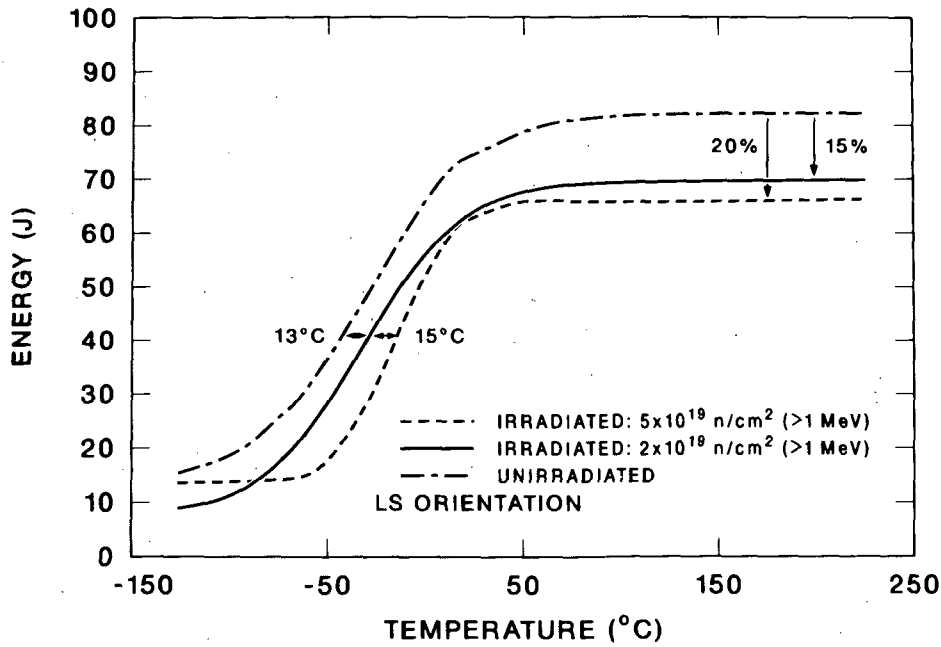


Fig. 4. Effect of irradiation on the Charpy impact energy of three-wire stainless steel cladding.

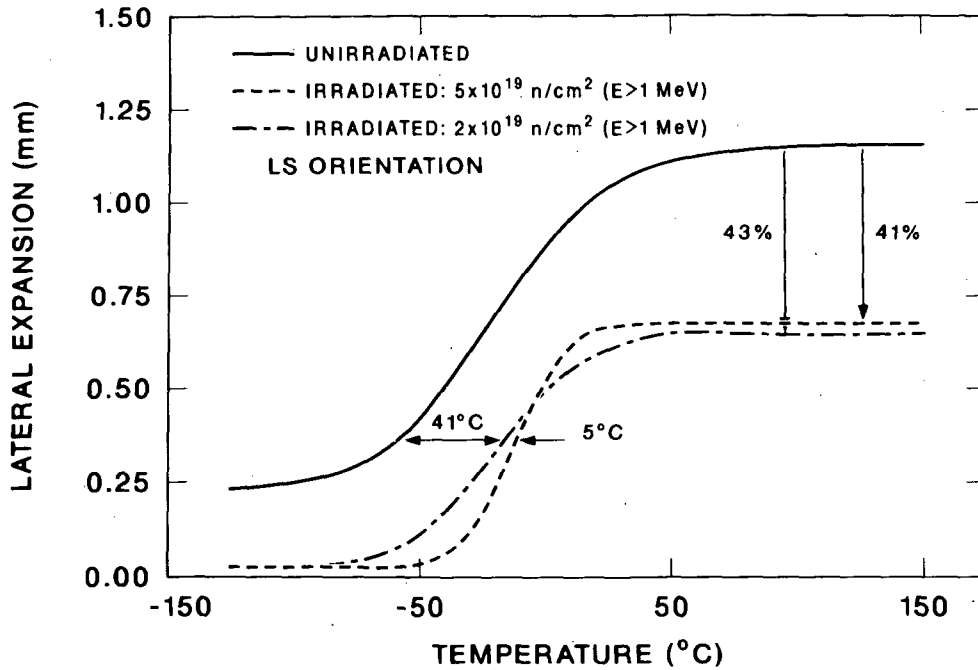


Fig. 5. Effect of irradiation on the Charpy V-notch lateral expansion of three-wire stainless steel cladding.

Table 1. Charpy impact test results for stainless steel three-wire series-arc cladding

Orientation <sup>a</sup>	Neutron fluence, neutrons/cm <sup>2</sup> (>1 MeV)	Transition temperature criterion (°C)		Energy (J)	
		41 J	68 J	Upper shelf	Lower shelf
		LS	0	-41	6
LS	$2 \times 10^{19}$	-28	56	70	9
LS	$5 \times 10^{19}$	-13	--	68	12
LT	0	-28	11	88	14
TL	0	-40	4	86	16
TS	0	-55	7	83	12

<sup>a</sup>With respect to the base metal where L is the rolling as well as the welding direction.

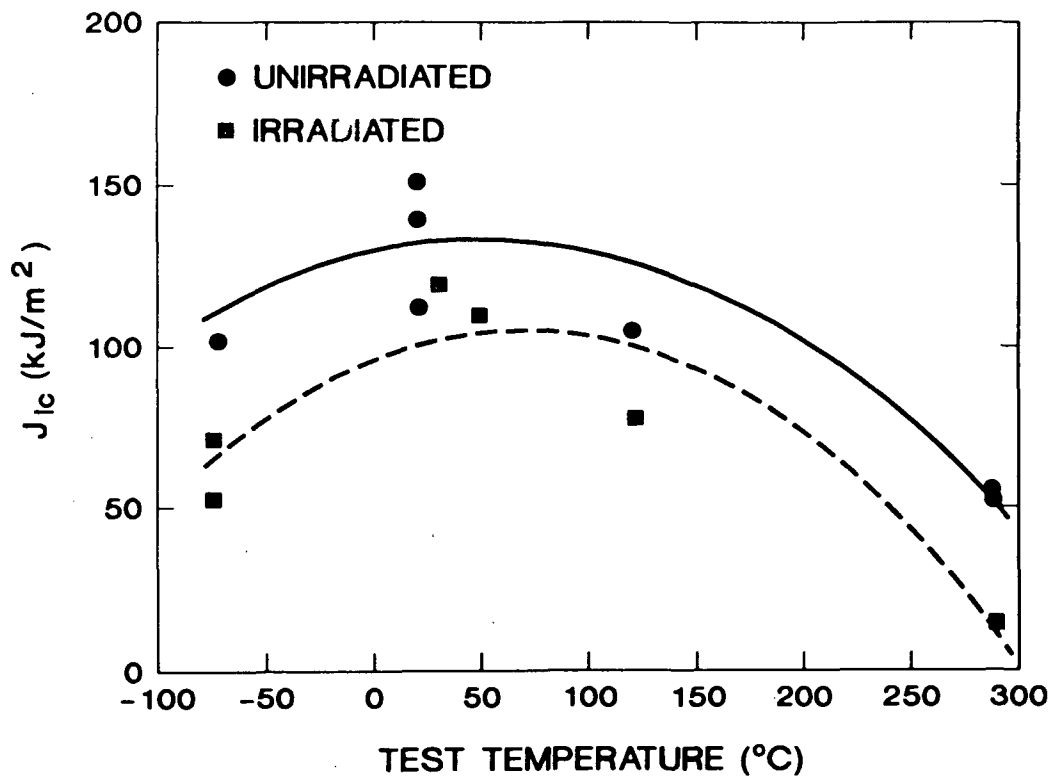


Fig. 6. Effect of irradiation on the ductile initiation fracture toughness of three-wire stainless steel cladding.

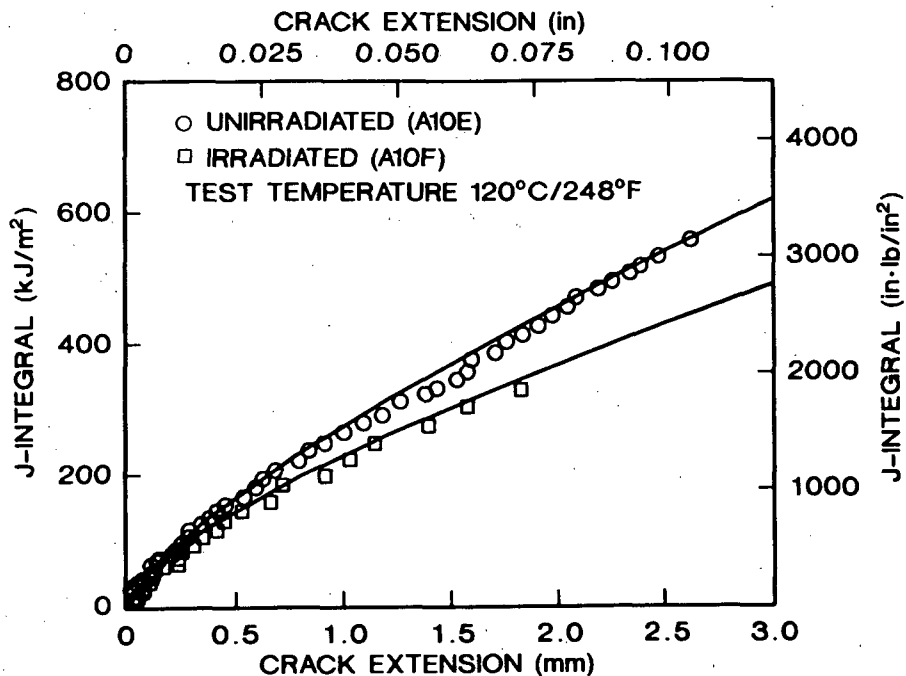


Fig. 7. Effect of irradiation on the tearing modulus of three-wire stainless steel cladding.

Irradiated 0.5TCS specimens tested from -75 to 288°C showed consistent decreases in both ductile initiation fracture toughness and tearing modulus in qualitative agreement with observed decreases in Charpy impact energy and lateral expansion.

It must be stressed that the results presented and discussed in this paper are only for a single case of a three-wire stainless steel cladding; hence, no conclusions can be drawn for different material chemistries and/or welding procedures.

Additional work in progress includes testing of precracked CVN and 12.5-mm compact specimens (0.5TCS) from the single-wire cladding. Furthermore, stainless steel cladding from the decommissioned West German Boiling Water Reactor at Gundremmingen will be examined using subsized specimen techniques to compare to our test reactor data. The subsized specimens will be machined from the recently acquired four trepans cut from the decommissioned reactor.

## II. CLAD PLATE EXPERIMENTS

A small crack near the inner surface of clad nuclear RPVs is an important consideration in the safety assessment of the structural integrity of the vessel. The behavior of such flaws is relevant to the PTS scenario and to the plant life extension issue. There are considerable experimental results which

have shown that, in the absence of cladding, a small surface flaw in an embrittled material subjected to severe thermal shock will become a long flaw. One example from Ref. 5 is shown in Fig. 8, which shows the extensive propagation and bifurcation on the surface of the TSE-7 cylinder originating from a 19-mm semicircular surface flaw. Other examples are given in Ref. 6.

There is a dearth of information on the behavior of small flaws in the presence of cladding, and questions remain about the role a tough surface cladding will play in preventing the propagation of small flaws along the surface. A clad plate research program was conducted as part of Oak Ridge National Laboratory's HSST program in order to investigate the behavior of small flaws in the presence of cladding. The objectives of this research were achieved by comparing the load-bearing capacity of clad and unclad flawed plates.

### EXPERIMENT DESCRIPTION AND RESULTS

A special plate specimen made of a typical RPV steel conforming to ASTM Specification for Pressure Vessel Plates, Alloy Steels, Quenched and Tempered, Manganese-Molybdenum and Manganese-Molybdenum-Nickel (A 533) Grade B has been developed to investigate the effects of cladding on the behavior of flaws (Fig. 9). It was commercially clad using the three-wire series-arc technique and stainless steel types 308, 309, and 312 weld wires. The three-wire series-arc technique was used in some of the older vessels.

CVN impact tests were performed on the cladding, heat-affected zone (HAZ), and base metal with specimens oriented in a direction corresponding to the flaw propagating along the surface of the clad-plate specimens (Fig. 10). Results of CVN impact testing on specimens oriented in a direction corresponding to the electron beam-induced flaw propagating in the thickness orientation were similar.<sup>7</sup> The CVN test results show that the cladding has a substantially lower ductile-to-brittle transition temperature than base metal as measured by the Charpy impact energy. The Charpy transition of the HAZ is also noticeably lower than that of the base metal. This is principally the result of the special heat treatment given to the base metal to raise its transition temperature. Details of the plate fabrication and heat treatment can be found in Ref. 7. Tests to determine nil-ductility temperature (NDT) using specimen P-3 according to the ASTM Test for Conducting Drop-Weight Test to Determine NDT of Ferritic Steels (E 208) were also performed and resulted in an NDT of 36°C for the base metal.

An electron beam weld is introduced into the base metal to provide a crack initiation site. The initially unflawed plate is loaded in four-point bending to approximate the stresses due to PTS. To initiate a sharp flaw, the plates were hydrogen charged while the load was maintained constant. The specific purpose of this test was to determine the arrest capacity of clad plates with various amounts of stored energy.

The pop-in, arrest loads, and corresponding crack lengths for the four plates tested at room temperature are shown schematically in Fig. 11. It may be noted that, as the potential energy stored in the plate increased, the length of the arrested flaw also increased as shown schematically by the shaded flaw shape in Fig. 11. Photographs of actual fracture surfaces of the plates are shown in Figs. 12 and 13. From these photographs it may be noted



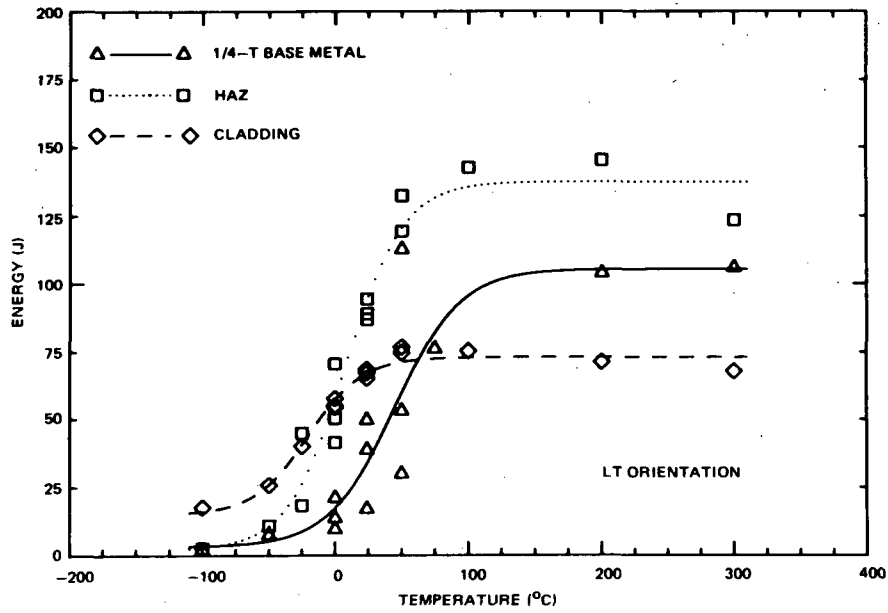


Fig. 10. Charpy impact energy of base metal, heat-affected zone, and cladding used in the clad plates. Specimen orientation corresponds to electron beam-induced flaw propagating along the surface.

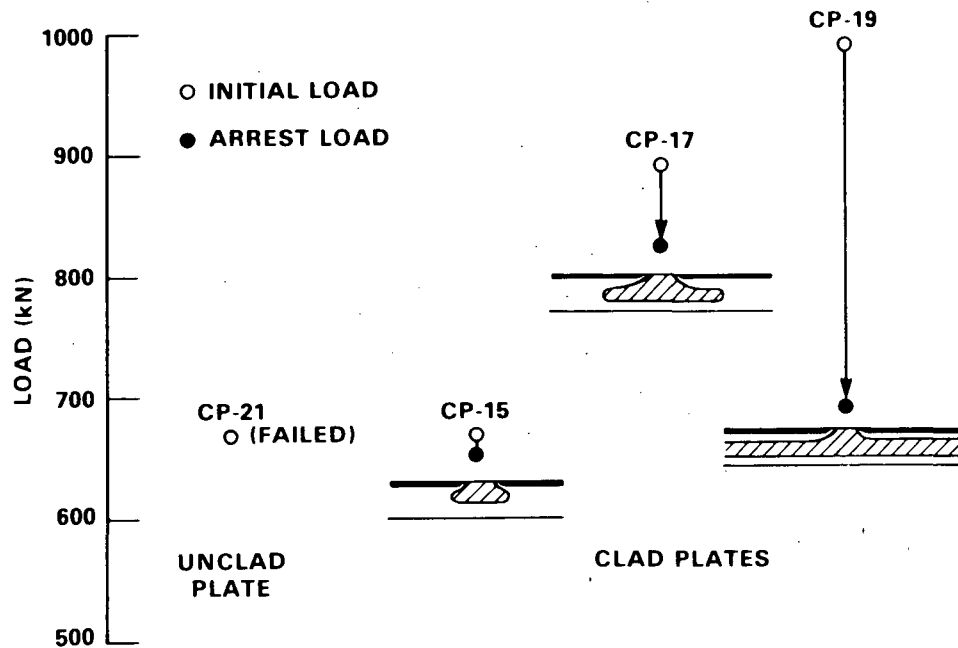


Fig. 11. Pop-in, arrest loads, and corresponding crack lengths for the four plates tested at room temperature.

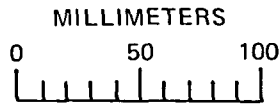
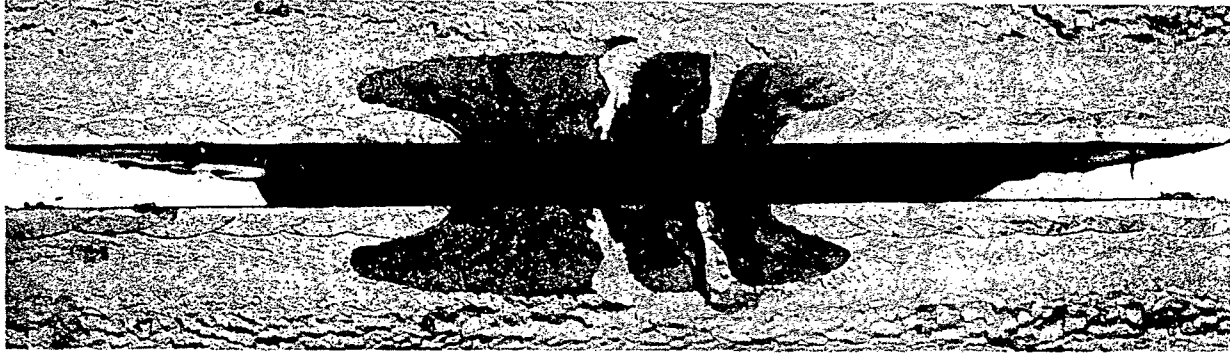


Fig. 12. Fracture surfaces of clad plate CP-17.



Fig. 13. Fracture surfaces of clad plate CP-19.

that in almost all cases a surface layer composed of HAZ and cladding arrested the flaw and prevented its propagation along the surface, causing it to tunnel below the surface.

#### DISCUSSION

The tough surface layer of cladding and HAZ seemed to have contributed significantly to the load-bearing capacity of the plates by arresting flaws at loads and temperatures that have ruptured unclad plates, as seen by comparing the results of the tests on clad plates CP-15, CP-17, CP-19, and unclad plate

CP-21. In fact, the clad plate CP-19 arrested a flaw subjected to a driving force (as measured by the initial load) almost 50% higher than that which broke an unclad plate. Moreover, the residual load-bearing capacity of plates (even with fairly large flaws) as measured by the arrest loads was generally greater than required to break the unclad plate (Fig. 11).

The HAZ played a prominent role in enhancing the load-carrying capacity of the clad plates. As measured by the CVN impact energy, the HAZ is the toughest of the three metallurgical zones of the clad plate specimens at 25°C, while the cladding is toughest at -25°C. It is not clear at this time whether cladding alone, without benefit of the tough strong HAZ which played a pronounced role in arresting propagating flaws, would have also elevated the load-bearing capacity beyond that of the unclad plate. In the case of radiation-embrittled RVPs, the HAZ will most likely undergo toughness degradation similar to that of the base metal, and therefore may not play such a prominent role in arresting propagating flaws.

#### ACKNOWLEDGMENTS

The authors gratefully acknowledge the personnel of Materials Engineering Associates, particularly J. R. Hawthorne, for capsule fabrication and irradiation. We acknowledge T. N. Jones, R. L. Swain, and E. T. Manneschildt for their experimental assistance; and P. H. Wilson and B. Q. Atkinson for editing and preparing the manuscript. We also acknowledge the support of our technical monitor, Michael Mayfield, the Materials Engineering Branch Chief, Chuck Serpan, Jr., and the U.S. Nuclear Regulatory Commission.

#### REFERENCES

1. W. R. Corwin et al., "Fracture Properties of a Neutron-Irradiated Stainless Steel Submerged Arc Weld Cladding Overlay," pp. 26-47 in NUREG/CP-0058, Vol. 4, *Proceedings of the Twelfth Water Reactor Safety Research Information Meeting*, Gaithersburg, Maryland, October 22-26, 1984.
2. W. R. Corwin et al., "Charpy Toughness and Tensile Properties of a Neutron-Irradiated Stainless Steel Submerged-Arc Weld Cladding Overlay," pp. 951-71 in *Effects of Radiation on Materials: Twelfth International Symposium*, ASTM STP 870, F. A. Garner and J. S. Perrin, eds., American Society for Testing and Materials, Philadelphia, 1985.
3. W. R. Corwin et al., "Fracture Behavior of a Neutron-Irradiated Stainless Steel Submerged Arc Weld Cladding Overlay," *Nucl. Eng. Des.* **89**, 199-221 (1985).
4. F. M. Haggag et al., "Effects of Irradiation on Strength and Toughness of Commercial LWR Vessel Cladding", pp. 177-193 in NUREG/CP-0091, Vol. 2, RF, R5, *Proceedings of the Fifteenth Water Reactor Safety Information Meeting*, Gaithersburg, Maryland, October 26-29, 1987.

5. R. D. Cheverton et al., *Pressure Vessel Fracture Studies Pertaining to the PWR Thermal-Shock Issue: Experiment TSE-7*, NUREG/CR-4304 (ORNL-6177), Oak Ridge National Laboratory, 1985.

6. S. K. Iskander, "A Method of LEFM Analysis of RPV During SBLOCA," *Int. J. Pressure Vessels Piping* 25, 279-298 (1986).

7. S. K. Iskander et al., "Effect of Stainless Steel Weld Overlay Cladding on the Structural Integrity of Flawed Steel Plates in Bending - Series 2" (to be published).



## GENERAL DEVELOPMENTS FROM NRC'S DEGRADED PIPING PROGRAM

by

Gery M. Wilkowski, J. Ahmad, R. Barnes, F. Brust, N. Ghadiali,  
D. Guerrieri, G. Kramer, M. Landow, C. Marschall, R. Olson,  
V. Papaspyropoulos, M. Rosenfeld, P. Scott, and P. Vieth

BATTELLE  
Columbus Division

### 1.0 Introduction

The NRC's Degraded Piping Program - Phase II started in April of 1984. Its main objective was to validate the fracture behavior of circumferentially cracked nuclear piping at quasi-static loading rates. The validation involved conducting pipe fracture experiments at LWR conditions which were used to assess various fracture analyses. These data were then used to validate and develop analysis procedures for leak-before-break or inservice flaw inspection criteria such as ASME Section XI IWB-3640 and 3650.

The full-scale experimental efforts involved conducting pipe fracture experiments on various nuclear grade pipes at LWR temperatures. A listing of piping materials investigated is given in Table 1. The pipe sizes ranged from 102-mm (4-inch) to 1067-mm (42-inch) diameter. Generally, the pipes were procured from cancelled nuclear power plants. In one case, a 711-mm (28-inch) diameter main recirculation pipe, which was removed from a BWR, was tested. Many of the experiments involved pipe pressurized with water at 288 C (550 F) under bending loads. Over 61 experiments were conducted and documented in detailed data record books. The data record books consist of four volumes containing data for assessment of current analyses and any future analyses that may be developed.

The material characterization efforts involved two aspects. The first aspect was to evaluate the material properties of each pipe necessary for flaw evaluation analyses. This typically included: chemical analyses, Charpy V-notch tests, tensile tests, and compact (Tension) [C(T)] tests. The C(T) specimen tests were conducted to obtain J-integral fracture resistance curve data for the pipe material at the pipe experiment test temperature. These data have subsequently been input into the NRC's data base on pipe material properties called PIFRAC. The second aspect of the material characterization effort involved specific investigations, such as

- an evaluation of crack instabilities in ferritic steels at LWR temperatures (which are believed to be due to dynamic strain aging),
- development of a test method to evaluate the toughness in the

through-thickness direction of a specimen which simulates the constraint condition in a surface cracked pipe,

- evaluation of methods to extrapolate J-R curves from small C(T) specimen data,
- assessment of material anisotropy on ductile fracture toughness, and
- various round-robin activities to validate calculation and testing techniques.

At the beginning of the Degraded Piping Program, it was believed that generally all nuclear piping failure stresses could be predicted by a limit-load analysis. The pipe fracture results from this program showed that this is not always true. A plastic-zone screening criterion was developed to show when limit-load failure was expected, and when elastic-plastic fracture mechanics would be needed to predict the potentially lower failure stresses than those predicted by the limit-load analyses.

Since that time, various engineering fracture mechanics analyses have been developed. These analyses use the J-integral fracture parameter and are frequently referred to as J-estimation schemes. The verification of these J-estimation schemes using pipe fracture data and more detailed finite element analyses have been a central focus of this program. The finite element analysis efforts have also been evaluated in round-robins for both laboratory specimen and cracked pipe experiments.

The material characterization, pipe experiment, and analytical efforts from the program are summarized in the following sections. Afterwards, the significance of some of these results and future needs are discussed.

## 2.0 Material Characterization Efforts

The main focus of this activity was to provide material characterization data from laboratory-specimen tests for pipes subjected to full-scale fracture tests. Included were chemical composition, tensile stress-strain curves, Charpy V-notch transition curves for ferritic steels, and J-resistance curves. The mechanical property tests were designed to simulate conditions existing in the full-scale pipe fracture test, including notch acuity, crack plane orientation, test temperature, and rate of loading. Specimens were machined from the same lot of pipe used in the pipe experiment; no mechanical flattening of the pipe was permitted. In addition to the data being used for analyzing pipe tests, they were transmitted to Materials Engineering Associates for inclusion in the NRC's Piping Fracture Mechanics Data Base (PIFRAC). Pipe materials that have been characterized in the Degraded Piping Program are indicated in Table 1.

In addition to conducting tests to characterize materials, several specific tasks were undertaken within the program to provide needed data. These tasks included:

- (1) Study of methods for predicting large-crack-growth J-R curves from small-specimen data. The Battelle study compared the usefulness of deformation J ( $J_D$ ) and modified J ( $J_M$ ) for extrapolating J-R curves. It also developed an empirical method for extrapolating J-R curves and revealed possible size effects on J-R curves, especially in weld-metal tests (Ref. 1).
- (2) Development of a special single-edge-notch test [SE(T)] to simulate a surface-cracked pipe bending experiment. Figure 1 is a schematic of the SE(T) specimen subjected to loading using rigid wedge grips. Note that the entire ligament is under tensile stress, just as it is in a surface-cracked pipe subjected to bending. In addition to developing experimental techniques for the SE(T) test, Battelle developed an estimation formula for calculating a J-R curve from the test data, verified the formula by finite element analysis, and applied the test method to evaluation of cracks in welds (Ref. 2). An interesting result of SE(T) tests at 288 C (550 F) is shown in Figure 2. Notice that the crack in Specimens A8-5 and A8-7 began in the HAZ and displayed a crack-opening angle similar to that for the base metal specimen. However, when the crack reached the fusion line in Specimen A8-5, it continued to extend along that boundary while exhibiting a much smaller crack-opening angle. This behavior may be indicative of a minimum toughness region at the fusion line in austenitic stainless steel weldments.
- (3) Study of anisotropy effects on crack-growth direction in ferritic-steel pipes. This study was prompted by observations in both pipe tests and C(T) specimen tests of cracks growing at a large angle to the intended direction in ferritic steels. Examination of a seamless pipe revealed nonmetallic inclusions oriented at 20 to 30 degrees from the pipe axis, apparently the result of twisting of the pipe during hot forming. Testing of C(T) specimens machined from the pipe in several different orientations revealed that the fracture resistance had a minimum value in the direction of the inclusions.
- (4) Participation in round robins with other NRC contractors on tensile testing, J-R curve calculations, and use of the direct-current electrical potential method to monitor crack growth in C(T) specimens.

During the course of the material characterization studies, a number of interesting and, in some cases, unexpected results were obtained. One

of the unexpected findings was dynamic crack jumps in some of the carbon steels at LWR operating temperatures of 550 F (288 C), possibly associated with dynamic strain aging. These crack jumps occurred intermittently between periods of slow stable tearing and were observed in both laboratory specimen fracture toughness tests (Figure 3a, upper curve) and full-scale pipe tests (Figure 3b). Although the fracture mode was ductile during the jumps, such instabilities are indicative of reduced toughness and could potentially led to sudden large leaks in flawed reactor pipes subjected to accident conditions. If the jumps are associated with dynamic strain aging, it is likely that their occurrence will be a function of both strain rate and temperature.

Other interesting results included: (1) flux welds are much less tough than welds made using inert gas in both austenitic and ferritic steels, and (2) most of the carbon steel pipes tested in the Degraded Piping Program exhibited tensile strength values at 300 and 550 F (149 and 288 C) that were greater than those at room temperature; this result indicates that many carbon steel pipes used in nuclear plants are susceptible to dynamic strain aging. Susceptibility to dynamic strain aging may be accompanied by several undesirable characteristics at LWR temperatures, including: (1) dynamic crack jumps, (2) reduced crack-initiation toughness, and (3) reduced tearing modulus (Ref. 3). On the other hand, a beneficial effect from dynamic strain aging is an increase in the material's strength at elevated temperatures.

### 3.0 Pipe Fracture Experiments

The scope of the full-scale pipe experiments included: (1) obtaining data on circumferentially cracked pipe, (2) using representative pipe materials, crack geometries, and loading conditions, (3) performing all experiments at elevated temperatures, (4) determining crack initiation, maximum load and crack growth in each experiment, (5) comparing experimental loads relative to net-section-collapse predicted failure loads, and (6) establishing a comprehensive pipe fracture data base for evaluating existing analytical fracture models.

In addition to verification of existing analysis methods, the extensive pipe fracture data base will be useful for evaluating fracture mechanics parameters developed or modified in the future. This data base has already been useful in evaluating flaw assessment criteria for cracks found in service, and has been used to benchmark the criteria presented in Section XI of the ASME Code; Article IWB-3640 for austenitic pipe and proposed Article IWB-3650 for ferritic pipe.

The test matrix consisted of 61 full-scale pipe fracture experiments conducted at Battelle's laboratories in Columbus and West Jefferson, Ohio. Flaw geometries included through-wall cracks, surface cracks and complex cracks. (A complex crack, as defined in this program, is a long internal surface crack that has propagated through the wall thickness for a short distance.) Figure 4 illustrates the number of experiments performed as a function of pipe diameter and crack

geometry. Evident from this figure is the wide range of pipe diameters studied in this program.

Figure 5 presents the data in a similar format, except that the number of experiments is shown as a function of loading method rather than crack geometry. Loading methods included four-point bending, pressure, pressure and bending, and bending with a high system compliance. Quasi-static loading rates were used in all cases.

A number of representative materials were evaluated in the pipe fracture experiments, as indicated in Table 1. Figure 6 shows the breakdown of experiments by material type. Pipe material wall thicknesses ranged from 0.25 to 3.41 inches (6.4 to 86.6 mm).

The test matrix rationale was to perform the simplest experiments early in the program and increase the complexity of the loading conditions and flaw geometries as the program progressed. Thus, many of the first year experiments evaluated through-wall-cracked pipe under simple bending, while the third and fourth year experiments evaluated surface cracks in welds under combined pressure and bending.

An example of a high-energy experiment is shown in Figure 7. This photograph shows the decompression behavior of a 16-inch (406-mm) diameter pipe after an internal surface crack has broken through the wall of the pipe under combined pressure and bending loads. In this particular experiment, the test pressure was 1,600 psig (11.0 MPa). The crack was embedded in the center of a low-toughness submerged-arc weld (SAW).

Two recent experiments have evaluated the load-carrying capacity of large diameter cold-leg pipes under simple bending loads. The first experiment evaluated a through-wall crack in the base metal, while the second experiment evaluated a similar crack in a shop manufactured weld. These experiments were challenging due to the extremely high bending moments required to propagate a crack in such a heavy-wall pipe. Figure 8 is a post-test photograph of the second cold-leg pipe experiment. A through-wall crack was tested in the centerline of an SAW in this experiment. A close-up of one crack tip is shown in Figure 9. Both crack tips initiated at the mid-wall of the pipe weld, but quickly grew out of the SAW weld and into the pipe base metal. As is evident from Figure 9, the crack growth direction was erratic, changing in a zig-zag fashion across the weld.

Results from all pipe experiments have been incorporated into an extensive pipe fracture data base. Data collected and reported in this data base consist of applied loads, load-line displacements of the test machine, internal pipe pressure, crack-opening displacements, direct-current electric potential measurements (for crack growth monitoring), rotations of the cracked pipe section, and pipe temperature.

In addition, the pipe fracture data base also summarizes pertinent material property data, such as chemical analyses, tensile results,

Charpy V-notch impact data, and J-resistance curve data. Five experiments from other research programs have been incorporated into the data base in addition to the Degraded Piping Program experiments.

Crack initiation and maximum moment data from all pipe experiments have been compared against limit-load analyses such as the net-section-collapse method. Figure 10 illustrates such a comparison for the two cold-leg pipe experiments discussed earlier. Net-section-collapse calculations were based on two values of flow stress for these materials. Both the actual tensile property data and the ASME code design stress were used to define the flow stress of the material. In the case of the weld metal experiment, both the base metal properties and the weld metal properties were used in the limit-load calculations. Thus, two sets of bars are shown in Figure 10 for the weld metal cold-leg pipe experiment. Comparisons to net-section-collapse predictions showed that, in both cases, experimental maximum loads exceeded the predicted loads when either the base metal data or design stress were used.

These comparisons to limit-load analyses have led to the development of a plastic-zone screening criterion to determine when net-section-collapse analyses are valid and when more complex elastic-plastic analyses are warranted. Such a criterion is shown in Figure 11. In this figure, experimental stress data are normalized against net-section-collapse predicted stresses for both through-wall-cracked and surface-cracked pipe. The data are plotted as a function of a non-dimensional plastic zone parameter. A statistical analyses was performed on these data and a lower bound failure curve was defined with a 95 percent confidence level. This is shown by the solid line in Figure 11. Such a criterion shows that even high-toughness stainless steel materials can fail below net-section-collapse predictions if the pipe diameter is sufficiently large. It also shows that surface-cracked pipes are less sensitive to toughness than are through-wall-cracked pipes.

A variety of other experiments were performed within this phase of the program. The crack instability behavior of pipe under bending was evaluated in several experiments. Conditions of unstable crack propagation were observed once maximum moment was achieved in pipes with long internal surface cracks or with complex cracks (such as found in the Duane Arnold nuclear plant). This instability behavior resulted in complete double-ended guillotine breaks in two experiments, and was found to be quite sensitive to changes in the compliance of the four-point-bending test machine for these two crack geometries.

Encouraging results were obtained from experiments in which circumferentially cracked pipe had been repaired by the weld-overlay-repair technique. In these experiments, a fatigue crack was grown completely through the wall of a stainless steel pipe and half-way around the circumference. A multiple pass TIG weld overlay repair was fabricated over the crack. Post-test results from these pressure and bending experiments showed tremendous plasticity in the base metal

before crack initiation occurred. The results were also used in a round-robin design analysis for weld-overlay repairs. The round-robin predictions showed that various vendors and engineering firms made consistent predictions that agreed well with the experimental results.

Another series of experiments evaluated cracks in solution-annealed versus as-welded low-toughness submerged-arc welded Type 304 stainless steel pipe. The solution-annealed weld metal had a higher toughness but lower stress-strain curve than the as-welded material. The pipe fracture experimental results showed the failure stresses were lower for the solution-annealed pipe experiments. This was the opposite trend than that predicted by J-estimation scheme analyses using the base metal stress-strain curve and the weld metal toughness data. These results suggested that both the stress-strain curves of the base metal and weld metal should be considered when analyzing cracks in a weld.

Finally, an interesting phenomenon was observed in a number of ferritic steel pipe specimens containing through-wall cracks under bending. Nearly all of these experiments showed significant out-of-plane crack growth behavior. In the case of one cold-leg pipe specimen (similar to the experiment shown in Figures 8 and 9), the through-wall crack turned from the circumferential direction and began propagating along the axis of the pipe. Thus, the crack followed the direction of lowest toughness rather than the direction of greatest principal stress. This result reveals that the material anisotropy due to the rolling and forming process is a significant factor in predicting the fracture behavior of through-wall-cracked pipe under bending.

#### 4.0 Analytical Efforts

The fracture mechanics analysis effort in the Degraded Piping Program - Phase II was aimed at providing the NRC with simple engineering models for predicting the integrity of nuclear power plant pipes containing cracks. The majority of the work was focused on predicting the behavior of circumferentially oriented cracks in pipes subjected to predominantly bending loads. A limited amount of effort was also devoted to combined internal pressure and bending loads. Through-wall cracks, part-through-wall internal surface cracks, as well as complex cracks in different pipe sizes and materials were considered. Both base-metal and weld cracks were analyzed. The majority of the modeling effort was based on the J-integral tearing instability (J/T) approach of elastic-plastic fracture mechanics (EPFM).

The application of the J/T approach requires two types of analytical models. These are for (a) establishing an appropriate J-resistance (J-R) curve using experimental data, and (b) calculating applied J and the tearing modulus (T) for the crack-structure configuration of interest. In the Degraded Piping Program, the work within Type (a) analyses included several activities. For example, finite element analyses were performed to aid the development of a simple method for extrapolating

J-R curves for large amounts of crack growth from laboratory specimen tests (Ref. 1). Elastic-plastic finite element analyses of 1.0 inch (25.4 mm) thick 1T, 3T, and 10T planar dimension specimens of both austenitic and carbon steels were performed (Ref. 1). An example of the (far-field) J-resistance curves resulting from these analyses on Type 304 stainless steel at 550 F (288 C) are shown in Figure 12. Such results were used in deciding how a J-resistance curve from a 1T specimen can be extrapolated to larger crack growth amounts normally encountered in through-wall crack analyses of pipes. The 10T specimen was also analyzed by a number of participants in an international analysis round-robin organized by Battelle (Ref. 4). Figure 13 shows a key result of the round robin in the form of predicted load versus applied displacement plots. The round-robin results also indicated that in general the far-field J values for large crack extension were in better agreement with the modified ( $J_M$ ) values rather than deformation ( $J_D$ ) values obtained by estimation methods.

The Type (a) analyses also included the evaluation of a single-edge notch specimen loaded under fixed-grip boundary conditions as a candidate for characterizing radial growth behavior of surface cracks in pipes (Ref. 2). The study suggested that in this specimen, as well as in circumferentially surface-cracked pipe in bending, there may be little or no J-controlled growth. If this is the case, further research aimed at more accurate prediction of surface-crack behavior in pipes may be needed.

Another activity within Type (a) analyses was aimed at developing and comparing J-R curves for cracks in welds by finite element analyses and by estimation methods. The results of this activity are reported in Reference 5.

The work in Type (b) analyses resulted in improved methods for analyzing pipes with through-wall cracks in bending. These methods, called LBB.GE and LBB.ENG (Ref. 6), and several other estimation analysis methods were evaluated by comparing their predictions with experimental data. Figure 14 represents an example of such evaluations in terms of predicted load versus displacement curves for a specific experiment. In terms of initiation and maximum load predictions, it was found that, with a few exceptions, the EPRI/GE estimation methods for through-wall cracked pipes gave underpredictions when used in conjunction with  $J_D$  resistance curves. Altogether, six different through-wall crack analysis methods were evaluated. A computer code called NRCPIPE, which allows convenient application of these methods for LBB evaluations, was developed for a personal computer.

In addition to estimation analyses, three-dimensional finite element analyses of through-wall cracked base metal as well as welded pipes were performed. A stainless steel 16-inch (406-mm) diameter pipe fracture experiment was analyzed by a number of participants as part of one of the three international round robins organized by Battelle. Figure 15 shows a key result of the round robin in the form of predicted load versus applied displacement plots. Note that a general

trend from this effort, as well as other efforts, is that the FEM analyses underpredict the experimental results for circumferential through-wall-cracked pipe in bending.

For circumferentially surface cracked pipes in bending, new J-estimation methods were developed (Ref. 7). These developments effectively utilized an existing two-dimensional estimation method to solve the three-dimensional surface crack problems. The predictions of these methods were compared with experimental data. Figure 16 shows an example of such a comparison.

## 5.0 Significance of Results

At the beginning of the Degraded Piping Program - Phase II, the status of the pipe fracture mechanics methodology was quite limited. For example;

- the net-section collapse (limit-load) analysis for circumferentially cracked pipe was developed and verified on small diameter stainless steel pipe,
- the EPRI/GE J-estimation elastic-plastic fracture mechanics analysis was developed, but had little verification,
- the NRC.LBB analysis method was under development,
- there was a limited amount of material property data, and
- there was a limited amount of pipe fracture data.

Some of the developments during the course of the Degraded Piping Program - Phase II are:

- the material property data base was greatly expanded,
- a detailed data base for circumferentially cracked pipe under slow monotonic loading was expanded,
- new J-integral based engineering analyses were developed and verified for circumferentially through-wall-cracked pipe stability evaluations used in LBB assessments,
- a finite length surface-cracked pipe elastic-plastic fracture mechanics engineering analysis was developed,
- the accuracy of finite element analyses of cracked pipe was assessed,
- an energy balance method was developed to predict the start of an instability and estimate the magnitude of crack growth in an instability event for both through-wall and surface-cracked pipe

under combined load-controlled and displacement-controlled stresses,

- a statistically based fracture analysis method to predict maximum loads of circumferentially cracked pipe was developed,
- a methodology to predict the fracture of circumferentially cracked piping systems subjected to dynamic loading such as earthquakes was initially conceived,
- a constraint correction for circumferential complex-cracked pipe was developed, and
- an assessment of Charpy versus  $J_{IC}$  correlations was made using data developed in this program.

These developments have subsequently been used to assess Leak-Before-Break (LBB) fracture analyses, and in-service flaw inspection methods. LBB developments include evaluation of through-wall circumferential cracked pipe J-estimation schemes, and development of experimental data to verify crack opening areas for leak-rate predictions. In-service flaw inspection criteria included assessments of the ASME Section XI IWB-3640 austenitic flaw evaluation procedure, and the IWB-3650 ferritic flaw evaluation procedure. This involved assessment of the inherent safety factors in the ASME analyses and development of fracture toughness data for development of reasonable lower bound material properties in the ASME analyses. Although numerous changes and improvements have been made to the ASME criteria, further improvements to unify and make secondary corrections are still needed.

Another assessment was on the weld-overlay repaired pipe fracture analyses. Fracture experiments were conducted on prototypical weld-overlay repaired pipe that initially had large circumferential through-wall cracks. This effort validated the NRC's NUREG-0313 Rev. 2 criteria for weld-overlay fracture analyses.

## 6.0 Future Needs

There are several areas of piping integrity that are in need of further efforts. Some of these resulted from the Degraded Piping Program results, while others were not within its scope. These are briefly described below.

The first area in need of further evaluation is fracture and crack-opening-area analyses of pipe fittings. Effort is needed to develop verified analyses for the LBB and in-service flaw inspection criteria of fittings. LBB and in-service flaw inspection criteria are currently based on the predictions of cracks in straight pipe. Pipe systems, however, may have cracks in fittings, i.e., elbows, tees, etc. Analyses verified by experimental data are needed for complete LBB analyses, and for future ASME Section XI Code flaw acceptance criteria.

The second area in need of further study is integration of the pipe fracture program results with the Piping Reliability Program results. The objective would be to assess the significance of possible interactions between pipe fracture studies and suggested code changes from the EPRI/NRC Piping Reliability Program. The EPRI/NRC Piping Reliability Program has recently completed efforts to suggest changes in the design rules for allowable stresses in nuclear piping. The basis for this suggestion comes from uncracked pipe fitting and pipe system tests. The Degraded Piping Program has developed considerable methodology for assessment of cracked pipe under quasi-static loading, while the NRC's IPIRG program is examining the behavior of cracked piping systems under dynamic loading. There has been very little consideration of acceptable flaws (which are much smaller than the Degraded Piping Program or IPIRG flaw geometries) on the suggested changes from the Piping Reliability Program. Thus, additional study is needed to examine the safety margins using the suggested pipe design stress rules if there are small flaws in critical areas.

A third area in need of additional efforts is development of a replacement criterion for the DEGB design rule. The elimination of the DEGB design criterion for pipe whip restraint and jet impingement removal has been a major step forward in improving piping safety and at the same time making plants more economical to run. The next logical step is to apply the elimination of the DEGB toward defining a maximum credible leakage area for more realistic designs for equipment qualification, pipe support design, redesign of internal reactor core supports for lower depressurization loads, etc. This effort will develop methodology that could be used to assess future licensing requests for replacement of the DEGB design rule.

A fourth area of further activity is to resolve issues from the Degraded Piping Program - Phase II that have not been sufficiently addressed. The Degraded Piping Program - Phase II program contained over 70 technical subtasks. Within those efforts many concerns were resolved, while others could not be resolved within the scope of the program. Furthermore, some of these issues were discovered during the course of the program. This effort is needed to assess the more significant issues for LBB or in-service flaw inspection criteria assessments.

Some of the more significant issues are:

- improvements in circumferential through-wall cracked pipe analyses for short crack lengths applicable to LBB analyses,
- improvements in the understanding of dynamic strain aging on the fracture behavior of carbon steels,
- assessment of the effects of anisotropy on fracture behavior of ferritic piping steels,

- generation of additional quasi-static straight pipe fracture data (i.e., large diameter pipe with surface cracks),
- generation of additional ferritic steel weld, bimetallic welds and fusion line toughness data, etc.,
- refinements to surface-cracked pipe estimation schemes for combined loading,
- generation of a data base on cyclic loading and dynamic rate effects on the strength and toughness of nuclear piping material,
- resolution of discrepancies between finite element analyses of cracked pipe experiments and experimental data, and
- development of improved criteria to uniformly handle crack-opening area and fracture predictions for welds.

The last area of effort that needs to be continued is validation of ASME Section XI Code procedures as well as coordination with NRC-NRR, ASTM and other NRC contractors. The objective of this effort is to assess proposed changes to the ASME Section XI Flaw Evaluation Working Group, and to coordinate pertinent research developments with the Working Group if they could impact the Code. For instance, at the September 1988 Pipe Flaw Evaluation Task Group meeting, a list of over 20 "maintenance" items for changes to the stainless steel and ferritic piping criteria was made. In order to implement these changes, input from the past Degraded Piping Program and additional new items is necessary.

## 7.0 References

1. Papaspyropoulos, V., Marschall, C., and Landow, M., "Predictions of J-R Curves with Large Crack Growth from Small Specimen Data", Technical Report for NRC Degraded Piping Program, prepared by Battelle Columbus Division, NUREG/CR-4575, September 1986.
2. Wilkowski, G. et al., "Degraded Piping Program - Phase II", Sixth Program Report, October 1986-September 1987, prepared by Battelle Columbus Division, NUREG/CR-4082, Vol. 6, April 1988.
3. Marschall, C., Landow, M., and Wilkowski, G., "Effect of Dynamic Strain Aging on Fracture Resistance of Carbon Steels Operating at Light-Water-Reactor Temperatures", paper presented at 21st National Symposium on Fracture Mechanics, Annapolis, MD, June 28-30, 1988; to be published by ASTM.
4. Ahmad, J. et al., "Elastic-Plastic Finite Element Analysis of Crack Growth in Large Compact Tension and Circumferentially Through-Wall-Cracked Pipe Specimen", Technical Report for NRC

Degraded Piping Program, prepared by Battelle Columbus Division, NUREG/CR-4573, October 1986.

5. Nakagaki, M., Marschall, C., and Brust, F., "Analysis of Cracks in Stainless Steel TIG Welds", Technical Report for NRC Degraded Piping Program, prepared by Battelle Columbus Division, NUREG/CR-4806, December 1986.
6. Brust, F., "Approximate Methods for Fracture Analyses of Through-Wall Cracked Pipes", Technical Report for NRC Degraded Piping Program, prepared by Battelle Columbus Division, NUREG/CR-4853, February 1987.
7. Scott, P. and Ahmad, J., "Experimental and Analytical Assessment of Circumferentially Surface-Cracked Pipes Under Bending", Technical Report for NRC Degraded Piping Program, prepared by Battelle Columbus Division, NUREG/CR-4872, April 1987.

TABLE 1. PIPES SUBJECTED TO FULL-SCALE TESTS AND TO MATERIAL CHARACTERIZATION STUDIES IN DEGRADED PIPING PROGRAM

	Diameter in Inches
Wrought Ferritic Pipe	
ASTM A106B	6 and 16
ASTM A333, Gr. 6	4, 10, and 24
ASTM A516, Gr. 70	28 and 37
SA Welds in Wrought Ferritic Pipe	
ASTM A516, Gr. 70	37
ASTM A106B	8 and 16
Wrought Austenitic Pipe	
Type 304 stainless	4, 6, 16, and 42
Type 316L stainless	16
Inconel 600	6
Cast Austenitic Pipe	
CF8M stainless	12 and 16
SA Welds in Wrought Austenitic Pipe	
Type 304 stainless	6 and 16
GTA Weld in Wrought Austenitic Pipe	4
GTA Weld Overlay on Wrought Austenitic Pipe	
Type 304 stainless	6

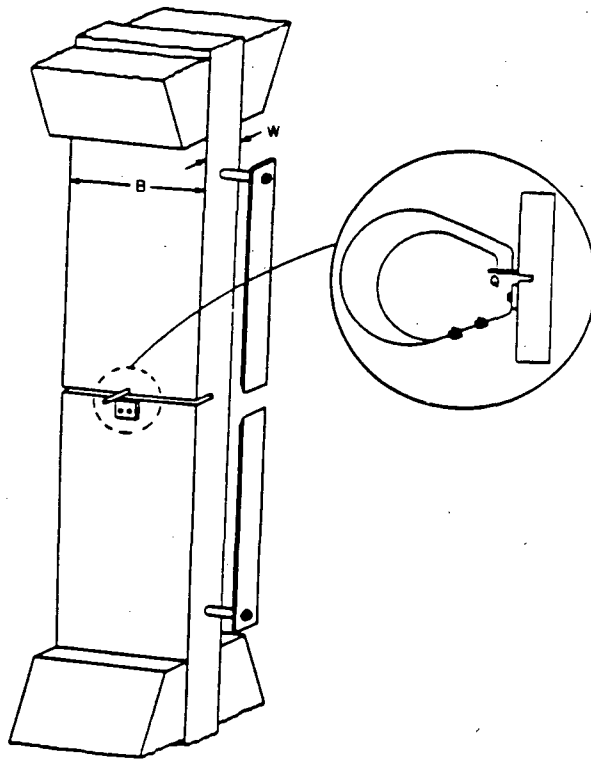


FIGURE 1. SCHEMATIC OF SE(T) TEST TO SIMULATE SURFACE CRACKED PIPE BENDING EXPERIMENT

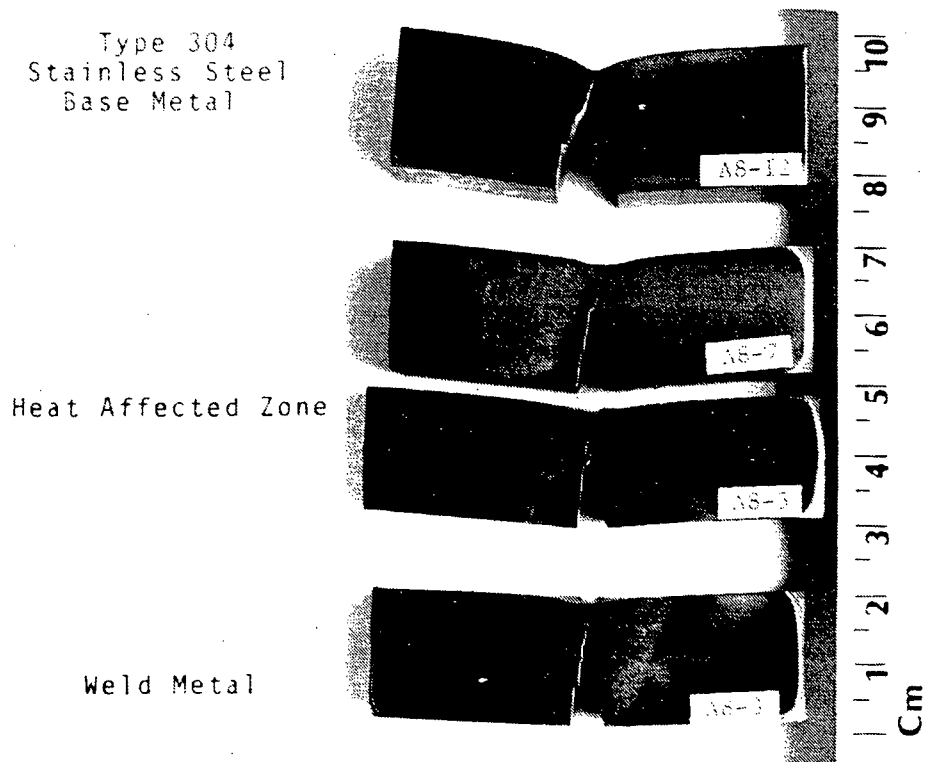


FIGURE 2. PHOTOGRAPH OF CROSS-SECTIONS NEAR THE CRACK IN SE(T) SPECIMENS TESTED AT 550 F (288 C)

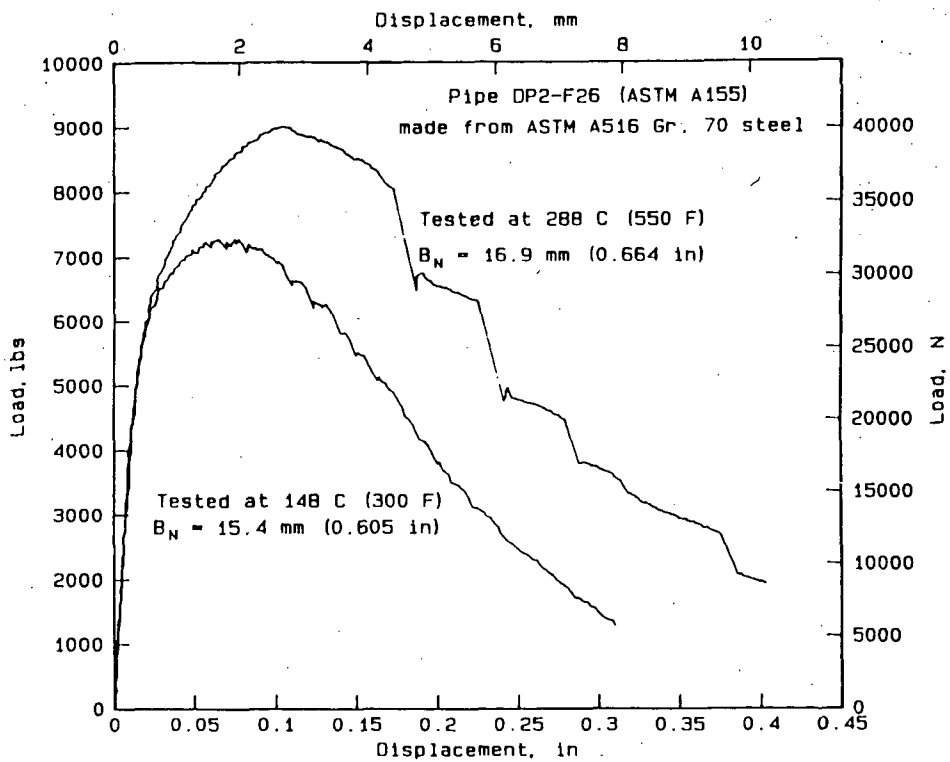


FIGURE 3a. UNSTABLE CRACK GROWTH IN COMPACT SPECIMENS

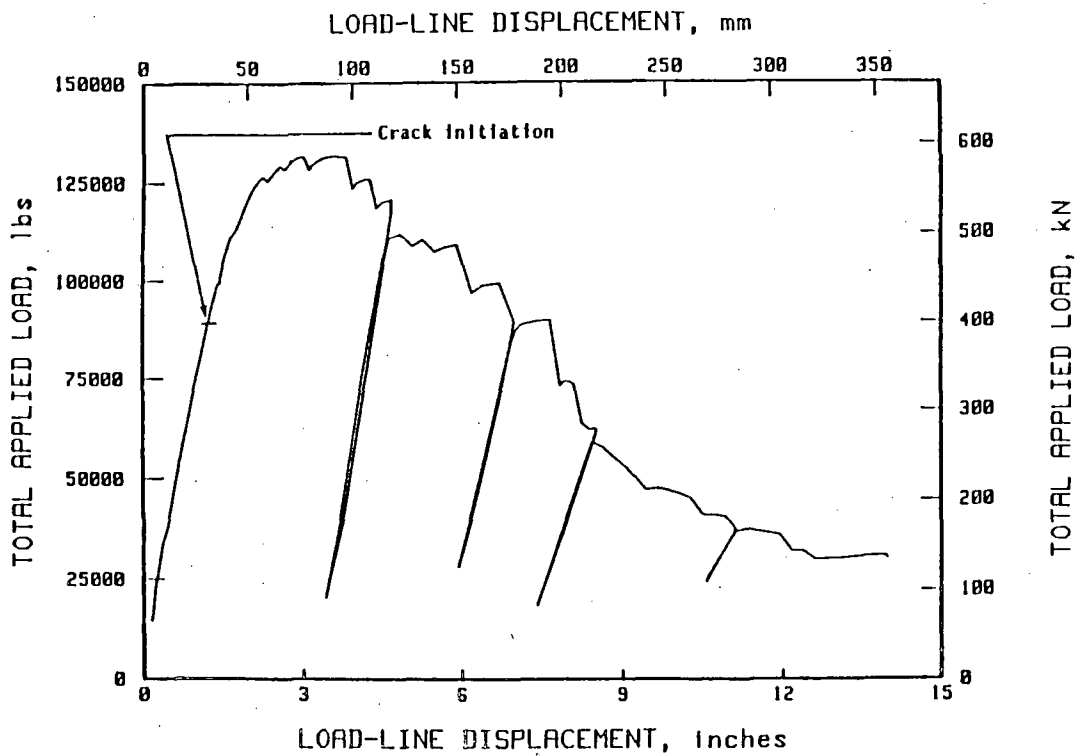


FIGURE 3b. UNSTABLE CRACK GROWTH IN PIPE FRACTURE TEST AT 550 F (288 C) (THE PIPE IS THE SAME PIPE AS IN FIGURE 3a)

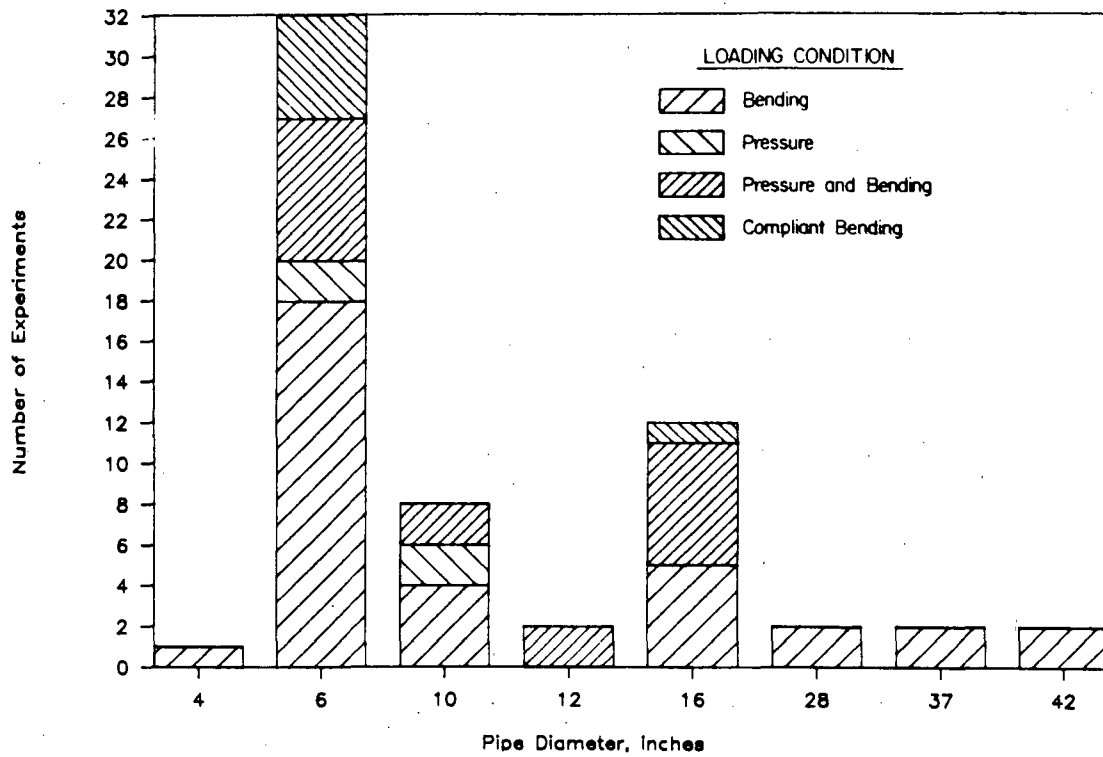


FIGURE 4. TEST MATRIX FROM THE FULL-SCALE PIPE FRACTURE EXPERIMENTS SHOWING THE NUMBER OF EXPERIMENTS BY DIAMETER AND LOADING TYPE

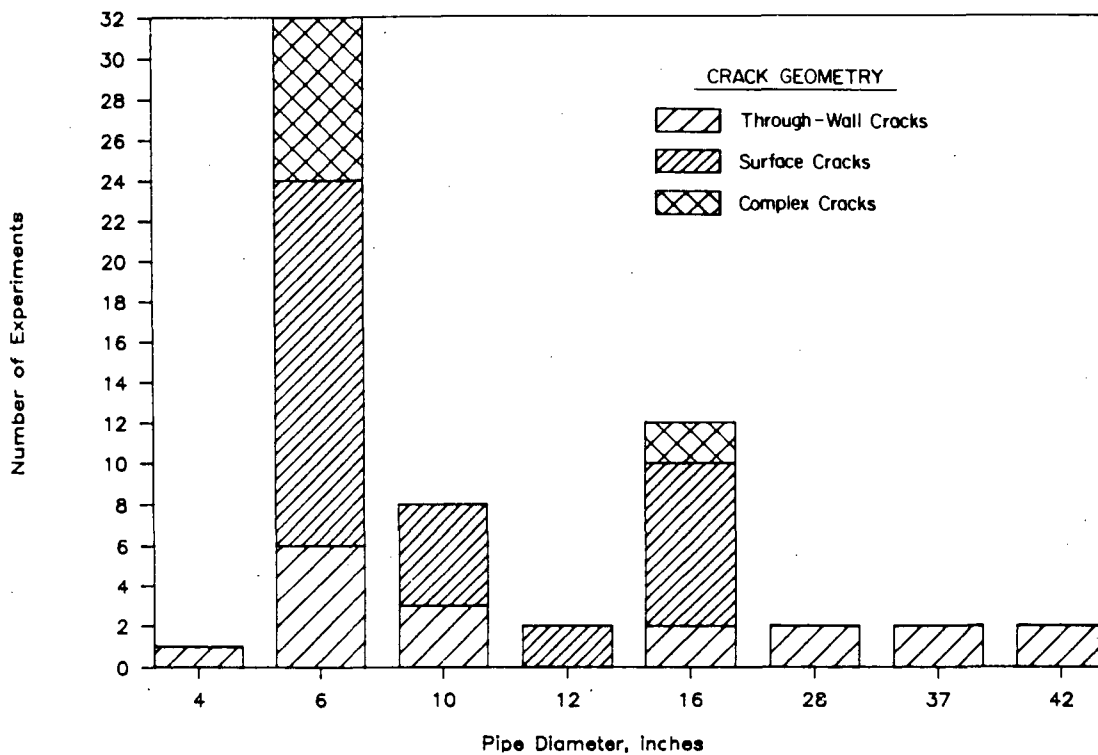


FIGURE 5. TEST MATRIX FROM THE FULL-SCALE PIPE FRACTURE EXPERIMENTS SHOWING THE NUMBER OF EXPERIMENTS BY DIAMETER AND CRACK GEOMETRY

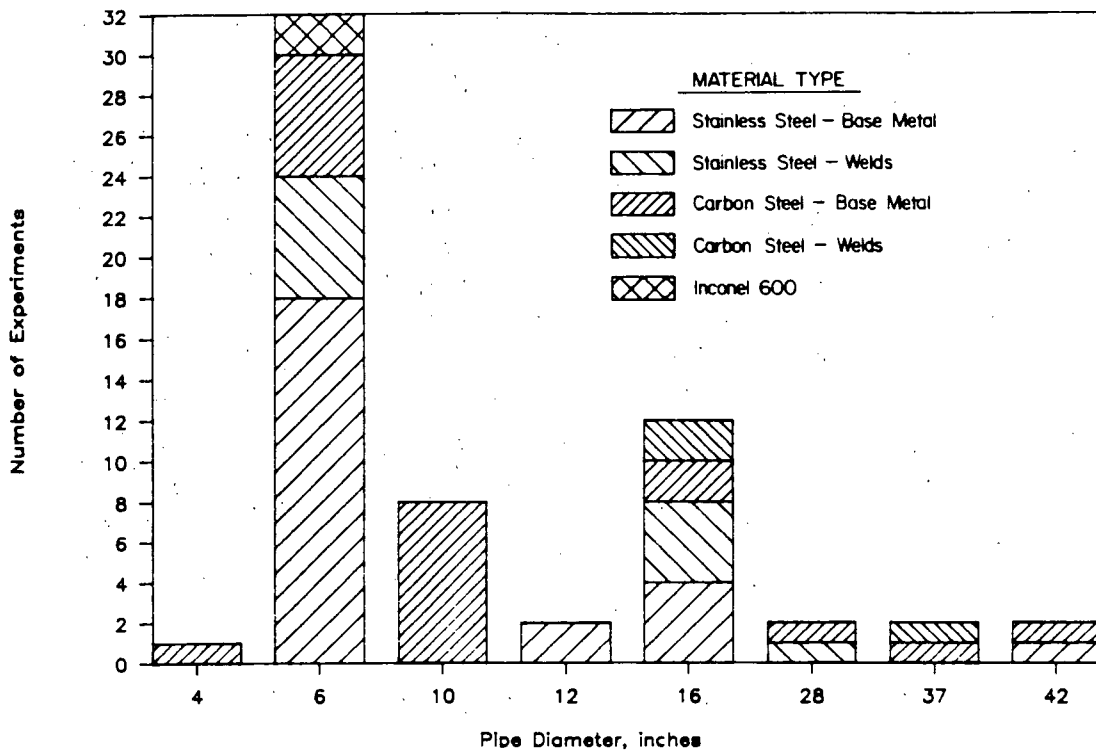


FIGURE 6. TEST MATRIX FROM THE FULL-SCALE PIPE FRACTURE EXPERIMENTS SHOWING THE NUMBER OF EXPERIMENTS BY DIAMETER AND MATERIAL TYPE

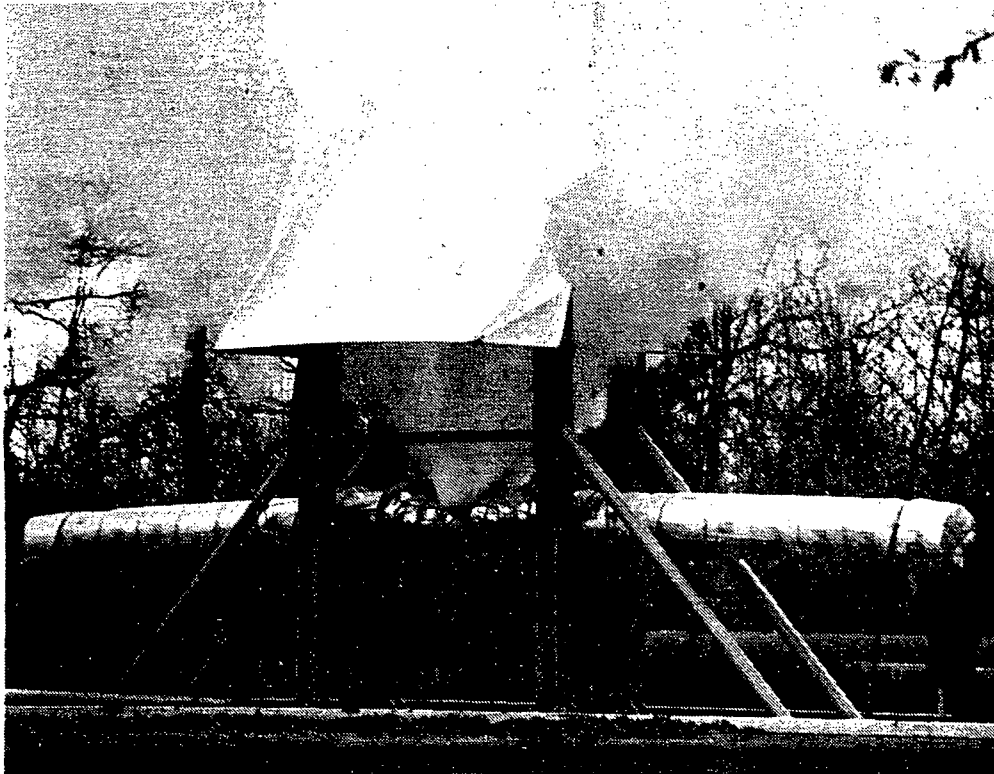


FIGURE 7. HIGH-ENERGY PIPE FRACTURE EXPERIMENT CONDUCTED UNDER PRESSURE AND BENDING AT ELEVATED TEMPERATURES

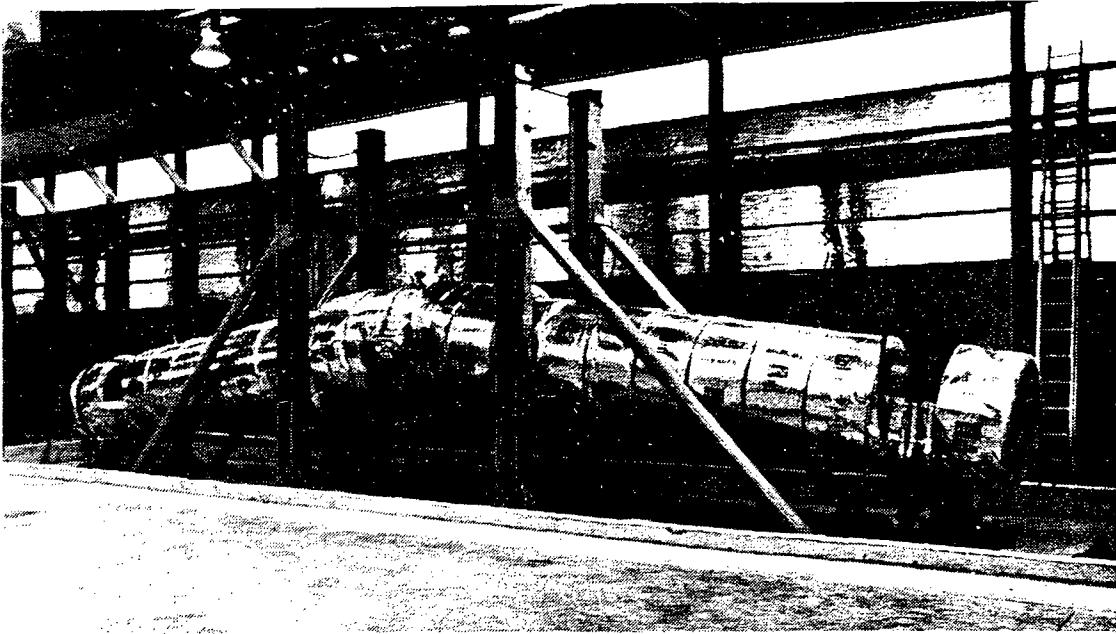


FIGURE 8. POST-TEST PHOTOGRAPH OF A LARGE DIAMETER COLD-LEG EXPERIMENT CONDUCTED UNDER BENDING AT ELEVATED TEMPERATURES



FIGURE 9. CLOSE-UP OF ONE CRACK TIP FROM THE COLD-LEG EXPERIMENT SHOWN IN FIGURE 8. THE THROUGH-WALL CRACK IN THIS EXPERIMENT WAS MACHINED INTO THE CENTERLINE OF A SUBMERGED-ARC WELD

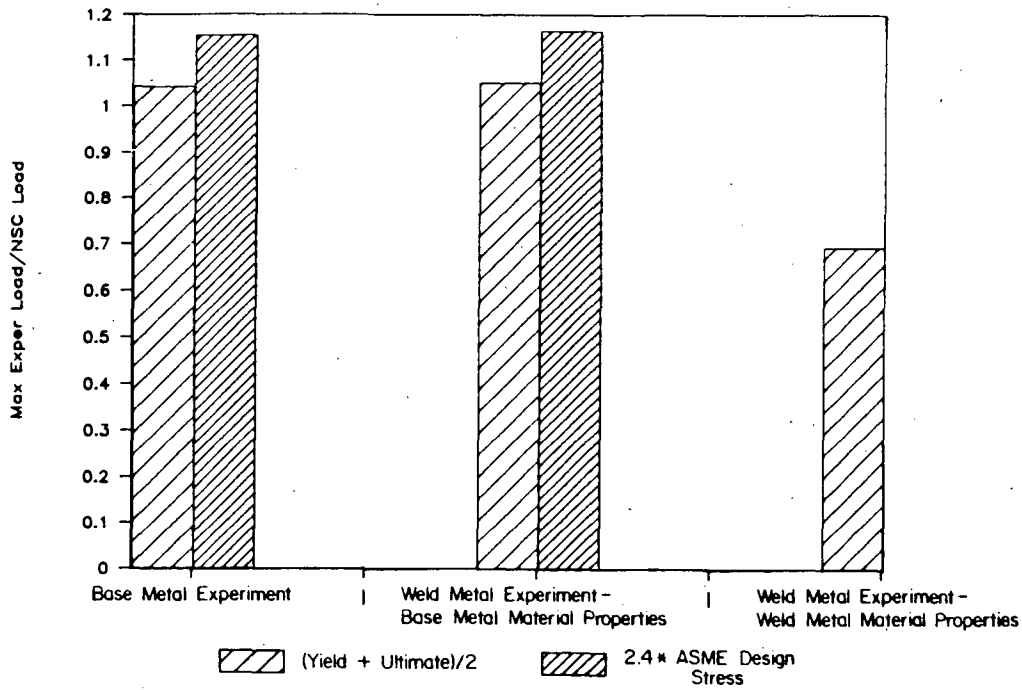


FIGURE 10. COMPARISON OF EXPERIMENTAL LOAD DATA FROM TWO COLD-LEG EXPERIMENTS TO NET-SECTION-COLLAPSE PREDICTED LOADS

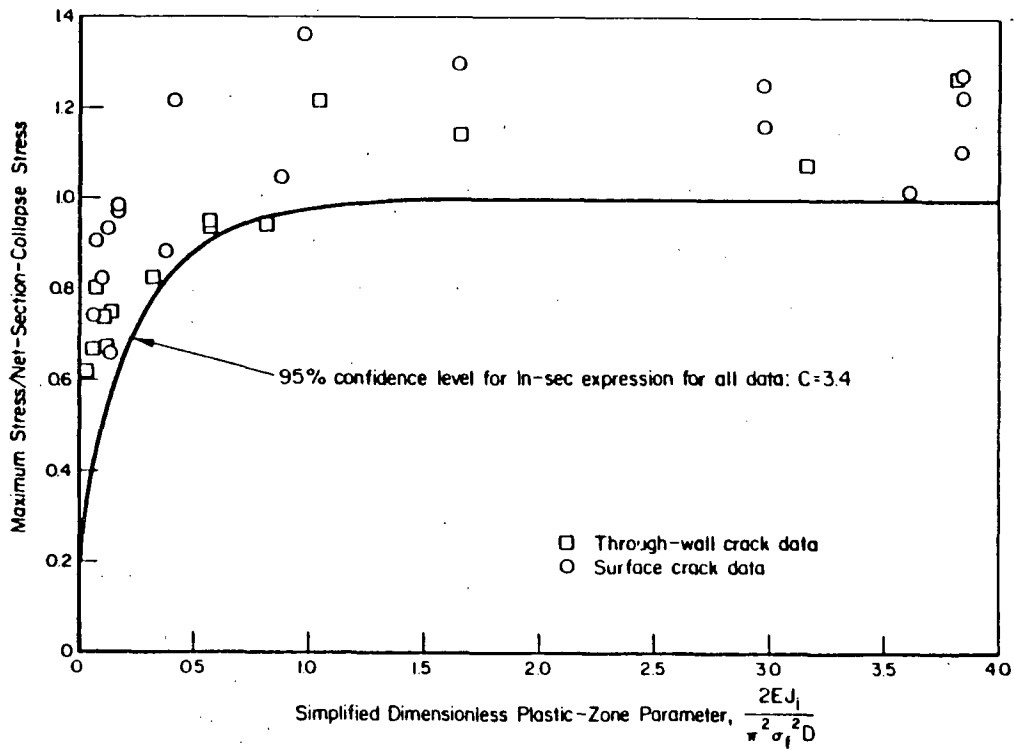


FIGURE 11. EMPIRICAL SCREENING CRITERIA DEVELOPED FROM THE FULL-SCALE PIPE FRACTURE EXPERIMENTS USING A DIMENSIONLESS PLASTIC-ZONE PARAMETER AND A FLOW STRESS VALUE =  $(\sigma_y + \sigma_u)/2$ .

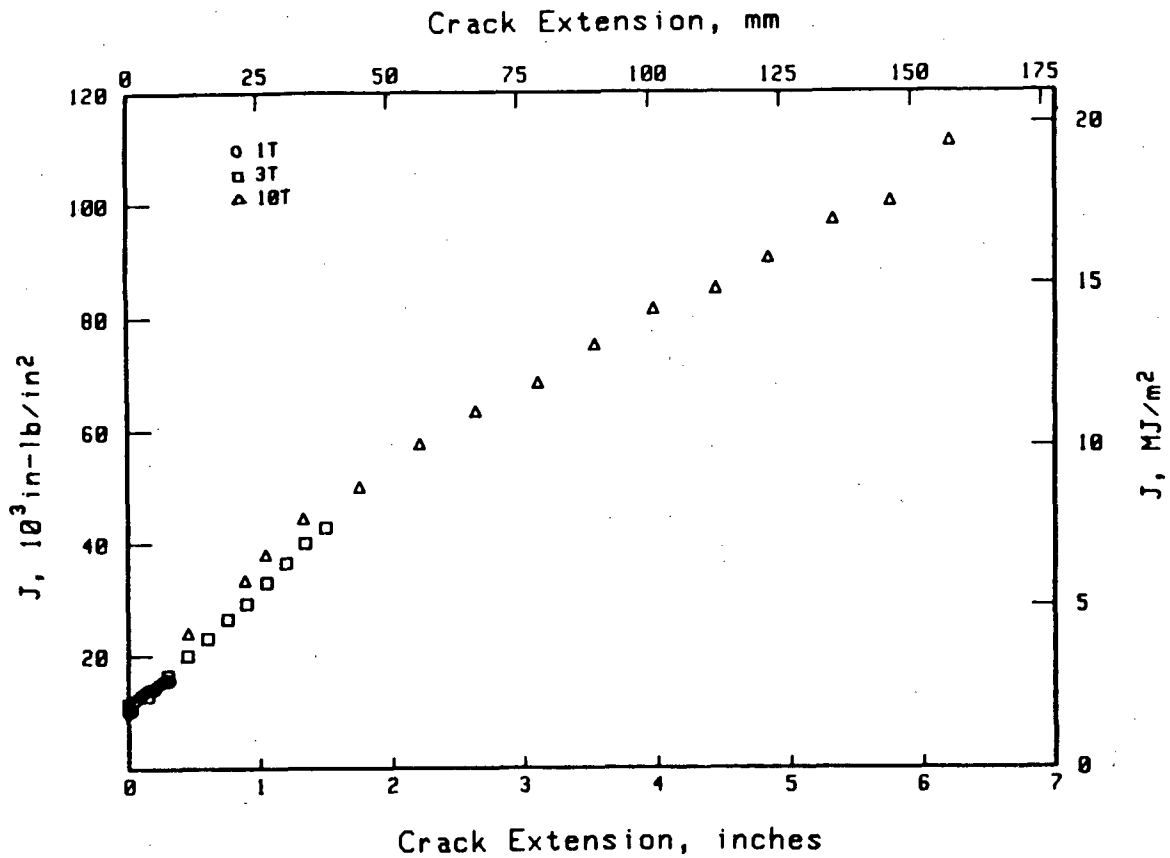


FIGURE 12. COMPARISON OF FAR-FIELD J-RESISTANCE CURVES FROM FINITE ELEMENT ANALYSIS FOR THE 1T, 3T, AND 10T NONSIDE-GROOVED TYPE 304 STAINLESS STEEL SPECIMENS AT 550 F (288 C)

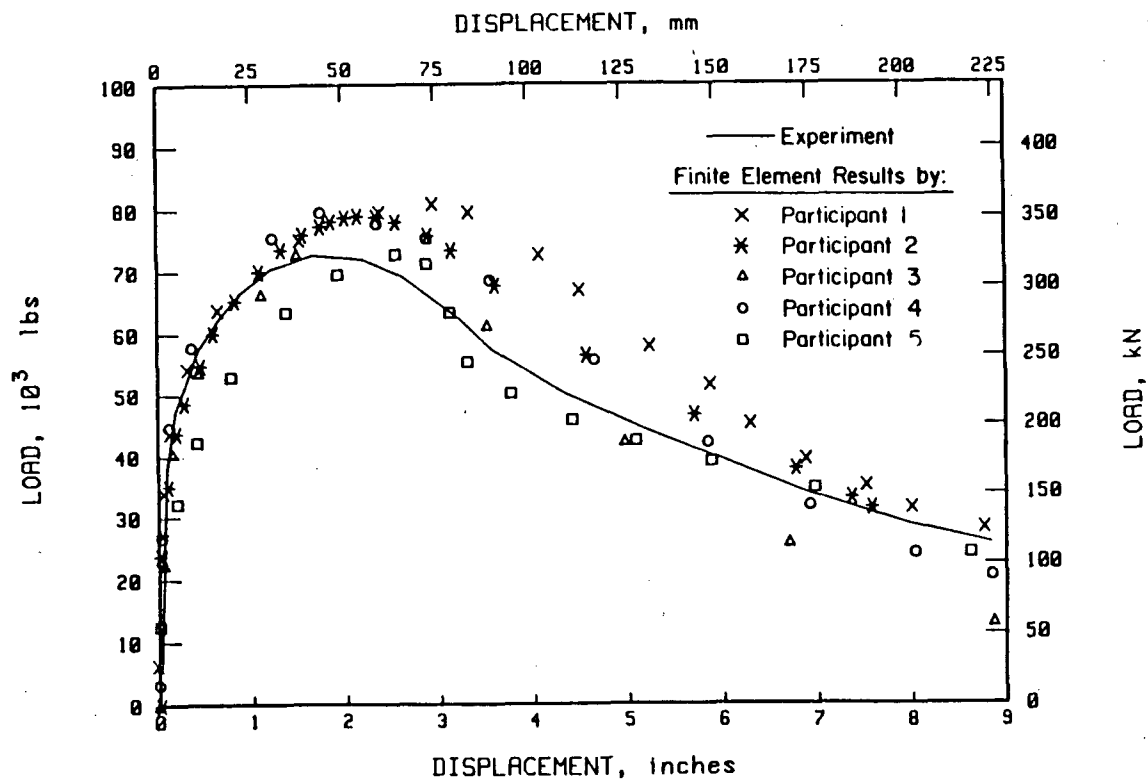


FIGURE 13. COMPARISON OF THE FINITE ELEMENT ANALYSIS RESULTS FOR THE C(T) SPECIMEN WITH EXPERIMENTAL DATA

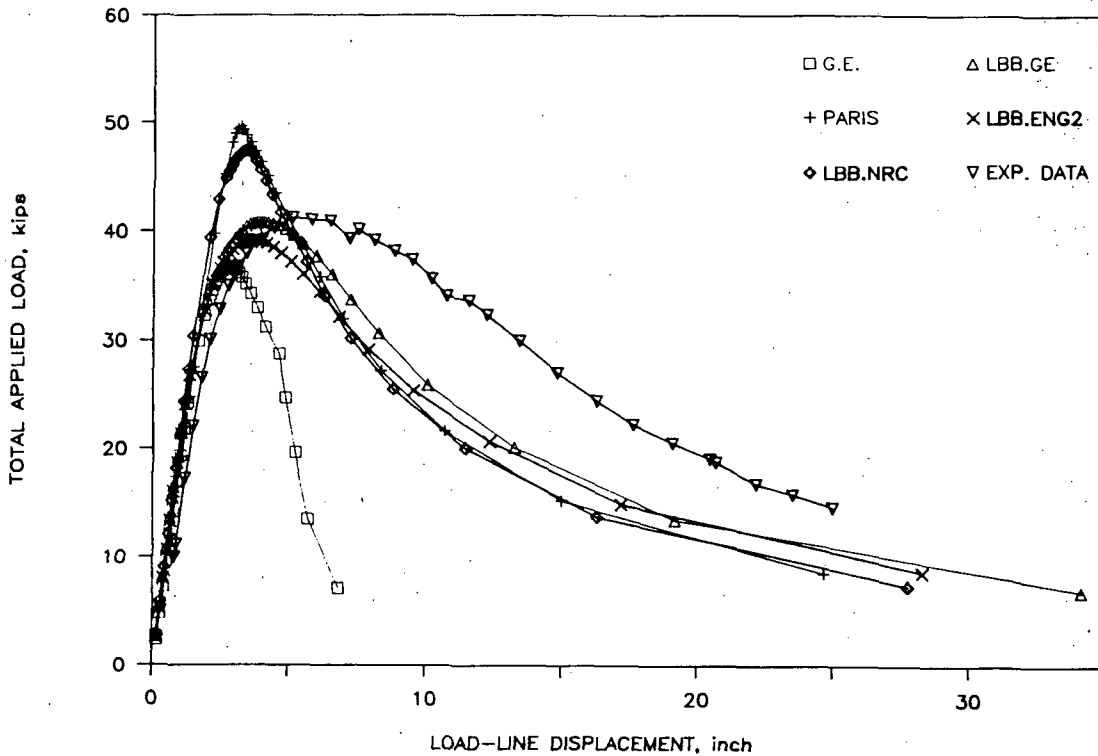


FIGURE 14. COMPARISONS OF PREDICTED LOAD-DISPLACEMENT CURVES USING POWER-LAW EXTRAPOLATION OF  $J_d$ -R CURVE TO EXPERIMENTAL RESULTS (16-INCH [406-MM] DIAMETER TP304 STAINLESS STEEL PIPE WITH TWC IN CENTER OF SAW)

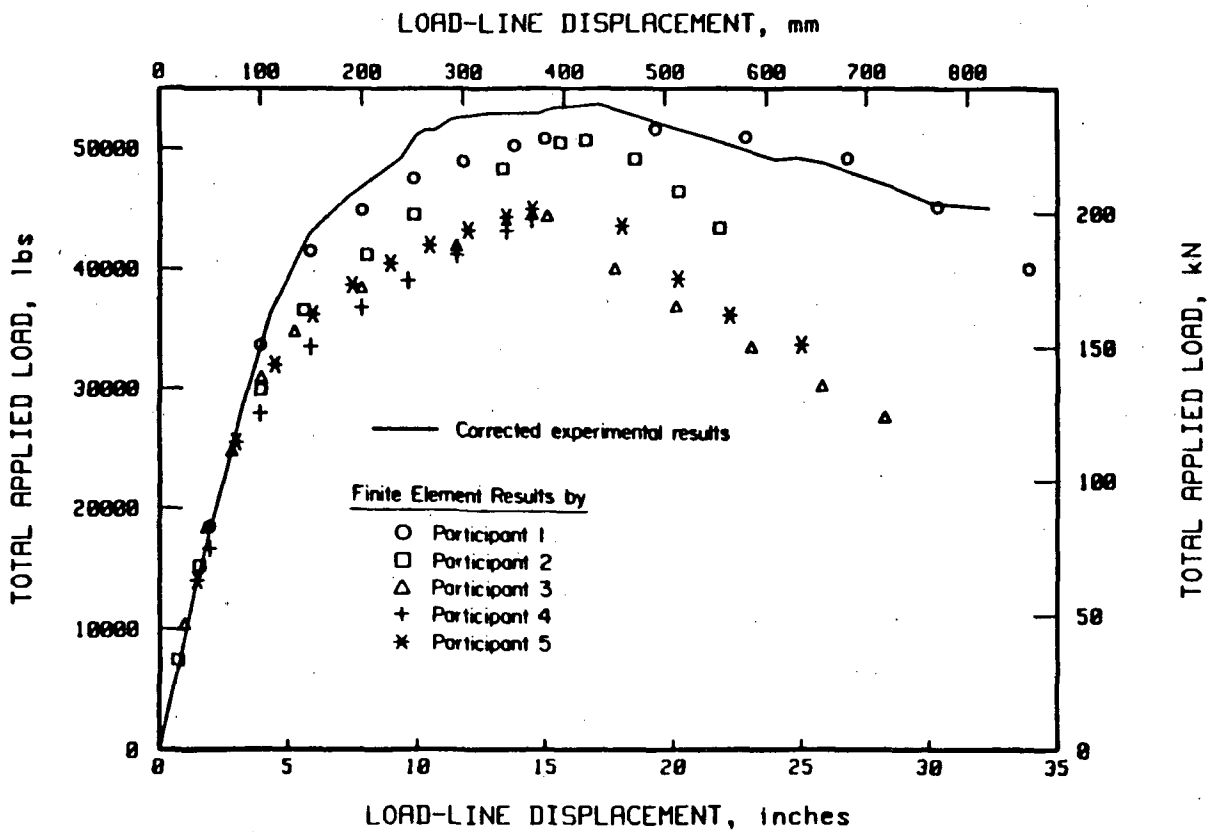


FIGURE 15. COMPARISON OF THE FINITE ELEMENT ANALYSIS RESULTS TO 16-INCH (406-MM) DIAMETER CIRCUMFERENTIALLY THROUGH-WALL CRACKED PIPE EXPERIMENTAL DATA

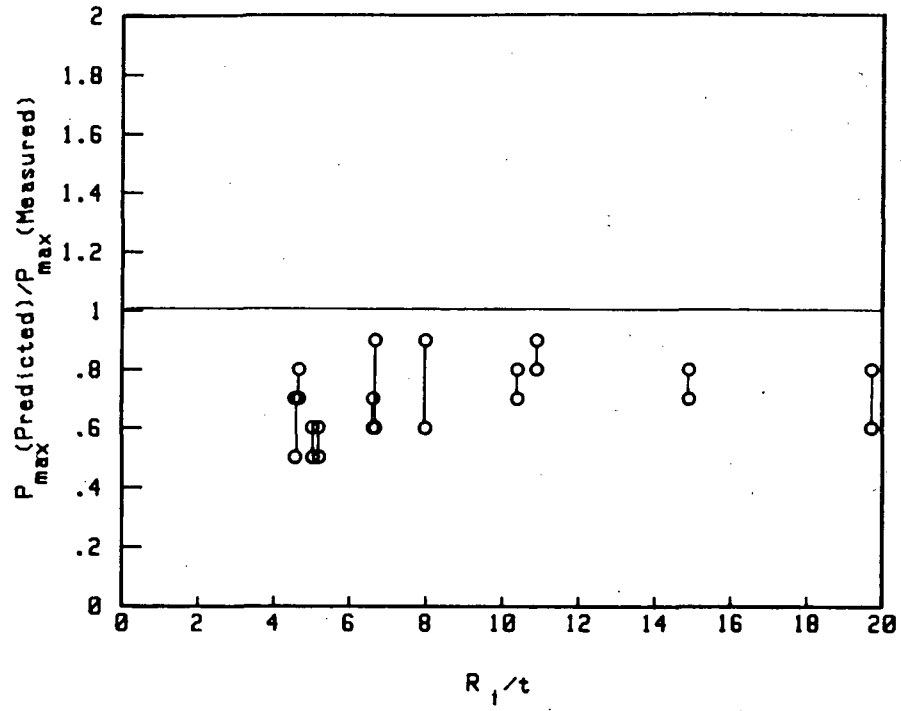


FIGURE 16. PREDICTION OF MAXIMUM LOAD BY THE SC.TKP METHOD FOR CIRCUMFERENTIAL SURFACE-CRACKED PIPE IN PURE BENDING

**BIBLIOGRAPHIC DATA SHEET**

SEE INSTRUCTIONS ON THE REVERSE

1. REPORT NUMBER (Assigned by PPMB: DPS, add Vol. No., if any)

NUREG/CP-0097  
Vol. 2

2. TITLE AND SUBTITLE

Proceedings of the Sixteenth Water Reactor Safety  
Information Meeting

3. LEAVE BLANK

4. DATE REPORT COMPLETED

MONTH YEAR

February 1989

6. DATE REPORT ISSUED

MONTH YEAR

March 1989

5. AUTHOR(S)

Compiled by Allen J. Weiss, BNL

7. PERFORMING ORGANIZATION NAME AND MAILING ADDRESS (Include Zip Code)

Office of Nuclear Regulatory Research  
U. S. Nuclear Regulatory Commission  
Washington, D. C. 20555

8. PROJECT/TASK/WORK UNIT NUMBER

9. FIN OR GRANT NUMBER

A-3282

10. SPONSORING ORGANIZATION NAME AND MAILING ADDRESS (Include Zip Code)

Same as Item 7 above

11a. TYPE OF REPORT

Proceedings of conference  
on safety research

b. PERIOD COVERED (Inclusive dates)

October 24-27, 1988

12. SUPPLEMENTARY NOTES

Proceedings prepared by Brookhaven National Laboratory

13. ABSTRACT (200 words or less)

This five-volume report contains 141 papers out of the 175 that were presented at the Sixteenth Water Reactor Safety Information Meeting held at the National Institute of Standards and Technology, Gaithersburg, Maryland, during the week of October 24-27, 1988. The papers are printed in the order of their presentation in each session and describe progress and results of programs in nuclear safety research conducted in this country and abroad. Foreign participation in the meeting included twenty different papers presented by researchers from Germany, Italy, Japan, Sweden, Switzerland, Taiwan and the United Kingdom. The titles of the papers and the names of the authors have been updated and may differ from those that appeared in the final program of the meeting.

14. DOCUMENT ANALYSIS - a. KEYWORDS/DESCRIPTORS

reactor safety research  
nuclear safety research  
decontamination and decommissioning

b. IDENTIFIERS/OPEN-ENDED TERMS

15. AVAILABILITY STATEMENT

Unlimited

16. SECURITY CLASSIFICATION

(This page)  
Unclassified

(This report)  
Unclassified

17. NUMBER OF PAGES

18. PRICE